TECHNISCHE UNIVERSITÄT MÜNCHEN

Professur für Mechanik auf Höchstleistungsrechnern

Computational modeling of patient-specific cardiac mechanics with model reduction-based parameter estimation and applications to novel heart assist technologies

Marc Hirschvogel

Vollständiger Abdruck der von der Fakultät für Maschinenwesen der Technischen Universität München zur Erlangung des akademischen Grades eines

Doktor-Ingenieurs (Dr.-Ing.)

genehmigten Dissertation.

Vorsitzender:	Prof. dr.ir. Daniel J. Rixen
Prüfer der Dissertation:	1. Prof. Dr.-Ing. Michael W. Gee
	2. Prof. Dr. David Nordsletten

Die Dissertation wurde am 11. Juni 2018 bei der Technischen Universität München eingereicht und durch die Fakultät für Maschinenwesen am 26. November 2018 angenommen.

Abstract

Cardiovascular disease entities are the most prevalent ones in the industrialized world, and therapies for patients suffering from heart failure are yet to be optimized or conclusively established. Due to the shortage in donor organs, heart transplantation as gold standard heart failure therapy fails to cover all needs, hence bridge-to-transplant or destination therapy vascular assist device (VAD) applications often are considered. Novel concepts of assist devices such as cardiac compression systems may promise better outcomes with reduced adverse event rates compared to current continuous-flow pumping technologies, but are yet to be established as VAD standard.
The present thesis deals with computational modeling of patient-specific mechanics of the heart and the vascular system, strategies for the efficient estimation of individual-specific parameters, and the assessment of novel extravascular assist devices for patients suffering from congestive heart failure from a computational mechanics modeling point of view.
The main and ultimate purpose of these in-silico models targets at investigating circumstances that are not or only hardly assessable in an experimental (in-vivo) setup, optimizing design variables of novel medical devices, and predicting their optimal operation point for the sake of the patient's benefit and quality of life. Ultimately, in-silico models may help to reduce the amount of animal experiments that are currently however inevitably required for the secure and reliable dimensioning of novel medical treatment strategies.

The heart is modeled as 3-dimensional (3D) anisotropic hyperelastic nonlinear solid with a fiber strain-dependent active stress approach to account for the cardiac contraction and the Frank-Starling mechanism (preload-dependent inotropy). Novel methods are developed to efficiently couple the finite element-discretized heart model to a closed-loop circulatory system 0-dimensional (0D) lumped-parameter model. A monolithic discretization and solution framework for the 3D-0D coupled problem is implemented that makes use of existing block preconditioning techniques to iteratively solve the linearized coupled system of equations on high-performance computing architectures in one monolithic Newton scheme. Different types of 0D vascular networks are implemented and combined with gas transport and dissociation models. The outcome is validated against standard physiological conditions, and reasonable results are obtained for varying ventricular pre- and afterload situations, changes in inotropy, and some exemplary disease events such as valve leakage or stenosis.
Furthermore, models for ventricular volumetric growth and remodeling (G&R) are implemented using variants of existing anisotropic volumetric growth laws, and a novel multiscale-in-time strategy is developed that allows to compute G&R phenomena for both volume and pressure overload conditions on a large time scale as consequence of an acute disease event happening on the small time scale. Long-term changes in pressure-volume relations are simulated for mitral valve regurgitation, aortic stenosis as well as myocardial infarction scenarios, and the results thereof are shown to comply with the typical syndromes and characteristics of systolic and diastolic heart failure. For the first time, an heuristic remodeling approach, hence a dependence of the tissue passive elastic (or active) properties on the volumetric growth stretch is introduced in the context of simulating ventricular growth, and reverse G&R phenomena are included in the analyses. Ultimately, these G&R models may help to predict the long-term development of myocardial disease progression and to evaluate the efficiency of medical treatment strategies against heart failure.

Methods for the computationally efficient and simultaneous estimation of homeostatic state conditions and key parameters like ventricular contractility, afterload and preload are developed. A novel multilevel strategy for the acceleration of a gradient-based optimization problem is implemented that makes use of low-fidelity surrogate modeling techniques to reduce the computational demand for optimizing the high-fidelity model. Different approaches such as coarse spatial (and temporal) discretizations, spatial dimensional reduction, as well as projection-based model order reduction are used to construct the surrogate models. For this purpose, model order reduction using proper orthogonal decomposition for the first time is implemented and applied to a monolithic 3D-0D coupled computational problem of the heart and the circulation, projecting the 3D heart governing equations to a lower dimensional subspace but maintaining the 0D circulation model as is.
Parameters are fitted to volume as well as time-resolved left ventricular pressure data gained from porcine in-vivo experiments for two different pharmacologically-induced heart failure scenarios, namely a low-afterload and a high-afterload heart failure case. The different types of surrogate models are compared with respect to their computational efficiency, and the calibrated states comply well with physiological expectations for these kinds of medications. The model order reduction surrogate thereby leads to the best performance with respect to the amount of iterations required on the high-fidelity model.

Last but not least, the models and methods are applied to simulating a novel extravascular cardiac augmentation device that is developed in close collaboration with an industrial partner. The novel implant relies on the concept of cardiac compression. The prototype consists of three inflatable thin-walled pads (pneumatic units) made out of polyurethan foil located inside and supported by a patient-specific shell (carrier unit) which is implanted beneath the pericardium. It operates by inflation of the pads exerting pulsatile pressure forces onto the epicardium, ECG-synchronized with the native cardiac function.
The experimental setup for the device is replicated in-silico, and simulations with gradually increasing ventricular augmentation pressures are performed. The in-silico results are in very good agreement with the experimental measurements: Increases in stroke volume and peak ventricular pressure are in the scatter range of the cohort of experiments, and qualitative deformation match well with the motion CT data set that had been recorded during the experiment. Furthermore, the in-silico models provide valuable insight into end-systolic wall stress and end-diastolic myofiber strain which are non-assessable quantities in an experimental setup. The results give a hint on how VADs may reduce driving forces that stimulate disease-related ventricular growth and remodeling, but are yet to be combined with the respective G&R approaches and still need experimental long-term studies to finally evaluate the VADs impact on reverse remodeling.
Finally, an optimization framework is introduced that allows to identify optimal design parameters of the implant for a given objective function, and the optimal placement of the left ventricular augmentation pads in order to maximize ventricular stroke work at given augmentation pressures is found.

Zusammenfassung

Erkrankungen des Herz-Kreislauf-Systems gehören zu den häufigsten in der modernen Welt, und Therapien für Herzinsuffizienzpatienten weisen noch immer Optimierungspotential auf oder sind noch nicht in letzter Konsequenz etabliert. Aufgrund der anhaltend geringen Verfügbarkeit von Spenderorganen kann die Herztransplantation als Goldstandard zur Behandlung von Herzinsuffizienz nicht alle Bedarfe decken, weshalb Herzunterstützungssysteme (engl. “vascular assist device”, VAD) zur Überbrückungs- oder Dauertherapie weiterhin eingesetzt werden. Neuartige Konzepte von Unterstützungssystemen wie ventrikuläre Kompressionsimplantate könnten bessere Behandlungsergebnisse mit reduzierten Komplikationsraten liefern als gegenwärtig eingesetzte kontinuierliche Flusspumpen, haben sich aber noch nicht als VAD-Standard etabliert.
Die vorliegende Arbeit behandelt die computergestützte patienten-spezifische Modellierung der Mechanik des Herzens und des Blutkreislaufs, Strategien zur effizienten individuellen Parameterschätzung, sowie die Beurteilung neuartiger extravaskulärer Herzunterstützungssysteme aus Sicht der computergestützten mechanischen Modellbildung.
Der primäre und schlussendliche Zweck dieser In-silico-Modelle zielt darauf ab, Gegebenheiten zu analysieren, die in einem experimentellen (In-vivo-)Umfeld kaum oder gar nicht untersucht werden können. Darüber hinaus können Design-Variablen neuer medizinischer Apparate optimiert und deren optimale Betriebsbedingungen zugunsten des Patienten und seiner Lebensqualität vorhergesagt werden. Letztendlich könnten In-silico-Modelle dabei helfen, die Anzahl der Tierversuche, die gegenwärtig unabdingbar zur sicheren und verlässlichen Auslegung neuartiger medizinischer Therapien gebraucht werden, zu reduzieren.

Das Herz wird als 3-dimensionaler (3D) anisotroper hyperelastischer nichtlinearer Festkörper mit einem von der Faserdehnung abhängigen aktiven Spannungsansatz modelliert, um Muskelkontraktion und den Frank-Starling-Mechanismus (vorlastabhängige Inotropie) abzubilden. Neuartige Ansätze werden entwickelt, um das mit finiten Elementen diskretisierte Herz effizient an ein 0-dimensionales (0D) geschlossenes Kreislaufmodell bestehend aus konzentrierten Elementen zu koppeln. Eine Umgebung zur monolithischen Diskretisierung und Lösung des 3D-0D-gekoppelten Problems wird implementiert, die von existierenden Block-Vorkonditionierungsmethoden Gebrauch macht, um das linearisierte gekoppelte Gleichungssystem in einem einzigen monolithischen Newton-Verfahren iterativ auf Höchstleistungsrechensystemen zu lösen.
Verschiedene 0D-Kreislaufansätze werden implementiert und mit Gastransport und -dissoziationsmodellen kombiniert. Die Ergebnisse werden mit physiologischen Bedingungen abgeglichen, und realistische Resultate für verschiedene Zustände ventrikulärer Vor- und Nachlast, Änderungen der Inotropie, und einigen beispielhaften Krankheitsbildern wie Herzklappeninsuffizienzen oder -stenosen werden erhalten.
Darüber hinaus werden Modelle für ventrikuläres Wachstum und Remodellierung (engl. “growth and remodeling”, G&R) unter Verwendung von Varianten bestehender anisotroper volumetrischer Wachstumsgesetze implementiert, und eine neuartige Mehrskalenstrategie wird entwickelt, die es erlaubt, G&R-Phänomene sowohl für Volumen- als auch Drucküberlastszenarien auf einer großen Zeitskala als Konsequenz einer akuten Erkrankung auf der kleinen Zeitskala zu simulieren. Langzeiteffekte auf die hämodynamischen Druck-Volumen-Kurven im Ventrikel werden für verschiedene Krankheitsbilder wie Mitralklappeninsuffizienz, Aortenklappenstenose oder Myokardinfarkt simuliert, und die Ergebnisse sind in guter Übereinstimmung mit typischen Syndromen

und Charakteristiken systolischer und diastolischer Herzinsuffizienz. Zum ersten Mal wurde ein heuristischer Remodellierungsansatz, d.h. eine Abhängigkeit der elastischen passiven (oder aktiven) Gewebeeigenschaften von der volumetrischen Wachstumsdehnung eingeführt im Zusammenhang mit der Simulation von ventrikulärem Wachstum, und reversible G&R-Phänomene werden in die Analysen miteinbezogen. Schlussendlich könnten diese G&R-Modelle Aufschluss über die Langzeitentwicklung myokardialer Krankheitsbilder geben und die Effizient medizinischer Therapien gegen Herzinsuffizienz bewerten.

Methoden für die rechnerisch effiziente und zeitgleiche Schätzung von homöostatischen Bedingungen und Schlüsselparametern wie ventrikuläre Kontraktilität, Nachlast sowie Vorlast werden entwickelt. Eine neuartige Mehrlevel-Strategie zur Beschleunigung eines gradienten-basierten Optimierungsproblems wird implementiert, die den Rechenaufwand zur Optimierung eines fein aufgelösten Modells hoher Güte mithilfe vergröberter Surrogat-Modelle geringer Güte reduziert. Verschiedene Reduktionsansätze wie vergröberte räumliche (und zeitliche) Diskretisierung, räumliche Dimensionsreduktion, sowie projektionsbasierte Modellreduktionsstrategien ("Model Order Reduction") werden verwendet, um Surrogat-Modelle zu generieren. Zu diesem Zweck wurden erstmalig Modellreduktionsansätze unter Zuhilfenahme von Singulärwertzerlegungen ("Proper Orthogonal Decomposition") für ein 3D-0D monolithisch gekoppeltes Herz-Kreislauf-Problem implementiert und angewandt, indem die das 3D-Herz beschreibenden Gleichungen in einen niedriger dimensionalen Unterraum projiziert werden, das 0D-Modell hingegen unverändert bleibt.
Parameter werden an linksventrikuläre Volumen- als auch zeitlich aufgelöste Druck-Daten aus In-vivo-Tierversuchen am Schwein kalibriert, jeweils zu zwei verschiedenen pharmakologisch induzierten Herzinsuffizienzszenarien: ein Szenario mit geringer und eines mit erhöhter Nachlast. Die verschiedenartigen Surrogat-Modelle werden bezüglich ihrer rechnerischen Effizienz verglichen, und die kalibrierten Zustände sind in Einklang mit physiologischen Erwartungen bei diesen Medikationen. Das auf Modellreduktion basierende Surrogat-Modell verhält sich am besten in Bezug auf die Anzahl der benötigten Iterationen auf dem fein aufgelösten Modell hoher Güte.

Schlussendlich werden die Modelle und Methoden angewandt auf die Simulation eines neuartigen extravaskulären Herzunterstützungssystems, das in enger Kooperation mit einem industriellen Partner entwickelt wird. Das neue Implantat beruht auf dem Konzept der ventrikulären Kompression. Der Prototyp besteht aus drei aufblasbaren dünnwandigen Kissen (pneumatischen Einheiten) aus Polyurethan-Folie, die in einer unter das Perikardium implantierbaren die Ventrikel umfassenden patienten-spezifisch gestalteten Schale (Trägereinheit) angeordnet sind und von dieser gehalten werden. Die Kissen werden inflatiert und üben pulsatilen Druck auf das Epikardium aus, EKG-synchronisiert mit der ursprünglichen Herzfunktion.
Das experimentelle Szenario für das Implantat wird in-silico repliziert, und Simulationen mit stufenweise erhöhtem ventrikulären Augmentationsdruck in den Kissen werden durchgeführt. Die In-silico-Ergebnisse sind dabei in sehr gutem Einklang mit den experimentellen Messungen: Erhöhungen des Schlagvolumens und des maximal generierten Ventrikeldrucks liegen in der Streubreite der Kohorte an experimentellen Messungen, und eine gute qualitative Übereinstimmung der Deformation des Herzens mit den CT-Daten, die während des Experiments aufgezeichnet wurden, wird gezeigt. Darüber hinaus erlauben die Modelldaten einen wertvollen Einblick in

end-systolische Wandspannungen und end-diastolische Dehnungen der Herzmuskelfasern, die durch Experimente alleine nicht gezeigt werden können. Die Modelle liefern einen Anhaltspunkt, wie ventrikuläre Unterstützungssysteme Triebkräfte für krankheitsbezogenes Wachstum und Remodellierung reduzieren könnten, müssen aber noch mit den entsprechenden G&R-Ansätzen kombiniert und durch experimentelle Langzeitstudien abgesichert werden, um Effekte der Umkehr der Remodellierung (engl. “reverse remodeling”) zu bestätigen.
Zu guter Letzt wird eine Optimierungsumgebung eingeführt, die es erlaubt, optimale das Implantat beschreibende Parameter für eine gegebene Zielfunktion zu identifizieren, und die ideale Positionierung der linksventrikulären Augmentationskissen zur Maximierung der Schlagarbeit des Ventrikels bei gegebenem Augmentationsdruck wird ermittelt.

Danksagung

Die vorliegende Arbeit entstand während meiner Tätigkeit als wissenschaftlicher Mitarbeiter am Fachgebiet Mechanik auf Höchstleistungsrechnern der Technischen Universität München (TUM) zwischen den Jahren 2012 und 2018. Die Zeit dort war für mich von unschätzbarem Wert und hat meinen fachlichen aber auch persönlichen Horizont extrem erweitert. Deshalb möchte ich diesen Abschnitt nutzen, um mich bei allen Personen, die mich während dieser Zeit begleitet haben, zu bedanken.

Allen voran möchte ich mich natürlich bei meinem Doktorvater, Prof. Dr. Michael Gee, für die Möglichkeit der Anfertigung dieser Arbeit und den mir gewährten Freiraum in der Ausgestaltung und Schwerpunktsetzung der Themen bedanken. Ich bin dankbar für das mir entgegengebrachte Vertrauen, für seine ständige Ansprechbarkeit und Verfügbarkeit sowie seine stets offene und hilfsbereite Art, die mir immer wieder neue Denkanstöße und Motivationsschübe für die Arbeit brachte. Ferner danke ich Prof. Dr. David Nordsletten vom King's College London bzw. der University of Michigan für die Übernahme des Mitberichts sowie Prof. Dr. Daniel Rixen für den Vorsitz der Prüfungskommission.

Ein weiterer Dank gilt dem industriellen Kooperationspartner, Prof. Dr. Stephen Wildhirt von der Firma AdjuCor® GmbH, ohne den es das Thema zu dieser Arbeit nicht gegeben hätte. Sein stets offenes Ohr, die Möglichkeit, medizinische Informationen zum Herzen und zur Herzinsuffizienz jederzeit aus erster Hand zu erhalten, und seine Bereitschaft, sich auch als Mediziner intensiv mit technischen Fragestellungen auseinanderzusetzen sind meiner Arbeit wesentlich zugutegekommen. In diesem Kontext möchte ich mich auch bei anderen Mitarbeitern der Firma AdjuCor bedanken, insbesondere Dr. Andreas Maier, der mir nicht nur schon zu Zeiten meiner Studienarbeit, sondern auch noch während der Promotion immer wieder kompetent mit Rat und Tat zur Seite stand.

Meinen ehemaligen Kollegen am Fachgebiet Mechanik auf Höchstleistungsrechnern danke ich für stets spannende fachliche und außerfachliche Diskussionen, entstandene Freundschaften, gemeinsame Urlaube, und manchen für die Bereitschaft, sich einem Tauchkurs bei mir zu unterziehen. Besonders bedanke ich mich bei meinem Bürokollegen Dr. Moritz Thon für manch lehrreichen Perspektivwechsel, dass Mathematiker ab und zu vielleicht doch die besseren Ingenieure sind, bei Marina Bassilious für das Vertrauen, als Studentin gleich zwei Studienarbeiten bei mir geschrieben zu haben, bei André Hemmler, der mir steter Leidensgenosse in Thematiken zu Kontakt- und Meshtying-Algorithmen war, sowie bei Alexander Schein für das Korrekturlesen des Kapitels zur Kontinuumsmechanik. Auch danke ich Dr. Lasse Jagschies, der als Pendant zu mir im Kooperationsprojekt für die Implantatsentwicklung zuständig war und stets wertvollen Input auch zu meiner Arbeit lieferte.

Ebenso möchte ich mich bei den ehemaligen Kollegen des Lehrstuhls für Numerische Mechanik bedanken, in dessen Räumlichkeiten ich das erste Jahr meiner Promotion zubringen durfte. Die stets entspannte und angenehme Arbeitsatmosphäre dort haben auch zum Erfolg meiner Arbeit beigetragen. Insbesondere danke ich Rui Fang, Andy Wirtz, Martin Pfaller sowie Dhrubajyoti Mukherjee, zu denen mich eine tiefe Freundschaft verbindet. Rui Fang danke ich besonders für die unzähligen Abende des gemeinsamen Musikproduzierens, und Andy Wirtz für die gemeinsame Bürozeit im ersten Jahr sowie seine stets unternehmensfreudige und motivierende Art.

Auch meinen Studenten danke ich für ihre geleistete Arbeit und den Beitrag, den sie durch ihre Studien- oder Abschlussarbeiten zum Erfolg meiner Arbeit beigetragen haben.

Annette Becker danke ich für die schöne gemeinsame Zeit zum Ende meiner Promotion und darüber hinaus sowie für ihre liebevolle Unterstützung in allen Lebenslagen. Dr. Anna Kirchhofer danke ich für das Korrekturlesen des medizinischen Einleitungsteils. Allen meinen weiteren Freunden sei gedankt für die immer schönen und ereignisreichen Erlebnisse, die ich mit euch verbringen durfte.
Darüber hinaus möchte ich mich auch bei Armin Maudrich und Walter Pischel bedanken, die durch ihr Engagement in der Frank Hirschvogel Stiftung aber auch in vielen anderen Gesellschafterthemen der Hirschvogel Automotive Group stets verlässliche und vertrauensvolle Ratgeber sind.
An dieser Stelle möchte ich mich auch bei meinen Eltern und meinem Bruder bedanken, ohne die ich niemals der Mensch geworden wäre, der ich jetzt bin. Auch wenn ihr nicht mehr physisch präsent seid, so trage ich euch immer in meinen Gedanken und meinem Herzen bei mir.
Meiner lieben Tante Lareine Kennedy und meinen Onkel Kevin und Stephen Kennedy danke ich für ihre immer offene und herzliche Art und die Gewissheit, jederzeit bei ihnen willkommen zu sein.
Schlussendlich danke ich Georg Dersch, der meiner Mutter bis zuletzt ein toller Partner war und mir in vielen Bereichen mit Rat und Tat zur Seite steht, sowie Claudia Drescher, die für einen Großteil meiner Promotionszeit als liebevolle Freundin an meiner Seite war.

München, im Dezember 2018 Marc Hirschvogel

Contents

Nomenclature

Representation of scalars, tensors and other quantities

q, Q	Scalar quantity
$\boldsymbol{q}, \boldsymbol{Q}$	Vector or 2nd order tensor quantity
$\boldsymbol{\mathcal{Q}}$	3rd order tensor quantity
$\mathbb{Q}$	4th order tensor quantity
$\mathbf{q}$	Discrete vector quantity
$\mathbf{Q}$	Discrete matrix quantity
$Q_{ij}q_j$	Exemplary tensor-vector product in coordinates: Einstein summation convention over indices that appear twice: $\sum_j Q_{ij}q_j$

Abbreviations

0D	Zero-dimensional
3D	Three-dimensional
AI	Apical infarction
ALE	Arbitrary Lagrangian-Eulerian
AS	Aortic stenosis
AVP	Atrioventricular plane
BiVAD	Biventricular assist device
CAD	Computer-aided design
CHF	Congestive heart failure
CT	Computed tomography
D-PVR	Diastatic pressure-volume relationship
DCM	Dilated cardiomyopathy
EAS	Enhanced assumed strain
ECG	Electrocardiogram
EDPVR	End-diastolic pressure-volume relationship
ESPVR	End-systolic pressure-volume relationship
FAS	Full approximation scheme
FEM	Finite element method
G&R	Growth and remodeling
GMRES	Generalized minimal residual method
HCM	Hypertrophic cardiomyopathy
HDM	High-dimensional model
HPC	High-performance computing
HF	Heart failure

KKT	Karush-Kuhn-Tucker
LU	Lower-upper (decomposition)
LV	Left ventricle
LVAD	Left ventricular assist device
MR	Mitral regurgitation
MRI	Magnetic resonance imaging
MULF	Modified Updated Lagrangian Formulation
POD	Proper orthogonal decomposition
PTC	Pseudo-transient continuation
RDM	Reduced-dimensional model
ROB	Reduced-order basis
ROM	Reduced-order model
RV	Right ventricle
RVAD	Right ventricular assist device
SIMPLE	Semi-Implicit Method for Pressure-Linked Equations
std	Standard
STL	Stereolithography, stereolithographic
TAH	Total artificial heart
VAD	Ventricular, or vascular assist device

Model, algorithm, or results abbreviations

0Dsyspul	Basic zero-dimensional systemic and pulmonary circulation model
0Dsyspulcap	Extended zero-dimensional systemic and pulmonary circulation model with capillaries
0Dsyspulcaprespir	Zero-dimensional systemic and pulmonary circulation, respiratory and gas transport model
2Dventr	Two-dimensional plane strain ventricular heart model
3Dventr	Three-dimensional ventricular heart model
3Datrioventr	Three-dimensional atrioventricular heart model
C	(Coarse) reduced-dimensional heart model based on coarse meshing
FAS-lsq	Full approximation scheme least-squares algorithm
HA-HF	High-afterload heart failure
hex8_h	8-node trilinear displacement-based hexahedral finite elements, with an (average) edge length of h $[\mathrm{mm}]$
LA-HF	Low-afterload heart failure
noremod	Without remodeling
p1, *p2*, *p3*	Pig number 1, 2, 3
PrescrHeart	Prescribed-dynamics heart model
R	Reduced-dimensional heart model based on model order reduction
remod_act	With remodeling relating to active material
remod_pas	With remodeling relating to passive material

ROM-ml	Reduced-order multilevel algorithm
S	(Surrogate) reduced-dimensional heart model based on plane strain and symmetry
tet4_h	4-node linear displacement-based tetrahedral finite elements, with an (average) edge length of h $[\mathrm{mm}]$
tet10_h	10-node quadratic displacement-based tetrahedral finite elements, with an (average) edge length of h $[\mathrm{mm}]$
VAD2013p	Model of prototype version of ventricular assist device (year 2013)
VADgen	Generalized ventricular assist device model
$\boxed{\mathrm{BL}}$	Baseline
$\boxed{\mathrm{A1}}$, $\boxed{\mathrm{A2}}$, $\boxed{\mathrm{A3}}$, $\boxed{\mathrm{A4}}$	Augmentation scenarios

Operators and symbols

$(\cdot)^{\mathrm{T}}$	Transpose of a tensor, or of a discrete vector/matrix
$(\cdot)^{-1}$	Inverse of a tensor or mapping, or of a discrete matrix
$(\cdot)^{-\mathrm{T}}$	Transpose of the inverse of a tensor, or of a discrete matrix
$\dot{(\cdot)}, \ddot{(\cdot)}$	First and second time derivative
$\hat{(\cdot)}$	Prescribed, or volume-averaged quantity
$\tilde{(\cdot)}$	Modified, or measured quantity
$\varnothing$	Average
$\varnothing(\cdot)$	Average of a quantity
$\lvert(\cdot)\rvert$	Absolute value
$\lvert(\cdot)\rvert_+, \lvert(\cdot)\rvert_-$	Positive, negative branch of a function
$\lvert\lvert(\cdot)\rvert\rvert_2$	2-norm of a vector
$\lvert\lvert(\cdot)\rvert\rvert_\infty$	Infinity norm of a vector
$\mathrm{d}(\cdot)$	Infinitesimal quantity
$\delta(\cdot)$	Virtual, or finitely perturbed quantity
$\Delta(\cdot)$	Increment, or (absolute) change of a quantity
$\det$	Determinant
diag	Diagonal matrix operator
rank	Rank of a matrix
Lin	Linearization operator
tr	Trance operator
$\mathbb{R}$	Space of real numbers
$\mathbb{I}_{(\cdot)}$	Indicator function (1, if $(\cdot)$ is true, 0 otherwise)
$\boldsymbol{\nabla}_0$	Nabla operator with respect to the reference (material) configuration
$\boldsymbol{\nabla}$	Nabla operator with respect to the current (spatial) configuration
$\mathcal{L}$	Laplace transform operator
i	Imaginary unit
$\otimes, \underline{\otimes}, \overline{\otimes}$	Dyadic products
δ_{ij}	Kronecker delta

$\mathcal{H}$	Heaviside function
$\frac{\mathrm{d}}{\mathrm{d}(\cdot)}, \frac{\partial}{\partial(\cdot)}$	First total, partial derivative with respect to $(\cdot)$
$\frac{\mathrm{d}^2}{\mathrm{d}(\cdot)^2}, \frac{\partial^2}{\partial(\cdot)^2}$	Second total, partial derivative with respect to $(\cdot)$
$\boldsymbol{\mathcal{E}}, \mathcal{E}_{ijk}$	Levi-Civita permutation tensor, and its coordinates
$\mathbf{0}$	Zero vector or zero 2nd order tensor
$\mathbf{1}$	2nd order identity tensor
$\mathbb{1}, \bar{\mathbb{1}}, \bar{\bar{\mathbb{1}}}$; $\mathbb{1}_{ijkl}, \bar{\mathbb{1}}_{ijkl}, \bar{\bar{\mathbb{1}}}_{ijkl}$	4th order identity, transposer, and trace tensor; and their coordinates
$\mathbf{0}$	Discrete zero vector or matrix
$\mathbf{1}$	Discrete identity matrix
$\mathcal{I}(t)$	Set of initial conditions (at time t)
$\mathcal{I}^\star$	Set of homeostatic state initial conditions

Heart funtion parameters and timings

CO	Cardiac output
SV	Stroke volume
$\mathrm{SV}_{\mathrm{net}}$	Net stroke volume
SW	Stroke work
EDV	End-diastolic volume
ESV	End-systolic volume
EDP	End-diastolic pressure
ESP	End-systolic pressure
PVP	Peak ventricular pressure
EF	Ejection fraction
$\mathrm{EF}_{\mathrm{net}}$	Net ejection fraction
RF	Regurgitant fraction
HR	Heart rate
T_{cycl}	Cardiac cycle time
t_{ed}	End-diastolic time
t_{es}	End-systolic time
t	Time variable
T	Total time for computation
t_0	Initial time for transient computations
N	Cardiac cycle
$\tilde{N}$	"Pseudo" cardiac cycle (updated initial conditions, but starting from t_0)
$N^\star$	Homeostatic cardiac cycle
$t_N, t_{N^\star}$	Start time of cardiac cycle N, homeostatic cardiac cycle $N^\star$
$\Delta t_{\mathrm{at,act}}$	Duration of atrial activation
t_{wall}	Wall time for computation
t_{CPU}	Net CPU time
T_{breath}	Time period of one breath
t_{sampl}	Sample rate of conductance catheter

Superscripts and subscripts (if multiple apply, separation by comma)

$(\cdot)_{\mathrm{min}}, (\cdot)^{\mathrm{min}}$	Minimum
$(\cdot)_{\mathrm{max}}, (\cdot)^{\mathrm{max}}$	Maximum
$(\cdot)^{\mathrm{lo}}, (\cdot)^{\mathrm{hi}}$	Lower, higher
$(\cdot)^{\mathrm{thres}}$	Threshold
$(\cdot)_{\mathrm{e}}$	Epicardium
$(\cdot)_{\mathrm{b}}$	Heart base
$(\cdot)_{\mathrm{b}^{\perp}}$	Direction perpendicular to heart base
$(\cdot)^{\mathrm{lid}}$	Lids
$(\cdot)^{\mathrm{remod}}$	Remodeled material
$(\cdot)^{\ell}$	Related to left heart (ventricle, atrium)
$(\cdot)^{r}$	Related to right heart (ventricle, atrium), or right ventricular location
$(\cdot)^{\ell_{\mathrm{a}}}$	Anterior left ventricular location
$(\cdot)^{\ell_{\mathrm{p}}}$	Posterior left ventricular location
$(\cdot)^{\mathrm{sys}}$	Systemic
$(\cdot)^{\mathrm{pul}}$	Pulmonary
$(\cdot)_{\mathrm{v}}$	Ventricular
$(\cdot)_{\mathrm{in}}, (\cdot)_{\mathrm{out}}$	In, out
$(\cdot)_{\mathrm{at}}$	Atrial
$(\cdot)_{\mathrm{ar}}$	Arterial
$(\cdot)_{\mathrm{ven}}$	Venous
$(\cdot)_{\mathrm{peri}}$	Peripheral
$(\cdot)_{\mathrm{spl}}$	Splanchnic
$(\cdot)_{\mathrm{espl}}$	Extra-splanchnic
$(\cdot)_{\mathrm{msc}}$	Muscular
$(\cdot)_{\mathrm{cer}}$	Cerebral
$(\cdot)_{\mathrm{cor}}$	Coronary
$(\cdot)_{\mathrm{cap}}$	Capillary
$(\cdot)_{\mathrm{alv}}$	Alveolar
$(\cdot)_{\mathrm{airw}}$	Related to airways
$(\cdot)_{\mathrm{ext}}$	External
$(\cdot)_{\mathrm{u}}$	Unstressed
$(\cdot)^{\mathrm{suc}}$	Suction
$(\cdot)^{[\mathrm{H}]}$	Heart
$(\cdot)^{[\mathrm{P}]}, (\cdot)_{\mathrm{P}}$	Pads
$(\cdot)^{[\mathrm{S}]}, (\cdot)_{\mathrm{S}}$	Shell

Kinematics

$\boldsymbol{x}_0, x_{0,i}$	Position in reference (material) configuration, and its coordinates
$\boldsymbol{x}, x_i$	Position in current (spatial) configuration, and its coordinates

$\hat{\boldsymbol{e}}_{0,1}, \hat{\boldsymbol{e}}_{0,2}, \hat{\boldsymbol{e}}_{0,3}$	Basis vectors of Cartesian coordinate system in reference (material) configuration
$\hat{\boldsymbol{e}}_1, \hat{\boldsymbol{e}}_2, \hat{\boldsymbol{e}}_3$	Basis vectors of Cartesian coordinate system in current (spatial) configuration
$\boldsymbol{\chi}$	Mapping between reference (material) and current (spatial) configuration
$\boldsymbol{u}$	Displacement
$\boldsymbol{v}$	Velocity
$\boldsymbol{a}$	Acceleration
$\boldsymbol{F}, F_{ij}$	Deformation gradient, and its coordinates
J	Determinant of deformation gradient
$\boldsymbol{C}, C_{ij}$	Right Cauchy-Green deformation tensor, and its coordinates
$\boldsymbol{B}, B_{ij}$	Left Cauchy-Green deformation tensor, and its coordinates
$\boldsymbol{U}$	Right stretch tensor
$\boldsymbol{V}$	Left stretch tensor
$\boldsymbol{Q}$	Proper orthogonal rotation tensor
$\boldsymbol{E}$	Green-Lagrange strain tensor
$\boldsymbol{e}$	Euler-Almansi strain tensor
$\boldsymbol{\gamma}$	Symmetric part of spatial velocity gradient
λ	(Uniaxial) stretch
$\lambda_1 \geq \lambda_2 \geq \lambda_3$	Principal stretches (eigenvalues) of right (left) stretch tensor
λ_{myo}	Myofiber stretch
$I_C, I\!I_C, I\!I\!I_C$	Principal invariants of right (left) Cauchy-Green deformation tensor
$\bar{I}_C, \bar{I\!I}_C, \bar{I\!I\!I}_C$	Modified (isochoric) principal invariants of right (left) Cauchy-Green deformation tensor
$\boldsymbol{n}_0$	Unit outward normal in reference (material) configuration
$\mathrm{d}\boldsymbol{A} = \mathrm{d}A\boldsymbol{n}_0$	Infinitesimal surface element in reference (material) configuration
$\boldsymbol{n}$	Unit outward normal in current (spatial) configuration
$\mathrm{d}\boldsymbol{a} = \mathrm{d}a\boldsymbol{n}$	Infinitesimal surface element in current (spatial) configuration
$\boldsymbol{f}_0, \boldsymbol{s}_0$	Fiber directions in reference (material) configuration
$I\!V_f \equiv I\!V$	First anisotropic invariant relating to first fiber
$I\!V_s \equiv V\!I$	First anisotropic invariant relating to second fiber
$V_f \equiv V$	Second anisotropic invariant relating to first fiber
$V_s \equiv V\!I\!I$	Second anisotropic invariant relating to second fiber
$V\!I\!I\!I_{fs} \equiv V\!I\!I\!I$	Anisotropic invariant relating to shear coupling of first and second fiber
$I\!X_{fs} \equiv I\!X$	Anisotropic invariant relating to scalar product of first and second fiber direction

Kinetics, constitutive laws, balance equations

$\mathrm{d}\boldsymbol{r}$	Infinitesimal resultant force vector
$\hat{\boldsymbol{b}}_0$	Body force vector in reference (material) configuration
$\hat{\boldsymbol{b}}$	Body force vector in current (spatial) configuration
$\boldsymbol{t}$	Cauchy traction vector
$\boldsymbol{t}_0$	First Piola-Kirchhoff traction vector

$\boldsymbol{\sigma}, \sigma_{ij}$	Cauchy stress tensor, and its coordinates
$\sigma_1 \geq \sigma_2 \geq \sigma_3$	Eigenvalues (principal normal stresses) of Cauchy stress tensor
$\hat{\boldsymbol{n}}_1, \hat{\boldsymbol{n}}_2, \hat{\boldsymbol{n}}_3$	Principal directions of Cauchy stress tensor
$\boldsymbol{P}, P_{ij}$	First Piola-Kirchhoff stress tensor, and its coordinates
$\boldsymbol{S}, S_{ij}$	Second Piola-Kirchhoff stress tensor, and its coordinates
$\boldsymbol{\tau}$	Kirchhoff stress tensor
$\overline{\boldsymbol{\sigma}}$	Spherical part of Cauchy stress tensor
$\tilde{\boldsymbol{\sigma}}$	Deviatoric part of Cauchy stress tensor
$I\!I_{\tilde{\sigma}}$	Second principal invariant of deviatoric stress tensor
$\overline{\sigma}$	Mean Cauchy stress
p	Hydrostatic pressure
σ_{vM}	Von Mises Cauchy stress
$\tau_{\max}$	Maximum Cauchy shear stress
$\mathcal{D}_{\mathrm{int}}$	Mechanical dissipation
Ψ	Strain energy function
$\bar{\Psi}$, Ψ_{vol}	Isochoric, volumetric part of strain energy function
$\mathbb{C}$, $\mathbb{C}_{ijkl}$	Elasticity (constitutive) tensor in reference (material) configuration, and its coordinates
m	Total mass
ρ_0	Density in reference (material) configuration
ρ	Density in current (spatial) configuration
$\boldsymbol{\phi}$	Test function (weighting function)
$\delta\mathcal{W}$	Virtual work

Heart, VAD, active and passive myocardial material laws

n_{mat}	Number of materials (region-wise constitutive laws)
k	Spring stiffness per unit reference surface area
c	Dashpot viscosity per unit reference surface area
μ	Shear modulus
$\mathbb{C}$	Elastic (Young's) modulus
ν	Poisson's ratio
κ	Bulk modulus
τ_{a}	Active stress
σ_0	Contractility
$\alpha_{\max}, \alpha_{\min}$	Upstroke and relaxation rates
$\hat{f}$	Normalized activation function
u	Scaled activation function
K	Activation function steepness
c_1, c_2	Activation function constants
a	Dimensionless Frank-Starling contractility scaling factor
a_0, a_f, a_s, a_{fs}	Passive myocardial material stiffnesses
b_0, b_f, b_s, b_{fs}	Dimensionless passive myocardial material parameters

$\mathbf{a}$	Heart long axis (through left ventricular bottom lumen and aortic valve)
$\mathbf{p}^{\ell}_{\mathrm{lum}}$	Left ventricular bottom lumen point
$\mathbf{p}_{\mathrm{AV}}$	Aortic valve point
$\mathbf{p}_{\mathrm{MV}}$	Posterior mitral valve leaflet point
$\mathbf{p}_{\mathrm{dist}}$	Most distal left ventricular point within atrioventricular plane
φ, z	Circumferential angular and axial coordinates for pad position description
d_{P}	Pad radial depth
$d_{\mathrm{P}}^{\mathrm{wall}}$	Pad wall thickness
d_{S}	Shell thickness
$h_{\mathrm{P}}^{\mathrm{s}}$	Pad bellows inset
$r_{\mathrm{P}}^{\mathrm{cor}}$	Pad corner radius
$r_{\mathrm{P}}^{\mathrm{s,i}}, r_{\mathrm{P}}^{\mathrm{s,o}}$	Pad seam inner, outer blend radii
$r_{\mathrm{P}}^{\mathrm{rim}}$	Pad rim blend radius
$d_{\mathrm{P}}^{\mathrm{brdg}}$	Pad bridge thickness (between two heart-oriented outer radii, two inner radii and two shell-oriented outer radii)
$t_{\mathrm{infl,s}}, t_{\mathrm{infl,e}}$	Begin, end of pad inflation
$t_{\mathrm{defl,s}}, t_{\mathrm{defl,e}}$	Begin, end of pad deflation
l_{φ}, l_z	Monitored circumferential, longitudinal distance that pad has already been moved
D_{φ}, D_z	Circumferential, longitudinal distance that pad should be moved
$\Delta_{\varphi}, \Delta_z$	Circumferential, longitudinal increments
a_z	User-specific blend parameter for longitudinal movement
$\mathcal{S}_{\mathrm{epi}}$	Epicardial surface
$\mathbf{x}_{\mathrm{mid}}$	Pad surface midpoint
$\boldsymbol{\xi}, \tilde{\boldsymbol{\xi}}$	Pad node coordinate vector, and its projection onto epicardial surface
$\mathbf{n}_{\mathrm{AVP}}$	Normal of atrioventricular plane
$\mathbf{n}_{\mathrm{epi}}$	Normal of epicardial surface at projected node
$\mathbf{n}_{\varphi}, \mathbf{n}_z$	Tangent in circumferential, longitudinal direction at projected node
$\tilde{\mathbf{n}}_z$	Tangent in longitudinal direction at pad surface midpoint
$\bar{\mathbf{n}}_z$	Tangent in modified longitudinal direction at projected node
d, d_{mid}	Distance from pad node, pad surface midpoint to axis $\mathbf{a}$
$\mathbf{n}_{\mathrm{cross}}$	Normal of cross-plane spanned by pad surface midpoint and axis $\mathbf{a}$ (at pad surface midpoint)

Growth & remodeling

$\boldsymbol{F}^{\mathrm{g}}$	Growth deformation gradient
$\boldsymbol{F}^{\mathrm{e}}$	Elastic deformation gradient
$\boldsymbol{L}^{\mathrm{g}}$	Growth velocity gradient
$\boldsymbol{C}^{\mathrm{e}}$	Elastic right Cauchy-Green deformation tensor
ϑ	Growth stretch
$\lambda_{\mathrm{myo}}^{\mathrm{e}}$	Elastic myofiber stretch
$\boldsymbol{S}^{\mathrm{e}}$	Elastic second Piola-Kirchhoff stress tensor

$\boldsymbol{\Sigma}^{\mathrm{e}}$	Elastic Mandel stress tensor
$\check{\boldsymbol{\mathbb{C}}}$	Elastic part of constitutive tensor (in reference configuration)
$\check{\boldsymbol{\mathbb{C}}}^{\mathrm{e}}$	Elastic part of constitutive tensor (in intermediate configuration)
$\tilde{\boldsymbol{\mathbb{C}}}$	Growth constitutive tensor
$\gamma, \gamma_{\mathrm{rev}}$	Growth, reverse growth nonlinearity
$\tau, \tau_{\mathrm{rev}}$	Growth, reverse growth time constant
k	Growth function
R_ϑ	Growth residual (for local Newton iteration)
ϕ	Fraction of non-grown (base) material
$\hat{\lambda}_{\mathrm{myo}}^{\mathrm{crit}}$	Prescribed critical myofiber stretch
$\hat{\Sigma}^{\mathrm{crit}}$	Prescribed critical volumetric Mandel stress
$(\hat{\lambda}_{\mathrm{myo}}^{\mathrm{crit}})_{\downarrow}$	Minimum myofiber stretch threshold
$(\hat{\Sigma}^{\mathrm{crit}})_{\downarrow}$	Minimum volumetric Mandel stress threshold
s	Safety factor for growth threshold
$\mathcal{N}$	Growth cycle
$t_{\mathcal{N}}$	Start time of growth cycle $\mathcal{N}$
T_{growth}	Growth cycle time
T_{load}	Load ramp-up or ramp-down time
t_{disease}	Acute disease initiation time
$t_{\mathrm{hom}}^{\mathrm{gr,ecc}}, t_{\mathrm{hom}}^{\mathrm{gr,con}}$	Time indicating homeostatic reference for eccentric, concentric growth
$t_{\mathrm{act}}^{\mathrm{gr,ecc}}, t_{\mathrm{act}}^{\mathrm{gr,con}}$	Time for evaluating overload state for eccentric, concentric growth

Contact mechanics

g_{n}	Gap function
$\boldsymbol{n}^{\mathrm{c}}$	Current unit outward normal at contact interface
$\check{\boldsymbol{x}}$	Projected (mapped) point from one body surface to the other
$\boldsymbol{t}^{\mathrm{c}}$	Total traction vector in contact interface
p_{n}	Contact stress in normal direction
$\boldsymbol{t}_{\mathrm{t}}$	Tangential traction vector in contact interface
$\boldsymbol{g}$	Gap vector

Domains and boundaries

Ω_0, Ω	Reference (material), current (spatial) configuration
Ω_0^{g}	Intermediate (grown) configuration
$\tilde{\Omega}_0$	Discretized reference (material) configuration
$\Omega_0^{(e)}$	Finite element sub-domain
$\Gamma_0^{\mathrm{D}}, \Gamma^{\mathrm{D}}$	Reference (material), current (spatial) Dirichlet boundary
$\Gamma_0^{\mathrm{N}}, \Gamma^{\mathrm{N}}$	Reference (material), current (spatial) Neumann boundary
Γ_0^{R}	Reference (material) Robin boundary
$\Gamma_0^{\mathrm{R,e}}$	Reference (material) Robin boundary at epicardium

$\Gamma_0^{\mathrm{R,b}}$	Reference (material) Robin boundary at heart base
$\Gamma_0^{\mathrm{R,ar}}$	Reference (material) Robin boundary at arterial outlets
$\Gamma_0^{\mathrm{R,ven}}$	Reference (material) Robin boundary at venous inlets
Γ_0^{lids}	Reference (material) endocardial lids (closures for heart cavities) boundary
$\Gamma_0^{\mathrm{0D}}, \Gamma^{\mathrm{0D}}$	Reference (material), current (spatial) coupling boundary
Γ_0^{mt}	Reference (material) tied contact (meshtying) boundary
$\Gamma_0^{\mathrm{c}}, \Gamma^{\mathrm{c}}$	Reference (material), current (spatial) contact boundary
$\Gamma_0^{\mathrm{D},x_2}$	Reference (material) Dirichlet boundary in x_2-direction (symmetry for 2D heart model)
$\Gamma_0^{\mathrm{D},x_3}$	Reference (material) Dirichlet boundary in x_3-direction (plane strain for 2D heart model)

Reduced-dimensional blood flow

ν	Kinematic viscosity
η	Dynamic viscosity
ρ	Density
r, z	Coordinates for axisymmetric description of reduced flow through vessel
r_0, l_0	Vessel radius and length
v_z	Axial vessel velocity
$(\cdot)^\star$	Non-dimensionalized quantity
J_0, Y_0	Zeroth-order Bessel functions
$\beta_1, \beta_2, \beta_3$	First three roots of J_0
λ_q, λ_p	Relaxation, retardation time scales
R	Resistance
$\tilde{R}$	Heart valve resistance (diode)
L	Inertance
E	Elastance
E_{A}	Elastance amplitude
C	Compliance
Z	(Arterial characteristic) impedance
Z_R, Z_L, Z_C	Impedance representation of resistance, inertance, compliance
ω	Angular frequency
p	Pressure
q	Flow
V	Volume
y_{at}	0D atrial activation function
π_{ar}	Auxiliary arterial pressure variable
τ_{ar}	Arterial windkessel time constant

Gas transport and dissociation

p_{CO_2}	Carbon-dioxide partial pressure
p_{O_2}	Oxygen partial pressure
f_{CO_2}	Carbon-dioxide gas fraction
f_{O_2}	Oxygen gas fraction
c_{CO_2}	Blood carbon-dioxide concentration
c_{O_2}	Blood oxygen concentration
$c_{\mathrm{tiss,CO}_2}$	Tissue carbon-dioxide concentration
$c_{\mathrm{tiss,O}_2}$	Tissue oxygen concentration
c_{Hb}	Blood hemoglobin concentration
S_{O_2}	Hemoglobin-oxygen dissociation curve
$p_{\mathrm{vap},37}^{\mathrm{water}}$	Vapor pressure of water at $37°\mathrm{C}$
$\hat{M}_{\mathrm{CO}_2}$	Metabolic rate of carbon-dioxide production (organ-specific)
$\hat{M}_{\mathrm{O}_2}$	Metabolic rate of oxygen consumption (organ-specific)
$\hat{M}_{\mathrm{CO}_2,\mathrm{total}}$	Total metabolic rate of carbon-dioxide production
$\hat{M}_{\mathrm{O}_2,\mathrm{total}}$	Total metabolic rate of oxygen consumption
p_{50,O_2}	Partial pressure of oxygen at $50\ \%$ saturation
n	Hill's constant
$\kappa_{\mathrm{CO}_2}, \tilde{\kappa}_{\mathrm{CO}_2}$	Diffusion capacity for carbon dioxide in the lung
$\kappa_{\mathrm{O}_2}, \tilde{\kappa}_{\mathrm{O}_2}$	Diffusion capacity for oxygen in the lung
α_{CO_2}	Solubility constant for carbon dioxide in blood/tissue
α_{O_2}	Solubility constant for oxygen in blood/tissue
V_{tiss}	Tissue volume
U_t	Time-varying pleural pressure
U_{m}	Atmospheric pressure
ω_{b}	Respiration (breathing) frequency
V_{T}	Tidal volume
V_{D}	Dead space volume
V_{lung}	Total lung volume
$\dot{V}_{\mathrm{t}}$	Total lung ventilation rate
$V_{\mathrm{m,gas}}$	Molar volume for an ideal gas at standard conditions
β	Point where effective oxygen consumption is $50\ \%$ of the maximum one

Discretization and solution

n_{el}	Number of finite elements
n_{nd}	Number of nodes
n_{dim}	Number of dimensions
n_{step}	Number of time steps
n_{core}	Number of cores
$n_{\mathrm{dof}}, n_{\mathrm{dof}}^{\mathrm{3D}}$	Number of structural degrees of freedom
$n_{\mathrm{dof}}^{\mathrm{0D}}$	Number of 0D model degrees of freedom

$\mathbf{u}^{(e)}$	Finite element displacement vector
$\mathbf{x}_0^{(e)}$	Finite element position vector
$\bar{\mathbf{x}}_0^{(e)}$	Finite element nodal coordinate vector
$\mathbf{N}^{(e)}$, N^k	Finite element shape function matrix, and its entries
ξ_1, ξ_2	(2D) finite element parameter space coordinates
$\mathbf{d}^{(e)}$, d_i^k	Finite element nodal displacement vector, and its entries
$\mathbf{S}^{(e)}$	Finite element second Piola-Kirchhoff stresses
$\mathbf{E}^{(e)}$	Finite element Green-Lagrange strains
$\hat{\mathbf{b}}_0^{(e)}$	Finite element body force vector
$\hat{\mathbf{t}}_0^{(e)}$	Finite element first Piola-Kirchhoff traction vector
$\mathbf{t}_0^{(\mathrm{R})(e)}$	Finite element first Piola-Kirchhoff traction vector from Robin boundary conditions
$\mathbf{t}_0^{(\mathrm{0D})(e)}$	Finite element first Piola-Kirchhoff traction vector from 0D circulation
$\mathbf{d}$	Global nodal displacement vector
$\mathbf{v}$	Global nodal velocity vector
$\mathbf{a}$	Global nodal acceleration vector
$\mathbf{p}$	0D circulation model state variable vector
$\mathbf{f}_{\mathrm{int}}, \mathbf{f}_{\mathrm{ext}}$	Global internal, external force vector
$\mathbf{M}$	Global mass matrix
$\mathbf{D}$	Global (Rayleigh) damping matrix
$c_{\mathrm{M}}, c_{\mathrm{K}}$	Mass, stiffness Rayleigh damping coefficients
$\mathbf{r}, \mathbf{r}^{\mathrm{S}}$	Structural residual vector
$\mathbf{r}^{\mathrm{0D}}$	0D circulatory system residual vector
$\mathbf{r}^{\mathrm{S-0D}}$	Total 3D-0D residual vector
$\mathbf{K}, \mathbf{K}^{\mathrm{S}}$	Structural dynamic effective tangential stiffness matrix
$\mathbf{K}_{\mathrm{T}}$	Tangential stiffness matrix
$\mathbf{K}^{\mathrm{0D}}$	0D circulatory system stiffness matrix
$\mathbf{K}^{\mathrm{0D,S}}$	Off-diagonal stiffness matrix, dependence of 0D model on structure (for 3D-0D coupled problem)
$\mathbf{K}^{\mathrm{S,0D}}$	Off-diagonal stiffness matrix, dependence of structure on 0D model (for 3D-0D coupled problem)
$\tilde{\mathbf{A}}$	Inverse of SIMPLE preconditioner matrix
$\bar{\alpha}$	SIMPLE blend parameter
$\check{\mathbf{S}}$	Schur complement operator
k_{ptc}	Pseudo-transient continuation parameter
γ, β	Newmark time integration parameters
$\alpha_{\mathrm{m}}, \alpha_{\mathrm{f}}$	Generalized-α time integration parameters
ρ_∞	Spectral radius of Generalized-α time integration algorithm
θ	Parameter of One-Step-θ time integration algorithm
$(\cdot)_n$	Quantity from previous time step n
$(\cdot)_{n+1}$	Quantity from current time step $n+1$
$(\cdot)_{n+1-\alpha_{\mathrm{m}}}$	Quantity at generalized instance in time, $n+1-\alpha_{\mathrm{m}}$
$(\cdot)_{n+1-\alpha_{\mathrm{f}}}$	Quantity at generalized instance in time, $n+1-\alpha_{\mathrm{f}}$
$(\cdot)_{n+\theta}$	Quantity at generalized instance in time, $n+\theta$

$(\cdot)^i$	Quantity from previous iteration i (unless overridden by context)
$(\cdot)^{i+1}$	Quantity from current iteration $i+1$

Norms, tolerances, errors

$\epsilon_{\text{res}}, \epsilon_{\text{res}}^{\text{S}}$	Structural residual norm tolerance for Newton scheme
$\epsilon_{\text{incr}}, \epsilon_{\text{incr}}^{\text{S}}$	Displacement increment norm tolerance for Newton scheme
$\epsilon_{\text{res}}^{\text{0D}}$	0D circulation residual tolerance for Newton scheme
$\epsilon_{\text{incr}}^{\text{0D}}$	0D model variable increment tolerance for Newton scheme
E_{fnorm}	Simplex error norm
ϵ_{grad}	Gradient norm tolerance
E_{cycl}	Cardiac cycle error norm
ϵ_{cycl}	Cardiac cycle tolerance
E_{growth}	Growth cycle error norm
ϵ_{growth}	Growth cycle tolerance

Parameter estimation, model order reduction

f	Objective function
n_{p}	Number of parameters
$\mathbf{x}$	Parameter vector
$\mathbf{x}^\star$	Optimum
$\mathbf{s}$	Search direction
α	Line search parameter
$\mathbf{w}$	Least-squares residual vector
$w_{\text{r}}, \tilde{w}_{\text{r}}$	Model output, measurement value
$\mathbf{J}$	Jacobian matrix
λ^i	Levenberg-Marquardt blend parameter in iteration i
S	Simplex
F	Facet of simplex S
λ_i	Linear combination factors for simplex
$\hat{\mathbf{x}}$	Centroid of facet
$\mathbf{x}_{\text{ref}}, \mathbf{x}_{\text{exp}}, \mathbf{x}_{\text{cont}}$	Reflected, expanded, contracted point
$\mathbf{x}_{\text{new}}$	New simplex point
n	Number of dimensions of simplex
γ, β, α	Simplex reflection, expansion, contraction parameter
$\hat{\mathbf{S}}$	Snapshot matrix
$\hat{\mathbf{D}}, \hat{\mathbf{C}}$	Covariance matrices
$\mathbf{\Phi}, \mathbf{\Psi}$	Eigenvector matrices of $\hat{\mathbf{D}}$, $\hat{\mathbf{C}}$
$\boldsymbol{\phi}, \boldsymbol{\psi}$	Eigenvectors of $\hat{\mathbf{D}}$, $\hat{\mathbf{C}}$
$\mathbf{\Lambda}$	Diagonal matrix of eigenvalues
n_{snap}	Number of snapshots

r_{b}	Number of reduced bases
$\mathbf{V}$	Reduced-order basis matrix
$\tilde{\mathbf{p}}$	Discrete vector of pressure measurements
b_p, b_V	Pressure, volume residual weighting factor
$b_{\mathrm{EF}}, b_{\mathrm{PVP}}, b_{\mathrm{EDP}}$	Ejection fraction, peak ventricular pressure, end-diastolic pressure residual weighting factor
$\mathbf{f}$	General residual vector function
$\mathbf{f}_{\mathrm{c}}$	General coarse level residual vector function
$\overline{\mathbf{f}}_{\mathrm{c}}$	General restricted (fixed) residual vector function
$\hat{\mathbf{f}}_{\mathrm{c}}$	General coarse level (fixed) residual vector function (at coarse level iterate)
$\overline{\mathbf{x}}_{\mathrm{c}}$	General restricted parameter vector
$\mathbf{R}, \mathbf{P}$	Restriction, prolongation operator
$\mathbf{R}_{\mathrm{w}}$	Least-squares residual restriction operator
n_{c}	Number of coarse level iterations
f_{c}	Coarse level objective function
$\mathbf{x}_{\mathrm{c}}$	Coarse level parameter vector
$\mathbf{w}_{\mathrm{c}}$	Coarse level least-squares residual vector
$\overline{\mathbf{w}}_{\mathrm{c}}$	Restricted (fixed) least-squares residual vector
$\widehat{\mathbf{w}}_{\mathrm{c}}$	Coarse level (fixed) least-squares residual vector (at coarse level iterate)
${}_{s}\mathbb{T}^{\mathrm{ff}}$	Intra-level transfer operator for post-V-cycle solve step
$\mathbb{T}^{\mathrm{ff}}$	Intra-level transfer operator between two V-cycles
$\mathbb{T}^{\mathrm{f}}_{\cdot\mathrm{c}}$	Inter-level transfer operator “fine” to “coarse”
$\mathbb{T}_{\mathrm{c}}^{\cdot\mathrm{f}}$	Inter-level transfer operator “coarse” to “fine”
$\mathcal{M}_{\mathrm{HDM}}, \mathcal{M}_{\mathrm{RDM}}$	Mathematical descriptors for high-, reduced-dimensional model
$\mathbb{L}$	Model reduction operator

1 Introduction

This thesis deals with computational modeling of patient-specific cardiac mechanics. It focuses on the ventricular and vascular system mechanics, on gas transport kinetics, as well as on modeling of heart failure disease entities like growth and remodeling phenomena. Furthermore, it presents novel efficient parameter estimation procedures and applies the developed methods and models in the context of novel heart assist technologies.
Here, a basic introduction to the scope of this thesis is presented. It starts with a motivation for the work in sec. 1.1, and continues with medical fundamentals on cardiovascular mechanics in sec. 1.2. The specific topic of heart failure as well as the medical treatment strategies thereof are presented in sec. 1.3, including a short introduction to current vascular assist device technologies. Finally, the research objective is detailed in sec. 1.4, and the outline of this thesis is presented in sec. 1.5.

1.1 Motivation

Cardiovascular diseases are one of the most prevalent entities of malady worldwide and still the leading cause of morbidity in the industrialized world [52, 130]. Amongst those, diseases directly relating to the heart and its ability to provide the necessary amount of blood flow to the body in order to maintain organ perfusion are the most abundant. Heart failure (HF) [99] with a prevalence of 5.8 million in the USA and over 23 million worldwide [19, 173] is a serious health problem and demands for tools and therapies that are effective, affordable, and beneficial for the patient's quality of life.
The reduced availability of donor hearts for patients suffering from end-stage congestive heart failure (CHF) necessitates and drives the development of ventricular assist device (VAD) technologies [160], that either serve as a bridge-to-transplant solution or may be a permanent terminal therapeutic strategy.
In order to overcome the deficiencies associated with current blood-pumping heart assist technologies, non-blood contacting extravascular ventricular support devices have been focus of research and are continuously being dealt with [98, 136, 137, 142, 170].

The primary motivation for this thesis emerged from a close collaboration of academic and industrial groups committed to the development of a novel extravascular biventricular augmentation device for patients suffering from CHF.
The core aspect of the present thesis is the development and implementation of mathematical and computational (in-silico) models and tools that serve to predictably assess the function, efficiency and security of the aforementioned novel VAD technology during its interaction with the patient-specific heart. The main motivation to do so lies in the belief that in-silico methods are able to predict circumstances and optimal operating conditions that are hardly or not at all

assessable in an experimental (in-vivo) setup. Hence, these methods at least enhance the insights gained from experiments and allow to derive potential for optimization that would not have been deducible from the in-vivo studies alone.
Ultimately, such computational approaches enable to judge the performance of a plenty of design variants and operating conditions for these kinds of implants and eventually allow to reduce the amount of in-vivo animal experiments that are currently inevitable for the reliable and secure development of medical devices.

For this purpose, various computational tools for modeling of the beating heart and its interaction with the vascular system are developed and implemented. They partly build upon recently developed in-silico heart models by various research groups around the world, with a multitude of novel extensions and integrative efforts as well as efficient solution and calibration strategies. Additionally, a framework for modeling of the novel implant and its design variants is developed, and predictive simulations of the interaction of the heart with the novel VAD technology are presented.

1.2 Cardiovascular mechanics

A brief introduction to cardiovascular mechanics with focus on the heart cycle is given. In depth treatments and physiological backgrounds may be found in [51].
The circulatory system in the body is mainly decomposed into two (sub-)circuits, namely the systemic (body) and the pulmonary (lung) circulation. The vitally important oxygen that is taken up from the lungs and binds to hemoglobin in the pulmonary capillary network has to be transported to the body, where oxygen consumption and carbon dioxide production take place.
The heart is the driving force of the cardiovascular system and simultaneously pumps oxygenated blood into the systemic circulation and deoxygenated as well as carbon dioxide-enriched blood into the pulmonary one. It is constituted out of four cardiac chambers, namely the left and right ventricle, and the left and right atrium. The ventricular cardiac chambers' task is to continuously supply both circulations with blood such that gas exchange and organ perfusion can happen. The atrial chambers' task basically is to guarantee uninterrupted non-pulsatile venous blood flow to the heart during the ventricular ejection phase. Prior to ventricular contraction, the atria perform a contraction themselves and actively complete ventricular filling. The heart and the circulatory system are sketched in fig. 1.1.

A heart cycle at resting conditions takes about $1\ \mathrm{s}$. The cycle is divided into two phases, the *systole* and the *diastole*. The systole is the time period during which ventricular contraction happens and blood is ejected into the aorta and the pulmonary artery, hence into the respective circuits. The *diastole* is the time period during which the ventricles relax and eventually fill again. At standard conditions, the diastole is about twice as long as the systole.
Four heart valves regulate the blood flow such that it remains unidirectional: The semilunar valves (aortic and pulmonary valve) separate the ventricles from the arteries, and the atrioventricular valves (mitral and tricuspid valve) regulate the flow between the atria and the ventricles. At the beginning of the systole, contractile force is built up in the ventricles, leading to a closure of mitral and tricuspid valve at end of the diastole. An isovolumic contraction phase follows

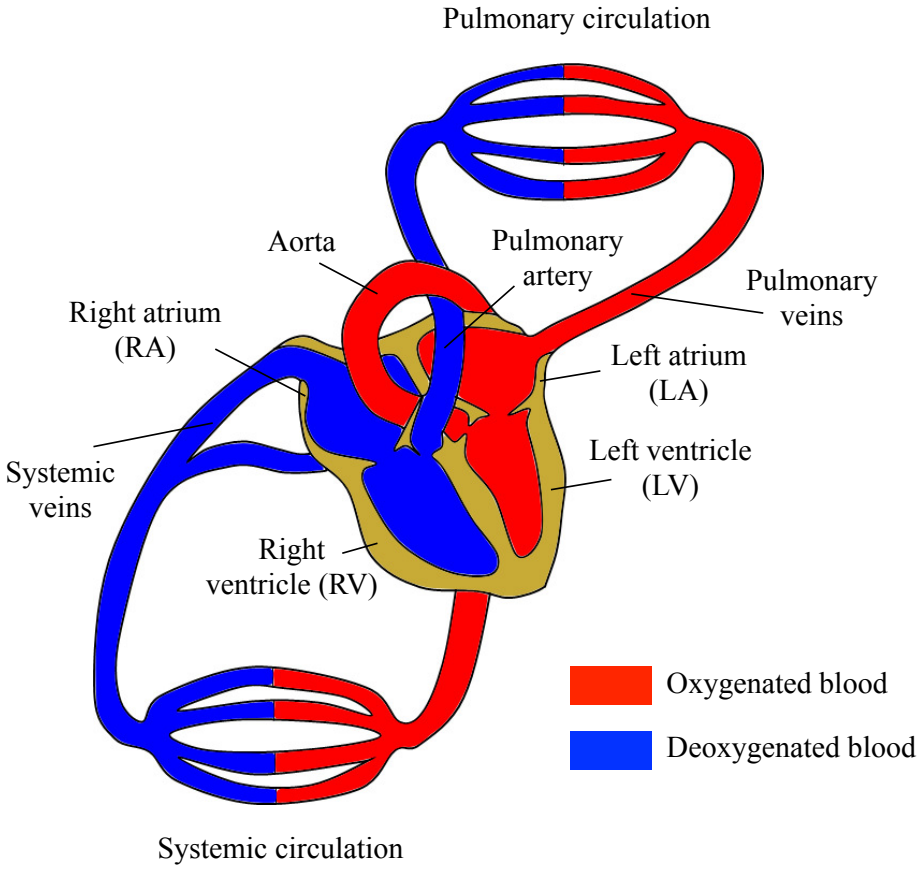

Figure 1.1: Schematic sketch of the cardiovascular system circulation with the heart as its driving unit: In the systole, the left ventricle (LV) pumps oxygenated blood (red) into the systemic circulation via the aorta, simultaneously to the RV delivering deoxygenated blood (blue) to the pulmonary circulation via the pulmonary artery. Oxygen consumption (carbon dioxide production) and re-oxygenation (carbon dioxide elimination) take place in the capillary networks of the systemic and pulmonary circulation, respectively. In the diastole, the ventricles relax and eventually fill through the left and right atrium (LA, RA) which guarantee uninterrupted non-pulsatile venous return to the heart.

(all valves closed) since aortic and pulmonary valve only open when left and right ventricular pressures surpass the pressures in the respective arteries, and blood ejects. Vice versa, when systole ends and ventricular relaxation starts, aortic and pulmonary valve close in order to avoid blood regurgitation: The isovolumic relaxation starts since all valves are shut until the ventricular pressure falls below the atrial one, eventually opening mitral and tricuspid valve such that the diastolic filling phase can happen. A schematic ventricular pressure-volume relationship is shown in fig. 1.2a, and fig. 1.2b shows the ventricular, atrial and arterial pressures over time t.

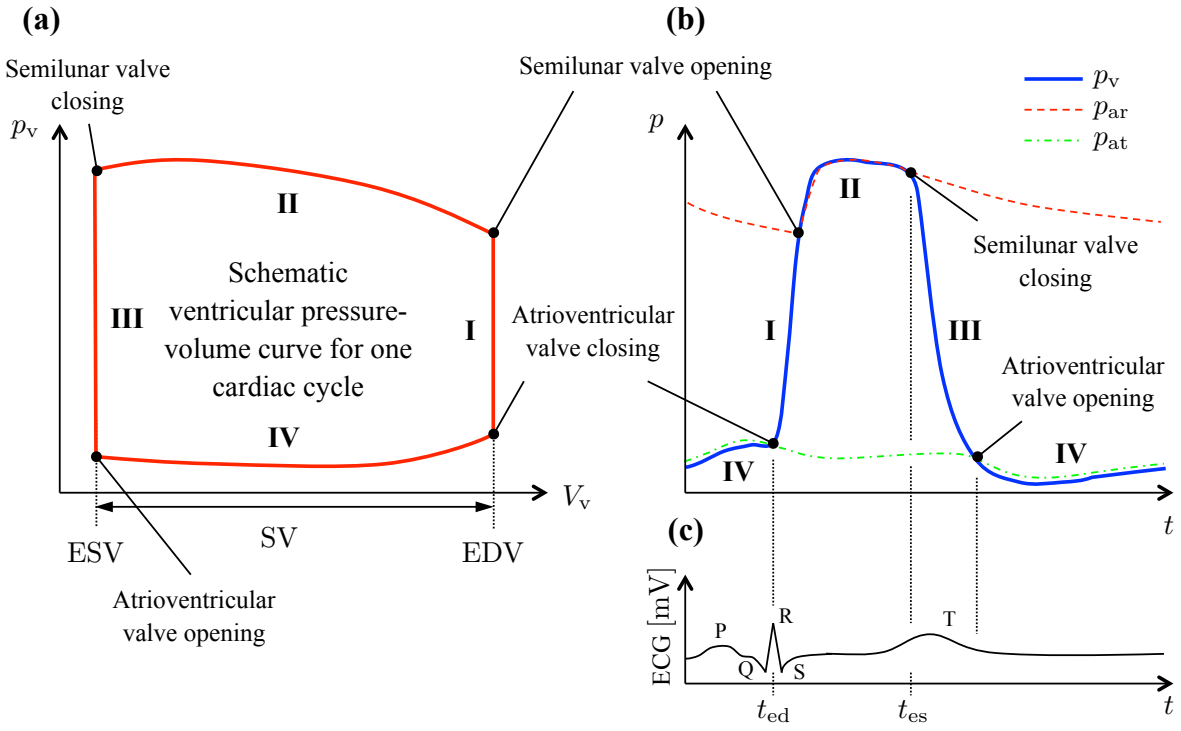

I isovolumic contraction phase
II ejection phase
III isovolumic relaxation phase
IV filling phase

Figure 1.2: Schematic sketches of: **(a)** Ventricular pressure-volume relationship, p_v over V_v, with end-diastolic and end-systolic volumes EDV and ESV, respectively, and the stroke volume SV (1.1) as the difference between the former and the latter. **(b)** Ventricular, atrial and arterial pressures p_v, p_at and p_ar over time t. **(c)** Electrocardiogram (ECG) curve, typically measured in $[\mathrm{mV}]$. End-diastolic and end-systolic timings denoted with t_ed and t_es, respectively.

The *stroke volume* SV determines the amount of blood that is pumped into the respective circulation by either of the ventricles in one cardiac cycle. It is the difference between the end-diastolic volume EDV and the end-systolic volume ESV:

$$\mathrm{SV} = \mathrm{EDV} - \mathrm{ESV}. \tag{1.1}$$

At a homeostatic state of the (healthy) circulatory system, left and right ventricular stroke volumes coincide.

A relative measure that determines the amount of ejected volume with respect to the end-diastolic volume is the *ejection fraction*:

$$\mathrm{EF} = \frac{\mathrm{SV}}{\mathrm{EDV}}. \tag{1.2}$$

The *cardiac output* is defined as the amount of volume that is pumped per time:

$$\mathrm{CO} = \mathrm{SV} \cdot \mathrm{HR}, \tag{1.3}$$

where $\mathrm{HR}\ [1/\mathrm{s}]$ is the heart rate, i.e. the amount of heart beats per second.

A healthy individual at rest has a left ventricular ejection fraction of around $\mathrm{EF}^{\ell} = 60\ \%$ and a right ventricular ejection fraction of about $\mathrm{EF}^{r} = 50\ \%$ [159]. Cardiac output is approximately $\mathrm{CO} = 5\ \mathrm{l/min}$. Note again that it coincides for both ventricles.

The contraction of the heart is initiated by an electrical impulse which is emitted by the sinoatrial node, leading to a depolarization of the myocardial cells. This first so-called P-wave in the electrocardiogram (ECG) curve results in contraction of the atria followed by electrical excitation of the ventricles, the so-called QRS-complex in the ECG. The end of the ventricular systole is marked by the T-wave in the ECG curve, representing the ventricles' repolarization. An exemplary ECG curve is sketched in fig. 1.2c.
Since the focus of this thesis is exclusively on the mechanics of the heart and the vascular system, electrophysiological phenomena are not dealt with to a further extent.

One of the most important mechanisms that determine the heart muscle's contractile dynamics is the so-called *Frank-Starling mechanism* [193]. It is an autoregulatory response to a change in the ventricular preload that increases (or lowers) contraction strength (*contractility*, or *inotropy*) of the cardiac muscle depending on the amount of volume entering the ventricles during diastole. If a larger amount of blood returns from the veins into one of the ventricles, a higher need in blood delivery is sensed in order to maintain an equal left and right ventricular cardiac output per stroke – inotropy rises. Vice versa, if the preload falls, the heart reacts to a reduced need in blood delivery, and inotropy is decreased again. However, at very high preloads, the myofibers become critically stretched and lose contractile ability again. The mechanism is used to maintain or re-establish homeostasis by assuring equal left and right ventricular cardiac output even at a sudden change in end-diastolic left or right ventricular volume.

1.3 Heart failure

Here, a short introduction to heart failure with its physiological mechanisms and therapeutic treatments is given, with a focus on vascular assist devices (VAD). A review on heart failure may be found in [99]. Section 1.3.1 briefly depicts the pathophysiology of heart failure, and VAD concepts are presented in sec. 1.3.2.

1.3.1 Pathophysiological mechanisms

Heart failure refers to symptoms of malfunction of the contractile performance of one or more heart chambers. Consequently, this underperformance of the heart leads to reduced organ perfusion and oxygen delivery to the body. Symptoms are shortness of breath, reduced ability of performing exercise, possibly accompanied by edema and tissue congestion due to the reduced flow and impaired circulation. The latter aspect is often referred to as *congestive* heart failure, which is however often used simultaneously to the term "heart failure" alone.
In general, heart failure is a chronic and progressive condition and may be caused by a multitude of pathophysiological mechanisms that are briefly highlighted here. Even though both, the left as well as the right ventricle may suffer from heart failure syndromes, and right ventricular failure as consequence of left ventricular malfunction eventually occurs, the focus here is set on pathophysiological changes with the left ventricle as consequence of mechanical overload.
Two distinct types of heart failure are discriminated:

- *systolic heart failure* describes the heart's disability to sufficient systolic performance, hence to provide the adequate amount of blood flow to the body;
- *diastolic heart failure* refers to an impairment of the diastolic filling phase of the ventricles due to increased stiffness of the ventricular wall.

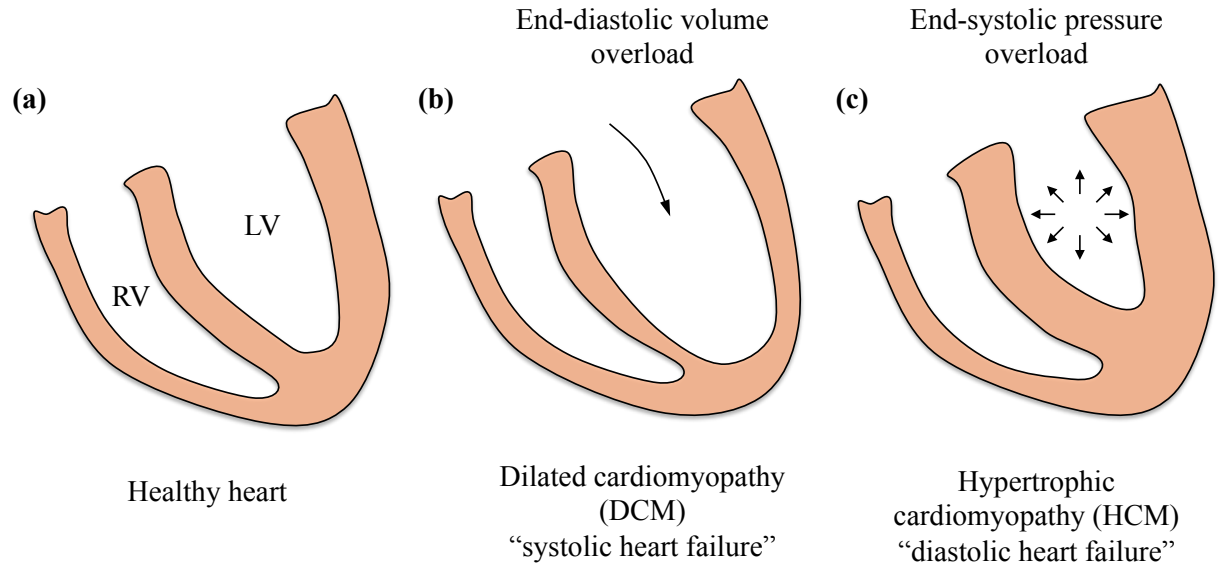

Figure 1.3: Ventricular myocardium with left (LV) and right (RV) ventricle. **(a)** Normal healthy heart. **(b)** Dilated heart after eccentric growth as consequence of end-diastolic volume overload, leading to systolic heart failure. **(c)** Thickened hypertrophied heart after concentric growth as consequence of end-systolic pressure overload, leading to diastolic heart failure.

While in systolic heart failure, ejection fraction falls due to increased end-diastolic and reduced stroke volume, it is virtually unaltered in diastolic heart failure due to greatly reduced end-diastolic and slightly reduced stroke volume.

Even though multiple mechanisms may cause either or both failure scenarios, a mechanistic view is likely to discriminate between *volume overload* stimulating systolic failure and *pressure overload* being the main driving force for the development of diastolic failure [175]. Figure 1.3 shows the two distinct types of overload and associated geometric changes of the (left) ventricle.

On the one hand, a state of volume overload occurs as the venous return to the heart at the end of the diastole is elevated, leading to a critical myofiber stretch which the heart tends to reduce. As consequence, additional sarcomeres are added in series which yields a reduction in strain but is accompanied by a ventricular dilation, referred to as *eccentric ventricular hypertrophy* and a *dilated cardiomyopathy* (DCM).
On the other hand, a state of pressure overload is present if the end-systolic cavity pressure is chronically elevated above physiological standard. This yields a high state of wall stress inside the myocardium, which is intended to be reduced by adding tissue in transverse myofiber direction. Consequently, the ventricular wall thickness increases, referred to as *concentric ventricular hypertrophy* and a *hypertrophic cardiomyopathy* (HCM).
Volume overload may be caused by acute events like aortic or mitral valve regurgitations (increasing preload), while pressure overload is most likely to establish if the afterload increases, e.g. as consequence of an aortic stenosis or hypertension.

The maladaptive changes in tissue that lead to the respective pathophysiology of DCM or HCM are referred to as *remodeling* [11]. They are further explained in chap. 2, sec. 2.3, along with approaches for modeling either one or the other phenomenon from a mechanical point of view.

1.3.2 Ventricular assist devices

Heart transplantation remains end-stage congestive heart failure's most promising treatment [160, 211]. However, due to the increasing organ demand, a continuous shortage in organ supply becomes more and more remarkable. The number of heart transplants currently being performed annually in the US ranges between 2000 and 2500 [106], while at any time, more than 3000 patients and rising are on the national waiting list for transplantation [75].
Due to that ever-present and constantly enlarging gap between supply and availability of donor hearts, vascular (or ventricular) assist devices (VAD) have prevailed to a noticeable treatment strategy of end-stage CHF for the last couple of decades. Even though the primary scopes of these devices are bridge-to-transplant solutions [169], improvements in device technology with reduction in adverse event rates qualify VADs for destination therapy [58, 180, 184, 212].

Assist devices for the left ventricle only are most common (LVADs) and are applied when right ventricular performance is adequate, while RVADs are used when solely the right heart's function is impaired. For patients with biventricular heart failure, so-called BiVADs composed of two separate assist devices are used.
Typical current VADs are made out of a continuous flow pumping unit that connects to the heart and the aorta via in- and outflow cannulas. A driveline exits the skin and is connected to a system controller that can be worn on a belt. First generation VADs were pulsatile flow pumps, which however have proven to be inferior to the continuous flow technologies despite some additional complications with respect to arterial pulsatility exhibited by the latter [40].

Depending on the the severity of impairment of the cardiac function, a total artificial heart (TAH) may be the only treatment option besides transplantation.
See [72, 185, 212] for more details on current mechanical circulatory assist devices, and especially [185] for an overview over all complications associated with VAD applications.

Within the scope of this thesis, a novel extravascular biventricular augmentation technology is investigated, which is developed by an industrial partner (AdjuCor® GmbH). First experimental results on this technology have been published by Jagschies et al. [98]. Its specific features and function parameters are detailed in chap. 5.
The novel support implant relies on the concept of cardiac compression devices. Their essential idea is not to partly bypass but to truly assist native ventricular function by exerting support pressures onto the epicardial surface, hence compressing the ventricles without the need to access a blood vessel. Therefore, any blood contact most often accompanied with increased thromboembolic event rates and the need for anticoagulation treatment is avoided. See [157] for a review on these kind of devices.

1.4 Research objective

This thesis aims at developing multiscale and multidimensional computational models for patient-specific cardiovascular conditions. In the following (sec. 1.4.1), a specification of requirements deduced from the motivational interlude in sec. 1.1 is derived. Thereafter, the specific contributions in terms of a methodological overview are highlighted in sec. 1.4.2.

1.4.1 Specification of requirements

The computational models and methods to be used, developed and implemented should allow the physiologically meaningful, parameterized, patient-specific, calibrated, validated, and computationally efficient assessment of the function and optimization potential of a novel cardiac extravascular augmentation technology interacting with the ventricular myocardium.
To date, none of the computational approaches for modeling of cardiac and vascular system mechanics in the literature fulfills all of the following requirements, therefore novel methods and models tailored for the specific problem at hand are needed.

Specifically, the models and methods for the heart and the assist device should comprise

- an accurate, patient-specific geometric representation of the ventricular myocardium, requiring a rule-based segmentation procedure from imaging data as well as a finite element meshing and input file preparation workflow applicable to arbitrary geometries;
- a reasonable consideration of boundary conditions, passive and active material behavior using state-of-the-art hyperelastic constitutive laws accounting for the myocardium's orthotropic behavior, the application of a rule-based but realistic fiber and sheet direction, together with a meaningful parameterization of the active contractile dynamics with time-controlled activation and relaxation times allowing to simulate various patient-specific conditions (rest, exercise, impaired relaxation, or similar);

- a sophisticated consideration of the fluid pressure and flow relationships in terms of a closed circulatory system that provides a physiological pressure loading condition for the heart on the one side, and returns meaningful integral pressure-volume relationships on the other, hence with the ability of linking local active or passive alterations in material behavior to global, integral cardiac performance indicators like stroke work and ejection fraction, including the meaningful assessment of homeostatic states of identical left and right ventricular cardiac output;

- an efficient computational framework and strategy to calibrate distinct, identifiable parameters of contraction strength, duration, and afterload to clinically relevant, observable measurements like ventricular pressure or volume in order to reproduce a physiological validated baseline condition;

- incorporation of growth and remodeling phenomena with considerations of the different time scales of heart beat dynamics and remodeling occurrences, and the possibility to link an acute event (infarction, valve disease) to long-term maladaptive changes in ventricular size and material behavior;

- an automated patient-independent modeling and simulation workflow for the aforementioned novel cardiac assist technology to efficiently compute design variants and allow for optimization procedures to access the design parameters and generate model variants; and

- a robust integration of all the models and methods in order to capture the different types of physical phenomena (solid mechanics with elastic and inelastic material behavior, multi-body contact and tied contact, coupling with circulatory system flow models) simultaneously in one monolithic computational setting on high-performance computing platforms.

1.4.2 Methodological overview

The above-mentioned requirements are fulfilled by developing modeling workflows, using and extending existing computational models, developing and implementing novel methods such as coupling schemes, parameter estimation procedures, and multiscale growth and remodeling approaches, and finally by proving the feasibility of the methods by meaningful results and validations with experimental data at hand.

A rule-based segmentation workflow for extracting the patient-specific ventricular geometry out of (motion) CT data sets at a distinct point in time is generated, both for providing the input data to a computational solid mechanics model of the ventricles (and the atria), as well as the core data that serves as basis for the manufacturing process of the aforementioned novel ventricular assist technology.

An automated model construction and finite element meshing workflow and pipeline is implemented that communicates with a CAD and FEM meshing software; specifically:

- a workflow for solid mechanics finite element heart model generation including meshing and making use of automated fiber and sheet direction incorporation methods, as well as

- a pipeline for modeling and construction of the assist device implant according to the design principles set by the industrial partner, readily providing the finite element discretized implant model to be computed together with the heart.

State-of-the-art anisotropic hyperelastic passive material laws are used for modeling of the patient-specific 3D heart, and an active stress material model used for the heart's contraction is extended to be capable of including strain-dependent behavior, hence the Frank-Starling mechanism, cf. sec. 1.2. Robin boundary conditions using spring and dashpot elements are implemented allowing for a realistic mechanical consideration of the truncated surrounding (at the atrioventricular base, or at venous inlets).

Furthermore, reduced-dimensional lumped-parameter (0D) pressure-flow and gas transport models for the entire closed circulatory system are derived by combining previous approaches and for the first time are implemented together with a monolithic 3D-0D coupled solution framework. This allows for the simultaneous implicit solution of 3D solid and 0D flow models in one monolithic Newton scheme, using available preconditioning techniques for the 3D-0D system of equations to meet the requirements for the solution of large-scale problems on high-performance computing (HPC) platforms.

Models for growth and remodeling are derived implementing and extending existing state-of-the-art anisotropic volumetric growth constitutive laws, combined with phenomenological approaches for remodeling in terms of growth-dependent changes in tissue passive elastic or active properties. A novel multiscale-in-time strategy is implemented that allows to simulate growth and remodeling phenomena on a large time scale as consequence of an acute disease event on the small time scale, including previously proposed reverse growth models.

Additionally, novel strategies for estimating key parameters that govern heart work (ventricular contractile properties, afterload, preload) are developed. An optimization framework is implemented with novel multilevel optimization methods that estimate parameters on a high-fidelity computational model by help of low-fidelity coarse surrogate models. Therefore, model order reduction techniques for the 3D heart are implemented and incorporated into the optimizer, and different types of reduced models are compared with respect to their computational performance.

Finally, all models and methods are applied to simulating a novel extravascular ventricular assist technology, and a validation with in-vivo experiments that were conducted with this kind of implant is performed. Last but not least, optimization algorithms for design and function parameters of the novel implant are developed, and proposals to enhance their computational efficiency by help of globalized model order reduction strategies are presented.

All computational models and solution schemes are implemented into the in-house multi-physics finite element software package Baci [207] in C++ programming language. Model and finite element input file generation scripts as well as optimization methods are implemented into a Python programming language-based framework that communicates with Baci and the HPC architecture, including an automated simulation processing and data handling chain.

1.5 Outline

After having presented all introductory remarks, physiological backgrounds to certain phenomena, as well as the research objective and the methodological approaches, the remainder of this thesis is organized as follows.
Chapter 2 introduces all modeling-related aspects. It starts with the mathematical backgrounds of continuum mechanics and reduced-dimensional flow models, and bridges over to the 3D-0D coupled problem description of the heart and the vascular system, introducing all the governing equations and modeling assumptions involved. Then, the models for myocardial growth and disease progression are introduced, including the time scale handling for both volume and pressure overload-induced cardiomyopathy.
Chapter 3 treats all discretization- and solution-related aspects. It opens with fundamentals on nonlinear finite element methods, finite difference schemes and nonlinear solution techniques, and then presents the monolithic approach to 3D-0D coupled cardiovascular mechanics. Numerous exemplary results for a patient-specific heart then are presented, i.e. pressure-volume relationships at different cardiovascular conditions and gas transport kinetics. Furthermore, growth and remodeling results for eccentric and concentric ventricular hypertrophy as consequence of an acute event (infarction, valve stenosis or regurgitation) are shown.
Chapter 4 then presents model reduction-based optimization algorithms. At first, a general introduction to nonlinear unconstrained optimization is given, before presenting model order reduction techniques for the 3D-0D coupled problem. Thereafter, the novel algorithms for parameter estimation are presented and compared. Results for a patient-specific heart calibrated to in-vivo measured pressure and volume data are shown.
Finally, chap. 5 addresses models for a novel heart assist technology developed in close collaboration with industrial partners. The previously developed methods and models are applied to the specific problem of a porcine failing heart treated with the extravascular implant. Validation with experimental data is performed, and optimization methods for functional parameters of the implant are introduced.

2 Modeling of cardiac mechanics and the vascular system

The mathematical and computational modeling of the cardiovascular system plays an ubiquitous role in biomedical engineering and has been topic of numerous contributions for the last couple of decades. Due to the huge biological complexity of the cardiovascular system and the manifoldness of processes happening on different spatial and temporal scales, models naturally have to be tailored towards a specific aspect and question at hand, while other phenomena with little or negligible influence on the quantities of interest have to be simplified or omitted during model design.
Amongst cardiovascular models, those concentrating on the mechanics and the electrophysiology of the heart as the central driving organ of the cardiovascular system are continuously prevailing and cover a vast field of research areas. An overview over a couple of recent models may be found in Quarteroni [165]. Specific references to models in the literature will be given in the respective sections of this thesis.

The models which are developed in this thesis focus on the *mechanics* of the heart and the vascular system with the aim of describing, predicting and understanding the heart's function, its diseases (e.g. myocardial infarction and chronic left or right ventricular insufficiency), diseases progression and impact of medical treatment thereof. Therefore, the myocardium (heart muscle) is modeled as a 3-dimensionally resolved nonlinear anisotropic elastic solid with an active material component in order to simulate the cardiac contraction. The geometry is *patient-specific* and extracted from medical imaging data such as CT or MRI scans.
The vascular network is taken into account by using a reduced-dimensional *lumped-parameter model* for the entire closed-loop circulatory system and hence links spatially resolved ventricular contraction, material behavior as well as disease progression and remodeling phenomena to integral hemodynamic quantities such as cardiac output, stroke work, and oxygen delivery.
Specifically end-diastolic and end-systolic homeostatic state volumes and pressures are important stimuli for maladaptive growth and remodeling processes such as eccentric and concentric ventricular cardiomyopathy. Both phenomena are extensively dealt with by a novel multiscale-in-time approach in order to link short term changes in hemodynamics to long term growth and remodeling effects.

The fundamentals of nonlinear solid mechanics and reduced-dimensional modeling of blood flow are detailed in sec. 2.1. The novel models which are developed in this thesis are described in sec. 2.2, including all relevant aspects such as geometry construction, governing equations, boundary conditions, specific material modeling and circulatory system properties.
Finally, sec. 2.3 deals with a novel multiscale-in-time approach for modeling myocardial growth and disease progression for both eccentric and concentric ventricular cardiomyopathy.

2.1 Fundamentals

2.1.1 Nonlinear solid mechanics

Here, basic governing equations of continuum mechanics are restated since they form the cornerstone of all mechanical analyses performed in this work. Kinematic descriptors, concepts of stress, balance equations and variational principles of initial boundary value problems are depicted.
While all kinematic and balance equations as well as the stress theorems hold for any type of material behavior (fluids, elastic or inelastic solids), the specific kinetics and constitutive models for isotropic and anisotropic hyperelastic solids are elaborated to a further extent. For a detailed treatment of continuum mechanics with a focus on constitutive theories for solids, the reader is referred to Holzapfel [88].

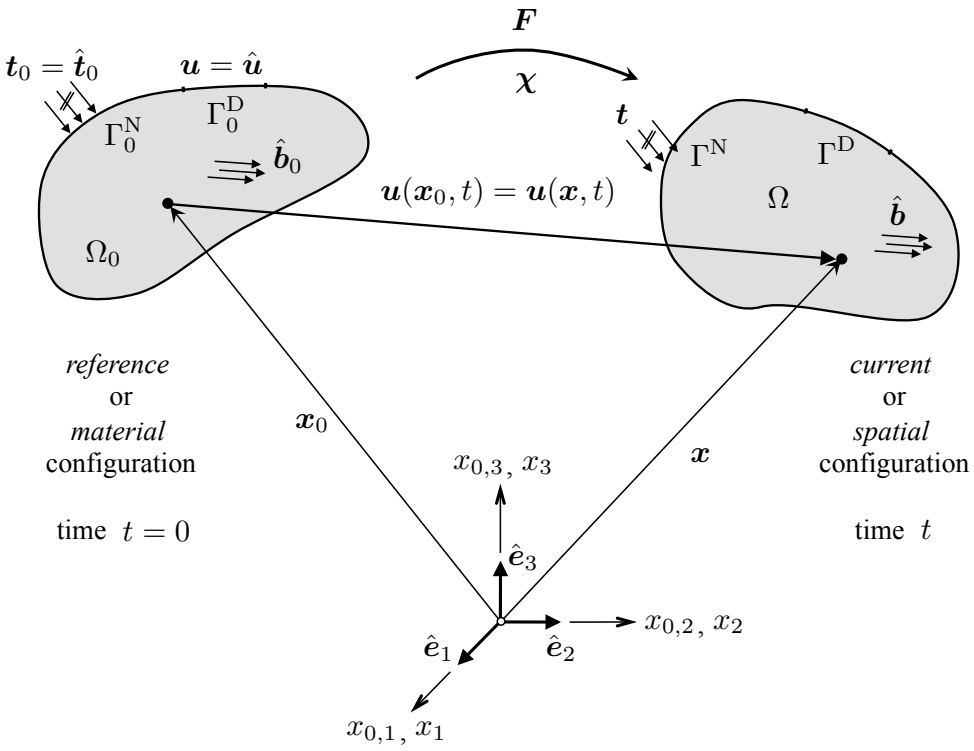

Figure 2.1: Nonlinear continuum mechanics setting: Deformation of a continuum body from reference (or material) to current (or spatial) configuration.

Figure 2.1 shows a generalized continuum mechanical setting in terms of the deformation of a continuous body subject to the motion $\boldsymbol{\chi}$. It is assumed that the same right-handed orthogonal reference frame for both, the *reference* or *material*, and the *current* or *spatial* configuration of the body is used. That is, material basis vectors $\hat{\boldsymbol{e}}_{0,i}$ and spatial basis vectors $\hat{\boldsymbol{e}}_i$ coincide, therefore their further distinction is omitted and only re-established for demonstrative purposes.
The reference configuration is denoted with $\Omega_0 \subset \mathbb{R}^3$, which is the domain occupied by material points $\boldsymbol{x}_0 = x_{0,i}\hat{\boldsymbol{e}}_i$ at time instance $t = 0$. By analogy, the current configuration $\Omega \subset \mathbb{R}^3$ is the domain occupied by spatial points $\boldsymbol{x} = x_i\hat{\boldsymbol{e}}_i$ at a time instance $t \neq 0$.
The boundary of the body is $\Gamma_0 = \Gamma_0^{\mathrm{D}} \cup \Gamma_0^{\mathrm{N}}$, which may be decomposed into a Dirichlet boundary

with prescribed displacements $\boldsymbol{u} = \hat{\boldsymbol{u}}$ and a Neumann boundary with prescribed tractions $\boldsymbol{t}_0 = \hat{\boldsymbol{t}}_0$. The two types of boundaries are disjoint: $\Gamma_0^{\mathrm{D}} \cap \Gamma_0^{\mathrm{N}} = \emptyset$. Furthermore, the body may be subject to forces per unit undeformed volume $\hat{\boldsymbol{b}}_0$, so-called body forces.

2.1.1.1 Kinematics

Let the motion (deformation map) $\boldsymbol{\chi}$ carry a material point $\boldsymbol{x}_0$ into its spatial counterpart $\boldsymbol{x}$ for all times t. It is assumed to be unique and invertible:

$$\boldsymbol{x} = \boldsymbol{\chi}(\boldsymbol{x}_0, t), \quad \boldsymbol{x}_0 = \boldsymbol{\chi}^{-1}(\boldsymbol{x}, t). \tag{2.1}$$

Consequently, the (material) displacement of a material point from reference to current configuration is the difference in position vectors,

$$\boldsymbol{u}(\boldsymbol{x}_0, t) = \boldsymbol{x}(\boldsymbol{x}_0, t) - \boldsymbol{x}_0, \tag{2.2}$$

while the material point's velocity and acceleration are the first and second time derivative of its displacement, respectively:

$$\boldsymbol{v}(\boldsymbol{x}_0, t) = \frac{\partial \boldsymbol{\chi}(\boldsymbol{x}_0, t)}{\partial t} = \frac{\partial \boldsymbol{u}(\boldsymbol{x}_0, t)}{\partial t} = \dot{\boldsymbol{u}}(\boldsymbol{x}_0, t), \tag{2.3}$$

$$\boldsymbol{a}(\boldsymbol{x}_0, t) = \frac{\partial^2 \boldsymbol{\chi}(\boldsymbol{x}_0, t)}{\partial t^2} = \frac{\partial \boldsymbol{v}(\boldsymbol{x}_0, t)}{\partial t} = \frac{\partial^2 \boldsymbol{u}(\boldsymbol{x}_0, t)}{\partial t^2} = \ddot{\boldsymbol{u}}(\boldsymbol{x}_0, t). \tag{2.4}$$

The displacement, velocity and acceleration fields may analogously be expressed in spatial coordinates $\boldsymbol{x}$:

$$\boldsymbol{u}(\boldsymbol{x}, t) = \boldsymbol{x} - \boldsymbol{x}_0(\boldsymbol{x}, t) = \boldsymbol{u}[\boldsymbol{\chi}(\boldsymbol{x}_0, t), t] = \boldsymbol{u}(\boldsymbol{x}_0, t), \tag{2.5}$$

$$\boldsymbol{v}(\boldsymbol{x}, t) = \boldsymbol{v}[\boldsymbol{\chi}(\boldsymbol{x}_0, t), t] = \boldsymbol{v}(\boldsymbol{x}_0, t), \tag{2.6}$$

$$\boldsymbol{a}(\boldsymbol{x}, t) = \boldsymbol{a}[\boldsymbol{\chi}(\boldsymbol{x}_0, t), t] = \boldsymbol{a}(\boldsymbol{x}_0, t). \tag{2.7}$$

However, if, for example, the velocity field is formulated with respect to spatial coordinates, the acceleration field emerges as its *material time derivative*, where the change of the current position $\boldsymbol{x}$ has to be accounted for:

$$\begin{aligned} \boldsymbol{a}(\boldsymbol{x}, t) = \dot{\boldsymbol{v}}(\boldsymbol{x}, t) = \frac{\mathrm{d}\boldsymbol{v}(\boldsymbol{x}, t)}{\mathrm{d}t} = \frac{\partial \boldsymbol{v}(\boldsymbol{x}, t)}{\partial t} + \frac{\partial \boldsymbol{v}(\boldsymbol{x}, t)}{\partial \boldsymbol{x}} \frac{\partial \boldsymbol{x}}{\partial t} = \\ = \frac{\partial \boldsymbol{v}(\boldsymbol{x}, t)}{\partial t} + (\boldsymbol{\nabla} \otimes \boldsymbol{v})\, \boldsymbol{v}. \end{aligned} \tag{2.8}$$

While a description with respect to the referential coordinates $\boldsymbol{x}_0$ is referred to as *Lagrangian* description, formulating with respect to the current spatial coordinates $\boldsymbol{x}$ is known as *Eulerian* description. A generalized descriptive concept with an independently moving observer is referred to as *Arbitrary Lagrangian-Eulerian* (ALE) description, which is not detailed here.

The deformation gradient carries a material infinitesimal line element into its spatial counterpart according to

$$\mathrm{d}\boldsymbol{x} = \boldsymbol{F}\, \mathrm{d}\boldsymbol{x}_0 \tag{2.9}$$

and therefore is defined as

$$\boldsymbol{F} = \frac{\partial \boldsymbol{x}(\boldsymbol{x}_0, t)}{\partial \boldsymbol{x}_0} = \mathbf{1} + \boldsymbol{\nabla}_0 \otimes \boldsymbol{u} = F_{ij}\, \hat{\boldsymbol{e}}_i \otimes \hat{\boldsymbol{e}}_{0,j}. \tag{2.10}$$

It is a so-called *two-point tensor* with one basis $\hat{\boldsymbol{e}}_{0,i}$ belonging to the reference and the other basis $\hat{\boldsymbol{e}}_i$ to the current frame.

The deformation gradient essentially captures rotations and stretches of line elements. The polar decomposition of the deformation gradient (2.10) into a proper orthogonal rotation tensor $\boldsymbol{Q}$ (obeying $\boldsymbol{Q}^{\mathrm{T}} = \boldsymbol{Q}^{-1}$ and $\det \boldsymbol{Q} = 1$) and a material (right) stretch tensor $\boldsymbol{U} = \boldsymbol{U}^{\mathrm{T}}$, or a spatial (left) stretch tensor $\boldsymbol{V} = \boldsymbol{V}^{\mathrm{T}}$ yields

$$\boldsymbol{F} = \boldsymbol{Q}\boldsymbol{U} = \boldsymbol{V}\boldsymbol{Q}. \tag{2.11}$$

In order to derive a deformation measure which is irrespective of rigid-body motions, the material *right Cauchy-Green deformation tensor*

$$\begin{aligned} \boldsymbol{C} = \boldsymbol{F}^{\mathrm{T}}\boldsymbol{F} &= F_{ij}F_{kl}\, (\hat{\boldsymbol{e}}_{0,j} \otimes \hat{\boldsymbol{e}}_i)(\hat{\boldsymbol{e}}_k \otimes \hat{\boldsymbol{e}}_{0,l}) = F_{ij}F_{il}\, \hat{\boldsymbol{e}}_{0,j} \otimes \hat{\boldsymbol{e}}_{0,l} = C_{jl}\, \hat{\boldsymbol{e}}_{0,j} \otimes \hat{\boldsymbol{e}}_{0,l} \\ &= (\boldsymbol{Q}\boldsymbol{U})^{\mathrm{T}}(\boldsymbol{Q}\boldsymbol{U}) = \boldsymbol{U}\boldsymbol{Q}^{-1}\boldsymbol{Q}\boldsymbol{U} = \boldsymbol{U}^2 \end{aligned} \tag{2.12}$$

as well as the spatial *left Cauchy-Green deformation tensor*

$$\begin{aligned} \boldsymbol{B} = \boldsymbol{F}\boldsymbol{F}^{\mathrm{T}} &= F_{ij}F_{kl}\, (\hat{\boldsymbol{e}}_i \otimes \hat{\boldsymbol{e}}_{0,j})(\hat{\boldsymbol{e}}_{0,l} \otimes \hat{\boldsymbol{e}}_k) = F_{ij}F_{kj}\, \hat{\boldsymbol{e}}_i \otimes \hat{\boldsymbol{e}}_k = B_{ik}\, \hat{\boldsymbol{e}}_i \otimes \hat{\boldsymbol{e}}_k \\ &= (\boldsymbol{V}\boldsymbol{Q})(\boldsymbol{V}\boldsymbol{Q})^{\mathrm{T}} = \boldsymbol{V}\boldsymbol{Q}\boldsymbol{Q}^{-1}\boldsymbol{V} = \boldsymbol{V}^2 \end{aligned} \tag{2.13}$$

are defined. As can be seen, both bases from $\boldsymbol{C}$ belong to the material frame, while the bases from $\boldsymbol{B}$ are defined in the spatial frame. Note that $\boldsymbol{B} = \boldsymbol{Q}\boldsymbol{C}\boldsymbol{Q}^{\mathrm{T}}$.
While many strain measures may be defined, two popular definitions of strain are the material *Green-Lagrange strain tensor* and the spatial *Euler-Almansi strain tensor*,

$$\boldsymbol{E} = \frac{1}{2}(\boldsymbol{C} - \mathbf{1}) \qquad \text{and} \qquad \boldsymbol{e} = \frac{1}{2}(\mathbf{1} - \boldsymbol{B}^{-1}). \tag{2.14}$$

Inserting (2.10) into (2.14) yields $\boldsymbol{E} = \frac{1}{2}\left(\boldsymbol{\nabla}_0 \otimes \boldsymbol{u} + (\boldsymbol{\nabla}_0 \otimes \boldsymbol{u})^{\mathrm{T}} + (\boldsymbol{\nabla}_0 \otimes \boldsymbol{u})^{\mathrm{T}}\boldsymbol{\nabla}_0 \otimes \boldsymbol{u}\right)$ and $\boldsymbol{e} = \frac{1}{2}\left(\boldsymbol{\nabla} \otimes \boldsymbol{u} + (\boldsymbol{\nabla} \otimes \boldsymbol{u})^{\mathrm{T}} - (\boldsymbol{\nabla} \otimes \boldsymbol{u})^{\mathrm{T}}\boldsymbol{\nabla} \otimes \boldsymbol{u}\right)$. One can show that both strain measures coincide for the geometrically linear theory and yield the classical engineering strain as symmetric part of the displacement gradient.

2.1.1.2 Kinetics and constitutive laws

If the body depicted in fig. 2.1 is imagined to be cut, continuity of forces over the cut boundary has to hold. An infinitesimal resultant force $\mathrm{d}\boldsymbol{r}$ that acts on a surface element $\mathrm{d}\boldsymbol{a} = \mathrm{d}a\, \boldsymbol{n}$ may be described either in the current cut configuration with spatial unit outward normal $\boldsymbol{n}$, or with respect to the reference configuration, where the surface element becomes $\mathrm{d}\boldsymbol{A} = \mathrm{d}A\, \boldsymbol{n}_0 = J^{-1}\boldsymbol{F}\, \mathrm{d}\boldsymbol{a}$ with material unit outward normal $\boldsymbol{n}_0$:

$$\mathrm{d}\boldsymbol{r} = \boldsymbol{t}\, \mathrm{d}a = \boldsymbol{t}_0\, \mathrm{d}A. \tag{2.15}$$

While $\boldsymbol{t}$ is called the (true) *Cauchy traction vector* describing the actual boundary stress, $\boldsymbol{t}_0$ is the (nominal) *first Piola-Kirchhoff traction vector*, both being force measured per unit surface area either in the current or in the reference configuration.

In order to quantify the full state of stress at a continuum point, three perpendicular cut planes would be necessary, since the traction vector depends on the actual unit outward normal. Thus, the full state of stress is characterized by a second-order tensor field relating the unit outward normal to the traction vector. Cauchy's stress theorem states

$$\boldsymbol{t}(\boldsymbol{x}, t, \boldsymbol{n}) = \boldsymbol{\sigma}(\boldsymbol{x}, t)\boldsymbol{n}, \tag{2.16}$$

$$\boldsymbol{t}_0(\boldsymbol{x}_0, t, \boldsymbol{n}_0) = \boldsymbol{P}(\boldsymbol{x}_0, t)\boldsymbol{n}_0, \tag{2.17}$$

where

$$\boldsymbol{\sigma} = \sigma_{ij}\, \hat{\boldsymbol{e}}_i \otimes \hat{\boldsymbol{e}}_j = \boldsymbol{\sigma}^{\mathrm{T}} \qquad \text{and} \qquad \boldsymbol{P} = P_{ij}\, \hat{\boldsymbol{e}}_i \otimes \hat{\boldsymbol{e}}_{0,j} \tag{2.18}$$

are the *Cauchy stress tensor* and the *first Piola-Kirchhoff stress tensor*, respectively. While the former is a spatial stress field, the latter, like the deformation gradient, is a two-point tensor with one basis in the reference and the other one in the current configuration. Its transpose, $\boldsymbol{P}^{\mathrm{T}}$, is frequently referred to as the nominal stress tensor.

In order to have a fully material stress measure, the so-called *second Piola-Kirchhoff stress tensor*

$$\boldsymbol{S} = \boldsymbol{F}^{-1}\boldsymbol{P} = J\boldsymbol{F}^{-1}\boldsymbol{\sigma}\boldsymbol{F}^{-\mathrm{T}} = S_{ij}\, \hat{\boldsymbol{e}}_{0,i} \otimes \hat{\boldsymbol{e}}_{0,j} = \boldsymbol{S}^{\mathrm{T}} \tag{2.19}$$

is defined. Since both of its bases are defined with respect to the material configuration and due to its symmetry, it represents a suitable quantity to define solid mechanics constitutive laws in a Total Lagrangian setting.

Solving an eigenvalue problem allows to represent $(2.18)_1$ in its spectral form

$$\boldsymbol{\sigma} = \sum_{a=1}^{3} \sigma_a\, \hat{\boldsymbol{n}}_a \otimes \hat{\boldsymbol{n}}_a, \tag{2.20}$$

where $\sigma_1 \geq \sigma_2 \geq \sigma_3$ are the eigenvalues (principal normal stresses) and $\hat{\boldsymbol{n}}_a$ the principal directions of $\boldsymbol{\sigma}$.
Furthermore, the state of stress may be additively split into a spherical (hydrostatic) part $\overline{\boldsymbol{\sigma}}$ causing change of volume and a deviatoric part $\tilde{\boldsymbol{\sigma}}$ causing change of shape, with

$$\overline{\boldsymbol{\sigma}} = \overline{\sigma}\, \mathbf{1} = \frac{1}{3}\mathrm{tr}\boldsymbol{\sigma}\, \mathbf{1} \qquad \text{and} \qquad \tilde{\boldsymbol{\sigma}} = \boldsymbol{\sigma} - \overline{\boldsymbol{\sigma}}. \tag{2.21}$$

The quantity $\overline{\sigma}$ is commonly referred to as *mean stress*, while the scalar $p = -\overline{\sigma}$ is the *hydrostatic pressure*. A state of pure shear stress (deviatoric stress) is given if $\overline{\sigma} = 0$. While brittle materials are most likely to fail if the maximum principal normal stress σ_1, cf. (2.20), exceeds a certain limit, ductile materials (especially ductile metals) rather fail if the deviatoric stress becomes critical. Two common deviatoric scalar stress metrics are the maximum shear stress $\tau_{\max}$ and the

von Mises stress σ_{vM}:

$$\tau_{\max} = \frac{1}{2}|\sigma_1 - \sigma_3| \qquad \text{and} \qquad \sigma_{\mathrm{vM}} = \sqrt{3\mathit{II}_{\tilde{\sigma}}}, \tag{2.22}$$

where $\mathit{II}_{\tilde{\sigma}} = \frac{1}{2}\tilde{\sigma}_{ij}\tilde{\sigma}_{ij}$ is the second principal invariant of the deviatoric stress tensor $\tilde{\boldsymbol{\sigma}}$ (note that its first invariant vanishes per definition, $I_{\tilde{\sigma}} = \mathrm{tr}\tilde{\boldsymbol{\sigma}} = \tilde{\sigma}_{ii} = 0$).

A so-called *constitutive law* relates the state of stress to the state of deformation of the continuum body, and essentially has to fulfill the second law of thermodynamics. This may be stated in terms of the *Clausius-Planck inequality*, which for an isothermal process determines the mechanical dissipation and for a closed system reads

$$\mathcal{D}_{\mathrm{int}} = \boldsymbol{P} : \dot{\boldsymbol{F}} - \dot{\Psi} = \left(\boldsymbol{P} - \frac{\partial \Psi(\boldsymbol{F})}{\partial \boldsymbol{F}}\right) : \dot{\boldsymbol{F}} \geq 0, \tag{2.23}$$

where Ψ is the *Helmholtz free-energy function* (energy per unit reference volume) or simply the *strain energy function* when considering a purely mechanical process. For a *hyperelastic* material, no dissipative effects (meaning no effects of viscosity, plasticity or damage) occur and the mechanical process is reversible, i.e. $\mathcal{D}_{\mathrm{int}} = 0$. For the first and second Piola-Kirchhoff stress, the following constitutive relations hold:

$$\boldsymbol{P} = \frac{\partial \Psi}{\partial \boldsymbol{F}}, \quad \boldsymbol{S} = 2\frac{\partial \Psi}{\partial \boldsymbol{C}} = \frac{\partial \Psi}{\partial \boldsymbol{E}}. \tag{2.24}$$

The strain energy is a scalar-valued tensor function and has to satisfy the important properties $\Psi(\boldsymbol{1}) = 0$ (no energy in the undeformed state), $\Psi(\boldsymbol{F}) \geq 0$ (positivity of energy), $\Psi(\boldsymbol{QF}) = \Psi(\boldsymbol{F})$ (invariance of energy under rigid-body modes) and $\Psi(\boldsymbol{F}) \to \infty$ if $J = \det\boldsymbol{F} \to \infty$ or $J = \det\boldsymbol{F} \to 0$ (infinite amount of energy required for an infinitely large expansion or compression of the body).
For *isotropic* hyperelasticity and due to the fact that the scalar-valued tensor function Ψ remains invariant under rigid-body modes, it can be represented with the principal invariants of its argument, for example in terms of the right Cauchy-Green deformation tensor $\boldsymbol{C}$, $\Psi = \Psi(I_C, \mathit{II}_C, \mathit{III}_C)$, with

$$\left.\begin{aligned} I_C &= \mathrm{tr}\boldsymbol{C} = C_{ii}, \\ \mathit{II}_C &= \frac{1}{2}\left((\mathrm{tr}\boldsymbol{C})^2 - \mathrm{tr}(\boldsymbol{C}^2)\right) = \frac{1}{2}(C_{ii}^2 - C_{ij}C_{ij}), \\ \mathit{III}_C &= \det\boldsymbol{C} = \frac{1}{6}\mathcal{E}_{ijk}\mathcal{E}_{lmn}C_{il}C_{jm}C_{kn} = J^2, \end{aligned}\right\} \tag{2.25}$$

where $\mathcal{E}_{ijk} = (\hat{\boldsymbol{e}}_i \times \hat{\boldsymbol{e}}_j) \cdot \hat{\boldsymbol{e}}_k$ are the coordinates of the well-known third-order Levi-Civita permutation tensor $\boldsymbol{\mathcal{E}} = \mathcal{E}_{ijk}\,\hat{\boldsymbol{e}}_i \otimes \hat{\boldsymbol{e}}_j \otimes \hat{\boldsymbol{e}}_k$.

The constitutive equation for the second Piola-Kirchhoff stress $(2.24)_2$ then particularizes in

$$\boldsymbol{S} = 2\frac{\partial \Psi}{\partial \boldsymbol{C}} = 2\left[\left(\frac{\partial \Psi}{\partial I_C} + I_C\frac{\partial \Psi}{\partial \mathit{II}_C}\right)\boldsymbol{1} - \frac{\partial \Psi}{\partial \mathit{II}_C}\boldsymbol{C} + \mathit{III}_C\frac{\partial \Psi}{\partial \mathit{III}_C}\boldsymbol{C}^{-1}\right]. \tag{2.26}$$

If the material is meant to be incompressible, an additional constraint $J = \mathit{III}_C = 1$ has to be incorporated into the constitutive equations:

$$\Psi = \Psi\left(I_C, \mathit{II}_C\right) - \frac{1}{2}p(\mathit{III}_C - 1), \quad \boldsymbol{S} = -p\boldsymbol{C}^{-1} + 2\left(\frac{\partial \Psi}{\partial I_C} + I_C\frac{\partial \Psi}{\partial \mathit{II}_C}\right)\mathbf{1} - 2\frac{\partial \Psi}{\partial \mathit{II}_C}\boldsymbol{C}, \tag{2.27}$$

where p is the Lagrange multiplier guaranteeing the constraint $\mathit{III}_C = 1$ and may be identified as the hydrostatic pressure.

Compressible isotropic hyperelasticity may be treated by a split of the deformation into an isochoric and volumetric part, $\boldsymbol{F} = (J^{1/3}\mathbf{1})\bar{\boldsymbol{F}} = J^{1/3}\bar{\boldsymbol{F}}$ and $\boldsymbol{C} = (J^{2/3}\mathbf{1})\bar{\boldsymbol{C}} = J^{2/3}\bar{\boldsymbol{C}}$,

$$\begin{aligned} \Psi(\boldsymbol{C}) &= \bar{\Psi}(\bar{\boldsymbol{C}}) + \Psi_{\mathrm{vol}}(J), \\ \Psi\left(I_C, \mathit{II}_C, \mathit{III}_C\right) &= \bar{\Psi}(\bar{I}_C, \bar{\mathit{II}}_C) + \Psi_{\mathrm{vol}}(J), \end{aligned} \tag{2.28}$$

with the modified (isochoric) invariants

$$\bar{I}_C = J^{-2/3}I_C, \quad \bar{\mathit{II}}_C = J^{-4/3}\mathit{II}_C \quad \text{and} \quad \bar{\mathit{III}}_C = 1. \tag{2.29}$$

In contrast to the Lagrange multiplier approach (2.27) with strict enforcement of the incompressibility constraint, (2.28) rather may be viewed as a penalty approach, where near-incompressible behavior can be achieved with Ψ_{vol} being appropriately large.

When dealing with *anisotropic hyperelasticity*, the strain energy becomes a function of the deformation and of one or more preferred directions, for example for two families of fibers with directions $\boldsymbol{f}_0$ and $\boldsymbol{s}_0$ in the reference configuration:

$$\Psi = \Psi(\boldsymbol{C}, \boldsymbol{f}_0 \otimes \boldsymbol{f}_0, \boldsymbol{s}_0 \otimes \boldsymbol{s}_0) = \Psi(\boldsymbol{Q}\boldsymbol{C}\boldsymbol{Q}^{\mathrm{T}}, \boldsymbol{Q}\boldsymbol{f}_0 \otimes \boldsymbol{f}_0\boldsymbol{Q}^{\mathrm{T}}, \boldsymbol{Q}\boldsymbol{s}_0 \otimes \boldsymbol{s}_0\boldsymbol{Q}^{\mathrm{T}}). \tag{2.30}$$

The strain energy Ψ is a scalar-valued isotropic tensor function obeying (2.30) if it is, additionally to invariants (2.25), a function of the set of so-called *pseudo-invariants*

$$\left.\begin{aligned} \mathit{IV}_f &= \boldsymbol{f}_0 \cdot \boldsymbol{C}\boldsymbol{f}_0 \equiv \mathit{IV}, & \mathit{IV}_s &= \boldsymbol{s}_0 \cdot \boldsymbol{C}\boldsymbol{s}_0 \equiv \mathit{VI}, \\ V_f &= \boldsymbol{f}_0 \cdot \boldsymbol{C}^2\boldsymbol{f}_0 \equiv V, & V_s &= \boldsymbol{s}_0 \cdot \boldsymbol{C}^2\boldsymbol{s}_0 \equiv \mathit{VII}, \\ \mathit{VIII}_{fs} &= \boldsymbol{f}_0 \cdot \boldsymbol{C}\boldsymbol{s}_0 \equiv \mathit{VIII}, & \mathit{IX}_{fs} &= (\boldsymbol{f}_0 \cdot \boldsymbol{s}_0)^2 \equiv \mathit{IX}. \end{aligned}\right\} \tag{2.31}$$

The invariants IV and VI correspond to the squared stretches in fiber direction. The invariant IX does not depend on the deformation and can be omitted for the formulation of strain energy functions.

The constitutive equation for the second Piola-Kirchhoff stress then generalizes to

$$\begin{aligned} \boldsymbol{S} = 2\frac{\partial \Psi}{\partial \boldsymbol{C}} = 2\Bigg[&\left(\frac{\partial \Psi}{\partial I_C} + I_C\frac{\partial \Psi}{\partial \mathit{II}_C}\right)\mathbf{1} - \frac{\partial \Psi}{\partial \mathit{II}_C}\boldsymbol{C} + \mathit{III}_C\frac{\partial \Psi}{\partial \mathit{III}_C}\boldsymbol{C}^{-1} + \\ &+ \frac{\partial \Psi}{\partial \mathit{IV}}\boldsymbol{f}_0 \otimes \boldsymbol{f}_0 + \frac{\partial \Psi}{\partial V}\left(\boldsymbol{f}_0 \otimes \boldsymbol{C}\boldsymbol{f}_0 + \boldsymbol{f}_0\boldsymbol{C} \otimes \boldsymbol{f}_0\right) + \frac{\partial \Psi}{\partial \mathit{VI}}\boldsymbol{s}_0 \otimes \boldsymbol{s}_0 + \\ &+ \frac{\partial \Psi}{\partial \mathit{VII}}\left(\boldsymbol{s}_0 \otimes \boldsymbol{C}\boldsymbol{s}_0 + \boldsymbol{s}_0\boldsymbol{C} \otimes \boldsymbol{s}_0\right) + \frac{1}{2}\frac{\partial \Psi}{\partial \mathit{VIII}}\left(\boldsymbol{f}_0 \otimes \boldsymbol{s}_0 + \boldsymbol{s}_0 \otimes \boldsymbol{f}_0\right)\Bigg]. \end{aligned} \tag{2.32}$$

If the matrix material is incompressible, $\mathit{III}_C \equiv 1$, the constitutive equation for $\boldsymbol{S}$ has a similar form to $(2.27)_2$, with the additional derivatives with respect to the pseudo-invariants from (2.32). For a compressible matrix material, here only the *isotropic part* $\Psi^{(isotr)}$ of the strain energy obeys the volumetric-deviatoric split [181] [1]

$$\Psi = \bar{\Psi}^{(isotr)}(\bar{I}_C, \bar{\mathit{II}}_C) + \Psi^{(aniso)}(\mathit{IV}, V, \mathit{VI}, \mathit{VII}, \mathit{VIII}) + \Psi^{(isotr)}_{\mathrm{vol}}(J). \tag{2.33}$$

The tangent to the stress-strain relationship may be seen as the material's (deformation-dependent) stiffness and plays an ubiquitous role when solving problems in the nonlinear realm with help of Newton-type iterative methods, cf. sec. 3.1.3. It is represented by the fourth-order tensor

$$\mathbb{C} = 2\frac{\partial \boldsymbol{S}}{\partial \boldsymbol{C}} = \frac{\partial \boldsymbol{S}}{\partial \boldsymbol{E}} = \mathbb{C}_{ijkl}\, \hat{\boldsymbol{e}}_i \otimes \hat{\boldsymbol{e}}_j \otimes \hat{\boldsymbol{e}}_k \otimes \hat{\boldsymbol{e}}_l, \tag{2.34}$$

also called the elasticity tensor in the material description. It always possesses so-called minor symmetries $\mathbb{C}_{ijkl} = \mathbb{C}_{jikl} = \mathbb{C}_{ijlk}$.
If the constitutive equation for the stress relies on a strain energy density, i.e. if the material is of hyperelastic nature (2.24), the elasticity tensor may be formulated as

$$\mathbb{C} = 4\frac{\partial^2 \Psi}{\partial \boldsymbol{C} \partial \boldsymbol{C}} = \frac{\partial^2 \Psi}{\partial \boldsymbol{E} \partial \boldsymbol{E}}. \tag{2.35}$$

In this case, $\mathbb{C}$ additionally possesses major symmetries $\mathbb{C}_{ijkl} = \mathbb{C}_{klij}$.

2.1.1.3 Balance equations

Conservation of mass For a closed mechanical system, the total mass m of the body is conserved, yielding the conservation of mass written either in the current or material configuration:

$$\frac{\mathrm{d}m}{\mathrm{d}t} = \frac{\mathrm{d}}{\mathrm{d}t}\int_{\Omega} \rho \,\mathrm{d}v = \int_{\Omega} (\dot{\rho} + \rho\, \boldsymbol{\nabla} \cdot \boldsymbol{v}) \mathrm{d}v = \frac{\mathrm{d}}{\mathrm{d}t}\int_{\Omega_0} \rho_0 \,\mathrm{d}V = \int_{\Omega_0} \dot{\rho}_0 \,\mathrm{d}V = 0, \tag{2.36}$$

where ρ is the spatial and $\rho_0 = J\rho$ the reference mass density. Since (2.36) has to hold for an arbitrary volume, conservation of mass in its local forms has to hold identically:

$$\dot{\rho} + \rho\, \boldsymbol{\nabla} \cdot \boldsymbol{v} = 0 \qquad \text{and} \qquad \dot{\rho}_0 = 0. \tag{2.37}$$

Balance of linear and angular momentum The balance of linear and angular momentum in continuum mechanics are the generalized versions of Newton's first and second law of motion. They state that the rate of change of linear (angular) momentum has to equal the sum of external

[1] In contrast to decoupled representations for compressible anisotropic materials according to [88], where the isochoric-voluemtric split is also applied to the pseudo-invariants (2.31), Sansour [181] concludes that for anisotropic fiber-reinforced materials, the split should be applied to the matrix material only. This is due to the fact that otherwise, the stress in the fibers would not contribute to the spherical part of the stress tensor $(2.21)_1$. This seems non-physical since a spherical state of stress causing deformation of the whole material should also produce stresses in the fibers. Furthermore, fiber stresses are expected to be of one-dimensional nature, which loses its validity when applying the split to the fibers, too.

forces (moments) acting on the body.
The balance of linear momentum in spatial description yields

$$\frac{\mathrm{d}}{\mathrm{d}t}\int\limits_{\Omega}\rho\boldsymbol{v}\,\mathrm{d}v=\int\limits_{\Omega}\hat{\boldsymbol{b}}\,\mathrm{d}v+\int\limits_{\Gamma}\hat{\boldsymbol{t}}\,\mathrm{d}a. \tag{2.38}$$

After application of Cauchy's theorem (2.16) and Gauss' divergence theorem,

$$\int\limits_{\Omega}\rho\boldsymbol{a}\,\mathrm{d}v=\int\limits_{\Omega}(\boldsymbol{\nabla}\cdot\boldsymbol{\sigma}+\hat{\boldsymbol{b}})\,\mathrm{d}v \tag{2.39}$$

is obtained. Analogously, (2.39) can be written with respect to the material configuration:

$$\int\limits_{\Omega_0}\rho_0\boldsymbol{a}\,\mathrm{d}V=\int\limits_{\Omega_0}(\boldsymbol{\nabla}_0\cdot\boldsymbol{P}+\hat{\boldsymbol{b}}_0)\,\mathrm{d}V. \tag{2.40}$$

Again, both expressions (2.39), (2.40) have to hold for an arbitrary volume, yielding their local forms, known as *Cauchy's first law of motion*:

$$\rho\dot{\boldsymbol{v}}=\boldsymbol{\nabla}\cdot\boldsymbol{\sigma}+\hat{\boldsymbol{b}}\qquad\text{and}\qquad\rho_0\dot{\boldsymbol{v}}=\boldsymbol{\nabla}_0\cdot(\boldsymbol{F}\boldsymbol{S})+\hat{\boldsymbol{b}}_0, \tag{2.41}$$

where (2.19) has been made use of.

The balance of angular momentum in spatial description with respect to a fixed origin $\mathbf{0}$ is

$$\begin{aligned}\frac{\mathrm{d}}{\mathrm{d}t}\int\limits_{\Omega}\boldsymbol{x}\times\rho\boldsymbol{v}\,\mathrm{d}v&=\int\limits_{\Omega}\boldsymbol{x}\times\hat{\boldsymbol{b}}\,\mathrm{d}v+\int\limits_{\Gamma}\boldsymbol{x}\times\hat{\boldsymbol{t}}\,\mathrm{d}a &(2.42)\\&=\int\limits_{\Omega}\boldsymbol{x}\times\hat{\boldsymbol{b}}\,\mathrm{d}v+\int\limits_{\Gamma}\boldsymbol{x}\times\boldsymbol{\sigma}\boldsymbol{n}\,\mathrm{d}a\\&=\int\limits_{\Omega}\boldsymbol{x}\times\hat{\boldsymbol{b}}\,\mathrm{d}v+\int\limits_{\Omega}\left(\boldsymbol{x}\times(\boldsymbol{\nabla}\cdot\boldsymbol{\sigma})+\boldsymbol{\mathcal{E}}:\boldsymbol{\sigma}^{\mathrm{T}}\right)\mathrm{d}v, &(2.43)\end{aligned}$$

having made use of the property $\int_a \boldsymbol{w}\times\boldsymbol{A}\boldsymbol{n}\,\mathrm{d}a=\int_v\left(\boldsymbol{w}\times(\boldsymbol{\nabla}\cdot\boldsymbol{A})+\boldsymbol{\mathcal{E}}:(\boldsymbol{\nabla}\otimes\boldsymbol{w})\boldsymbol{A}^{\mathrm{T}}\right)\mathrm{d}v$ where $\boldsymbol{A}$ is some second-order tensor, $\boldsymbol{w}$ an arbitrary vector field and $\boldsymbol{n}$ a unit outward normal. Inserting $(2.41)_1$ into re-arranged (2.43) leads to the local form particularizing in the symmetry of the Cauchy stress tensor, also known as *Cauchy's second law of motion*:

$$\boldsymbol{\mathcal{E}}:\boldsymbol{\sigma}^{\mathrm{T}}=\mathbf{0}\quad\text{or}\quad\mathcal{E}_{ijk}\sigma_{kj}=0,\quad\Rightarrow\boldsymbol{\sigma}=\boldsymbol{\sigma}^{\mathrm{T}}\quad\text{or}\quad\sigma_{ij}=\sigma_{ji}. \tag{2.44}$$

For the sake of completeness, the balance of angular momentum in material description as equivalence to (2.42) is stated and reads

$$\frac{\mathrm{d}}{\mathrm{d}t}\int\limits_{\Omega_0}\boldsymbol{x}\times\rho_0\boldsymbol{v}\,\mathrm{d}V=\int\limits_{\Omega_0}\boldsymbol{x}\times\hat{\boldsymbol{b}}_0\,\mathrm{d}V+\int\limits_{\Gamma_0}\boldsymbol{x}\times\hat{\boldsymbol{t}}_0\,\mathrm{d}A. \tag{2.45}$$

Note that similar symmetry observations may be deduced from (2.45) by re-writing $\int_{\Gamma_0} \boldsymbol{x} \times \hat{\boldsymbol{t}}_0 \, \mathrm{d}A = \int_{\Gamma_0} \boldsymbol{x} \times \boldsymbol{P}\boldsymbol{n}_0 \, \mathrm{d}A = \int_{\Omega_0} \left(\boldsymbol{x} \times (\boldsymbol{\nabla}_0 \cdot \boldsymbol{P}) + \boldsymbol{\mathcal{E}} : (\boldsymbol{\nabla}_0 \otimes \boldsymbol{x}) \boldsymbol{P}^{\mathrm{T}} \right) \mathrm{d}V$. After insertion of $(2.41)_2$ into the re-written form of (2.45), $\boldsymbol{\mathcal{E}} : (\boldsymbol{\nabla}_0 \otimes \boldsymbol{x}) \boldsymbol{P}^{\mathrm{T}} = \boldsymbol{\mathcal{E}} : (\boldsymbol{F}\boldsymbol{P}^{\mathrm{T}}) = \boldsymbol{0}$ follows analogously to $(2.44)_1$, where the symmetry of the so-called Kirchhoff stress $\boldsymbol{\tau} = \boldsymbol{P}\boldsymbol{F}^{\mathrm{T}} = J\boldsymbol{\sigma}$ and thus that one of the Cauchy stress is shown equivalently to (2.43). Note further however that the first Piola-Kirchhoff stress $\boldsymbol{P}$ is not symmetric.

Balance of mechanical energy For a purely mechanical system, the balance of energy is a direct consequence of Cauchy's first law of motion and is stated here for the sake of completeness, however its local forms do not provide additional information compared to (2.41).
Its spatial representation reads

$$\frac{\mathrm{d}}{\mathrm{d}t} \int_{\Omega} \frac{1}{2} \rho \boldsymbol{v}^2 \, \mathrm{d}v + \int_{\Omega} \boldsymbol{\sigma} : \boldsymbol{\gamma} \, \mathrm{d}v = \int_{\Gamma} \hat{\boldsymbol{t}} \cdot \boldsymbol{v} \, \mathrm{d}a + \int_{\Omega} \hat{\boldsymbol{b}} \cdot \boldsymbol{v} \, \mathrm{d}v, \tag{2.46}$$

with the symmetric part of the spatial velocity gradient

$$\boldsymbol{\gamma} = \frac{1}{2} \left(\boldsymbol{\nabla} \otimes \boldsymbol{v} + (\boldsymbol{\nabla} \otimes \boldsymbol{v})^{\mathrm{T}} \right). \tag{2.47}$$

In material description, (2.46) is expressed as

$$\frac{\mathrm{d}}{\mathrm{d}t} \int_{\Omega_0} \frac{1}{2} \rho_0 \boldsymbol{v}^2 \, \mathrm{d}V + \int_{\Omega_0} J\boldsymbol{\sigma} : \boldsymbol{\gamma} \, \mathrm{d}V = \int_{\Gamma_0} \hat{\boldsymbol{t}}_0 \cdot \boldsymbol{v} \, \mathrm{d}A + \int_{\Omega_0} \hat{\boldsymbol{b}}_0 \cdot \boldsymbol{v} \, \mathrm{d}V. \tag{2.48}$$

Note that the stress power or rate of internal mechanical work may be alternatively expressed: $\int_{\Omega_0} J\boldsymbol{\sigma} : \boldsymbol{\gamma} \, \mathrm{d}V = \int_{\Omega_0} \boldsymbol{P} : \dot{\boldsymbol{F}} \, \mathrm{d}V = \int_{\Omega_0} \boldsymbol{S} : \dot{\boldsymbol{E}} \, \mathrm{d}V = \int_{\Omega_0} \boldsymbol{S} : \frac{1}{2} \dot{\boldsymbol{C}} \, \mathrm{d}V$.

2.1.1.4 Initial boundary value problem and variational principles

In order to address problems in nonlinear continuum mechanics, the solution of an initial boundary value problem in the time span $t \in [0, T]$ of the type

$$\boldsymbol{\nabla}_0 \cdot \boldsymbol{P} + \hat{\boldsymbol{b}}_0 = \rho_0 \ddot{\boldsymbol{u}} \qquad \text{in } \Omega_0 \times [0, T], \tag{2.49}$$

$$\boldsymbol{u} = \hat{\boldsymbol{u}} \qquad \text{on } \Gamma_0^{\mathrm{D}} \times [0, T], \tag{2.50}$$

$$\boldsymbol{t}_0 = \boldsymbol{P}\boldsymbol{n}_0 = \hat{\boldsymbol{t}}_0 \qquad \text{on } \Gamma_0^{\mathrm{N}} \times [0, T], \tag{2.51}$$

$$\boldsymbol{u}(\boldsymbol{x}_0, 0) = \hat{\boldsymbol{u}}_0(\boldsymbol{x}_0) \qquad \text{in } \Omega_0, \tag{2.52}$$

$$\dot{\boldsymbol{u}}(\boldsymbol{x}_0, 0) = \hat{\boldsymbol{v}}_0(\boldsymbol{x}_0) \qquad \text{in } \Omega_0, \tag{2.53}$$

has to be found, here formulated with respect to the material (known) configuration, which is common practice in solid mechanics. The partial differential equation (2.49), being the local balance of linear momentum in the material description $(2.41)_2$, is subject to initial and boundary conditions (on the Dirichlet and Neumann boundaries Γ_0^{D} and Γ_0^{N}, cf. fig. 2.1). In order to close the system, a constitutive equation connecting kinetic and kinematic quantities, here in terms of $\boldsymbol{P}$ and $\boldsymbol{u}$, is needed, for example (2.24), with the kinematics being described by some suitable

deformation measure, e.g. (2.12). The set of equations (2.49)–(2.53) is called the *strong form* of the initial boundary value problem, since it requires the point-wise fulfillment of the partial differential equation (2.49).

Multiplying (2.49) by a smooth arbitrary so-called *test function* or *weighting function* $\boldsymbol{\phi} = \boldsymbol{\phi}(\boldsymbol{x}_0)$ with the property that it has to vanish on the boundary Γ_0^{D}, $\boldsymbol{\phi} = \boldsymbol{0}$, and integrating over the domain Ω_0, the *weak form* of Cauchy's first law of motion with respect to the material configuration is obtained:

$$\int_{\Omega_0} (-\boldsymbol{\nabla}_0 \cdot \boldsymbol{P} - \hat{\boldsymbol{b}}_0 + \rho_0 \ddot{\boldsymbol{u}}) \cdot \boldsymbol{\phi} \, \mathrm{d}V = 0, \tag{2.54}$$

with the initial conditions $\int_{\Omega_0} \boldsymbol{u}(\boldsymbol{x}_0, 0) \cdot \boldsymbol{\phi} \, \mathrm{d}V = \int_{\Omega_0} \hat{\boldsymbol{u}}_0(\boldsymbol{x}_0) \cdot \boldsymbol{\phi} \, \mathrm{d}V$ and $\int_{\Omega_0} \dot{\boldsymbol{u}}(\boldsymbol{x}_0, 0) \cdot \boldsymbol{\phi} \, \mathrm{d}V = \int_{\Omega_0} \hat{\boldsymbol{v}}_0(\boldsymbol{x}_0) \cdot \boldsymbol{\phi} \, \mathrm{d}V$. Since no special requirements but that for the Dirichlet boundary have been set on the weighting function, $\boldsymbol{\phi}$ may be identified as the *first variation* of the displacement field $\boldsymbol{u}$, denoted by $\delta\boldsymbol{u} = \tilde{\boldsymbol{u}} - \boldsymbol{u} = (\boldsymbol{u} + \varepsilon\boldsymbol{w}) - \boldsymbol{u} = \varepsilon\boldsymbol{w}$, where $\boldsymbol{w}$ is some new vector field yielding a slightly perturbed configuration with respect to the actual displacement state $\boldsymbol{u}$, and $\varepsilon \to 0$. Thus, $\delta\boldsymbol{u}$ is arbitrary and infinitesimal and is called *virtual* displacement.

After insertion of Cauchy's stress theorem (2.16), the relation for the second Piola-Kirchhoff stress $\boldsymbol{S}$ (2.19), and application of Gauss' divergence theorem, (2.54) yields the well-known *principle of virtual work* in the material description:

$$\delta\mathcal{W} := \int_{\Omega_0} \rho_0 \ddot{\boldsymbol{u}} \cdot \delta\boldsymbol{u} \, \mathrm{d}V + \int_{\Omega_0} \boldsymbol{S} : \delta\boldsymbol{E} \, \mathrm{d}V - \int_{\Omega_0} \hat{\boldsymbol{b}}_0 \cdot \delta\boldsymbol{u} \, \mathrm{d}V - \int_{\Gamma_0^{\mathrm{N}}} \hat{\boldsymbol{t}}_0 \cdot \delta\boldsymbol{u} \, \mathrm{d}A = 0, \quad \forall \, \delta\boldsymbol{u}, \tag{2.55}$$

with the initial conditions $\int_{\Omega_0} \boldsymbol{u}(\boldsymbol{x}_0, 0) \cdot \delta\boldsymbol{u} \, \mathrm{d}V = \int_{\Omega_0} \hat{\boldsymbol{u}}_0(\boldsymbol{x}_0) \cdot \delta\boldsymbol{u} \, \mathrm{d}V$ and $\int_{\Omega_0} \dot{\boldsymbol{u}}(\boldsymbol{x}_0, 0) \cdot \delta\boldsymbol{u} \, \mathrm{d}V = \int_{\Omega_0} \hat{\boldsymbol{v}}_0(\boldsymbol{x}_0) \cdot \delta\boldsymbol{u} \, \mathrm{d}V$. Since the Neumann boundary conditions are already incorporated in (2.55), they are often referred to as *natural* boundary conditions, while the Dirichlet conditions are sometimes called *essential* boundary conditions. The differential equation associated with the variational form (2.55) is called *Euler-Lagrange equation*.
As for the stress power, the internal virtual work of the stress field along the virtual deformation field may be expressed alternatively: $\int_{\Omega_0} \boldsymbol{S} : \delta\boldsymbol{E} \, \mathrm{d}V = \int_{\Omega_0} \boldsymbol{P} : \delta\boldsymbol{F} \, \mathrm{d}V = \int_{\Omega} \boldsymbol{\sigma} : \delta\boldsymbol{e} \, \mathrm{d}v$. Stress and strain pairs of which the double contraction yields work per undeformed reference or deformed current volume are said to be *work-conjugate*.

The principle of virtual work (2.55) may also be formulated with respect to the current spatial configuration, which is omitted here. Furthermore, (2.55) may also be derived in a "top-down" manner requiring the stationarity of potential energy (in the quasi-static case, where $\ddot{\boldsymbol{u}} = \dot{\boldsymbol{u}} = \boldsymbol{0}$), meaning its first variation with respect to its kinematic variable $\boldsymbol{u}$ has to vanish. However, that approach would necessitate the existence of a potential both for the internal mechanical work (hyperelastic material, cf. sec. 2.1.1.2) as well as the external one (conservative loading). In contrast, the "bottom-up" derivation and therefore (2.55) holds for any class of materials and external loading conditions, since no special constitutive equation has been assumed for $\boldsymbol{S}$.

The advantage of the weak form over the strong form comes into play when (approximate) solutions of the initial boundary value problem, e.g. in the context of the finite element method are searched. The requirement of point-wise fulfillment of a partial differential equation is replaced by that of an integral weighted one, for which the differentiability requirements of the solution $\boldsymbol{u}$ have been weakened: After insertion of constitutive and kinematic relations, second-order spatial derivatives of the displacement are involved in (2.49), while (2.55) only captures first-order spatial derivatives of $\boldsymbol{u}$. Therefore, (2.55) is the starting point for a spatial discretization approach with the finite element method, which will be detailed in sec. 3.1.1.
Since the only field of unknowns in (2.55) is the displacement field $\boldsymbol{u}$, it is called a *single-field variational principle*. However, more general multi-field variational principles may be introduced with additional fields of unknowns, e.g. the hydrostatic pressure in the case of incompressible material behavior, or some kinematic quantity like the strain field. For a further treatment of this topic, the reader is referred to [88] and references therein.

2.1.1.5 Contact mechanics

A very brief introduction to contact and tied contact mechanics ("mesh tying") is given since these methods are applied in chap. 5 for the specific setting of a heart and a ventricular assist device. Details on contact mechanics may be found in Wriggers [217]. The computational concepts and methods that are used in this thesis here have been published by Popp et al. [162, 163], see also the thesis by Popp [161].
Figure 2.2 depicts a continuum mechanical setting of two bodies $\Omega_0^{[1]}$ and $\Omega_0^{[2]}$ subject to the motions $\boldsymbol{\chi}^{[1]}$ and $\boldsymbol{\chi}^{[2]}$, respectively. The focus is set exclusively on the contact problem – the description of Neumann and Dirichlet boundaries is omitted, cf. fig. 2.1. Both bodies are required to fulfill the continuum mechanics initial boundary value problem (2.49)–(2.53) presented in sec. 2.1.1.4.
In contact mechanics, the contact boundary of both bodies, $\Gamma_0^{\mathrm{c}[1]}$ and $\Gamma_0^{\mathrm{c}[2]}$, is a priori unknown, hence the actual contact happens in the *current configuration* with the current boundaries $\Gamma^{\mathrm{c}[1]}$ and $\Gamma^{\mathrm{c}[2]}$ that meet. Thus, the determination of what part of the body comes into contact with the other has to be performed during the nonlinear solution process and introduces an additional source of nonlinearity to the problem.
A quantity that measures the distance from a point of body $[1]$ to a normal projection of that point onto the boundary of body $[2]$ is the so-called *gap function*

$$g_{\mathrm{n}} = -\boldsymbol{n}^{\mathrm{c}} \cdot (\boldsymbol{x}^{[1]} - \check{\boldsymbol{x}}^{[2]}), \tag{2.56}$$

where $\boldsymbol{n}^{\mathrm{c}}$ is a current unit outward normal at the contact interface.

Classical methods in computational contact mechanics determine the point $\check{\boldsymbol{x}}^{[2]}$ by a closest point projection (in the computational sense referred to as node-to-segment strategies), while in the context of so-called *mortar* approaches, the point $\check{\boldsymbol{x}}^{[2]}$ is determined by a smooth mapping onto the surface $\Gamma^{\mathrm{c}[2]}$ (segment-to-segment approach). See [161] for details.

Balance of linear momentum requires that the tractions in the contact interface obey

$$\boldsymbol{t}^{\mathrm{c}[1]} = -\boldsymbol{t}^{\mathrm{c}[2]}. \tag{2.57}$$

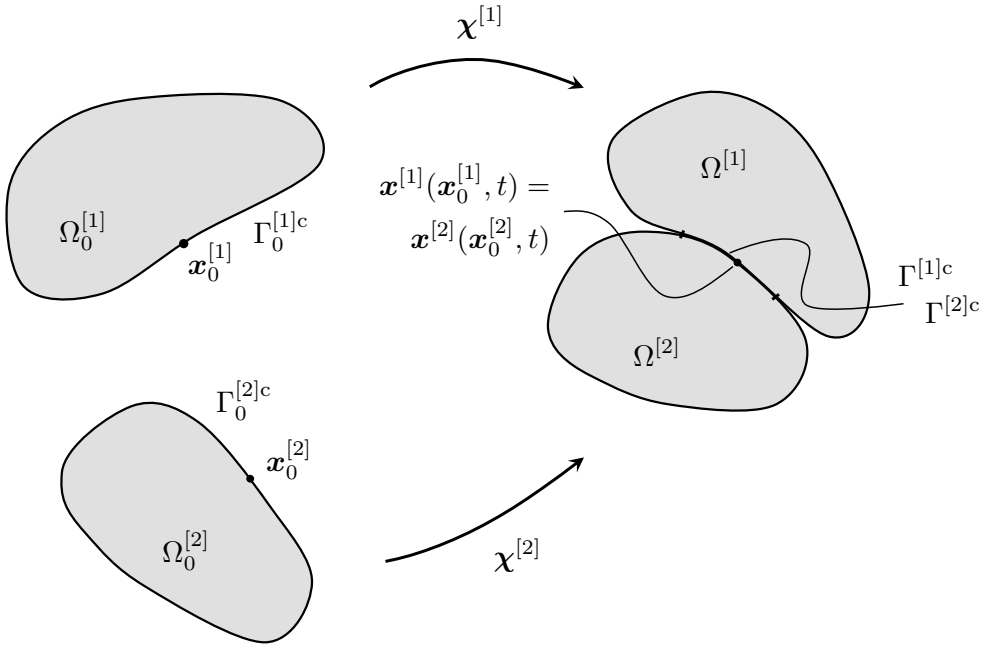

Figure 2.2: Contact (tied contact) continuum setting.

The contact traction may be split into a normal and a tangential component:

$$\boldsymbol{t}^{\mathrm{c}[1]} = p_{\mathrm{n}}\boldsymbol{n}^{\mathrm{c}} + \boldsymbol{t}_{\mathrm{t}}, \tag{2.58}$$

where p_{n} is the stress in normal direction (in non-adhesive contact, $p_{\mathrm{n}} \leq 0$) and $\boldsymbol{t}_{\mathrm{t}}$ the tangential traction vector.

Throughout this thesis, only *normal* (frictionless) contact (with vanishing tangential components in (2.58)), as well as tied contact are considered.

The (non-adhesive) normal contact constraint is formulated with the Karush-Kuhn-Tucker (KKT) conditions, requiring

$$g_{\mathrm{n}} \geq 0, \quad p_{\mathrm{n}} \leq 0, \quad p_{\mathrm{n}} p_{\mathrm{n}} = 0, \tag{2.59}$$

i.e. the gap (2.56) is either greater or equal to zero, while the normal traction is either zero or is negative.

For the tied contact case, it is typically assumed that the two bodies already meet and are tied in the reference configuration, deducing that $\Gamma_0^{\mathrm{c}[1]} = \Gamma_0^{\mathrm{c}[2]} \equiv \Gamma_0^{\mathrm{c}}$. The constraint simply requires the gap vector

$$\boldsymbol{g} = \boldsymbol{x}^{[1]} - \check{\boldsymbol{x}}^{[2]} \stackrel{!}{=} \boldsymbol{0} \tag{2.60}$$

to vanish.

Weak formulations of the contact and tied contact problem as well as their discretization and numerical solution strategies are omitted here with reference to the respective literature [161–163, 217].

2.1.2 Reduced-dimensional fluid models

Reduced-dimensional and lumped-parameter fluid dynamics models are a popular approach for describing blood flow mechanics in arteries. Here, basic concepts of 0-dimensional pressure-flow models are introduced since they form the backbone of all fluid mechanics analyses performed in this work.
A special focus is put on the so-called *windkessel* effect that the blood flow from the heart exhibits when entering the large arteries. In general, a windkessel may be viewed as a compliant chamber that transforms a pulsatile into a rather continuous steady flow by damping the oscillatory component of the wave to a certain extent. A classical example would be that of a pump and a spout, where the fluctuating component of the pulsatile flow is damped by an air chamber, leading to a regular flow at the outlet, cf. fig. 2.3a.
In physiology, the elastic arteries ("air chamber") cause a comparable effect on the pulsatile blood flow provided by the heart ("pump"), resulting in a steady flow in the peripheral parts of the body ("spout") guaranteeing non-interrupted organ perfusion. Figure 2.3b depicts the physiological analogy to the windkessel effect.

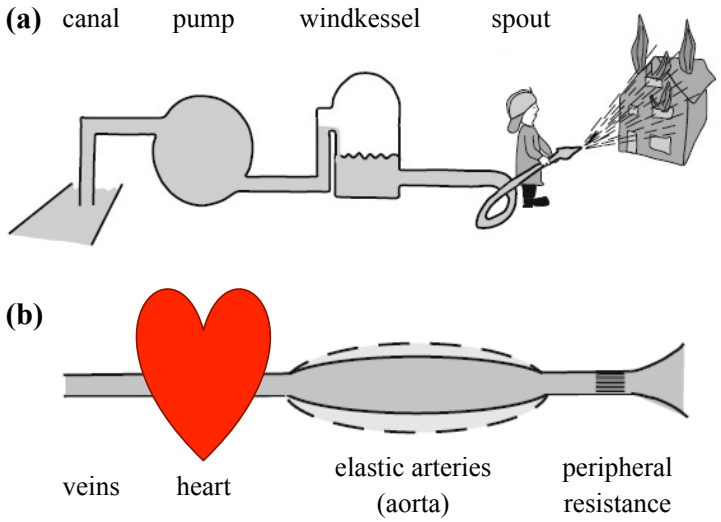

Figure 2.3: Modified from Westerhof et al. (2009) "The arterial windkessel" [210] (with permission). **(a)** Windkessel effect of an air chamber on the pulsatile flow of a pump, resulting in a rather continuous flow at the outlet (spout). **(b)** Physiological analogy, where the elastic arteries act as windkessel for the non-steady blood flow from the heart, leading to a regular non-interrupted flow in the periphery.

Windkessel models of blood flow in large arteries were first described by Hales [80] in the mid-18th and Frank [61] in the late 19th century. A recent overview of windkessel models used for describing blood flow in arteries is found in Westerhof et al. [210].

Here, a short introduction to these types of models is given, starting with a derivation of a 0-dimensional flow of incompressible fluid through a *rigid* vessel, with Poiseuille's relation [198] between pressure and flow as a special case thereof. The derivation follows a publication by Olufsen and Nadim [154].

Afterwards, the concept of *compliance* is introduced to these models, essentially then adding the actual windkessel effect by some assumption on the elasticity of the vessel. Some physiological backgrounds and mathematical perspectives of compliance in arteries may be found in Keener and Sneyd [102].

The 3-dimensional incompressible Navier-Stokes equations in Eulerian description follow from $(2.41)_1$ by use of (2.8) and read

$$\rho\left(\frac{\partial \boldsymbol{v}}{\partial t} + (\boldsymbol{\nabla}\otimes\boldsymbol{v})\,\boldsymbol{v}\right) = \boldsymbol{\nabla}\cdot\boldsymbol{\sigma} + \hat{\boldsymbol{b}}, \tag{2.61}$$

$$\boldsymbol{\nabla}\cdot\boldsymbol{v} = 0, \tag{2.62}$$

where $(2.37)_1$ with $\dot{\rho} = 0$ has been made use of. The Cauchy stress for a Newtonian fluid with kinematic viscosity ν is

$$\boldsymbol{\sigma} = -p\mathbf{1} + 2\nu\boldsymbol{\gamma}, \tag{2.63}$$

with p as the pressure and the shear rate tensor (2.47).

Now, axisymmetric unidirectional (hence 1-dimensional) flow of dynamic viscosity $\eta = \rho\nu$ in cylindrical coordinates r and z through a rigid straight vessel of length l_0 and radius r_0 shall be considered, cf. fig. 2.4.

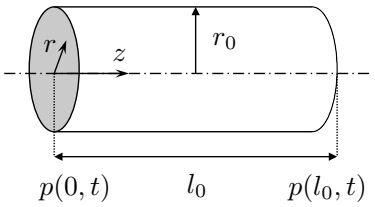

Figure 2.4: Rigid straight vessel of length l_0 and radius r_0.

After applying the coordinate transformation and the dimensional reduction to (2.61), the axisymmetric 1-dimensional Navier-Stokes equations read

$$\rho\frac{\partial v_z}{\partial t} + \frac{\partial p}{\partial z} - \frac{\eta}{r}\frac{\partial}{\partial r}\left(r\frac{\partial v_z}{\partial r}\right) = 0, \tag{2.64}$$

where the axial velocity v_z has been introduced.

Assuming that the velocity profile is independent of the axial coordinate z yields a linearly varying pressure over the length l_0, which can be written as

$$-\frac{\partial p}{\partial z} = \frac{p(0,t) - p(l_0,t)}{l_0} = \frac{\Delta p}{l_0}p^\star. \tag{2.65}$$

The non-dimensionalized pressure gradient is $p^\star$ and Δp is the characteristic change in pressure.

Writing (2.64) in non-dimensionalized form with

$$t^\star = \frac{t\nu}{r_0^2}, \quad r^\star = \frac{r}{r_0} \quad \text{and} \quad v_z^\star(r^\star, t^\star) = \frac{v_z(r_0, t) l_0 \eta}{\Delta p r_0^2} \tag{2.66}$$

yields

$$\frac{\partial v_z^\star}{\partial t^\star} - \frac{1}{r^\star}\frac{\partial v_z^\star}{\partial r^\star} - \frac{\partial^2 v_z^\star}{\partial r^{\star 2}} = p^\star(t^\star). \tag{2.67}$$

This equation then can be solved by applying a Laplace transformation

$$\mathcal{L}\{v_z^\star(r^\star, t^\star)\} = \int_0^\infty v_z^\star(r^\star, t^\star) e^{-st^\star} \mathrm{d}t^\star = \overline{v}_z^\star(r^\star, s), \tag{2.68}$$

yielding

$$\frac{\mathrm{d}^2 \overline{v}_z^\star}{\mathrm{d}r^{\star 2}} + \frac{1}{r^\star}\frac{\mathrm{d}\overline{v}_z^\star}{\mathrm{d}r^\star} + (\mathrm{i}\sqrt{s})^2 \overline{v}_z^\star = -\overline{p}^\star(s) \tag{2.69}$$

in the image domain. For no initial flow ($\overline{v}_z^\star(r^\star, 0) = 0$), the general solution of (2.69) is

$$\overline{v}_z^\star(r^\star, s) = c_1 J_0(\mathrm{i}\, r^\star \sqrt{s}) + c_2 Y_0(\mathrm{i}\, r^\star \sqrt{s}) + \frac{\overline{p}^\star(s)}{s}, \tag{2.70}$$

with arbitrary constants c_1 and c_2 and the zeroth-order Bessel functions J_0 and Y_0.

After exploiting the singularity of Y_0 at $r^\star = 0$ and applying no-slip boundary conditions $\overline{v}_z^\star(1, s) = 0$, the solution in terms of the dimension-less flow rate $\overline{q}^\star(s) = 2\pi \int_0^1 \overline{v}_z^\star(r^\star, s) r^\star \mathrm{d}r^\star$ reads

$$\overline{q}^\star(s) = \frac{\pi \overline{p}^\star(s)}{s}\left(1 - \frac{2J_1(\mathrm{i}\sqrt{s})}{\mathrm{i}\sqrt{s} J_0(\mathrm{i}\sqrt{s})}\right). \tag{2.71}$$

Back-transformation of (2.71) to the time domain yields

$$q^\star(t^\star) = \frac{\pi}{8} p^\star(t^\star) - 4\pi \sum_{n=1}^{\infty} \frac{f_n(t^\star)}{\beta_n^4}, \tag{2.72}$$

with

$$f_n(t^\star) = \int_0^{t^\star} e^{-\beta_n^2 (t^\star - \tilde{t}^\star)} p^{\star\prime}(\tilde{t}^\star) \mathrm{d}\tilde{t}^\star \tag{2.73}$$

and β_n as the roots of the Bessel function $J_0(\beta_n) = 0$ (first three: $\beta_1 \approx 2.40483$, $\beta_2 \approx 5.52008$ and $\beta_3 \approx 8.65373$).

The amount of terms included in the sum of (2.72) determines the order of the model. Here, exemplarily, only the 0th and 1st order solutions are presented.
For $n = 0$, the sum in (2.72) simply vanishes, and the dimensionless as well as re-dimensionalized pressure-flow relationships

$$q^\star = \frac{\pi}{8} p^\star \quad \Rightarrow \; q = \frac{\pi r_0^4}{8\eta l_0} p \tag{2.74}$$

are obtained. As can be seen, Poiseuille's pressure-flow relation of laminar steady flow in a rigid vessel, $p = Rq$, is recovered, where the fluid's *resistance* can be identified as

$$R = \frac{8\eta l_0}{\pi r_0^4}. \tag{2.75}$$

If accounting for a 1st-order model, the following solution for $n = 1$ is obtained:

$$\lambda_q \frac{\mathrm{d}q^\star}{\mathrm{d}t^\star} + q^\star = \frac{\pi}{8}\left(\lambda_p \frac{\mathrm{d}p^\star}{\mathrm{d}t^\star} + p^\star\right) \quad \Rightarrow \quad \frac{\lambda_q r_0^2}{\nu}\frac{\mathrm{d}q}{\mathrm{d}t} + q = \frac{\pi r_0^4}{8\eta l_0}\left(\frac{\lambda_p r_0^2}{\nu}\frac{\mathrm{d}p}{\mathrm{d}t} + p\right), \tag{2.76}$$

with $\lambda_q = \frac{1}{\beta_1^2} \approx 0.1729$ being interpretable as a relaxation time and $\lambda_p = \frac{1-\frac{32}{\beta_1^4}}{\beta_1^2} \approx 0.0075$ as a retardation time. Since $\lambda_p \ll \lambda_q$, the effect of change in pressure over time is significantly smaller than that of the pressure itself. Consequently, if that time is neglected ($\lambda_p \to 0$), $(2.76)_2$ becomes

$$\frac{\lambda_q r_0^2}{\nu}\frac{\mathrm{d}q}{\mathrm{d}t} + q = \frac{\pi r_0^4}{8\eta l_0} p. \tag{2.77}$$

As can be seen compared to Poiseuille's flow $(2.74)_2$, a time dependence of the flow has been introduced in (2.77). After re-arrangement isolating p, the factor in front of the time derivative consequently can be interpreted as an *inertance*

$$L = \frac{8\lambda_q \rho l_0}{\pi r_0^2}. \tag{2.78}$$

Re-writing (2.77) in terms of (2.75) and (2.78) yields a lumped-parameter balance of linear momentum:

$$L\frac{\mathrm{d}q}{\mathrm{d}t} + Rq = p. \tag{2.79}$$

Relation (2.79) is subsequently referred to as (0D) momentum balance and will be the basis of the pressure-flow relations that are used for modeling of vascular networks. However, it should be noted that either including λ_p in (2.76) or allowing for higher order solutions in (2.72) ($n > 1$), reduced-dimensional pressure-flow models of greater complexity may be derived. Especially for blood flow in vessels with a radius of $r_0 > 0.5\ \mathrm{cm}$, Olufsen and Nadim [154] deduce that at least a 2nd order model ($n = 2$) shall be used in order to adequately describe the temporal evolutions of pressure and flow.

The inclusion of compliance into 0D pressure-flow models in general is not straightforward when deriving the equations from basic fluid dynamics principles. There exist different concepts with a couple of underlying assumptions, e.g. the leakage approach by Berger [20] or the one by Keener and Sneyd [102], both being briefly discussed in [154].
To the contrary, 0D pressure-flow models have been derived from electrical circuit analogies by simply adding a capacitor (in the mechanical analogy, a compliance) to the aforementioned models. By viewing pressure as voltage and flow as current, the analogs of resistance and inertance virtually become resistance and *inductance*, and the inclusion of a capacitor does not hinder the consistent derivation of the corresponding electrical governing equations. Figure 2.5 shows the hydraulic and electric circuit analogies for a couple of well-established models: the Poiseuille flow,

the so-called *2-element windkessel* with a capacitor in parallel to the resistance, the *3-element windkessel* with an additional resistance in series in front of the 2-element windkessel, as well as the *4-element windkessel* according to [195], where an inductor has been added in parallel to the first resistance of the 3-element windkessel model.

The second resistance introduced in fig. 2.5c for the 3-element windkessel is often referred to as "aortic characteristic resistance" or "aortic characteristic *impedance*". Its introduction emerged from the fact that the 2-element windkessel model originally proposed by Frank [61] was suitable to describe aortic pressure decay in the diastole, but insufficiently approximated the systolic pressure over time. The characteristic impedance can be computed by the quotient of wave speed times blood density and the cross-sectional vessel area, hence it may be viewed as a link between lumped model behavior and aspects of wave transmission. This is further discussed by Westerhof et al. [210].
Stergiopulos et al. [195] concluded that an additional inductance in parallel to the aortic characteristic resistance – denoted as "total arterial inertance" – leads to better estimates of total arterial compliance.

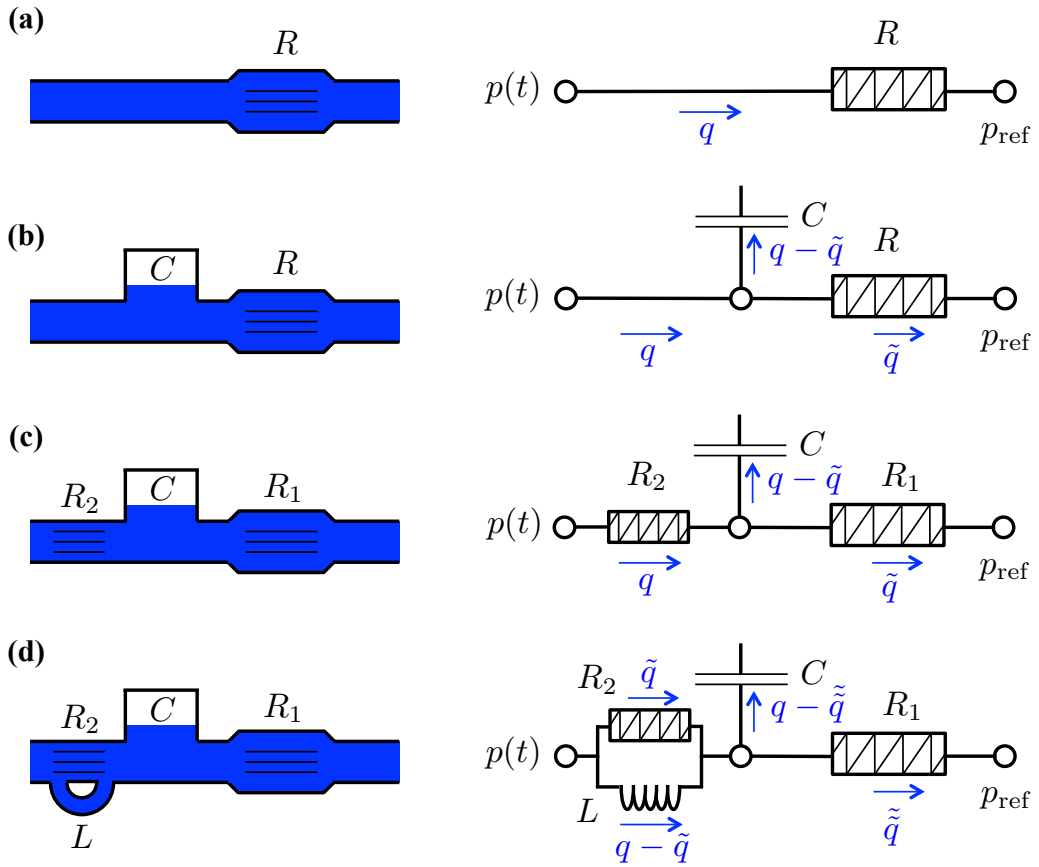

Figure 2.5: Hydraulic (left) and electric (right) circuit analogies of different lumped-parameter models. **(a)** Poiseuille flow. **(b)** 2-element windkessel. **(c)** 3-element windkessel. **(d)** 4-element windkessel according to [195].

The model in fig. 2.5a corresponds Poiseuille's flow $(2.74)_2$ and can be written as

$$\frac{p - p_{\mathrm{ref}}}{R} = q \tag{2.80}$$

considering a reference pressure p_{ref}.

Here, compliance in the mechanical sense is introduced by combining the momentum equation (2.79) with conservation of volume by allowing the volume V of the compartment (vessel) to change over time (similar to Berger [20]):

$$\frac{\mathrm{d}V}{\mathrm{d}t} = q_{\mathrm{in}} - q, \tag{2.81}$$

where q_{in} is the arriving (incoming) flux into the compartment. Now, a constitutive equation is needed to link the volume change to the pressure. In good approximation, a linear relationship between a change in volume ΔV as consequence of a change in pressure Δp may be assumed,

$$\Delta V = C \Delta p, \tag{2.82}$$

where C is the compliance of the vessel.

The 2-element windkessel equation (fig. 2.5b) then can be written as

$$C\frac{\mathrm{d}p}{\mathrm{d}t} + \frac{p - p_{\mathrm{ref}}}{R} = q \tag{2.83}$$

combining (2.81) and (2.82) with (2.79) for $L = 0$.

The equation for the 3-element windkessel (fig. 2.5c) reads

$$C\frac{\mathrm{d}p}{\mathrm{d}t} + \frac{p - p_{\mathrm{ref}}}{R_1} = \left(1 + \frac{R_2}{R_1}\right) q + R_2 C \frac{\mathrm{d}q}{\mathrm{d}t} \tag{2.84}$$

and can be derived by combining the 2-element windkessel (2.83) with conservation of volume (2.81) with $\dot{V} = 0$ and momentum (2.79) with $L = 0$ applied to the additional R_2-part.

Analogously, 4-element windkessel governing equations can be derived. The model according to [195] (fig. 2.5d) with the inertance parallel to R_2 yields

$$\frac{LC}{R_2}\frac{\mathrm{d}^2 p}{\mathrm{d}t^2} + \left(\frac{L}{R_1 R_2} + C\right)\frac{\mathrm{d}p}{\mathrm{d}t} + \frac{p - p_{\mathrm{ref}}}{R_1} = q + \left(\frac{L}{R_1} + \frac{L}{R_2}\right)\frac{\mathrm{d}q}{\mathrm{d}t} + LC\frac{\mathrm{d}^2 q}{\mathrm{d}t^2}. \tag{2.85}$$

However, if the inertance is in series to R_2, the governing equation reads

$$C\frac{\mathrm{d}p}{\mathrm{d}t} + \frac{p - p_{\mathrm{ref}}}{R_1} = \left(1 + \frac{R_2}{R_1}\right) q + \left(R_2 C + \frac{L}{R_1}\right)\frac{\mathrm{d}q}{\mathrm{d}t} + LC\frac{\mathrm{d}^2 q}{\mathrm{d}t^2}. \tag{2.86}$$

2.2 3D-0D coupled cardiovascular mechanics

A model for the simulation of the patient-specific heart interacting with the systemic and pulmonary circulation is developed. The primary, but not the exclusive driving force for the modeling assumptions chosen here originated from the endeavor to formulate integrative mathematical models and to establish state-of-the-art computational tools that serve the better understanding of heart failure and medical treatments thereof, especially by novel ventricular assist technologies, cf. chap. 5. This "application-driven" foundational research sets the scope for the requirements on the model in terms of feasibility, accuracy, predictability, and computational robustness and efficiency. Specifically, these are

- a patient-specific accurate 3-dimensional geometric representation of the myocardium accounting for anatomical particularities and rule-based generic but realistic fiber architecture, material behavior, and the prestressed state of the heart [68];

- considerations of the surrounding tissue in terms of visco-elastic support boundary conditions at the truncations from the body environmental tissue (arteries, veins, atrioventricular plane);

- a sophisticated accounting for the coupling of the heart to a closed systemic and pulmonary circulation in order to link active ventricular contraction properties (strength, duration) to relevant, experimentally observable, integral quantities such as cardiac output, pressures and flows for the homeostatic state of the cardiovascular system, necessitating adequate (here reduced-dimensional) flow models and a computational strategy to couple the different physics and dimensions (3-dimensional solid mechanics, 0-dimensional fluid flow);

- a reasonable parameterization of the model in terms of quantities that are directly relatable to physiological phenomena (contractile properties of the myocardium, resistive and compliant features of the vasculature that govern the afterload), and that allow for a meaningful parameter estimation procedure to be applied, cf. sec. 4; and

- a mathematical description that allows for robust and efficient computational coupling and solution schemes, in terms of both the nonlinear solver and the solver used for the linear system of equations that arises during Newton iteration, cf. chap. 3.

Especially the latter aspect is of uttermost importance since the mathematical modeling itself already has to look ahead and keep in mind the computational feasibility of addressing the problem at hand. Therefore, the description in terms of field equations, boundary conditions and coupling constraints should be derived in close interrelation with the development of the computational modeling methods. Chapter 3 will cope with all discretization- and solution-related aspects in order to solve the models presented here.
The combination of the above-mentioned items comprising a novel mathematical and subsequently, a computational model is elaborated in the following sections. The fundaments of the presented models are published in Hirschvogel et al. [86].

Two model variants for the patient-specific heart are established and may be employed depending on the specific question at hand:

- a 3D model of the left and right ventricular myocardium, which is truncated at a well-defined atrioventricular plane, subsequently denoted as *3Dventr*, and
- a 3D model comprising a structural resolution of all the four heart chambers, left and right ventricular, and left and right atrial myocardium, in the following denoted as *3Datrioventr*.

All modeling-related aspects, namely the segmentation of the heart from medical imaging, e.g. CT data, the construction of the geometric representation, i.e. the mathematical solution domain, and finally the formulation of the specific solid mechanical problem statement are dealt with in sec. 2.2.1.

Three model variants of the closed-loop vascular network that build upon another are considered:

- a basic circulation model that accounts for the whole arterial and the entire venous compartment of the systemic and pulmonary circulation by multi-element windkessel models, subsequently denoted as *0Dsyspul*;
- an extended circulation model that additionally takes into account the systemic and pulmonary capillary network, in the following denoted as *0Dsyspulcap*; and
- the extended capillary circulation model supplemented by a 0D oxygen and carbon dioxide transport and dissociation model, named *0Dsyspulcaprespir*.

The vasculature models are detailed in sec. 2.2.2.

The 3D heart and the 0D circulatory system are coupled in the sense that the circulation receives flow from the heart and returns pressure from the vasculature, which then acts onto the endocardial cavity lumen of the respective heart chamber. In order to adequately describe the coupling, the heart cavities have to allow for mathematical assessment of their volumes, hence their respective lumen has to form an enclosed surface area with respect to the surrounding. The coupling conditions between the 3D and the 0D model are expressed in sec. 2.2.3.

Figure 2.6 depicts the coupled model *3Dventr* | *0Dsyspul*, and fig. 2.7 shows the coupled model *3Datrioventr* | *0Dsyspulcap*. The models' primary variables are the structural displacement field $\boldsymbol{u}$ as well as vascular pressures p and fluxes q. Model *3Dventr* | *0Dsyspul*, besides slight technical modifications, is published in Hirschvogel et. al [86].

Little literature to date describes the coupling of a *closed-loop* vascular model to a *3D patient-specific* heart, the only known by the author is from Kerckhoffs et al. [104], while a similar closed circulation is coupled to some generic 3D heart model in Lumens et al. [131]. The models therein essentially differ to the ones presented here with respect to the mathematical formulation and the computational approach, which is detailed and discussed in chap. 3.
Also, closed-loop modeling of the cardiovascular system was addressed, for instance, by Neal et al. [147] or Blanco et al. [23], however not including a 3D patient-specific heart geometry. Veress et al. [206] coupled a systemic circulation as simplification of the model in [147] to a generic left ventricular geometry, similar to [150] or a recent contribution by Shavik et al. [189]. However, multiple models exist that couple single (non-connected) pre- and afterload 0D models to each

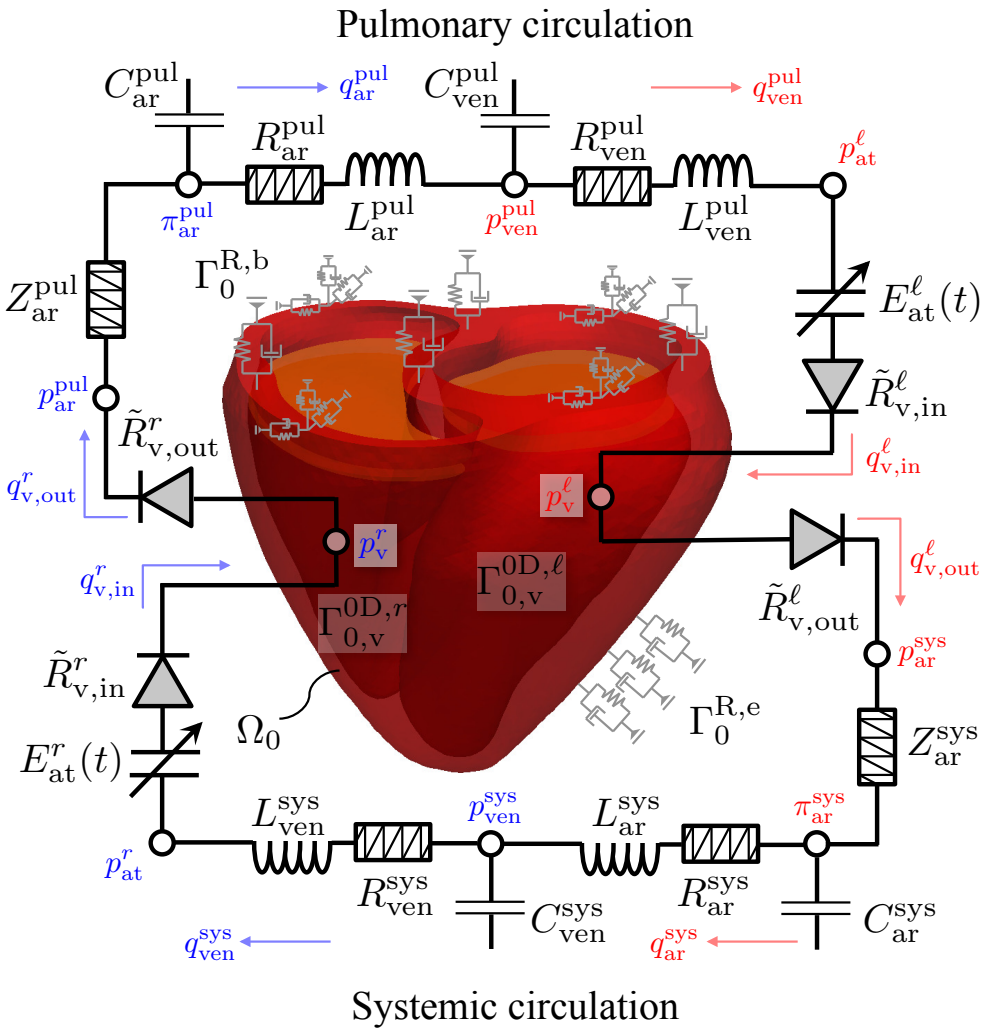

Figure 2.6: Model *3Dventr | 0Dsyspul*: Atria are modeled with time-varying elastances $E(t)$; circulation parameters are resistances R, compliances C, inertances L and impedances Z; circulation variables are pressures p, π and fluxes q; superscripts ℓ and r: left and right heart (ventricle, atrium); sys and pul: systemic and pulmonary circulation; subscripts v, at, ar and ven: "ventricular", "atrial", "arterial" and "venous".

the left and right ventricle of patient-specific hearts separately, cf. Sainte-Marie et al. [178] or Fritz et al. [62].

Furthermore, this is the first approach to couple all four cardiac chambers of a patient-specific 3D heart (*3Datrioventr*) to a closed circulation. Even though patient-specific 4-chamber geometries have been used in the literature to date, cf. again Fritz et al. [62] or the growth models by Genet et al. [71] which are to be discussed, these either use 0D pre- and afterload models for the ventricles only [62] or simply do account for the influence of the circulation just in terms of pressure boundary conditions [71]. Additionally, there are models with 4-chamber patient-specific geometries which exclusively deal with the electrophysiology of the heart, cf. Schenone et al. [183], which is not topic of this work here.

It should be noted that efforts also have been made modeling 3-dimensional fluid-structure interaction phenomena in the heart, cf. Watanabe et al. [209], Nordsletten et al. [151, 152] or Laadhari et al. [115]. Also models by Gao et al. [64, 65], Griffith et al. [76] and Astorino et al. [9] present approaches for heart valve modeling by help of immersed boundary methods. However, those approaches greatly increase the computational complexity and would violate the model requirements which have been stated initially.

The inclusion of oxygen and carbon dioxide transport and dissociation, and hence the extension of the *0Dsyspul* circulation model to account for capillary pressures and flows (*0Dsyspulcap*) was inspired by an integrative fully 0-dimensional model of the cardiorespiratory system by Trenhago et al. [202]. The approach therein is adopted from Christiansen and Dræby [41, 42] as well as from models by Ursino and Magosso [203, 204].
Due to the different time scales on the one hand of the cardiovascular mechanical and on the other of the respiratory and transport models in order to achieve periodicity, here the one-way coupling between these two models is exploited by a novel prescribed-dynamics approach to mimic the 3D heart in every phase of the cardiac cycle making use of the precomputed periodic pressure-volume data for each chamber. The one-way coupling and the prescribed-dynamics approach are dealt with in sec. 2.2.3.

Finally, the importance of homeostatic state solutions is highlighted, and the requirements for periodicity are stated in sec. 2.2.4.

2.2.1 3D (atrio-)ventricular solid mechanics model

2.2.1.1 Patient-specific segmentation and geometry construction

The heart is segmented from CT imaging data using MIMICS® software (Materialise.com). The time snapshot for segmentation is chosen to $80\ \%$ of the time span between two end-diastolic time instances (denoted by t_{ed}), hence $0.2 \cdot T_{\mathrm{cycl}}$ prior to ventricular excitation (contraction), with T_{cycl} being the duration of a complete cardiac cycle.

After segmentation and smoothing, three stereolithographic (STL) geometries are exported: the whole (atrio-)ventricular contour as bulk body, as well as the left and the right (atrio-)ventricular

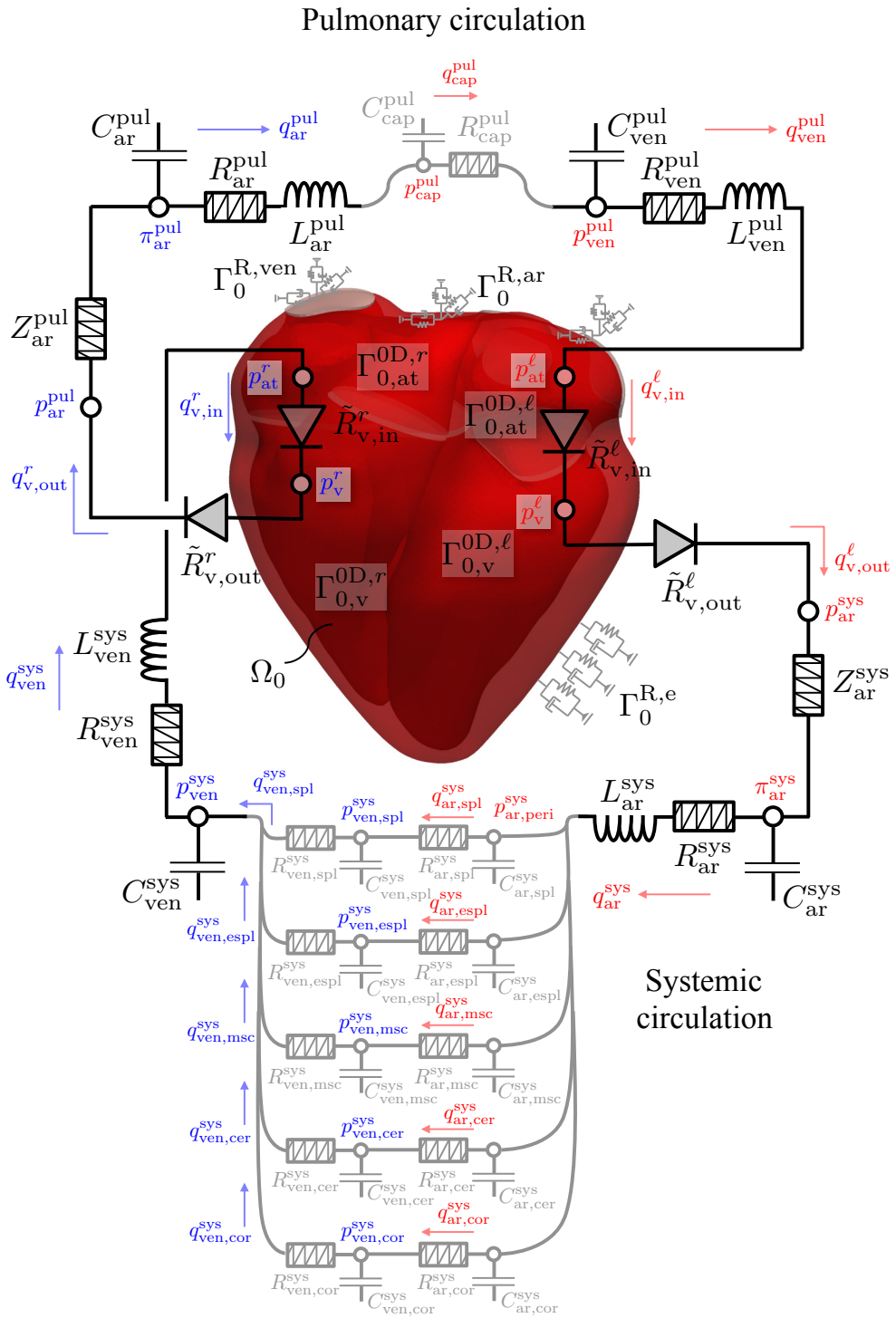

Figure 2.7: Model *3Datrioventr | 0Dsyspulcap*: Circulation parameters are resistances R, compliances C, inertances L and impedances Z; circulation variables are pressures p, π and fluxes q; superscripts ℓ and r: left and right heart (ventricle, atrium); sys and pul: systemic and pulmonary circulation; primary subscripts v, at, ar, ven and cap: "ventricular", "atrial", "arterial", "venous" and "capillary"; secondary subscripts peri, spl, espl, msc, cer and cor (for the systemic arterial capillaries): "peripheral", "splanchnic", "extra-splanchnic", "muscular", "cerebral" and "coronary".

lumina. Valves are not explicitly segmented. The process of model construction (and subsequent finite element meshing) is performed using TRELIS® software (csimsoft.com) with its respective Python interface. The chain from STL import to model output (including finite element meshing as well as the fiber incorporation, cf. the following section for the latter subject) is automatized and applicable to arbitrary patient-specific heart geometries. A condensed version of the whole process is depicted in fig. 2.8. When only accounting for the ventricular myocardium (*3Dventr*), all three STLs are cut at the atrioventricular plane (AVP), cf. its definition in fig. 2.8d. At that cut, covering lids are added and imprinted to the endocardium, and an extrusion of bulk material of $10\ \mathrm{mm}$ is performed at the heart base.

2.2.1.2 Idealized modeling of fiber and sheet directions

In order to adequately describe the heart muscle from a continuum mechanical point of view, it is essential to incorporate its anisotropy into the model for the description of both the passive and the active mechanical behavior. The muscle fiber, here denoted by the vector field $\boldsymbol{f}_0$, which is responsible for generating active contraction force during ventricular systole has a distinct alignment pattern that may differ significantly from one individual to the other. In general, the muscle fiber changes its orientation throughout the ventricular wall. Typically, on the epicardium, the muscle fiber has an inclination of -50° to -70° with respect to the circumference of the ventricles, and rotates to about 50° to 70° on the endocardial wall.
Furthermore, the heart is considered to exhibit orthotropic passive material behavior [54, 89], hence a second sheet direction that stands orthogonal to the muscle fiber direction is introduced, here denoted by the vector field $\boldsymbol{s}_0$. The plane spanned by the two distinct directions is assumed to be parallel to the vessel wall, even though this idealization does not strictly hold, cf. the annotations in [89]. A more detailed characterization of the morphology of the heart may be found in there and in [123]. Early experimental characterizations of the heart's fiber architecture were published by Streeter et al. [196].
Magnetic resonance tomography may be used to determine the patient-specific myocardial muscle fiber orientations [93], and efforts have been made of incorporating that individual information into computational heart models [145]. However, data is rare and the estimation procedures not well-established, which is why a rule-based fiber model is used for all patient-specific heart geometries throughout this thesis. Specifically, the fiber direction is assumed to vary from -60° on the epicardium to 60° on the endocardium with respect to the ventricles' circumferential direction. The sheet direction is assumed accordingly, however with an angular shift of $+90^\circ$ on both surfaces.
Technically, the fiber and sheet angles are prescribed on the respective surfaces, and a Poisson problem is solved on the then discretized heart in order to obtain a smooth transition throughout the ventricular wall [145, 216]. Figures 2.9 and 2.10 depict an anterior and a posterior view, respectively, each for both heart models *3Dventr* and *3Datrioventr*.
The muscle fiber direction $\boldsymbol{f}_0$ is shown in green, and the sheet direction $\boldsymbol{s}_0$ is shown in light-grey.

The myofiber orientation in the atria is rather complex and consists of multiple layers and bundles. Even though there have been efforts to generate rule-based atria-specific fiber orientation patterns for computational models focusing on the atrial electrophysiology [91, 92, 112], here these

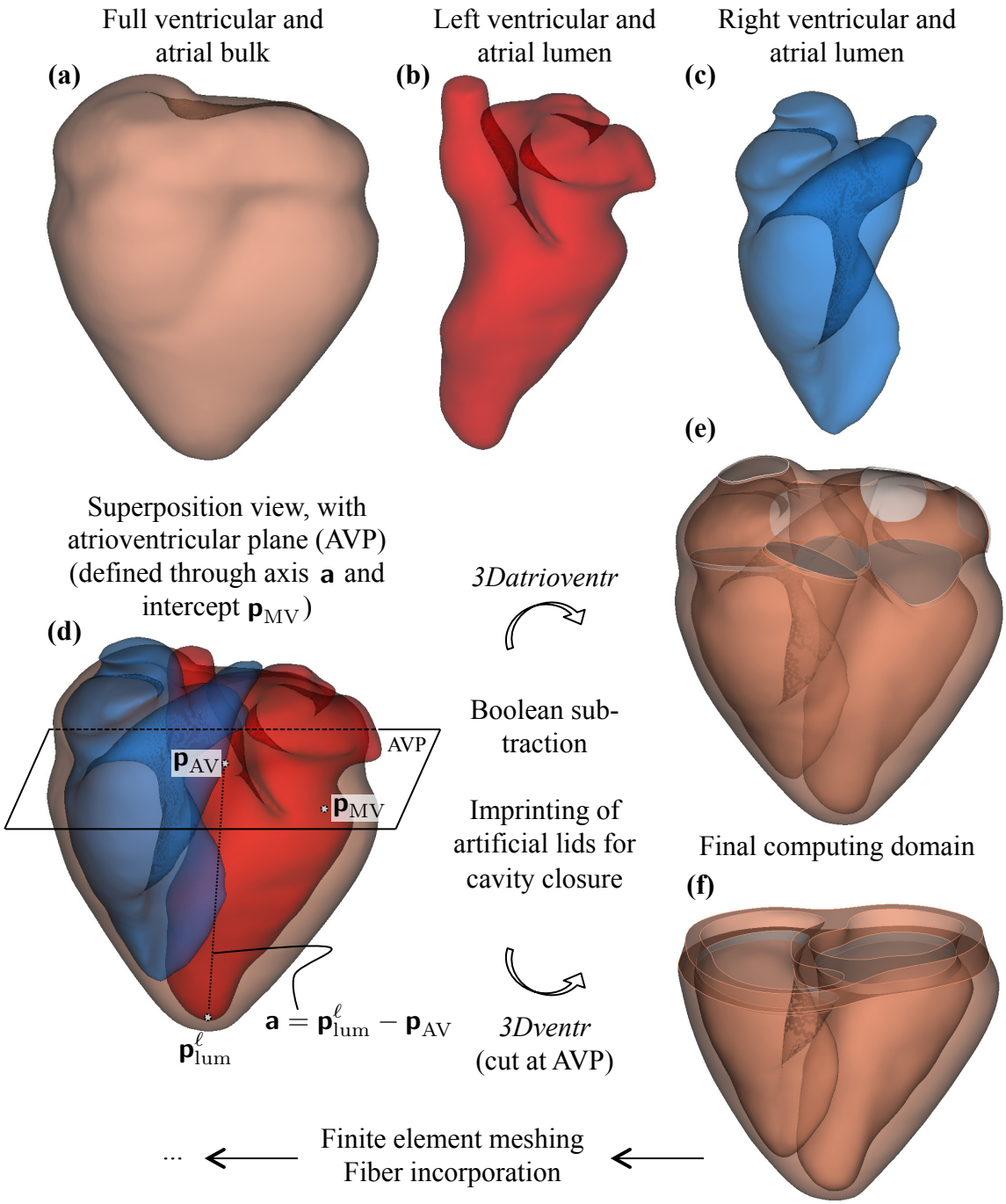

Figure 2.8: Model generation chain. **(a)** Bulk atrioventricular contour body. **(b)** Left atrioventricular blood lumen. **(c)** Right atrioventricular blood lumen. **(d)** Superposition view of all three bodies prior to boolean subtraction. **(e)**,**(f)** Final geometry for model *3Datrioventr* and *3Dventr* (additional cut at atrioventricular plane AVP) after boolean subtraction of the lumina from the full body, including the "artificial" lids serving as closures for the cavities for adequate mathematical assessment of the enclosed volume by surface integrals. This is the mathematical domain Ω_0, devoid of any fiber information. Meshing and subsequent fiber incorporation is performed directly after geometry construction.

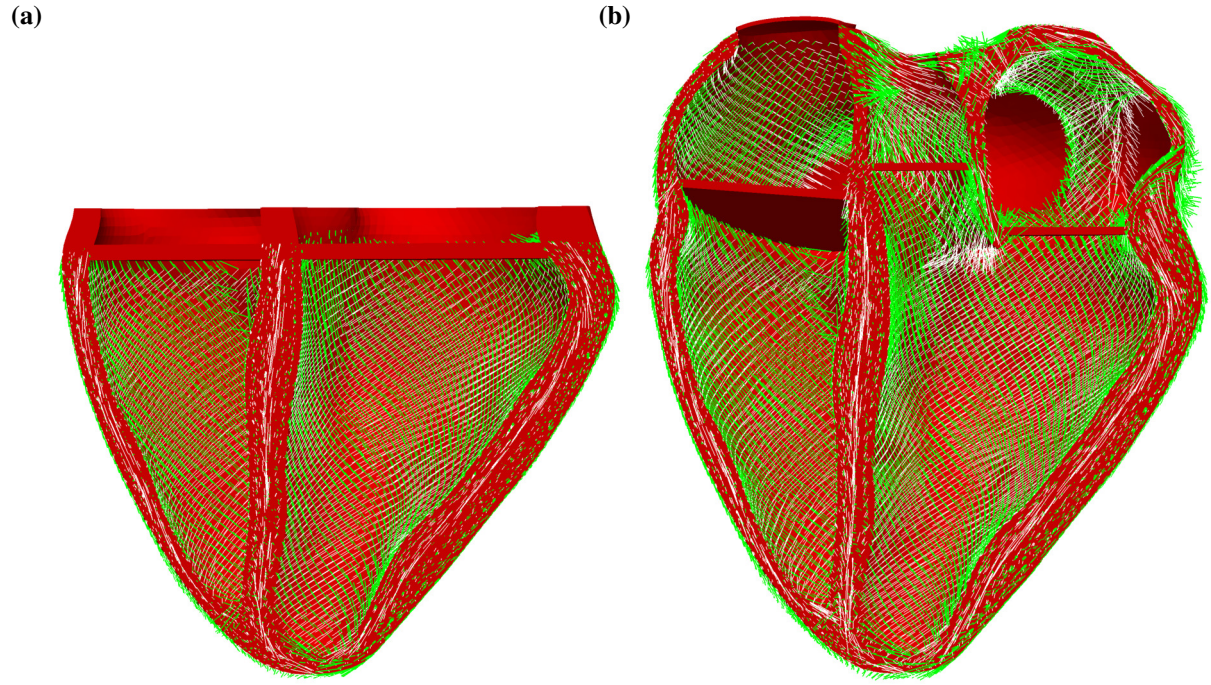

Figure 2.9: Anterior coronary cut view. Muscle fiber direction $\boldsymbol{f}_0$ shown in green, sheet direction $\boldsymbol{s}_0$ shown in light-grey. **(a)** 2-chamber anterior coronary cut view (model *3Dventr*). **(b)** 4-chamber anterior coronary cut view (model *3Datrioventr*).

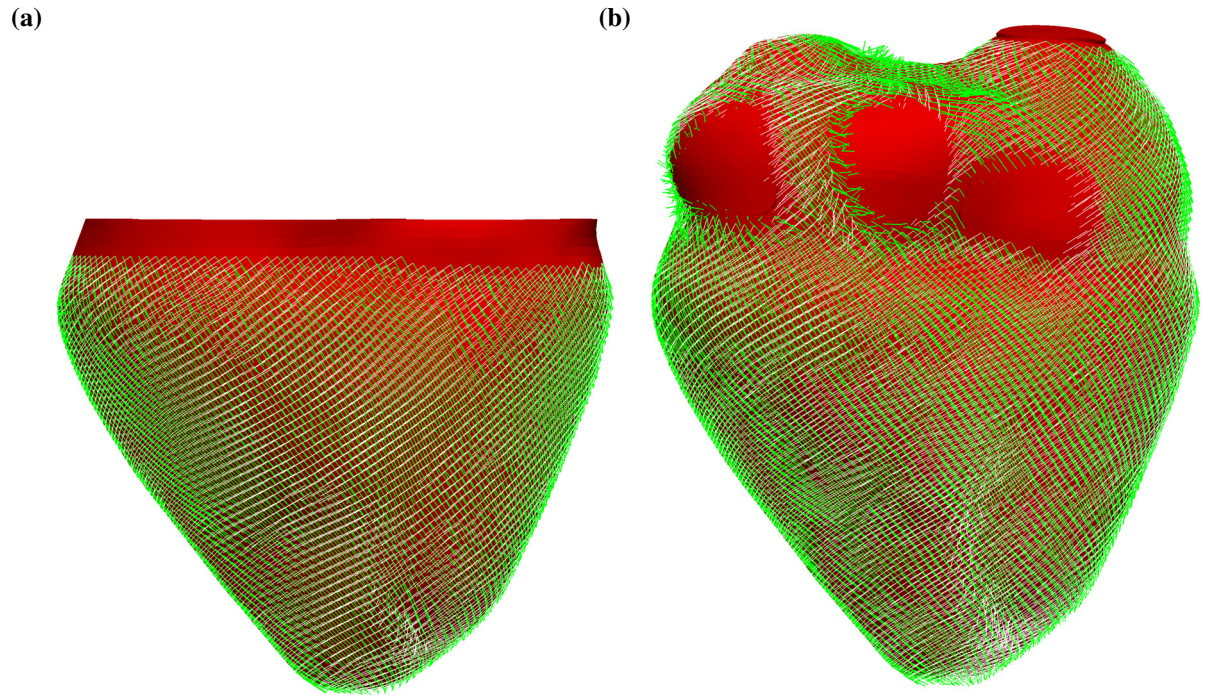

Figure 2.10: Posterior view. Muscle fiber direction $\boldsymbol{f}_0$ shown in green, sheet direction $\boldsymbol{s}_0$ shown in light-grey. **(a)** 2-chamber posterior view (model *3Dventr*). **(b)** 4-chamber posterior view (model *3Datrioventr*).

methods are not used but a continuous transition of fiber and sheet directions from the ventricles to the atria is maintained.[2]

2.2.1.3 Initial boundary value problem

The 3D ventricular continuum mechanics models, *3Dventr* and *3Datrioventr*, are depicted in fig. 2.6 and fig. 2.7, respectively, coupled to the *0Dsyspul* and *0Dsyspulcap* circulations which will be detailed in sec. 2.2.2.
The reference configuration, being ventricular (and atrial) myocardium (drawn in red) as well as artificial lids used as closures for the volumes (drawn in orange and grey, respectively) is $\Omega_0 \subset \mathbb{R}^3$.

Balance equations and boundary conditions The balance of linear momentum (2.49) for nonlinear elastodynamics for the specific problem (no body forces) reads

$$\boldsymbol{\nabla}_0 \cdot (\boldsymbol{F}\boldsymbol{S}) = \rho_0 \ddot{\boldsymbol{u}} \quad \text{in } \Omega_0 \times [t_0, T], \tag{2.87}$$

where t_0 denotes the initial time for the transient problem and T the total time. On the ventricular (subscript v) and atrial (subscript at) "coupling" boundaries $\Gamma_{0,\mathrm{v}}^{0\mathrm{D},i}$, $\Gamma_{0,\mathrm{at}}^{0\mathrm{D},i}$ ($i = \ell, r$ standing for "left" and "right", respectively), a so-called *follower load*, i.e. a pressure boundary condition pointing in the direction of the *current* unit outward normal is enforced. Hence, the boundary condition formulated with respect to the current configuration Ω is

$$\boldsymbol{t} = \boldsymbol{\sigma}\boldsymbol{n} = -p_c^i \, \boldsymbol{n} \quad \text{on } \Gamma_c^{0\mathrm{D},i} \times [t_0, T], \tag{2.88}$$

cf. Cauchy's stress theorem (2.16). For convenience and since a Total Lagrangian description is chosen for all mechanical analyses here, it is formulated with respect to the reference configuration Ω_0, cf. (2.17):

$$\boldsymbol{t}_0 = \boldsymbol{P}\boldsymbol{n}_0 = -p_c^i \, J\boldsymbol{F}^{-\mathrm{T}}\boldsymbol{n}_0 \quad \text{on } \Gamma_{0,c}^{0\mathrm{D},i} \times [t_0, T], \tag{2.89}$$

with $c = \mathrm{v}$ (*3Dventr*), $c = \mathrm{v}, \mathrm{at}$ (*3Datrioventr*). From the solid mechanics point of view, they may be seen as Neumann boundary conditions, however note that the pressures p_c^i are not prescribed but result from a strong coupling between the heart and the vascular system. They are variables of the 0D circulation that again implicitly depend upon the primary variable of the solid mechanics problem, namely the displacement field $\boldsymbol{u}$.

Furthermore, generalized so-called *Robin boundary conditions* [78] are introduced at locations where the heart has been truncated from the body environment. These types of boundary conditions explicitly depend upon the value of the primary variable at the boundary, hence the displacement field or its time derivative (velocity). Therefore, they simply can be viewed as springs or dashpots per unit reference surface area and intend to model the (visco-)elastic effects of the embedding surrounding.

[2] It should be emphasized that this simplification naturally only allows for qualitative atrial mechanical behavior. However, reasonable atrial pressure-volume relationships are obtained, and the physiologically meaningful effect of atrial contraction on end-diastolic ventricular pressure and volume justifies the modeling assumptions. Refer to the results and their discussion presented in chap. 3.

On the one hand, the pericardium that would cover the epicardial surface is not structurally resolved, hence its influence is taken into account on the epicardial boundary $\Gamma_0^{\mathrm{R,e}}$ in form of springs and dashpots that act in reference surface normal direction only:

$$\boldsymbol{t}_0 = -(\boldsymbol{n}_0 \otimes \boldsymbol{n}_0)\,(k_{\mathrm{e}}\boldsymbol{u} + c_{\mathrm{e}}\dot{\boldsymbol{u}}) \quad \text{on } \Gamma_0^{\mathrm{R,e}} \times [0,T]. \tag{2.90}$$

On the other hand, model *3Dventr* is truncated at the atrioventricular plane (heart base), denoted by the boundary $\Gamma_0^{\mathrm{R,b}}$, while model *3Datrioventr* is truncated at arterial outlets and venous inlets, denoted by the boundaries $\Gamma_0^{\mathrm{R,ar}}$ and $\Gamma_0^{\mathrm{R,ven}}$, respectively.
For the heart base (model *3Dventr*), it is assumed that a higher portion of stiffness acts normal to the atrioventricular truncation than tangential to it, hence different heart base spring and dashpot moduli for the perpendicular direction ($\mathrm{b}^{\perp}$) and the "all-direction" case (b) are introduced:

$$\boldsymbol{t}_0 = -k_{\mathrm{b}}\boldsymbol{u} - c_{\mathrm{b}}\dot{\boldsymbol{u}} - (\boldsymbol{n}_0 \otimes \boldsymbol{n}_0)\,(k_{\mathrm{b}^{\perp}}\boldsymbol{u} + c_{\mathrm{b}^{\perp}}\dot{\boldsymbol{u}}) \quad \text{on } \Gamma_0^{\mathrm{R,b}} \times [0,T]. \tag{2.91}$$

For the boundaries at the arterial and venous truncations belonging to model *3Datrioventr*, springs and dashpots act on the "artificial" lids for cavity closure (outer grey portions of Ω_0 in fig. 2.7):

$$\boldsymbol{t}_0 = -k_{\mathrm{ar}}\boldsymbol{u} - c_{\mathrm{ar}}\dot{\boldsymbol{u}} \quad \text{on } \Gamma_0^{\mathrm{R,ar}} \times [0,T], \tag{2.92}$$

$$\boldsymbol{t}_0 = -k_{\mathrm{ven}}\boldsymbol{u} - c_{\mathrm{ven}}\dot{\boldsymbol{u}} \quad \text{on } \Gamma_0^{\mathrm{R,ven}} \times [0,T]. \tag{2.93}$$

The parameters for the Robin boundary conditions are listed in tab. 2.1. Note that no Dirichlet boundary conditions are present. Initial conditions for the displacement and velocity field at $t = t_0$ vanish and are of minor importance since the output of the model only is of relevance at its periodic orbit being the homeostatic state of the cardiovascular system. Refer to sec. 2.2.4 for further details on periodic state computation.

The continuum mechanical initial boundary value problem for the solid mechanics part in its weak form, cf. (2.55), then yields for the model *3Dventr*

$$\begin{aligned}
&\int_{\Omega_0} \rho_0 \ddot{\boldsymbol{u}} \cdot \delta\boldsymbol{u}\,\mathrm{d}V + \int_{\Omega_0} \boldsymbol{S} : \delta\boldsymbol{E}\,\mathrm{d}V \\
&+ \int_{\Gamma_0^{\mathrm{R,e}}} (\boldsymbol{n}_0 \otimes \boldsymbol{n}_0)\,(k_{\mathrm{e}}\boldsymbol{u} + c_{\mathrm{e}}\dot{\boldsymbol{u}}) \cdot \delta\boldsymbol{u}\,\mathrm{d}A + \int_{\Gamma_0^{\mathrm{R,b}}} [k_{\mathrm{b}}\boldsymbol{u} + c_{\mathrm{b}}\dot{\boldsymbol{u}} + (\boldsymbol{n}_0 \otimes \boldsymbol{n}_0)\,(k_{\mathrm{b}^{\perp}}\boldsymbol{u} + c_{\mathrm{b}^{\perp}}\dot{\boldsymbol{u}})] \cdot \delta\boldsymbol{u}\,\mathrm{d}A \\
&+ \sum_{i=\ell,r} \int_{\Gamma_{0,\mathrm{v}}^{0\mathrm{D},i}} p_{\mathrm{v}}^{i}\, J\boldsymbol{F}^{-\mathrm{T}}\boldsymbol{n}_0 \cdot \delta\boldsymbol{u}\,\mathrm{d}A = 0, \quad \forall\, \delta\boldsymbol{u},
\end{aligned} \tag{2.94}$$

and for the model *3Datrioventr*

$$\int_{\Omega_0} \rho_0 \ddot{\boldsymbol{u}} \cdot \delta\boldsymbol{u} \,\mathrm{d}V + \int_{\Omega_0} \boldsymbol{S} : \delta\boldsymbol{E} \,\mathrm{d}V$$
$$+ \int_{\Gamma_0^{\mathrm{R,e}}} (\boldsymbol{n}_0 \otimes \boldsymbol{n}_0)\,(k_{\mathrm{e}}\boldsymbol{u} + c_{\mathrm{e}}\dot{\boldsymbol{u}}) \cdot \delta\boldsymbol{u} \,\mathrm{d}A + \sum_{j=\mathrm{ar,ven}} \int_{\Gamma_0^{\mathrm{R},j}} (k_j\boldsymbol{u} + c_j\dot{\boldsymbol{u}}) \cdot \delta\boldsymbol{u} \,\mathrm{d}A$$
$$+ \sum_{i=\ell,r} \int_{\Gamma_{0,\mathrm{v}}^{0\mathrm{D},i}} p_{\mathrm{v}}^i \, J\boldsymbol{F}^{-\mathrm{T}}\boldsymbol{n}_0 \cdot \delta\boldsymbol{u} \,\mathrm{d}A + \sum_{i=\ell,r} \int_{\Gamma_{0,\mathrm{at}}^{0\mathrm{D},i}} p_{\mathrm{at}}^i \, J\boldsymbol{F}^{-\mathrm{T}}\boldsymbol{n}_0 \cdot \delta\boldsymbol{u} \,\mathrm{d}A = 0, \quad \forall\, \delta\boldsymbol{u}. \tag{2.95}$$

Constitutive equations: Passive material, active stress and the Frank-Starling mechnanism In order to close the system, a constitutive equation for the second Piola-Kirchhoff stress (2.19), $\boldsymbol{S}$, has to be formulated, cf. sec. 2.1.1.2. Here, an additive decomposition of the stress into a (hyperelastic) passive part and an active contribution, so-called *active stress* [2], is performed:

$$\boldsymbol{S} = \frac{\partial \Psi}{\partial \boldsymbol{E}} + \tau_{\mathrm{a}}(t)\boldsymbol{f}_0 \otimes \boldsymbol{f}_0. \tag{2.96}$$

The passive material stress response stems from a hyperelastic strain energy function Ψ. It accounts for anisotropy in two distinct, locally orthogonal directions, the muscle fiber direction $\boldsymbol{f}_0$ and the sheet direction $\boldsymbol{s}_0$ (green and grey directions in fig. 2.9, fig. 2.10, respectively), and possesses an isotropic ground substance which the fibers are "embedded" into. The specific form of the strain energy function was introduced by Holzapfel and Ogden [89] for myocardial tissue and reads

$$\Psi = \frac{a_0}{2b_0}\left(e^{b(\bar{I}_C-3)} - 1\right) + \sum_{i=f,s} \frac{a_i}{2b_i}\left(e^{b_i(\mathit{IV}_i-1)^2} - 1\right) + \frac{a_{fs}}{2b_{fs}}\left(e^{b_{fs}\mathit{VIII}_{fs}^2} - 1\right) + \frac{\kappa}{2}(J-1)^2, \tag{2.97}$$

here making use of the isochoric-volumetric split of the deformation according to (2.33). The modified invariant of the right Cauchy-Green deformation tensor (2.12) is defined according to $(2.29)_1$, and the anisotropic invariants are according to (2.31). Note, however, that the latter are not subject to the isochoric-volumetric split [181]. The myocardium is assumed to behave nearly incompressible, hence the bulk modulus κ for the volumetric part of the strain energy has to be chosen appropriately large, cf. tab. 2.2 for the material parameters.

The "artificial" lids that serve as cavity closures are modeled with a "dummy" Neo-Hookean material,

$$\Psi^{\mathrm{lid}} = \frac{\mu^{\mathrm{lid}}}{2}(\bar{I}_C - 3) + \frac{\kappa^{\mathrm{lid}}}{2}(J-1)^2. \tag{2.98}$$

For model *3Dventr*, parameters are $\mu^{\mathrm{lid}} = 50$ kPa and $\kappa^{\mathrm{lid}} = 10$ kPa (low bulk stiffness); and for model *3Datrioventr*, ventricular lid parameters are $\mu^{\mathrm{lid}} = 20$ kPa and $\kappa^{\mathrm{lid}} = 1000$ kPa, whereas parameters for the atrial lids are set to $\mu^{\mathrm{lid}} = 500$ kPa and $\kappa^{\mathrm{lid}} = 25\,000$ kPa. Furthermore, ventricular (atrial) lids exhibit the same active stress like the ventricles (atria) in order to support ventricular (atrial) contraction, hence their constitutive equation is (2.96). For model *3Dventr*, the

extrusion at the heart base, cf. sec. 2.2.1.1, is devoid of any active component.

The (time-dependent) active stress $\tau_\mathrm{a}(t)$ acts along the muscle fiber direction $\boldsymbol{f}_0$. It stems from an evolution equation, here a simplification of the law in Bestel et al. [21] following arguments in [186]:

$$\dot{\tau}_\mathrm{a} = -|u|\tau_\mathrm{a} + a\,\sigma_0|u|_+, \tag{2.99}$$

with $|u|$ for the absolute value of u and $|u|_+ := \max(0, u)$. The function u scales the activation function $\hat{f}(t) \in [0, 1]$ with the active stress upstroke and relaxation rates α_max and α_min, respectively:

$$u = \hat{f}(t) \cdot \alpha_\mathrm{max} + (1 - \hat{f}(t)) \cdot \alpha_\mathrm{min}. \tag{2.100}$$

The normalized input activation function here has been developed to

$$\begin{aligned}\hat{f}(t) = (K(t - c_1) + 1) \cdot \mathcal{H}[K(t - c_1) + 1] - K(t - c_1) \cdot \mathcal{H}[K(t - c_1)] \\ - K(t - c_2) \cdot \mathcal{H}[K(t - c_2)] + (K(t - c_2) - 1) \cdot \mathcal{H}[K(t - c_2) - 1],\end{aligned} \tag{2.101}$$

with

$$c_1 = t_\mathrm{contr} + \frac{\alpha_\mathrm{max}}{K(\alpha_\mathrm{max} - \alpha_\mathrm{min})} \tag{2.102}$$

and

$$c_2 = t_\mathrm{relax} - \frac{\alpha_\mathrm{max}}{K(\alpha_\mathrm{max} - \alpha_\mathrm{min})} \tag{2.103}$$

as well as the Heaviside function

$$\mathcal{H}[(\cdot)] := \begin{cases} 0, & (\cdot) < 0, \\ 1, & (\cdot) \geq 0. \end{cases} \tag{2.104}$$

This specific choice of input activation function (2.101) allows for full control of begin and end of muscle activation by setting the timing quantities t_contr and t_relax as desired, e.g. taken from ECG or pressure over time data.
Figure 2.11 exemplarily depicts the development of the active stress τ_a, the normalized input activation $\hat{f}$ as well as u, $|u|$ and $|u|_+$ over one cardiac cycle, $t \in [0, T_\mathrm{cycl}]$.
Note that if $K \to \infty$ in (2.101), $\hat{f}(t)$ degenerates to a Heaviside input function with value 1 for $t_\mathrm{contr} \leq t \leq t_\mathrm{relax}$ and value 0 otherwise. However, if K is chosen too large, the kinks at active stress initialization (at $t = t_\mathrm{contr}$) and relaxation (at $t = t_\mathrm{relax}$) would become too pronounced and may cause difficulties for the numerical solution schemes. Thus, throughout this thesis, $K = 5$ is chosen.

The quantity σ_0 in (2.99) is the *contractility* of the cardiac muscle and represents the asymptotic value of the active stress τ_a. Its magnitude determines the strength of muscle contraction and in "real-life" depends upon several biological conditions. The Frank-Starling mechanism, cf. the introductory notes in chap. 1, sec. 1.2, is an important preload-dependent autoregulatory mechanism of the heart that is used to maintain homeostasis, hence an equal left and right ventricular stroke volume.
The Frank-Starling mechanism thereby is a local phenomenon that happens at the scale of cells, which eventually sense the increased preload by their state of strain. Hence, in order to model that

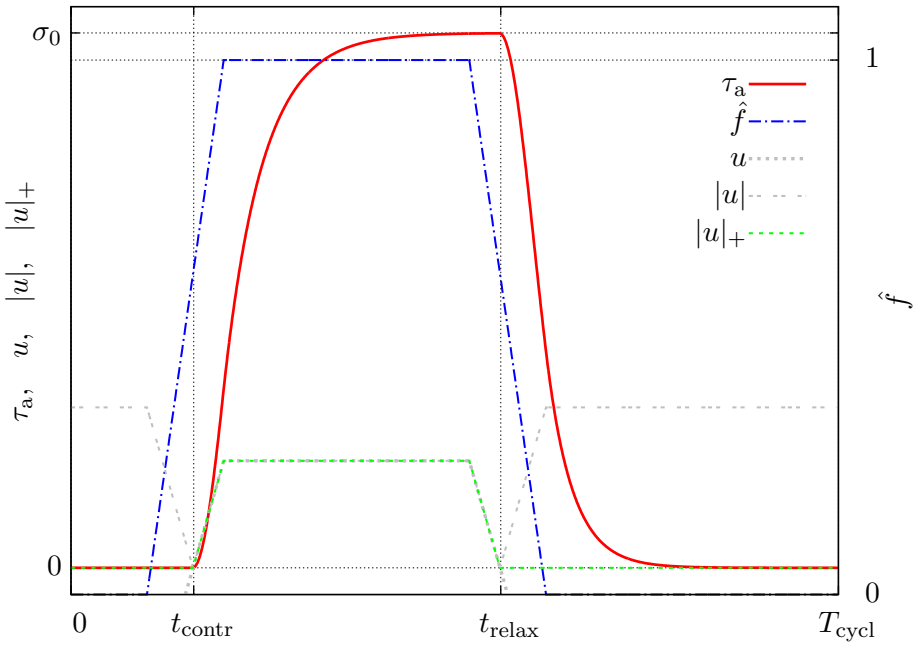

Figure 2.11: Exemplary development of the (ventricular) active stress τ_a (Backward Euler solution of (2.99) with $a \equiv 1$), the normalized (ventricular) input activation $\hat{f}$ as well as u, $|u|$ and $|u|_+$ over one cardiac cycle.

phenomenon, a strain dependency has to be introduced into the active stress evolution equation (2.99), here done in terms of the factor $a = a(\lambda_{myo})$ being some function of the elastic myofiber stretch

$$\lambda_{myo} = \sqrt{\boldsymbol{f}_0 \cdot \boldsymbol{C}\boldsymbol{f}_0}. \tag{2.105}$$

Here, a novel function for modeling the Frank-Starling law is introduced:

$$\dot{a}(\lambda_{myo}) = \dot{g}(\lambda_{myo})\, \mathbb{I}_{|u|_- > 0}, \tag{2.106}$$

with $|u|_- := \max(0, -u)$ and u according to (2.100). For the strain-dependent function g, an expression of the type

$$g(\lambda_{myo}) = \begin{cases} a_{min}, & \lambda_{myo} \leq \hat{\lambda}_{myo}^{thres,lo}, \\ a_{min} + \frac{1}{2}(a_{max} - a_{min})\left(1 - \cos\frac{\pi(\lambda_{myo} - \hat{\lambda}_{myo}^{thres,lo})}{\hat{\lambda}_{myo}^{max,lo} - \hat{\lambda}_{myo}^{thres,lo}}\right), & \hat{\lambda}_{myo}^{thres,lo} \leq \lambda_{myo} \leq \hat{\lambda}_{myo}^{max,lo}, \\ a_{max}, & \hat{\lambda}_{myo}^{max,lo} \leq \lambda_{myo} \leq \hat{\lambda}_{myo}^{thres,hi}, \\ a_{min} + \frac{1}{2}(a_{max} - a_{min})\left(1 - \cos\frac{\pi(\lambda_{myo} - \hat{\lambda}_{myo}^{max,hi})}{\hat{\lambda}_{myo}^{max,hi} - \hat{\lambda}_{myo}^{thres,hi}}\right), & \hat{\lambda}_{myo}^{thres,hi} \leq \lambda_{myo} \leq \hat{\lambda}_{myo}^{max,hi}, \\ a_{min}, & \lambda_{myo} \geq \hat{\lambda}_{myo}^{max,hi} \end{cases} \tag{2.107}$$

is proposed. Therein, a_{min} and a_{max} are the minimum and maximum contractility scaling factors. The constants $\hat{\lambda}_{myo}^{thres,lo}$ and $\hat{\lambda}_{myo}^{max,lo}$ are the lower threshold and maximum stretch between which contractility is increased, while $\hat{\lambda}_{myo}^{thres,hi}$ and $\hat{\lambda}_{myo}^{max,hi}$ are the higher threshold and maximum stretch between which contractility is decreased again. The actual strength of the heart to contract ($a\,\sigma_0$)

at a given state of preload is also referred to as the heart's *inotropy*.
Figure 2.12 plots the Frank-Starling factor a over the myofiber stretch λ_{myo}. Expression (2.106) represents some hysteresis which is passed through depending on the state of activation. While $a(\lambda_{\text{myo}})$ rises during ventricular filling (diastole) up to a certain maximum (lower) stretch value and would drop again if surpassing the plateau beyond the (upper) stretch threshold, it remains at the value it has taken right before ventricular contraction starts ($t = t_{\text{contr}}$). Otherwise, an immediate fall-back to the baseline value would occur, since fibers shorten during ventricular systole. Only when the activation is trespassed, the function may drop back to its baseline value for the time branch $t > t_{\text{relax}}$. It should be noted that (2.106) is constructed such that no jump in τ_{a} occurs during ventricular relaxation.

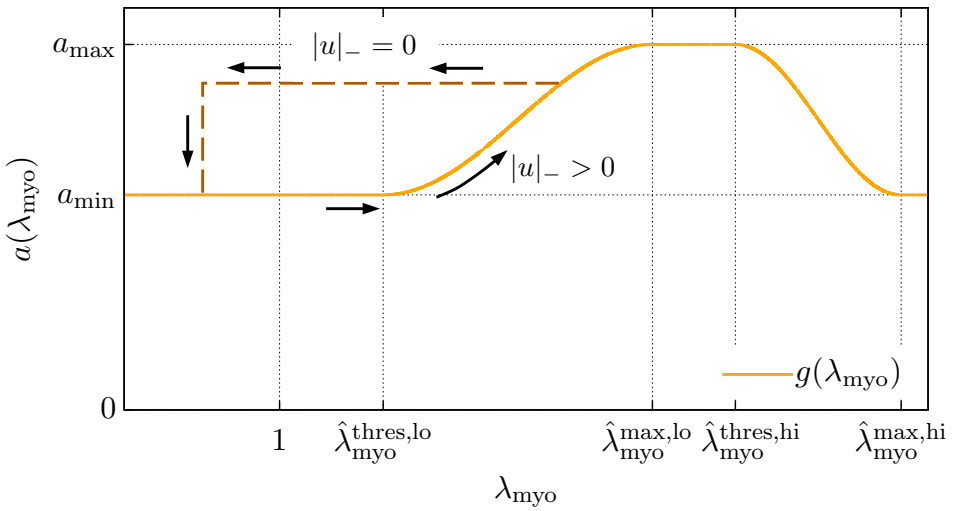

Figure 2.12: Frank-Starling factor a as function of the myofiber stretch λ_{myo}.

A couple of different models for the Frank-Starling mechanism have been proposed in the literature to date, cf. the models by Chapelle [37], Caruel et al. [33] and Sainte-Marie et al. [178], all basically relying on the active tissue model by Bestel et al. [21]. However, no explicit analytical functional dependence of the Frank-Starling factor (here a) is proposed, and little data is available to robustly calibrate (2.107).

The material tangent (2.34) for the passive-active constitutive heart muscle model then becomes

$$\begin{aligned}\mathbb{C} = 2\frac{\partial \boldsymbol{S}}{\partial \boldsymbol{C}} = 4\frac{\partial^2 \Psi}{\partial \boldsymbol{C}\partial \boldsymbol{C}} + 2\frac{\partial \tau_{\text{a}}}{\partial \boldsymbol{C}} \otimes \boldsymbol{f}_0 \otimes \boldsymbol{f}_0 = 4\frac{\partial^2 \Psi}{\partial \boldsymbol{C}\partial \boldsymbol{C}} + 2\frac{\partial \tau_{\text{a}}}{\partial \lambda_{\text{myo}}}\frac{\partial \lambda_{\text{myo}}}{\partial \boldsymbol{C}} \otimes \boldsymbol{f}_0 \otimes \boldsymbol{f}_0 = \\ = 4\frac{\partial^2 \Psi}{\partial \boldsymbol{C}\partial \boldsymbol{C}} + \frac{\partial \tau_{\text{a}}}{\partial \lambda_{\text{myo}}}\frac{1}{\lambda_{\text{myo}}}\, \boldsymbol{f}_0 \otimes \boldsymbol{f}_0 \otimes \boldsymbol{f}_0 \otimes \boldsymbol{f}_0. \end{aligned} \tag{2.108}$$

It should be noted that the active stress only contributes to the material tangent if the Frank-Starling mechanism is considered, thus $\frac{\partial \tau_{\text{a}}}{\partial \boldsymbol{C}} \neq \boldsymbol{0}$. The time-discrete solution of the active stress evolution equation (2.99) yielding the solution τ_{a} will be discussed in chapter 3.2.1.

Figure 2.13 plots the driving forces for the 3D-0D coupled cardiovascular models. In case of model *3Dventr*, the ventricular active stress and the atrial elastance are the external time-controlled inputs (fig. 2.13a), and for model *3Datrioventr*, ventricular as well as atrial active stress are prescribed (fig. 2.13b).

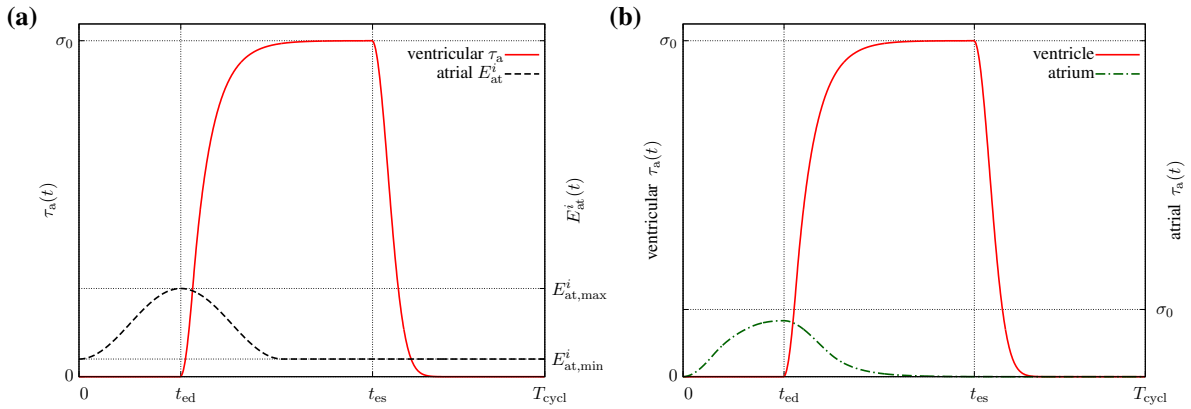

Figure 2.13: Prescribed driving forces of cardiovascular simulations: Exemplary development of active stresses (Backward Euler solution of (2.99) with $a \equiv 1$) and atrial elastance (2.112) over one cardiac cycle $t \in [0, T_{\text{cycl}}]$; atrial start of contraction is $t = 0$, atrial start of relaxation is t_{ed}. **(a)** Model *3Dventr*: Time-course of (3D) ventricular active stress and (0D) atrial elastance. **(b)** Model *3Datrioventr*: Time-course of (3D) ventricular and atrial active stress.

Parameters The parameters of the 3D (atrio-)ventricular solid mechanics models, *3Dventr* and *3Datrioventr*, are separated into ones that remain fixed for all computations carried out in this thesis, and into ones that are considered for parameter estimation (cf. chap. 4) or are changed depending on the "case study".
The former group comprises all parameters for the Robin boundary conditions, cf. tab. 2.1, as well as all passive parameters for the elastic behavior of the myocardium (ventricles and atria), which are taken from Holzapfel and Ogden [89] and rely on experiments performed by Dokos et al. [54]. They are listed in tab. 2.2, including the bulk modulus κ, which had been chosen such that a Poisson's ratio of approximately $\nu \approx 0.49$ is obtained, and the (reference) density ρ_0, assumed to that of water.

The latter parameter group (study-dependent ones) comprises those which relate to the active contractile properties of ventricles and atria. These are the contractility σ_0, the upstroke and relaxation rates $\alpha_{\max}$ and $\alpha_{\min}$, and the Frank-Starling factor a from the active stress evolution equation, cf. (2.99), (2.100), (2.106), and (2.107), respectively. Additionally, the timings for the beginning of ventricular (atrial) contraction t_{contr}, for the start of ventricular (atrial) relaxation t_{relax}, cf. (2.101), as well as the cardiac cycle time T_{cycl} govern the individual cardiac dynamics.

The base parameters are listed in tab. 2.3. If not stated otherwise, these base values are chosen for the specific problem at hand. Here, due to the absence of reliable data but without loss of

Table 2.1: Parameters of embedding Robin boundary conditions: for 2-chamber model *3Dventr* at heart base (subscripts b, $\mathrm{b}^{\perp}$), for 4-chamber model *3Datrioventr* at arterial and venous in-/outlets (subscripts ar, ven), and at epicardium (subscript e) for both models

3Dventr	k_{b} $[\frac{\mathrm{kPa}}{\mathrm{mm}}]$	$k_{\mathrm{b}^{\perp}}$ $[\frac{\mathrm{kPa}}{\mathrm{mm}}]$	k_{e} $[\frac{\mathrm{kPa}}{\mathrm{mm}}]$	c_{b} $[\frac{\mathrm{kPa\cdot s}}{\mathrm{mm}}]$	$c_{\mathrm{b}^{\perp}}$ $[\frac{\mathrm{kPa\cdot s}}{\mathrm{mm}}]$	c_{e} $[\frac{\mathrm{kPa\cdot s}}{\mathrm{mm}}]$
	0.25	1.25	0.075	0.0005	0.0005	0.005
3Datrioventr	k_{ar} $[\frac{\mathrm{kPa}}{\mathrm{mm}}]$	k_{ven} $[\frac{\mathrm{kPa}}{\mathrm{mm}}]$	k_{e} $[\frac{\mathrm{kPa}}{\mathrm{mm}}]$	c_{ar} $[\frac{\mathrm{kPa\cdot s}}{\mathrm{mm}}]$	c_{ven} $[\frac{\mathrm{kPa\cdot s}}{\mathrm{mm}}]$	c_{e} $[\frac{\mathrm{kPa\cdot s}}{\mathrm{mm}}]$
	0.5	0.25	0.075	0.0005	0.0005	0.005

Table 2.2: Passive myocardial material parameters according to Holzapfel and Ogden [89], density ρ_0 chosen to that of water, bulk modulus κ chosen such that a Poisson's ratio of approximately 0.49 is obtained (near-incompressibility)

a_0 [kPa]	a_f [kPa]	a_s [kPa]	a_{fs} [kPa]	κ [kPa]
0.059	18.472	2.481	0.216	10^3
b_0 $[-]$	b_f $[-]$	b_s $[-]$	b_{fs} $[-]$	ρ_0 $[\frac{\mathrm{kg}}{\mathrm{mm}^3}]$
8.023	16.026	11.120	11.436	10^{-6}

generality, only the ventricles are assumed to obey the Frank-Starling mechanism for the model *3Datrioventr*, even though atria may alter their contraction depending on their preload, too [6]. Furthermore, even if provided by the model, a contractility re-reduction at very high fiber strains is not taken into account since the Frank-Starling model so far is not calibrated to experimental data but only accounted for on a phenomenological basis, hence $\hat{\lambda}_{\mathrm{myo}}^{\mathrm{thres,hi}} \to \infty$ and $\hat{\lambda}_{\mathrm{myo}}^{\mathrm{max,hi}} \to \infty$ in (2.107). Also, the Frank-Starling mechanism is not considered for model *3Dventr* but only for the more recent *3Datrioventr* model.

Prestressing Organs such as blood vessels or the myocardium usually are in a loaded state at the time of medical imaging. Therefore, a computational model that makes use of geometries that are gained from CT or MRI data via segmentation should take into account that the geometry is situated in a deformed state. This is especially important when specific constitutive laws with experimentally obtained material parameters are used, since these experiments usually are performed on unloaded tissue samples. Due to the inherent nonlinear stress-strain constitutive behavior of soft tissue, it is of importance to perform computations on the right level of loading in order to obtain reasonable deformations.

Prior to all transient 3D-0D coupled computations that are carried out, the patient-specific heart is "prestressed" to the diastolic cavity pressures and to the initial active stress values that are present at the time instance the geometry was segmented from CT imaging data, namely $0.2 \cdot T_{\mathrm{cycl}}$ prior to ventricular contraction. A so-called Modified Updated Lagrangian Formulation (MULF) that was proposed by Gee et al. [68] is used.
During this process, per definition happening in the time span $t \in [0, t_0]$, the quasi-static balance

Table 2.3: Base parameters of the active contractile dynamics

		3Dventr	*3Datrioventr*		
			ventricles	atria	
σ_0	[kPa]	70.0	100.0	20.0	contractility
$\alpha_{\max}$	[1/s]	10.0	10.0	5.0	upstroke rate
$\alpha_{\min}$	[1/s]	-30.0	-30.0	-20.0	relaxation rate
K	[−]	5.0	5.0	5.0	activation function steepness
$a_{\max}$	[−]	1.0	1.0	1.0	maximum contractility scaling factor
$a_{\min}$	[−]	1.0	2/3	1.0	minimum contractility scaling factor
$\hat{\lambda}_{\text{myo}}^{\text{thres,lo}}$	[−]	$\to \infty$	1.01	$\to \infty$	lower stretch threshold
$\hat{\lambda}_{\text{myo}}^{\text{max,lo}}$	[−]	$\to \infty$	1.2	$\to \infty$	lower stretch limit
$\hat{\lambda}_{\text{myo}}^{\text{thres,hi}}$	[−]	$\to \infty$	$\to \infty$	$\to \infty$	upper stretch threshold
$\hat{\lambda}_{\text{myo}}^{\text{max,hi}}$	[−]	$\to \infty$	$\to \infty$	$\to \infty$	upper stretch limit
t_{ed}	[s]	0.2	0.2		end-diastolic time
t_{es}	[s]	0.53	0.53		end-systolic time
T_{cycl}	[s]	1.0	1.0		cardiac cycle time
t_{contr}	[s]	t_{ed}	t_{ed}	0.0	contraction time
t_{relax}	[s]	t_{es}	t_{es}	t_{ed}	relaxation time

of linear momentum

$$\boldsymbol{\nabla}_0 \cdot (\boldsymbol{F}\boldsymbol{S}) = \boldsymbol{0} \quad \text{in } \Omega_0 \times [0, t_0] \tag{2.109}$$

instead of (2.87) is considered. The cavity pressures $\hat{p}_c^i = p_c^i(t_0)$ that will serve as initial conditions for the 3D-0D coupled problem are prescribed on the endocardial surfaces, hence (2.89) becomes

$$\boldsymbol{t}_0 = \boldsymbol{P}\boldsymbol{n}_0 = -\hat{p}_c^i \, J\boldsymbol{F}^{-\mathrm{T}}\boldsymbol{n}_0 \quad \text{on } \Gamma_{0,c}^{0\mathrm{D},i} \times [0, t_0]. \tag{2.110}$$

Robin boundary conditions (2.90)–(2.93) remain the same as for the transient problem.

After the quasi-static prestressing phase, the deformation gradient (2.10) is stored in a history deformation gradient, $\tilde{\boldsymbol{F}} \leftarrow \boldsymbol{F}(t_0)$, while the displacement state is forgotten, $\boldsymbol{u} := \boldsymbol{0}$. For the subsequent transient problem, the deformation gradient $\boldsymbol{F}\tilde{\boldsymbol{F}}$ instead of $\boldsymbol{F}$ is used.
By analogy, the elastic springs in the Robin boundary conditions (2.90)–(2.93) are prestressed as well. Their deflection $\tilde{\boldsymbol{u}}$ is stored prior to forgetting the displacement state and subsequently added to the actual displacement during computation of the transient problem, $\boldsymbol{u} + \tilde{\boldsymbol{u}}$. Note that the dashpots do not contribute to the prestressed state.

2.2.2 0D circulation modeling

Here, the previously introduced circulation models *0Dsyspul*, *0Dsyspulcap* and *0Dsyspulcaprespir* are presented. The following subsections are subdivided into one part concentrating on blood flow mechanics, sec. 2.2.2.1, and another part treating transport and dissociation of oxygen and carbon dioxide, cf. sec. 2.2.2.2.

2.2.2.1 Blood flow mechanics

For the 2-chamber ventricular heart *3Dventr*, the atria are considered by 0-dimensional so-called *elastance models* [177]. These are reduced "chambers" which provide a simple relation between atrial pressure p_{at}^i and the atrial volume V_{at}^i ($i = \ell$ for "left", $i = r$ for "right"). The pressure-volume relation reads

$$p_{\mathrm{at}}^i = E_{\mathrm{at}}^i(t) \cdot (V_{\mathrm{at}}^i - V_{\mathrm{at,u}}^i), \tag{2.111}$$

with $V_{\mathrm{at,u}}^i$ being the unstressed dead volume of the chamber and the time varying atrial elastance

$$E_{\mathrm{at}}^i(t) = E_{\mathrm{at,A}}^i \cdot y_{\mathrm{at}}^i(t) + E_{\mathrm{at,min}}^i, \tag{2.112}$$

where $E_{\mathrm{at,A}}^i = E_{\mathrm{at,max}}^i - E_{\mathrm{at,min}}^i$ is the atrial elastance amplitude, while $E_{\mathrm{at,max}}^i$ and $E_{\mathrm{at,min}}^i$ denote the maximum and minimum atrial elastance, respectively. The normalized atrial activation function is

$$y_{\mathrm{at}}^i(t) = \begin{cases} \frac{1}{2}\left(1 - \cos\frac{2\pi t}{\Delta t_{\mathrm{at,act}}}\right), & t \leq \Delta t_{\mathrm{at,act}}, \\ 0, & t > \Delta t_{\mathrm{at,act}}. \end{cases} \tag{2.113}$$

Therein, the duration of the atrial activation here is considered $\Delta t_{\mathrm{at,act}} = 2\,(t_{\mathrm{ed}} - t_0)$, assuming that atrial activation starts at $t = t_0$ which is the time instance $0.2 \cdot T_{\mathrm{cycl}}$ prior to ventricular activation ("$80\ \%$", with "$100\ \%$" indicating the end of the diastole at $t = t_{\mathrm{ed}}$).

For a coupling of the 0D circulatory system model the 4-chamber atrioventricular heart *3Datrioventr*, atrial chamber volumes V_{at}^i, like ventricular volumes, stem from the 3D solid mechanics problem.

The heart valves are not modeled as structurally resolved entities but are considered in terms of 0-dimensional diodes that either oppose to flow by a very high resistance when closed, or give way to flow by a very small resistance when opened. Hence, they are modeled by a Poiseuille-like flow law (2.79) without inertance and with variable resistance depending on the difference in pressures in front of and beyond the valve.
The semilunar valves of the heart relate left ($i = \ell$) or right ($i = r$) ventricular out-flux $q_{\mathrm{v,out}}^i$ to the difference in ventricular pressure p_{v}^i and systemic or pulmonary arterial pressure $p_{\mathrm{ar}}^{\mathrm{sys}}$ or $p_{\mathrm{ar}}^{\mathrm{pul}}$ (aortic or pulmonary valve, respectively). Thus, their pressure-flow relations read

$$q_{\mathrm{v,out}}^{\ell} = \frac{1}{\tilde{R}_{\mathrm{v,out}}^{\ell}}(p_{\mathrm{v}}^{\ell} - p_{\mathrm{ar}}^{\mathrm{sys}}), \qquad q_{\mathrm{v,out}}^{r} = \frac{1}{\tilde{R}_{\mathrm{v,out}}^{r}}(p_{\mathrm{v}}^{r} - p_{\mathrm{ar}}^{\mathrm{pul}}), \tag{2.114}$$

with

$$\tilde{R}_{\mathrm{v,out}}^{\ell} := \begin{cases} R_{\mathrm{v,out}}^{\ell,\max}, & p_{\mathrm{v}}^{\ell} < p_{\mathrm{ar}}^{\mathrm{sys}}, \\ R_{\mathrm{v,out}}^{\ell,\min}, & p_{\mathrm{v}}^{\ell} \geq p_{\mathrm{ar}}^{\mathrm{sys}}, \end{cases} \qquad \tilde{R}_{\mathrm{v,out}}^{r} := \begin{cases} R_{\mathrm{v,out}}^{r,\max}, & p_{\mathrm{v}}^{r} < p_{\mathrm{ar}}^{\mathrm{pul}}, \\ R_{\mathrm{v,out}}^{r,\min}, & p_{\mathrm{v}}^{r} \geq p_{\mathrm{ar}}^{\mathrm{pul}}. \end{cases} \tag{2.115}$$

The atrioventricular valves relate left or right ventricular in-flux $q_{\mathrm{v,in}}^i$ to the difference in ventricular pressure p_{v}^i and atrial pressure p_{at}^i (mitral or tricuspid valve, respectively):

$$q_{\mathrm{v,in}}^{\ell} = \frac{1}{\tilde{R}_{\mathrm{v,in}}^{\ell}}(p_{\mathrm{at}}^{\ell} - p_{\mathrm{v}}^{\ell}), \qquad q_{\mathrm{v,in}}^{r} = \frac{1}{\tilde{R}_{\mathrm{v,in}}^{r}}(p_{\mathrm{at}}^{r} - p_{\mathrm{v}}^{r}), \tag{2.116}$$

with

$$\tilde{R}^{\ell}_{\mathrm{v,in}} := \begin{cases} R^{\ell,\min}_{\mathrm{v,in}}, & p^{\ell}_{\mathrm{v}} \leq p^{\ell}_{\mathrm{at}}, \\ R^{\ell,\max}_{\mathrm{v,in}}, & p^{\ell}_{\mathrm{v}} > p^{\ell}_{\mathrm{at}}, \end{cases} \qquad \tilde{R}^{r}_{\mathrm{v,in}} := \begin{cases} R^{r,\min}_{\mathrm{v,in}}, & p^{r}_{\mathrm{v}} \leq p^{r}_{\mathrm{at}}, \\ R^{r,\max}_{\mathrm{v,in}}, & p^{r}_{\mathrm{v}} > p^{r}_{\mathrm{at}}. \end{cases} \tag{2.117}$$

In (2.115) and (2.117), maximum resistances are orders of magnitudes greater than minimum resistances, $R^{i,\max}_{\mathrm{v,out}} \gg R^{i,\min}_{\mathrm{v,out}}$ and $R^{i,\max}_{\mathrm{v,in}} \gg R^{i,\min}_{\mathrm{v,in}}$.

In the following, a basic systemic and pulmonary circulation as depicted in fig. 2.6, and an extended circulation including the capillary network, cf. fig. 2.7, are introduced. The parameters and state variables are provided in the figures. Resistances and impedances are denoted with R and Z [3], respectively, compliances with C, inertances with L, and elastances with E. The state variables are pressures p and fluxes q. Auxiliary pressure variables π are condensed out of the system of equations.
The governing equations are reduced-dimensional balances of mass (volume) and balances of momentum, applied to each compartment of the circulatory system. The respective volume of the compartment either stems from the law of compliance (2.82) or elastance (2.111), or as input from the 3D heart model (ventricular and atrial chambers).

Basic systemic and pulmonary circulation The circulation model *0Dsyspul* shown in fig. 2.6 is introduced. It is based on approaches in Kerckhoffs et al. [104] and Blanco et al. [23], and in its specific form published in Hirschvogel et al. [86]. Preparatory work for the implementation of the governing equations has been performed in the Master's thesis by [16], also by usage of a 0D heart chamber model, and extension of the coupling to a 3D 4-chamber heart geometry has been implemented in the Bachelor's thesis by [144] (both supervised by the author of this work). The systemic and pulmonary circulation each are divided into an arterial and a venous compartment, both modeled as (windkessel) network with compliant, resistant, and inertant properties, cf. sec. 2.1.2. The governing equations are combinations of (2.79), (2.81) and (2.82) and here are written in terms of flux (volume over time):

left atrial mass
$$\frac{\mathrm{d}V^{\ell}_{\mathrm{at}}(\boldsymbol{u})}{\mathrm{d}t} - q^{\mathrm{pul}}_{\mathrm{ven}} + q^{\ell}_{\mathrm{v,in}} = 0, \tag{2.118}$$

mitral valve momentum
$$\frac{1}{\tilde{R}^{\ell}_{\mathrm{v,in}}}(p^{\ell}_{\mathrm{at}} - p^{\ell}_{\mathrm{v}}) - q^{\ell}_{\mathrm{v,in}} = 0, \tag{2.119}$$

left ventricular mass
$$\frac{\mathrm{d}V^{\ell}_{\mathrm{v}}(\boldsymbol{u})}{\mathrm{d}t} - q^{\ell}_{\mathrm{v,in}} + q^{\ell}_{\mathrm{v,out}} = 0, \tag{2.120}$$

aortic valve momentum
$$\frac{1}{\tilde{R}^{\ell}_{\mathrm{v,out}}}(p^{\ell}_{\mathrm{v}} - p^{\mathrm{sys}}_{\mathrm{ar}}) - q^{\ell}_{\mathrm{v,out}} = 0, \tag{2.121}$$

systemic arterial mass
$$C^{\mathrm{sys}}_{\mathrm{ar}}\left(\frac{\mathrm{d}p^{\mathrm{sys}}_{\mathrm{ar}}}{\mathrm{d}t} - Z^{\mathrm{sys}}_{\mathrm{ar}}\frac{\mathrm{d}q^{\ell}_{\mathrm{v,out}}}{\mathrm{d}t}\right) - q^{\ell}_{\mathrm{v,out}} + q^{\mathrm{sys}}_{\mathrm{ar}} = 0, \tag{2.122}$$

[3] Note that the "aortic characteristic impedance" is conveniently denoted by Z, even though here it is nothing but a resistor acting in front of the arterial compliance-resistance-inertance compartment. In the electrical analogy, each circuit element has its impedance representation: for a compliance it is $Z_C = 1/(\mathrm{i}\omega C)$, for an inertance $Z_L = \mathrm{i}\omega L$ and for a resistance simply $Z_R = R$, where $\mathrm{i} := \sqrt{-1}$ is the imaginary unit and ω the angular frequency.

systemic arterial momentum
$$\frac{L_{\mathrm{ar}}^{\mathrm{sys}}}{R_{\mathrm{ar}}^{\mathrm{sys}}}\frac{\mathrm{d}q_{\mathrm{ar}}^{\mathrm{sys}}}{\mathrm{d}t}+\frac{1}{R_{\mathrm{ar}}^{\mathrm{sys}}}(p_{\mathrm{ven}}^{\mathrm{sys}}-p_{\mathrm{ar}}^{\mathrm{sys}}+Z_{\mathrm{ar}}^{\mathrm{sys}}q_{\mathrm{v,out}}^{\ell})+q_{\mathrm{ar}}^{\mathrm{sys}}=0, \tag{2.123}$$

systemic venous mass
$$C_{\mathrm{ven}}^{\mathrm{sys}}\frac{\mathrm{d}p_{\mathrm{ven}}^{\mathrm{sys}}}{\mathrm{d}t}-q_{\mathrm{ar}}^{\mathrm{sys}}+q_{\mathrm{ven}}^{\mathrm{sys}}=0, \tag{2.124}$$

systemic venous momentum
$$\frac{L_{\mathrm{ven}}^{\mathrm{sys}}}{R_{\mathrm{ven}}^{\mathrm{sys}}}\frac{\mathrm{d}q_{\mathrm{ven}}^{\mathrm{sys}}}{\mathrm{d}t}+\frac{1}{R_{\mathrm{ven}}^{\mathrm{sys}}}(p_{\mathrm{at}}^{r}-p_{\mathrm{ven}}^{\mathrm{sys}})+q_{\mathrm{ven}}^{\mathrm{sys}}=0, \tag{2.125}$$

right atrial mass
$$\frac{\mathrm{d}V_{\mathrm{at}}^{r}(\boldsymbol{u})}{\mathrm{d}t}-q_{\mathrm{ven}}^{\mathrm{sys}}+q_{\mathrm{v,in}}^{r}=0, \tag{2.126}$$

tricuspid valve momentum
$$\frac{1}{\tilde{R}_{\mathrm{v,in}}^{r}}(p_{\mathrm{at}}^{r}-p_{\mathrm{v}}^{r})-q_{\mathrm{v,in}}^{r}=0, \tag{2.127}$$

right ventricular mass
$$\frac{\mathrm{d}V_{\mathrm{v}}^{r}(\boldsymbol{u})}{\mathrm{d}t}-q_{\mathrm{v,in}}^{r}+q_{\mathrm{v,out}}^{r}=0, \tag{2.128}$$

pulmonary valve momentum
$$\frac{1}{\tilde{R}_{\mathrm{v,out}}^{r}}(p_{\mathrm{v}}^{r}-p_{\mathrm{ar}}^{\mathrm{pul}})-q_{\mathrm{v,out}}^{r}=0, \tag{2.129}$$

pulmonary arterial mass
$$C_{\mathrm{ar}}^{\mathrm{pul}}\left(\frac{\mathrm{d}p_{\mathrm{ar}}^{\mathrm{pul}}}{\mathrm{d}t}-Z_{\mathrm{ar}}^{\mathrm{pul}}\frac{\mathrm{d}q_{\mathrm{v,out}}^{r}}{\mathrm{d}t}\right)-q_{\mathrm{v,out}}^{r}+q_{\mathrm{ar}}^{\mathrm{pul}}=0, \tag{2.130}$$

pulmonary arterial momentum
$$\frac{L_{\mathrm{ar}}^{\mathrm{pul}}}{R_{\mathrm{ar}}^{\mathrm{pul}}}\frac{\mathrm{d}q_{\mathrm{ar}}^{\mathrm{pul}}}{\mathrm{d}t}+\frac{1}{R_{\mathrm{ar}}^{\mathrm{pul}}}(p_{\mathrm{ven}}^{\mathrm{pul}}-p_{\mathrm{ar}}^{\mathrm{pul}}+Z_{\mathrm{ar}}^{\mathrm{pul}}q_{\mathrm{v,out}}^{r})+q_{\mathrm{ar}}^{\mathrm{pul}}=0, \tag{2.131}$$

pulmonary venous mass
$$C_{\mathrm{ven}}^{\mathrm{pul}}\frac{\mathrm{d}p_{\mathrm{ven}}^{\mathrm{pul}}}{\mathrm{d}t}-q_{\mathrm{ar}}^{\mathrm{pul}}+q_{\mathrm{ven}}^{\mathrm{pul}}=0, \tag{2.132}$$

pulmonary venous momentum
$$\frac{L_{\mathrm{ven}}^{\mathrm{pul}}}{R_{\mathrm{ven}}^{\mathrm{pul}}}\frac{\mathrm{d}q_{\mathrm{ven}}^{\mathrm{pul}}}{\mathrm{d}t}+\frac{1}{R_{\mathrm{ven}}^{\mathrm{pul}}}(p_{\mathrm{at}}^{\ell}-p_{\mathrm{ven}}^{\mathrm{pul}})+q_{\mathrm{ven}}^{\mathrm{pul}}=0. \tag{2.133}$$

Superscripts ℓ, r, sys and pul refer to “left”, “right”, “systemic” and “pulmonary”, respectively, while subscripts at, v, ar and ven refer to “atrial”, “ventricular”, “arterial” and “venous”, respectively.

Extended systemic and pulmonary circulation with capillaries In the following, the circulation model *0Dsyspulcap* shown in fig. 2.7 is presented. It is an extension to the above-introduced *0Dsyspul* model. Its main motivation emerges from the desire to compute transport and dissociation of substances into a distinguished network of capillaries that consume oxygen and produce carbon dioxide, hence act as source and sink with decidedly determinable production and consumption rates. However, one step back, a transport and dissociation model of some grade of detail (*0Dsyspulcaprespir*, which will be introduced later) necessitates a vascular network and the respective blood compartments that provide transport ability and storage capacity. Therefore, the circulation *0Dsyspulcap* presented here up to now only accounts for the blood flow and is a diversification of the previously stated model *0Dsyspul*, where capillary pressures and flows are considered as well. The fundaments of this extended blood circulation model are based on Trenhago et al. [202] as well as on Ursino and Magosso [203, 204].
The systemic periphery is subdivided into “splanchnic”, “extra-splanchnic”, “muscular”, “cerebral” and “coronary” capillaries, denoted by secondary subscripts spl, espl, msc, cer and cor,

respectively. Each, the arterial and venous capillaries (actually being arterioles and venules), are modeled with a 2-element windkessel (2.83). Quantities relating to the whole systemic arterial periphery carry the secondary subscript peri.
The whole pulmonary capillary bed is modeled with a single 2-element windkessel and is denoted by the subscript cap. The governing equations are stated in the following, where the extension to the basic circulation model is highlighted in grey:

left atrial mass
$$\frac{\mathrm{d}V_{\mathrm{at}}^{\ell}(\boldsymbol{u})}{\mathrm{d}t} - q_{\mathrm{ven}}^{\mathrm{pul}} + q_{\mathrm{v,in}}^{\ell} = 0, \tag{2.134}$$

mitral valve momentum
$$\frac{1}{\tilde{R}_{\mathrm{v,in}}^{\ell}}(p_{\mathrm{at}}^{\ell} - p_{\mathrm{v}}^{\ell}) - q_{\mathrm{v,in}}^{\ell} = 0, \tag{2.135}$$

left ventricular mass
$$\frac{\mathrm{d}V_{\mathrm{v}}^{\ell}(\boldsymbol{u})}{\mathrm{d}t} - q_{\mathrm{v,in}}^{\ell} + q_{\mathrm{v,out}}^{\ell} = 0, \tag{2.136}$$

aortic valve momentum
$$\frac{1}{\tilde{R}_{\mathrm{v,out}}^{\ell}}(p_{\mathrm{v}}^{\ell} - p_{\mathrm{ar}}^{\mathrm{sys}}) - q_{\mathrm{v,out}}^{\ell} = 0, \tag{2.137}$$

systemic arterial mass
$$C_{\mathrm{ar}}^{\mathrm{sys}}\left(\frac{\mathrm{d}p_{\mathrm{ar}}^{\mathrm{sys}}}{\mathrm{d}t} - Z_{\mathrm{ar}}^{\mathrm{sys}}\frac{\mathrm{d}q_{\mathrm{v,out}}^{\ell}}{\mathrm{d}t}\right) - q_{\mathrm{v,out}}^{\ell} + q_{\mathrm{ar}}^{\mathrm{sys}} = 0, \tag{2.138}$$

systemic arterial momentum
$$\frac{L_{\mathrm{ar}}^{\mathrm{sys}}}{R_{\mathrm{ar}}^{\mathrm{sys}}}\frac{\mathrm{d}q_{\mathrm{ar}}^{\mathrm{sys}}}{\mathrm{d}t} + \frac{1}{R_{\mathrm{ar}}^{\mathrm{sys}}}(p_{\mathrm{ar,peri}}^{\mathrm{sys}} - p_{\mathrm{ar}}^{\mathrm{sys}} + Z_{\mathrm{ar}}^{\mathrm{sys}}q_{\mathrm{v,out}}^{\ell}) + q_{\mathrm{ar}}^{\mathrm{sys}} = 0, \tag{2.139}$$

systemic capillary mass
$$\left(\sum_{j=\mathrm{spl,espl,msc,cer,cor}} C_{\mathrm{ar},j}^{\mathrm{sys}}\right)\frac{\mathrm{d}p_{\mathrm{ar,peri}}^{\mathrm{sys}}}{\mathrm{d}t} + \sum_{j=\mathrm{spl,espl,msc,cer,cor}} q_{\mathrm{ar},j}^{\mathrm{sys}} - q_{\mathrm{ar}}^{\mathrm{sys}} = 0, \tag{2.140}$$

sys. cap. art. splanchnic mom.
$$\frac{1}{R_{\mathrm{ar,spl}}^{\mathrm{sys}}}(p_{\mathrm{ven,spl}}^{\mathrm{sys}} - p_{\mathrm{ar,peri}}^{\mathrm{sys}}) + q_{\mathrm{ar,spl}}^{\mathrm{sys}} = 0, \tag{2.141}$$

sys. cap. art. splanchnic mom.
$$\frac{1}{R_{\mathrm{ar,espl}}^{\mathrm{sys}}}(p_{\mathrm{ven,espl}}^{\mathrm{sys}} - p_{\mathrm{ar,peri}}^{\mathrm{sys}}) + q_{\mathrm{ar,espl}}^{\mathrm{sys}} = 0, \tag{2.142}$$

sys. cap. art. muscular mom.
$$\frac{1}{R_{\mathrm{ar,msc}}^{\mathrm{sys}}}(p_{\mathrm{ven,msc}}^{\mathrm{sys}} - p_{\mathrm{ar,peri}}^{\mathrm{sys}}) + q_{\mathrm{ar,msc}}^{\mathrm{sys}} = 0, \tag{2.143}$$

sys. cap. art. cerebral mom.
$$\frac{1}{R_{\mathrm{ar,cer}}^{\mathrm{sys}}}(p_{\mathrm{ven,cer}}^{\mathrm{sys}} - p_{\mathrm{ar,peri}}^{\mathrm{sys}}) + q_{\mathrm{ar,cer}}^{\mathrm{sys}} = 0, \tag{2.144}$$

sys. cap. art. coronary mom.
$$\frac{1}{R_{\mathrm{ar,cor}}^{\mathrm{sys}}}(p_{\mathrm{ven,cor}}^{\mathrm{sys}} - p_{\mathrm{ar,peri}}^{\mathrm{sys}}) + q_{\mathrm{ar,cor}}^{\mathrm{sys}} = 0, \tag{2.145}$$

sys. cap. ven. splanchnic mass
$$C_{\mathrm{ven,spl}}^{\mathrm{sys}}\frac{\mathrm{d}p_{\mathrm{ven,spl}}^{\mathrm{sys}}}{\mathrm{d}t} + q_{\mathrm{ven,spl}}^{\mathrm{sys}} - q_{\mathrm{ar,spl}}^{\mathrm{sys}} = 0, \tag{2.146}$$

sys. cap. ven. splanchnic mom.
$$\frac{1}{R_{\mathrm{ven,spl}}^{\mathrm{sys}}}(p_{\mathrm{ven}}^{\mathrm{sys}} - p_{\mathrm{ven,spl}}^{\mathrm{sys}}) + q_{\mathrm{ven,spl}}^{\mathrm{sys}} = 0, \tag{2.147}$$

sys. cap. ven. extra-splnch. mass
$$C_{\mathrm{ven,espl}}^{\mathrm{sys}}\frac{\mathrm{d}p_{\mathrm{ven,espl}}^{\mathrm{sys}}}{\mathrm{d}t} + q_{\mathrm{ven,espl}}^{\mathrm{sys}} - q_{\mathrm{ar,espl}}^{\mathrm{sys}} = 0, \tag{2.148}$$

sys. cap. ven. extra-splnch. mom.
$$\frac{1}{R_{\mathrm{ven,espl}}^{\mathrm{sys}}}(p_{\mathrm{ven}}^{\mathrm{sys}} - p_{\mathrm{ven,espl}}^{\mathrm{sys}}) + q_{\mathrm{ven,espl}}^{\mathrm{sys}} = 0, \tag{2.149}$$

sys. cap. ven. muscular mass
$$C^{\mathrm{sys}}_{\mathrm{ven,msc}}\frac{\mathrm{d}p^{\mathrm{sys}}_{\mathrm{ven,msc}}}{\mathrm{d}t}+q^{\mathrm{sys}}_{\mathrm{ven,msc}}-q^{\mathrm{sys}}_{\mathrm{ar,msc}}=0, \tag{2.150}$$

sys. cap. ven. muscular mom.
$$\frac{1}{R^{\mathrm{sys}}_{\mathrm{ven,msc}}}(p^{\mathrm{sys}}_{\mathrm{ven}}-p^{\mathrm{sys}}_{\mathrm{ven,msc}})+q^{\mathrm{sys}}_{\mathrm{ven,msc}}=0, \tag{2.151}$$

sys. cap. ven. cerebral mass
$$C^{\mathrm{sys}}_{\mathrm{ven,cer}}\frac{\mathrm{d}p^{\mathrm{sys}}_{\mathrm{ven,cer}}}{\mathrm{d}t}+q^{\mathrm{sys}}_{\mathrm{ven,cer}}-q^{\mathrm{sys}}_{\mathrm{ar,cer}}=0, \tag{2.152}$$

sys. cap. ven. cerebral mom.
$$\frac{1}{R^{\mathrm{sys}}_{\mathrm{ven,cer}}}(p^{\mathrm{sys}}_{\mathrm{ven}}-p^{\mathrm{sys}}_{\mathrm{ven,cer}})+q^{\mathrm{sys}}_{\mathrm{ven,cer}}=0, \tag{2.153}$$

sys. cap. ven. coronary mass
$$C^{\mathrm{sys}}_{\mathrm{ven,cor}}\frac{\mathrm{d}p^{\mathrm{sys}}_{\mathrm{ven,cor}}}{\mathrm{d}t}+q^{\mathrm{sys}}_{\mathrm{ven,cor}}-q^{\mathrm{sys}}_{\mathrm{ar,cor}}=0, \tag{2.154}$$

sys. cap. ven. coronary mom.
$$\frac{1}{R^{\mathrm{sys}}_{\mathrm{ven,cor}}}(p^{\mathrm{sys}}_{\mathrm{ven}}-p^{\mathrm{sys}}_{\mathrm{ven,cor}})+q^{\mathrm{sys}}_{\mathrm{ven,cor}}=0, \tag{2.155}$$

systemic venous mass
$$C^{\mathrm{sys}}_{\mathrm{ven}}\frac{\mathrm{d}p^{\mathrm{sys}}_{\mathrm{ven}}}{\mathrm{d}t}+q^{\mathrm{sys}}_{\mathrm{ven}}-\sum_{j=\mathrm{spl,espl,msc,cer,cor}}q^{\mathrm{sys}}_{\mathrm{ven},j}=0, \tag{2.156}$$

systemic venous mom.
$$\frac{L^{\mathrm{sys}}_{\mathrm{ven}}}{R^{\mathrm{sys}}_{\mathrm{ven}}}\frac{\mathrm{d}q^{\mathrm{sys}}_{\mathrm{ven}}}{\mathrm{d}t}+\frac{1}{R^{\mathrm{sys}}_{\mathrm{ven}}}(p^{r}_{\mathrm{at}}-p^{\mathrm{sys}}_{\mathrm{ven}})+q^{\mathrm{sys}}_{\mathrm{ven}}=0, \tag{2.157}$$

right atrial mass
$$\frac{\mathrm{d}V^{r}_{\mathrm{at}}(\boldsymbol{u})}{\mathrm{d}t}-q^{\mathrm{sys}}_{\mathrm{ven}}+q^{r}_{\mathrm{v,in}}=0, \tag{2.158}$$

tricuspid valve momentum
$$\frac{1}{\tilde{R}^{r}_{\mathrm{v,in}}}(p^{r}_{\mathrm{at}}-p^{r}_{\mathrm{v}})-q^{r}_{\mathrm{v,in}}=0, \tag{2.159}$$

right ventricular mass
$$\frac{\mathrm{d}V^{r}_{\mathrm{v}}(\boldsymbol{u})}{\mathrm{d}t}-q^{r}_{\mathrm{v,in}}+q^{r}_{\mathrm{v,out}}=0, \tag{2.160}$$

pulmonary valve momentum
$$\frac{1}{\tilde{R}^{r}_{\mathrm{v,out}}}(p^{r}_{\mathrm{v}}-p^{\mathrm{pul}}_{\mathrm{ar}})-q^{r}_{\mathrm{v,out}}=0, \tag{2.161}$$

pulmonary arterial mass
$$C^{\mathrm{pul}}_{\mathrm{ar}}\left(\frac{\mathrm{d}p^{\mathrm{pul}}_{\mathrm{ar}}}{\mathrm{d}t}-Z^{\mathrm{pul}}_{\mathrm{ar}}\frac{\mathrm{d}q^{r}_{\mathrm{v,out}}}{\mathrm{d}t}\right)-q^{r}_{\mathrm{v,out}}+q^{\mathrm{pul}}_{\mathrm{ar}}=0, \tag{2.162}$$

pulmonary arterial momentum
$$\frac{L^{\mathrm{pul}}_{\mathrm{ar}}}{R^{\mathrm{pul}}_{\mathrm{ar}}}\frac{\mathrm{d}q^{\mathrm{pul}}_{\mathrm{ar}}}{\mathrm{d}t}+\frac{1}{R^{\mathrm{pul}}_{\mathrm{ar}}}(p^{\mathrm{pul}}_{\mathrm{cap}}-p^{\mathrm{pul}}_{\mathrm{ar}}+Z^{\mathrm{pul}}_{\mathrm{ar}}q^{r}_{\mathrm{v,out}})+q^{\mathrm{pul}}_{\mathrm{ar}}=0, \tag{2.163}$$

pulmonary capillary mass
$$C^{\mathrm{pul}}_{\mathrm{cap}}\frac{\mathrm{d}p^{\mathrm{pul}}_{\mathrm{cap}}}{\mathrm{d}t}-q^{\mathrm{pul}}_{\mathrm{ar}}+q^{\mathrm{pul}}_{\mathrm{cap}}=0, \tag{2.164}$$

pulmonary capillary momentum
$$\frac{1}{R^{\mathrm{pul}}_{\mathrm{cap}}}(p^{\mathrm{pul}}_{\mathrm{ven}}-p^{\mathrm{pul}}_{\mathrm{cap}})+q^{\mathrm{pul}}_{\mathrm{cap}}=0, \tag{2.165}$$

pulmonary venous mass
$$C^{\mathrm{pul}}_{\mathrm{ven}}\frac{\mathrm{d}p^{\mathrm{pul}}_{\mathrm{ven}}}{\mathrm{d}t}-q^{\mathrm{pul}}_{\mathrm{cap}}+q^{\mathrm{pul}}_{\mathrm{ven}}=0, \tag{2.166}$$

pulmonary venous momentum
$$\frac{L^{\mathrm{pul}}_{\mathrm{ven}}}{R^{\mathrm{pul}}_{\mathrm{ven}}}\frac{\mathrm{d}q^{\mathrm{pul}}_{\mathrm{ven}}}{\mathrm{d}t}+\frac{1}{R^{\mathrm{pul}}_{\mathrm{ven}}}(p^{\ell}_{\mathrm{at}}-p^{\mathrm{pul}}_{\mathrm{ven}})+q^{\mathrm{pul}}_{\mathrm{ven}}=0. \tag{2.167}$$

It should be noted that the pressure in the systemic arterial periphery, $p^{\mathrm{sys}}_{\mathrm{ar,peri}}$, is the same for all five arterial capillary compartments (arterioles) due to continuity requirements.

Due to the large amount of parameters within this model on the one hand, and the desire of determinability to a certain extent on the other, some considerations with regard to the distribution of resistances and compliances are carried out.
The equivalent resistance in case of a parallel alignment is the inverse of the sum over the reciprocal resistances, while for a serial alignment the sum of all resistances yields the equivalent one.
In the systemic arterial periphery, the total peripheral resistance may be computed by the five arteriole resistances in parallel:

$$R^{\mathrm{sys}}_{\mathrm{ar,peri}} = \left(\frac{1}{R^{\mathrm{sys}}_{\mathrm{ar,spl}}} + \frac{1}{R^{\mathrm{sys}}_{\mathrm{ar,espl}}} + \frac{1}{R^{\mathrm{sys}}_{\mathrm{ar,msc}}} + \frac{1}{R^{\mathrm{sys}}_{\mathrm{ar,cer}}} + \frac{1}{R^{\mathrm{sys}}_{\mathrm{ar,cor}}} \right)^{-1}, \tag{2.168}$$

and the total systemic arterial resistance then emerges from a serial alignment of the peripheral and the proximal resistance:

$$R^{\mathrm{sys}}_{\mathrm{ar}(\mathit{total})} = R^{\mathrm{sys}}_{\mathrm{ar,peri}} + R^{\mathrm{sys}}_{\mathrm{ar}}. \tag{2.169}$$

For the systemic venules and veins, similar considerations hold:

$$R^{\mathrm{sys}}_{\mathrm{ven,peri}} = \left(\frac{1}{R^{\mathrm{sys}}_{\mathrm{ven,spl}}} + \frac{1}{R^{\mathrm{sys}}_{\mathrm{ven,espl}}} + \frac{1}{R^{\mathrm{sys}}_{\mathrm{ven,msc}}} + \frac{1}{R^{\mathrm{sys}}_{\mathrm{ven,cer}}} + \frac{1}{R^{\mathrm{sys}}_{\mathrm{ven,cor}}} \right)^{-1}, \tag{2.170}$$

and

$$R^{\mathrm{sys}}_{\mathrm{ven}(\mathit{total})} = R^{\mathrm{sys}}_{\mathrm{ven,peri}} + R^{\mathrm{sys}}_{\mathrm{ven}}. \tag{2.171}$$

In contrast to resistances, the equivalent compliances behave additively in parallel alignment and reciprocally in serial alignment. However, here the connection of compliances always may be viewed as a parallel one since no flux entering a capacitor is trespassed to another one. Hence, in the systemic arterial capillaries, total peripheral compliance is

$$C^{\mathrm{sys}}_{\mathrm{ar,peri}} = C^{\mathrm{sys}}_{\mathrm{ar,spl}} + C^{\mathrm{sys}}_{\mathrm{ar,espl}} + C^{\mathrm{sys}}_{\mathrm{ar,msc}} + C^{\mathrm{sys}}_{\mathrm{ar,cer}} + C^{\mathrm{sys}}_{\mathrm{ar,cor}}, \tag{2.172}$$

and total arterial compliance

$$C^{\mathrm{sys}}_{\mathrm{ar}(\mathit{total})} = C^{\mathrm{sys}}_{\mathrm{ar,peri}} + C^{\mathrm{sys}}_{\mathrm{ar}}. \tag{2.173}$$

Again, the venous compartment behaves analogously:

$$C^{\mathrm{sys}}_{\mathrm{ven,peri}} = C^{\mathrm{sys}}_{\mathrm{ven,spl}} + C^{\mathrm{sys}}_{\mathrm{ven,espl}} + C^{\mathrm{sys}}_{\mathrm{ven,msc}} + C^{\mathrm{sys}}_{\mathrm{ven,cer}} + C^{\mathrm{sys}}_{\mathrm{ven,cor}}, \tag{2.174}$$

and

$$C^{\mathrm{sys}}_{\mathrm{ven}(\mathit{total})} = C^{\mathrm{sys}}_{\mathrm{ven,peri}} + C^{\mathrm{sys}}_{\mathrm{ven}}. \tag{2.175}$$

Total pulmonary arterial resistance and compliance then yield

$$R^{\mathrm{pul}}_{\mathrm{ar}(\mathit{total})} = R^{\mathrm{pul}}_{\mathrm{ar}} + R^{\mathrm{pul}}_{\mathrm{cap}} \quad \text{and} \quad C^{\mathrm{pul}}_{\mathrm{ar}(\mathit{total})} = C^{\mathrm{pul}}_{\mathrm{ar}} + C^{\mathrm{pul}}_{\mathrm{cap}}, \tag{2.176}$$

while total pulmonary venous resistance and compliance remains unaltered with respect to model *0Dsyspul*.

Table 2.4: Model *0Dsyspulcap*: Relative systemic arterial and venous peripheral resistances and compliances with respect to the total peripheral ones (2.168), (2.170), (2.172) and (2.174), respectively; weights according to Ursino and Magosso [203]

j	spl	espl	msc	cer	cor
$R^{\mathrm{sys}}_{\mathrm{ar},j}/R^{\mathrm{sys}}_{\mathrm{ar,peri}}$	3.35	3.56	4.54	6.65	19.95
$C^{\mathrm{sys}}_{\mathrm{ar},j}/C^{\mathrm{sys}}_{\mathrm{ar,peri}}$	0.55	0.18	0.14	0.11	0.03
$R^{\mathrm{sys}}_{\mathrm{ven},j}/R^{\mathrm{sys}}_{\mathrm{ven,peri}}$	3.4	3.53	4.47	6.66	19.93
$C^{\mathrm{sys}}_{\mathrm{ven},j}/C^{\mathrm{sys}}_{\mathrm{ven,peri}}$	0.55	0.18	0.14	0.1	0.03

The resistance (compliance) fractions of the respective organs to the overall systemic peripheral resistance (compliance) are chosen according to absolute values presented in Ursino and Magosso [203] and are listed in tab. 2.4.

Furthermore, the distribution of peripheral with respect to total resistance and compliance is given in tab. 2.5. However, only values indicated by ‡ are taken from Ursino and Magosso [203], while the others are roughly estimated.[4]

Table 2.5: Model *0Dsyspulcap*: Fractions of peripheral to total resistance and compliance, respectively; values indicated by ‡ from Ursino and Magosso [203]

$R^{\mathrm{sys}}_{\mathrm{ar,peri}}/R^{\mathrm{sys}}_{\mathrm{ar}(\mathit{total})}$	$C^{\mathrm{sys}}_{\mathrm{ar,peri}}/C^{\mathrm{sys}}_{\mathrm{ar}(\mathit{total})}$	$R^{\mathrm{sys}}_{\mathrm{ven,peri}}/R^{\mathrm{sys}}_{\mathrm{ven}(\mathit{total})}$	$C^{\mathrm{sys}}_{\mathrm{ven,peri}}/C^{\mathrm{sys}}_{\mathrm{ven}(\mathit{total})}$
$0.94^{\ddagger}$	0.05	0.2	0.8

$R^{\mathrm{pul}}_{\mathrm{cap}}/R^{\mathrm{pul}}_{\mathrm{ar}(\mathit{total})}$	$C^{\mathrm{pul}}_{\mathrm{cap}}/C^{\mathrm{pul}}_{\mathrm{ar}(\mathit{total})}$
0.5	0.5

Base parameters for the blood flow mechanics models Due to the relatively large amount of parameters, a reasonable parameterization of the models in terms of a few, functionally characteristic quantities is chosen. For example, the time constant $\tau^{\mathrm{sys}}_{\mathrm{ar}}$ of the systemic arterial windkessel model may be approximately estimated if only two pressure values, namely the end-systolic and end-diastolic arterial pressure $\tilde{p}^{\mathrm{sys}}_{\mathrm{ar}}(t_{\mathrm{es}})$ and $\tilde{p}^{\mathrm{sys}}_{\mathrm{ar}}(t_{\mathrm{ed}})$, respectively, are known, i.e. obtained from basic non-invasive measurements. That time constant describes the speed of pressure decay if no flux enters the windkessel model, and is the product of arterial compliance and resistance:

$$\tau^{\mathrm{sys}}_{\mathrm{ar}} = C^{\mathrm{sys}}_{\mathrm{ar}(\mathit{total})} R^{\mathrm{sys}}_{\mathrm{ar}(\mathit{total})} \approx \frac{T_{\mathrm{cycl}} - t_{\mathrm{es}} + t_{\mathrm{ed}}}{\ln \frac{\tilde{p}^{\mathrm{sys}}_{\mathrm{ar}}(t_{\mathrm{es}})}{\tilde{p}^{\mathrm{sys}}_{\mathrm{ar}}(t_{\mathrm{ed}})}}. \tag{2.177}$$

[4] Ursino and Magosso [203] fractions indicate that a significant portion (93 %) of systemic arterial compliance should lie in the periphery, which is doubted and produces unphysiological pressure curves. Furthermore, 72 % of pulmonary arterial resistance and only 12 % of compliance should be proximal to the heart, which is also doubted since the smaller capillaries should not be less resistive and more compliant than the larger proximal vessels. Additionally, the authors do not have a proximal systemic venous compartment, such that those fractions are roughly estimated.

Typically, $\tau_{\mathrm{ar}}^{\mathrm{sys}}$ has physiological values between $1.0\ \mathrm{s} \sim 2.5\ \mathrm{s}$, while the pulmonary arterial time constant usually is much lower and remains rather constant regardless of the state of health ($\tau_{\mathrm{ar}}^{\mathrm{pul}} \approx \tau_{\mathrm{ar}}^{\mathrm{sys}}/5 \sim \tau_{\mathrm{ar}}^{\mathrm{sys}}/6$ [182]). Hence, without loss of generality, it is chosen here to $\tau_{\mathrm{ar}}^{\mathrm{pul}} = 0.3\ \mathrm{s}$. Supposing that the time constant and systemic arterial resistance, $R_{\mathrm{ar}(\mathit{total})}^{\mathrm{sys}}$, are considered as the variable "inputs of choice", the compliance results from (2.177) according to

$$C_{\mathrm{ar}(\mathit{total})}^{\mathrm{sys}} = \frac{\tau_{\mathrm{ar}}^{\mathrm{sys}}}{R_{\mathrm{ar}(\mathit{total})}^{\mathrm{sys}}}. \tag{2.178}$$

In contrast to systemic arterial compliance which is mainly located in the aorta and the big vessels, pulmonary arterial compliance rather is distributed over the whole arterial tree. Pulmonary arterial resistance is significantly lower than its systemic arterial counterpart, i.e. a little over a tenth of the systemic one [182]. Hence, the following dependencies for the pulmonary arterial compartment are assumed:

$$R_{\mathrm{ar}(\mathit{total})}^{\mathrm{pul}} = \frac{1}{8} R_{\mathrm{ar}(\mathit{total})}^{\mathrm{sys}} \quad \text{and} \quad C_{\mathrm{ar}(\mathit{total})}^{\mathrm{pul}} = \frac{\tau_{\mathrm{ar}}^{\mathrm{pul}}}{R_{\mathrm{ar}(\mathit{total})}^{\mathrm{pul}}}. \tag{2.179}$$

Systemic veins have an extensive storage capacity and their compliance is about thirty times higher than the systemic arterial one [69]. However, this does not hold equally for pulmonary veins; their compliance can be considered only a little over twice the pulmonary arterial one [200]. Thus, the venous compliances are set to

$$C_{\mathrm{ven}(\mathit{total})}^{\mathrm{sys}} = 30 \cdot C_{\mathrm{ar}(\mathit{total})}^{\mathrm{sys}} \quad \text{and} \quad C_{\mathrm{ven}}^{\mathrm{pul}} = 2.5 \cdot C_{\mathrm{ar}(\mathit{total})}^{\mathrm{pul}}. \tag{2.180}$$

The systemic venous resistance is significantly lower than the arterial one, while the pulmonary venous resistance is approximately equal to its arterial counterpart [63]:

$$C_{\mathrm{ven}(\mathit{total})}^{\mathrm{sys}} = \frac{1}{5} R_{\mathrm{ar}(\mathit{total})}^{\mathrm{sys}} \quad \text{and} \quad R_{\mathrm{ven}}^{\mathrm{pul}} = R_{\mathrm{ar}(\mathit{total})}^{\mathrm{pul}}. \tag{2.181}$$

The systemic arterial impedance is only about 5–7 $\%$ of the systemic arterial resistance [210], and pulmonary arterial impedance is neglected:

$$Z_{\mathrm{ar}}^{\mathrm{sys}} = \frac{1}{20} R_{\mathrm{ar}(\mathit{total})}^{\mathrm{sys}} \quad \text{and} \quad Z_{\mathrm{ar}}^{\mathrm{pul}} = 0. \tag{2.182}$$

The inertance of the systemic arterial system is set to $L_{\mathrm{ar}}^{\mathrm{sys}} = 0.667 \cdot 10^{-6}\ \frac{\mathrm{kPa \cdot s^2}}{\mathrm{mm^3}}$, according to a value estimated in [195]. Pulmonary arterial inertance as well as all venous inertances are set to zero due to the lack of reliable data and the general difficulties to estimate them [210].

Base parameters for the blood flow models are shown in tab. 2.6. Other vascular parameters (resistances, compliances) are, in general, assumed to depend on the (total) systemic arterial resistance as well as on the systemic and pulmonary arterial windkessel time constant. These above-introduced dependencies are summarized in tab. 2.7. Note that for the basic circulation model *0Dsyspul*, no distinction between parameters referring to the *total* tree and different subgroups thereof is given, hence $(\cdot)_{(\cdot)(\mathit{total})}^{(\cdot)} \equiv (\cdot)_{(\cdot)}^{(\cdot)}$.

Table 2.6: Base parameters of the blood flow mechanics models

parameters for 0D atrial models (apply only to model *3Dventr*)		
$\Delta t_{\mathrm{at,act}}$ $[\mathrm{s}]$	$2\,(t_{\mathrm{ed}} - t_0)$	duration of 0D atrial activation
$E^{\ell}_{\mathrm{at,min}}$ $[\frac{\mathrm{kPa}}{\mathrm{mm}^3}]$	$9 \cdot 10^{-6}$	left atrial baseline elastance
$E^{\ell}_{\mathrm{at,A}}$ $[\frac{\mathrm{kPa}}{\mathrm{mm}^3}]$	$20 \cdot 10^{-6}$	left atrial elastance amplitude
$E^{r}_{\mathrm{at,min}}$ $[\frac{\mathrm{kPa}}{\mathrm{mm}^3}]$	$8 \cdot 10^{-6}$	right atrial baseline elastance
$E^{r}_{\mathrm{at,A}}$ $[\frac{\mathrm{kPa}}{\mathrm{mm}^3}]$	$10 \cdot 10^{-6}$	right atrial elastance amplitude
valve resistances		
$R^{\ell,\mathrm{min}}_{\mathrm{v,in}}$ $[\frac{\mathrm{kPa\cdot s}}{\mathrm{mm}^3}]$	10^{-6}	opened mitral valve resistance
$R^{\ell,\mathrm{max}}_{\mathrm{v,in}}$ $[\frac{\mathrm{kPa\cdot s}}{\mathrm{mm}^3}]$	10^{1}	closed mitral valve resistance
$R^{\ell,\mathrm{min}}_{\mathrm{v,out}}$ $[\frac{\mathrm{kPa\cdot s}}{\mathrm{mm}^3}]$	10^{-6}	opened aortic valve resistance
$R^{\ell,\mathrm{max}}_{\mathrm{v,out}}$ $[\frac{\mathrm{kPa\cdot s}}{\mathrm{mm}^3}]$	10^{1}	closed aortic valve resistance
$R^{r,\mathrm{min}}_{\mathrm{v,in}}$ $[\frac{\mathrm{kPa\cdot s}}{\mathrm{mm}^3}]$	10^{-6}	opened tricuspid valve resistance
$R^{r,\mathrm{max}}_{\mathrm{v,in}}$ $[\frac{\mathrm{kPa\cdot s}}{\mathrm{mm}^3}]$	10^{1}	closed tricuspid valve resistance
$R^{r,\mathrm{min}}_{\mathrm{v,out}}$ $[\frac{\mathrm{kPa\cdot s}}{\mathrm{mm}^3}]$	10^{-6}	opened pulmonary valve resistance
$R^{r,\mathrm{max}}_{\mathrm{v,out}}$ $[\frac{\mathrm{kPa\cdot s}}{\mathrm{mm}^3}]$	10^{1}	closed pulmonary valve resistance
inertances		
$L^{\mathrm{sys}}_{\mathrm{ar}}$ $[\frac{\mathrm{kPa\cdot s}^2}{\mathrm{mm}^3}]$	$0.667 \cdot 10^{-6}$	systemic arterial inertance
$L^{\mathrm{sys}}_{\mathrm{ven}}$ $[\frac{\mathrm{kPa\cdot s}^2}{\mathrm{mm}^3}]$	0	systemic venous inertance
$L^{\mathrm{pul}}_{\mathrm{ar}}$ $[\frac{\mathrm{kPa\cdot s}^2}{\mathrm{mm}^3}]$	0	pulmonary arterial inertance
$L^{\mathrm{pul}}_{\mathrm{ven}}$ $[\frac{\mathrm{kPa\cdot s}^2}{\mathrm{mm}^3}]$	0	pulmonary venous inertance
time constants and arterial resistances		
$\tau^{\mathrm{sys}}_{\mathrm{ar}}$ $[\mathrm{s}]$	1.652	systemic arterial windkessel time constant (2.177)
$\tau^{\mathrm{pul}}_{\mathrm{ar}}$ $[\mathrm{s}]$	0.3	pulmonary arterial windkessel time constant
$R^{\mathrm{sys}}_{\mathrm{ar}(\mathit{total})}$ $[\frac{\mathrm{kPa\cdot s}}{\mathrm{mm}^3}]$	$120 \cdot 10^{-6}$	(total) systemic arterial resistance

Table 2.7: Vascular resistance, compliance, and impedance parameters dependent on the systemic arterial resistance $R^{\mathrm{sys}}_{\mathrm{ar}(\mathit{total})}$

i	$R^{i}_{\mathrm{ar}(\mathit{total})}$	$C^{i}_{\mathrm{ar}(\mathit{total})}$	Z^{i}_{ar}	$R^{i}_{\mathrm{ven}(\mathit{total})}$	$C^{i}_{\mathrm{ven}(\mathit{total})}$
sys	$R^{\mathrm{sys}}_{\mathrm{ar}(\mathit{total})}$	$\tau^{\mathrm{sys}}_{\mathrm{ar}} / R^{\mathrm{sys}}_{\mathrm{ar}(\mathit{total})}$	$R^{\mathrm{sys}}_{\mathrm{ar}(\mathit{total})}/20$	$R^{\mathrm{sys}}_{\mathrm{ar}(\mathit{total})}/5$	$30 \cdot C^{\mathrm{sys}}_{\mathrm{ar}(\mathit{total})}$
pul	$R^{\mathrm{sys}}_{\mathrm{ar}(\mathit{total})}/8$	$8 \cdot \tau^{\mathrm{pul}}_{\mathrm{ar}} / R^{\mathrm{sys}}_{\mathrm{ar}(\mathit{total})}$	0	$R^{\mathrm{sys}}_{\mathrm{ar}(\mathit{total})}/8$	$2.5 \cdot C^{\mathrm{pul}}_{\mathrm{ar}(\mathit{total})}$

2.2.2.2 Gas transport and dissociation

A model for oxygen and carbon dioxide transport and dissociation, including the oxygen uptake and carbon dioxide elimination by the lungs in terms of gas-blood diffusion is proposed. At the organ level, metabolic consumption of oxygen and production of carbon dioxide happens, distinguished into five different organ levels: the "splanchnic" (spl), "extra-splanchnic" (espl), "muscular" (msc), "cerebral" (cer) and "coronary" (cor) compartments.
The integrated cardiovascular-respiratory system model is abbreviated with *0Dsyspulcaprespir*. Its cardiovascular mechanics part is governed by equations (2.134)–(2.167). The model is based on Trenhago et al. [202], which partly relies on the one proposed by Christiansen and Dræby [41, 42]. However, here a different model for the lung mechanics is chosen, namely one according to Ben-Tal [18]. Additionally, simplified dissociation rules [84] for oxygen and carbon dioxide are chosen here in contrast to the models in [41, 42, 202]. Further reduced-dimensional models of the cardiovascular and respiratory systems may be found in [17, 56, 122], while Broomé et al. [30] propose a reduced-dimensional model for hemodynamics with a simplified oxygen transport without gas uptake by the lungs.

Lung mechanics A 0-dimensional flexible lung model including gas exchange is considered as it is presented by Ben-Tal [18]. Its mechanics are described – analogously to 0D flow models – with an alveolar inertance L_{alv}, resistance R_{alv} and elastance E_{alv}. The mass and momentum balances here are written as two first-order differential equations for the alveolar volume V_{alv} and alveolar flux q_{alv}:

$$\dot{V}_{\mathrm{alv}} - q_{\mathrm{alv}} = 0, \tag{2.183}$$

$$L_{\mathrm{alv}}\dot{q}_{\mathrm{alv}} + R_{\mathrm{alv}}q_{\mathrm{alv}} + E_{\mathrm{alv}}(V_{\mathrm{alv}} - V_{\mathrm{alv,u}}) - p_{\mathrm{alv}} + U_t = 0, \tag{2.184}$$

with $V_{\mathrm{alv,u}}$ as the unstressed volume of the lung.

The alveolar pressure p_{alv} in (2.184) is governed by the ordinary differential equation

$$\dot{p}_{\mathrm{alv}} - \frac{1}{V_{\mathrm{alv}}}\left(U_{\mathrm{m}}\left[\frac{U_{\mathrm{m}} - p_{\mathrm{alv}}}{R_{\mathrm{airw}}} + \tilde{\kappa}_{\mathrm{CO_2}}(p^{\mathrm{pul}}_{\mathrm{CO_2,cap}} - f_{\mathrm{CO_2,alv}}p_{\mathrm{alv}}) + \tilde{\kappa}_{\mathrm{O_2}}(p^{\mathrm{pul}}_{\mathrm{O_2,cap}} - f_{\mathrm{O_2,alv}}p_{\mathrm{alv}})\right] - p_{\mathrm{alv}}q_{\mathrm{alv}}\right) = 0, \tag{2.185}$$

where $p^{\mathrm{pul}}_{\mathrm{CO_2,cap}}$ and $p^{\mathrm{pul}}_{\mathrm{O_2,cap}}$ are the pulmonary capillary partial pressures of carbon dioxide ($\mathrm{CO_2}$) and oxygen ($\mathrm{O_2}$), respectively. They are state variables of the transport equations that will be introduced later.

The concentrations of carbon dioxide and oxygen (volume fractions) inside the alveolar compartments are $f_{\mathrm{CO_2,alv}}$ and $f_{\mathrm{O_2,alv}}$, respectively. They are governed by the ordinary differential equations

$$\dot{f}_{\mathrm{CO_2,alv}} - \frac{1}{V_{\mathrm{alv}}}\left[\tilde{\kappa}_{\mathrm{CO_2}}(p^{\mathrm{pul}}_{\mathrm{CO_2,cap}} - f_{\mathrm{CO_2,alv}}p_{\mathrm{alv}}) + (f_{\mathrm{CO_2,in}} - f_{\mathrm{CO_2,alv}})q_{\mathrm{in}} - f_{\mathrm{CO_2,alv}}\left\{\tilde{\kappa}_{\mathrm{O_2}}(p^{\mathrm{pul}}_{\mathrm{O_2,cap}} - f_{\mathrm{O_2,alv}}(p_{\mathrm{alv}} - p^{\mathrm{water}}_{\mathrm{vap},37})) + \tilde{\kappa}_{\mathrm{CO_2}}(p^{\mathrm{pul}}_{\mathrm{CO_2,cap}} - f_{\mathrm{CO_2,alv}}(p_{\mathrm{alv}} - p^{\mathrm{water}}_{\mathrm{vap},37}))\right\}\right] = 0 \tag{2.186}$$

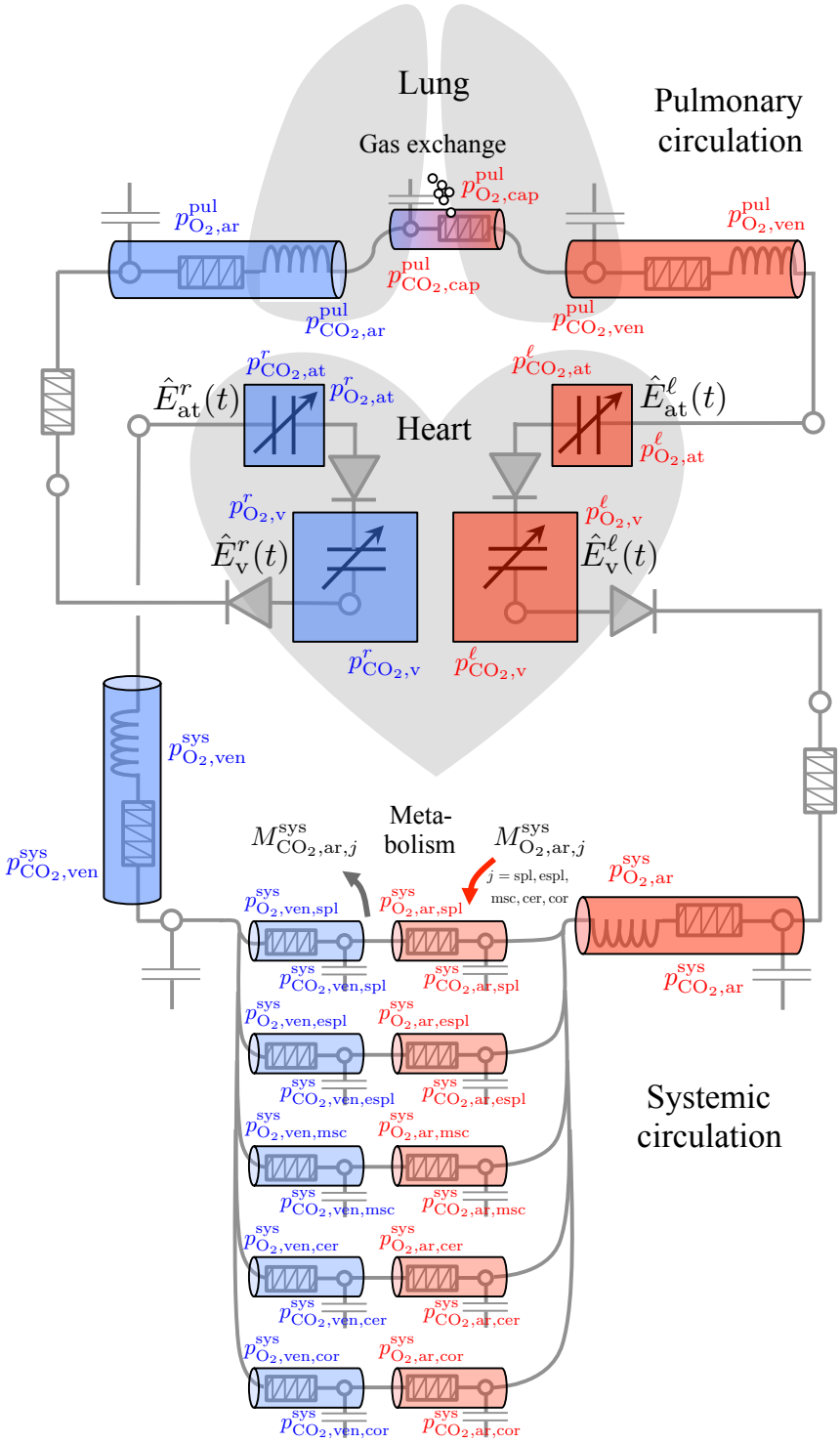

Figure 2.14: Model *PrescrHeart* | *0Dsyspulcaprespir*: Prescribed-dynamics heart together with the cardio-respiratory system; all four heart chambers are 0-dimensional elastance models with prescribed elastance functions $\hat{E}^i_c(t)$ ($c = \mathrm{v}, \mathrm{at}$, $i = \ell, r$) according to (2.221).

and

$$\dot{f}_{\mathrm{O}_2,\mathrm{alv}} - \frac{1}{V_{\mathrm{alv}}}\Big[\tilde{\kappa}_{\mathrm{O}_2}(p^{\mathrm{pul}}_{\mathrm{O}_2,\mathrm{cap}} - f_{\mathrm{O}_2,\mathrm{alv}}p_{\mathrm{alv}}) + (f_{\mathrm{O}_2,\mathrm{in}} - f_{\mathrm{O}_2,\mathrm{alv}})q_{\mathrm{in}} - f_{\mathrm{O}_2,\mathrm{alv}}\Big\{\tilde{\kappa}_{\mathrm{O}_2}(p^{\mathrm{pul}}_{\mathrm{O}_2,\mathrm{cap}} - f_{\mathrm{O}_2,\mathrm{alv}}(p_{\mathrm{alv}} - p^{\mathrm{water}}_{\mathrm{vap},37})) + \tilde{\kappa}_{\mathrm{CO}_2}(p^{\mathrm{pul}}_{\mathrm{CO}_2,\mathrm{cap}} - f_{\mathrm{CO}_2,\mathrm{alv}}(p_{\mathrm{alv}} - p^{\mathrm{water}}_{\mathrm{vap},37}))\Big\}\Big] = 0, \tag{2.187}$$

stating that the rates of change of CO_2 and O_2 concentration in the lung have to balance the leaving or incoming amount of gas due to transport (convection) and the change of gas quantities as consequence of diffusion across the alveolar-capillary barrier. The vapor pressure of water at $37°\mathrm{C}$ is $p^{\mathrm{water}}_{\mathrm{vap},37} = 47.1\ \mathrm{mmHg}$.
The inspired concentrations of carbon dioxide and oxygen are

$$f_{\mathrm{CO}_2,\mathrm{in}} = \begin{cases} \frac{f_{\mathrm{CO}_2,\mathrm{alv}}V_{\mathrm{D}} + f_{\mathrm{CO}_2,\mathrm{ext}}(V_{\mathrm{T}} - V_{\mathrm{D}})}{V_{\mathrm{T}}}, & V_{\mathrm{T}} \geq V_{\mathrm{D}}, \\ f_{\mathrm{CO}_2,\mathrm{alv}}, & V_{\mathrm{T}} < V_{\mathrm{D}} \end{cases} \tag{2.188}$$

and

$$f_{\mathrm{O}_2,\mathrm{in}} = \begin{cases} \frac{f_{\mathrm{O}_2,\mathrm{alv}}V_{\mathrm{D}} + f_{\mathrm{O}_2,\mathrm{ext}}(V_{\mathrm{T}} - V_{\mathrm{D}})}{V_{\mathrm{T}}}, & V_{\mathrm{T}} \geq V_{\mathrm{D}}, \\ f_{\mathrm{O}_2,\mathrm{alv}}, & V_{\mathrm{T}} < V_{\mathrm{D}}, \end{cases} \tag{2.189}$$

respectively, where V_{D} is the dead space volume and V_{T} the previously introduced tidal volume (volume of inspired air per breath). The external atmospheric gas fractions (concentrations) of carbon dioxide and oxygen are $f_{\mathrm{CO}_2,\mathrm{ext}} = 0.0004$ and $f_{\mathrm{O}_2,\mathrm{ext}} = 0.21$, respectively. The inspired air flow in (2.186) and (2.187) is

$$q_{\mathrm{in}} = \begin{cases} \frac{U_{\mathrm{m}} - p_{\mathrm{alv}}}{R_{\mathrm{airw}}}, & U_{\mathrm{m}} > p_{\mathrm{alv}}, \\ 0, & U_{\mathrm{m}} \leq p_{\mathrm{alv}}. \end{cases} \tag{2.190}$$

The time-varying pleural pressure U_t in (2.184) is an external input to the lung model and is given by the function

$$U_t = U_{\mathrm{m}} - R_{\mathrm{airw}}\,\omega_{\mathrm{b}}\frac{V_{\mathrm{T}}}{2}\sin(\omega_{\mathrm{b}}\,t) - E_{\mathrm{alv}}(V_{\mathrm{lung}} - \frac{V_{\mathrm{T}}}{2}\cos(\omega_{\mathrm{b}}\,t)), \tag{2.191}$$

with the external atmospheric pressure U_{m}, the tidal volume V_{T}, the total lung volume V_{lung}, and the breathing frequency ω_{b}.

The diffusion capacities for CO_2 and O_2 across the hemato-alveolar membrane are

$$\tilde{\kappa}_{\mathrm{CO}_2} = V_{\mathrm{m,gas}}\,\kappa_{\mathrm{CO}_2} \quad \text{and} \quad \tilde{\kappa}_{\mathrm{O}_2} = V_{\mathrm{m,gas}}\,\kappa_{\mathrm{O}_2}, \tag{2.192}$$

either expressed in $[\frac{\mathrm{mmol}}{\mathrm{s{\cdot}kPa}}]$ or $[\frac{\mathrm{mm}^3}{\mathrm{s{\cdot}kPa}}]$ with help of the molar volume of an ideal gas $V_{\mathrm{m,gas}} = 22.4 \cdot 10^3\ \frac{\mathrm{mm}^3}{\mathrm{mmol}}$ (at standard conditions for temperature and pressure).

The parameters for the 0D lung are summarized in tab. 2.8.

Transport model The gas transport model follows Trenhago et al. [202], essentially being a modification of [41, 42] to allow for the unsteady realm. It relies on considerations of conservation of the concentration c_i of a species i within a compartment of volume V and flux q, and additional conservation of the entire compartment volume, cf. (2.81):

$$\frac{\mathrm{d}(c_i V)}{\mathrm{d}t} = q_{\mathrm{in}} c_{i,\mathrm{in}} - q c_i \qquad \text{and} \qquad \frac{\mathrm{d}V}{\mathrm{d}t} = q_{\mathrm{in}} - q, \tag{2.193}$$

where q_{in} and $c_{i,\mathrm{in}}$ are the incoming (upstream) fluxes and concentrations, respectively. Combining $(2.193)_1$ and $(2.193)_2$ then yields

$$V \frac{\mathrm{d}c_i}{\mathrm{d}t} = q_{\mathrm{in}}(c_{i,\mathrm{in}} - c_i). \tag{2.194}$$

The dissociation of gases in blood and tissue is of complex nature and depends upon multiple biochemical and physical conditions. A gas dissociation model governs the amount of gas matter c_i that somehow is absorbed or released by the blood and the tissue. The blood dissociation functions for carbon dioxide and oxygen, c_{CO_2} and c_{O_2}, respectively, are compartment-specific and in general depend upon another. Here, they are written in terms of the partial pressures of carbon dioxide and oxygen, p_{CO_2} and p_{O_2}, respectively, which are the state variables of the transport model:

$$c_{\mathrm{CO}_2} = c_{\mathrm{CO}_2}(p_{\mathrm{CO}_2}, p_{\mathrm{O}_2}) \quad \text{and} \quad c_{\mathrm{O}_2} = c_{\mathrm{O}_2}(p_{\mathrm{CO}_2}, p_{\mathrm{O}_2}). \tag{2.195}$$

The tissue dissociation functions are $c_{\mathrm{tiss},\mathrm{CO}_2}$ and $c_{\mathrm{tiss},\mathrm{O}_2}$. They are assumed to be independent of one another:

$$c_{\mathrm{tiss},\mathrm{CO}_2} = c_{\mathrm{tiss},\mathrm{CO}_2}(p_{\mathrm{CO}_2}) \quad \text{and} \quad c_{\mathrm{tiss},\mathrm{O}_2} = c_{\mathrm{tiss},\mathrm{O}_2}(p_{\mathrm{O}_2}). \tag{2.196}$$

The specific dissociation laws are elaborated after having introduced the transport equations for the closed circulation.

For two inter-dependent species CO_2 and O_2, the transport equations according to (2.194) can be derived for each compartment of the vascular model, cf. fig. 2.14. For the sake of brevity, the arguments of (2.195) and (2.196) are omitted in the following.

As for the mechanics model (2.134)–(2.167), the equations are introduced starting from the left atrium. The left heart cavities represent pure transport compartments, yielding

$$V_{\mathrm{at}}^{\ell} \begin{bmatrix} \frac{\partial c^{\ell}_{\mathrm{CO}_2,\mathrm{at}}}{\partial p^{\ell}_{\mathrm{CO}_2,\mathrm{at}}} & \frac{\partial c^{\ell}_{\mathrm{CO}_2,\mathrm{at}}}{\partial p^{\ell}_{\mathrm{O}_2,\mathrm{at}}} \\ \frac{\partial c^{\ell}_{\mathrm{O}_2,\mathrm{at}}}{\partial p^{\ell}_{\mathrm{CO}_2,\mathrm{at}}} & \frac{\partial c^{\ell}_{\mathrm{O}_2,\mathrm{at}}}{\partial p^{\ell}_{\mathrm{O}_2,\mathrm{at}}} \end{bmatrix} \begin{bmatrix} \dot{p}^{\ell}_{\mathrm{CO}_2,\mathrm{at}} \\ \dot{p}^{\ell}_{\mathrm{O}_2,\mathrm{at}} \end{bmatrix} = q^{\mathrm{pul}}_{\mathrm{ven}} \begin{bmatrix} c^{\mathrm{pul}}_{\mathrm{CO}_2,\mathrm{ven}} - c^{\ell}_{\mathrm{CO}_2,\mathrm{at}} \\ c^{\mathrm{pul}}_{\mathrm{O}_2,\mathrm{ven}} - c^{\ell}_{\mathrm{O}_2,\mathrm{at}} \end{bmatrix} \tag{2.197}$$

for the left atrium and

$$V_{\mathrm{v}}^{\ell} \begin{bmatrix} \frac{\partial c^{\ell}_{\mathrm{CO}_2,\mathrm{v}}}{\partial p^{\ell}_{\mathrm{CO}_2,\mathrm{v}}} & \frac{\partial c^{\ell}_{\mathrm{CO}_2,\mathrm{v}}}{\partial p^{\ell}_{\mathrm{O}_2,\mathrm{v}}} \\ \frac{\partial c^{\ell}_{\mathrm{O}_2,\mathrm{v}}}{\partial p^{\ell}_{\mathrm{CO}_2,\mathrm{v}}} & \frac{\partial c^{\ell}_{\mathrm{O}_2,\mathrm{v}}}{\partial p^{\ell}_{\mathrm{O}_2,\mathrm{v}}} \end{bmatrix} \begin{bmatrix} \dot{p}^{\ell}_{\mathrm{CO}_2,\mathrm{v}} \\ \dot{p}^{\ell}_{\mathrm{O}_2,\mathrm{v}} \end{bmatrix} = q^{\ell}_{\mathrm{v,in}} \begin{bmatrix} c^{\ell}_{\mathrm{CO}_2,\mathrm{at}} - c^{\ell}_{\mathrm{CO}_2,\mathrm{v}} \\ c^{\ell}_{\mathrm{O}_2,\mathrm{at}} - c^{\ell}_{\mathrm{O}_2,\mathrm{v}} \end{bmatrix} \tag{2.198}$$

for left ventricle. Analogously, the large systemic arterial vessels transport the gas species down to the organ level, thus the transport equation for the systemic arterial compartment reads

$$V_{\mathrm{ar}}^{\mathrm{sys}} \begin{bmatrix} \frac{\partial c_{\mathrm{CO_2,ar}}^{\mathrm{sys}}}{\partial p_{\mathrm{CO_2,ar}}^{\mathrm{sys}}} & \frac{\partial c_{\mathrm{CO_2,ar}}^{\mathrm{sys}}}{\partial p_{\mathrm{O_2,ar}}^{\mathrm{sys}}} \\ \frac{\partial c_{\mathrm{O_2,ar}}^{\mathrm{sys}}}{\partial p_{\mathrm{CO_2,ar}}^{\mathrm{sys}}} & \frac{\partial c_{\mathrm{O_2,ar}}^{\mathrm{sys}}}{\partial p_{\mathrm{O_2,ar}}^{\mathrm{sys}}} \end{bmatrix} \begin{bmatrix} \dot{p}_{\mathrm{CO_2,ar}}^{\mathrm{sys}} \\ \dot{p}_{\mathrm{O_2,ar}}^{\mathrm{sys}} \end{bmatrix} = q_{\mathrm{v,out}}^{\ell} \begin{bmatrix} c_{\mathrm{CO_2,v}}^{\ell} - c_{\mathrm{CO_2,ar}}^{\mathrm{sys}} \\ c_{\mathrm{O_2,v}}^{\ell} - c_{\mathrm{O_2,ar}}^{\mathrm{sys}} \end{bmatrix}. \tag{2.199}$$

At the splanchnic (spl), extra-splanchnic (espl), muscular (msc), cerebral (cer) and coronary (cor) organ levels, additional oxygen and carbon dioxide dissociation in the organ tissue, denoted by $V_{\mathrm{tiss},j}$ and the dissociation functions (2.196) takes place. Furthermore, the organs consume oxygen and produce carbon dioxide, taken into account by the organ-specific carbon dioxide production and oxygen consumption metabolic rates $\hat{M}_{\mathrm{CO_2},j}$ and $\hat{M}_{\mathrm{O_2},j}$, respectively. The transport equations for the five organ compartments then read

$$\left(V_{\mathrm{ar},j}^{\mathrm{sys}} \begin{bmatrix} \frac{\partial c_{\mathrm{CO_2,ar},j}^{\mathrm{sys}}}{\partial p_{\mathrm{CO_2,ar},j}^{\mathrm{sys}}} & \frac{\partial c_{\mathrm{CO_2,ar},j}^{\mathrm{sys}}}{\partial p_{\mathrm{O_2,ar},j}^{\mathrm{sys}}} \\ \frac{\partial c_{\mathrm{O_2,ar},j}^{\mathrm{sys}}}{\partial p_{\mathrm{CO_2,ar},j}^{\mathrm{sys}}} & \frac{\partial c_{\mathrm{O_2,ar},j}^{\mathrm{sys}}}{\partial p_{\mathrm{O_2,ar},j}^{\mathrm{sys}}} \end{bmatrix} + V_{\mathrm{tiss},j} \begin{bmatrix} \frac{\partial c_{\mathrm{tiss,CO_2},j}}{\partial p_{\mathrm{CO_2,ar},j}^{\mathrm{sys}}} & 0 \\ 0 & \frac{\partial c_{\mathrm{tiss,O_2},j}}{\partial p_{\mathrm{O_2,ar},j}^{\mathrm{sys}}} \end{bmatrix} \right) \begin{bmatrix} \dot{p}_{\mathrm{CO_2,ar},j}^{\mathrm{sys}} \\ \dot{p}_{\mathrm{O_2,ar},j}^{\mathrm{sys}} \end{bmatrix} =$$

$$= q_{\mathrm{ar},j,\mathrm{in}}^{\mathrm{sys}} \begin{bmatrix} c_{\mathrm{CO_2,ar}}^{\mathrm{sys}} - c_{\mathrm{CO_2,ar},j}^{\mathrm{sys}} \\ c_{\mathrm{O_2,ar}}^{\mathrm{sys}} - c_{\mathrm{O_2,ar},j}^{\mathrm{sys}} \end{bmatrix} + \begin{bmatrix} \hat{M}_{\mathrm{CO_2},j} \\ -\hat{M}_{\mathrm{O_2},j} \frac{c_{\mathrm{tiss,O_2},j}}{\beta + c_{\mathrm{tiss,O_2},j}} \end{bmatrix}, \quad j = \mathrm{spl}, \mathrm{espl}, \mathrm{msc}, \mathrm{cer}, \mathrm{cor}. \tag{2.200}$$

Therein, the $\mathrm{O_2}$ consumption rate scales with the tissue oxygen saturation, and the constant β defines when the effective oxygen consumption is $50\ \%$ of the imposed value $\hat{M}_{\mathrm{O_2},j}$ (Michaelis-Menten kinetic form [139]).
The carbon dioxide consumption and oxygen production rates per organ are assumed to be fractions of the total rates $\hat{M}_{\mathrm{CO_2,total}}$ and $\hat{M}_{\mathrm{O_2,total}}$ and are weighted according to the size of the respective organ compartment [41]:

$$\hat{M}_{\mathrm{CO_2},j} = \hat{M}_{\mathrm{CO_2,total}} \frac{V_{\mathrm{tiss},j}}{\sum_j V_{\mathrm{tiss},j}} \quad \text{and} \quad \hat{M}_{\mathrm{O_2},j} = \hat{M}_{\mathrm{O_2,total}} \frac{V_{\mathrm{tiss},j}}{\sum_j V_{\mathrm{tiss},j}}, \tag{2.201}$$

$$j = \mathrm{spl}, \mathrm{espl}, \mathrm{msc}, \mathrm{cer}, \mathrm{cor}. \tag{2.202}$$

Since flow from the main arterial vessels branches into five parallel compartments, care has to be taken considering the organ in-fluxes $q_{\mathrm{ar},j,\mathrm{in}}^{\mathrm{sys}}$ from upstream, which is insufficiently clarified in [202]. These fluxes are no primary variables of (2.134)–(2.167), hence auxiliary equations are introduced to solve for them by considering mass (volume) balances for each single arterial organ compartment, $j = \mathrm{spl}, \mathrm{espl}, \mathrm{msc}, \mathrm{cer}, \mathrm{cor}$:

$$C_{\mathrm{ar},j}^{\mathrm{sys}} \dot{p}_{\mathrm{ar,peri}}^{\mathrm{sys}} - q_{\mathrm{ar},j,\mathrm{in}}^{\mathrm{sys}} + q_{\mathrm{ar},j}^{\mathrm{sys}} = 0. \tag{2.203}$$

Note, however, that the upstream concentrations washed into the organs are all identical, namely that of the upstream main arterial compartment, $c_{\mathrm{CO_2,ar}}^{\mathrm{sys}}$.

The organic venules compartments then continue transportation to the larger systemic venous vessels according to

$$V^{\mathrm{sys}}_{\mathrm{ven},j} \begin{bmatrix} \frac{\partial c^{\mathrm{sys}}_{\mathrm{CO_2},\mathrm{ven},j}}{\partial p^{\mathrm{sys}}_{\mathrm{CO_2},\mathrm{ven},j}} & \frac{\partial c^{\mathrm{sys}}_{\mathrm{CO_2},\mathrm{ven},j}}{\partial p^{\mathrm{sys}}_{\mathrm{O_2},\mathrm{ven},j}} \\ \frac{\partial c^{\mathrm{sys}}_{\mathrm{O_2},\mathrm{ven},j}}{\partial p^{\mathrm{sys}}_{\mathrm{CO_2},\mathrm{ven},j}} & \frac{\partial c^{\mathrm{sys}}_{\mathrm{O_2},\mathrm{ven},j}}{\partial p^{\mathrm{sys}}_{\mathrm{O_2},\mathrm{ven},j}} \end{bmatrix} \begin{bmatrix} \dot{p}^{\mathrm{sys}}_{\mathrm{CO_2},\mathrm{ven},j} \\ \dot{p}^{\mathrm{sys}}_{\mathrm{O_2},\mathrm{ven},j} \end{bmatrix} = q^{\mathrm{sys}}_{\mathrm{ar},j} \begin{bmatrix} c^{\mathrm{sys}}_{\mathrm{CO_2},\mathrm{ar},j} - c^{\mathrm{sys}}_{\mathrm{CO_2},\mathrm{ven},j} \\ c^{\mathrm{sys}}_{\mathrm{O_2},\mathrm{ar},j} - c^{\mathrm{sys}}_{\mathrm{O_2},\mathrm{ven},j} \end{bmatrix}, \tag{2.204}$$

$$j = \mathrm{spl}, \mathrm{espl}, \mathrm{msc}, \mathrm{cer}, \mathrm{cor}.$$

At the junction to the larger systemic venous vessels, all flows from the five organic venules unite again:

$$V^{\mathrm{sys}}_{\mathrm{ven}} \begin{bmatrix} \frac{\partial c^{\mathrm{sys}}_{\mathrm{CO_2},\mathrm{ven}}}{\partial p^{\mathrm{sys}}_{\mathrm{CO_2},\mathrm{ven}}} & \frac{\partial c^{\mathrm{sys}}_{\mathrm{CO_2},\mathrm{ven}}}{\partial p^{\mathrm{sys}}_{\mathrm{O_2},\mathrm{ven}}} \\ \frac{\partial c^{\mathrm{sys}}_{\mathrm{O_2},\mathrm{ven}}}{\partial p^{\mathrm{sys}}_{\mathrm{CO_2},\mathrm{ven}}} & \frac{\partial c^{\mathrm{sys}}_{\mathrm{O_2},\mathrm{ven}}}{\partial p^{\mathrm{sys}}_{\mathrm{O_2},\mathrm{ven}}} \end{bmatrix} \begin{bmatrix} \dot{p}^{\mathrm{sys}}_{\mathrm{CO_2},\mathrm{ven}} \\ \dot{p}^{\mathrm{sys}}_{\mathrm{O_2},\mathrm{ven}} \end{bmatrix} = \sum_j q^{\mathrm{sys}}_{\mathrm{ven},j} \begin{bmatrix} \frac{\sum_j q^{\mathrm{sys}}_{\mathrm{ven},j}\, c^{\mathrm{sys}}_{\mathrm{CO_2},\mathrm{ven},j}}{\sum_j q^{\mathrm{sys}}_{\mathrm{ven},j}} - c^{\mathrm{sys}}_{\mathrm{CO_2},\mathrm{ven}} \\ \frac{\sum_j q^{\mathrm{sys}}_{\mathrm{ven},j}\, c^{\mathrm{sys}}_{\mathrm{O_2},\mathrm{ven},j}}{\sum_j q^{\mathrm{sys}}_{\mathrm{ven},j}} - c^{\mathrm{sys}}_{\mathrm{O_2},\mathrm{ven}} \end{bmatrix}. \tag{2.205}$$

$$(\text{summation index } j = \mathrm{spl}, \mathrm{espl}, \mathrm{msc}, \mathrm{cer}, \mathrm{cor})$$

Due to the junction, the incoming upstream flux is a mixture of all venous organ fluxes $\sum_j q^{\mathrm{sys}}_{\mathrm{ven},j}$, while the upstream concentrations washed into the venous compartment have to be weighted with the amount flowing into the compartment, $\frac{\sum_j q^{\mathrm{sys}}_{\mathrm{ven},j}\, c^{\mathrm{sys}}_{\mathrm{ven},j}}{\sum_j q^{\mathrm{sys}}_{\mathrm{ven},j}}$. Again, [202] misses clarification; cf. [56].

The right atrium receives the flow from the systemic venous compartment,

$$V^{r}_{\mathrm{at}} \begin{bmatrix} \frac{\partial c^{r}_{\mathrm{CO_2},\mathrm{at}}}{\partial p^{r}_{\mathrm{CO_2},\mathrm{at}}} & \frac{\partial c^{r}_{\mathrm{CO_2},\mathrm{at}}}{\partial p^{r}_{\mathrm{O_2},\mathrm{at}}} \\ \frac{\partial c^{r}_{\mathrm{O_2},\mathrm{at}}}{\partial p^{r}_{\mathrm{CO_2},\mathrm{at}}} & \frac{\partial c^{r}_{\mathrm{O_2},\mathrm{at}}}{\partial p^{r}_{\mathrm{O_2},\mathrm{at}}} \end{bmatrix} \begin{bmatrix} \dot{p}^{r}_{\mathrm{CO_2},\mathrm{at}} \\ \dot{p}^{r}_{\mathrm{O_2},\mathrm{at}} \end{bmatrix} = q^{\mathrm{sys}}_{\mathrm{ven}} \begin{bmatrix} c^{\mathrm{sys}}_{\mathrm{CO_2},\mathrm{ven}} - c^{r}_{\mathrm{CO_2},\mathrm{at}} \\ c^{\mathrm{sys}}_{\mathrm{O_2},\mathrm{ven}} - c^{r}_{\mathrm{O_2},\mathrm{at}} \end{bmatrix}, \tag{2.206}$$

transporting to the right ventricle,

$$V^{r}_{\mathrm{v}} \begin{bmatrix} \frac{\partial c^{r}_{\mathrm{CO_2},\mathrm{v}}}{\partial p^{r}_{\mathrm{CO_2},\mathrm{v}}} & \frac{\partial c^{r}_{\mathrm{CO_2},\mathrm{v}}}{\partial p^{r}_{\mathrm{O_2},\mathrm{v}}} \\ \frac{\partial c^{r}_{\mathrm{O_2},\mathrm{v}}}{\partial p^{r}_{\mathrm{CO_2},\mathrm{v}}} & \frac{\partial c^{r}_{\mathrm{O_2},\mathrm{v}}}{\partial p^{r}_{\mathrm{O_2},\mathrm{v}}} \end{bmatrix} \begin{bmatrix} \dot{p}^{r}_{\mathrm{CO_2},\mathrm{v}} \\ \dot{p}^{r}_{\mathrm{O_2},\mathrm{v}} \end{bmatrix} = q^{r}_{\mathrm{v,in}} \begin{bmatrix} c^{r}_{\mathrm{CO_2},\mathrm{at}} - c^{r}_{\mathrm{CO_2},\mathrm{v}} \\ c^{r}_{\mathrm{O_2},\mathrm{at}} - c^{r}_{\mathrm{O_2},\mathrm{v}} \end{bmatrix}, \tag{2.207}$$

which in turn pumps into the pulmonary circulation for re-oxygenation. The balance equation for the pulmonary arteries reads

$$V^{\mathrm{pul}}_{\mathrm{ar}} \begin{bmatrix} \frac{\partial c^{\mathrm{pul}}_{\mathrm{CO_2},\mathrm{ar}}}{\partial p^{\mathrm{pul}}_{\mathrm{CO_2},\mathrm{ar}}} & \frac{\partial c^{\mathrm{pul}}_{\mathrm{CO_2},\mathrm{ar}}}{\partial p^{\mathrm{pul}}_{\mathrm{O_2},\mathrm{ar}}} \\ \frac{\partial c^{\mathrm{pul}}_{\mathrm{O_2},\mathrm{ar}}}{\partial p^{\mathrm{pul}}_{\mathrm{CO_2},\mathrm{ar}}} & \frac{\partial c^{\mathrm{pul}}_{\mathrm{O_2},\mathrm{ar}}}{\partial p^{\mathrm{pul}}_{\mathrm{O_2},\mathrm{ar}}} \end{bmatrix} \begin{bmatrix} \dot{p}^{\mathrm{pul}}_{\mathrm{CO_2},\mathrm{ar}} \\ \dot{p}^{\mathrm{pul}}_{\mathrm{O_2},\mathrm{ar}} \end{bmatrix} = q^{r}_{\mathrm{v,out}} \begin{bmatrix} c^{r}_{\mathrm{CO_2},\mathrm{v}} - c^{\mathrm{pul}}_{\mathrm{CO_2},\mathrm{ar}} \\ c^{r}_{\mathrm{O_2},\mathrm{v}} - c^{\mathrm{pul}}_{\mathrm{O_2},\mathrm{ar}} \end{bmatrix}, \tag{2.208}$$

which eventually passes the deoxygenated blood to the pulmonary capillary bed. There, the gas exchange with the lung occurs, and the blood becomes re-oxygenated for the further supply to the left heart and systemic circulation. Therefore, the pulmonary capillary balance equation yields

$$\begin{aligned} V^{\mathrm{pul}}_{\mathrm{cap}} \begin{bmatrix} \frac{\partial c^{\mathrm{pul}}_{\mathrm{CO_2},\mathrm{cap}}}{\partial p^{\mathrm{pul}}_{\mathrm{CO_2},\mathrm{cap}}} & \frac{\partial c^{\mathrm{pul}}_{\mathrm{CO_2},\mathrm{cap}}}{\partial p^{\mathrm{pul}}_{\mathrm{O_2},\mathrm{cap}}} \\ \frac{\partial c^{\mathrm{pul}}_{\mathrm{O_2},\mathrm{cap}}}{\partial p^{\mathrm{pul}}_{\mathrm{CO_2},\mathrm{cap}}} & \frac{\partial c^{\mathrm{pul}}_{\mathrm{O_2},\mathrm{cap}}}{\partial p^{\mathrm{pul}}_{\mathrm{O_2},\mathrm{cap}}} \end{bmatrix} \begin{bmatrix} \dot{p}^{\mathrm{pul}}_{\mathrm{CO_2},\mathrm{cap}} \\ \dot{p}^{\mathrm{pul}}_{\mathrm{O_2},\mathrm{cap}} \end{bmatrix} &= q^{\mathrm{pul}}_{\mathrm{ar}} \begin{bmatrix} c^{\mathrm{pul}}_{\mathrm{CO_2},\mathrm{ar}} - c^{\mathrm{pul}}_{\mathrm{CO_2},\mathrm{cap}} \\ c^{\mathrm{pul}}_{\mathrm{O_2},\mathrm{ar}} - c^{\mathrm{pul}}_{\mathrm{O_2},\mathrm{cap}} \end{bmatrix} + \\ &+ \begin{bmatrix} \kappa_{\mathrm{CO_2}}(f_{\mathrm{CO_2},\mathrm{alv}}\,(p_{\mathrm{alv}} - p^{\mathrm{water}}_{\mathrm{vap},37}) - p^{\mathrm{pul}}_{\mathrm{CO_2},\mathrm{cap}}) \\ \kappa_{\mathrm{O_2}}(f_{\mathrm{O_2},\mathrm{alv}}\,(p_{\mathrm{alv}} - p^{\mathrm{water}}_{\mathrm{vap},37}) - p^{\mathrm{pul}}_{\mathrm{O_2},\mathrm{cap}}) \end{bmatrix}, \end{aligned} \tag{2.209}$$

where $f_{\mathrm{CO}_2,\mathrm{alv}}$ and $f_{\mathrm{O}_2,\mathrm{alv}}$ are the alveolar carbon dioxide and oxygen gas fractions governed by (2.186) and (2.187), respectively, and p_{alv} is the alveolar pressure, cf. (2.185).

The pulmonary veins then carry the oxygenated blood and feed it back to the left atrium, cf. (2.197):

$$V_{\mathrm{ven}}^{\mathrm{pul}} \begin{bmatrix} \frac{\partial c_{\mathrm{CO}_2,\mathrm{ven}}^{\mathrm{pul}}}{\partial p_{\mathrm{CO}_2,\mathrm{ven}}^{\mathrm{pul}}} & \frac{\partial c_{\mathrm{CO}_2,\mathrm{ven}}^{\mathrm{pul}}}{\partial p_{\mathrm{O}_2,\mathrm{ven}}^{\mathrm{pul}}} \\ \frac{\partial c_{\mathrm{O}_2,\mathrm{ven}}^{\mathrm{pul}}}{\partial p_{\mathrm{CO}_2,\mathrm{ven}}^{\mathrm{pul}}} & \frac{\partial c_{\mathrm{O}_2,\mathrm{ven}}^{\mathrm{pul}}}{\partial p_{\mathrm{O}_2,\mathrm{ven}}^{\mathrm{pul}}} \end{bmatrix} \begin{bmatrix} \dot{p}_{\mathrm{CO}_2,\mathrm{ven}}^{\mathrm{pul}} \\ \dot{p}_{\mathrm{O}_2,\mathrm{ven}}^{\mathrm{pul}} \end{bmatrix} = q_{\mathrm{cap}}^{\mathrm{pul}} \begin{bmatrix} c_{\mathrm{CO}_2,\mathrm{cap}}^{\mathrm{pul}} - c_{\mathrm{CO}_2,\mathrm{ven}}^{\mathrm{pul}} \\ c_{\mathrm{O}_2,\mathrm{cap}}^{\mathrm{pul}} - c_{\mathrm{O}_2,\mathrm{ven}}^{\mathrm{pul}} \end{bmatrix}. \tag{2.210}$$

Note that all compartment volumes in (2.197)–(2.210) are not constant but are governed by the law of compliance (2.82) or the specific elastic properties of the cardiac chambers. While the absolute value of all 0D compartments is not of importance for the mechanical model (2.134)–(2.167) since only fluxes enter the balance equations, the storage capacity of the models is of relevance regarding the gas transport and dissociation laws. All 0D compliant compartment volumes thus can be computed as function of their pressure p depending on the compliance C via

$$V(p) = Cp + V_{\mathrm{u}}, \tag{2.211}$$

where V_{u} the unstressed volume of the compartment. Atrial 0D compartment volumes are calculated from (2.218), cf. sec. 2.2.3.2 in the following. Unstressed volumes are listed in tab. 2.9.

Dissociation laws There exists a vast amount of laws describing the dissociation of oxygen and carbon dioxide in the human body. The first pioneering works on the oxygen dissociation curve of hemoglobin go back to the early 20th century, cf. the works by Hill [84] and Adair [1]. Since then, a multitude of variants and diversifications of these models have been proposed, cf. [47, 188] as well as references therein. A more complex mathematical model describing the hemoglobin-oxygen dissociation curve as well as the carbon dioxide dissociation was proposed by Siggaard-Andersen et al. [191], which was also adopted by [41, 42, 202].
For simplicity, here the dependencies of gas dissociation on the pH value and on the temperature are neglected, similar to the dissociation functions used in Ellwein et al. [56]. Also, dependencies of the oxygen concentration on the carbon dioxide partial pressure and vice versa (Haldane effect [190]), as implied by (2.195), are not considered for the models here, even though a diversification of the specific forms of dissociation functions is not inhibited by the respective formulations of the transport equations. Hence, (2.197)–(2.210) remain valid regardless of the complexity and interdependencies of c_{CO_2} and c_{O_2}.

For the solubility of carbon dioxide in blood and tissue, a simple linear relationship between the concentration and the partial pressure according to Henry's law is assumed:

$$c_{\mathrm{CO}_2} = \alpha_{\mathrm{CO}_2}\, p_{\mathrm{CO}_2} \quad \text{and} \quad c_{\mathrm{tiss},\mathrm{CO}_2} = \alpha_{\mathrm{CO}_2}\, p_{\mathrm{CO}_2}, \tag{2.212}$$

where α_{CO_2} is the solubility constant.

Regarding the oxygen solution in blood, only a rather small portion is physically solved (around 1.4 % [51]) according to Henry's law, while the lion's share binds to hemoglobin according to the hemoglobin-oxygen dissociation curve S_{O_2}. In tissue, oxygen solution is entirely governed by Henry's law. Hence, the dissociation functions read

$$c_{\mathrm{O}_2} = \alpha_{\mathrm{O}_2}\, p_{\mathrm{O}_2} + c_{\mathrm{Hb}}\, S_{\mathrm{O}_2}(p_{\mathrm{O}_2}) \qquad \text{and} \qquad c_{\mathrm{tiss},\mathrm{CO}_2} = \alpha_{\mathrm{CO}_2}\, p_{\mathrm{CO}_2}. \tag{2.213}$$

Therein, α_{O_2} is the solubility constant of O_2, and c_{Hb} is the hemoglobin concentration of the blood.

Here, the simplest form of the hemoglobin-oxygen dissociation curve according to Hill [84] is chosen:

$$S_{\mathrm{O}_2} = \frac{\left(\frac{p_{\mathrm{O}_2}}{p_{50,\mathrm{O}_2}}\right)^n}{1 + \left(\frac{p_{\mathrm{O}_2}}{p_{50,\mathrm{O}_2}}\right)^n}, \tag{2.214}$$

with Hill's constant n and the partial pressure of O_2 at $50\ \%$ saturation $p_{50,\mathrm{O}_2} = 26.8\ \mathrm{mmHg}$. The constants and parameters are summarized in tab. 2.9.

Hill's hemoglobin oxygen saturation curve (2.214) is depicted in fig. 2.15. The curve corresponds well to the complex pH- and CO_2 saturation-dependent hemoglobin oxygen saturation function at a blood pH value of 7.4, which can be assumed as standard conditions [103].

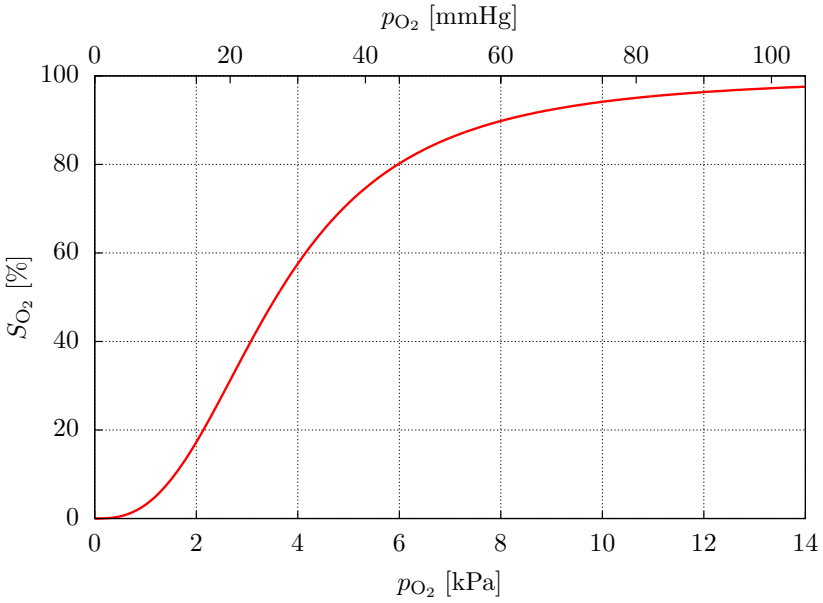

Figure 2.15: Hemoglobin oxygen saturation curve S_{O_2} as function of the oxygen blood partial pressure p_{O_2} (2.214), according to Hill [84].

Parameters In the following, an overview of all parameters of the 0D lung as well as the gas transport and dissociation model is given. The parameters are separated into "fixed" ones that do not vary for a specific individual (only inter-patient variability), at least not on a short time scale, and parameters that might be adjusted to the individual's current cardiorespiratory state

(intra-patient variability), e.g. rest or exercise conditions.
Table 2.8 lists all parameters associated to the lung model, eq. (2.183)–(2.187), and tab. 2.9 depicts all parameters that are associated to the gas transport equations, (2.197)–(2.210), as well as the ones from the dissociation laws (2.212)–(2.214).

Table 2.8: Parameters of 0D lung model: separation into "fixed" parameters for a specific individual (inter-patient) and parameters that might be adjusted to specific conditions of that individual (intra-patient)

fixed parameters:			
R_{airw} $[\frac{\text{kPa}\cdot\text{s}}{\text{mm}^3}]$	$1.33 \cdot 10^{-7}$	overall resistance of the conducting airways	[18]
L_{alv} $[\frac{\text{kPa}\cdot\text{s}^2}{\text{mm}^3}]$	$9.87 \cdot 10^{-10}$	alveolar inertance	[171]
R_{alv} $[\frac{\text{kPa}\cdot\text{s}}{\text{mm}^3}]$	0	alveolar resistance	[171]
E_{alv} $[\frac{\text{kPa}}{\text{mm}^3}]$	$3.33 \cdot 10^{-7}$	alveolar elastance	[18]
$V_{\text{alv,u}}$ $[\text{mm}^3]$	0	unstressed alveolar volume	[18]
U_{m} $[\text{kPa}]$	10^2	atmospheric air pressure	
κ_{CO_2} $[\frac{\text{mmol}}{\text{s}\cdot\text{kPa}}]$	$23.7 \cdot 10^{-2}$	diffusion capacity for CO_2 in the lung	[18]
κ_{O_2} $[\frac{\text{mmol}}{\text{s}\cdot\text{kPa}}]$	$11.7 \cdot 10^{-2}$	diffusion capacity for O_2 in the lung	[18]
$V_{\text{m,gas}}$ $[\frac{\text{mm}^3}{\text{mmol}}]$	$22.4 \cdot 10^3$	molar volume for an ideal gas at standard conditions	
$f_{\text{CO}_2,\text{ext}}$ $[-]$	0.0004	gas fraction of CO_2 in the atmosphere	
$f_{\text{O}_2,\text{ext}}$ $[-]$	0.21	gas fraction of O_2 in the atmosphere	
$p_{\text{vap,37}}^{\text{water}}$ $[\text{kPa}]$	6.279	vapor pressure of water at $37°\text{C}$	
V_{D} $[\text{mm}^3]$	$150 \cdot 10^3$	dead space lung volume	[18]
V_{lung} $[\text{mm}^3]$	$5.0 \cdot 10^6$	total lung volume	
parameters that may be adjusted to specific conditions (e.g. rest, exercise):			
V_{T} $[\text{mm}^3]$	$600 \cdot 10^3$	tidal volume (volume of inspired air per breath)	
T_{breath} $[\text{s}]$	4.5	time period of one breath	
ω_{b} $[\frac{1}{\text{s}}]$	$2\pi/T_{\text{breath}}$	respiration (breathing) frequency	

2.2.3 Coupling conditions

The heart and the vascular models are strongly coupled, meaning that the physics of the cardiovascular system affect the deformation and contraction pattern of the heart and vice versa. Hence, this phenomenon has to be modeled as a two-way coupled mechanical problem. The specific coupling conditions are stated below, sec. 2.2.3.1. The respective numerical solution is elaborated in chap. 3.
In contrast, the cardiovascular and the respiratory problem exhibit a one-way coupling only: The transport equations (2.197)–(2.210) hold information on fluxes and volumes of the cardiovascular models, however the latter, (2.134)–(2.167), are independent of any respiratory state variables like partial pressures or gas fractions. Therefore, and due to the fact that periodic orbit solutions of the cardiorespiratory model require a significantly larger amount of heart beats than the mechanical model alone, a novel *prescribed-dynamics* approach for the heart is introduced in order to allow an

Table 2.9: Parameters of 0D gas transport and dissociation model: separation into "fixed" parameters for a specific individual (inter-patient) and parameters that might be adjusted to specific conditions of that individual (intra-patient)

fixed parameters:				
$V_{\mathrm{tiss,spl}}$	$[\mathrm{mm}^3]$	$3243.0 \cdot 10^3$	splanchnic tissue volume (liver and kidney)	[41]
$V_{\mathrm{tiss,espl}}$	$[\mathrm{mm}^3]$	$217.0 \cdot 10^3$	extra-splanchnic tissue volume	[41]
$V_{\mathrm{tiss,msc}}$	$[\mathrm{mm}^3]$	$26773.0 \cdot 10^3$	muscular tissue volume	[41]
$V_{\mathrm{tiss,spl}}$	$[\mathrm{mm}^3]$	$1300.0 \cdot 10^3$	cerebral tissue volume	[41]
$V_{\mathrm{tiss,spl}}$	$[\mathrm{mm}^3]$	$307.0 \cdot 10^3$	coronary tissue volume	[41]
$V^{\ell}_{\mathrm{at,u}}$	$[\mathrm{mm}^3]$	$5.0 \cdot 10^3$	unstressed left atrial volume	
$V^{\ell}_{\mathrm{v,u}}$	$[\mathrm{mm}^3]$	$10.0 \cdot 10^3$	unstressed left ventricular volume	
$V^{\mathrm{sys}}_{\mathrm{ar,u}}$	$[\mathrm{mm}^3]$	0	unstressed systemic arterial volume	[203]
$V^{\mathrm{sys}}_{\mathrm{ar,spl,u}}$	$[\mathrm{mm}^3]$	$274.4 \cdot 10^3$	unstressed systemic arterial splanchnic volume	[203]
$V^{\mathrm{sys}}_{\mathrm{ar,espl,u}}$	$[\mathrm{mm}^3]$	$134.6 \cdot 10^3$	unstressed systemic arterial extra-splanchnic volume	[203]
$V^{\mathrm{sys}}_{\mathrm{ar,msc,u}}$	$[\mathrm{mm}^3]$	$105.8 \cdot 10^3$	unstressed systemic arterial muscular volume	[203]
$V^{\mathrm{sys}}_{\mathrm{ar,cer,u}}$	$[\mathrm{mm}^3]$	$72.1 \cdot 10^3$	unstressed systemic arterial cerebral volume	[203]
$V^{\mathrm{sys}}_{\mathrm{ar,cor,u}}$	$[\mathrm{mm}^3]$	$24.0 \cdot 10^3$	unstressed systemic arterial coronary volume	[203]
$V^{\mathrm{sys}}_{\mathrm{ven,spl,u}}$	$[\mathrm{mm}^3]$	$1121.0 \cdot 10^3$	unstressed systemic venous splanchnic volume	[203]
$V^{\mathrm{sys}}_{\mathrm{ven,espl,u}}$	$[\mathrm{mm}^3]$	$550.0 \cdot 10^3$	unstressed systemic venous extra-splanchnic volume	[203]
$V^{\mathrm{sys}}_{\mathrm{ven,msc,u}}$	$[\mathrm{mm}^3]$	$432.1 \cdot 10^3$	unstressed systemic venous muscular volume	[203]
$V^{\mathrm{sys}}_{\mathrm{ven,cer,u}}$	$[\mathrm{mm}^3]$	$294.6 \cdot 10^3$	unstressed systemic venous cerebral volume	[203]
$V^{\mathrm{sys}}_{\mathrm{ven,cor,u}}$	$[\mathrm{mm}^3]$	$98.2 \cdot 10^3$	unstressed systemic venous coronary volume	[203]
$V^{\mathrm{sys}}_{\mathrm{ven,u}}$	$[\mathrm{mm}^3]$	$100.0 \cdot 10^3$	unstressed systemic venous volume	
$V^{r}_{\mathrm{at,u}}$	$[\mathrm{mm}^3]$	$4.0 \cdot 10^3$	unstressed right atrial volume	
$V^{r}_{\mathrm{v,u}}$	$[\mathrm{mm}^3]$	$8.0 \cdot 10^3$	unstressed right ventricular volume	
$V^{\mathrm{pul}}_{\mathrm{ar,u}}$	$[\mathrm{mm}^3]$	0	unstressed pulmonary arterial volume	[203]
$V^{\mathrm{pul}}_{\mathrm{cap,u}}$	$[\mathrm{mm}^3]$	$123.0 \cdot 10^3$	unstressed pulmonary capillary volume	[203]
$V^{\mathrm{pul}}_{\mathrm{ven,u}}$	$[\mathrm{mm}^3]$	$120.0 \cdot 10^3$	unstressed pulmonary venous volume	[203]
n	$[-]$	2.7	Hill coefficient	[84]
$p_{50,\mathrm{O_2}}$	$[\mathrm{kPa}]$	3.573	partial pressure of $\mathrm{O_2}$ at $50\ \%$ saturation	[84]
$\alpha_{\mathrm{CO_2}}$	$[\frac{\mathrm{mmol}}{\mathrm{kPa \cdot mm^3}}]$	$24.75 \cdot 10^{-8}$	$\mathrm{CO_2}$ solubility constant	[18]
$\alpha_{\mathrm{O_2}}$	$[\frac{\mathrm{mmol}}{\mathrm{kPa \cdot mm^3}}]$	$1.05 \cdot 10^{-8}$	$\mathrm{O_2}$ solubility constant	[18]
c_{Hb}	$[\frac{\mathrm{mmol}}{\mathrm{mm^3}}]$	$9.3 \cdot 10^{-6}$	hemoglobin concentration of the blood	[41]
parameters that may be adjusted to specific conditions (e.g. rest, exercise):				
$\hat{M}_{\mathrm{CO_2,total}}$	$[\frac{\mathrm{mmol}}{\mathrm{s}}]$	0.193	total metabolic $\mathrm{CO_2}$ production rate	
$\hat{M}_{\mathrm{O_2,total}}$	$[\frac{\mathrm{mmol}}{\mathrm{s}}]$	0.238	total metabolic $\mathrm{O_2}$ max. consumption rate	
β	$[\frac{\mathrm{mmol}}{\mathrm{mm^3}}]$	10^{-8}	point where effective $\mathrm{O_2}$ consumption is $50\ \%$ of max.	

efficient yet accurate representation of the heart by exploiting the precomputed pressure-volume relations of each heart chamber. This approach is introduced in sec. 2.2.3.2.

2.2.3.1 Cardio-vascular coupling

The coupling conditions of the 3D heart and the 0D vascular system state the dependencies of the model governing equations on the primary variables of the other model. The coupling variables of the 0D circulatory system are the ventricular (and atrial) pressures p_{v}^i (and p_{at}^i). They act as boundary traction onto the endocardial chamber cavity surfaces and hence contribute to the external virtual work $\delta\mathcal{W}_{\mathrm{ext}}$, cf. the whole weak form (2.94) and (2.95), respectively.

In case of model *3Dventr*, only the virtual work of the ventricular pressures has to be taken into account,

$$\delta\mathcal{W}_{\mathrm{ext}} = -\sum_{i=\ell,r} \int\limits_{\Gamma_{0,\mathrm{v}}^{0\mathrm{D},i}} p_{\mathrm{v}}^i \, J\boldsymbol{F}^{-\mathrm{T}}\boldsymbol{n}_0 \cdot \delta\boldsymbol{u} \, \mathrm{d}A, \tag{2.215}$$

while for model *3Datrioventr*, ventricular and atrial cavity pressures contribute to the external virtual work:

$$\delta\mathcal{W}_{\mathrm{ext}} = -\sum_{i=\ell,r} \int\limits_{\Gamma_{0,\mathrm{v}}^{0\mathrm{D},i}} p_{\mathrm{v}}^i \, J\boldsymbol{F}^{-\mathrm{T}}\boldsymbol{n}_0 \cdot \delta\boldsymbol{u} \, \mathrm{d}A - \sum_{i=\ell,r} \int\limits_{\Gamma_{0,\mathrm{at}}^{0\mathrm{D},i}} p_{\mathrm{at}}^i \, J\boldsymbol{F}^{-\mathrm{T}}\boldsymbol{n}_0 \cdot \delta\boldsymbol{u} \, \mathrm{d}A. \tag{2.216}$$

Vice versa, the 3D solid mechanics state variable – the displacement field $\boldsymbol{u}$ – governs the rate of change of ventricular and atrial cavity volumes that enter the mass balance equations of the 0D model, cf. (2.118), (2.120), (2.126), (2.128) for model *0Dsyspul* and (2.134), (2.136), (2.158), (2.160) for model *0Dsyspulcap*. They are computed as boundary integral over the coupling surfaces $\Gamma_{0,c}^{0\mathrm{D},i}$ *and* the inner lid surfaces[5] denoted by $\Gamma_{0,c}^{\mathrm{lids},i}$, cf. fig. 2.6 and fig. 2.7. Therefore, the rate of change of the enclosed chamber volumes can be expressed as

$$\frac{\mathrm{d}V_c^i(\boldsymbol{u})}{\mathrm{d}t} = \frac{\mathrm{d}}{\mathrm{d}t}\left(\frac{1}{3}\int\limits_{\Gamma_c^{0\mathrm{D},i}\cup\Gamma_c^{\mathrm{lids},i}} \boldsymbol{x}\cdot\boldsymbol{n}\,\mathrm{d}a\right) = \frac{1}{3}\frac{\mathrm{d}}{\mathrm{d}t}\int\limits_{\Gamma_{0,c}^{0\mathrm{D},i}\cup\Gamma_{0,c}^{\mathrm{lids},i}} (\boldsymbol{u}+\boldsymbol{x}_0)\cdot J\boldsymbol{F}^{-\mathrm{T}}\boldsymbol{n}_0\,\mathrm{d}A, \quad i=\ell,r, \tag{2.217}$$

where $c = \mathrm{v}$ in case of model *3Dventr*, and $c = \mathrm{v}, \mathrm{at}$ in case of model *3Datrioventr*.

2.2.3.2 One-way cardiovascular-respiratory coupling and prescribed-dynamics heart

The time span until a stable homeostatic state of carbon dioxide and oxygen saturation is occupied is of orders of magnitudes greater than that for a stable periodic mechanical state of the cardiovascular system. While mechanical periodicity may already be obtained after 5–20 cardiac

[5] In order to mathematically assess the cavity volumes correctly by boundary integrals, it is mandatory that the bounding surfaces fully enclose the volume. However, since the lids are "artificial" structures with "dummy" (compliant) material properties, the coupling pressures are only exerted to the boundary belonging to the myocardium, cf. (2.215) and (2.216), respectively.

cycles depending on the initial condition guess, transport and dissociation periodicity requires cycle numbers of > 1000, cf. Trenhago et al. [202] requiring 20 cycles for the cardiovascular system state variables and $15\,000$ cycles for the respiratory and gas partial pressure state variables to exhibit periodicity.
Since the models in [41, 42, 56, 202] all are of 0-dimensional nature where the heart cavities are modeled by time-varying elastances, hence no field equations with spatial derivatives are involved, a numerical solution of the model equations on a physical time span of hours or days is of acceptable computational cost. However, spatially resolved models often yield discretizations where the number of spatial degrees of freedom (here for the heart only) is significantly greater than the number of state variables describing the whole 0D model. Thus, the computational burden is expected to be significant in order to compute a stable homeostatic state for the whole cardiorespiratory system if a 3D heart is involved.

Due to the above-mentioned one-way coupling between the cardiovascular mechanical models (2.134)–(2.167) and the respiratory (2.183)–(2.187) as well as gas transport kinetics (2.197)–(2.210), the a priori computed homeostatic mechanical state of the heart can be used as input to the respiratory and gas transport models.

As for the atria of model *3Dventr*, each heart chamber c is replaced by a time-varying elastance model, cf. (2.111), yielding a pressure-volume relation

$$p_c^i = \hat{E}_c^i(t) \cdot (V_c^i - V_{\mathrm{at,u}}^i). \tag{2.218}$$

Hence, the left and right atrial mass balances, cf. (2.81), read

$$\frac{\mathrm{d}}{\mathrm{d}t}\left(\frac{p_{\mathrm{at}}^\ell}{\hat{E}_{\mathrm{at}}^\ell}\right) - q_{\mathrm{ven}}^{\mathrm{pul}} + q_{\mathrm{v,in}}^\ell = 0 \qquad \text{and} \qquad \frac{\mathrm{d}}{\mathrm{d}t}\left(\frac{p_{\mathrm{at}}^r}{\hat{E}_{\mathrm{at}}^r}\right) - q_{\mathrm{ven}}^{\mathrm{sys}} + q_{\mathrm{v,in}}^r = 0, \tag{2.219}$$

which substitute (2.134) and (2.136), respectively. Analogously, the left and right ventricular mass balances read

$$\frac{\mathrm{d}}{\mathrm{d}t}\left(\frac{p_{\mathrm{v}}^\ell}{\hat{E}_{\mathrm{v}}^\ell}\right) - q_{\mathrm{v,in}}^\ell + q_{\mathrm{v,out}}^\ell = 0 \qquad \text{and} \qquad \frac{\mathrm{d}}{\mathrm{d}t}\left(\frac{p_{\mathrm{v}}^r}{\hat{E}_{\mathrm{v}}^r}\right) - q_{\mathrm{v,in}}^r + q_{\mathrm{v,out}}^r = 0, \tag{2.220}$$

substituting (2.158) and (2.160), respectively

The prescribed time-varying elastance now makes use of the time course of the ventricular (and atrial) pressures $\hat{p}_c^i(t)$ and volumes $\hat{V}_c^i(t)$ that stem from the precomputed homeostatic mechanical state:

$$\hat{E}_c^i(t) = \frac{\hat{p}_c^i(t)}{\hat{V}_c^i(t) - V_{c,\mathrm{u}}^i}. \tag{2.221}$$

This approach prescribing the elastance instead of the primary variables and volumes may be seen as a dimensional reduction that mimics the precomputed pressure-volume relation of the 3D heart and maintains a smooth behavior of 0D pressure and flux variables at the transition from one cardiac cycle to the other. This smoothness in terms of continuity of pressures and fluxes would get lost if the primary variables of (2.134)–(2.167) were prescribed directly by values from the precomputed homeostatic state, since periodicity is only fulfilled up to a certain tolerance (2.222).

2.2.4 Evaluation of homeostatic states

The models that have been presented are closed circulations, and their solutions have to obey some periodicity requirements in order to be viewed as reasonable or valid. Due to the respective mathematical formulations, the cardiovascular models inherently will tend to a periodic orbit regardless of their initial conditions. For the models *0Dsyspul* and *0Dsyspulcap*, a so-called *homeostatic state* is considered achieved if some of the state variables and compartment volumes become periodic, hence if their value at the beginning of the respective cardiac cycle at time t_N coincides up to a certain tolerance with their value at the end of that cycle, at time $t_N + T_{\mathrm{cycl}}$. Additionally, for unidirectional flow through the cardiac cycle, left and right ventricular stroke volumes SV^i $(i = \ell, r)$ have to coincide, too. For this purpose, the so-called cycle error criterion

$$\begin{aligned} E_{\mathrm{cycl}} = \max \Bigg\{ & \left| \frac{p_{\mathrm{ar}}^{\mathrm{sys}}(t_N+T_{\mathrm{cycl}}) - p_{\mathrm{ar}}^{\mathrm{sys}}(t_N)}{p_{\mathrm{ar}}^{\mathrm{sys}}(t_N)} \right|, \\ & \left| \frac{p_{\mathrm{ar}}^{\mathrm{pul}}(t_N+T_{\mathrm{cycl}}) - p_{\mathrm{ar}}^{\mathrm{pul}}(t_N)}{p_{\mathrm{ar}}^{\mathrm{pul}}(t_N)} \right|, \left| \frac{p_{\mathrm{ven}}^{\mathrm{sys}}(t_N+T_{\mathrm{cycl}}) - p_{\mathrm{ven}}^{\mathrm{sys}}(t_N)}{p_{\mathrm{ven}}^{\mathrm{sys}}(t_N)} \right|, \\ & \left| \frac{p_{\mathrm{ven}}^{\mathrm{pul}}(t_N+T_{\mathrm{cycl}}) - p_{\mathrm{ven}}^{\mathrm{pul}}(t_N)}{p_{\mathrm{ven}}^{\mathrm{pul}}(t_N)} \right|, \left| \frac{V_{\mathrm{v}}^{\ell}(t_N+T_{\mathrm{cycl}}) - V_{\mathrm{v}}^{\ell}(t_N)}{V_{\mathrm{v}}^{\ell}(t_N)} \right|, \\ & \left| \frac{V_{\mathrm{v}}^{r}(t_N+T_{\mathrm{cycl}}) - V_{\mathrm{v}}^{r}(t_N)}{V_{\mathrm{v}}^{r}(t_N)} \right|, \left| \frac{\mathrm{SV}^{\ell} - \mathrm{SV}^{r}}{\mathrm{SV}^{\ell}} \right| \Bigg\} \leq \epsilon_{\mathrm{cycl}}, \end{aligned} \tag{2.222}$$

is defined, where V_{v}^{ℓ} and V_{v}^{r} are left and right ventricular cavity volumes, respectively, and ϵ_{cycl} is the cycle error tolerance.

Two scenarios for computing a homeostatic state are considered in this context:

- Homeostatic state initial conditions of the circulation are not known, and a prestressed homeostatic state on the imaged configuration is desired;
- Some homeostatic state initial conditions have been precomputed or estimated, and a new homeostatic state is searched after a perturbing event occurred, e.g. a myocardial infarction or the application of a ventricular assist device.

For these purposes, the set of variables at a time instance t is defined,

$$\mathcal{I}(t) = \{(\mathbf{p})_1(t), ..., (\mathbf{p})_{n_{\mathrm{dof}}^{\mathrm{0D}}}(t), \tau_{\mathrm{a}}|_{(1)}(t), ..., \tau_{\mathrm{a}}|_{(n_{\mathrm{mat}})}(t)\}, \tag{2.223}$$

where the initial active stress state is set region-wise, where n_{mat} is the total number of constitutive laws (one per region), e.g. allowing for a discrimination between atrial and ventricular material or an infarction zone. Hence, the simplifying assumption is made that each material point belonging to a distinct region possesses the same initial active stress state.

2.2.4.1 Prestressed homeostatic state on the imaged configuration

If the homeostatic state initial conditions of the circulation are not known, a semi-educated guess has to be chosen and the following algorithmic pattern for the computation of a homeostatic state

on the prestressed imaged configuration has to be run through:

while $E_{\mathrm{cycl}} > \epsilon_{\mathrm{cycl}}$ **do**
i) prestress [68] heart to initial ventricular pressures $p_{\mathrm{v}}^{\ell}(t_0)$, $p_{\mathrm{v}}^{r}(t_0)$ / atrial pressures $p_{\mathrm{at}}^{\ell}(t_0)$, $p_{\mathrm{at}}^{r}(t_0)$, and to initial active stress states $\tau_{\mathrm{a}}(t_0)$ (may differ depending on chamber and individual material law)

ii) compute one transient cardiac cycle with $\mathcal{I}(t_0)$

iii) evaluate end-cyclic 0D vascular variables and active stress state:
$\mathcal{I}(t_0 + T_{\mathrm{cycl}}) = \{(\mathbf{p})_1(t_0 + T_{\mathrm{cycl}}), ..., (\mathbf{p})_{n_{\mathrm{dof}}^{\mathrm{0D}}}(t_0 + T_{\mathrm{cycl}}), \tau_{\mathrm{a}}|_{(1)}(t_0 + T_{\mathrm{cycl}}), ..., \tau_{\mathrm{a}}|_{(n_{\mathrm{mat}})}(t_0 + T_{\mathrm{cycl}})\}$

iv) update initial conditions: $\mathcal{I}(t_0) \leftarrow \mathcal{I}(t_0 + T_{\mathrm{cycl}})$

else
set homeostatic state initial conditions: $\mathcal{I}^{\star} := \mathcal{I}(t_0 + T_{\mathrm{cycl}})$
STOP.

2.2.4.2 Transient computation of alternating homeostatic state

If a set of homeostatic state initial conditions $\mathcal{I}^{\star}$ is given, e.g. computed by the procedure in sec. 2.2.4.1 or estimated with help of the methods of chap. 4, a normal transient computation lasting multiple cardiac cycles can be performed in order to compute a new homeostatic state after some *event* has happened. The following algorithmic pattern can be run through:

set homeostatic initial conditions $\mathcal{I}(t_0) := \mathcal{I}^{\star}$, prestress [68] heart to initial ventricular pressures $p_{\mathrm{v}}^{\ell\star}$, $p_{\mathrm{v}}^{r\star}$ / atrial pressures $p_{\mathrm{at}}^{\ell\star}$, $p_{\mathrm{at}}^{r\star}$, and to initial active stress states $\tau_{\mathrm{a}}^{\star}$ (may differ depending on chamber and individual material law)

while $E_{\mathrm{cycl}} > \epsilon_{\mathrm{cycl}}$ **or not yet** *event* **do**
compute transient cardiac cycles with $\mathcal{I}^{\star}$

else
STOP.

2.3 Multiscale modeling of myocardial growth and disease progression

Understanding pathologies of growth and remodeling (G&R) in the heart is of uttermost importance for deriving effective medical treatment strategies against cardiomyopathy and end-stage congestive heart failure (CHF). Amongst a multitude of causes for the development of CHF, a critical state of mechanical loading is one prominent stimulus for cardiac G&R, ultimately leading to systolic or diastolic heart failure.

The models presented here aim at quantifying the long-term maladaptive changes in the cardiac tissue at the cell level as a consequence of an acute disease event, e.g. myocardial infarction, mitral regurgitation or aortic stenosis. Depending on the type of event and the distinct location, a critical mechanical overload state may arise, here strictly discriminated between *volume overload* caused by an increased venous return at the end of the diastole, and *pressure overload* caused by a sustained elevated ventricular cavity pressure during systole [175].
Both phenomena induce growth (cardiac hypertrophy) which may be distinguished into *eccentric hypertrophy* in response to a state of chronic volume overload, and *concentric hypertrophy* as a consequence of persistent pressure overload.
Volume overload leads to a dilation of the ventricles and a reduction in cardiac contractility, thus its pathology is referred to as *dilated cardiomyopathy* (DCM), ultimately yielding *systolic heart failure*. The pathology of pressure overload, to the contrary, is referred to as *hypertrophic cardiomyopathy* (HCM), ultimately yielding *diastolic heart failure* due to an impairment of ventricular relaxation and filling of the thickened and stiffened ventricular wall, while contractile properties remain virtually unaltered [99]. Refer to chap. 1, sec. 1.3 for some pathophysiological backgrounds to heart failure.

Remodeling of tissue describes the change of its morphology and structure as consequence of some external stimulus. Here, focus is set on myocardial (ventricular) remodeling accompanying the maladaptive changes in size and shape of the heart due to volumetric growth [11], triggered by a state of sustained pressure or volume overload. Remodeling phenomena happen as result of some injury of the heart muscle, e.g. a myocardial infarction, or other incidents that ultimate in chronic overload scenarios that increase or invoke inflammatory processes leading to alterations in the tissue's microstructure and mechanical properties.
While there are physiologically desirable effects of ventricular remodeling, e.g. the in the athlete's heart [140], remodeling due to chronic hypertension or myocardial infarction are pathologic and ultimately may lead to end-stage CHF.

In order to model the G&R phenomena described, the theory of volumetric growth as it first has been introduced by Rodriguez et al. [172] is employed. However, it should be noted that even though the terminus *growth and remodeling* (G&R) often is used to describe models that are capturing growth phenomena, the aspect of remodeling, meaning a change in tissue constituents and hence an alteration in its mechanical response characteristics, is *per se* not included in volumetric growth constitutive models.
An alternative approach to the volumetric growth theory that inherently includes turnover of tissue

constituents and thus may be viewed as a true G&R model is the constrained mixture theory introduced by Humphrey and Rajagopal [94]. This approach is not considered within the scope of this thesis.
However, here, a phenomenological remodeling model is introduced that makes the simplifying assumption that the portion of grown matter may have different mechanical properties which are continuously distributed.

Since growth and remodeling phenomena take place on a time scale of days to months compared to the dynamics of the cardiovascular system that alter (periodically) within seconds, a model owing to reasonably capture the long-term kinetics of G&R as a consequence of a short-term event needs some considerations and assumptions with regards to the different time scales involved.

In the following, a novel multiscale-in-time approach is presented to model the two distinct types of cardiomyopathy, volume overload-induced DCM and pressure overload-induced HCM. It essentially combines short-term cardiovascular dynamics with long-term growth and remodeling kinetics by using homeostatic states on the small time scale as stimulus for G&R on the large time scale.
At first, the constitutive models used for growth, including a brief introduction to growth continuum mechanics, are introduced in sec. 2.3.1, and a phenomenological remodeling approach depending on the state of growth is introduced in sec. 2.3.2. Then, the multiscale approach for DCM and HCM is presented in sec. 2.3.3.

2.3.1 Anisotropic volumetric growth models

The concept of finite deformation mechanics of volumetric growth is briefly depicted and is introduced as an extension to the continuum mechanical problem described in sec. 2.1.1. It relies on a kinematical approach first introduced for finite strain elasto-plasticity by Lee [117] which was adopted by Rodriguez et al. [172] in the context of isotropic growth of soft elastic tissue. A further in-depth treatment of the topic, especially with focus on numerical implementation aspects, may be found in Himpel et al. [85]. General growth constitutive models including orthotropic growth are depicted in Lubarda and Hoger [129], with Liu et al. [128] focusing on the numerical implementation aspects, while a good review of growth mechanics applied in the biomechanics context is provided by Menzel et al. [138].

Within the theory of finite deformation volumetric growth, the deformation gradient (2.10) is multiplicatively split into a growth part $\boldsymbol{F}^{\mathrm{g}}$ describing the stretches that occur solely as consequence of some growth stimulus, and an elastic part $\boldsymbol{F}^{\mathrm{e}}$ capturing stretches *and* rigid-body rotations as consequence of the mechanical loading on the one hand, *and* as consequence of compatibility which potentially could have been violated during growth on the other:

$$\boldsymbol{F} = \boldsymbol{F}^{\mathrm{e}}\boldsymbol{F}^{\mathrm{g}}(\vartheta). \tag{2.224}$$

Therein, the dependence of the growth deformation gradient on the growth stretch ϑ is introduced. Figure 2.16 depicts the split of the overall deformation, introducing an *intermediate* or *grown* configuration in addition to the classical concept of reference and current configuration (fig. 2.1).

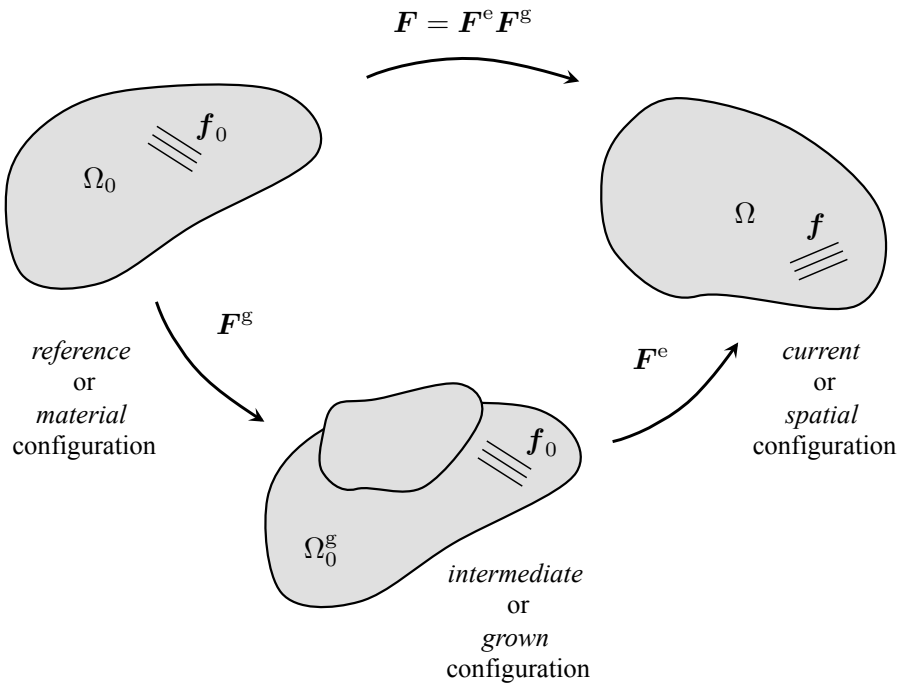

Figure 2.16: Growth continuum with multiplicative split of the deformation gradient $\boldsymbol{F}$ into a growth part $\boldsymbol{F}^{\mathrm{g}}$ and an elastic part $\boldsymbol{F}^{\mathrm{e}}$; intermediate (or grown) configuration Ω_0^{g}, additionally to the concept of reference and current configuration Ω_0 and Ω, respectively.

It should be highlighted that the specific order of execution of deformations is of importance, i.e. $\boldsymbol{F}^{\mathrm{e}}$ is acting on the intermediate configuration and $\boldsymbol{F}^{\mathrm{g}}$ on the reference state. Thus, since the growth deformation invokes a pure state of stretch, no re-orientation of directions (for example a fiber direction $\boldsymbol{f}_0$) occurs from the reference to the intermediate configuration but is entirely lumped into $\boldsymbol{F}^{\mathrm{e}}$ being executed after growth has happened. Furthermore, as stated above, the intermediate configuration may, in general, be incompatible, which is indicated by the portion of grown matter disjointed from the rest of the body. If growth produces an incompatible intermediate state, additional elastic stresses will arise in the final current configuration to restore compatibility.

In the intermediate configuration, the elastic right Cauchy-Green deformation tensor, cf. (2.12), as well as the elastic second Piola-Kirchhoff stress, cf. (2.19), are defined:

$$\boldsymbol{C}^{\mathrm{e}} = \boldsymbol{F}^{\mathrm{e}^{\mathrm{T}}}\boldsymbol{F}^{\mathrm{e}} = \boldsymbol{F}^{\mathrm{g}^{-1}}\boldsymbol{C}\boldsymbol{F}^{\mathrm{g}^{-\mathrm{T}}} \qquad \text{and} \qquad \boldsymbol{S}^{\mathrm{e}} = \boldsymbol{F}^{\mathrm{g}}\boldsymbol{S}\boldsymbol{F}^{\mathrm{g}^{\mathrm{T}}}. \tag{2.225}$$

The Clausius-Plack inequality (2.23) in presence of inelastic growth now becomes

$$\mathcal{D}_{\mathrm{int}} = \left(\boldsymbol{P} - \frac{\partial \Psi(\boldsymbol{F})}{\partial \boldsymbol{F}}\right) : \dot{\boldsymbol{F}} + \boldsymbol{\Sigma}^{\mathrm{e}} : \boldsymbol{L}^{\mathrm{g}} \geq 0, \tag{2.226}$$

with the elastic *Mandel stress tensor*

$$\boldsymbol{\Sigma}^{\mathrm{e}} = \boldsymbol{C}^{\mathrm{e}}\boldsymbol{S}^{\mathrm{e}} \tag{2.227}$$

defined in the intermediate grown configuration, which is work-conjugate to the growth velocity gradient

$$\boldsymbol{L}^{\mathrm{g}} = \dot{\boldsymbol{F}}^{\mathrm{g}} \boldsymbol{F}^{\mathrm{g}^{-1}}. \tag{2.228}$$

The total second Piola-Kirchhoff stress (2.19) now is a function of the deformation (2.12) and of the growth internal variable ϑ which itself is again dependent on the deformation:

$$\boldsymbol{S} = \boldsymbol{S}(\boldsymbol{C}, \vartheta(\boldsymbol{C})). \tag{2.229}$$

The material tangent (2.34), written with respect to the reference state, then generalizes to

$$\mathbb{C} = 2\frac{\partial \boldsymbol{S}}{\partial \boldsymbol{C}} + 2\left(\frac{\partial \boldsymbol{S}}{\partial \boldsymbol{F}^{\mathrm{g}}} : \frac{\partial \boldsymbol{F}^{\mathrm{g}}}{\partial \vartheta}\right) \otimes \frac{\partial \vartheta}{\partial \boldsymbol{C}} = \check{\mathbb{C}} + \tilde{\mathbb{C}}, \tag{2.230}$$

omitting the arguments of (2.229) for the sake of brevity.

The derivative of the second Piola-Kirchhoff stress $\boldsymbol{S}$ with respect to the growth deformation gradient $\boldsymbol{F}^{\mathrm{g}}$ in (2.230) is independent of the specific choice of an evolution equation for ϑ, namely the growth law, and particularizes in

$$\begin{aligned}
\frac{\partial \boldsymbol{S}}{\partial \boldsymbol{F}^{\mathrm{g}}} &= \frac{\partial}{\partial \boldsymbol{F}^{\mathrm{g}}}\left(\boldsymbol{F}^{\mathrm{g}^{-1}} \boldsymbol{S}^{\mathrm{e}} \boldsymbol{F}^{\mathrm{g}^{-\mathrm{T}}}\right) = \\
&= \frac{\partial \boldsymbol{F}^{\mathrm{g}^{-1}}}{\partial \boldsymbol{F}^{\mathrm{g}}} \boldsymbol{S}^{\mathrm{e}} \boldsymbol{F}^{\mathrm{g}^{-\mathrm{T}}} + \boldsymbol{F}^{\mathrm{g}^{-1}}\left[\frac{\partial \boldsymbol{S}^{\mathrm{e}}}{\partial \boldsymbol{C}^{\mathrm{e}}} : \frac{\partial \boldsymbol{C}^{\mathrm{e}}}{\partial \boldsymbol{F}^{\mathrm{g}}}\right] \boldsymbol{F}^{\mathrm{g}^{-\mathrm{T}}} + \boldsymbol{F}^{\mathrm{g}^{-1}} \boldsymbol{S}^{\mathrm{e}} \frac{\partial \boldsymbol{F}^{\mathrm{g}^{-\mathrm{T}}}}{\partial \boldsymbol{F}^{\mathrm{g}}} = \\
&= \frac{\partial \boldsymbol{F}^{\mathrm{g}^{-1}}}{\partial \boldsymbol{F}^{\mathrm{g}}} \boldsymbol{S}^{\mathrm{e}} \boldsymbol{F}^{\mathrm{g}^{-\mathrm{T}}} + \boldsymbol{F}^{\mathrm{g}^{-1}} \boldsymbol{S}^{\mathrm{e}} \frac{\partial \boldsymbol{F}^{\mathrm{g}^{-\mathrm{T}}}}{\partial \boldsymbol{F}^{\mathrm{g}}} + \boldsymbol{F}^{\mathrm{g}^{-1}}\left[\frac{1}{2}\check{\mathbb{C}}^{\mathrm{e}} : \frac{\partial}{\partial \boldsymbol{F}^{\mathrm{g}}}\left(\boldsymbol{F}^{\mathrm{g}^{-\mathrm{T}}} \boldsymbol{C} \boldsymbol{F}^{\mathrm{g}^{-1}}\right)\right] \boldsymbol{F}^{\mathrm{g}^{-\mathrm{T}}} = \\
&= \frac{\partial \boldsymbol{F}^{\mathrm{g}^{-1}}}{\partial \boldsymbol{F}^{\mathrm{g}}} \boldsymbol{S}^{\mathrm{e}} \boldsymbol{F}^{\mathrm{g}^{-\mathrm{T}}} + \boldsymbol{F}^{\mathrm{g}^{-1}} \boldsymbol{S}^{\mathrm{e}} \frac{\partial \boldsymbol{F}^{\mathrm{g}^{-\mathrm{T}}}}{\partial \boldsymbol{F}^{\mathrm{g}}} + \\
&\qquad + \boldsymbol{F}^{\mathrm{g}^{-1}}\left[\frac{1}{2}\check{\mathbb{C}}^{\mathrm{e}} : \left(\frac{\partial \boldsymbol{F}^{\mathrm{g}^{-\mathrm{T}}}}{\partial \boldsymbol{F}^{\mathrm{g}}} \boldsymbol{C} \boldsymbol{F}^{\mathrm{g}^{-1}} + \boldsymbol{F}^{\mathrm{g}^{-\mathrm{T}}} \boldsymbol{C} \frac{\partial \boldsymbol{F}^{\mathrm{g}^{-1}}}{\partial \boldsymbol{F}^{\mathrm{g}}}\right)\right] \boldsymbol{F}^{\mathrm{g}^{-\mathrm{T}}} = \\
&= -\left(\boldsymbol{F}^{\mathrm{g}^{-1}} \overline{\otimes} \boldsymbol{S} + \boldsymbol{S} \underline{\otimes} \boldsymbol{F}^{\mathrm{g}^{-1}}\right) - \left(\boldsymbol{F}^{\mathrm{g}^{-1}} \overline{\otimes} \boldsymbol{F}^{\mathrm{g}^{-1}}\right) : \frac{1}{2}\check{\mathbb{C}}^{\mathrm{e}} : \left(\boldsymbol{F}^{\mathrm{g}^{-\mathrm{T}}} \overline{\otimes} \boldsymbol{C}^{\mathrm{e}} + \boldsymbol{C}^{\mathrm{e}} \underline{\otimes} \boldsymbol{F}^{\mathrm{g}^{-\mathrm{T}}}\right),
\end{aligned} \tag{2.231}$$

with the dyadic products connecting two second-order tensors defined as

$$\mathbb{1} = \mathbf{1} \,\overline{\otimes}\, \mathbf{1} = \delta_{ik}\delta_{jl}\, \hat{\boldsymbol{e}}_i \otimes \hat{\boldsymbol{e}}_j \otimes \hat{\boldsymbol{e}}_k \otimes \hat{\boldsymbol{e}}_l, \tag{2.232}$$

$$\bar{\mathbb{1}} = \mathbf{1} \,\underline{\otimes}\, \mathbf{1} = \delta_{il}\delta_{jk}\, \hat{\boldsymbol{e}}_i \otimes \hat{\boldsymbol{e}}_j \otimes \hat{\boldsymbol{e}}_k \otimes \hat{\boldsymbol{e}}_l, \tag{2.233}$$

$$\bar{\bar{\mathbb{1}}} = \mathbf{1} \otimes \mathbf{1} = \delta_{ij}\delta_{kl}\, \hat{\boldsymbol{e}}_i \otimes \hat{\boldsymbol{e}}_j \otimes \hat{\boldsymbol{e}}_k \otimes \hat{\boldsymbol{e}}_l, \tag{2.234}$$

cf. [39, 107], where δ_{ij} is the well-known Kronecker delta, taking the value 1 for $i = j$ and 0 otherwise.[6]

[6] Equations (2.232) and (2.233) define the fourth-order identity and transposer tensors fulfilling the properties $\mathbb{1} : \boldsymbol{A} = \boldsymbol{A}$ and $\bar{\mathbb{1}} : \boldsymbol{A} = \boldsymbol{A}^{\mathrm{T}}$, respectively, while the fourth-order operator $\bar{\bar{\mathbb{1}}}$ (2.234) acts on a second-order tensor according to $\bar{\bar{\mathbb{1}}} : \boldsymbol{A} = \mathrm{tr}\boldsymbol{A}\, \mathbf{1}$.

In the following sections, specific growth laws suitable for modeling of *dilated cardiomyopathy* (DCM), here meaning eccentric ventricular growth, and *hypertrophic cardiomyopathy* (HCM), here meaning concentric ventricular growth, are introduced. They are closely related to anisotropic growth laws in Göktepe et al. [73], Rausch et al. [167] and Genet et al. [71], however with the option for reversal of growth according to Lee et al. [119]. Also, the combination of these growth laws with electro-mechanical models has been proposed, cf. another work by Lee et al. [121]. Strain-based growth laws from [71] for both eccentric and concentric ventricular hypertrophy have been implemented and applied to patient-specific geometries in the Bachelor's thesis by [90] (supervised by the author of this work).
Early theoretical models for ventricular growth have been proposed by Lin and Taber [127] as well as Taber and Chabert [199], and Kroon et al. [111] applied growth to a simplified generic left ventricular geometry with help of computational methods. Recent models of cardiac growth may be found in another work by Genet et al. [70], where the focus lies on growth-induced prestrain, and Kerckhoffs et al. [105], where some different growth evolution equations to the above-mentioned are introduced. A specific application of growth as consequence of a ventricular infarction is elaborated in Klepach et al. [108]. Finally, a good review for cardiac growth and remodeling is found in Lee et al. [120], and some comparison of different growth laws for myocardial hypertrophy has been performed by Witzenburg and Holmes [213].

2.3.1.1 Strain-driven eccentric growth

Dilated cardiomyopathy (DCM) as consequence of volume overload is triggered during the diastolic filling phase of the heart. This phase is characterized by relatively low ventricular pressures but large cavity volumes. It is assumed that volume overload is present if the myofibers exhibit a sustained critical state of strain at the end of the diastole, hence a strain-driven growth law seems adequate in order to model DCM.
Further, the typical pathological geometric changes associated with DCM are eccentric ventricular hypertrophy, meaning that growth happens longitudinally in myofiber direction $\boldsymbol{f}_0$, cf. fig. 2.9 and fig. 2.10. A myofiber stretch-driven growth law from Göktepe et al. [73] is used, with appropriate extensions in order to allow for reversal in growth [119].

The growth deformation gradient for this law reads

$$\boldsymbol{F}^{\mathrm{g}} = \boldsymbol{1} + (\vartheta - 1)\boldsymbol{f}_0 \otimes \boldsymbol{f}_0, \tag{2.235}$$

and the growth stretch ϑ is governed by the following evolution equation:

$$\dot{\vartheta} = k(\vartheta)\left(\lambda^{\mathrm{e}}_{\mathrm{myo}} - \hat{\lambda}^{\mathrm{crit}}_{\mathrm{myo}}\right). \tag{2.236}$$

Therein, $\lambda^{\mathrm{e}}_{\mathrm{myo}}$ is the *elastic* myofiber stretch,

$$\lambda^{\mathrm{e}}_{\mathrm{myo}} = \frac{1}{\vartheta}\lambda_{\mathrm{myo}} = \frac{1}{\vartheta}\sqrt{\boldsymbol{f}_0 \cdot \boldsymbol{C}\boldsymbol{f}_0}, \tag{2.237}$$

which is the split (2.224) applied to the total myofiber stretch (2.105).

The growth function here reads

$$k(\vartheta) = \begin{cases} \frac{1}{\tau}\left(\frac{\vartheta_{\max}-\vartheta}{\vartheta_{\max}-\vartheta_{\min}}\right)^{\gamma}, & \lambda_{\mathrm{myo}}^{\mathrm{e}} \geq \hat{\lambda}_{\mathrm{myo}}^{\mathrm{crit}}, \\ \frac{1}{\tau_{\mathrm{rev}}}\left(\frac{\vartheta-\vartheta_{\min}}{\vartheta_{\max}-\vartheta_{\min}}\right)^{\gamma_{\mathrm{rev}}}, & \lambda_{\mathrm{myo}}^{\mathrm{e}} < \hat{\lambda}_{\mathrm{myo}}^{\mathrm{crit}}, \end{cases} \tag{2.238}$$

where τ and τ_{rev} are growth and reversal growth time constants, and γ as well as γ_{rev} are growth and reversal growth nonlinearities, respectively. Furthermore, $\vartheta_{\max}$ and $\vartheta_{\min}$ are used to restrict growth and reversal growth to an upper and lower limit, respectively. Finally, $\hat{\lambda}_{\mathrm{myo}}^{\mathrm{crit}}$ is a prescribed critical myofiber stretch above which growth occurs or below which a reversal in growth may happen.

The growth law-specific contributions to the material tangent $\mathbb{C}$ (2.230) are

$$\frac{\partial \boldsymbol{F}^{\mathrm{g}}}{\partial \vartheta} = \boldsymbol{f}_0 \otimes \boldsymbol{f}_0 \tag{2.239}$$

and

$$\frac{\partial \vartheta}{\partial \boldsymbol{C}} = \frac{\partial \vartheta}{\partial \lambda_{\mathrm{myo}}^{\mathrm{e}}}\frac{\partial \lambda_{\mathrm{myo}}^{\mathrm{e}}}{\partial \boldsymbol{C}} = \frac{\partial \vartheta}{\partial \lambda_{\mathrm{myo}}^{\mathrm{e}}}\frac{\partial\left(\frac{1}{\vartheta}\lambda_{\mathrm{myo}}\right)}{\partial \boldsymbol{C}} = \frac{\partial \vartheta}{\partial \lambda_{\mathrm{myo}}^{\mathrm{e}}}\frac{1}{\vartheta}\frac{\partial\sqrt{\boldsymbol{f}_0 \cdot \boldsymbol{C}\boldsymbol{f}_0}}{\partial \boldsymbol{C}} = \frac{\partial \vartheta}{\partial \lambda_{\mathrm{myo}}^{\mathrm{e}}}\frac{1}{2\vartheta\lambda_{\mathrm{myo}}}\boldsymbol{f}_0 \otimes \boldsymbol{f}_0, \tag{2.240}$$

while the partial derivative of the solution ϑ with respect to the growth stimulus $\lambda_{\mathrm{myo}}^{\mathrm{e}}$ only is expressible after having applied a numerical solution algorithm to (2.236), since it is an ordinary differential equation and nonlinear in ϑ. Refer to the following chapter, sec. 3.3.1.1, for the numerical solution aspects.

2.3.1.2 Stress-governed concentric growth

Hypertrophic cardiomyopathy (HCM) as consequence of sustained pressure overload is rather triggered in the systolic heart phase where the ventricles are exposed to high pressures at lowest cavity volumes at a state where the muscle is contracted and the myofibers therefore are shortened. Pressure overload is present if the afterload the heart has to work against during ejection is critically high, leading to a persistently elevated end-systolic load onto the endocardium. Thus, a critical state of wall stress is assumed to be the growth stimulus for this type of overload scenario. The pathological geometric changes due to pressure overload are of concentrically thickened ventricular walls, since adaptive growth processes seek at decreasing the wall stress by adding tissue in transverse cross-fiber directions. Here, a similar stress-driven growth law to the one used in Göktepe et al. [73] is chosen, however not with only-radial growth but with growth in all directions but the myofiber direction $\boldsymbol{f}_0$, as it has been used in [71] in context of a strain-driven concentric law. Again, adaptions for including reversal growth according to [119] are added.

For this law, the growth deformation gradient reads

$$\boldsymbol{F}^{\mathrm{g}} = \vartheta\boldsymbol{1} + (1-\vartheta)\boldsymbol{f}_0 \otimes \boldsymbol{f}_0, \tag{2.241}$$

and the growth stretch ϑ is governed by the evolution equation

$$\dot{\vartheta} = k(\vartheta)(\mathrm{tr}\,\boldsymbol{\Sigma}^{\mathrm{e}} - \hat{\Sigma}^{\mathrm{crit}}). \tag{2.242}$$

Therein, $\boldsymbol{\Sigma}^{\mathrm{e}}$ is the elastic Mandel stress tensor (2.227).

The growth function here reads

$$k(\vartheta) = \begin{cases} \frac{1}{\tau}\left(\frac{\vartheta_{\max}-\vartheta}{\vartheta_{\max}-\vartheta_{\min}}\right)^{\gamma}, & \mathrm{tr}\,\boldsymbol{\Sigma}^{\mathrm{e}} \geq \hat{\Sigma}^{\mathrm{crit}}, \\ \frac{1}{\tau_{\mathrm{rev}}}\left(\frac{\vartheta-\vartheta_{\min}}{\vartheta_{\max}-\vartheta_{\min}}\right)^{\gamma_{\mathrm{rev}}}, & \mathrm{tr}\,\boldsymbol{\Sigma}^{\mathrm{e}} < \hat{\Sigma}^{\mathrm{crit}}, \end{cases} \tag{2.243}$$

where τ and τ_{rev} again are growth and reversal growth time constants, and γ as well as γ_{rev} are growth and reversal growth nonlinearities, respectively. Like for the stretch-driven growth, $\vartheta_{\max}$ and $\vartheta_{\min}$ are used to restrict growth and reversal growth to an upper and lower limit, respectively. Finally, $\hat{\Sigma}^{\mathrm{crit}}$ is a prescribed critical Mandel stress above which growth occurs or below which a reversal in growth may happen.

The growth law-specific contributions to the material tangent $\mathbb{C}$ (2.230) are

$$\frac{\partial \boldsymbol{F}^{\mathrm{g}}}{\partial \vartheta} = \boldsymbol{1} - \boldsymbol{f}_0 \otimes \boldsymbol{f}_0 \tag{2.244}$$

and

$$\begin{aligned} \frac{\partial \vartheta}{\partial \boldsymbol{C}} &= \frac{\partial \vartheta}{\partial \mathrm{tr}\,\boldsymbol{\Sigma}^{\mathrm{e}}} \frac{\partial \mathrm{tr}\,\boldsymbol{\Sigma}^{\mathrm{e}}}{\partial \boldsymbol{C}} = \frac{\partial \vartheta}{\partial \mathrm{tr}\,\boldsymbol{\Sigma}^{\mathrm{e}}} \frac{\partial (\boldsymbol{C}^{\mathrm{e}} : \boldsymbol{S}^{\mathrm{e}})}{\partial \boldsymbol{C}} = \frac{\partial \vartheta}{\partial \mathrm{tr}\,\boldsymbol{\Sigma}^{\mathrm{e}}} \left[\frac{\partial \boldsymbol{C}^{\mathrm{e}}}{\partial \boldsymbol{C}} : \boldsymbol{S}^{\mathrm{e}} + \boldsymbol{C}^{\mathrm{e}} : \frac{\partial \boldsymbol{S}^{\mathrm{e}}}{\partial \boldsymbol{C}} \right] = \\ &= \frac{\partial \vartheta}{\partial \mathrm{tr}\,\boldsymbol{\Sigma}^{\mathrm{e}}} \left[\frac{\partial}{\partial \boldsymbol{C}} \left(\boldsymbol{F}^{\mathrm{g}^{-\mathrm{T}}} \boldsymbol{C} \boldsymbol{F}^{\mathrm{g}^{-1}} \right) : \boldsymbol{F}^{\mathrm{g}} \boldsymbol{S} \boldsymbol{F}^{\mathrm{g}^{\mathrm{T}}} + \boldsymbol{F}^{\mathrm{g}^{-\mathrm{T}}} \boldsymbol{C} \boldsymbol{F}^{\mathrm{g}^{-1}} : \frac{\partial}{\partial \boldsymbol{C}} \left(\boldsymbol{F}^{\mathrm{g}} \boldsymbol{S} \boldsymbol{F}^{\mathrm{g}^{\mathrm{T}}} \right) \right] = \\ &= \frac{\partial \vartheta}{\partial \mathrm{tr}\,\boldsymbol{\Sigma}^{\mathrm{e}}} \left[\boldsymbol{F}^{\mathrm{g}^{-\mathrm{T}}} \mathbb{1}\, \boldsymbol{F}^{\mathrm{g}^{-1}} : \boldsymbol{F}^{\mathrm{g}} \boldsymbol{S} \boldsymbol{F}^{\mathrm{g}^{\mathrm{T}}} + \boldsymbol{F}^{\mathrm{g}^{-\mathrm{T}}} \boldsymbol{C} \boldsymbol{F}^{\mathrm{g}^{-1}} : \boldsymbol{F}^{\mathrm{g}} \frac{\partial \boldsymbol{S}}{\partial \boldsymbol{C}} \boldsymbol{F}^{\mathrm{g}^{\mathrm{T}}} \right] = \\ &= \frac{\partial \vartheta}{\partial \mathrm{tr}\,\boldsymbol{\Sigma}^{\mathrm{e}}} \left[\boldsymbol{F}^{\mathrm{g}^{-\mathrm{T}}} \left(\mathbb{1} : \boldsymbol{S} + \boldsymbol{C} : \frac{1}{2} \check{\mathbb{C}} \right) \boldsymbol{F}^{\mathrm{g}^{\mathrm{T}}} \right] = \\ &= \frac{\partial \vartheta}{\partial \mathrm{tr}\,\boldsymbol{\Sigma}^{\mathrm{e}}} \left[\boldsymbol{S} + \boldsymbol{C} : \frac{1}{2} \check{\mathbb{C}} \right], \end{aligned} \tag{2.245}$$

with $\check{\mathbb{C}} = \boldsymbol{F}^{\mathrm{g}^{-1}} \boldsymbol{F}^{\mathrm{g}^{-1}} \check{\mathbb{C}}^{\mathrm{e}} \boldsymbol{F}^{\mathrm{g}^{-\mathrm{T}}} \boldsymbol{F}^{\mathrm{g}^{-\mathrm{T}}}$ being the pull-back of the elastic modulus in the intermediate configuration to the reference configuration, and the fourth-order unity tensor $\mathbb{1}$ according to (2.232).

Again, the partial derivative of the solution ϑ with respect to the growth stimulus $\mathrm{tr}\,\boldsymbol{\Sigma}^{\mathrm{e}}$ in (2.245) only is expressible after having applied a numerical solution algorithm to (2.242) due to the nonlinearity in ϑ, cf. the next chapter, sec. 3.3.1.2.

2.3.2 Phenomenological remodeling

Mathematical and computational models for growth and, explicitly, remodeling of biological tissue have been proposed in the literature to date [3]. A unified approach to growth *and* remodeling is the constrained mixture theory [94] mentioned earlier which would be an alternative framework to the volumetric growth theory, which itself is not able to capture remodeling phenomena.

As mentioned in the introductory remarks to this section, the terminus G&R most often does not strictly apply to the cardiac growth models presented in the literature to date, cf. sec. 2.3.1, since an explicit change in passive or active mechanical tissue constituents and hence an alteration of their mechanical properties is not considered. To date, no cardiac volumetric growth model was extended to be capable of capturing "true" remodeling effects [120].

Here, a phenomenological approach to include remodeling into volumetric growth constitutive models is chosen. In a slightly modified variant, it has been proposed by Thon et al. [201] and relies on the assumption that the portion of grown matter exhibits different passive or active mechanical properties than the (non-grown) "base" material.

Analogously to the isochoric-volumetric split in finite strain hyperelasticity, the elastic second Piola-Kirchhoff stress $(2.225)_2$ is additively decomposed into a part governing the non-grown base material, $\boldsymbol{S}^{\mathrm{e}}_{(base)}$, and a part that governs the grown added material, $\boldsymbol{S}^{\mathrm{e}}_{(grown)}$. A growth-dependent weighting $\phi = \phi(\vartheta) \in [0,1]$ is introduced, being the fraction of the non-grown, healthy base material:

$$\boldsymbol{S}^{\mathrm{e}} = \phi(\vartheta)\boldsymbol{S}^{\mathrm{e}}_{(base)} + (1-\phi(\vartheta))\boldsymbol{S}^{\mathrm{e}}_{(grown)}. \tag{2.246}$$

For longitudinal (uni-axial) growth as assumed for eccentric strain-driven ventricular hypertrophy, the fraction of non-grown material is

$$\phi = \frac{1}{\vartheta}, \tag{2.247}$$

and for transversal (bi-axial) growth as assumed for concentric stress-driven ventricular hypertrophy, it becomes

$$\phi = \frac{1}{\vartheta^2}. \tag{2.248}$$

The elastic material tangent for the phenomenological remodeling law then yields

$$\begin{aligned}\check{\mathbb{C}}^{\mathrm{e}} &= 2\left(\phi\frac{\partial \boldsymbol{S}^{\mathrm{e}}_{(base)}}{\partial \boldsymbol{C}^{\mathrm{e}}} + \frac{\partial\phi}{\partial \boldsymbol{C}^{\mathrm{e}}}\otimes\boldsymbol{S}^{\mathrm{e}}_{(base)} + (1-\phi)\frac{\partial \boldsymbol{S}^{\mathrm{e}}_{(grown)}}{\partial \boldsymbol{C}^{\mathrm{e}}} - \frac{\partial\phi}{\partial \boldsymbol{C}^{\mathrm{e}}}\otimes\boldsymbol{S}^{\mathrm{e}}_{(grown)}\right) = \\ &= \phi\,\check{\mathbb{C}}^{\mathrm{e}}_{(base)} + (1-\phi)\,\check{\mathbb{C}}^{\mathrm{e}}_{(grown)} + 2\frac{\partial\phi}{\partial\vartheta}\frac{\partial\vartheta}{\partial \boldsymbol{C}^{\mathrm{e}}}\otimes(\boldsymbol{S}^{\mathrm{e}}_{(base)} - \boldsymbol{S}^{\mathrm{e}}_{(grown)}),\end{aligned} \tag{2.249}$$

where $\partial\vartheta/\partial\boldsymbol{C}^{\mathrm{e}}$ is the elastic analog to either (2.240) or (2.245) depending on the specific growth law.

It is worth mentioning that for the isochoric-volumetric split commonly used in finite strain hyperelasticity, an additive decomposition of the strain energy (2.28) yields an additive decomposition of the second Piola-Kirchhoff stress, and no dependence on the specific energy functional but only on its derivative with respect to strain invariants occurs in the constitutive model. However, the mass fraction $\phi = \phi(\vartheta)$ in (2.246) depends on the deformation, since $\vartheta = \vartheta(\boldsymbol{C})$. Hence, an additive split according to (2.246) would *not* be equal to applying the same type of split to the strain energy $\Psi = \phi(\vartheta)\,\Psi_{(base)} + (1-\phi(\vartheta))\,\Psi_{(grown)}$. This approach is not chosen here since otherwise the explicit form of the energy functional would enter the expression (2.246), and questions would arise how to consider (partly) non-hyperelastic constitutive models like active stress (2.96), or effects of viscosity, damage and plasticity.

2.3.3 Multiscale-in-time approach for cardiac growth and remodeling

A computational model that accounts for long-term growth and remodeling invoked by a short-term event has to consider the different temporal scales of cardiovascular dynamics and G&R kinetics. While a heart beat and alterations of the dynamics of the cardiovascular state take place on a time scale of seconds to minutes, G&R phenomena in the heart occur on a time span of days to months depending on the specific stimulus [44].

Here, a novel multiscale-in-time approach is presented that allows to model G&R on a large time scale as result of a short time scale acute event. The essential feature of this approach is the continuity of vascular pressures and the mechanical as well as the growth state inside the tissue for all times. Hence, the final homeostatic grown configuration captures all residual stresses and strains as well as the fraction of remodeled material that has developed during G&R.

The approach relies on a separation of time scales into a short one solving the 3D-0D coupled cardiovascular mechanics problem, namely the 3D structural model (2.94) (*3Dventr*) or (2.95) (*3Datrioventr*) coupled to the 0D vascular system (2.118)–(2.133) (*0Dsyspul*) or (2.134)–(2.167) (*0Dsyspulcap*), and a large time scale solving the growth problem.

Figures 2.17 and 2.18 depict the multiscale approach for modeling eccentric strain-driven growth for dilated cardiomyopathy and concentric stress-driven growth for hypertrophic cardiomyopathy, respectively. The figures outline the time course of the ventricular and atrial pressures and active stress throughout the multiscale problem and sketch the different time scale sub-problems that are solved.
Per definition, the multiscale computation is initialized with precomputed homeostatic state initial conditions, cf. sec. 2.2.4.1. Prestressing occurs during the time span $[0, t_0]$. The very first cycle fulfills (2.222) and is used to set the point-wise differing homeostatic state values of the critical growth threshold. This guarantees that the critical value above which growth is initiated depends on a healthy known state, hence G&R only occurs if this state is violated by some pathological incident which only then, after the first cardiac cycle, is introduced at the time t_{disease}. This may be a myocardial infarction in some distinct area, an alteration in valve behavior such as mitral regurgitation or aortic stenosis, or some other event that is capable of producing overload scenarios which eventually lead to ventricular G&R. Thereafter, the amount of heart cycles required to re-fulfill (2.222) is computed, ending the first small time scale with a switch-over to the large one. On the large time scale, the heart is decoupled from the vascular system, and a quasi-static balance of linear momentum

$$\boldsymbol{\nabla}_0 \cdot (\boldsymbol{F}\boldsymbol{S}) = \boldsymbol{0} \quad \text{in } \Omega_0 \times [t_{\mathcal{N}}, t_{\mathcal{N}} + T_{\mathrm{growth}} + 2\,T_{\mathrm{load}}] \tag{2.250}$$

is solved, where the current growth cycle is denoted with $\mathcal{N} \in [0, \mathcal{N}_{\mathrm{growth}}]$. The net time for the calculation of the growth kinetics is T_{growth}, which is the time span during which growth may happen. The non-physical "artificial" time span T_{load} characterizes a "conditioning" of the model to the growth stimulating state of load that has been extracted from the small time scale and a

release thereof, happening before and after entering the net growth large time scale.[7]
The Robin boundary conditions (2.90)–(2.93) remain present throughout the whole multiscale simulation.
However, after decoupling the vascular model, the cavity pressures $\hat{p}_c^i$ are prescribed with a Neumann load:

$$\boldsymbol{t}_0 = \boldsymbol{P}\boldsymbol{n}_0 = -\hat{p}_c^i \, J\boldsymbol{F}^{-\mathrm{T}}\boldsymbol{n}_0 \quad \text{on } \Gamma_{0,c}^{\mathrm{0D},i} \times [t_{\mathcal{N}}, t_{\mathcal{N}} + T_{\mathrm{growth}}], \tag{2.251}$$

where the "conditioning" phase during the time spans $[t_{\mathcal{N}}, t_{\mathcal{N}} + T_{\mathrm{load}}]$ ("ramp-up") and $[t_{\mathcal{N}} + T_{\mathrm{growth}}, t_{\mathcal{N}} + T_{\mathrm{growth}} + T_{\mathrm{load}}]$ ("ramp-down") is not described.

Additionally, the active stress $\hat{\tau}_{\mathrm{a}}$ at the respective growth stimulating time instance is prescribed. Hence, on the large time scale, the constitutive equation for the second Piola-Kirchhoff stress (2.96) becomes

$$\boldsymbol{S} = \frac{\partial \Psi}{\partial \boldsymbol{E}} + \hat{\tau}_{\mathrm{a}} \boldsymbol{f}_0 \otimes \boldsymbol{f}_0. \tag{2.252}$$

In (2.251) and (2.252), the pressures $\hat{p}_c^i$ and the (point-wise varying) active stress $\hat{\tau}_{\mathrm{a}}$ are no longer variables but are prescribed quantities that remain fixed during the time span $[t_{\mathcal{N}}, t_{\mathcal{N}} + T_{\mathrm{growth}}]$. They emerge from the growth stimulating time instance of the *previous* short time scale computation and depend on the type of growth that is considered, eccentric growth for dilated cardiomyopathy or concentric growth for hypertrophic cardiomyopathy.
Hence, the large time scale mechanical state may be seen as "frozen" with regards to the external loads, capturing either the end-diastolic or end-systolic small time scale instance which stimulates G&R. Note that, without loss of generality, the exact values of the external loads from the growth-stimulating small time scale instance are used. However, one may also think of using some time-averaged quantities to trigger G&R.

After finishing the large time scale computation, the small time scale is re-visited with the circulation 0D state variable initial conditions $\mathcal{I}(t_{N^\star} + T_{\mathrm{cycl}})$, cf. (2.223), where $t_{N^\star}$ denotes the time when the homeostatic cycle $N^\star$ from the previous small time scale started.

The alternation between the time scales is continued until the so-called growth error E_{growth} fulfills a tolerance $\epsilon_{\mathrm{growth}}$:

$$\begin{aligned} E_{\mathrm{growth}} = \max \Bigg\{ &\left| \frac{\mathrm{EDV}^\ell(t_{\mathcal{N}}) - \mathrm{EDV}^\ell(t_{\mathcal{N}-1})}{\mathrm{EDV}^\ell(t_{\mathcal{N}-1})} \right|, \left| \frac{\mathrm{EDV}^r(t_{\mathcal{N}}) - \mathrm{EDV}^r(t_{\mathcal{N}-1})}{\mathrm{EDV}^r(t_{\mathcal{N}-1})} \right|, \\ &\left| \frac{\mathrm{ESV}^\ell(t_{\mathcal{N}}) - \mathrm{ESV}^\ell(t_{\mathcal{N}-1})}{\mathrm{ESV}^\ell(t_{\mathcal{N}-1})} \right|, \left| \frac{\mathrm{ESV}^r(t_{\mathcal{N}}) - \mathrm{ESV}^r(t_{\mathcal{N}-1})}{\mathrm{ESV}^r(t_{\mathcal{N}-1})} \right| \Bigg\} \leq \epsilon_{\mathrm{growth}}, \end{aligned} \tag{2.253}$$

where EDV^i and ESV^i are the left ($i = \ell$) and right ($i = r$) ventricular end-diastolic and end-systolic volumes, respectively.

[7] In the computational sense, this time may be denoted as load ramp-up and ramp-down. However, since a quasi-static problem is solved on the large time scale, the actual duration of T_{load} does not influence the solution.

2.3.3.1 Dilated cardiomyopathy (DCM)

The specific particularities for the multiscale approach to strain-triggered DCM are highlighted, cf. fig. 2.17. The underlying growth law is presented in sec. 2.3.1.1. After prestressing, the first homeostatic healthy baseline state is computed, and at the *end-diastolic* time instance $t_{\text{hom}}^{\text{gr,ecc}} = t_0 + t_{\text{ed}}$ denoting the time governing the homeostatic reference state for eccentric ventricular growth, the actual elastic myofiber stretch (2.237) is "recorded" and stored into the point-wise differing critical baseline elastic myofiber stretch if it is greater than a lower bound $(\hat{\lambda}_{\text{myo}}^{\text{crit}})_{\downarrow}$:

$$\hat{\lambda}_{\text{myo}}^{\text{crit}} \leftarrow \begin{cases} s\,\lambda_{\text{myo}}^{\text{e}}, & \text{if } \lambda_{\text{myo}}^{\text{e}} > (\hat{\lambda}_{\text{myo}}^{\text{crit}})_{\downarrow}, \\ (\hat{\lambda}_{\text{myo}}^{\text{crit}})_{\downarrow}, & \text{else,} \end{cases} \tag{2.254}$$

which enters the growth law (2.236), using a safety factor s.

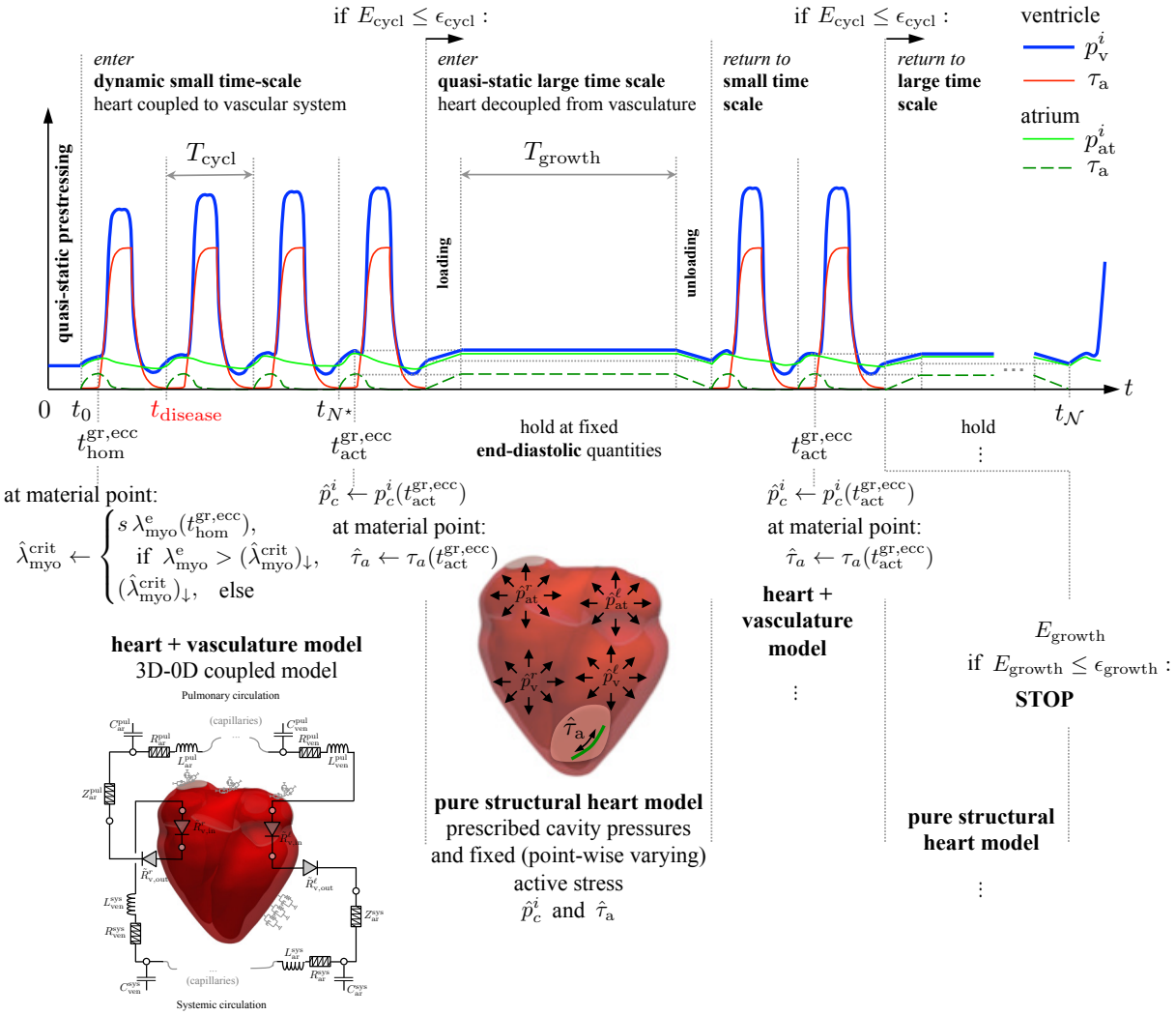

Figure 2.17: Multiscale-in-time approach for eccentric strain-driven growth as consequence of end-diastolic volume overload leading to dilated cardiomyopathy (DCM).

At the time instance $t_{\text{act}}^{\text{gr,ecc}} = t_{N^\star} + t_{\text{ed}}$, which denotes the point at which the critical state of volume overload is evaluated, being the end-diastolic point of the homeostatic cardiac cycle $N^\star$ starting at $t_{N^\star}$, the growth stimulating cavity pressures for all four cardiac chambers as well as the active stress state at every material point are stored in order to be applied to the quasi-static large time scale computation in (2.251) and (2.252), respectively:

$$\hat{p}_c^i \leftarrow p_c^i(t_{\text{act}}^{\text{gr,ecc}}) \quad \text{and} \quad \hat{\tau}_{\text{a}} \leftarrow \tau_{\text{a}}(t_{\text{act}}^{\text{gr,ecc}}). \tag{2.255}$$

The cycling between small and large time scale is continued until (2.253) is met.

2.3.3.2 Hypertrophic cardiomyopathy (HCM)

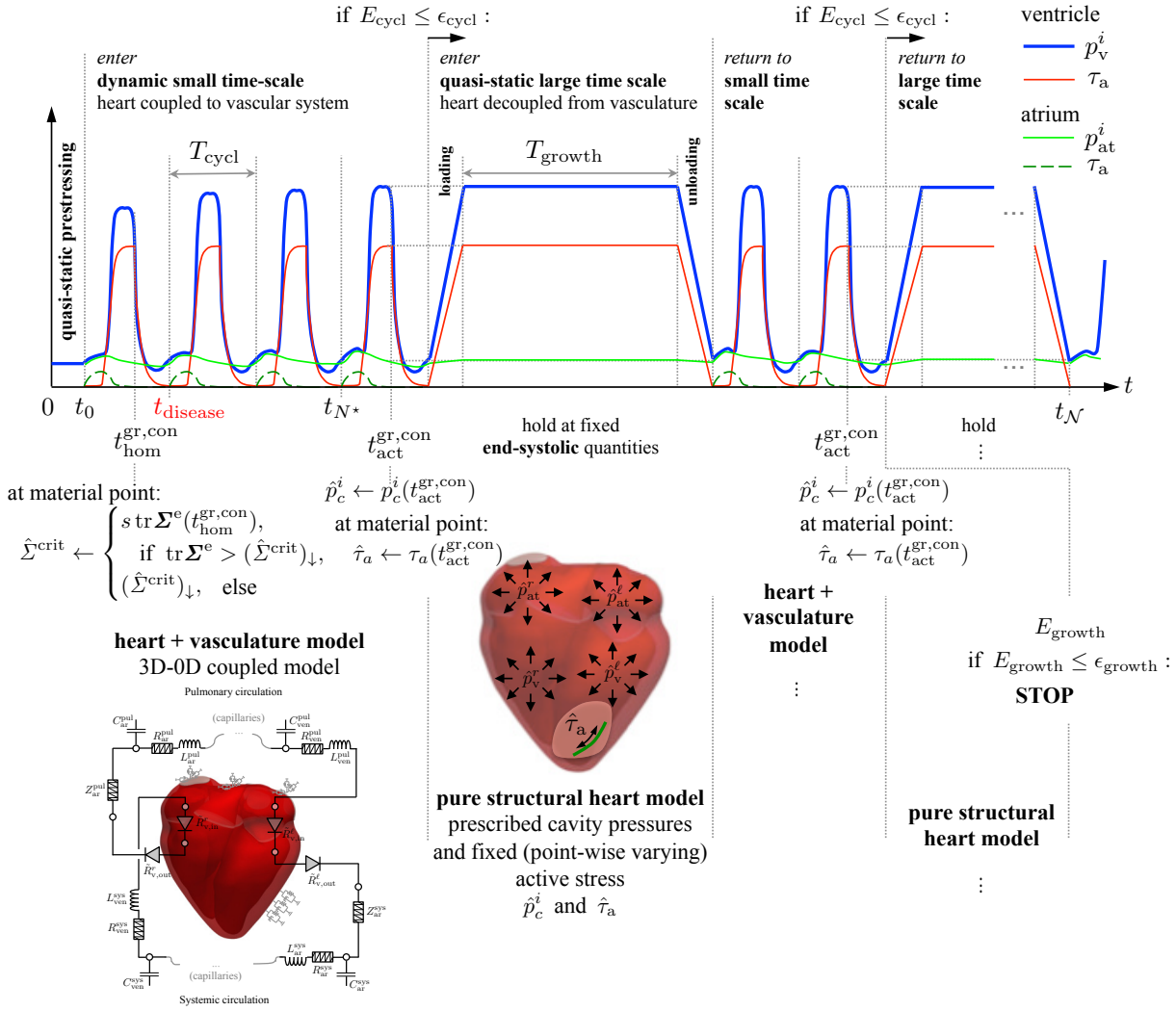

Figure 2.18: Multiscale-in-time approach for concentric stress-driven growth as consequence of end-systolic pressure overload leading to hypertrophic cardiomyopathy (HCM).

Here, the characteristic features of the multiscale approach to stress-triggered HCM are highlighted, cf. fig. 2.18. The underlying growth law is presented in sec. 2.3.1.2. After prestressing,

the first homeostatic healthy baseline state is computed, and at the *end-systolic* time instance $t_{\mathrm{hom}}^{\mathrm{gr,con}} = t_0 + t_{\mathrm{es}}$ denoting the time governing the homeostatic reference state for concentric ventricular growth, the actual trace of the elastic Mandel stress, cf. (2.227), is "recorded" and stored into the point-wise differing critical baseline elastic volumetric Mandel stress if it is greater than a lower bound $(\hat{\Sigma}^{\mathrm{crit}})_{\downarrow}$:

$$\hat{\Sigma}^{\mathrm{crit}} \leftarrow \begin{cases} s \operatorname{tr} \boldsymbol{\Sigma}^{\mathrm{e}}, & \text{if } \operatorname{tr} \boldsymbol{\Sigma}^{\mathrm{e}} > (\hat{\Sigma}^{\mathrm{crit}})_{\downarrow}, \\ (\hat{\Sigma}^{\mathrm{crit}})_{\downarrow}, & \text{else}, \end{cases} \tag{2.256}$$

which enters the growth law (2.242), using a safety factor s.

At the time instance $t_{\mathrm{act}}^{\mathrm{gr,con}} = t_{N^\star} + t_{\mathrm{es}}$, which denotes the point at which the critical state of pressure overload is evaluated, being the end-systolic point of the homeostatic cardiac cycle $N^\star$ starting at $t_{N^\star}$, the growth stimulating cavity pressures for all four cardiac chambers as well as the active stress state at every material point are stored in order to be applied to the quasi-static large time scale computation in (2.251) and (2.252), respectively:

$$\hat{p}_c^i \leftarrow p_c^i(t_{\mathrm{act}}^{\mathrm{gr,con}}) \quad \text{and} \quad \hat{\tau}_{\mathrm{a}} \leftarrow \tau_{\mathrm{a}}(t_{\mathrm{act}}^{\mathrm{gr,con}}). \tag{2.257}$$

Again, the cycling between small and large time scale is continued until (2.253) is met.

3 Discretization and solution methods for cardiovascular mechanics

Models capable of describing the complex mechanical behavior of the heart and its interaction with the circulatory system as they have been introduced in chap. 2 require robust and efficient computational discretization and solution strategies due to the coupling of sub-models with different spatial and temporal scales.
While, for example, the myocardium is treated as 3-dimensionally resolved nonlinear elastic solid, the vascular system is a 0-dimensional lumped-parameter model where the temporal scales have been integrated, setting the requirements for the discretization methods in order to maintain the intended physical behavior.
Furthermore, the heart and the vascular system strongly influence one another, thus robust coupling schemes are required for the exchange of information between the 3D solid mechanics and the 0D vascular model during the nonlinear solution process.

All spatially resolved entities, the only-ventricular heart model *3Dventr* or the 4-chamber heart model *3Datrioventr*, are discretized in space using the displacement-based finite element method in a Total Lagrangian frame. The resulting spatially discretized solid mechanics balance equations as well as all other 0D models – circulation models *0Dsyspul*, *0Dsyspulcap* or the cardiorespiratory model *0Dsyspulcaprespir* – are discretized in time using finite difference methods.
The strong coupling of the 3D heart to the 0D circulation here is performed by a novel monolithic discretization and solution approach with consistent linearization such that the entire coupled nonlinear problem can be solved in one monolithic Newton-Raphson scheme. For the linearized system of equations, an existing preconditioner is used for the efficient iterative solution of the block matrix system arising in each Newton iteration. For the solid mechanics part of the problem state-of-the-art algebraic multigrid preconditioners are utilized, while the comparably small 0D model block is inverted directly.

This chapter is organized as follows. The fundamentals of spatial and temporal discretization strategies, here finite element and finite difference methods, are briefly depicted in sec. 3.1. The novel monolithic discretization and solution strategy for the 3D-0D coupled problems as well as various results for patient-specific heart-vascular mechanics and gas transport are presented in sec. 3.2. Finally, the algorithmic treatment of the multiscale growth and remodeling approach that has been presented in the previous chapter is presented in sec. 3.3, including the results for volume overload-induced dilated cardiomyopathy and pressure overload-induced hypertrophic cardiomyopathy.
Discussions on results and algorithmic aspects accompany the results presentations of the respective sections.

3.1 Fundamentals

3.1.1 Nonlinear finite element methods for solid mechanics

Since spatial discretizations throughout this thesis exclusively are performed using the finite element method, a short introduction to its basic concept and the respective notations is given here. Specifically, focus is set on the discretization of nonlinear solid mechanics (cf. sec. 2.1.1) in a Total Lagrangian description. For an in-depth treatment of various aspects of the topic, the reader is referred to Zienkiewicz [225, 226] and Wriggers [218].

The starting point of the (displacement-based) finite element method is the weak form of the initial boundary value problem of finite deformation nonlinear solid mechanics (2.55), here stated with respect to the (known) reference configuration. The basic idea is not to find some global function for the displacement field $\boldsymbol{u}$ in order to satisfy (2.55) (which would render infeasible for complex geometries), but to find solutions at discrete points (nodes) belonging to smaller (interconnected) sub-domains which allow a unique mathematical description and interpolation of the solution by so-called *shape functions* with only local support. Thus, the finite element method can be seen as a discretization of the function space of the admissible solutions. The whole domain Ω_0 is split into sub-domains $\Omega_0^{(e)}$ called *finite elements*:

$$\Omega_0 \approx \bigcup_{e=1}^{n_{\mathrm{el}}} \Omega_0^{(e)} = \tilde{\Omega}_0, \tag{3.1}$$

where the discretized overall domain is denoted with $\tilde{\Omega}_0$ and n_{el} is the total number of finite elements making up that domain.

The displacement vector of one finite element $\mathbf{u}^{(e)}$ is a linear combination of shape functions stored in the matrix $\mathbf{N}^{(e)}$ and discrete nodal values denoted by $\mathbf{d}^{(e)}$:

$$\mathbf{u}^{(e)}(\mathbf{x}_0, t) = \mathbf{N}^{(e)}(\mathbf{x}_0)\, \mathbf{d}^{(e)}(t). \tag{3.2}$$

Analogously, the geometry is approximated using the same set of shape functions (called the *isoparametric concept*), mapping a finite element defined in some parameter space to the real space. The finite element position vector thus yields

$$\mathbf{x}_0^{(e)} = \mathbf{N}^{(e)}\, \bar{\mathbf{x}}_0^{(e)}, \tag{3.3}$$

with the vector of nodal coordinates $\bar{\mathbf{x}}_0^{(e)}$. The isoparametric concept in the 2-dimensional case is depicted in fig. 3.1.
For a linear 2-dimensional quadrilateral element as indicated in fig. 3.1, (3.2) becomes

$$\mathbf{u}^{(e)} = \begin{bmatrix} N^1 & 0 & N^2 & 0 & N^3 & 0 & N^4 & 0 \\ 0 & N^1 & 0 & N^2 & 0 & N^3 & 0 & N^4 \end{bmatrix} \begin{bmatrix} d_1^1 \\ d_2^1 \\ d_1^2 \\ d_2^2 \\ d_1^3 \\ d_2^3 \\ d_1^4 \\ d_2^4 \end{bmatrix}, \tag{3.4}$$

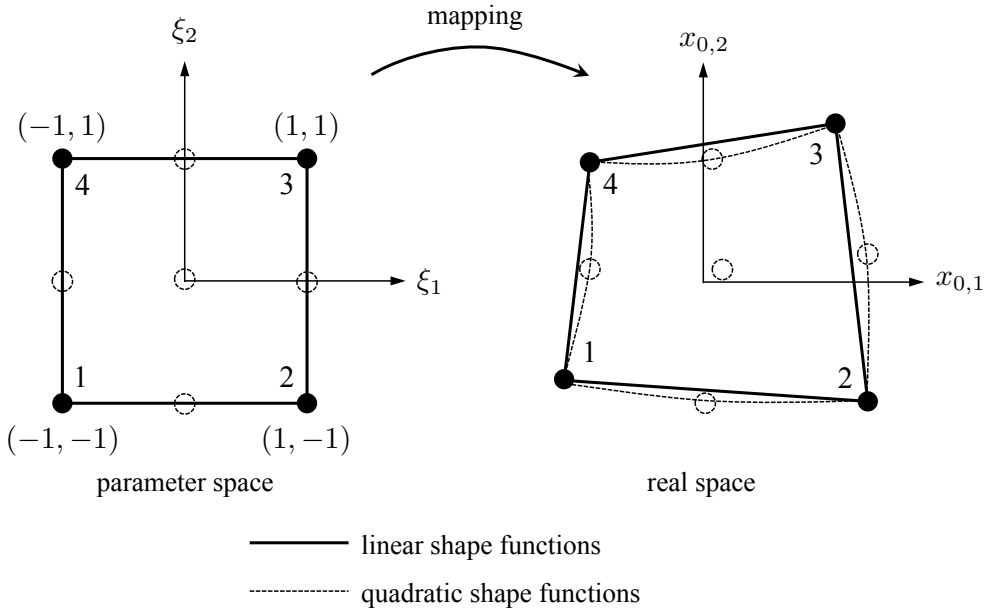

Figure 3.1: Exemplary (2-dimensional) quadrilaterial finite element: Isoparametric concept.

with the shape functions being e.g. Lagrangian polynomials like $N^1 = \frac{1}{4}(1-\xi_1)(1-\xi_2)$, $N^2 = \frac{1}{4}(1+\xi_1)(1-\xi_2)$, $N^3 = \frac{1}{4}(1+\xi_1)(1+\xi_2)$ and $N^4 = \frac{1}{4}(1-\xi_1)(1+\xi_2)$. They take the value 1 at their respective node and the value 0 at all other nodes. Furthermore, they fulfill the so-called *partition of unity*, meaning that they sum up to 1 at every location inside the finite element. Potentially, higher-order (Lagrangian) polynomials, e.g. quadratic ones, may be used, indicated by the dashed lines in fig. 3.1, where additional nodes have to be introduced. The shape functions however have to be at least linear in order meet the requirements for differentiability of the displacement, cf. sec. 2.1.1.4.
The concept analogously transfers to the 3-dimensional case and to other types of elements (besides quadrilateral also triangular elements in two dimensions, or hexahedral, tetrahedral, wedge or pyramidal elements in three dimensions).
Now, the principle of virtual work (2.55) can be approximated by

$$\delta\mathcal{W} \approx \sum_{e=1}^{n_{\mathrm{el}}} \left[\int_{\Omega_0^{(e)}} \delta\mathbf{u}^{\mathrm{T}}\, \rho_0 \ddot{\mathbf{u}}\, \mathrm{d}V + \int_{\Omega_0^{(e)}} \delta\mathbf{E}^{\mathrm{T}}\, \mathbf{S}\, \mathrm{d}V - \int_{\Omega_0^{(e)}} \delta\mathbf{u}^{\mathrm{T}}\, \hat{\mathbf{b}}_0\, \mathrm{d}V - \int_{\Gamma_0^{\mathrm{N}(e)}} \delta\mathbf{u}^{\mathrm{T}}\, \hat{\mathbf{t}}_0\, \mathrm{d}A \right]^{(e)} = 0, \quad \forall\, \delta\mathbf{u}, \tag{3.5}$$

where the second Piola-Kirchhoff stress tensor as well as the (virtual) Green-Lagrange strain tensor have been written as 6×1 arrays $\mathbf{S}$ and $\delta\mathbf{E}$ due to their symmetry. The weighing function (virtual displacement) is analogously interpolated to (3.2):

$$\delta\mathbf{u}^{(e)}(\mathbf{x}_0) = \mathbf{N}^{(e)}(\mathbf{x}_0)\, \delta\mathbf{d}^{(e)}, \tag{3.6}$$

which is referred to as *Bubnov-Galerkin approach*. An alternative treatment would be the *Petrov-Galerkin approach*, where differing shape functions for the weighting function from those for the

primary variable are used.

Inserting (3.2) and (3.6) into (3.5), re-writing the equation and assembling the global system of equations yields an expression of the type

$$\delta\mathbf{d}^{\mathrm{T}} \left(\mathbf{M}\,\ddot{\mathbf{d}} + \mathbf{f}_{\mathrm{int}}(\mathbf{d}) - \mathbf{f}_{\mathrm{ext}} \right) = 0, \tag{3.7}$$

with the global discrete displacement vector $\mathbf{d}$, the mass matrix $\mathbf{M}$, the (nonlinear) internal force vector $\mathbf{f}_{\mathrm{int}}$ (including all kinematic and constitutive contributions) and the external force vector $\mathbf{f}_{\mathrm{ext}}$ (including contributions of prescribed body forces and boundary tractions). [1]
The discretized global principle of virtual work (3.7) has to hold for an arbitrary vector of virtual displacements $\delta\mathbf{d}$, yielding the final global balance of linear momentum as the system of nonlinear equations

$$\mathbf{M}\,\ddot{\mathbf{d}} + \mathbf{f}_{\mathrm{int}}(\mathbf{d}) - \mathbf{f}_{\mathrm{ext}} = \mathbf{0}. \tag{3.8}$$

Its size depends on the overall number of finite element nodes n_{nd}, where every node has n_{dim} unknowns, with n_{dim} being the number of spatial dimensions (here, most often $n_{\mathrm{dim}} = 3$).
In order to add some damping to the system of equations without the necessity to incorporate it into the constitutive equation, a common practice in engineering is the introduction of a damping matrix $\mathbf{D}$ as a linear combination of c_{M} times mass matrix and c_{K} times initial tangential stiffness matrix (3.21), with the two parameters c_{M} $[1/\mathrm{s}]$ and c_{K} $[\mathrm{s}]$. The concept is known as *Rayleigh damping*. Thus, (3.8) expands to

$$\mathbf{M}\,\ddot{\mathbf{d}} + \mathbf{D}\,\dot{\mathbf{d}} + \mathbf{f}_{\mathrm{int}}(\mathbf{d}) - \mathbf{f}_{\mathrm{ext}} = \mathbf{0}. \tag{3.9}$$

Now, the original (spatial and temporal) partial differential equation (explicitly, Cauchy's first law of motion, with Cauchy's second law of motion being implicitly fulfilled) has been transformed into an ordinary differential equation in time (3.9). In general, a temporal discretization has to be carried out in order to find the transient solution $\mathbf{d}(t)$ of (3.9), which will be dealt with in the following section.

3.1.2 Time discretization

In contrast to the finite element method, where a function space is discretized, time discretization is performed using the finite difference method, meaning a discretization of the differential operator in terms of $\mathrm{d}(\cdot)/\mathrm{d}t \approx [(\cdot)_{n+1} - (\cdot)_n]/\Delta t$. The integer n denotes the time stepping index and indicates the old, known state, while $n+1$ indicates the actual step of which a solution is searched for. Here, only *one-step* time integration schemes are considered, which solely require information of the previous time step.
In general, one may differ between *explicit* and *implicit* time integration schemes: While the former exclusively express the discretized differential operator as a function of the old, known

[1] Note that here, only the internal force vector is assumed to depend (nonlinearly) on the displacement state, while all external (body and traction) forces are considered as "dead" not depending on the deformed state of the geometry. However, this loses its validity if, for example, a pressure boundary loading (*follower load*, always poiting into the *current* unit outward normal) is considered, which is ubiquitous in cardiac mechanics and many other applications. This topic will be dealt with in the specific following sections.

state of the system at t_n, $[(\cdot)_{n+1} - (\cdot)_n]/\Delta t = f[(\cdot)_n]$, the latter formulate with respect to the unknown state at t_{n+1}: $[(\cdot)_{n+1} - (\cdot)_n]/\Delta t = f[(\cdot)_{n+1}]$.
Implicit schemes can be constructed such that they are *unconditionally stable*, which means that the solution $(\cdot)_{n+1}$ remains bounded for a limited increase of the time step size $\Delta t = t_{n+1} - t_n$, provided that the "true" (if existent, the analytical) solution is bounded. Explicit schemes, to the contrary, are not unconditionally stable and may produce unbounded unphysical solutions if the time step size is not appropriately small [110].
However, in contrast to explicit algorithms, which directly can be re-arranged to achieve the solution $(\cdot)_{n+1}$, implicit algorithms require a solution process, which may necessitate an iterative numerical procedure depending on the degree of nonlinearity of $f[(\cdot)_{n+1}]$.
In general, explicit schemes are preferred when high-frequency impact problems are dealt with, while implicit schemes rather are applied in the low-frequency range where a comparably large time step size can be used. Throughout this thesis, all time-dependent problems are discretized using implicit one-step time integration schemes.

For the second-order ordinary differential equation in time (3.9) which is obtained after spatial discretization of the solid mechanics problem, the Generalized-α time integration scheme [43] is utilized. It relies on Newmark's method [149] which directly integrates a second-order differential equation by assuming a linear progression of the acceleration over one time step. The velocity $\mathbf{v} = \dot{\mathbf{d}}$ and acceleration $\mathbf{a} = \ddot{\mathbf{d}}$ are approximated according to

$$\mathbf{v}_{n+1} = \frac{\gamma}{\beta \Delta t}(\mathbf{d}_{n+1} - \mathbf{d}_n) - \frac{\gamma - \beta}{\beta}\mathbf{v}_n - \frac{\gamma - 2\beta}{2\beta}\Delta t\, \mathbf{a}_n, \tag{3.10}$$

$$\mathbf{a}_{n+1} = \frac{1}{\beta \Delta t^2}(\mathbf{d}_{n+1} - \mathbf{d}_n) - \frac{1}{\beta \Delta t}\mathbf{v}_n - \frac{1 - 2\beta}{2\beta}\mathbf{a}_n, \tag{3.11}$$

with the parameters $\gamma \in [0, 1]$ and $\beta \in [0, \frac{1}{2}]$.
The Generalized-α method performs a linear combination of the discretized equation of motion at time t_{n+1} (unknown state) and time t_n (known, old state):

$$\mathbf{M}\,\mathbf{a}_{n+1-\alpha_\mathrm{m}} + \mathbf{D}\,\mathbf{v}_{n+1-\alpha_\mathrm{f}} + \mathbf{f}_{\mathrm{int},\,n+1-\alpha_\mathrm{f}} - \mathbf{f}_{\mathrm{ext},\,n+1-\alpha_\mathrm{f}} = \mathbf{0}, \tag{3.12}$$

where

$$\mathbf{v}_{n+1-\alpha_\mathrm{f}} = (1 - \alpha_\mathrm{f})\mathbf{v}_{n+1} + \alpha_\mathrm{f}\mathbf{v}_n, \tag{3.13}$$

$$\mathbf{a}_{n+1-\alpha_\mathrm{m}} = (1 - \alpha_\mathrm{m})\mathbf{a}_{n+1} + \alpha_\mathrm{m}\mathbf{a}_n, \tag{3.14}$$

$$\mathbf{f}_{\mathrm{int},\,n+1-\alpha_\mathrm{f}} = (1 - \alpha_\mathrm{f})\mathbf{f}_{\mathrm{int},\,n+1} + \alpha_\mathrm{f}\mathbf{f}_{\mathrm{int},\,n}, \tag{3.15}$$

$$\mathbf{f}_{\mathrm{ext},\,n+1-\alpha_\mathrm{f}} = (1 - \alpha_\mathrm{f})\mathbf{f}_{\mathrm{ext},\,n+1} + \alpha_\mathrm{f}\mathbf{f}_{\mathrm{ext},\,n}, \tag{3.16}$$

with $\alpha_\mathrm{m}, \alpha_\mathrm{f} \in [0, 1]$.
The algorithm allows to add controllable numerical dissipation into the system without losing the merits of unconditional stability and second-order accuracy for a specific choice of the parameters. Introducing the so-called spectral radius ρ_∞, which is the maximum eigenvalue of the algorithm's amplification matrix, the two conditions are satisfied for

$$\alpha_\mathrm{m} = \frac{2\rho_\infty - 1}{\rho_\infty + 1}, \quad \alpha_\mathrm{f} = \frac{\rho_\infty}{\rho_\infty + 1}, \quad \beta = \frac{1}{4}(1 - \alpha_\mathrm{m} + \alpha_\mathrm{f})^2 \quad \text{and} \quad \gamma = \frac{1}{2} - \alpha_\mathrm{m} + \alpha_\mathrm{f}, \tag{3.17}$$

where $\rho_\infty \in [0,1]$. Relation $(3.17)_4$ asserts second-order accuracy, while dissipation in the high-frequency domain is maximized if $(3.17)_3$, hence minimizing dissipation in the important low-frequency domain. A spectral radius of $\rho_\infty = 1$ means no numerical dissipation, while $\rho_\infty = 0$ immediately annihilates high-frequency responses. See [43] for further details on this algorithm.

All 0-dimensional models, namely reduced-order fluids and windkessel models (cf. sec. 2.1.2) or transport equations, are written in terms of first-order differential equations in time and are discretized with a One-Step-θ scheme [14, 197], according to

$$\frac{(\cdot)_{n+1} - (\cdot)_n}{\Delta t} = \theta f[(\cdot)_{n+1}] + (1-\theta) f[(\cdot)_n], \tag{3.18}$$

with $\theta \in]0,1]$. Note that for $\theta = 0$, an explicit scheme, namely the *Forward-Euler method*, would be obtained, which is not considered here. Second-order accuracy is obtained for $\theta = 0.5$ (trapezoidal rule), while $\theta = 1$ yields the *Backward-Euler method* with a maximum of numerical dissipation for this algorithm.

3.1.3 Nonlinear solution techniques

The space and time discrete momentum balance (3.12), abbreviated with $\mathbf{r} = \mathbf{r}(\mathbf{d}_{n+1})$, is nonlinear in the discrete vector of unknowns $\mathbf{d}_{n+1}$ (nodal displacements) which has to be solved for. Hence, an iterative solution technique has to be used to find an approximate solution within each time step $n+1$. Here, solution schemes of Newton-type are employed, which require the linearization of (3.12) with respect to the vector of unknowns, denoted as

$$\mathrm{Lin}\,\mathbf{r}(\mathbf{d}^i_{n+1}) = \mathbf{r}(\mathbf{d}^i_{n+1}) + \left.\frac{\partial \mathbf{r}(\mathbf{d}_{n+1})}{\partial \mathbf{d}_{n+1}}\right|^i \Delta \mathbf{d}^{i+1}_{n+1}. \tag{3.19}$$

For the Generalized-α time integration utilized here, the so-called *dynamic effective tangential stiffness matrix* reads

$$\mathbf{K}(\mathbf{d}^i_{n+1}) = \left.\frac{\partial \mathbf{r}(\mathbf{d}_{n+1})}{\partial \mathbf{d}_{n+1}}\right|^i = \frac{1-\alpha_\mathrm{m}}{\beta \Delta t^2}\mathbf{M} + \frac{(1-\alpha_\mathrm{f})\gamma}{\beta \Delta t}\mathbf{D} + (1-\alpha_\mathrm{f}) \left.\frac{\partial \mathbf{f}_\mathrm{int}(\mathbf{d}_{n+1})}{\partial \mathbf{d}_{n+1}}\right|^i, \tag{3.20}$$

which is a sparse matrix due to the locality of the finite element shape functions, cf. sec. 3.1.1. The *tangential stiffness matrix*

$$\mathbf{K}_\mathrm{T}(\mathbf{d}_{n+1}) = \frac{\partial \mathbf{f}_\mathrm{int}(\mathbf{d}_{n+1})}{\partial \mathbf{d}_{n+1}} \tag{3.21}$$

includes geometric and material stiffness contributions from the finite elements, i.e. the discrete representation of the material tangent (2.34).

Newton's method searches for the root $\Delta \mathbf{d}^{i+1}_{n+1}$ of the linearized equation (3.19),

$$\mathrm{Lin}\,\mathbf{r}(\mathbf{d}^i_{n+1}) \stackrel{!}{=} \mathbf{0}, \quad \Rightarrow \mathbf{K}(\mathbf{d}^i_{n+1}) \Delta \mathbf{d}^{i+1}_{n+1} = -\mathbf{r}(\mathbf{d}^i_{n+1}) \tag{3.22}$$

and updates the displacement successively after each iteration i,

$$\mathbf{d}_{n+1}^{i+1} = \mathbf{d}_{n+1}^{i} + \Delta\mathbf{d}_{n+1}^{i+1}. \tag{3.23}$$

The procedure of successive linear solution of (3.22) and iterative update (3.23) is carried on until a stopping criterion is met, e.g. in terms of the 2-norm of both the residual and the displacement increment vector,

$$||\mathbf{r}(\mathbf{d}_{n+1}^{i})||_2 \leq \epsilon_{\mathrm{res}} \quad \text{and} \quad ||\Delta\mathbf{d}_{n+1}^{i+1}||_2 \leq \epsilon_{\mathrm{incr}}, \tag{3.24}$$

respectively. The values for the tolerances ϵ_{res} and ϵ_{incr} depend upon the particular problem at hand (scaling, physical system of units), here for the solid mechanical problem having the units of force and length, respectively.

Newton's method obtains a quadratic convergence rate when its initial guess is sufficiently close to the solution, however may diverge if physics change too drastically within the time step considered (for instance, a too steep increase of external loading, bifurcation problems, snap-through phenomena, or non-smooth physical behavior such as contact or valve dynamics). Hence, the method may be combined with line search algorithms or some other regularization techniques such as pseudo-transient continuation (PTC) [67]. The latter will be dealt with in sec. 3.2.2 in terms of a special adaptivity of the nonlinear solution strategy.

Note that in the geometrically and materially linearized theory, (3.21) is independent of the displacement state, and the series of linear solves per time step within Newton's method is replaced by only one solve of a linear system of equations directly yielding the solution $\mathbf{d}_{n+1}$ for the considered step.

3.2 Monolithic discretization and solution of 3D-0D coupled cardiac dynamics

The heart is an inherent part of the circulatory system and its central driving unit. Hence, the mechanics of the heart, i.e. its contractile kinetics, are tightly interconnected to the fluid dynamics of the blood in the circulation. When the heart contracts, the blood pressure in its ventricles rises while chamber volume remains virtually unaltered until semilunar valve opening and blood ejection occurs. When the heart starts to relax, ventricular blood pressure drops while chamber volume again stays constant at its minimum value until eventually atrioventricular valve opening and filling of the heart occurs – and the cycle starts again, cf. chap. 1, sec. 1.2.
Therefore, at each time instance of the cardiac cycle, the mechanical dependencies of the variables that describe the heart are *strongly* dependent on the state variables describing the blood pressures and flows in the vascular system – and vice versa.

Due to this inherently strong coupling between the 3D solid mechanics model and the 0D fluid circulation model, a unified monolithic discretization and solution strategy for the 3D-0D coupled transient cardiovascular dynamics problem is proposed. To date, this is the first monolithic 3D-0D coupled solution approach for a 3D patient-specific (atrio-)ventricular mechanical model coupled

to a closed-loop circulatory system model. The approach has been published in Hirschvogel et al. [86] for the heart model *3Dventr*.
Monolithic solution schemes of 3D-0D coupled solid-fluid cardiovascular problems have previously been presented in literature, e.g. by Sainte-Marie et al. [178]. Another approach is presented by Fritz et al. [62]. There, a patient-specific 4-chamber heart is used, however only the ventricles are coupled to a 0D model.
However, in both of these approaches, only the ventricles are coupled to single 0D pre- and afterload models, and venous return from one ventricle into the other is not accounted for, hence no closed complex circulation and with the ability to couple to four cardiac chambers has been used. Further, a direct solver was applied to tackle the resulting linearized system of equations.

In nearly all other contributions where 3D solid mechanical heart models are coupled to circulatory system models, cf. for example Kerckhoffs et al. [104], presenting a closed-loop model that is capable of venous return coupling to a ventricular patient-specific heart, partitioned coupling schemes with a separation of solid mechanics and circulatory system solves are employed. While these approaches are very promising with regard to their modularity, i.e. using different software packages or modules and hence tailored nonlinear and linear solvers for each sub-problem separately, they require staggered multiple nonlinear solution loops for each sub-problem with interchange of state variables until an outer convergence is achieved. Additionally, special relaxation techniques are required for the isovolumic heart phases due to the classical balloon dilemma [114] of a Dirichlet constrained incompressible fluid (the 0D blood when the ventricles' valves are closed).

Section 3.2.1 depicts the space and time discrete problem formulation, and the consistently linearized system of equations including the linear solution process are shown in sec. 3.2.2. Thereafter, various exemplary results for the 3D-0D coupled heart-vasculature model are shown in sec. 3.2.3, including solutions of the gas transport cardiorespiratory model *0Dsyspulcaprespir*. Finally, the results as well as the algorithmic approaches are discussed in sec. 3.2.4.

3.2.1 Space and time discrete problem formulation

The 3D solid mechanics problem of the heart is spatially discretized using the finite element method, cf. its fundamentals depicted in sec. 3.1.1. The principle of virtual work for the specific problem, (2.94) for model *3Dventr* and (2.95) for model *3Datrioventr*, reads according to (3.5) in its discretized form

$$\delta\mathcal{W} \approx \sum_{e=1}^{n_{\mathrm{el}}} \left[\int\limits_{\Omega_0^{(e)}} \delta\mathbf{u}^{\mathrm{T}}\, \rho_0 \ddot{\mathbf{u}}\, \mathrm{d}V + \int\limits_{\Omega_0^{(e)}} \delta\mathbf{E}^{\mathrm{T}}\, \mathbf{S}\, \mathrm{d}V + \right.$$

$$\left. + \sum_j \int\limits_{\Gamma_0^{\mathrm{R},j(e)}} \delta\mathbf{u}^{\mathrm{T}}\, \mathbf{t}_0^{(\mathrm{R})}(\mathbf{u},\dot{\mathbf{u}})\, \mathrm{d}A + \sum_c \sum_{i=\ell,r} \int\limits_{\Gamma_{0,c}^{\mathrm{0D},i(e)}} \delta\mathbf{u}^{\mathrm{T}}\, \mathbf{t}_0^{(\mathrm{0D})}(\mathbf{u},p_c^i)\, \mathrm{d}A \right]^{(e)} = 0, \quad \forall\, \delta\mathbf{u}, \quad (3.25)$$

where $\mathbf{t}_0^{(\mathrm{R})}$ is the discretized traction of the Robin boundary conditions ($j = \mathrm{b}, \mathrm{e}$ for model *3Dventr* and $j = \mathrm{ar}, \mathrm{ven}, \mathrm{e}$ for model *3Datrioventr*), and $\mathbf{t}_0^{(\mathrm{0D})}$ is the discretized follower load traction stemming from the vascular system ($c = \mathrm{v}$ for model *3Dventr* and $c = \mathrm{v}, \mathrm{at}$ for model *3Datrioventr*).

After assembly, the semi-discrete global balance of linear momentum according to (3.9) reads

$$\mathbf{M}\,\ddot{\mathbf{d}} + \mathbf{D}\,\dot{\mathbf{d}} + \mathbf{f}_{\mathrm{int}}(\mathbf{d}, \dot{\mathbf{d}}) - \mathbf{f}_{\mathrm{ext}}(\mathbf{d}, \mathbf{p}) = \mathbf{0} \quad \text{in } \tilde{\Omega}_0 \times [t_0, T], \tag{3.26}$$

where $\mathbf{d}$ is the vector of solid mechanics state variables (displacements) and $\mathbf{p}$ the vector containing the state variables of the 0D model (pressures and flows), while only a subset out of the latter, namely the atrial and ventricular cavity pressures, enter (3.26).

Time discretization is performed using finite differences, cf. some fundamentals thereof in sec. 3.1.2. Specifically, the space-discrete balance of linear momentum (3.26) is discretized in time with the Generalized-α method, and the fully discretized system of equations according to (3.12) yields

$$\mathbf{r}^{\mathrm{S}} = \mathbf{M}\,\mathbf{a}_{n+1-\alpha_{\mathrm{m}}} + \mathbf{D}\,\mathbf{v}_{n+1-\alpha_{\mathrm{f}}} + \mathbf{f}_{\mathrm{int},\,n+1-\alpha_{\mathrm{f}}} - \mathbf{f}_{\mathrm{ext},\,n+1-\alpha_{\mathrm{f}}}, \tag{3.27}$$

denoted as the solid mechanics residual $\mathbf{r}^{\mathrm{S}}$.

At each material integration point, the evolution equation of the active stress constitutive model (2.99) has to be solved, here done with a Backward-Euler method, (3.18) with $\theta = 1$. Since the evolution equation is linear in the active stress variable, it can be re-arranged directly yielding the active stress $\tau_{\mathrm{a},n+1}$ at the current time step $n+1$:

$$\begin{aligned} \frac{\tau_{\mathrm{a},n+1} - \tau_{\mathrm{a},n}}{\Delta t} &= -|u|\tau_{\mathrm{a},n+1} + a_{n+1}\sigma_0|u|_+, \\ \Rightarrow \tau_{\mathrm{a},n+1} &= \frac{\tau_{\mathrm{a},n} + a_{n+1}\,\sigma_0\,|u|_+\Delta t}{1 + |u|\Delta t}, \end{aligned} \tag{3.28}$$

where $\tau_{\mathrm{a},n}$ represents the old, known value of the previous time step n.

The Frank-Starling law (2.106) is discretized as follows:

$$\begin{aligned} &\text{if } |u|_- > 0\text{:} \\ &\qquad a_{n+1} = g(\lambda_{\mathrm{myo},n+1}), \\ &\text{else:} \\ &\qquad a_{n+1} = a_n, \end{aligned} \tag{3.29}$$

with g defined according to (2.107).

The 0D vascular system model, (2.118)–(2.133) for model *0Dsyspul* or (2.134)–(2.167) for model *0Dsyspulcap*, as well as (2.183)–(2.187) for the lung mechanics and (2.197)–(2.210) for the gas transport kinetics of model *0Dsyspulcaprespir*, is discretized in time using an implicit One-Step-θ

scheme, cf. (3.18). The time-discrete 0D model residual $\mathbf{r}^{\mathrm{0D}}$ for the vascular model *0Dsyspul* thus particularizes in

$$\mathbf{r}^{\mathrm{0D}} = \begin{bmatrix}
\frac{V_{\mathrm{at}}^{\ell}(\mathbf{d}_{n+1})-V_{\mathrm{at}}^{\ell}(\mathbf{d}_n)}{\Delta t} - q_{\mathrm{ven},n+\theta}^{\mathrm{pul}} + q_{\mathrm{v,in},n+\theta}^{\ell} \\
\frac{\theta}{\tilde{R}_{\mathrm{v,in},n+1}^{\ell}}(p_{\mathrm{at},n+1}^{\ell} - p_{\mathrm{v},n+1}^{\ell}) + \frac{1-\theta}{\tilde{R}_{\mathrm{v,in},n}^{\ell}}(p_{\mathrm{at},n}^{\ell} - p_{\mathrm{v},n}^{\ell}) - q_{\mathrm{v,in},n+\theta}^{\ell} \\
\frac{V_{\mathrm{v}}^{\ell}(\mathbf{d}_{n+1})-V_{\mathrm{v}}^{\ell}(\mathbf{d}_n)}{\Delta t} - q_{\mathrm{v,in},n+\theta}^{\ell} + q_{\mathrm{v,out},n+\theta}^{\ell} \\
\frac{\theta}{\tilde{R}_{\mathrm{v,out},n+1}^{\ell}}(p_{\mathrm{v},n+1}^{\ell} - p_{\mathrm{ar},n+1}^{\mathrm{sys}}) + \frac{1-\theta}{\tilde{R}_{\mathrm{v,out},n}^{\ell}}(p_{\mathrm{v},n}^{\ell} - p_{\mathrm{ar},n}^{\mathrm{sys}}) - q_{\mathrm{v,out},n+\theta}^{\ell} \\
C_{\mathrm{ar}}^{\mathrm{sys}}\left(\frac{p_{\mathrm{ar},n+1}^{\mathrm{sys}}-p_{\mathrm{ar},n}^{\mathrm{sys}}}{\Delta t} - Z_{\mathrm{ar}}^{\mathrm{sys}}\frac{q_{\mathrm{v,out},n+1}^{\ell}-q_{\mathrm{v,out},n}^{\ell}}{\Delta t}\right) - q_{\mathrm{v,out},n+\theta}^{\ell} + q_{\mathrm{ar},n+\theta}^{\mathrm{sys}} \\
\frac{L_{\mathrm{ar}}^{\mathrm{sys}}}{R_{\mathrm{ar}}^{\mathrm{sys}}}\frac{q_{\mathrm{ar},n+1}^{\mathrm{sys}}-q_{\mathrm{ar},n}^{\mathrm{sys}}}{\Delta t} + \frac{1}{R_{\mathrm{ar}}^{\mathrm{sys}}}(p_{\mathrm{ven},n+\theta}^{\mathrm{sys}} - p_{\mathrm{ar},n+\theta}^{\mathrm{sys}} + Z_{\mathrm{ar}}^{\mathrm{sys}}q_{\mathrm{v,out},n+\theta}^{\ell}) + q_{\mathrm{ar},n+\theta}^{\mathrm{sys}} \\
C_{\mathrm{ven}}^{\mathrm{sys}}\frac{p_{\mathrm{ven},n+1}^{\mathrm{sys}}-p_{\mathrm{ven},n}^{\mathrm{sys}}}{\Delta t} - q_{\mathrm{ar},n+\theta}^{\mathrm{sys}} + q_{\mathrm{ven},n+\theta}^{\mathrm{sys}} \\
\frac{L_{\mathrm{ven}}^{\mathrm{sys}}}{R_{\mathrm{ven}}^{\mathrm{sys}}}\frac{q_{\mathrm{ven},n+1}^{\mathrm{sys}}-q_{\mathrm{ven},n}^{\mathrm{sys}}}{\Delta t} + \frac{1}{R_{\mathrm{ven}}^{\mathrm{sys}}}(p_{\mathrm{at},n+\theta}^{r} - p_{\mathrm{ven},n+\theta}^{\mathrm{sys}}) + q_{\mathrm{ven},n+\theta}^{\mathrm{sys}} \\
\frac{V_{\mathrm{at}}^{r}(\mathbf{d}_{n+1})-V_{\mathrm{at}}^{r}(\mathbf{d}_n)}{\Delta t} - q_{\mathrm{ven},n+\theta}^{\mathrm{sys}} + q_{\mathrm{v,in},n+\theta}^{r} \\
\frac{\theta}{\tilde{R}_{\mathrm{v,in},n+1}^{r}}(p_{\mathrm{at},n+1}^{r} - p_{\mathrm{v},n+1}^{r}) + \frac{1-\theta}{\tilde{R}_{\mathrm{v,in},n}^{r}}(p_{\mathrm{at},n}^{r} - p_{\mathrm{v},n}^{r}) - q_{\mathrm{v,in},n+\theta}^{r} \\
\frac{V_{\mathrm{v}}^{r}(\mathbf{d}_{n+1})-V_{\mathrm{v}}^{r}(\mathbf{d}_n)}{\Delta t} - q_{\mathrm{v,in},n+\theta}^{r} + q_{\mathrm{v,out},n+\theta}^{r} \\
\frac{\theta}{\tilde{R}_{\mathrm{v,out},n+1}^{r}}(p_{\mathrm{v},n+1}^{r} - p_{\mathrm{ar},n+1}^{\mathrm{pul}}) + \frac{1-\theta}{\tilde{R}_{\mathrm{v,out},n}^{r}}(p_{\mathrm{v},n}^{r} - p_{\mathrm{ar},n}^{\mathrm{pul}}) - q_{\mathrm{v,out},n+\theta}^{r} \\
C_{\mathrm{ar}}^{\mathrm{pul}}\left(\frac{p_{\mathrm{ar},n+1}^{\mathrm{pul}}-p_{\mathrm{ar},n}^{\mathrm{pul}}}{\Delta t} - Z_{\mathrm{ar}}^{\mathrm{pul}}\frac{q_{\mathrm{v,out},n+1}^{r}-q_{\mathrm{v,out},n}^{r}}{\Delta t}\right) - q_{\mathrm{v,out},n+\theta}^{r} + q_{\mathrm{ar},n+\theta}^{\mathrm{pul}} \\
\frac{L_{\mathrm{ar}}^{\mathrm{pul}}}{R_{\mathrm{ar}}^{\mathrm{pul}}}\frac{q_{\mathrm{ar},n+1}^{\mathrm{pul}}-q_{\mathrm{ar},n}^{\mathrm{pul}}}{\Delta t} + \frac{1}{R_{\mathrm{ar}}^{\mathrm{pul}}}(p_{\mathrm{ven},n+\theta}^{\mathrm{pul}} - p_{\mathrm{ar},n+\theta}^{\mathrm{pul}} + Z_{\mathrm{ar}}^{\mathrm{pul}}q_{\mathrm{v,out},n+\theta}^{r}) + q_{\mathrm{ar},n+\theta}^{\mathrm{pul}} \\
C_{\mathrm{ven}}^{\mathrm{pul}}\frac{p_{\mathrm{ven},n+1}^{\mathrm{pul}}-p_{\mathrm{ven},n}^{\mathrm{pul}}}{\Delta t} - q_{\mathrm{ar},n+\theta}^{\mathrm{pul}} + q_{\mathrm{ven},n+\theta}^{\mathrm{pul}} \\
\frac{L_{\mathrm{ven}}^{\mathrm{pul}}}{R_{\mathrm{ven}}^{\mathrm{pul}}}\frac{q_{\mathrm{ven},n+1}^{\mathrm{pul}}-q_{\mathrm{ven},n}^{\mathrm{pul}}}{\Delta t} + \frac{1}{R_{\mathrm{ven}}^{\mathrm{pul}}}(p_{\mathrm{at},n+\theta}^{\ell} - p_{\mathrm{ven},n+\theta}^{\mathrm{pul}}) + q_{\mathrm{ven},n+\theta}^{\mathrm{pul}}
\end{bmatrix}_{(\textit{0Dsyspul})}, \tag{3.30}$$

where a quantity $(\cdot)$ at time instance $t_{n+\theta}$ is denoted with $(\cdot)_{n+\theta} := \theta(\cdot)_{n+1} + (1-\theta)(\cdot)_n$, cf. sec. 3.1.2. The vector of discrete state variables (of model *0Dsyspul*) at the current time step $n+1$ is

$$\begin{aligned}\mathbf{p}_{n+1} = \big[&p_{\mathrm{at}}^{\ell} \;\; q_{\mathrm{v,in}}^{\ell} \;\; q_{\mathrm{v,out}}^{\ell} \;\; p_{\mathrm{v}}^{\ell} \;\; p_{\mathrm{ar}}^{\mathrm{sys}} \;\; q_{\mathrm{ar}}^{\mathrm{sys}} \;\; p_{\mathrm{ven}}^{\mathrm{sys}} \;\; q_{\mathrm{ven}}^{\mathrm{sys}} \\ &p_{\mathrm{at}}^{r} \;\; q_{\mathrm{v,in}}^{r} \;\; q_{\mathrm{v,out}}^{r} \;\; p_{\mathrm{v}}^{r} \;\; p_{\mathrm{ar}}^{\mathrm{pul}} \;\; q_{\mathrm{ar}}^{\mathrm{pul}} \;\; p_{\mathrm{ven}}^{\mathrm{pul}} \;\; q_{\mathrm{ven}}^{\mathrm{pul}}\big]_{(\textit{0Dsyspul})\,n+1}^{\mathrm{T}}.\end{aligned} \tag{3.31}$$

Models *0Dsyspulcap* and *0Dsyspulcaprespir* are discretized analogously to (3.30), thus their discrete representations are omitted. Note that atrial volumes V_{at}^{i} are represented by the 0D elastance models (2.111) in case of an only-ventricular 3D heart (model *3Dventr*), thus they do not depend on the (volume-describing subset of the) discrete structural displacement state $\mathbf{d}_{n+1}$ at time instance t_{n+1}. Furthermore, for the model *0Dsyspulcaprespir*, atrial and ventricular volumes are decoupled from the 3D problem and are treated with the prescribed-dynamics approach detailed in sec. 2.2.3.2.

3.2.2 Consistent linearization and monolithic Newton iteration

The 3D solid mechanics problem (3.27) as well as the 0D model (3.30) are implicitly discretized in time and formulated with respect to the unknown state variables $\mathbf{d}_{n+1}$ (sized $n_{\mathrm{dof}}^{\mathrm{3D}}$) and $\mathbf{p}_{n+1}$

(sized $n_{\mathrm{dof}}^{\mathrm{0D}}$) of 3D and 0D model which has to be solved for. Hence, it is required that both residual expressions vanish at the current time step $n+1$:

$$\mathbf{r}^{\mathrm{S-0D}} = \begin{bmatrix} \mathbf{r}^{\mathrm{S}}(\mathbf{d},\mathbf{p}) \\ \mathbf{r}^{\mathrm{0D}}(\mathbf{p},\mathbf{d}) \end{bmatrix}_{n+1} \overset{!}{=} \begin{bmatrix} \mathbf{0} \\ \mathbf{0} \end{bmatrix}. \tag{3.32}$$

Here, a Newton-Raphson scheme, cf. sec. 3.1.3, is applied to the coupled system of nonlinear equations, requiring a simultaneous solution of both 3D and 0D problem in one monolithic iterative process. The linearization (3.19) for the Newton scheme then has to account for both variables $\mathbf{d}_{n+1}$ and $\mathbf{p}_{n+1}$ and reads

$$\begin{aligned} \mathrm{Lin}\,\mathbf{r}^{\mathrm{S-0D}}(\mathbf{d}_{n+1}^{i},\mathbf{p}_{n+1}^{i}) = \mathbf{r}^{\mathrm{S-0D}}(\mathbf{d}_{n+1}^{i},\mathbf{p}_{n+1}^{i}) + \\ + \left.\frac{\partial \mathbf{r}^{\mathrm{S-0D}}(\mathbf{d}_{n+1},\mathbf{p}_{n+1})}{\partial \mathbf{d}_{n+1}}\right|^{i} \Delta\mathbf{d}_{n+1}^{i+1} + \left.\frac{\partial \mathbf{r}^{\mathrm{S-0D}}(\mathbf{d}_{n+1},\mathbf{p}_{n+1})}{\partial \mathbf{p}_{n+1}}\right|^{i} \Delta\mathbf{p}_{n+1}^{i+1}. \end{aligned} \tag{3.33}$$

Requiring (3.33) to vanish in each Newton iteration i, it can be re-written to the linearized monolithic system of equations

$$\begin{bmatrix} \mathbf{K}^{\mathrm{S}} & \mathbf{K}^{\mathrm{S,0D}} \\ \mathbf{K}^{\mathrm{0D,S}} & \mathbf{K}^{\mathrm{0D}} \end{bmatrix}_{n+1}^{i} \begin{bmatrix} \Delta\mathbf{d} \\ \Delta\mathbf{p} \end{bmatrix}_{n+1}^{i+1} = - \begin{bmatrix} \mathbf{r}^{\mathrm{S}} \\ \mathbf{r}^{\mathrm{0D}} \end{bmatrix}_{n+1}^{i} \tag{3.34}$$

which has to be solved for $\Delta\mathbf{d}_{n+1}^{i+1}$ and $\Delta\mathbf{p}_{n+1}^{i+1}$ prior to updating the solution according to

$$\mathbf{d}_{n+1}^{i+1} = \mathbf{d}_{n+1}^{i} + \Delta\mathbf{d}_{n+1}^{i+1} \quad \text{and} \quad \mathbf{p}_{n+1}^{i+1} = \mathbf{p}_{n+1}^{i} + \Delta\mathbf{p}_{n+1}^{i+1} \tag{3.35}$$

in each Newton iteration i until

$$||\mathbf{r}^{\mathrm{S}}(\mathbf{d}_{n+1}^{i},\mathbf{p}_{n+1}^{i})||_2 \leq \epsilon_{\mathrm{res}}^{\mathrm{S}} \quad \text{and} \quad ||\Delta\mathbf{d}_{n+1}^{i}||_2 \leq \epsilon_{\mathrm{incr}}^{\mathrm{S}} \tag{3.36}$$

and

$$||\mathbf{r}^{\mathrm{0D}}(\mathbf{p}_{n+1}^{i},\mathbf{d}_{n+1}^{i})||_2 \leq \epsilon_{\mathrm{res}}^{\mathrm{0D}} \quad \text{and} \quad ||\Delta\mathbf{p}_{n+1}^{i}||_2 \leq \epsilon_{\mathrm{incr}}^{\mathrm{0D}}. \tag{3.37}$$

Therein, the structural effective dynamic stiffness matrix $\mathbf{K}^{\mathrm{S}} \in \mathbb{R}^{n_{\mathrm{dof}}^{\mathrm{3D}} \times n_{\mathrm{dof}}^{\mathrm{3D}}}$ according to (3.20) reads

$$\begin{aligned} \mathbf{K}^{\mathrm{S}}\big|_{n+1}^{i} &= \left.\frac{\partial \mathbf{r}^{\mathrm{S}}}{\partial \mathbf{d}}\right|_{n+1}^{i} = \\ &= \frac{1-\alpha_{\mathrm{m}}}{\beta\Delta t^2}\mathbf{M} + \frac{(1-\alpha_{\mathrm{f}})\gamma}{\beta\Delta t}\mathbf{D} + (1-\alpha_{\mathrm{f}})\left.\frac{\partial \mathbf{f}_{\mathrm{int}}(\mathbf{d})}{\partial \mathbf{d}}\right|_{n+1}^{i} - (1-\alpha_{\mathrm{f}})\left.\frac{\partial \mathbf{f}_{\mathrm{ext}}(\mathbf{d},\mathbf{p})}{\partial \mathbf{d}}\right|_{n+1}^{i}, \end{aligned} \tag{3.38}$$

where the dependence of the external force vector on the displacement state has to be accounted for (follower pressure load).

The off-diagonal stiffness matrix $\mathbf{K}^{\mathrm{S,0D}} \in \mathbb{R}^{n_{\mathrm{dof}}^{\mathrm{3D}} \times n_{\mathrm{dof}}^{\mathrm{0D}}}$, governing the dependence of the solid mechanical problem on the 0D vascular model reads

$$\mathbf{K}^{\mathrm{S,0D}}\big|_{n+1}^{i} = \left.\frac{\partial \mathbf{r}^{\mathrm{S}}}{\partial \mathbf{p}}\right|_{n+1}^{i} = -(1-\alpha_{\mathrm{f}})\left.\frac{\partial \mathbf{f}_{\mathrm{ext}}(\mathbf{d},\mathbf{p})}{\partial \mathbf{p}}\right|_{n+1}^{i}. \tag{3.39}$$

Vice versa, the second off-diagonal stiffness block $\mathbf{K}^{\mathrm{0D,S}} \in \mathbb{R}^{n_{\mathrm{dof}}^{\mathrm{0D}} \times n_{\mathrm{dof}}^{\mathrm{3D}}}$ describes the dependence of the 0D model on the structural displacement field and reads

$$\begin{aligned}\mathbf{K}^{\mathrm{0D,S}}\big|_{n+1}^{i} &= \left.\frac{\partial \mathbf{r}^{\mathrm{0D}}}{\partial \mathbf{d}}\right|_{n+1}^{i} = \\ &= \frac{1}{\Delta t}\left[\frac{\partial V_{\mathrm{at}}^{\ell}(\mathbf{d})}{\partial \mathbf{d}}^{\mathrm{T}} \;\; \mathbf{0} \;\; \frac{\partial V_{\mathrm{v}}^{\ell}(\mathbf{d})}{\partial \mathbf{d}}^{\mathrm{T}} \;\; \mathbf{0} \;\; \dots \;\; \mathbf{0} \;\; \frac{\partial V_{\mathrm{at}}^{r}(\mathbf{d})}{\partial \mathbf{d}}^{\mathrm{T}} \;\; \mathbf{0} \;\; \frac{\partial V_{\mathrm{v}}^{r}(\mathbf{d})}{\partial \mathbf{d}}^{\mathrm{T}} \;\; \mathbf{0} \;\; \dots \;\; \mathbf{0}\right]_{n+1}^{i\;\mathrm{T}}. \end{aligned} \tag{3.40}$$

The stiffness matrix $\mathbf{K}^{\mathrm{0D}}\big|_{n+1}^{i} = \left.\frac{\partial \mathbf{r}^{\mathrm{0D}}}{\partial \mathbf{p}}\right|_{n+1}^{i} \in \mathbb{R}^{n_{\mathrm{dof}}^{\mathrm{0D}} \times n_{\mathrm{dof}}^{\mathrm{0D}}}$ depends on the specific 0D model. For the model *0Dsyspul* with its discrete representation (3.30) and for the model *0Dsyspulcap*, it is straightforward due to only linear or piecewise-linear functions involved and therefore is omitted here.

All 0D models as well as a 3D-0D monolithic solution framework are implemented into the in-house multi-physics finite element software package Baci [207].

In order to solve the linear system of equations (3.34), a 2×2 block SIMPLE-like preconditioner (Semi-Implicit Method for Pressure-Linked Equations) [57] within a parallel GMRES [176] solver implemented in Trilinos [82] is used. The preconditioner that is applied to the global system matrix is denoted as $\left(\tilde{\mathbf{A}}_{n+1}^{i}\right)^{-1}$. The matrix $\tilde{\mathbf{A}}$ reads

$$\begin{bmatrix} \mathbf{K}^{\mathrm{S}} & \mathbf{K}^{\mathrm{S,0D}} \\ \mathbf{K}^{\mathrm{0D,S}} & \mathbf{K}^{\mathrm{0D}} \end{bmatrix}_{n+1}^{i} \approx \tag{3.41}$$

$$\approx \begin{bmatrix} \mathbf{1} & \mathbf{0} \\ \mathbf{K}^{\mathrm{0D,S}}\left(\mathbf{K}^{\mathrm{S}}\right)^{-1} & \mathbf{1} \end{bmatrix}_{n+1}^{i} \begin{bmatrix} \mathbf{K}^{\mathrm{S}} & \mathbf{0} \\ \mathbf{0} & -\check{\mathbf{S}} \end{bmatrix}_{n+1}^{i} \begin{bmatrix} \mathbf{1} & \left(\mathrm{diag}\left(\mathbf{K}^{\mathrm{S}}\right)\right)^{-1}\mathbf{K}^{\mathrm{S,0D}} \\ \mathbf{0} & \bar{\alpha}\,\mathbf{1} \end{bmatrix}_{n+1}^{i} = \tilde{\mathbf{A}}_{n+1}^{i}, \tag{3.42}$$

with $\bar{\alpha} \in \,]0,1]$ and the Schur complement operator

$$\check{\mathbf{S}}_{n+1}^{i} = \mathbf{K}^{\mathrm{0D}}\big|_{n+1}^{i} - \mathbf{K}^{\mathrm{0D,S}}\big|_{n+1}^{i}\left(\mathrm{diag}\left(\mathbf{K}^{\mathrm{S}}\big|_{n+1}^{i}\right)\right)^{-1}\mathbf{K}^{\mathrm{S,0D}}\big|_{n+1}^{i}. \tag{3.43}$$

For the inverse $\left(\mathbf{K}^{\mathrm{S}}\right)^{-1}$ of the large structural block, an algebraic multigrid preconditioner is used, while the small 0D block $\mathbf{K}^{\mathrm{0D}}$ is inverted directly using an LU solver.

There exist specific numerical problems with rapid changes in physical conditions from one time step to another (e.g., types of problems that are dealt with in chap. 5: thin-walled structures under time-varying loading, sudden contact phenomena, etc.) that challenge a Newton-type nonlinear solution procedure. If these changes between two subsequent steps become too drastic, a Newton scheme may fail to converge to the equilibrium solution. Hence, robust strategies are required that prevent Newton's method from diverging, or in case of divergence, that are capable of performing the respective time step again with modified algorithmic settings.

While a priori error estimators for the time integrator and subsequent adaptive time stepping procedures are well-established tools in order to maintain a certain level of accuracy along with savings in computation time [224], in many cases they most probably will not prevent Newton's method from diverging or the program running into floating point exceptions if a step beyond the equilibrium point is performed.
Here, methods that detect problems in the linear solver or divergence at a fixed number of nonlinear iterations are used, and the time step is stopped or repeated using a pseudo-transient continuation (PTC) [67] technique on the structural block of the system matrix. Hence, in case of detected problems in the linear or nonlinear solution process, the linear system of equations (3.34) becomes

$$\begin{bmatrix} \mathbf{K}^{\mathrm{S}} + k_{\mathrm{ptc}}\mathbf{1} & \mathbf{K}^{\mathrm{S,0D}} \\ \mathbf{K}^{\mathrm{0D,S}} & \mathbf{K}^{\mathrm{0D}} \end{bmatrix}_{n+1}^{i} \begin{bmatrix} \Delta\mathbf{d} \\ \Delta\mathbf{p} \end{bmatrix}_{n+1}^{i+1} = - \begin{bmatrix} \mathbf{r}^{\mathrm{S}} \\ \mathbf{r}^{\mathrm{0D}} \end{bmatrix}_{n+1}^{i}, \tag{3.44}$$

with

$$k_{\mathrm{ptc}}^{i} := k_{\mathrm{ptc}}^{i-1} \frac{||\mathbf{r}^{\mathrm{S}}||_2^{i}}{||\mathbf{r}^{\mathrm{S}}||_2^{i-1}}. \tag{3.45}$$

In case of further divergence, i.e. if the initial value of (3.45) was not appropriately large, it is doubled and the PTC solution is performed once again. Only after ten non-successful attempts, the computation is finally stopped. In case of convergence of the nonlinear solver and successful accomplishment of the time step, (3.45) is set to zero, hence a standard Newton scheme with the system (3.34) is performed for the subsequent steps.
It should be noted that a similar strategy may be applied to the time step size Δt, i.e. halving it until convergence of the nonlinear solver is achieved. However, in case of snap-through, buckling or large deflection phenomena (thin-walled pressure-loaded structures), a PTC adaption has proven to work more robustly and more efficient than time step size reduction for the problems addressed in this thesis.

3.2.3 Exemplary results for a patient-specific heart

Results for a patient-specific heart are presented, here using a porcine (atrio-)ventricular geometry that is generated according to the procedure in sec. 2.2.1.1. Standard conditions are shown in sec. 3.2.3.1, and the model's behavior under varying afterload, preload and inotropic states is presented in sec. 3.2.3.2. Finally, a couple of valve diseases are simulated in sec. 3.2.3.3. Conclusively, gas transport kinetics are dealt with in sec. 3.2.3.4. The results are validated to textbook physiology for different alterations from the standard conditions.

If not stated otherwise, the contraction dynamics and 0D circulation base parameters that are listed in tab. 2.3 and tab. 2.6 are chosen. The 3D heart is meshed with linear displacement-based tetrahedral elements with an average element edge length of $h \approx 1 \text{ mm}$ (*3Dventr*) as well as $h \approx 1.25 \text{ mm}$ (*3Datrioventr*). The respective discretizations are denoted with *tet4_1* and *tet4_1.25*. Refer to appendix A.1.1.1 for further details and sketches of the meshes. For one cardiac cycle, $n_{\text{step}} = 500$ time steps of equal size are used.
Gas transport and dissociation parameters are chosen according to tab. 2.8 and tab. 2.9.

Table 3.1 lists the algorithmic base parameters, i.e. time integration parameters, damping coefficients as well as tolerances for the Newton iteration.

Table 3.1: Algorithmic base parameters (0D model tolerances for Newton iteration are given without unit and apply for residuals / increments formulated in fluxes or pressures)

n_{step}	$[-]$	500	number of time steps
ρ_∞	$[-]$	0.8	spectral radius of Generalized-α time integration
θ	$[-]$	0.5	parameter for One-Step-θ time integration
c_{M}	$[1/\text{s}]$	0	Rayleigh damping mass factor
c_{K}	$[\text{s}]$	0.0001	Rayleigh damping stiffness factor
$\epsilon_{\text{res}}^{\text{S}}$	$[\text{mN}]$	10^{-6}	solid mechanics residual tolerance for Newton iteration
$\epsilon_{\text{res}}^{\text{0D}}$		10^{-6}	0D model residual tolerance for Newton iteration
$\epsilon_{\text{incr}}^{\text{S}}$	$[\text{mm}]$	10^{-8}	solid mechanics increment tolerance for Newton iteration
$\epsilon_{\text{incr}}^{\text{0D}}$		10^{-6}	0D model increment tolerance for Newton iteration
ϵ_{cycl}	$[-]$	0.03	periodicity tolerance for cardiac cycle

3.2.3.1 Standard conditions

Standard conditions (subsequently referred to as “control”) for the cardiovascular system are computed using a semi-educated guess of initial conditions for all circulation system variables and applying the procedure outlined in sec. 2.2.4.1 in order to achieve a prestressed homeostatic state on the initial geometric configuration.

Figure 3.2 shows pressures and pressure-volume relationships as well as the end-systolic deformed configuration of the ventricular model *3Dventr* coupled to the circulatory model *0Dsyspul* (cf. fig. 2.6), and tab. 3.2 the corresponding left and right ventricular function indicators in terms of end-diastolic and end-systolic pressures and volumes as well as stroke work.

Figure 3.3 shows the results obtained for the atrioventricular model *3Datrioventr* coupled to the extended circulation *0Dsyspulcap* (cf. fig. 2.7), and tab. 3.3 the corresponding left and right ventricular function indicators in terms of end-diastolic and end-systolic pressures and volumes as well as stroke work.

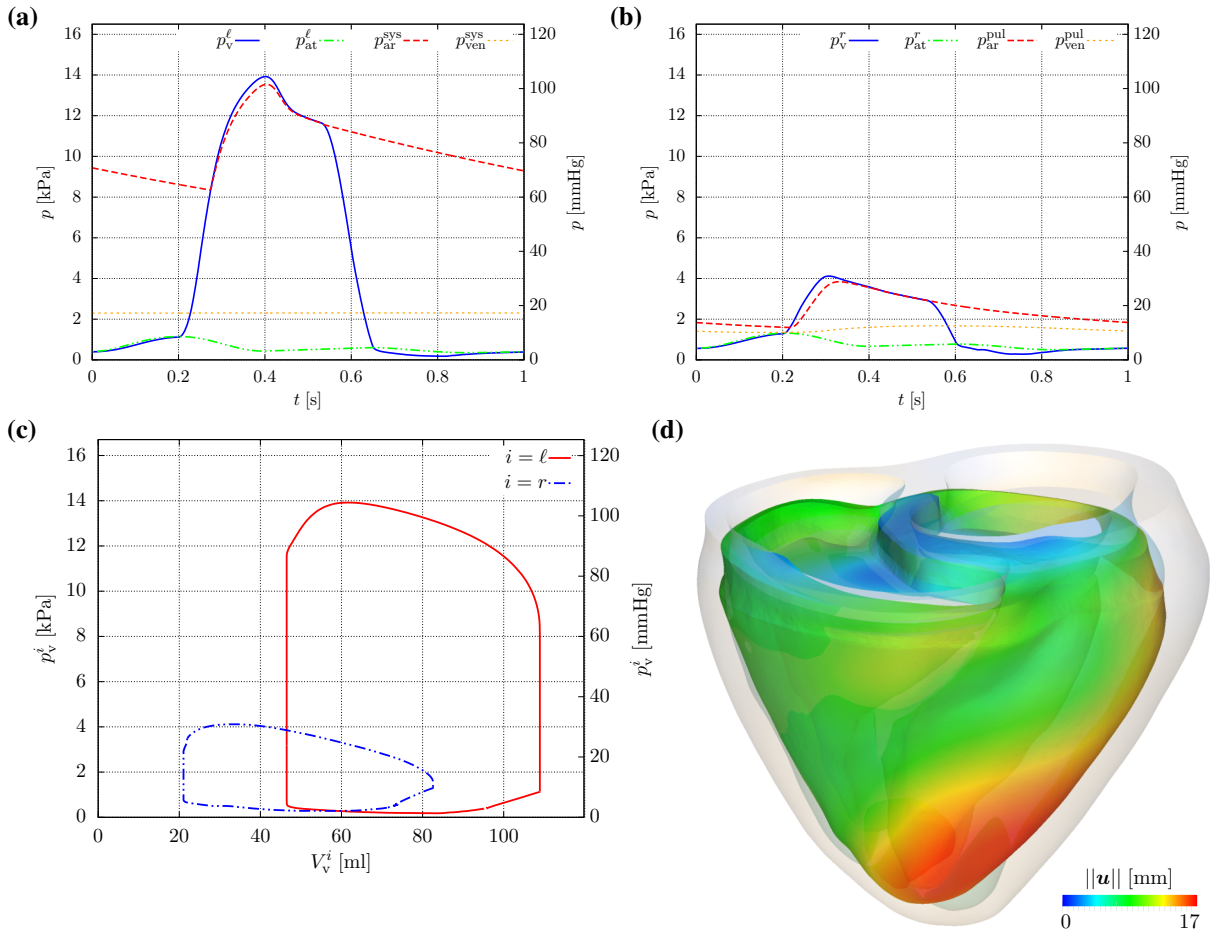

Figure 3.2: Model *3Dventr*$_{tet4\_1}$ | *0Dsyspul*: Healthy baseline (control) state of a subject-specific porcine ventricular geometry. **(a)** Left heart and systemic pressures over time. **(b)** Right heart and pulmonary pressures over time. **(c)** Left ($i = \ell$) and right ($i = r$) ventricular pressure-volume loops. **(d)** Initial (light-gray, at $t = t_0$) vs. periodic end-systolic (colored, at $t = t_0 + t_{\mathrm{es}}$) configuration: Displacement magnitude.

Table 3.2: Model *3Dventr*$_{tet4\_1}$ | *0Dsyspul*: Left ($i = \ell$) and right ($i = r$) ventricular function indicators end-diastolic volume EDV, stroke volume SV, ejection fraction EF, end-diastolic pressure EDP, end-systolic pressure ESP, peak ventricular pressure PVP, cardiac output CO, and stroke work SW

i	EDV^i [ml]	SV^i [ml]	EF^i [−]	EDP^i [kPa]	ESP^i [kPa]	PVP^i [kPa]	CO^i [$\frac{\mathrm{l}}{\mathrm{min}}$]	SW^i [mJ]
ℓ	108.9	62.4	0.57	1.12	11.7	13.9	3.74	774.7
r	82.6	61.5	0.75	1.28	2.96	4.12	3.69	180.6

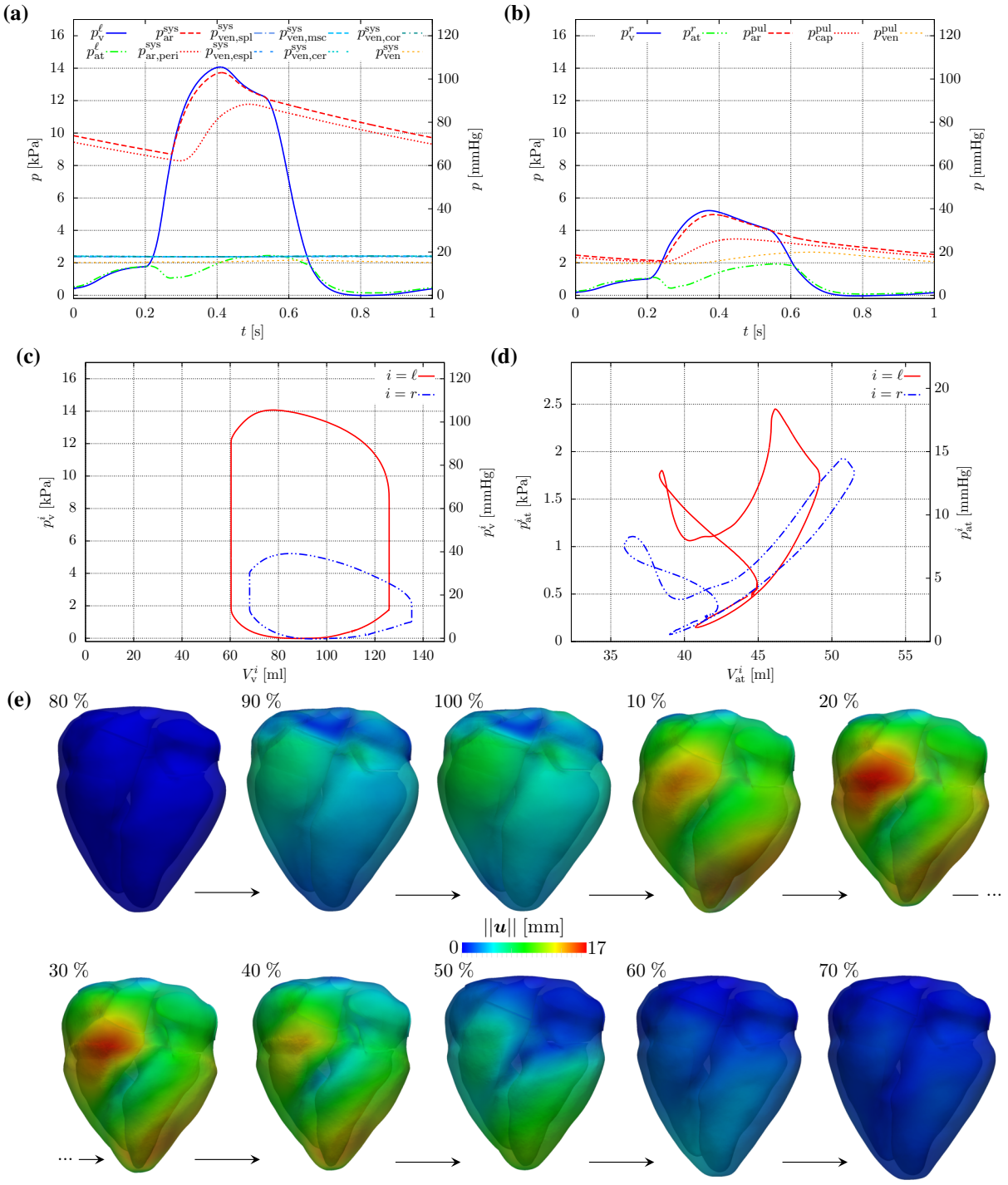

Figure 3.3: Model *3Datrioventr*$_{tet4\_1.25}$ | *0Dsyspulcap*: Healthy baseline (control) state of a subject-specific porcine ventricular geometry. **(a)** Left heart and systemic pressures over time. **(b)** Right heart and pulmonary pressures over time. **(c)** Left ($i = \ell$) and right ($i = r$) ventricular pressure-volume loops. **(d)** Left ($i = \ell$) and right ($i = r$) atrial pressure-volume loops. **(e)** Deformation in percent of heart cycle: 100 % indicates end of diastole (maximum filling), color is displacement magnitude.

Table 3.3: Model *3Datrioventr*$_{tet4\_1.25}$ | *0Dsyspulcap*: Left ($i = \ell$) and right ($i = r$) ventricular function indicators end-diastolic volume EDV, stroke volume SV, ejection fraction EF, end-diastolic pressure EDP, end-systolic pressure ESP, peak ventricular pressure PVP, cardiac output CO, and stroke work SW

i	EDV^i [ml]	SV^i [ml]	EF^i [−]	EDP^i [kPa]	ESP^i [kPa]	PVP^i [kPa]	CO^i [$\frac{\mathrm{l}}{\mathrm{min}}$]	SW^i [mJ]
ℓ	125.9	65.5	0.52	1.76	12.3	14.1	3.93	828.1
r	135.3	67.2	0.50	0.99	4.15	5.22	4.03	273.7

3.2.3.2 Changes in afterload, preload, and inotropy: End-systolic, end-diastolic, diastatic pressure-volume relationships, and the Frank-Starling law

The performance of the models under varying conditions of preload and afterload is assessed. The term *preload* refers to the maximum cavity volume at the end of the diastole, hence the maximum state of stretch sensed by the myofibers. The term *afterload* is associated with the pressure the heart has to work against during systole.

The so-called *end-systolic pressure-volume relationship* (ESPVR) defines the maximum pressure that the ventricle can develop at any given left ventricular volume. Over a narrow range of loading conditions, the ESPVR is linear, however becomes nonlinear over a wider range [101, 205]. It is obtained by connecting the upper left points of ventricular pressure-volume relationships under varying conditions of afterload, hence the pressure-volume pairs at the end of the systole. In physiology, it represents a global index of contractility.
The *end-diastolic pressure-volume relationship* (EDPVR) determines the passive filling curve of the ventricles and in general is curvilinear. At ideal quasi-static passive filling, changes in preload occur along the EDPVR. The so-called *diastatic pressure-volume relationship* (D-PVR) describes the passive filling curve before atrial contraction, which is in general not the same as the EDPVR [223] since atrial contraction alters passive ventricular behavior. The slope of EDPVR (and D-PVR) quantify the passive chamber stiffness.

Figure 3.4a presents the left ventricular pressure-volume relationships for four different inotropic states (varying contractility σ_0) of the model *3Datrioventr* with circulation *0Dsyspulcap* – each state at 10 different afterloads. The afterload here is varied by *exclusively* changing the (total) systemic arterial resistance $R^{\mathrm{sys}}_{\mathrm{ar}(total)}$, hence *without* adapting the other vascular parameters according to tab. 2.7 but assuming them to be calculated using the base total resistance (tab. 2.6). Resistances are varied in the range $R^{\mathrm{sys}}_{\mathrm{ar}(total)} \in [40\ \frac{\mathrm{mPa\cdot s}}{\mathrm{mm}^3}, 220\ \frac{\mathrm{mPa\cdot s}}{\mathrm{mm}^3}]$ in increments of $20\ \frac{\mathrm{mPa\cdot s}}{\mathrm{mm}^3}$. For each of the 40 runs, circulation variable initial conditions of the afore-presented control case were set, and the transient simulations were performed according to the procedure in sec. 2.2.4.2 until (2.222) fell below $3\ \%$.
ESPVR is sketched by the solid black lines connecting the upper left end-systolic pressure-volume pairs, and regions of near-linearity are drawn by straight lines next to the respective "true" curves. Curvilinearity tends to shift from higher to lower afterloads for decreasing contractility, and steepness decreases at lower inotropic states. Volume axis intercepts are not drawn, but in general are obtained by extrapolating ESPVR.

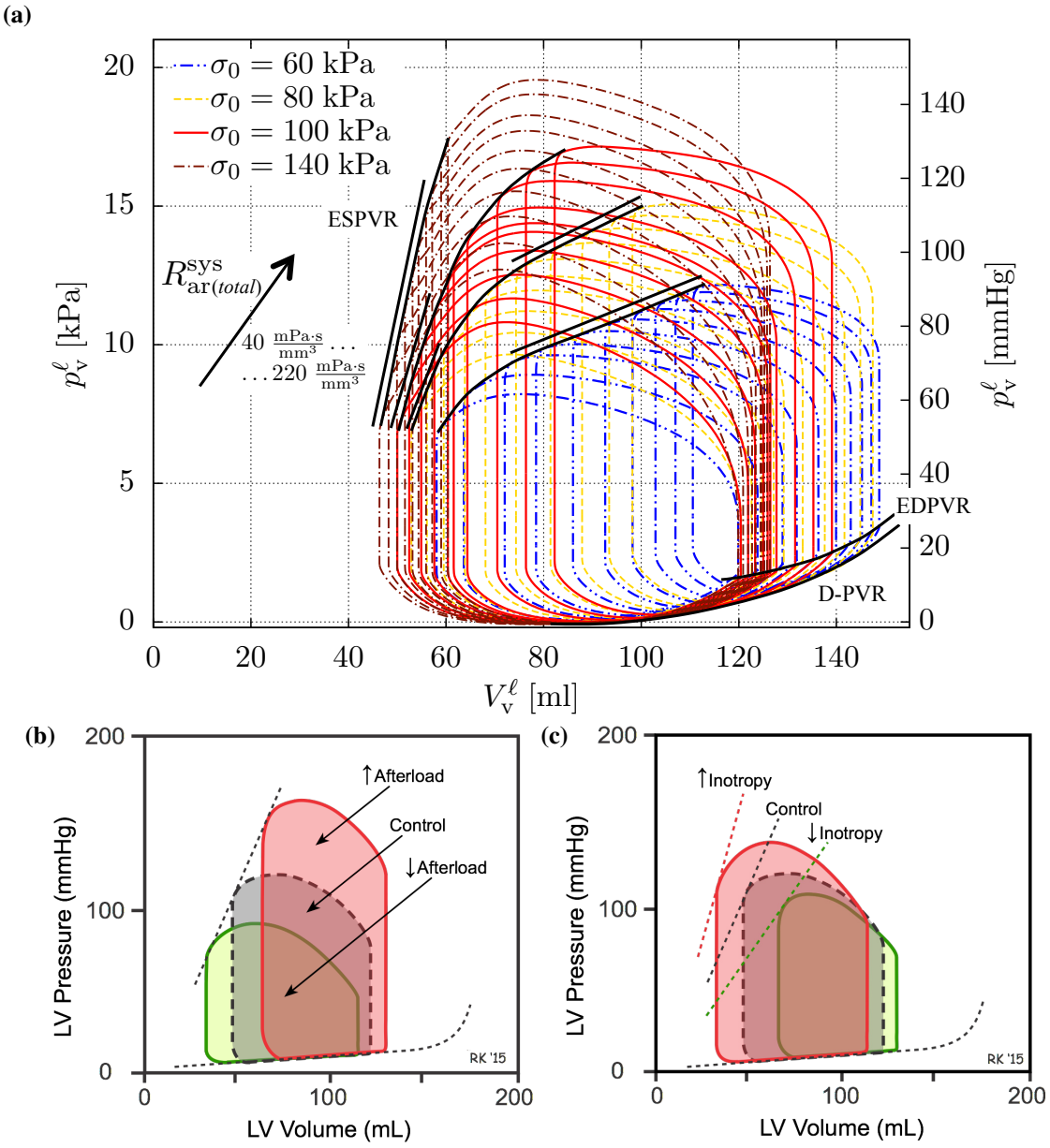

Figure 3.4: Effects on left ventricular pressure-volume relationships for changes in afterload, preload and inotropy. **(a)** Model *3Datrioventr*$_{tet4\_1.25}$ | *0Dsyspulcap*: End-systolic, end-diastolic, diastatic pressure-volume relationships (ESPVR, EDPVR, D-PVR) under different inotropic states (contractility σ_0) as well as changes in afterload (total systemic arterial resistance $R^{\text{sys}}_{\text{ar}(total)}$). **(b)** Textbook physiology on changes in afterload, and **(c)** changes in inotropy, both taken from www.cyphysiology.com (with permission).

EDPVR and D-PVR are indicated by solid black lines connecting the end-diastolic and end-diastatic pressure-volume pairs, respectively. Both are curvilinear, with a slightly steeper slope of D-PVR.

Figure 3.5a presents the left ventricular pressure-volume relationships for the base contractile state ($\sigma_0 = 100$ kPa) for five different states of afterload (*exclusively* varying $R^{\mathrm{sys}}_{\mathrm{ar}(total)} \in [40\ \frac{\mathrm{mPa\cdot s}}{\mathrm{mm}^3}, 200\ \frac{\mathrm{mPa\cdot s}}{\mathrm{mm}^3}]$ in increments of $40\ \frac{\mathrm{mPa\cdot s}}{\mathrm{mm}^3}$ *without* change of other vascular parameters according to tab. 2.7) – for impaired (no) atrial contraction as well as the respective control states (intact atria). When ventricular filling is purely passive (impaired atria), EDPVR and D-PVR coincide.

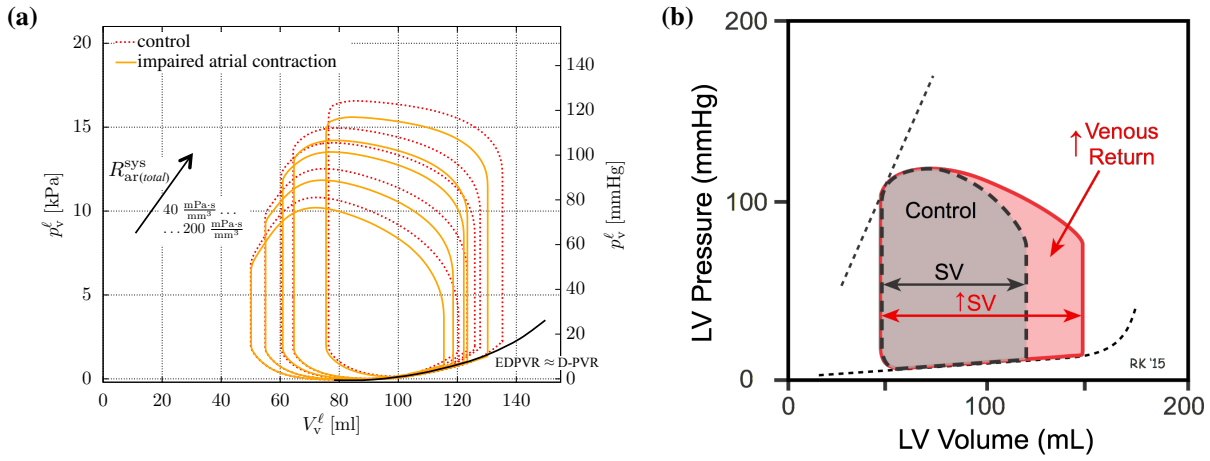

Figure 3.5: **(a)** Model *3Datrioventr*$_{tet4\_1.25}$ | *0Dsyspulcap*: End-diastolic and diastatic left ventricular pressure-volume relationship (EDPVR and D-PVR), and the Frank-Starling mechanism: Control vs. impaired atrial contraction. **(b)** Textbook demonstration of the Frank-Starling law, taken from www.cyphysiology.com (with permission): A higher end-diastolic volume due to increased venous return leads to stronger contraction, and stroke volume is increased by about the added return volume.

Effects of the Frank-Starling mechanism may be readily conceived: The portion of increased preload by atrial contraction is added to the stroke volume, and the ventricles contract to the same respective end-systolic volume as compared to the impaired atrium case. The Frank-Starling effect is sketched in fig. 3.5b, taken from www.cyphysiology.com (with permission): The higher end-diastolic volume due to elevated venous return yields a stroke volume that is increased by about that additional return volume.

3.2.3.3 Valve diseases

Valve diseases are computed with respect to the control state which was calculated in sec. 3.2.3.1. The disease is suddenly introduced after two cardiac cycles. The transient computation is carried out according to the procedure in sec. 2.2.4.2. However, in case of valve regurgitations, absolute left and right stroke volumes do not necessarily have to coincide at homeostatic state [7], thus a modification of (2.222) neglecting the stroke volume error is considered for these cases. Results are shown for model *3Dventr* coupled to circulation *0Dsyspul*.

Mitral valve diseases A mitral valve insufficiency or disease is simulated by changing its resistive properties. Mitral valve regurgitation is simulated by reducing the valve's maximum resistance from the base value to $R_{\mathrm{v,in}}^{\ell,\max} = 10^{-5}\ \frac{\mathrm{kPa \cdot s}}{\mathrm{mm}^3}$. A stenosis is mimicked by increasing the valve's minimum resistance to $R_{\mathrm{v,in}}^{\ell,\min} = 2.5 \cdot 10^{-5}\ \frac{\mathrm{kPa \cdot s}}{\mathrm{mm}^3}$.

Figure 3.6b and fig. 3.6d show textbook qualitative left ventricular pressure-volume relationships (with permission from www.cvphysiology.com) with respect to a control state as they would occur for mitral valve leakage (regurgitation) as well as for mitral valve stenosis, respectively. The related simulation results are shown in fig. 3.6a and fig. 3.6c, respectively.

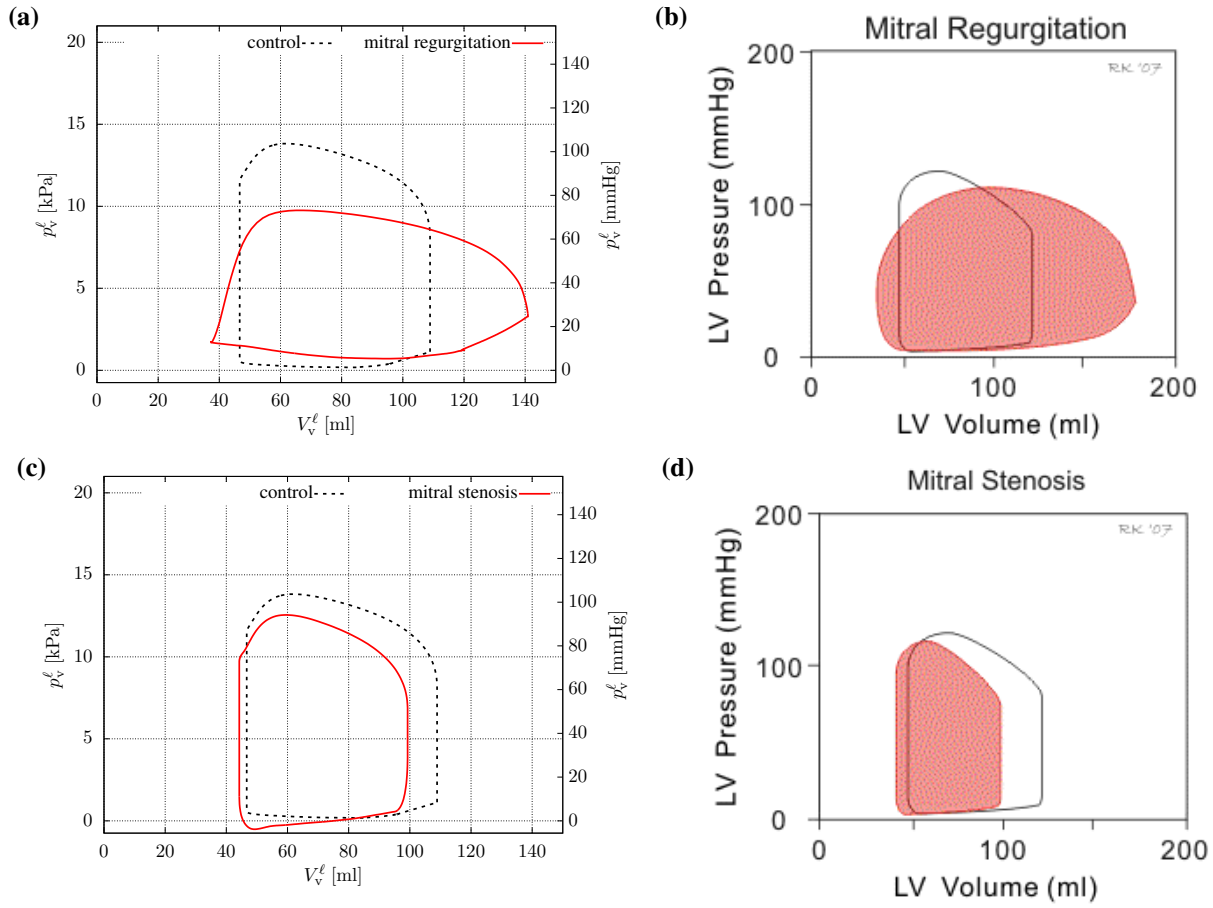

Figure 3.6: Model *3Dventr*$_{tet4\_1}$ | *0Dsyspul*: Mitral valve diseases. **(a)** Simulated left ventricular pressure-volume loop, control vs. mitral regurgitation, mitral valve's maximum resistance changed from its base value to $R_{\mathrm{v,in}}^{\ell,\max} = 10^{-5}\ \frac{\mathrm{kPa \cdot s}}{\mathrm{mm}^3}$. **(b)** Schematic textbook left ventricular pressure-volume loop, control (black) vs. mitral regurgitation (filled red), taken from www.cvphysiology.com (with permission). **(c)** Simulated left ventricular pressure-volume loop, control vs. mitral stenosis, mitral valve's minimum resistance changed from its base value to $R_{\mathrm{v,in}}^{\ell,\min} = 2.5 \cdot 10^{-5}\ \frac{\mathrm{kPa \cdot s}}{\mathrm{mm}^3}$. **(d)** Schematic textbook left ventricular pressure-volume loop, control (black) vs. mitral stenosis (filled red), taken from www.cvphysiology.com (with permission).

In case of mitral valve regurgitation, the pressure-volume relation widens and flattens. End-diastolic volume drastically increases (volume overload) to $141\ \mathrm{ml}$. A significant amount of stroke volume is not ejected into the aorta but back into the left atrium. Here, this so called regurgitant fraction is $67\ \%$. Net stroke volume and net ejection fraction fall to $34\ \mathrm{ml}$ and $24\ \%$, respectively. Total left and right ventricular stroke volume do not coincide at homeostasis [7].
A stenosis of the mitral valve, to the contrary, leads to a left shift of the pressure-volume relationship. Filling is impaired, and end-diastolic volume falls to $99\ \mathrm{ml}$. Stroke volume and ejection fraction are slightly reduced to $55\ \mathrm{ml}$ and $55\ \%$, respectively.

Aortic valve diseases As for the mitral valve, a malperformance of the aortic valve is simulated by altering the resistive properties. Aortic regurgitation is simulated by reducing the valve's maximum resistance from the base value to $R_{\mathrm{v,out}}^{\ell,\max} = 5 \cdot 10^{-5}\ \frac{\mathrm{kPa \cdot s}}{\mathrm{mm}^3}$. A stenosis of the aortic valve is achieved by increasing the valve's minimum resistance to $R_{\mathrm{v,out}}^{\ell,\min} = 5 \cdot 10^{-5}\ \frac{\mathrm{kPa \cdot s}}{\mathrm{mm}^3}$.

Figure 3.7b and fig. 3.7d show textbook qualitative left ventricular pressure-volume relationships (with permission from www.cvphysiology.com) with respect to a control state as they would occur for a leakage of the aortic valve (aortic valve regurgitation) as well as for an aortic valve stenosis, respectively. The simulation results for these diseases are shown in fig. 3.7a and fig. 3.7c, respectively.

Aortic regurgitation produces large end-diastolic volumes, here $138\ \mathrm{ml}$ (volume overload). Net stroke volume and net ejection fraction are $42\ \mathrm{ml}$ and $30\ \%$, with a regurgitant fraction of $55\ \%$. As for the mitral regurgitation, left and right ventricular stroke volumes do not coincide at homeostasis.
Aortic valve stenosis produces greatly increased systolic pressures the ventricle has to work against (pressure overload). The pressure-volume relation shifts to the right, stroke volume and ejection fraction fall to $50\ \mathrm{ml}$ and $36\ \%$, respectively. End-diastolic and end-systolic pressures rise to $3\ \mathrm{kPa}$ and $18\ \mathrm{kPa}$, respectively. Aortic stenosis produces a secondary increase in end-diastolic volume (fig. 3.7c) which is not directly distinguishable in the textbook fig. 3.7d but in the associated fig. 3.4b (pressure-volume loop changes for varying afterload).

Flow distributions for valve diseases The solutions for the left heart and systemic vascular flows (variables q) is studied for the four valve disease scenarios. Figure 3.8a shows the (healthy) control state (solution for the second cardiac cycle using the initial conditions of the model in fig. 3.3). The homeostatic state fluxes for aortic regurgitation are depicted in fig. 3.8b. The uni-directionality (positivity) of ventricular out-flux gets lost, and $q_{\mathrm{v,out}}^{\ell}$ becomes negative during diastole. In case of mitral regurgitation (fig. 3.8d), ventricular in-flux $q_{\mathrm{v,in}}^{\ell}$ is negative during systole. If a stenosis of the aortic valve is present, $q_{\mathrm{v,out}}^{\ell}$ gets diminished (fig. 3.8c), while $q_{\mathrm{v,in}}^{\ell}$ is reduced in case of a mitral valve stenosis (fig. 3.8e). The respective start time for the homeostatic heart cycle is denoted with $t_{N^\star}$, which varies depending on the disease.

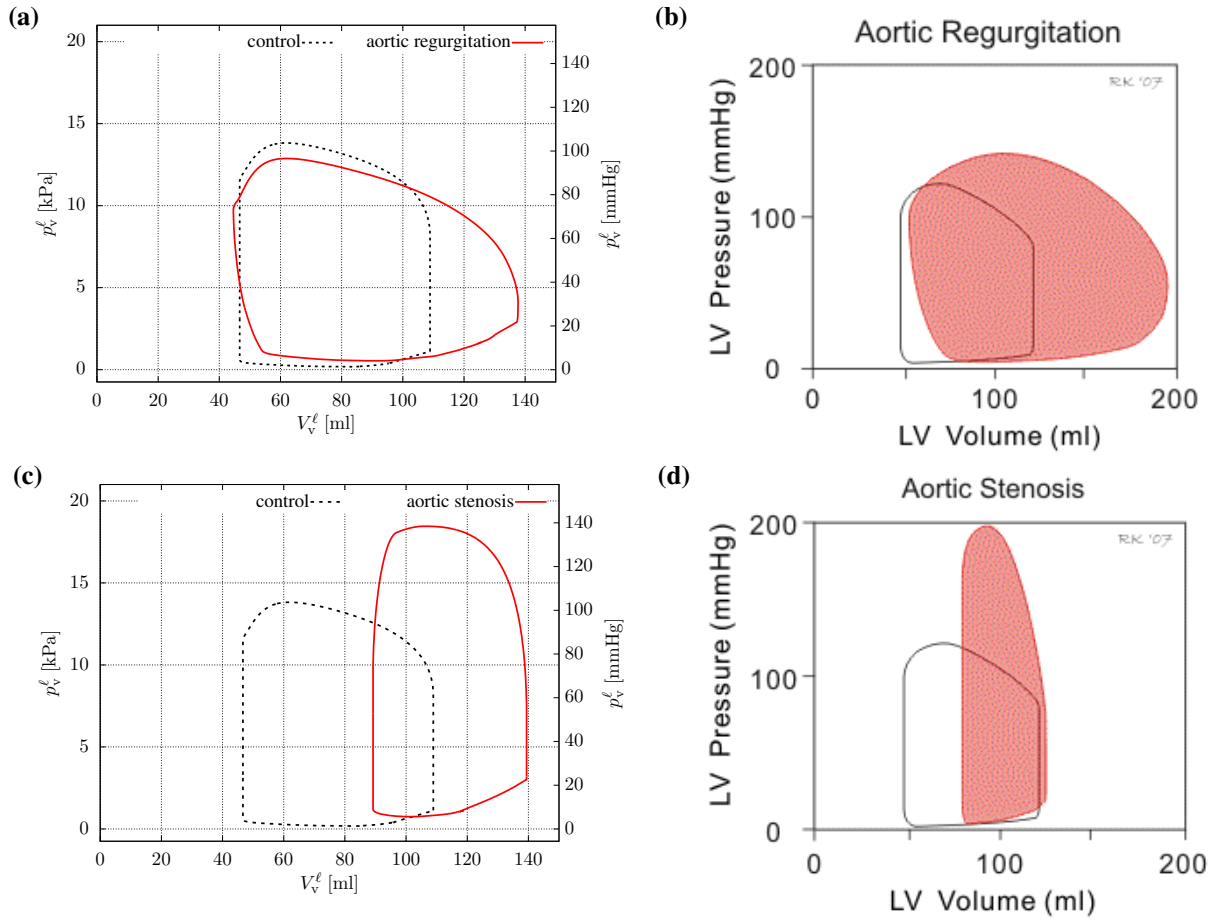

Figure 3.7: Model *3Dventr*$_{tet4\_1}$ | *0Dsyspul*: Aortic valve diseases. **(a)** Simulated left ventricular pressure-volume loop, control vs. aortic regurgitation, aortic valve's maximum resistance changed from its base value to $R_{\mathrm{v,out}}^{\ell,\max} = 5 \cdot 10^{-5}\ \frac{\mathrm{kPa \cdot s}}{\mathrm{mm}^3}$. **(b)** Schematic textbook left ventricular pressure-volume loop, control (black) vs. aortic regurgitation (filled red), taken from www.cvphysiology.com (with permission). **(c)** Simulated left ventricular pressure-volume loop, control vs. aortic stenosis, aortic valve's minimum resistance changed from its base value to $R_{\mathrm{v,out}}^{\ell,\min} = 5 \cdot 10^{-5}\ \frac{\mathrm{kPa \cdot s}}{\mathrm{mm}^3}$. **(d)** Schematic textbook left ventricular pressure-volume loop, control (black) vs. aortic stenosis (filled red), taken from www.cvphysiology.com (with permission).

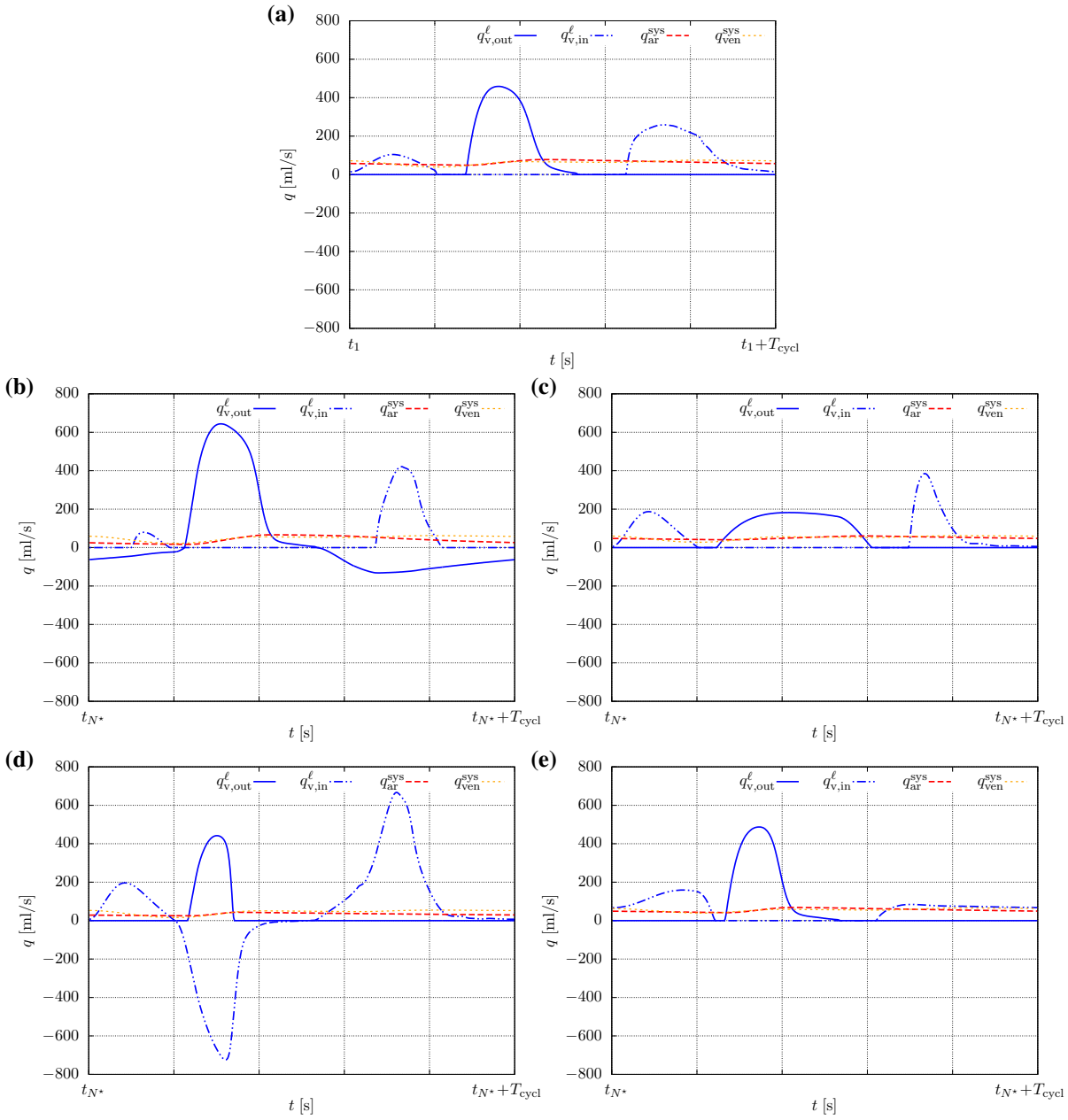

Figure 3.8: Model *3Dventr*$_{tet4\_1}$ | *0Dsyspul*: Left heart and systemic fluxes over time for control and valve disease states; respective homeostatic cycle is denoted with $N^\star$. **(a)** Control, second homeostatic cardiac cycle. **(b)** Aortic regurgitation. **(c)** Aortic stenosis. **(d)** Mitral regurgitation. **(e)** Mitral stenosis.

3.2.3.4 Gas transport and dissociation

The gas transport problem is computed with the prescribed-dynamics approach detailed in sec. 2.2.3.2. As input, the standard conditions from model *3Datrioventr$_{tet4_1.25}$ | 0Dsyspulcap* are used. A total ventilation rate of $\dot{V}_\mathrm{t} = V_\mathrm{T}/T_\mathrm{breath} = 8\ \mathrm{l/min}$ (tidal volume per duration of one breath) is achieved for the given parameters, cf. tab. 2.8.

Figure 3.9 depicts the mechanical pressure solutions for the last ten cycles as well as for the very last periodic cycle ($N^\star = 10\,000$) for the standard conditions. Accordance between fig. 3.9c and fig. 3.3a, as well as between fig. 3.9d and fig. 3.3b may be ascertained.

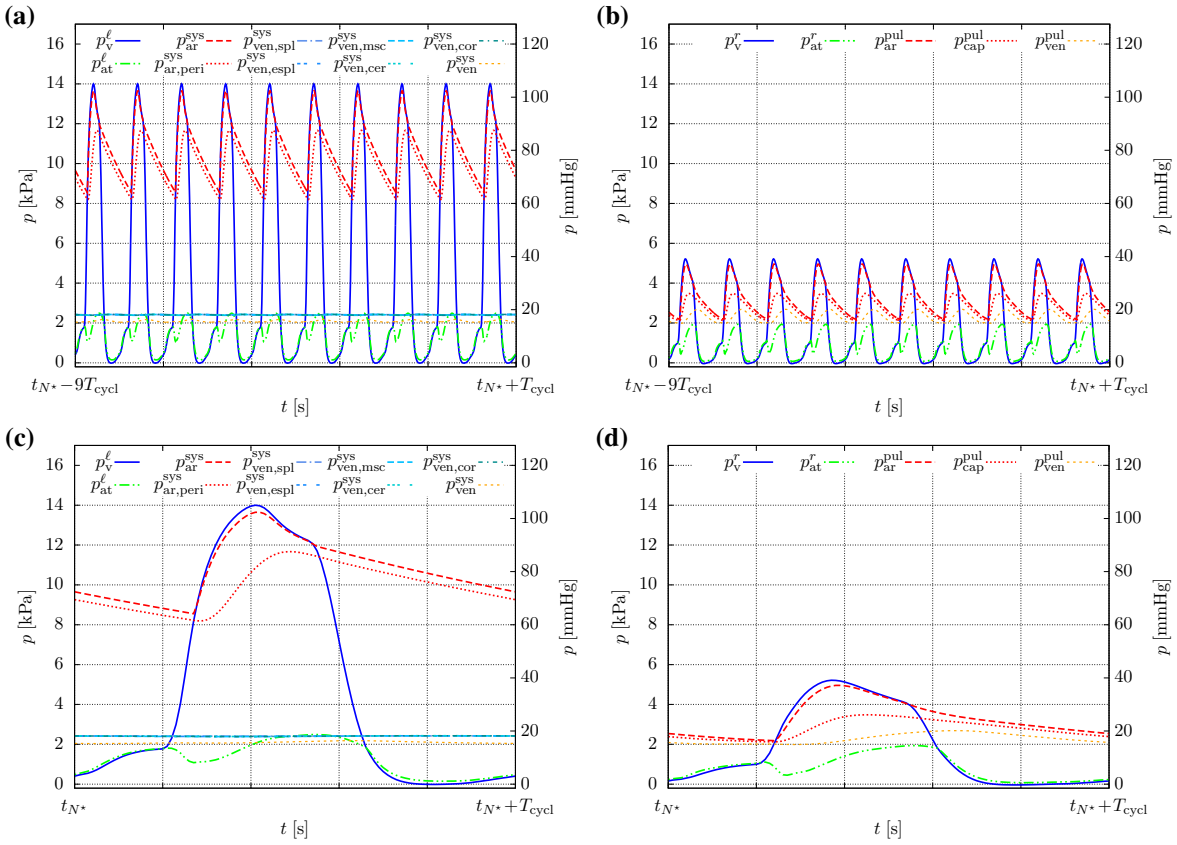

Figure 3.9: Model *PrescrHeart$_{3Datrioventr_{tet4_1.25}}$ | 0Dsyspulcaprespir*: Prescribed-dynamics solution. **(a)** Left heart and systemic pressures over the last ten cardiac cycles. **(b)** Right heart and pulmonary pressures over the last ten cardiac cycles. **(c)** Left heart and systemic pressures over the final cardiac cycle. **(d)** Right heart and pulmonary pressures over the final cardiac cycle.

Figure 3.10a shows the compartment volumes, (2.211) or calculated from the elastance models (2.218), for the last ten cycles including the sum $\sum V$ over all volumes. Total blood volume is conserved, hence $\sum V$ is constant over all cycles. A more detailed (zoomed) view of the time course of the compartment volumes (omitting the sum) is shown in fig. 3.10b.
Table 3.4 shows the averaged results over the last ten cycles of arterial and venous oxygen and carbon dioxide partial pressures as well as the systemic arterial and mixed-venous oxygen

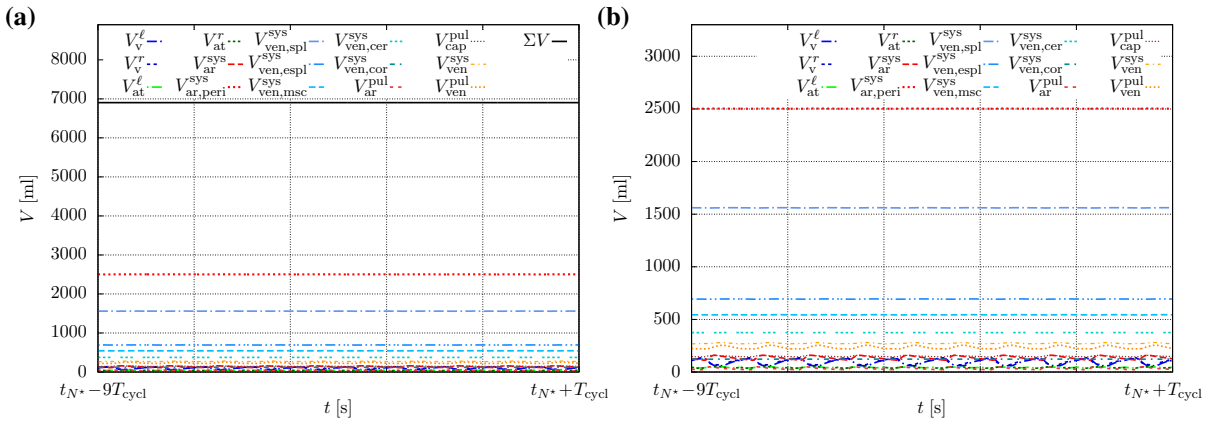

Figure 3.10: Model *PrescrHeart*$_{\textit{3Datrioventr}_{\textit{tet4\_1.25}}}$ | *0Dsyspulcaprespir*: Prescribed-dynamics solution, conservation of total blood volume. **(a)** Compartment volumes, including the sum $\sum V$ over all volumes. **(b)** Detailed (zoomed) view of compartment volumes over the last ten cardiac cycles.

saturation. Norm values are presented below the simulated results. All oxygen-related values are within the range of the norm. Arterial carbon dioxide partial pressure is slightly underestimated, and venous carbon dioxide partial pressure is overestimated by a factor of > 2.

Table 3.4: Model *PrescrHeart*$_{\textit{3Datrioventr}_{\textit{tet4\_1.25}}}$ | *0Dsyspulcaprespir*: Systemic arterial and venous oxygen partial pressure $p_{\mathrm{O_2,ar}}^{\mathrm{sys}}$ and $p_{\mathrm{O_2,ven}}^{\mathrm{sys}}$, systemic arterial oxygen saturation $S_{\mathrm{O_2,ar}}^{\mathrm{sys}}$, mixed-venous oxygen saturation $S_{\mathrm{O_2,ar}}^{\mathrm{pul}}$, systemic arterial and venous carbon dioxide partial pressure $p_{\mathrm{CO_2,ar}}^{\mathrm{sys}}$ and $p_{\mathrm{CO_2,ven}}^{\mathrm{sys}}$. Simulation, and norm values according to www.medicoconsult.de/blutgasanalyse and [45].

$\varnothing$	$p_{\mathrm{O_2,ar}}^{\mathrm{sys}}$ [kPa]	$p_{\mathrm{O_2,ven}}^{\mathrm{sys}}$ [kPa]	$S_{\mathrm{O_2,ar}}^{\mathrm{sys}}$ [%]	$S_{\mathrm{O_2,ar}}^{\mathrm{pul}}$ [%]	$p_{\mathrm{CO_2,ar}}^{\mathrm{sys}}$ [kPa]	$p_{\mathrm{CO_2,ven}}^{\mathrm{sys}}$ [kPa]
simulation	11.96	5.07	96.3	72.0	4.14	15.85
norm	9.5–13.9	4.8–5.9	94–98	70–80	4.7–6.1	4.9–6.7

Figures 3.11a–d show the systemic arterial and venous oxygen partial pressures, the total alveolar pressure, the alveolar carbon dioxide and oxygen partial pressures and gas fractions, as well as the alveolar volume and flux over time, respectively.
Systemic arterial and venous oxygen partial pressures oscillate in small amplitudes slightly below $12\ \mathrm{kPa}$ and slightly above $5\ \mathrm{kPa}$ (fig. 3.11a and fig. 3.11b), respectively. Alveolar pressure (fig. 3.11c) hardly perceptibly oscillates around the prescribed atmospheric pressure $U_{\mathrm{m}} = 100\ \mathrm{kPa} = 1\ \mathrm{bar}$ (cf. tab. 2.8). Alveolar carbon dioxide and oxygen gas fractions oscillate around $3\ \%$ and $15\ \%$, respectively. The alveolar partial pressures of carbon dioxide and oxygen are directly computable by multiplying the gas fractions with the total alveolar pressure and hence are no primary variables of the model. Alveolar volume (fig. 3.11d) oscillates around total lung volume V_{lung} slightly below the amplitude of the tidal volume V_{T}. Alveolar flux q_{alv} here is the positive rate of change of alveolar volume (2.184).

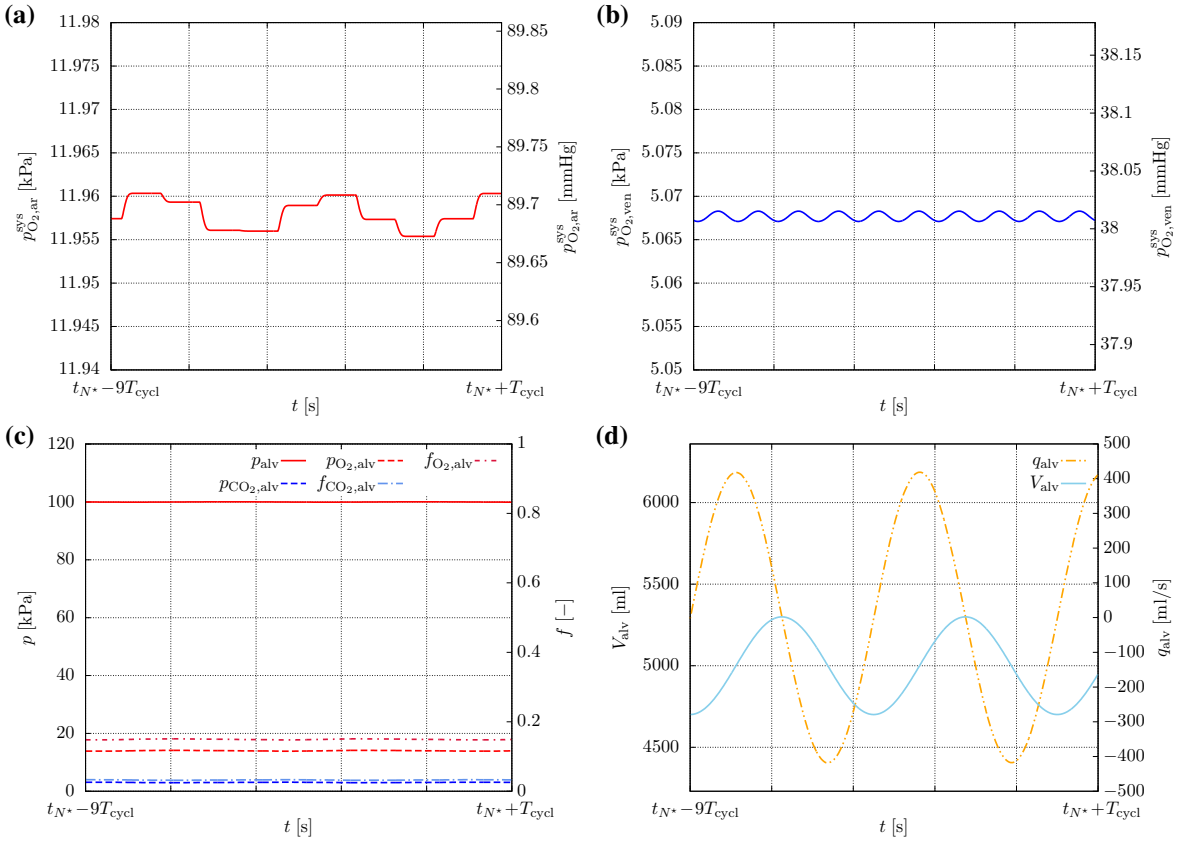

Figure 3.11: Model *PrescrHeart*$_{\textit{3Datrioventr}_{\textit{tet4\_1.25}}}$ | *0Dsyspulcaprespir*: Solutions of the gas transport problem for the last ten cycles over time t. **(a)** Systemic arterial oxygen partial pressure $p^{\text{sys}}_{\text{O}_2,\text{ar}}$. **(b)** Systemic venous oxygen partial pressure $p^{\text{sys}}_{\text{O}_2,\text{ven}}$. **(c)** Total alveolar pressure p_{alv}, alveolar carbon dioxide and oxygen partial pressures as well as gas fractions $p_{\text{CO}_2,\text{alv}}$ and $p_{\text{O}_2,\text{alv}}$ as well as $f_{\text{CO}_2,\text{alv}}$ and $f_{\text{O}_2,\text{alv}}$, respectively. **(d)** Alveolar volume V_{alv} and flux q_{alv}.

3.2.4 Discussion

The models and methods presented for simulating physiological cardiovascular conditions are tailored towards the patient-specific 3D resolution of the ventricular and atrial myocardium and their mechanical behavior. Coupled to lumped-parameter closed-loop vascular network models, homeostatic states of the cardio-circulatory system can be assessed, and a link between local continuum mechanical behavior of the heart muscle to integral cardiac functionality indicators such as cardiac output and stroke work can be drawn. This feature is considered essential for the assessment of how growth and remodeling phenomena are triggered and vice versa affect the cardiac work (cf. sec. 3.3), and becomes highly relevant for the prediction of function and efficiency of novel cardiac compression-based ventricular assist devices (cf. chap. 5).
To date, this is the first model that includes a 3D resolution of all four cardiac chambers, their interaction with a closed circulation, and a straightforward one-way coupling of the mechanical solutions to gas transport and dissociation mechanisms, cf. sec. 2.2 of chap. 2 for some review of other approaches from the contemporary literature.
However, limitations may be seen in the material (constitutive), boundary condition, and fiber data, which do not rely on patient-specific measurements but are generic or rule-based. Especially atrial fiber architecture does not correspond to a physiological pattern and would not be applicable to models for atrial electrophysiology and excitation propagation [91, 92]. However, if only accounting for the mechanical performance and its contribution to overall myocardial function, non-physiological atrial fiber patterns may be sufficient, however might lack of accurately addressing the passive mechanical behavior in terms of atrial systolic deformation patterns, or stresses and strains inside the tissue. Therefore, more complex and more realistic atrial fiber patterns should be incorporated into these models, cf. the proposed methods by Krueger et al. [112], for example.

To efficiently address the multi-dimensional coupling of 3D nonlinear solid mechanics and 0D pressure-flow models, a monolithic discretization and solution framework is established and implemented together with a time integration of all 0D governing equations. The monolithic 3D-0D coupling is considered superior to any partitioned coupling schemes (as, for instance, presented by [104] for a 2-chamber patient-specific heart coupled to a 0D circulation), since isovolumic heart phases naturally require a relaxation technique for partitioned approaches to circumvent the classical balloon dilemma [114] in fluid-structure interaction in presence of a Dirichlet-constrained fluid.
Furthermore, partitioned solutions have to be tightly 2-way coupled due to the strong interdependencies of 0D and 3D models, and hence a far greater amount of linear solves would be required compared to the monolithic approach. However, it should be emphasized that the advantage of partitioned schemes on the one hand lies in the choice of field-specific (independent 3D and 0D) linear solvers and preconditioners that can be tailored towards the specific physical problem, whereas an (implicit) monolithic approach always requires a preconditioning technique for the global system of equations. On the other hand, partitioned algorithms may be designed highly modularly, even by combining different software packages that address the respective physical fields independently, while on the other hand monolithic schemes most often require an extra implementation as well as linearization procedures for the field-interdependencies in order to efficiently solve the coupled problem in one monolithic Newton algorithm.

As mentioned in the introductory remarks, little literature proposes monolithic coupling schemes for 3D solid and 0D fluid mechanical models, cf. the contributions by Sainte-Marie et al. [178] or Fritz et al. [62]. Therein, no circulatory system but only single pre- and afterload models for the ventricles only are used. Additionally, the approach in Fritz et al. [62] seems to rely on condensing out the pressure variables and directly incorporating the whole vascular model into the solid mechanics balance equation. This approach is considered impracticable since it increases the bandwidth of the system matrix and thus renders the linear solution more demanding. Furthermore, [178] and [62] use direct linear solvers and hence are restricted to limited sizes of the underlying forward problem.

The simulated standard conditions are physiologically realistic and could correspond to a healthy individual at rest. All parameters are chosen either according to physiological considerations (blood flow parameters, tab. 2.7 and tab. 2.6, as well as respiration, gas transport and dissociation parameters, tab. 2.8 and tab. 2.9), rely on state-of-the-art experimental data (myocardial passive properties, tab. 2.2), or are result of well-educated guesses combined with reasonability considerations for the case that no data exists (Robin boundary parameters, tab. 2.1). The driving parameters that govern the dynamical behavior of the myocardium (tab. 2.3) may be set to individual requirements, i.e. with respect to heart rate, end-diastolic and end-systolic timings, contraction speed and strength.

The performance of the model under varying preloads and afterloads is assessed by changing the peripheral arterial resistance under different inotropic states (contractility), presented in fig. 3.4a. The end-systolic pressure-volume relationship (ESPVR) in physiology is used as index of ventricular contractility, even though its independence on the afterload is still controversial [24]. The model shows consistency of local cell-based contractile behavior to the global ESPVR contractility index: A reduction in inotropy yields decreased ESPVR steepness and vice versa, cf. the textbook pressure-volume loops of fig. 3.4b and fig. 3.4c. The results also comply with the in-silico model results by Shavik et al. [189], who however couple a generic simplified only-left ventricular finite element model to a closed-loop circulation. Results therein preen themselves on showing load-independence and linearity of ESPVR, even though clear evidence is present that ESPVR is nonlinear for a larger spectrum of load ranges [101, 205].
End-diastolic pressure-volume relationship (EDPVR) is an index of ventricular stiffness, and passive filling occurs along that curve. However, evidence is given that the *diastatic* pressure-volume relationship (D-PVR) is a better index of compliance since effects of atrial systole are excluded [223]. The model *3Datrioventr* here is capable of showing both EDPVR and D-PVR. However, while D-PVR is usually less steep than EDPVR [223], here no significantly but slightly steeper D-PVR curve compared to the EDPVR curve is obtained, cf. fig. 3.4a. Probably, this effect may be explained by the assumed load-independence of atrial contraction, even though atria also exhibit a Frank-Starling mechanism [6].
To the best of the author's knowledge, this is the first model capable of showing distinguishable EDPVR and D-PVR curves. Shavik et al. [189] again show passive filling perfectly occurring along the EDPVR curve for varying preloads, which however is no surprise since a quasi-static solid mechanics model was used. Effects of inertia and viscosity – which are included in the present model – lead to tiny deviations of end-diastatic (end-diastolic) points from the D-PVR

(EDPVR for the impaired atrial contraction, cf. fig. 3.5a).

The effect of the Frank-Starling mechanism, namely the increase of contractile force at higher preloads in order to empty that additional amount of added volume to the same end-systolic volume may be conceived comparing the respective impaired atrial with the control pressure-volume loops from fig. 3.5a. Higher atrial contractility leads to increased venous return and hence higher end-diastolic volume. This is in good accordance to what is concluded from physiological observations, cf. the textbook curves in fig. 3.5b.

Furthermore, the model's behavior under different kinds of valve diseases is investigated and compared to textbook pressure-volume relations. In case of all four abnormalities – mitral and aortic valve regurgitation and stenosis – model output in terms of the general trend in pressure-volume loop alterations complies very well to what is observed, cf. the textbook pressure-volume loops in fig. 3.6 and fig. 3.7.

Gas transport and dissociation was computed for the standard conditions, and a good accordance of all oxygen-related values to norm data (tab. 3.4) is ascertained. However, the slight underestimation of arterial carbon dioxide content and the great overestimation (factor > 2) of the venous CO_2 partial pressure remains to be investigated and may be due to insufficient CO_2 elimination in the lung compartment.
Here, the alveolar ventilation rate ($\dot{V}_{\mathrm{alv}}$) nearly corresponds to the total ventilation due to breathing, $\dot{V}_{\mathrm{t}} = V_{\mathrm{T}}/T_{\mathrm{breath}}$, since alveolar resistance was neglected and alveolar elastance and inertance are small (tab. 2.8). However, these parameters from [171] might have to be resought in presence of the fact that alveolar ventilation is only about $70\ \%$ of total ventilation [51].
The dissociation functions for carbon dioxide and oxygen are chosen as simple as possible and do not include the respective interdependencies as in the models of [41, 191, 202]. Further studies are needed to more robustly calibrate these models to distinct conditions in order to be able to reliably assess the gas kinetics for a specific individual.
Furthermore, as the model of Trenhago et al. [202], no control and feedback control systems for the whole cardiovascular-respiratory model are implemented yet, hence a perturbation of one model parameter does not naturally induce adaptation mechanisms in a different branch of the model. A classical example would be an exercise condition: This is accompanied not only by an increase in heart rate but also a change in systolic-diastolic duration relationship, a fall of skeletal muscle vascular resistance [87], a decrease in pulmonary vascular resistance [109, 168], as well as an increase in cardiac contractility, lung ventilation, and metabolism. Therefore, a bunch of parameters would have to be changed, and it remains unclear in which consecutive order such that the desired output is achieved or still lies within physiological bounds.

3.3 Multiscale growth and remodeling (G&R): Algorithmic aspects and results

The algorithmic and solution aspects of the multiscale growth and remodeling (G&R) models presented in sec. 2.3 as well as the results are presented. Section 3.3.1 deals with the solution and

implementation of the strain- and stress-based growth laws, and sec. 3.3.2 presents the results of the multiscale computations for eccentric ventricular growth for dilated cardiomyopathy (DCM) as well as for concentric ventricular growth for hypertrophic cardiomyopathy (HCM). Finally, the algorithms and the results are discussed in sec. 3.3.3.

3.3.1 Return mapping schemes for volumetric growth constitutive laws

During each outer Newton iteration in order to solve the global discretized system of equations (3.32), the nonlinear growth evolution equation (2.236) or (2.242) has to be solved in order to obtain a *non-equilibrium* solution ϑ with respect to the outer iteration. Here, a Backward-Euler time integration scheme, being (3.18) with $\theta = 1$ is chosen, yielding a time-discrete growth evolution that is nonlinear in the current growth stretch ϑ_{n+1} that belongs to the actual time step $n+1$ which has to be solved for.
Hence, at *frozen* outer iteration state of the global Newton scheme, an integration point-wise *local* Newton scheme has to be applied in order to solve the time-discrete nonlinear growth evolution equation. When entering the local Newton scheme, only the accumulated growth stretch from the previous time step is assumed to be present, hence the initial guess is an *elastic* deformation (predictor) and the growth variable has to be integration point-wise iterated to obtain the true elasto-plastic (elasto-growth) state (correction step). A scheme of this type is usually denoted as *return mapping scheme*.

3.3.1.1 Strain-governed eccentric growth for dilated cardiomyopathy

The integration point-wise solution of the strain-driven growth law presented in sec. 2.3.1.1 suited for modeling of eccentric ventricular growth due to end-diastolic volume overload is detailed.

The Backward-Euler time integration scheme applied to (2.236) yields the discretized version of the evolution equation,

$$\frac{\vartheta_{n+1} - \vartheta_n}{\Delta t} = k(\vartheta_{n+1}) \left(\frac{1}{\vartheta_{n+1}} \lambda_{\mathrm{myo}} - \hat{\lambda}^{\mathrm{crit}}_{\mathrm{myo}} \right), \tag{3.46}$$

where ϑ_{n+1} is the current unknown state to be solved for, and ϑ_n is the old, known state from the previous converged time step. Unfortunately, (3.46) is nonlinear in ϑ_{n+1}, on the one hand due to the nonlinearity in the growth function k, (2.238), on the other due to the dependence of the growth stimulating elastic myofiber stretch $\lambda^{\mathrm{e}}_{\mathrm{myo}}$, cf. (2.237).

The local Newton scheme in order to solve (3.46) then yields a residual expression of the type

$$R_\vartheta = \frac{\vartheta_{n+1} - \vartheta_n}{\Delta t} - k(\vartheta_{n+1}) \left(\frac{\lambda_{\mathrm{myo}}}{\vartheta_{n+1}} - \hat{\lambda}^{\mathrm{crit}}_{\mathrm{myo}} \right) \stackrel{!}{=} 0. \tag{3.47}$$

The tangent reads

$$\frac{\mathrm{d}R_\vartheta}{\mathrm{d}\vartheta_{n+1}} = \frac{1}{\Delta t} + \frac{\mathrm{d}k(\vartheta_{n+1})}{\mathrm{d}\vartheta_{n+1}} \left(\frac{\lambda_{\mathrm{myo}}}{\vartheta_{n+1}} - \hat{\lambda}^{\mathrm{crit}}_{\mathrm{myo}} \right) + k(\vartheta_{n+1}) \frac{\lambda_{\mathrm{myo}}}{\vartheta^2_{n+1}}, \tag{3.48}$$

with

$$\frac{\mathrm{d}k(\vartheta_{n+1})}{\mathrm{d}\vartheta_{n+1}} = \begin{cases} -\frac{\gamma}{\tau}\left(\frac{\vartheta_{\max}-\vartheta_{n+1}}{\vartheta_{\max}-\vartheta_{\min}}\right)^{\gamma-1}\frac{1}{\vartheta_{\max}-\vartheta_{\min}}, & \lambda^{\mathrm{e}}_{\mathrm{myo}} \geq \hat{\lambda}^{\mathrm{crit}}_{\mathrm{myo}}, \\ \frac{\gamma_{\mathrm{rev}}}{\tau_{\mathrm{rev}}}\left(\frac{\vartheta_{n+1}-\vartheta_{\min}}{\vartheta_{\max}-\vartheta_{\min}}\right)^{\gamma_{\mathrm{rev}}-1}\frac{1}{\vartheta_{\max}-\vartheta_{\min}}, & \lambda^{\mathrm{e}}_{\mathrm{myo}} < \hat{\lambda}^{\mathrm{crit}}_{\mathrm{myo}}. \end{cases} \tag{3.49}$$

3.3.1.2 Stress-governed concentric growth for hypertrophic cardiomyopathy

Here, the integration point-wise solution of the stress-driven growth law presented in sec. 2.3.1.2 that was introduced in order to model concentric growth due to end-systolic pressure overload is detailed.

The Backward-Euler time integration scheme applied to (2.242) yields the discretized version of the evolution equation,

$$\frac{\vartheta_{n+1}-\vartheta_n}{\Delta t} = k(\vartheta_{n+1})\left(\mathrm{tr}\,\boldsymbol{\Sigma}^{\mathrm{e}}(\vartheta_{n+1}) - \hat{\Sigma}^{\mathrm{crit}}\right), \tag{3.50}$$

where again ϑ_{n+1} is the current unknown state to be solved for, and ϑ_n is the old, known state from the previous converged time step. Here also, (3.50) is nonlinear in ϑ_{n+1}, on the one hand due to the nonlinearity in the growth function k, (2.243), on the other due to the dependence of the growth stimulating volumetric component of the Mandel stress $\mathrm{tr}\,\boldsymbol{\Sigma}^{\mathrm{e}}$, cf. (2.227).

The local Newton scheme in order to solve (3.50) then yields a residual expression of the type

$$R_\vartheta = \frac{\vartheta_{n+1}-\vartheta_n}{\Delta t} - k(\vartheta_{n+1})\left(\mathrm{tr}\,\boldsymbol{\Sigma}^{\mathrm{e}}(\vartheta_{n+1}) - \hat{\Sigma}^{\mathrm{crit}}\right) \stackrel{!}{=} 0. \tag{3.51}$$

The tangent reads

$$\frac{\mathrm{d}R_\vartheta}{\mathrm{d}\vartheta_{n+1}} = \frac{1}{\Delta t} + \frac{\mathrm{d}k(\vartheta_{n+1})}{\mathrm{d}\vartheta_{n+1}}\left(\mathrm{tr}\,\boldsymbol{\Sigma}^{\mathrm{e}}(\vartheta_{n+1}) - \hat{\Sigma}^{\mathrm{crit}}\right) + k(\vartheta_{n+1})\frac{\partial \mathrm{tr}\,\boldsymbol{\Sigma}^{\mathrm{e}}(\vartheta_{n+1})}{\partial \vartheta_{n+1}} \tag{3.52}$$

with

$$\frac{\mathrm{d}k(\vartheta_{n+1})}{\mathrm{d}\vartheta_{n+1}} = \begin{cases} -\frac{\gamma}{\tau}\left(\frac{\vartheta_{\max}-\vartheta_{n+1}}{\vartheta_{\max}-\vartheta_{\min}}\right)^{\gamma-1}\frac{1}{\vartheta_{\max}-\vartheta_{\min}}, & \mathrm{tr}\,\boldsymbol{\Sigma}^{\mathrm{e}} \geq \hat{\Sigma}^{\mathrm{crit}}, \\ \frac{\gamma_{\mathrm{rev}}}{\tau_{\mathrm{rev}}}\left(\frac{\vartheta_{n+1}-\vartheta_{\min}}{\vartheta_{\max}-\vartheta_{\min}}\right)^{\gamma_{\mathrm{rev}}-1}\frac{1}{\vartheta_{\max}-\vartheta_{\min}}, & \mathrm{tr}\,\boldsymbol{\Sigma}^{\mathrm{e}} < \hat{\Sigma}^{\mathrm{crit}} \end{cases} \tag{3.53}$$

and the derivative of the first invariant of the Mandel stress tensor unfortunately needing further considerations:

$$\frac{\partial \mathrm{tr}\,\boldsymbol{\Sigma}^{\mathrm{e}}}{\partial \vartheta_{n+1}} = \frac{\partial \mathrm{tr}(\boldsymbol{C}^{\mathrm{e}}\boldsymbol{S}^{\mathrm{e}})}{\partial \vartheta_{n+1}} = \frac{\partial(\boldsymbol{C}^{\mathrm{e}} : \boldsymbol{S}^{\mathrm{e}})}{\partial \vartheta_{n+1}} = \frac{\partial \boldsymbol{C}^{\mathrm{e}}}{\partial \vartheta_{n+1}} : \boldsymbol{S}^{\mathrm{e}} + \boldsymbol{C}^{\mathrm{e}} : \frac{\partial \boldsymbol{S}^{\mathrm{e}}}{\partial \vartheta_{n+1}}, \tag{3.54}$$

where the derivatives of the elastic Cauchy-Green tensor $(2.225)_1$ and the elastic second Piola-Kirchhoff stress tensor $(2.225)_2$ with respect to the current growth stretch are

$$\begin{aligned} \frac{\partial \boldsymbol{C}^{\mathrm{e}}}{\partial \vartheta_{n+1}} &= \frac{\partial}{\partial \vartheta_{n+1}}\left(\boldsymbol{F}^{\mathrm{g}^{-\mathrm{T}}}\boldsymbol{C}\boldsymbol{F}^{\mathrm{g}^{-1}}\right) = \\ &= \frac{\partial \boldsymbol{F}^{\mathrm{g}^{-\mathrm{T}}}}{\partial \boldsymbol{F}^{\mathrm{g}^{\mathrm{T}}}} : \frac{\partial \boldsymbol{F}^{\mathrm{g}^{\mathrm{T}}}}{\partial \vartheta_{n+1}}\boldsymbol{C}\boldsymbol{F}^{\mathrm{g}} + \boldsymbol{F}^{\mathrm{g}^{-\mathrm{T}}}\boldsymbol{C}\frac{\partial \boldsymbol{F}^{\mathrm{g}^{-1}}}{\partial \boldsymbol{F}^{\mathrm{g}}} : \frac{\partial \boldsymbol{F}^{\mathrm{g}}}{\partial \vartheta_{n+1}} = \\ &= -\boldsymbol{F}^{\mathrm{g}^{-\mathrm{T}}}\frac{\partial \boldsymbol{F}^{\mathrm{g}^{\mathrm{T}}}}{\partial \vartheta}\boldsymbol{C}^{\mathrm{e}} - \boldsymbol{C}^{\mathrm{e}}\frac{\partial \boldsymbol{F}^{\mathrm{g}}}{\partial \vartheta}\boldsymbol{F}^{\mathrm{g}^{-1}} \end{aligned} \tag{3.55}$$

and

$$\frac{\partial \boldsymbol{S}^{\mathrm{e}}}{\partial \vartheta_{n+1}} = \frac{\partial \boldsymbol{S}^{\mathrm{e}}}{\partial \boldsymbol{C}^{\mathrm{e}}} : \frac{\partial \boldsymbol{C}^{\mathrm{e}}}{\partial \vartheta_{n+1}} = \frac{1}{2}\check{\mathbb{C}}^{\mathrm{e}} : \frac{\partial \boldsymbol{C}^{\mathrm{e}}}{\partial \vartheta_{n+1}}, \tag{3.56}$$

respectively.

3.3.2 Results

Two exemplary scenarios of volume overload-induced dilated cardiomyopathy (DCM) and one example of pressure overload-induced hypertrophic cardiomyopathy (HCM) are presented. Volume overload is induced by mitral regurgitation as well as left ventricular infarction, cf. sec. 3.3.2.1, and a state of pressure overload is achieved by assuming an aortic valve stenosis, cf. sec. 3.3.2.2. Furthermore, reverse growth and remodeling phenomena are presented in sec. 3.3.2.3 by simulating a mitral valve repair after volume overload growth due to mitral regurgitation.

Without loss of generality, the large time scale period is set to $T_{\mathrm{growth}} = 10^6\ \mathrm{s} \approx 11.6\ \mathrm{d}$. Further parameters for the growth laws are listed in 3.5.

Table 3.5: G&R parameters: Time constants τ and τ_{rev} have units "stretch times time" or "stress times time" depending on the growth law

		volume overload	pressure overload	
T_{growth}	[s]	10^6		large time scale duration per (outer) cycle
$\vartheta_{\min}$	[−]	1.0		minimum growth stretch
$\vartheta_{\max}$	[−]	3.0	2.0	maximum growth stretch
τ	[s] / [kPa·s]	$0.025{\cdot}10^6$	$25{\cdot}10^6$	growth time constant
τ_{rev}	[s] / [kPa·s]	$0.025{\cdot}10^6$	$25{\cdot}10^6$	reverse growth time constant
γ	[−]	1.0		growth nonlinearity
γ_{rev}	[−]	1.0		reverse growth nonlinearity
s	[−]	1.001	1.01	threshold safety factor
$(\hat{\lambda}^{\mathrm{crit}}_{\mathrm{myo}})_{\downarrow}$	[−]	1.02	−	minimum myofiber stretch threshold
$(\hat{\Sigma}^{\mathrm{crit}})_{\downarrow}$	[kPa]	−	30.0	minimum volumetric stress threshold

G&R phenomena may take place everywhere in the ventricular and atrial myocardium except in regions where an infarction is assumed. Additionally, G&R is disabled for the "dummy" lids that are modeled by the strain energy (2.98).
Algorithmic parameters are chosen according to tab. 3.1, however with $c_{\mathrm{K}} = 0$ due to technical reasons. The number of time steps per cardiac cycle is reduced to $n_{\mathrm{step}} = 200$ for volume overload and $n_{\mathrm{step}} = 300$ for pressure overload, since a coarser spatial discretization (*tet4_2*, cf. appendix A.1) is chosen for the sake of computational efficiency.
The tolerance for the error (2.253) in two subsequent grown small time scale states is chosen to $\epsilon_{\mathrm{growth}} = 1.5\ \%$.

3.3.2.1 Volume overload: Dilated cardiomyopathy

Here, volume overload G&R for two exemplary acute disease events is considered, namely mitral regurgitation (MR) as well as apical infarction (AI). Both events are introduced after the first homeostatic heart cycle. For simplicity, the remodeling of the portion of grown material only shall affect the active stress (referred to as *remod_act*), hence the constitutive equation for $\boldsymbol{S}^{\mathrm{e}}_{(grown)}$ in (2.246) is (2.96) with $\tau_{\mathrm{a}} \equiv 0$ at all times, and the passive strain energy function remains (2.97). Comparisons to growth without remodeling are carried out (referred to as *noremod*).

Mitral regurgitation A mitral valve insufficiency, here a mitral regurgitation (MR), is induced by setting the mitral valve's maximum resistance from its base value (cf. tab. 2.6) to $R_{\mathrm{v,in}}^{\ell,\max} = 10^{-5}\ \frac{\mathrm{kPa \cdot s}}{\mathrm{mm}^3}$.
Figure 3.12 shows the multiscale results for MR-induced volume overload resulting in eccentric ventricular hypertrophy. In fig. 3.12a, volume results per multiscale cycles $\mathcal{N}$ are shown: The respective top plot shows the small time scale cavity volumes for all four cardiac chambers, the bottom left plot the end-diastolic cavity volumes and the bottom right plot the relative wall volume change on the large time scale as consequence of eccentric growth. Only the first two multiscale cycles ($\mathcal{N} = 1$ and $\mathcal{N} = 2$) as well as the last one ($\mathcal{N} = 5$) are shown. Small time scale cycles (N) and small time scale cycle errors (2.222) as well as the associated large scale error (2.253) are depicted next to the upper left plots of fig. 3.12a.
Figure 3.12b shows the pressure-volume relationships for the control state, the MR base state (homeostatic state after MR but prior to any G&R), and the converged grown state with active remodeling (*remod_act*) as well as without (*noremod*).
Figure 3.12c depicts the elastic myofiber stretch (2.237) on the end-diastolic configuration for the control, MR base and MR grown *remod_act* case. Finally, fig. 3.12d shows the growth stretch ϑ as well as the remodeling factor (2.247) on the end-diastolic configuration of the final MR grown *remod_act* state.

Left ventricular function indicators are listed in tab. 3.6.

Table 3.6: Left ventricular function indicators end-diastolic volume EDV^{ℓ}, net stroke volume $\mathrm{SV}^{\ell}_{\mathrm{net}}$ (total minus regurgitant volume), net ejection fraction $\mathrm{EF}^{\ell}_{\mathrm{net}}$ (net stroke per end-diastolic volume), regurgitant fraction RF^{ℓ}, end-diastolic and end-systolic pressures EDP^{ℓ} and ESP^{ℓ}, respectively; for control, MR base, MR grown *remod_act* and MR grown *noremod* state

	EDV^{ℓ} [ml]	$\mathrm{SV}^{\ell}_{\mathrm{net}}$ [ml]	$\mathrm{EF}^{\ell}_{\mathrm{net}}$ [−]	RF^{ℓ} [−]	EDP^{ℓ} [kPa]	ESP^{ℓ} [kPa]
control	124.7	64.1	0.51	−	1.83	11.9
MR base	140.8	44.3	0.31	0.54	2.95	4.92
MR grown *remod_act*	182.2	47.4	0.26	0.59	2.65	8.04
MR grown *noremod*	179.1	49.1	0.27	0.58	2.57	7.19

MR leads to a reduction of peak ventricular pressure and a widening of the pressure-volume relationship, without clear isovolumic phases. The regurgitant fraction is over $50\ \%$, hence a

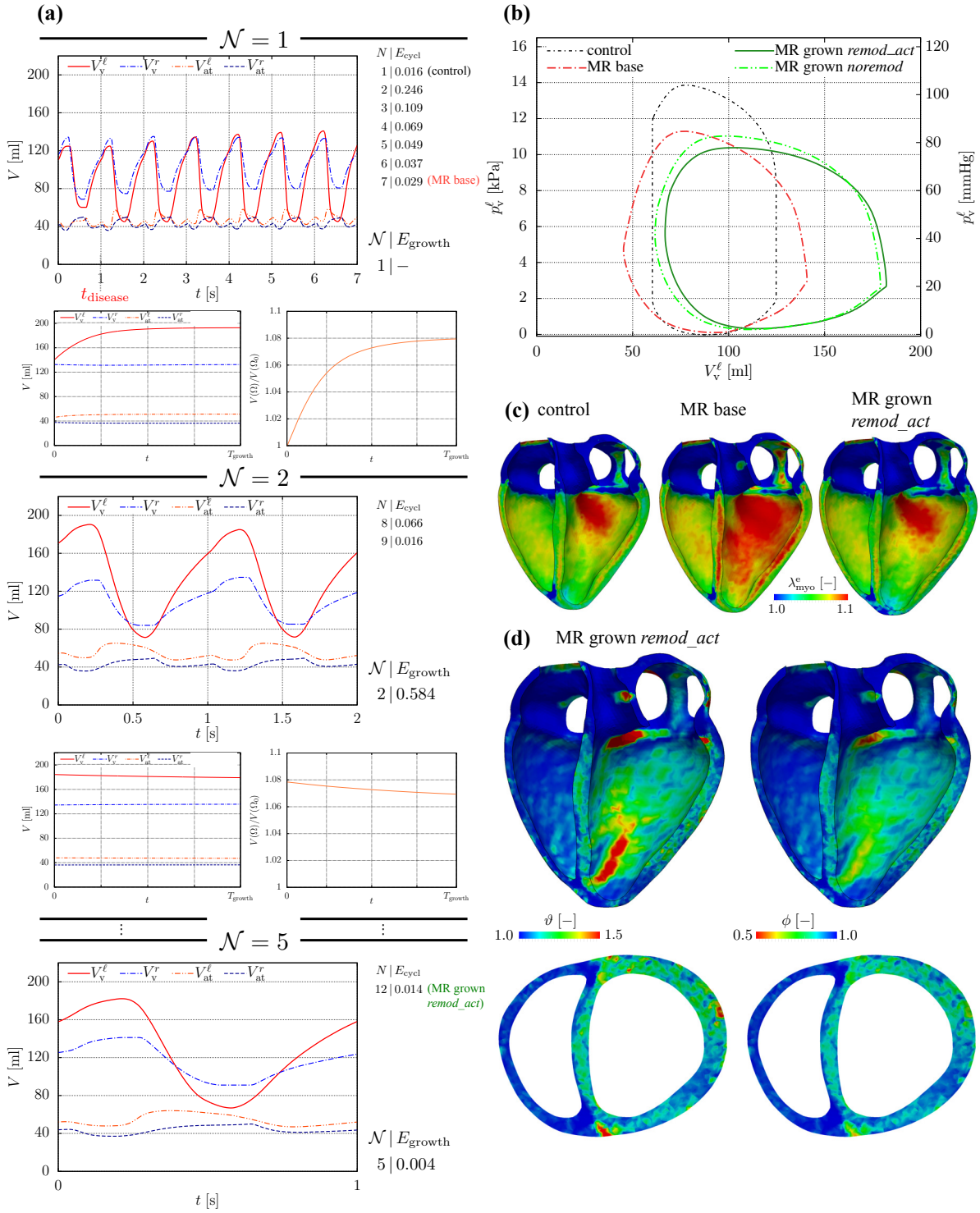

Figure 3.12: Model *3Datrioventr*$_{tet4\_2}$ | *0Dsyspulcap*: Multiscale volume-overload computation of eccentric growth after mitral regurgitation (MR). **(a)** Outer cycles $\mathcal{N}$, cavity volumes on small time scale (top plot), end-diastolic cavity volumes (bottom left plot) and relative myocardial wall volume change (bottom right plot) on large time scale. **(b)** Left-ventricular pressure-volume relationships: Control vs. MR base vs. MR grown *noremod* vs. MR grown *remod_act*. **(c)** End-diastolic elastic myofiber stretch $\lambda_{\text{myo}}^{\text{e}}$ (coronary cut view): Control vs. MR base vs. MR grown *remod_act*. **(d)** End-diastolic growth stretch ϑ and remodeling factor ϕ for MR grown *remod_act*.

significant part of stroke volume is not ejected into the aorta but back into the atrium. G&R leads to an increase in end-diastolic volume of $28\ \%$ (*remod_act*) and $27\ \%$ (*noremod*). Ejection fraction sinks significantly with acute MR and even more pronouncedly after G&R. As seen from fig. 3.12b, EDPVR virtually remains unaltered after acute MR with respect to control, however greatly decreases after G&R.

Left ventricular infarction A left ventricular apical infarction (AI) is induced by assuming a portion of the left ventricle located at the apex to be devoid of any contractile behavior, hence the contractility σ_0 in (2.99) is set to zero. Thus, its constitutive equation is identical to that of the grown matter. Per definition, the infarct region cannot grow.
Figure 3.13 shows the multiscale results for AI-induced volume overload resulting in eccentric ventricular hypertrophy. In fig. 3.13a, volume results per multiscale cycles $\mathcal{N}$ are shown: The respective top plot shows the small time scale cavity volumes for all four cardiac chambers, the bottom left plot the end-diastolic cavity volumes and the bottom right plot the relative wall volume change on the large time scale as consequence of eccentric growth. All three multiscale cycles ($\mathcal{N} = 1, 2, 3$) are shown. Small time scale cycles (N) and small time scale cycle errors (2.222) as well as the associated large scale error (2.253) are depicted next to the upper left plots of fig. 3.13a.
Figure 3.13b shows the pressure-volume relationships for the control state, the AI base state (homeostatic state after AI but prior to any G&R), and the converged grown state with active remodeling (*remod_act*) as well as without (*noremod*).
Figure 3.13c depicts the elastic myofiber stretch (2.237) on the end-diastolic configuration for the control, AI base and AI grown *remod_act* case. Finally, fig. 3.13d shows the growth stretch ϑ as well as the remodeling factor (2.247) on the end-diastolic configuration of the final AI grown *remod_act* state. Note that the infarct region a priori is assumed to behave as the diseased grown material but itself cannot grow, hence $\phi = 0$ and $\vartheta = 1$ in this region.

Left ventricular function indicators are listed in tab. 3.7.

Table 3.7: Left ventricular function indicators end-diastolic volume EDV^ℓ, stroke volume SV^ℓ, ejection fraction EF^ℓ, end-diastolic and end-systolic pressures EDP^ℓ and ESP^ℓ, respectively; for control, AI base, AI grown *remod_act* and AI grown *noremod* state

	EDV^ℓ [ml]	SV^ℓ [ml]	EF^ℓ [−]	EDP^ℓ [kPa]	ESP^ℓ [kPa]
control	124.7	64.1	0.51	1.83	11.9
AI base	135.5	57.4	0.42	2.52	10.7
AI grown *remod_act*	170.9	55.2	0.32	2.58	11.1
AI grown *noremod*	163.6	58.8	0.36	2.34	11.5

An apical infarction leads to a rightward shift in the pressure-volume curve. Stroke volume does not drop substantially after acute AI. G&R leads to an increase in end-diastolic volume of $26\ \%$ (*remod_act*) and $21\ \%$ (*noremod*). Ejection fraction drops with acute AI, and significantly more pronouncedly after G&R. EDPVR remains virtually unaltered.

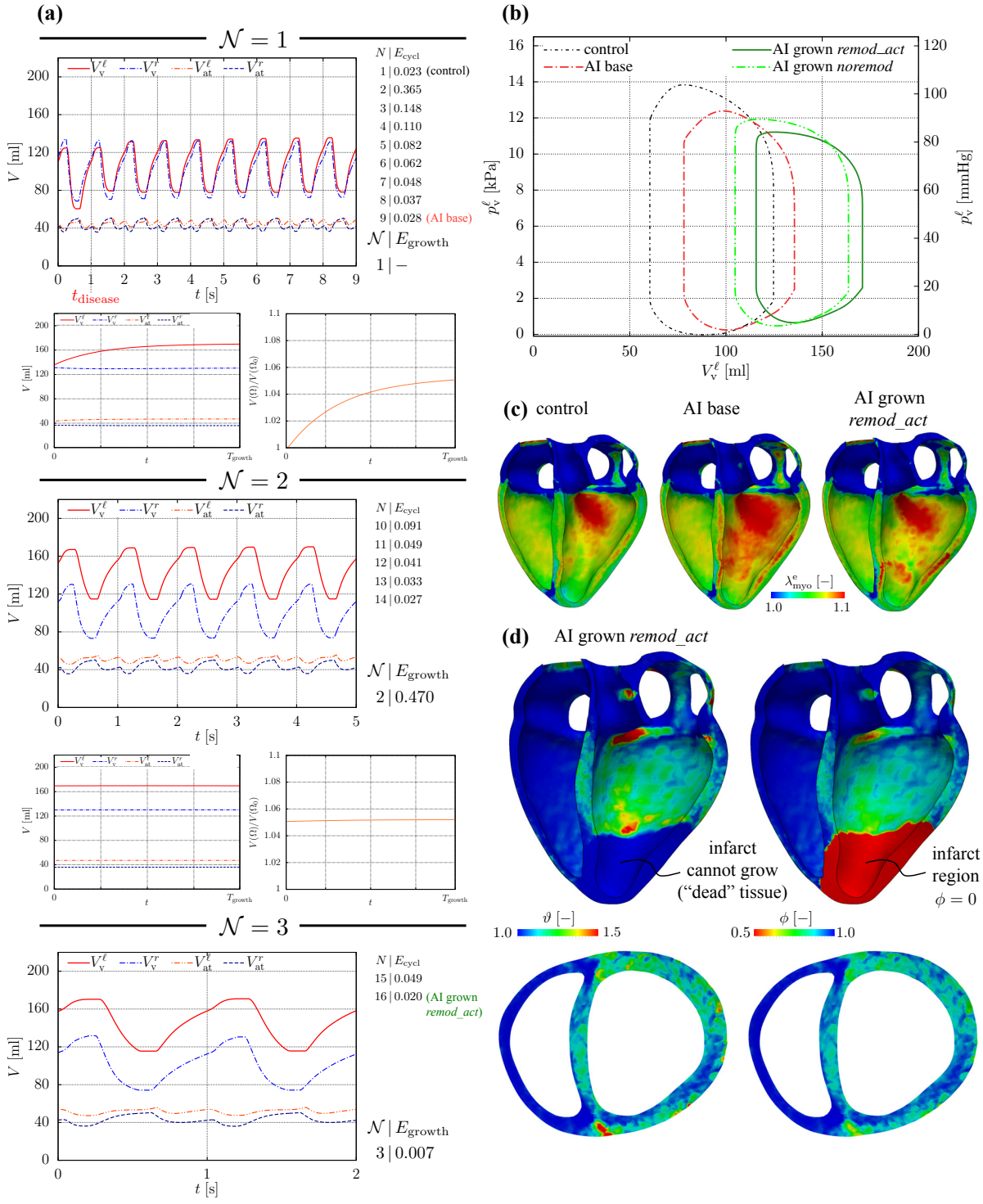

Figure 3.13: Model *3Datrioventr*$_{tet4\_2}$ | *0Dsyspulcap*: Multiscale volume-overload computation of eccentric growth after apical infarct (AI). **(a)** Outer cycles $\mathcal{N}$, cavity volumes on small time scale (top plot), end-diastolic cavity volumes (bottom left plot) and relative myocardial wall volume change (bottom right plot) on large time scale. **(b)** Left-ventricular pressure-volume relationships: Control vs. AI base vs. AI grown *noremod* vs. AI grown *remod_act*. **(c)** End-diastolic elastic myofiber stretch $\lambda_{\text{myo}}^{\text{e}}$ (coronary cut view): Control vs. AI base vs. AI grown *remod_act*. **(d)** End-diastolic growth stretch ϑ and remodeling factor ϕ for AI grown *remod_act*.

3.3.2.2 Pressure overload: Hypertrophic cardiomyopathy

A state of pressure overload is achieved by modeling of a stenosis of the aortic valve (AS). It is induced by setting the aortic valve's minimum resistance from its base value (cf. tab. 2.6) to $R_{\mathrm{v,out}}^{\ell,\mathrm{min}} = 5 \cdot 10^{-5}\ \frac{\mathrm{kPa \cdot s}}{\mathrm{mm}^3}$ after the first homeostatic cardiac cycle.
The remodeling of the portion of grown material here only shall affect the passive behavior (referred to as *remod_pas*), hence the constitutive equation for $\boldsymbol{S}^{\mathrm{e}}_{(grown)}$ in (2.246) is identical to (2.96), however the strain energy of the grown material is assumed to be a simple Neo-Hookean material of the form

$$\Psi^{\mathrm{remod}} = \frac{\mu^{\mathrm{remod}}}{2}(\bar{I}_C - 3) + \frac{\kappa^{\mathrm{remod}}}{2}(J-1)^2, \tag{3.57}$$

instead of (2.97). The shear and bulk moduli are set to $\mu^{\mathrm{remod}} = 60\ \mathrm{kPa}$ and $\kappa^{\mathrm{remod}} = 3000\ \mathrm{kPa}$, respectively. Again, comparisons to growth without remodeling are carried out (referred to as *noremod*).

Figure 3.14 shows the multiscale results for AS-induced pressure overload resulting in concentric ventricular hypertrophy. In fig. 3.14a, volume results per multiscale cycles $\mathcal{N}$ are shown: The respective top plot shows the small time scale cavity volumes for all four cardiac chambers, the bottom left plot the end-systolic cavity volumes and the bottom right plot the relative wall volume change on the large time scale as consequence of concentric growth. Only the first two multiscale cycles ($\mathcal{N} = 1$ and $\mathcal{N} = 2$) as well as the last one ($\mathcal{N} = 6$) are shown. Small time scale cycles (N) and small time scale cycle errors (2.222) as well as the associated large scale error (2.253) are depicted next to the upper left plots of fig. 3.14a.
Figure 3.14b shows the pressure-volume relationships for the control state, the AS base state (homeostatic state after AS but prior to any G&R), and the converged grown state with passive remodeling (*remod_pas*) as well as without (*noremod*).
Figure 3.14c depicts the elastic volumetric Mandel stress (2.227) on the end-systolic configuration for the control, AS base and AS grown *remod_pas* case. Finally, fig. 3.14d shows the growth stretch ϑ as well as the remodeling factor (2.248) on the end-systolic configuration of the final AS grown *remod_pas* state.

Left ventricular function indicators are listed in tab. 3.8.

Table 3.8: Left ventricular function indicators end-systolic volume ESV^ℓ, stroke volume SV^ℓ, ejection fraction EF^ℓ, end-diastolic and end-systolic pressures EDP^ℓ and ESP^ℓ, respectively; for control, AS base, AS grown *remod_pas* and AS grown *noremod* state

	ESV^ℓ [ml]	SV^ℓ [ml]	EF^ℓ [−]	EDP^ℓ [kPa]	ESP^ℓ [kPa]
control	60.6	64.1	0.51	1.83	11.9
AS base	96.3	52.1	0.35	3.58	19.1
AS grown *remod_pas*	88.0	42.8	0.33	3.76	14.1
AS grown *noremod*	97.2	50.1	0.34	3.86	18.0

A stenosis of the aortic valve leads to greatly increased end-systolic left ventricular pressures, accompanied by a rightward shift of the pressure-volume curve and secondary increase in end-

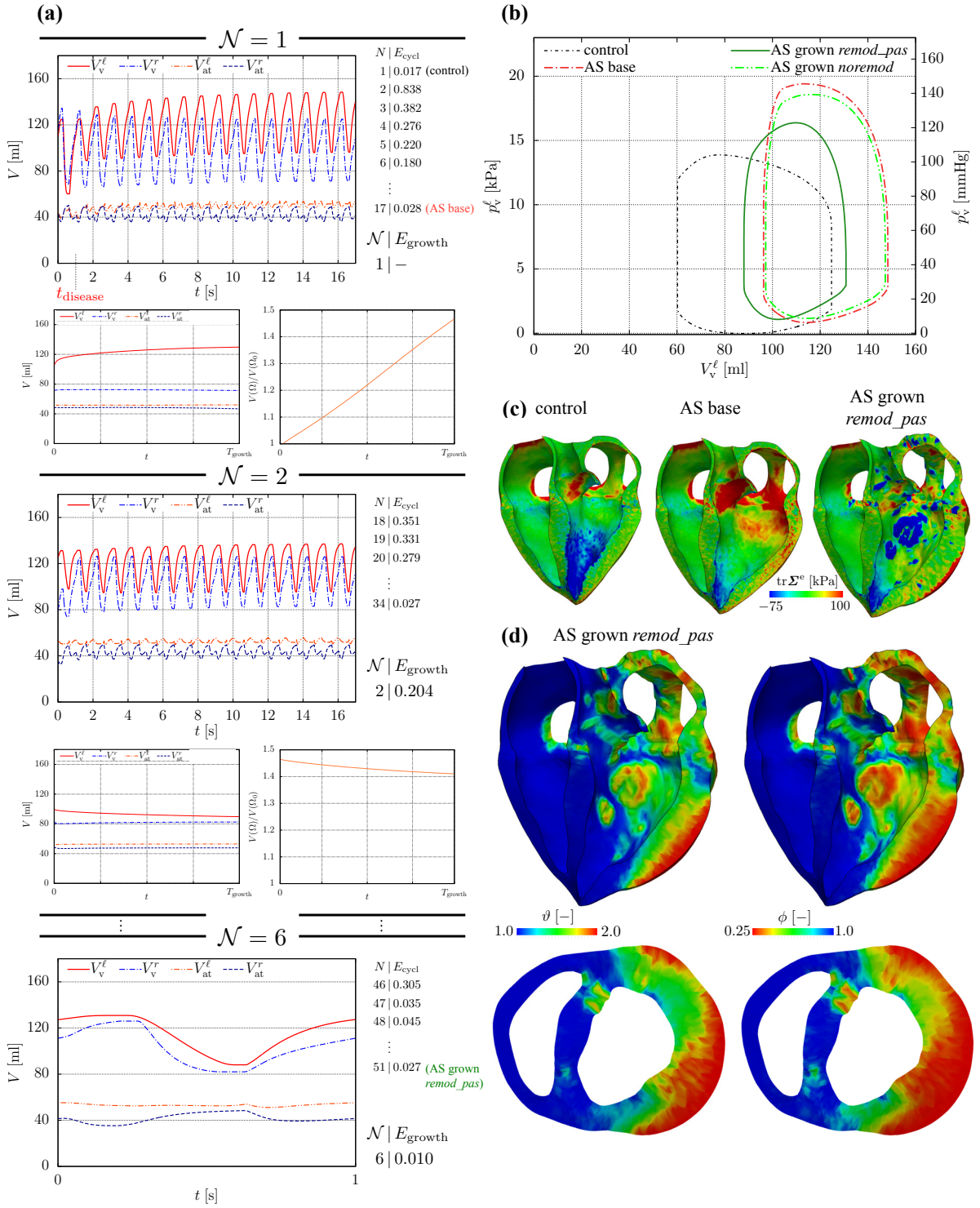

Figure 3.14: Model *3Datrioventr*$_{tet4\_2}$ | *0Dsyspulcap*: Multiscale pressure-overload computation of concentric growth after aortic valve stenosis (AS). **(a)** Outer cycles $\mathcal{N}$, cavity volumes on small time scale (top plot), end-systolic cavity volumes (bottom left plot) and relative myocardial wall volume change (bottom right plot) on large time scale. **(b)** Left-ventricular pressure-volume relationships: Control vs. AS base vs. AS grown *noremod* vs. AS grown *remod_pas*. **(c)** End-systolic elastic first invariant of Mandel stress $\text{tr}\,\boldsymbol{\Sigma}^{\text{e}}$ (coronary cut view): Control vs. AS base vs. AS grown *remod_pas*. **(d)** End-systolic growth stretch ϑ and remodeling factor ϕ for AS grown *remod_pas*.

diastolic volume and pressure. Ejection fraction drops due to acute AS but then remains nearly the same even after G&R has occurred, regardless of considering remodeling or not. EDPVR increases after G&R (*remod_pas*) but remains nearly unaltered for acute AS or when remodeling effects are not accounted for (*noremod*).

3.3.2.3 Reverse G&R after mitral valve repair

For demonstrative purposes, reverse G&R phenomena are simulated that eventually occur as consequence of a relief of the acute disease event. Here, the case of volume overload due to mitral regurgitation is considered, cf. sec. 3.3.2.1 and the results presented in fig. 3.12. After the final converged grown state ($\mathcal{N} = 5$), a mitral valve repair is performed by setting its maximum resistance back to its base value (cf. tab. 2.6). Two different reverse growth kinetics governed by the parameter τ_{rev} are considered: the base kinetics, cf. tab. 3.5, as well as accelerated kinetics by setting $\tau_{\mathrm{rev}} = 0.005 \cdot 10^6$ s (indicated by $\tau_{\mathrm{rev}} \downarrow$). Figure 3.15 shows the pressure-volume relationships for the control, the MR base and the MR grown (*remod_act*) state, as well as that grown state just after mitral valve repair (MR repair), and the same state after reverse growth has happened (MR reverse) – both for baseline (upper legend) and increased reverse growth kinetics (lower legend, $\tau_{\mathrm{rev}} \downarrow$).

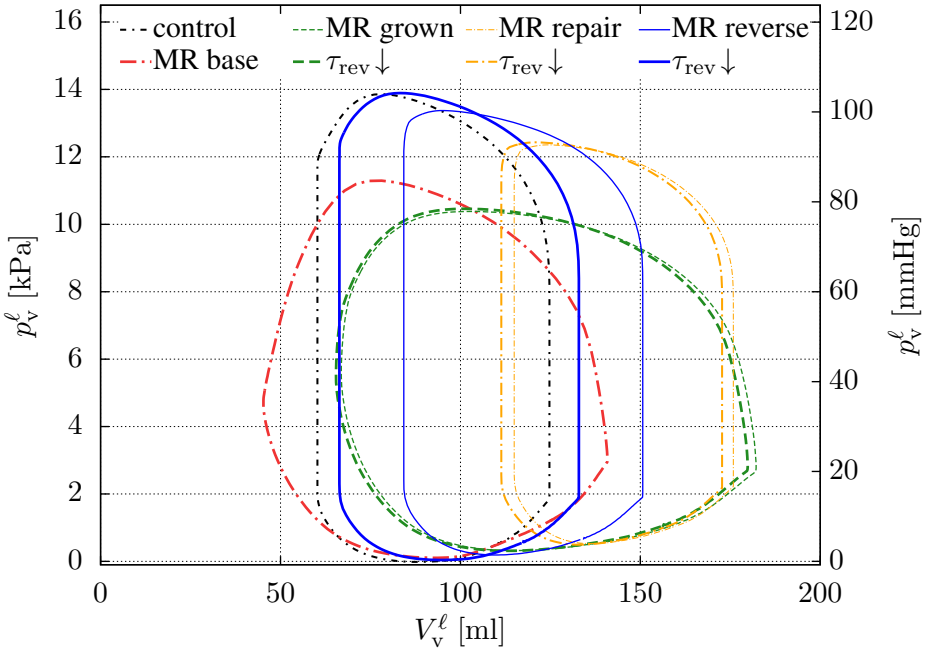

Figure 3.15: Left ventricular pressure-volume relationships for reverse G&R after mitral valve repair for two different reverse growth kinetics, base and reduced ($\tau_{\mathrm{rev}} \downarrow$): Comparison of control, MR base, MR grown, MR repair and MR reverse (each *remod_act*).

Reverse growth stagnates at some point using baseline reverse growth kinetics since changes per large time scale become negligible and fall below the chosen tolerance for (2.253). Increasing the kinetics by reducing τ_{rev} produces a more significant reversal of G&R phenomena, with the final pressure-volume relation approximating the original control state.

3.3.3 Discussion

The present approach for the first time incorporates a patient-specific 4-chamber heart model coupled to a closed circulatory system into a multiscale analysis of ventricular growth and remodeling (G&R) using acute disease events happening on a global integrated scale to trigger G&R phenomena on a local spatial scale. The multiscale-in-time strategy asserts continuity of all local mechanical quantities, hence the residual growth strains are preserved throughout the entire computation without the need to perform a relaxation of the grown state or to prescribe the growth stimulating force on integration point level.

To date, the only growth model for a patient-specific biventricular heart geometry coupled to a closed circuit system was presented by Kerckhoffs et al. [105]. Therein, comparable to here, stimulating disease events like mitral regurgitation and aortic stenosis are used to generate the respective overload scenarios, and a separation of time scales is performed for simulating cardiovascular and growth mechanics. In contrast to here, growth on the large time scale is prescribed as function of the deviation between baseline and disease strain values.
A further ventricular growth model that makes use of a separation of time scales is the one by Lee et al. [121], which additionally incorporates electromechanical effects. However, therein only a left ventricular geometry coupled to a single pre- and afterload 0D model is used, and volume overload is simply generated by modeling a myocardial infarction leading to myofiber overstretch in healthy tissue due to impaired contractile performance of the infarcted region. Due to the missing circulation, the model therein lacks of quantifying the (additional) volume overload that arises due to increased venous return as consequence of left ventricular malfunction. Additionally, the time scale separation therein relies on relaxing the residual growth stresses after each growth update of the geometry, which however might be a valid modeling assumption given that these residual stresses could play a minor role [156].
Other applications of growth models to ventricular geometries solely triggering growth by applying a prescribed load onto the ventricular endocardium are those by Göktepe et al. [73] (using strain- and stress-based growth laws for volume and pressure overload), Rausch et al. [167] using only stress-based growth laws for modeling of hypertension-induced growth, or Genet et al. [71] with strain-based growth models for both eccentric and concentric hypertrophy, the latter also making use of a patient-specific 4-chamber atrioventricular geometry. While the models from these contributions excellently demonstrate how growth affects ventricular shape change, they lack of linking global acute cardiovascular events to local maladaptive changes in ventricular tissue due to the missing cardio-circulatory coupling.
Furthermore, as stated by the review of Lee et al. [120], no cardiac volumetric growth model to date has truly incorporated effects of remodeling yet, even though the aforementioned publications often refer to their approaches as G&R models. Hence, to the best of the author's knowledge, this is the first contribution to link the growth stretch in some way to changes in tissue passive elastic or active properties.

The choice for end-diastolic strain as a stimulant for eccentric growth due to volume overload and end-systolic stress as the trigger for concentric growth due to pressure overload is reasonable and consistent with other established approaches [73]. However, Omens [155] primarily concludes that the stimulus for cardiac hypertrophy, be it stress or strain, is simply not profoundly known,

even though some evidence is stated that end-diastolic strain could be the stimulus for volume overload eccentric ventricular hypertrophy. Kerckhoffs et al. [105] use a strain-based growth law for modeling of both eccentric and concentric ventricular hypertrophy, also citing the work of Omens [155] that strain in general would be the more reasonable growth stimulus, which however is not stated to that clarity therein.
However, since volume overload happens at the end of the diastole where strains are highest and stresses are rather low, and to the contrary pressure overload occurs during systole where wall stresses are highest and myofiber tensile strains are virtually not present, strain as stimulant for eccentric and stress as that for concentric growth are readily reasoned.
It should be noted that the current implementation of the growth models only allows for computing *either* eccentric *or* concentric growth, hence both phenomena cannot be addressed. The remark in [105] that no a priori choice of the type of growth should be undertaken but that this choice is implicitly performed by the overload scenario certainly is valid. However, even though the aortic stenosis also produces a state of volume overload (cf. fig. 3.14b), it is assumed that the pressure overload is the more prominent driving factor for G&R and would reduce the end-diastolic myofiber strain (hence the volume overload) due to wall thickening.

The present results obtained from volume and pressure overload-induced cardiomyopathy simulations only allow for limited comparisons to experimental data since no associated studies on long-term maladaptive G&R progression were available for the specific porcine heart that is considered here. Provided a meaningful baseline state (cf. sec. 3.2.3.1) as well as the modeling of external G&R stimulants (valve diseases, myocardial infarction) to comply with physiological observations (cf. sec. 3.2.3.3), the modeling of G&R phenomena with the present approach is justified and allows for general observations and comparisons to textbook data.
Figure 3.16 depicts textbook pressure-volume loop sketches for systolic (fig. 3.16a) and diastolic (fig. 3.16b) dysfunction with respect to the control state.

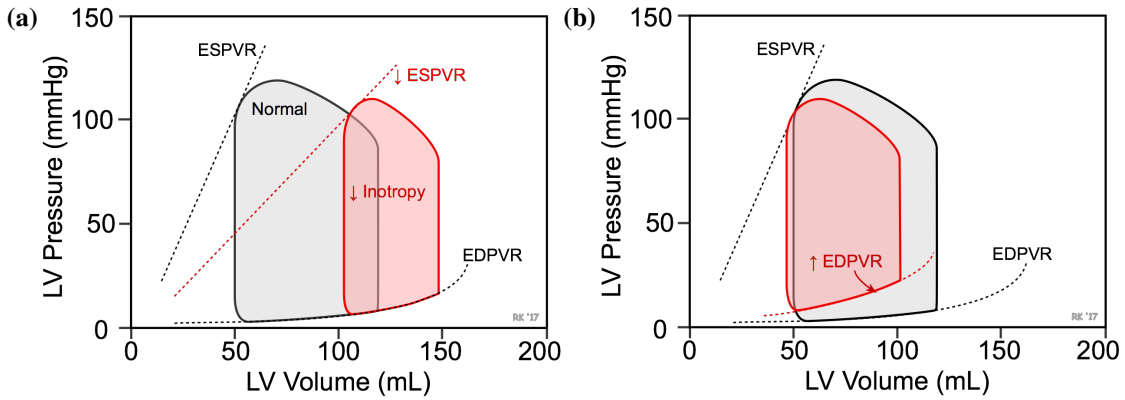

Figure 3.16: Textbook pressure-volume loop changes, taken from www.cvphysiology.com (with permission). **(a)** Pressure-volume loop change due to systolic dysfunction. **(b)** Pressure-volume loop change due to diastolic dysfunction.

Mitral regurgitation has been modeled by a change in closed-valve resistive properties. It leads to a regurgitation fraction comparable to what has been monitored with canine data ($56\ \% \pm 18\ \%$) by Dell'Italia et al. [50], cf. the results in tab. 3.6. The increase in end-diastolic volume here

is lower than reported in [50], however initial volumes are significantly different (factor 2) and hence not comparable.
Ventricular stiffness in terms of end-diastolic pressure-volume relationship (EDPVR) remains unaltered for acute MR and decreases for chronic MR as stated by Zile et al. [227], which is in good accordance to the results presented here. Furthermore, Zile et al. [227] state an increase in end-diastolic pressure for acute MR without a further increase for chronic MR, which also is in accordance with the results presented here. Further experimental studies on MR may be found in Young et al. [222].
The G&R-induced drop in ejection fraction is in accordance with typical syndromes of systolic heart failure [38]. The change in pressure-volume loop from the acute MR to the chronic MR case complies well with physiological observations, cf. fig. 3.12b and fig. 3.16a.

The myocardial infarction at the apex was modeled by deactivating the contractile performance of the apical region, even though more sophisticated infarction models including a distinct border zone as the one presented by Klepach et al. [108] or Lee et al. [121] may be considered. Here, the infarction leads to a volume overload due to an increased venous return as consequence of left ventricular malperformance. Even though stroke volume does not drop significantly after acute infarction, the volume overload stimulates G&R and finally ultimates in a significant drop in ejection fraction without a further remarkable decrease in stroke volume since the Frank-Starling mechanism tries to partly maintain cardiac output at higher preloads. As for the regurgitation case, the drop in ejection fraction complies with systolic heart failure syndromes [38].
Effects of left ventricular remodeling after myocardial infarction (MI) have been experimentally investigated, for instance, by Angeli et al. [5] in a swine model. Figure 3.17 (with permission from [5]) shows left ventricular pressure volume loops at baseline as well as one and six weeks after myocardial infarction in a swine model. Even though a 1:1 comparison due to the significantly different ventricular sizes is tedious, good qualitative agreement between fig. 3.13b and fig. 3.17 may be readily conceived – given the fact that no steps of calibration to any data have been performed so far. Similar agreements between fig. 3.13b and fig. 3.16a with regards to the trends of pressure-volume relationship changes can be stated.

A chronic aortic valve stenosis leads to a stiffened ventricle (higher EDPVR) with elevated end-diastolic pressure, cf. Yarbrough et al. [220] and Mistiaen [141]. Ejection fraction due to G&R remains virtually the same as for the acute aortic stenosis case, hence the typical preservation of ejection fraction for diastolic heart failure and hypertrophic cardiomyopathy may be confirmed [81], cf. also fig. 3.14b and fig. 3.16b.
G&R on the large time scale exhibits rapid myocardial wall volume increase without stagnation after T_{growth} has elapsed, cf. fig. 3.14a, bottom right plot of the $\mathcal{N} = 1$ section. A return to the small time scale however settles the growth kinetics for the subsequent cycle, where a slight correction in terms of a reduction in wall volume occurs (bottom right plot of fig. 3.14a in $\mathcal{N} = 2$ block) due to identical forward and reverse growth kinetics. Consequently, since small and large time scales are inherently coupled and mutually revisited until an outer convergence criterion (2.253) is met, the multiscale algorithm is supposed to be independent of the duration of T_{growth} provided the detectability of changes in terms of the given outer cycle tolerance. Hence, the fact that growth has not yet settled on the $\mathcal{N} = 1$ large time scale is of minor importance to the final grown settled state.

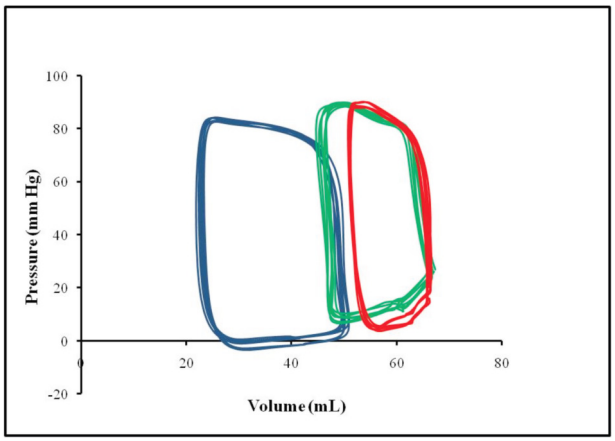

Figure 3.17: Left ventricular pressure-volume relationships in a swine model at baseline (blue, most left curve), one week after myocardial infarction (green curve, in the middle), and six weeks thereafter (red, right curve), taken from [5] (with permission).

Reverse G&R phenomena are computed straightforwardly by assuming a sudden acute reversal of mitral regurgitation, i.e. after a mitral valve repair. Reverse ventricular and atrial remodeling are well-recognized processes, and some studies investigated the association of these effects with mitral valve repair and improvements in mitral regurgitation [113, 194].
Here, different kinetics of reverse growth have been used: a scenario using the same time constant τ_{rev} as for the forward growth, and the same setting but with reduced reverse growth time constant, cf. fig. 3.15. In general, the growth laws used here are able to display asymptotic growth towards the upper stretch threshold and asymptotic decay of the accumulated plastic growth deformation towards the lower stretch threshold. Thus, a relief of the acute disease event, here performed by restoring native mitral valve function, naturally will lead to a reversal of the accumulated growth for $T_{\text{growth}} \to \infty$. However, true reverse growth kinetics are not certainly known, and are yet to be more reliably determined in order to assess and quantify the dynamics of reverse G&R when applying a certain treatment (valve repair, vascular assist device, other).

4 Parameter estimation and model order reduction for 3D-0D coupled cardiac dynamics

An indispensable task in modeling is the adequate choice of model parameters in order to obtain outcomes which are in accordance with the nature of the underlying physical problem. Most often, these model parameters emerge from measurements or other kind of data extracted from the "real-world problem" which is considered to be modeled, such as (elastic) material properties, geometric features or magnitudes of specific boundary conditions, for example.
A computational process which deals with a (rule-based) determination of model parameters on the basis of measurement samples is called *parameter estimation*. In general, only a subset of model parameters may be qualified for parameter estimation purposes, namely those sensitive to the underlying data, while others have to be chosen either as a result of reasonability considerations, well-educated guesses or general prominence, i.e. a priori knowledge (e.g., the elastic modulus of steel). The science that deals with the likelihood of model outcomes given the fact that (some) parameters are not sufficiently known is referred to as *uncertainty quantification*, which leaves the scope of this thesis.

In complex biological systems such as the cardiovascular system, inter- and intra-patient variability of conditions plays an ubiquitous role and calls for robust data-based parameter estimation processes in order to derive reliable computational models.
For models of the heart and the vascular system, loads of approaches for estimating diverse spatially resolved or lumped-parameters have been proposed in the literature to date. Amongst those there are models concentrating on the estimation of regionally varying properties of ventricular contractility, cf. Chabiniok et al. [34–36], Sainte-Marie et al. [178] or Marchesseau et al. [134], or approaches that also include the estimation of passive ventricular behavior, cf. Hadjicharalambous et al. [79] and Asner et al. [8] or Avazmohammadi et al. [10].

Here, parameter estimation for the 3D-0D coupled cardiovascular model as detailed in chap. 2 is considered. Novel procedures for parameter and initial condition estimation are proposed which rely on techniques from nonlinear optimization and model order reduction, hence basic aspects thereof are dealt with in the following section 4.1 in an introductory manner. Thereafter, the concept of model order reduction, for the first time, is applied in the context of 3D-0D coupled closed-loop cardiovascular dynamics problems, outlined in sec. 4.2. Then, the novel estimation methods are presented in sec. 4.3 and their results for a patient-specific porcine heart at different conditions of medication are outlined and discussed.

4.1 Fundamentals

4.1.1 Nonlinear unconstrained optimization

In the following, a very brief introduction to nonlinear optimization is given, focusing on the minimization problem of a scalar-valued objective function f depending on a vector of n_p variables (parameters) $\mathbf{x} = [x_1 \;\; x_2 \;\; \dots \;\; x_{n_\mathrm{p}}]^\mathrm{T}$ not subject to constraints. For a detailed in-depth treatment of various optimization techniques, the reader is referred to [158], for example.

The task is stated as

$$\min_{\mathbf{x}\in\mathbb{R}^{n_\mathrm{p}}} f(\mathbf{x}). \tag{4.1}$$

The function f is minimized by a set of "optimal" parameters $\mathbf{x}^\star$ if the gradient at that point vanishes and if its Hessian matrix is positive definite. Hence, the sufficient condition for a local minimum can be expressed as

$$\boldsymbol{\nabla} f(\mathbf{x}^\star) = \frac{\partial f}{\partial \mathbf{x}}(\mathbf{x}^\star) = \mathbf{0} \qquad \text{and} \qquad \boldsymbol{\nabla}^2 f(\mathbf{x}^\star) = \frac{\partial^2 f}{\partial \mathbf{x}\,\partial \mathbf{x}}(\mathbf{x}^\star) > \mathbf{0}. \tag{4.2}$$

For all optimization problems dealt with in this thesis, the objective function is nonlinear in the parameters and cannot be formulated as an analytical expression in terms of the parameter vector. Since a vast bunch of different techniques may be applied to find a stationary point fulfilling $(4.2)_1$, only techniques which are applied in the context of problem types addressed in this thesis are outlined. They are classified into algorithms which explicitly compute the gradient of the objective function, $\boldsymbol{\nabla} f$, and so-called *gradient-free* algorithms, which try to fulfill (4.2) in an approximate sense.

4.1.1.1 Gradient-based methods

A classical approach in order to find the minimizer $\mathbf{x}^\star$ of the objective function f is the *gradient-descent method*. It simply determines the search direction $\mathbf{s}$ as the negative gradient and updates the parameters $\mathbf{x}$ as a scaling along that direction:

$$\mathbf{s}^i = -\boldsymbol{\nabla} f(\mathbf{x}^i) \qquad \text{and} \qquad \mathbf{x}^{i+1} = \mathbf{x}^i + \alpha\,\mathbf{s}^i, \tag{4.3}$$

where $\alpha > 0$ should be determined by a *line search method* such that $f(\mathbf{x}^i + \alpha\,\mathbf{s}^i) \to \min$. The gradient-descent method may approach the "valley" region around the minimum fairly quickly but slows down as the slope decreases, potentially necessitating a significant amount of iterations to finally arrive at the stationary point if the valley is flat and long.

Alternatively, the stationary condition $(4.2)_1$ can be considered as a nonlinear system of equations to solve for the parameter vector $\mathbf{x}$. Hence, Newton's method, cf. sec. 3.1.3, may be applied, requiring the linearization of the gradient at the current estimate $\mathbf{x}^i$ which is nothing but the Hessian matrix $\boldsymbol{\nabla}^2 f$. Analogously to $(3.22)_2$ and (3.23), the Newton iteration and update rules for the optimization problem then yield

$$\boldsymbol{\nabla}^2 f(\mathbf{x}^i)\Delta\mathbf{x}^{i+1} = -\boldsymbol{\nabla} f(\mathbf{x}^i) \qquad \text{and} \qquad \mathbf{x}^{i+1} = \mathbf{x}^i + \Delta\mathbf{x}^{i+1}. \tag{4.4}$$

In contrast to many applications in nonlinear mechanics, where a system most often is at its equilibrium state (at rest) in the initial configuration, facilitating the task to find a neighboring state of equilibrium for Newton's method after a (sufficiently small) change in external conditions from one time step to the next, an initial guess to (4.4) most probably will be far away from the stationary point and out of scope of the convergence radius of a Newton-type strategy.
Hence, Newton's method for nonlinear optimization most often will have to be combined with globalization strategies such as line search methods in order to restrict the step lengths for points that do not lie within the region of convergence. Therefore, a parameter $\alpha < 1$ may be introduced that reduces the step according to

$$\Delta \mathbf{x}^{i+1} = -\alpha \left[\boldsymbol{\nabla}^2 f(\mathbf{x}^i) \right]^{-1} \boldsymbol{\nabla} f(\mathbf{x}^i). \tag{4.5}$$

In each iteration, α is found by help of a line search method such as Armijo's rule, for example. An algorithm with an iteration rule like (4.5) is also referred to as *damped* Newton method.

For optimization problems where f cannot be expressed as an analytical function of the parameters $\mathbf{x}$, the gradient $\boldsymbol{\nabla} f$ has to be computed in an approximate sense, i.e. with help of (forward) finite differences:

$$\begin{aligned} \boldsymbol{\nabla} f &= \left[\frac{\partial f}{\partial x_1} \quad \dots \quad \frac{\partial f}{\partial x_{n_\mathrm{p}}} \right]^\mathrm{T} \approx \\ &\approx \left[\frac{f(x_1 + \delta x_1, ..., x_{n_\mathrm{p}}) - f(x_1, ..., x_{n_\mathrm{p}})}{\delta x_1} \quad \dots \quad \frac{f(x_1, ..., x_{n_\mathrm{p}} + \delta x_{n_\mathrm{p}}) - f(x_1, ..., x_{n_\mathrm{p}})}{\delta x_{n_\mathrm{p}}} \right]^\mathrm{T}, \end{aligned} \tag{4.6}$$

where $\delta x_1, \dots, \delta x_{n_\mathrm{p}}$ are small perturbations of the respective parameters. In order to compute (4.6), the function f has to be evaluated $n_\mathrm{p} + 1$ times per iteration step of the optimization algorithm.
Additionally, when using a Newton-type scheme, the computation of the Hessian matrix $\boldsymbol{\nabla}^2 f$ with help of further finite differencing of (4.6) may become an infeasible task in terms of computational effort and accuracy, especially if a larger number of parameters is considered and the evaluation of the objective function itself is of non-negligible computational cost.
Thus, a bunch of approximate formulas has been developed comprising the class of *quasi-Newton methods*, which essentially approximate the inverse of the Hessian matrix in a suitable manner. One of the most popular schemes amongst this class is the *BFGS method*, named after the initials of its inventors (Broyden, Fletcher, Goldfarb, Shanno) [31, 60, 74, 187].

A special case of nonlinear optimization, a so-called *least-squares problem*, is present if the objective function can be expressed as

$$f(\mathbf{x}) = \frac{1}{2} \mathbf{w}(\mathbf{x})^\mathrm{T} \mathbf{w}(\mathbf{x}) \quad \equiv \quad \frac{1}{2} ||\mathbf{w}(\mathbf{x})||_2^2 \quad \equiv \quad \frac{1}{2} \sum_{i=1}^{m} w_i^2(\mathbf{x}), \tag{4.7}$$

with

$$\mathbf{w}(\mathbf{x}) = \left[w_1(\mathbf{x}) \quad \dots \quad w_m(\mathbf{x}) \right]^\mathrm{T} \quad = \quad \left[w_{\mathrm{r},1}(\mathbf{x}) - \tilde{w}_{\mathrm{r},1} \quad \dots \quad w_{\mathrm{r},m}(\mathbf{x}) - \tilde{w}_{\mathrm{r},m} \right]^\mathrm{T} \tag{4.8}$$

as the *least-squares residuals*. Objective functions of type (4.7) are classical formulations for data fitting purposes, where the deviation of a model value $w_{\mathrm{r},k}(\mathbf{x})$ to a respective "measurement" $\tilde{w}_{\mathrm{r},k}$ is intended to become as small as possible. The gradient of f then yields

$$\boldsymbol{\nabla} f = \frac{1}{2}\left(\frac{\partial \mathbf{w}}{\partial \mathbf{x}}\right)^{\mathrm{T}} \mathbf{w} + \frac{1}{2}\mathbf{w}^{\mathrm{T}}\frac{\partial \mathbf{w}}{\partial \mathbf{x}} = \left(\frac{\partial \mathbf{w}}{\partial \mathbf{x}}\right)^{\mathrm{T}} \mathbf{w} = \mathbf{J}^{\mathrm{T}}\mathbf{w}, \tag{4.9}$$

where the so-called *Jacobian matrix* is introduced, here approximated using forward finite differences:

$$\begin{aligned}\mathbf{J} = \frac{\partial \mathbf{w}}{\partial \mathbf{x}} &= \begin{bmatrix} \frac{\partial w_1}{\partial x_1} & \cdots & \frac{\partial w_1}{\partial x_{n_\mathrm{p}}} \\ \vdots & \ddots & \vdots \\ \frac{\partial w_m}{\partial x_1} & \cdots & \frac{\partial w_m}{\partial x_{n_\mathrm{p}}} \end{bmatrix} \approx \\ &\approx \begin{bmatrix} \frac{w_1(x_1+\delta x_1,\ldots,x_{n_\mathrm{p}})-w_1(x_1,\ldots,x_{n_\mathrm{p}})}{\delta x_1} & \cdots & \frac{w_1(x_1,\ldots,x_{n_\mathrm{p}}+\delta x_{n_\mathrm{p}})-w_1(x_1,\ldots,x_{n_\mathrm{p}})}{\delta x_{n_\mathrm{p}}} \\ \vdots & \ddots & \vdots \\ \frac{w_m(x_1+\delta x_1,\ldots,x_{n_\mathrm{p}})-w_m(x_1,\ldots,x_{n_\mathrm{p}})}{\delta x_1} & \cdots & \frac{w_m(x_1,\ldots,x_{n_\mathrm{p}}+\delta x_{n_\mathrm{p}})-w_m(x_1,\ldots,x_{n_\mathrm{p}})}{\delta x_{n_\mathrm{p}}} \end{bmatrix}. \end{aligned} \tag{4.10}$$

The Hessian matrix becomes

$$\boldsymbol{\nabla}^2 f = \mathbf{J}^{\mathrm{T}}\mathbf{J} + \sum_{i=1}^{m} w_i \boldsymbol{\nabla}^2 w_i. \tag{4.11}$$

In a region close to the minimum, the last term in (4.11) becomes small comparable to the first term, and its negligence leads to the so-called *Gauss-Newton algorithm*, with the iteration rule according to $(4.4)_1$:

$$\mathbf{J}^{i^{\mathrm{T}}}\mathbf{J}^i \Delta \mathbf{x}^{i+1} = -\mathbf{J}^{i^{\mathrm{T}}}\mathbf{w}^i. \tag{4.12}$$

A very popular and robust scheme for nonlinear least-squares problems is (4.12) equipped with a regularization technique, yielding the well-known *Levenberg-Marquardt algorithm* [124, 135]:

$$\left[\mathbf{J}^{i^{\mathrm{T}}}\mathbf{J}^i + \lambda^i \operatorname{diag}(\mathbf{J}^{i^{\mathrm{T}}}\mathbf{J}^i)\right] \Delta \mathbf{x}^{i+1} = -\mathbf{J}^{i^{\mathrm{T}}}\mathbf{w}^i. \tag{4.13}$$

If the regularization parameter $\lambda \to \infty$, (4.13) degenerates to a gradient-descent method (4.3), while the Gauss-Newton method (4.12) is recovered for $\lambda = 0$. Thus, the merits of both algorithms may be combined in (4.13) when initializing λ as sufficiently "large" and adapting its value to tend to zero when approaching the valley of the objective function.
There exists a bunch of adaptive methods for the Levenberg-Marquardt algorithm, e.g. in terms of a gradient norm scaling

$$\lambda^i := \lambda^{i-1}\frac{||\boldsymbol{\nabla} f^i||_\infty}{||\boldsymbol{\nabla} f^{i-1}||_\infty} \tag{4.14}$$

which will be used for least-squares problems dealt with in this thesis.

Finally, note that $m \geq n_\mathrm{p}$, i.e. the number of least-squares residuals m has to be greater or at least equal to the number of parameters n_p. Otherwise, the Gauss-Newton tangent $\mathbf{J}^{\mathrm{T}}\mathbf{J}$ becomes rank-deficient and the system of equations is underdetermined. If $m = n_\mathrm{p}$, the Jacobian is a square matrix and an "exact" solution fulfilling each least-squares residual can be obtained, since after left-multiplication of (4.12) with $\mathbf{J}^{-\mathrm{T}}$, a classical Newton method to find the root of $\mathbf{w}$ emerges. Thus, the minimum of the objective function is $f = 0$.

4.1.1.2 Gradient-free optimization: The Nelder-Mead simplex method

There exist cases in nonlinear unconstrained optimization where the computation of a gradient to the objective function in terms of finite differencing (4.6) does not provide a sufficient amount of accuracy or is of too great computational expense. Especially the former aspect is concomitant if the underlying forward model for evaluation of the objective function f captures non-smooth behavior, e.g. as a result of its discretization or inherent physics. One may think of an optimization problem where a change in parameters $\mathbf{x}$ has influence on the spatial discrete representation of the forward model, e.g. in structural shape optimization [208], where a tight link between the discrete model for analysis and its original geometric representation is needed. A specific application in the context of this thesis, cf. chap. 5, is the optimization of the location of pneumatic units for ventricular "compression" devices, where the inherently non-smooth situation of contact between two bodies (heart and implant) and its finite element discretization are not sufficiently sensitive with respect to a finite perturbation $\delta\mathbf{x}$ in the location parameters. A further discussion of this issue is carried out in sec. 5.4.
For these kinds of problem types, gradient-free methods may be an option of choice, amongst which the *Nelder-Mead simplex algorithm* [148] is a very popular one. Further progresses and algorithms of derivative-free optimization are discussed in [46].

The Nelder-Mead method, sometimes also known as (downhill) simplex method (not to be confused with the simplex method in linear programming), produces a convex hull of affinely independent vectors $\mathbf{x}_0, \ldots, \mathbf{x}_n \in \mathbb{R}^n$. Hence, $\mathbf{x}_1 - \mathbf{x}_0, \ldots, \mathbf{x}_n - \mathbf{x}_0$ are linearly independent. The simplex is denoted as

$$S = \left\{ \sum_{i=0}^{n} \lambda_i \, \mathbf{x}_i \,|\, \lambda_i \geq 0, \sum_{i=0}^{n} \lambda_i = 1 \right\}. \tag{4.15}$$

The algorithm is depicted in fig. 4.1 for two dimensions. After the initial simplex is defined, the objective function f is evaluated at each point, and the points are denoted according to their function value, $f(\mathbf{x}_{\max}) = \max\limits_{i=0,\ldots,n} f(\mathbf{x}_i)$ and $f(\mathbf{x}_{\min}) = \min\limits_{i=0,\ldots,n} f(\mathbf{x}_i)$, and then sorted such that $\mathbf{x}_{\max} = \mathbf{x}_0$.
First of all, the centroid $\hat{\mathbf{x}}$ of all points except the point with the maximum function value is calculated, which is the centroid of the resulting facet F:

$$\hat{\mathbf{x}} = \frac{1}{n} \sum_{i=1}^{n} \mathbf{x}_i = \frac{1}{n} \sum_{i=0}^{n} \left(\mathbf{x}_i - \mathbf{x}_{\max} \right). \tag{4.16}$$

The point with the maximum function value on the facet is denoted as $f(\mathbf{x}^F_{\max}) = \max\limits_{i=1,\ldots,n} f(\mathbf{x}_i)$.

The algorithm then starts finding a new simplex by a *reflection* of the point with the maximum function value along the facet:

$$\mathbf{x}_{\mathrm{ref}} = \hat{\mathbf{x}} + \gamma(\hat{\mathbf{x}} - \mathbf{x}_{\max}), \quad 0 < \gamma \leq 1. \tag{4.17}$$

Three cases then are distinguished:

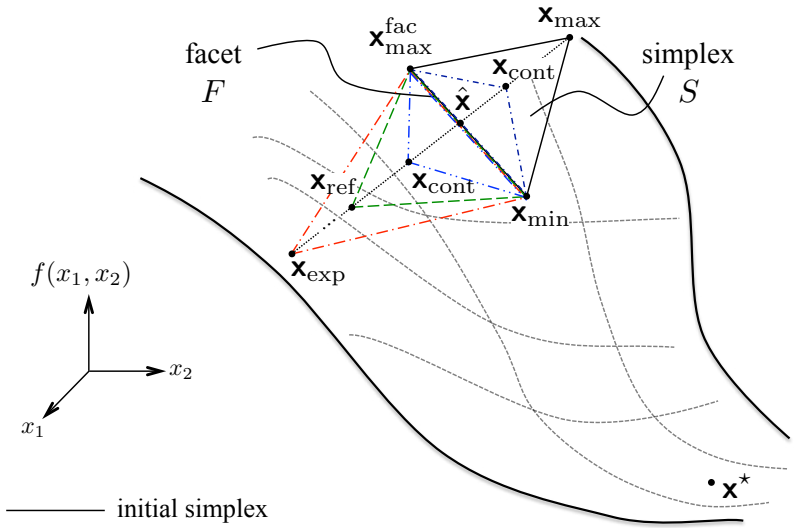

new simplex, if

- - - - - - $f(\mathbf{x}_{\min}) < f(\mathbf{x}_{\text{ref}}) < f(\mathbf{x}_{\max}^F)$ OR $f(\mathbf{x}_{\text{ref}}) < f(\mathbf{x}_{\min})$ and $f(\mathbf{x}_{\text{exp}}) > f(\mathbf{x}_{\text{ref}})$
- · - · - · $f(\mathbf{x}_{\text{ref}}) < f(\mathbf{x}_{\min})$ and $f(\mathbf{x}_{\text{exp}}) < f(\mathbf{x}_{\text{ref}})$
- - · - · - $f(\mathbf{x}_{\text{cont}}) < f(\mathbf{x}_{\max})$ and $f(\mathbf{x}_{\max}) > f(\mathbf{x}_{\text{ref}}) > f(\mathbf{x}_{\max}^F)$
- · · - · · $f(\mathbf{x}_{\text{cont}}) < f(\mathbf{x}_{\max})$ and $f(\mathbf{x}_{\text{ref}}) > f(\mathbf{x}_{\max})$

Figure 4.1: Visualization of the Nelder-Mead simplex method in $\mathbb{R}^2$.

- The reflection yields a point with minimum function value $f(\mathbf{x}_{\text{ref}}) < f(\mathbf{x}_{\min})$: Try an *expansion* in order to see if a further point along that direction produces an even lower function value,

$$\mathbf{x}_{\text{exp}} = \hat{\mathbf{x}} + \beta(\mathbf{x}_{\text{ref}} - \hat{\mathbf{x}}), \quad \beta > 1, \tag{4.18}$$

  and choose the new point according to

$$\mathbf{x}_{\text{new}} = \begin{cases} \mathbf{x}_{\text{exp}}, & \text{if } f(\mathbf{x}_{\text{exp}}) < f(\mathbf{x}_{\text{ref}}), \\ \mathbf{x}_{\text{ref}}, & \text{else.} \end{cases} \tag{4.19}$$

- The reflection yields a point with maximum function value $f(\mathbf{x}_{\text{ref}}) > f(\mathbf{x}_{\max}^F)$: A *contraction* is performed in order to find a closer point along that direction with lower function value,

$$\mathbf{x}_{\text{cont}} = \begin{cases} \hat{\mathbf{x}} + \alpha(\mathbf{x}_{\max} - \hat{\mathbf{x}}), & \text{if } f(\mathbf{x}_{\text{ref}}) > f(\mathbf{x}_{\max}), \\ \hat{\mathbf{x}} + \alpha(\mathbf{x}_{\text{ref}} - \hat{\mathbf{x}}), & \text{else,} \end{cases} \quad 0 < \alpha < 1. \tag{4.20}$$

  The new point is set either to the contracted one, or a total contraction is performed, where all corners of the simplex are re-set except of the one with minimum function value:

$$\begin{cases} \mathbf{x}_{\text{new}} = \mathbf{x}_{\text{cont}}, & \text{if } f(\mathbf{x}_{\text{cont}}) < f(\mathbf{x}_{\max}), \\ \mathbf{x}_{\text{new},i} = \frac{1}{2}\left(\mathbf{x}_i + \mathbf{x}_{\min}\right), \ i = 0, \ldots, n, & \text{else.} \end{cases} \tag{4.21}$$

- The reflection yields a point with medium function value $f(\mathbf{x}_{\min}) < f(\mathbf{x}_{\mathrm{ref}}) < f(\mathbf{x}^F_{\max})$, and the reflected point may be set as the new one:

$$\mathbf{x}_{\mathrm{new}} = \mathbf{x}_{\mathrm{ref}}. \tag{4.22}$$

Here, the algorithm is considered converged if

$$E_{\mathrm{fnorm}} = \sqrt{\sum_{i=0}^{n} \frac{\left(f(\mathbf{x}_i) - f(\mathbf{x}_{\min})\right)^2}{n}} \leq \epsilon_{\mathrm{f}}. \tag{4.23}$$

4.1.2 Projection-based model order reduction using proper orthogonal decomposition

A brief introduction to model order reduction methods using proper orthogonal decomposition (POD) is given. Model reduction strategies have widely been used in the scientific computing and engineering community due to the impelling demand for in-time solutions of parameterized (initial) boundary value problems while maintaining an acceptable accuracy for the problem at hand [83, 166].
Here, POD-based model order reduction strategies applied in the context of nonlinear finite element-discretized structural dynamics problems are considered. A recent contribution for these specific applications is the one by Farhat et al. [59], with specific applications to contact mechanics in [13]. Further applications, e.g. to blood flow or aeroelastic problems, are given by [4, 133]. A general overview of POD methods with applications to engineering problems is given by Liang et al. [125, 126].

The process of model order reduction-based computing comprises an *offline phase* during which one or multiple parametric instances of the full, subsequently called *high-dimensional model* (HDM) are computed in order to generate a reduced-order basis (ROB), and an *online phase* during which the reduced-order model (ROM) is solved. The ROM thereby is generated by projecting the HDM to a lower dimensional subspace spanned by the ROB. In general, a ROM is used in order to assess new parametric configurations for which no HDM solution is given – in a fraction of the time that would be needed to solve the HDM. Depending on the problem, multiple offline phases may be required in order to recompute or update the ROB if the interpolatory abilities of the ROM are loosened.

The central part of POD-based model reduction is the collection of snapshots from the solution of the underlying high-dimensional problem. These may be static solutions of multiple parametric realizations of the HDM, or the HDM solution of a dynamic problem at different instances in time.
Here, for transient nonlinear structural dynamics problems, the time-dependent discrete displacement vector $\mathbf{d}(t)$ of the finite element- and finite difference-discretized HDM is used as snapshot quantity. Hence, at n_{snap} discrete instances in time, the solution is stored into the snapshot matrix $\hat{\mathbf{S}} \in \mathbb{R}^{n_{\mathrm{dof}} \times n_{\mathrm{snap}}}$:

$$\hat{\mathbf{S}} = \begin{bmatrix} \mathbf{d}_1 & \dots & \mathbf{d}_{n_{\mathrm{snap}}} \end{bmatrix}, \tag{4.24}$$

where n_{dof} is the number of degrees of freedom of the underlying discretized HDM. The snapshot matrix (4.24) here has full column rank.

Now, a proper orthonormal basis, the so-called POD basis of rank r_{b} for the set of snapshots spanned by the n_{snap} snapshot vectors is searched. However, instead of forming the symmetric matrix $\hat{\mathbf{D}} \in \mathbb{R}^{n_{\mathrm{dof}} \times n_{\mathrm{dof}}}$,

$$\hat{\mathbf{D}} = \hat{\mathbf{S}}\hat{\mathbf{S}}^{\mathrm{T}}, \tag{4.25}$$

which still is large since n_{dof} is large, the symmetric covariance matrix $\hat{\mathbf{C}} \in \mathbb{R}^{n_{\mathrm{snap}} \times n_{\mathrm{snap}}}$ of significantly smaller dimension (provided $n_{\mathrm{snap}} \ll n_{\mathrm{dof}}$),

$$\hat{\mathbf{C}} = \hat{\mathbf{S}}^{\mathrm{T}}\hat{\mathbf{S}}, \tag{4.26}$$

is used to solve the eigenvalue problem

$$\hat{\mathbf{C}}\,\boldsymbol{\psi}_j = \lambda_j\,\boldsymbol{\psi}_j, \quad j = 1, \ldots, n_{\mathrm{snap}}, \tag{4.27}$$

since the non-zero eigenvalues of $\hat{\mathbf{D}}$ are the same as those of $\hat{\mathbf{C}}$. The covariance matrix $\hat{\mathbf{C}}$ is symmetric and positive-semidefinite, hence its eigenvalues all are real and positive.

If $\mathrm{rank}(\hat{\mathbf{C}}) = r_{\mathrm{b}}$, then the first r_{b} POD modes are

$$\boldsymbol{\phi}_j = \frac{1}{\sqrt{\lambda_j}}\hat{\mathbf{S}}\boldsymbol{\psi}_j, \quad j = 1, \ldots, r_{\mathrm{b}}. \tag{4.28}$$

Let the eigenvectors of $\hat{\mathbf{D}}$ and $\hat{\mathbf{C}}$ be

$$\boldsymbol{\Phi} = \begin{bmatrix} \boldsymbol{\phi}_1 & \ldots & \boldsymbol{\phi}_{r_{\mathrm{b}}} \end{bmatrix} \quad \text{and} \quad \boldsymbol{\Psi} = \begin{bmatrix} \boldsymbol{\psi}_1 & \ldots & \boldsymbol{\psi}_{r_{\mathrm{b}}} \end{bmatrix}, \tag{4.29}$$

respectively, with the property

$$\boldsymbol{\Psi}^{\mathrm{T}}\boldsymbol{\Psi} = \mathbf{1}_{r_{\mathrm{b}}}. \tag{4.30}$$

Consequently, $\boldsymbol{\Phi}$ may be written as

$$\boldsymbol{\Phi} = \hat{\mathbf{S}}\boldsymbol{\Psi}\boldsymbol{\Lambda}^{-\frac{1}{2}}, \tag{4.31}$$

with the diagonal matrix of eigenvalues

$$\boldsymbol{\Lambda} = \begin{bmatrix} \lambda_1 & & (0) \\ & \ddots & \\ (0) & & \lambda_{r_{\mathrm{b}}} \end{bmatrix}. \tag{4.32}$$

The columns of $\boldsymbol{\Phi}$ are eigenvectors of $\hat{\mathbf{D}}$ ordered by decreasing eigenvalues, since

$$\boldsymbol{\Phi}^{\mathrm{T}}\hat{\mathbf{D}}\boldsymbol{\Phi} = \boldsymbol{\Psi}^{\mathrm{T}}\hat{\mathbf{C}}\boldsymbol{\Psi} = \boldsymbol{\Lambda}. \tag{4.33}$$

The optimal orthogonal basis of size $k \leq r_{\mathrm{b}}$ then is

$$\mathbf{V} = \begin{bmatrix} \boldsymbol{\Phi}_k & \boldsymbol{\Phi}_{r_{\mathrm{b}}-k} \end{bmatrix} \begin{bmatrix} \mathbf{1}_k \\ \mathbf{0} \end{bmatrix}. \tag{4.34}$$

Here, the model reduction process entirely operates at the fully discrete level, performing the dimensional reduction on the linearized system of equations $(3.22)_2$ yielding a reduced system

$$\mathbf{V}^{\mathrm{T}}\mathbf{K}_{n+1}^{i}\mathbf{V}\,\Delta\tilde{\mathbf{d}}_{n+1}^{i+1} = -\mathbf{V}^{\mathrm{T}}\mathbf{r}_{n+1}^{i} \tag{4.35}$$

which has to be solved for the reduced displacement increment $\Delta\tilde{\mathbf{d}}_{n+1}^{i+1}$ in every Newton iteration i. After each performed reduced linear solution of (4.35), the full displacement increment vector is reconstructed,

$$\Delta\mathbf{d}_{n+1}^{i+1} = \mathbf{V}\,\Delta\tilde{\mathbf{d}}_{n+1}^{i+1}, \tag{4.36}$$

and then updated according to (3.23). The termination criterion however is not (3.24) but

$$||\mathbf{V}^{\mathrm{T}}\mathbf{r}(\mathbf{d}_{n+1}^{i})||_2 \leq \epsilon_{\mathrm{res}} \quad \text{and} \quad ||\Delta\tilde{\mathbf{d}}_{n+1}^{i+1}||_2 \leq \epsilon_{\mathrm{incr}}. \tag{4.37}$$

4.2 3D-0D coupled model order reduction

The presented model order reduction techniques are applied to the 3D-0D coupled cardiovascular mechanics problem, performing the reduction on the 3D heart without changing the 0D governing equations. These techniques for the first time are applied in the context of modeling the heart and the circulatory system, however already have been applied to a 3D-0D coupled problem in the thesis of [116]. Therein, a heart coupled to single 0D pre- and afterload models is employed, using the 3D-0D framework that has been developed and implemented here. Furthermore, model reduction techniques applied to pure solid mechanics models of the heart have been presented, for instance, in [164].

The reduced linear system of equations is presented in sec. 4.2.1, and exemplary results as well as error estimates are shown in sec. 4.2.2. The results are briefly discussed in sec. 4.2.3.

4.2.1 Linear reduced monolithic system of equations

Model order reduction for the 3D-0D coupled problem addresses the computationally demanding 3D solid mechanics description of the heart. Therefore, the linearized 3D-0D coupled system of equations (3.34) is reduced according to (4.35) and reads

$$\begin{bmatrix} \mathbf{V}^{\mathrm{T}}\mathbf{K}^{\mathrm{S}}\mathbf{V} & \mathbf{V}^{\mathrm{T}}\mathbf{K}^{\mathrm{S,0D}} \\ \mathbf{K}^{\mathrm{0D,S}}\mathbf{V} & \mathbf{K}^{\mathrm{0D}} \end{bmatrix}_{n+1}^{i} \begin{bmatrix} \Delta\tilde{\mathbf{d}} \\ \Delta\mathbf{p} \end{bmatrix}_{n+1}^{i+1} = - \begin{bmatrix} \mathbf{V}^{\mathrm{T}}\mathbf{r}^{\mathrm{S}} \\ \mathbf{r}^{\mathrm{0D}} \end{bmatrix}_{n+1}^{i}, \tag{4.38}$$

with the recovered full displacement increment (4.36) and the reduced-order basis (4.34). It has to be solved for $\Delta\tilde{\mathbf{d}}_{n+1}^{i+1}$ and $\Delta\mathbf{p}_{n+1}^{i+1}$ prior to updating according to (3.35) until (4.37), $(3.37)_3$ and $(3.37)_4$.

The respective reduction of (3.34) yielding (4.38) is implemented into the 3D-0D monolithic solution framework that itself has been implemented into the in-house multi-physics finite element software package Baci [207]. For the sake of computational efficiency, the reduced-order basis

(4.34) is stored as an *Epetra multi-vector* [82] such that the cost for matrix-matrix or matrix-vector products required to construct (4.38) is minimized.
The reduced system then can be solved with a direct linear solver (e.g. UMFPACK [48]) instead of the 2×2 block-preconditioned GMRES (chap. 3, sec. 3.2.2).

In order to quantify the performance of the reduced order model, the a-posteriori error estimate

$$||\mathbf{r}^{\mathrm{S}}(\mathbf{V}\,\tilde{\mathbf{d}}_{n+1}^{i+1})||_2 \tag{4.39}$$

is used. Hence, the quality of the ROM is simply measured in terms of the full structural residual 2-norm evaluated with the reconstructed full displacement vector at the end of each time step.

4.2.2 Exemplary results and error estimations

A couple of numerical examples are presented and the performance of the ROM under varying sizes of the reduced-order basis (ROB) (4.34), different amounts of snapshots (4.24), a reduction in time steps, and at changed parametric configurations is presented.

As high-dimensional model (HDM), *3Dventr*$_{\textit{tet4\_1}}$ | *0Dsyspul* is used, specifically the standard conditions presented in sec. 3.2.3.1, fig. 3.2. The discretization (*tet4_1*) is presented in appendix A.1.1.1 (fig. A.1). The HDM problem is solved on $n_{\mathrm{core}} = 112$ Xeon Haswell cores with $n_{\mathrm{step}} = 500$ time steps for one cardiac cycle, and the displacement vector at each time step is saved. Hence, a maximum of $n_{\mathrm{snap}} = 500$ snapshots (displacement states) for the computation of the ROB can be used, with the maximum theoretical number of reduced-basis vectors $r_{\mathrm{b}} = n_{\mathrm{snap}}$. For all ROM computations, the same amount of $n_{\mathrm{core}} = 112$ Xeon Haswell cores is used even though the direct linear solve operation is performed by UMFPACK in serial. However, besides the linear solve, a great amount of computational effort lies in the construction of (4.38) and the residual evaluations that are performed on the full-sized vector. Hence, all operations that happen outside of the linear solve routine are as expensive as for the HDM, with even additional costs due to the matrix-matrix and matrix-vector products for the reductional and displacement increment reconstruction process.

Figure 4.2 shows the performance of the ROM under a varying number of reduced-basis vectors. Each time, all available snapshots are used, and the number of time steps is fixed to $n_{\mathrm{step}} = 500$ for all computations. The left and right ventricular pressure-volume relations are shown in fig. 4.2a and 4.2b, respectively, and the left and right ventricular volumes over time in fig. 4.2c and 4.2d, respectively. The ROM error (4.39) over time is shown in fig. 4.2e, and fig. 4.2f depicts the overall wall time t_{wall} for the transient computation of the single cardiac cycle.[1] This time measures the start of the solution process (no setup) to final program termination, including the proper orthogonal decomposition (POD) solving (4.27) at the very beginning. Prestressing, which is performed as an extra computation prior to the transient simulations, is not included in t_{wall}.

[1] Since the homeostatic state initial conditions from the previously computed problem from sec. 3.2.3.1 are used, the cycle error (2.222) most often is fulfilled by the ROMs.

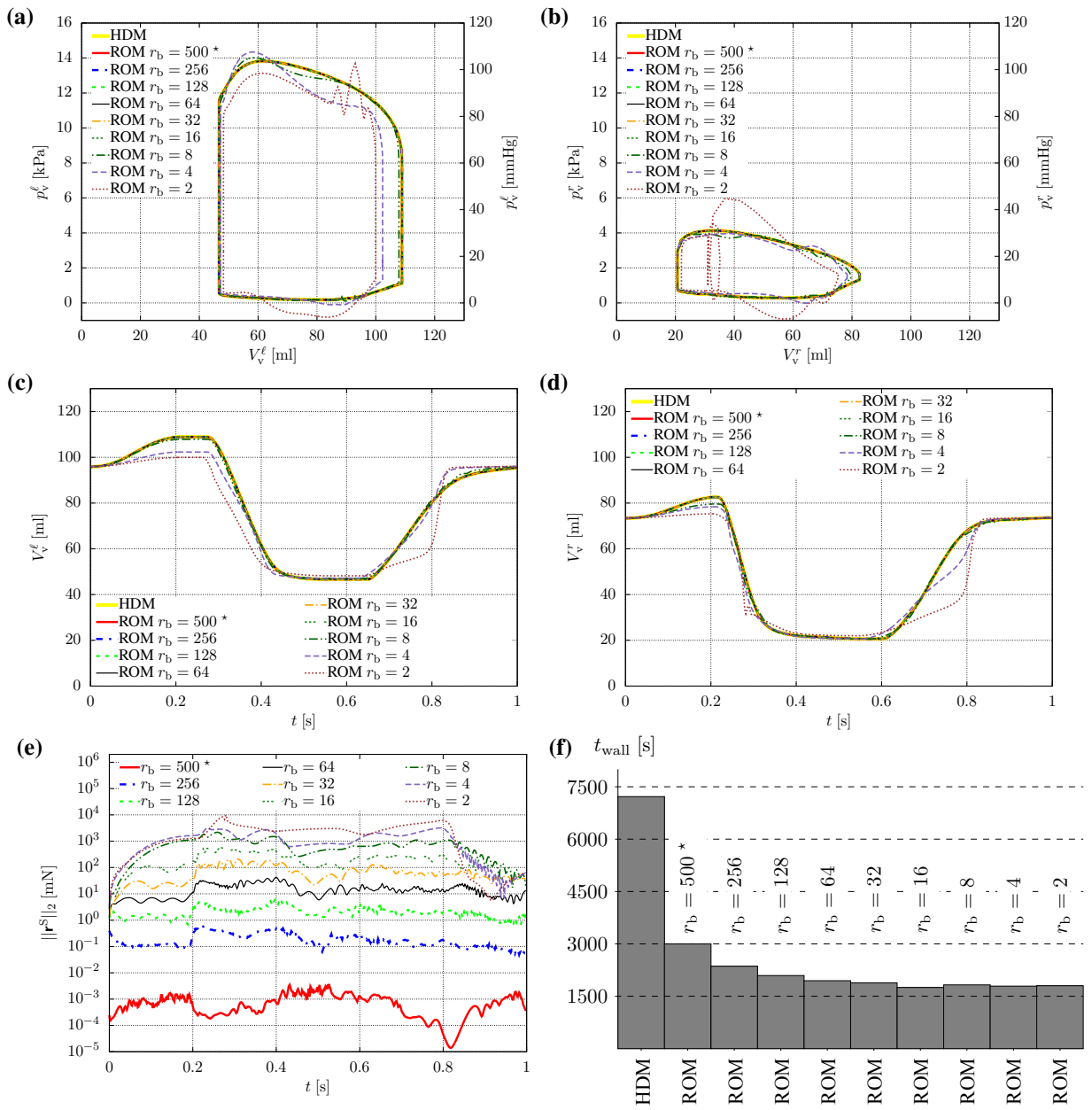

Figure 4.2: Model *3Dventr$_{tet4_1}$ | 0Dsyspul*: Performance of ROM under varying number of reduced-basis vectors r_b, using all snapshots ($n_{snap} = 500$). ⋆: not all 500 but only 486 reduced-basis vectors considered due to round-off errors. **(a)** Left ventricular pressure-volume relation. **(b)** Right ventricular pressure-volume relation. **(c)** Left ventricular volume over time. **(d)** Right ventricular volume over time. **(e)** ROM error $||\mathbf{r}^S||_2$ over time. **(f)** Total wall time for transient computation (one cardiac cycle, prestressing excluded).

Table 4.1 depicts relative stroke work errors for both the left and the right ventricle as well as the time step-averaged ROM error (4.39) with respect to the HDM for the case of varying numbers of reduced-basis vectors r_b.

Table 4.1: Relative errors in left ($i = \ell$) and right ($i = r$) ventricular stroke work $|\mathrm{SW}^i_\mathrm{ROM} - \mathrm{SW}^i_\mathrm{HDM}|/\mathrm{SW}^i_\mathrm{HDM}$ for the ROM with respect to the HDM, as well as time step-averaged ROM error $\varnothing||\mathbf{r}^\mathrm{S}||_2$ [mN], for varying number of reduced-basis vectors r_b using all $n_\mathrm{snap} = 500$ snapshots (*: not all 500 but only 486 reduced-basis vectors considered due to round-off errors)

r_b	$500^\star$	256	128	64	32	16	8	4	2
$\lvert\mathrm{SW}^\ell_\mathrm{ROM} - \mathrm{SW}^\ell_\mathrm{HDM}\rvert/\mathrm{SW}^\ell_\mathrm{HDM}$	0.00	$3.00 \cdot 10^{-5}$	$3.00 \cdot 10^{-5}$	$2.60 \cdot 10^{-4}$	$8.50 \cdot 10^{-4}$	$2.10 \cdot 10^{-4}$	$2.53 \cdot 10^{-2}$	0.13	0.17
$\lvert\mathrm{SW}^r_\mathrm{ROM} - \mathrm{SW}^r_\mathrm{HDM}\rvert/\mathrm{SW}^r_\mathrm{HDM}$	0.00	$3.00 \cdot 10^{-5}$	$5.00 \cdot 10^{-5}$	$1.00 \cdot 10^{-4}$	$7.00 \cdot 10^{-4}$	$4.12 \cdot 10^{-3}$	$6.41 \cdot 10^{-2}$	$8.01 \cdot 10^{-2}$	0.21
$\varnothing\|\|\mathbf{r}^\mathrm{S}\|\|_2$ [mN]	$8.34 \cdot 10^{-4}$	0.20	2.14	$1.50 \cdot 10^{1}$	$6.89 \cdot 10^{1}$	$2.04 \cdot 10^{2}$	$7.04 \cdot 10^{2}$	$1.27 \cdot 10^{3}$	$2.30 \cdot 10^{3}$

Figure 4.3 shows the ROM solutions for varying number of snapshots n_snap. Every $(500/n_\mathrm{snap})$th snapshot is taken, each time however using all available $r_\mathrm{b} = n_\mathrm{snap}$ reduced-basis vectors. Left and right ventricular pressure-volume relationships are shown in fig. 4.3a and fig. 4.3b, respectively. The ROM error is plotted in fig. 4.3c.

Table 4.2 depicts relative stroke work errors for both the left and the right ventricle as well as the time step-averaged ROM error (4.39) with respect to the HDM for the case of varying numbers of snapshots n_snap.

Table 4.2: Relative errors in left ($i = \ell$) and right ($i = r$) ventricular stroke work $|\mathrm{SW}^i_\mathrm{ROM} - \mathrm{SW}^i_\mathrm{HDM}|/\mathrm{SW}^i_\mathrm{HDM}$ for the ROM with respect to the HDM, for varying number of snapshots n_snap (only every $(500/n_\mathrm{snap})$th snapshot taken) using all $r_\mathrm{b} = n_\mathrm{snap}$ reduced-basis vectors

n_snap	250	100	50	25	10	5
$\lvert\mathrm{SW}^\ell_\mathrm{ROM} - \mathrm{SW}^\ell_\mathrm{HDM}\rvert/\mathrm{SW}^\ell_\mathrm{HDM}$	$3.00 \cdot 10^{-5}$	$3.00 \cdot 10^{-5}$	$5.00 \cdot 10^{-5}$	$4.30 \cdot 10^{-4}$	$1.71 \cdot 10^{-3}$	0.11
$\lvert\mathrm{SW}^r_\mathrm{ROM} - \mathrm{SW}^r_\mathrm{HDM}\rvert/\mathrm{SW}^r_\mathrm{HDM}$	$3.00 \cdot 10^{-5}$	$8.00 \cdot 10^{-5}$	$2.00 \cdot 10^{-4}$	$3.34 \cdot 10^{-3}$	0.15	0.23
$\varnothing\|\|\mathbf{r}^\mathrm{S}\|\|_2$ [mN]	0.88	9.26	$3.72 \cdot 10^{1}$	$1.53 \cdot 10^{2}$	$5.63 \cdot 10^{2}$	$2.02 \cdot 10^{3}$

Figure 4.4 depicts the performance of the ROM under varying number of time steps n_step. All reduced-basis vectors and all snapshots are used. Left and right ventricular pressure-volume loops are depicted in fig. 4.4a and fig. 4.4b, respectively, and the ROM error is shown in fig. 4.4c. The wall times are depicted in fig. 4.4d. ROMs are always generated from the HDM with $n_\mathrm{step} = 500$ time steps. The HDM does not allow a further reduction of time steps than 250, however the ROM can handle significantly larger steps.

Table 4.3 depicts relative stroke work errors for both the left and the right ventricle as well as the time step-averaged ROM error (4.39) with respect to the HDM for the case of varying numbers of time steps n_step.

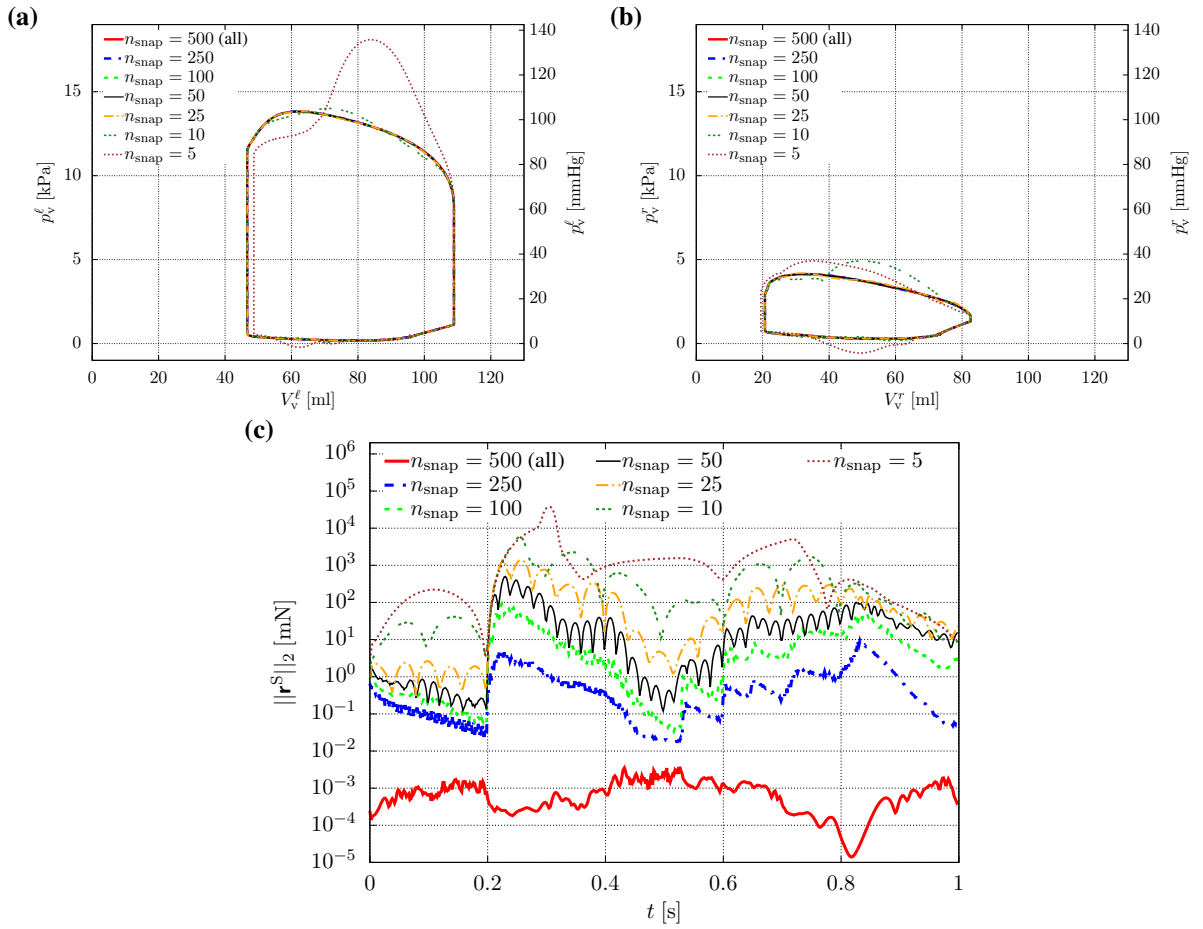

Figure 4.3: Model *3Dventr*$_{\text{tet4\_1}}$ | *0Dsyspul*: Performance of ROM under varying number of snapshots n_{snap} (only every $(500/n_{\text{snap}})$th snapshot taken) using all $r_{\text{b}} = n_{\text{snap}}$ reduced-basis vectors. **(a)** Left ventricular pressure-volume relation. **(b)** Right ventricular pressure-volume relation. **(c)** ROM error $||\mathbf{r}^{\text{S}}||_2$ over time.

Table 4.3: Relative errors in left ($i = \ell$) and right ($i = r$) ventricular stroke work $|\text{SW}^i_{\text{ROM}} - \text{SW}^i_{\text{HDM}}|/\text{SW}^i_{\text{HDM}}$ for the ROM with respect to the HDM, for varying number of time steps n_{step} using all $n_{\text{snap}} = 500$ snapshots and all $r_{\text{b}} = n_{\text{snap}}$ reduced-basis vectors

n_{step}	250	100	50
$\lvert\text{SW}^{\ell}_{\text{ROM}} - \text{SW}^{\ell}_{\text{HDM}}\rvert/\text{SW}^{\ell}_{\text{HDM}}$	$2.12 \cdot 10^{-3}$	$7.54 \cdot 10^{-3}$	$2.38 \cdot 10^{-2}$
$\lvert\text{SW}^{r}_{\text{ROM}} - \text{SW}^{r}_{\text{HDM}}\rvert/\text{SW}^{r}_{\text{HDM}}$	$3.59 \cdot 10^{-3}$	$1.27 \cdot 10^{-2}$	$4.06 \cdot 10^{-2}$
$\varnothing\lvert\lvert\mathbf{r}^{\text{S}}\rvert\rvert_2$ [mN]	7.27	$2.56 \cdot 10^{1}$	$4.8 \cdot 10^{1}$

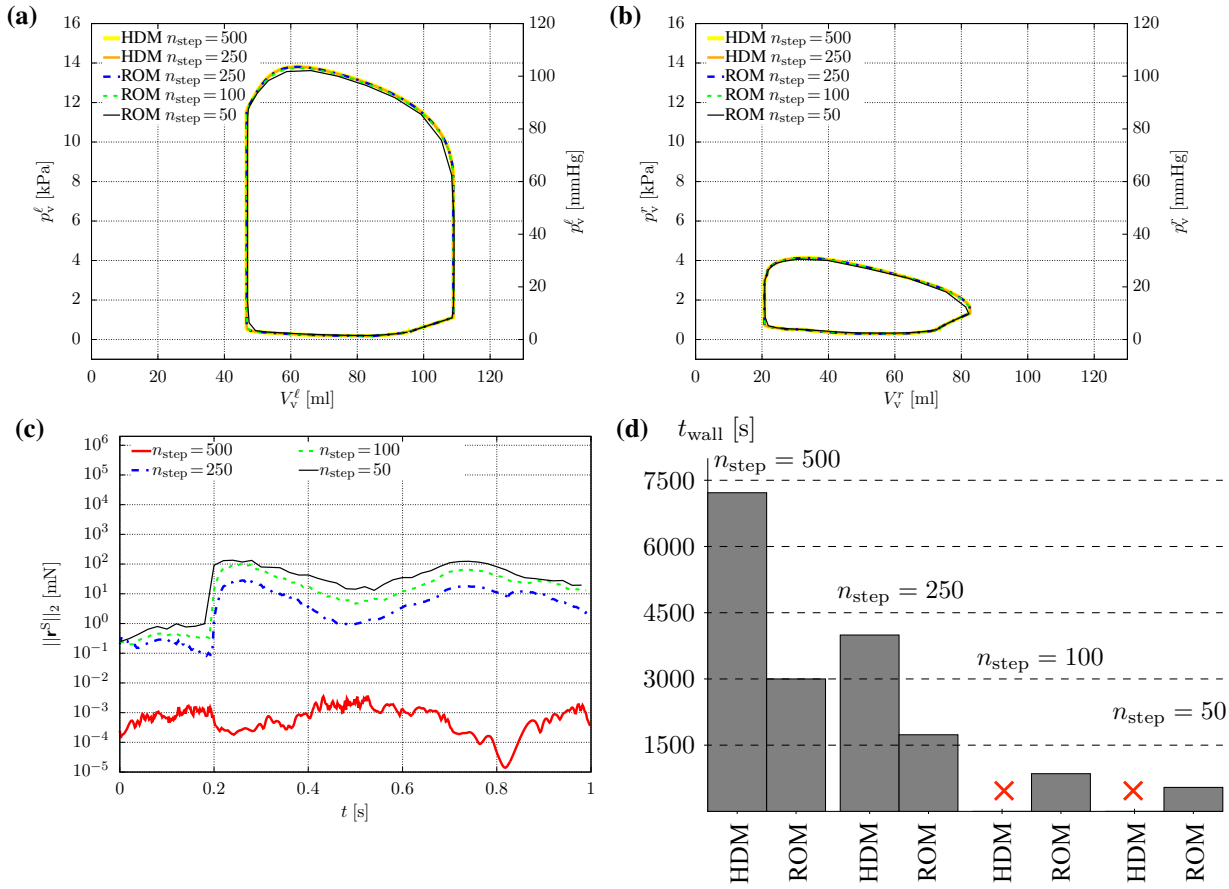

Figure 4.4: Model *3Dventr*$_{tet4\_1}$ | *0Dsyspul*: Performance of ROM under varying number of time steps n_{step} using all $n_{\text{snap}} = 500$ snapshots and all $r_{\text{b}} = n_{\text{snap}}$ reduced-basis vectors. **(a)** Left ventricular pressure-volume relation. **(b)** Right ventricular pressure-volume relation. **(c)** ROM error $||\mathbf{r}^{\text{S}}||_2$ over time. **(d)** Total wall time for transient computation (one cardiac cycle, prestressing excluded). Red cross means that HDM was not computable with this number of time steps using a standard Newton as nonlinear solver.

Figure 4.5 shows the performance of the ROM under different parametric configurations. Specifically, the contractility σ_0 is varied under base afterload (resistance $R_{\text{ar}}^{\text{sys}}$), and then the resistance $R_{\text{ar}}^{\text{sys}}$ is varied under base inotropic state (contractility σ_0), however *without* adjusting the other vascular parameters according to tab. 2.7 but assuming them to be calculated using the base total resistance (tab. 2.6). ROMs are all calculated from the HDM with base parameters ($\sigma_0 = 70$ kPa, $R_{\text{ar}}^{\text{sys}} = 120\ \frac{\text{mPa·s}}{\text{mm}^3}$).

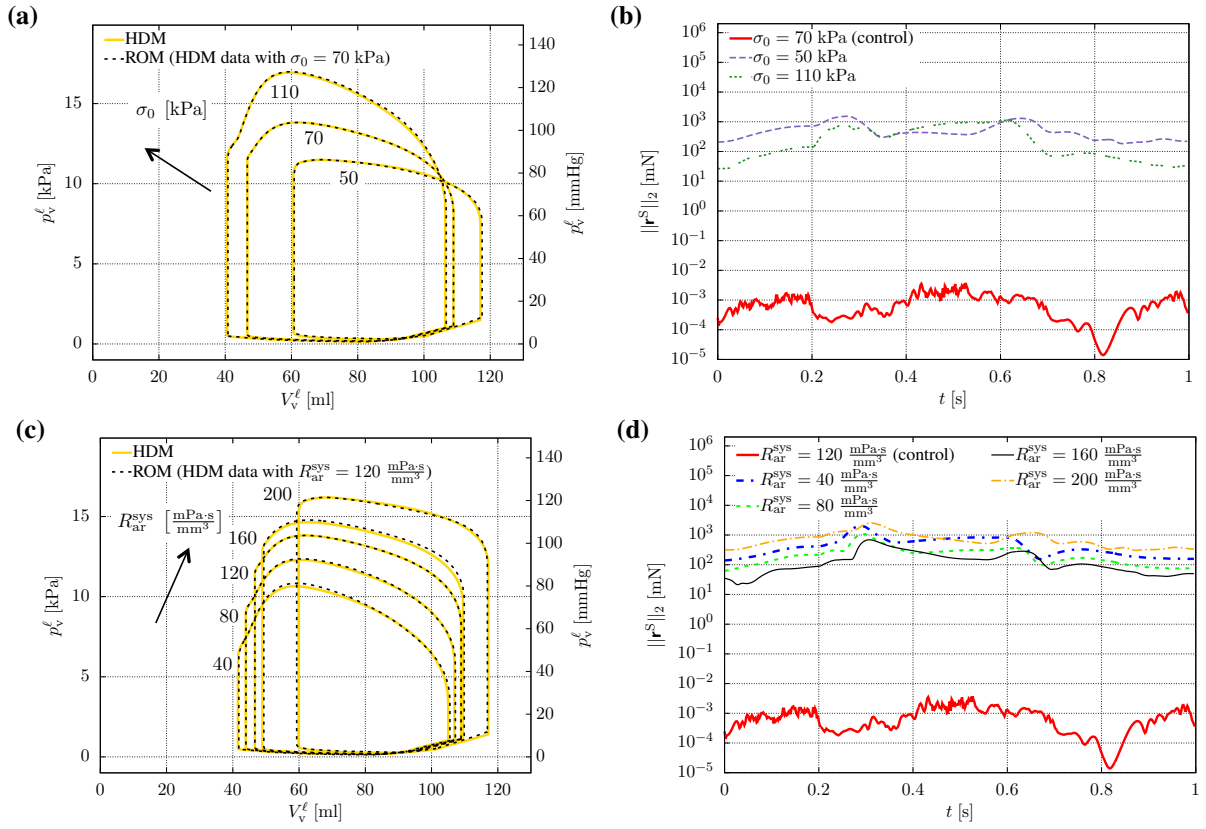

Figure 4.5: Model *3Dventr$_{tet4_1}$ | 0Dsyspul*: Performance of ROM under varying parametric configuration using all $n_{\text{snap}} = 500$ snapshots and all $r_{\text{b}} = n_{\text{snap}}$ reduced-basis vectors generated from the "control" HDM (base parameters from tab. 2.3 and tab. 2.6, namely $\sigma_0 = 70$ kPa and $R_{\text{ar}}^{\text{sys}} = 120\ \frac{\text{mPa·s}}{\text{mm}^3}$). **(a)** Left ventricular pressure-volume relation under change in contractility (inotropy). **(b)** ROM error $||\mathbf{r}^{\text{S}}||_2$ over time under change in contractility (inotropy). **(c)** Left ventricular pressure-volume relation under change in afterload. **(d)** ROM error $||\mathbf{r}^{\text{S}}||_2$ over time under change in afterload.

Table 4.4 shows relative stroke work errors for both the left and the right ventricle as well as the time step-averaged ROM error (4.39) with respect to the HDM for the case of varying parametric configurations (change in afterload $R_{\text{ar}}^{\text{sys}}$, change in contractility σ_0).

Table 4.4: Relative errors in left ($i = \ell$) and right ($i = r$) ventricular stroke work $|\mathrm{SW}^i_{\mathrm{ROM}} - \mathrm{SW}^i_{\mathrm{HDM}}|/\mathrm{SW}^i_{\mathrm{HDM}}$ for the ROM with respect to the HDM, varying parametric configuration using all $n_{\mathrm{snap}} = 500$ snapshots and all $r_{\mathrm{b}} = n_{\mathrm{snap}}$ reduced-basis vectors generated from the "control" HDM (base parameters from tab. 2.3 and tab. 2.6, namely $\sigma_0 = 70$ kPa and $R^{\mathrm{sys}}_{\mathrm{ar}} = 120\ \frac{\mathrm{mPa\cdot s}}{\mathrm{mm}^3}$)

	$R^{\mathrm{sys}}_{\mathrm{ar}}\ [\frac{\mathrm{mPa\cdot s}}{\mathrm{mm}^3}]$				σ_0 [kPa]	
	40	80	160	200	50	110
$\lvert\mathrm{SW}^\ell_{\mathrm{ROM}} - \mathrm{SW}^\ell_{\mathrm{HDM}}\rvert/\mathrm{SW}^\ell_{\mathrm{HDM}}$	$1.26 \cdot 10^{-2}$	$6.96 \cdot 10^{-3}$	$1.08 \cdot 10^{-2}$	$1.42 \cdot 10^{-3}$	$3.42 \cdot 10^{-3}$	$5.52 \cdot 10^{-3}$
$\lvert\mathrm{SW}^r_{\mathrm{ROM}} - \mathrm{SW}^r_{\mathrm{HDM}}\rvert/\mathrm{SW}^r_{\mathrm{HDM}}$	$6.18 \cdot 10^{-3}$	$4.01 \cdot 10^{-3}$	$3.54 \cdot 10^{-3}$	$2.42 \cdot 10^{-2}$	$4.07 \cdot 10^{-2}$	$7.00 \cdot 10^{-3}$
$\varnothing \lvert\lvert\mathbf{r}^{\mathrm{S}}\rvert\rvert_2$ [mN]	$5.02 \cdot 10^2$	$2.44 \cdot 10^2$	$1.57 \cdot 10^2$	$7.92 \cdot 10^2$	$5.43 \cdot 10^2$	$3.55 \cdot 10^2$

4.2.3 Discussion

As mentioned before, this is the first time that model order reduction techniques have been applied to a monolithic 3D-0D coupled problem describing the 3D nonlinear solid mechanics of the heart and the 0D pressure-flow relationships for the closed circulatory system.
The performance of the reduced-order model (ROM) was tested for a single (homeostatic) heart cycle of a high-dimensional model (HDM) that was used as input for the proper orthogonal decomposition (POD).

At first, its behavior with respect to a varying size of the reduced-order basis (ROB) is analyzed. A reduction of the ROB from $r_{\mathrm{b}} = 500$ to $r_{\mathrm{b}} = 16$ reduced-basis vectors yielded visually non-distinguishable pressure-volume relationships (relative stroke work errors below $1\ \%$). Less modes however lead to significantly greater errors and did not further decrease wall time (fig. 4.2, tab. 4.1). The maximum measured wall time speedup with respect to the HDM for this case is 4.12.

Also, taking a reduced number of snapshots still allows for good accuracies. For example, using only $n_{\mathrm{snap}} = 25$ snapshots (hence every 20th) may be sufficient depending on the problem at hand, with relative stroke work errors below $1\ \%$ (fig. 4.3, tab. 4.2). However, a too drastic increase of the snapshot increment is not recommendable since important features of the cardiac cycle then may be missed.

An important property of the ROM compared to the HDM is its tolerance for large time steps when using a standard Newton scheme to solve the nonlinear problem (fig. 4.4, tab. 4.3). While for the special case here the HDM still is computable with $n_{\mathrm{step}} = 250$ instead of $n_{\mathrm{step}} = 500$ (default), a further reduction leads to divergence of Newton's method and would necessitate more robust – hence more expensive – nonlinear solution techniques. However, the ROM still converges well even for $n_{\mathrm{step}} = 50$ time steps over one cardiac cycle, with little overall error compared to the HDM using all $n_{\mathrm{step}} = 500$ steps. Considering the ability of time step reduction, wall time speedups become more remarkable ($n^{\mathrm{ROM}}_{\mathrm{step}} = 50$ vs. $n^{\mathrm{HDM}}_{\mathrm{step}} = 500$: speedup 13.3; $n^{\mathrm{ROM}}_{\mathrm{step}} = 50$ vs. $n^{\mathrm{HDM}}_{\mathrm{step}} = 250$: speedup 7.4), and could be increased when combining time step and ROB size reduction simultaneously.

Finally, the ROM's performance under different parametric configurations is evaluated. Changes in afterload and inotropy are computed on the ROM generated from the default HDM input data. Even for large changes in these parameters, ROM pressure-volume data is visually only little distinguishable to the respective HDM (fig. 4.5, tab. 4.4). Therefore, the ROM may be used even if parameters differ from the underlying HDM, however a more general and robust quantification of the ROM's accuracy under different parametric configurations remains to be performed.
Furthermore, global ROMs performing the POD on HDM inputs from different parametric settings may be constructed that lead to an even better interpolatory behavior of the ROM. Even though this feature is implemented, it is yet to be evaluated, and its analysis leaves the scope of this thesis.

The main limitation of the present model order reduction implementation is the need for evaluating the full HDM problem in every Newton iteration in order to construct the reduced linear system of equations (4.38) to be solved. Additionally, the processes of projection (matrix-matrix and matrix-vector multiplication) themselves are time-consuming and depend on the size of the underlying HDM. While the linear solve then is significantly faster than for the system (3.34), the speedup is diminished by evaluation and projection operations, and the total amount of cores used for computation is intended to be the same as for the HDM in order to achieve measurable speedups.
In order to circumvent evaluating the whole $n_{\mathrm{dof}}^{\mathrm{3D}} \times n_{\mathrm{dof}}^{\mathrm{3D}}$-sized HDM, hyper reduction techniques have been proposed that essentially produce reduced nonlinear systems of equations, and in combination with the POD yield significant speedups. For nonlinear structural dynamics problems refer again to Farhat et al. [59] for comparisons of ROMs with and without hyper reduction. However, this topic leaves the scope of this thesis and is subject of future investigations.

4.3 Multilevel parameter and homeostatic state estimation

The focus here is set on the estimation of model parameters in cardiovascular dynamics such that (time-resolved) measurements of left ventricular pressure and data on left ventricular stroke volume (ejection fraction) are reproduced by the 3D-0D coupled computational model of the heart and the vascular system as it is detailed in chap. 2.
The specific data was gathered from animal experiments on pigs which have been conducted for experimental assessment of a novel extravascular ventricular assist technology, cf. chap. 5 and [98]. Two cases of pharmacologically-induced heart failure models are considered, namely

- a *low-afterload heart failure* state, subsequently denoted as *LA-HF*, which was created by injection of β_1-blockade with vasodilatory effects [174] leading to widening of the arteries and reduction of vascular resistance, ultimately causing a state of low heart rate, weak contractility and hence reduced cardiac output; and

- a *high-afterload heart failure* scenario, in the following denoted as *HA-HF*, which was induced by additional infusion of phenylephrine leading to a constriction of the peripheral arterioles and therefore increased vascular resistance [192] and subsequently elevated ventricular contractility.

Hence, parameters which are responsive to external medical treatment conditions and exhibit short time-scale variability have been chosen for estimation, since the alteration of measured ventricular data was on a time-scale of minutes after the medical treatment had been applied. A qualified pair of parameters would be a systemic vascular compliance or resistance ($R_{\mathrm{ar}}^{\mathrm{sys}}$), and the heart's autoregulatory response to a change of that quantity in terms of contractile force, i.e. the contractility (σ_0) as the asymptotic value of the active stress τ_{a}, cf. (2.99).
Given that information of the time-course of (left) ventricular pressure is present, the qualified pair of parameters is enhanced by the muscle's contraction and relaxation speeds that govern the slope of the pressure build-up and decrease in isovolumic contraction and relaxation phases (upstroke and relaxation rates $\alpha_{\max}$ and $\alpha_{\min}$, respectively), cf. (2.100).
As an advancement to the procedure in [86], left atrial contractility ($E_{\mathrm{at,A}}^{\ell}$ in case of model *3Dventr*, $\sigma_{0(at)}$ in case of model *3Datrioventr*) is incorporated into the parameter estimation process as it governs end-diastolic ventricular pressure which the other parameters are not directly able to determine.

The vector of model parameters to be estimated thus reads

$$\mathbf{x} = \Big[\sigma_0 \quad \alpha_{\max} \quad \alpha_{\min} \quad R_{\mathrm{ar}(\mathit{total})}^{\mathrm{sys}} \quad E_{\mathrm{at,A}}^{\ell}\Big]_{(\mathit{3Dventr})}^{\mathrm{T}} \tag{4.40}$$

for the model *3Dventr* and

$$\mathbf{x} = \Big[\sigma_0 \quad \alpha_{\max} \quad \alpha_{\min} \quad R_{\mathrm{ar}(\mathit{total})}^{\mathrm{sys}} \quad \sigma_{0(\mathit{at})}\Big]_{(\mathit{3Datrioventr})}^{\mathrm{T}} \tag{4.41}$$

in case of the model *3Datrioventr*.

The data of m_p discrete left ventricular pressure measurements stemming from an eight-electrode conductance catheter [12] equally distributed over one cardiac cycle with a sample rate of $t_{\mathrm{sampl}} = 0.01\ \mathrm{s}$ are stored in the discrete vector

$$\tilde{\mathbf{p}} = [\tilde{p}_{\mathrm{v}}^{\ell,1} \ \dots \ \tilde{p}_{\mathrm{v}}^{\ell,m_p}]^{\mathrm{T}}, \tag{4.42}$$

and its peak and end-diastolic values are denoted as

$$\widetilde{\mathrm{PVP}}^{\ell} = \max(\tilde{\mathbf{p}}) \qquad \text{and} \qquad \widetilde{\mathrm{EDP}}^{\ell} = \tilde{\mathbf{p}}[t_{\mathrm{ed}}/t_{\mathrm{sampl}}], \tag{4.43}$$

respectively.

Finally, measured left ventricular ejection fraction

$$\widetilde{\mathrm{EF}}^{\ell} = \frac{\widetilde{\mathrm{SV}}^{\ell}}{\widetilde{\mathrm{EDV}}^{\ell}} \tag{4.44}$$

stemming from CT volumetry analyses performed according to Simpsons's rule [95] at the Clinic of Diagnostic and Interventional Radiology in Ulm, Germany, is considered.[2] Measured stroke

[2] Without loss of generality, ejection fraction instead of volume-over-time resolved data is considered, since complete experimentally measured synchronized pressure-volume data was unavailable and the imaging data did not provide the temporal resolution required. Furthermore, total model vs. motion CT estimated volume might differ due to different atrioventricular offsets, thus ejection fraction as a relative measure seems the more reasonable quantity to consider.

and end-diastolic volumes $\widetilde{\mathrm{SV}}^{\ell}$ and $\widetilde{\mathrm{EDV}}^{\ell}$ thus only implicitly enter the parameter estimation process.

Given the data at hand, a least-squares objective function according to (4.7) of the type

$$f(\mathbf{x}) = \frac{1}{2}\left(\left(\frac{||\Delta\mathbf{p}(\mathbf{x})||_2}{||\tilde{\mathbf{p}}||_2}\right)^2 + \left(\frac{\Delta\mathrm{PVP}^{\ell}(\mathbf{x})}{\widetilde{\mathrm{PVP}}^{\ell}}\right)^2 + \left(\frac{\Delta\mathrm{EDP}^{\ell}(\mathbf{x})}{\widetilde{\mathrm{EDP}}^{\ell}}\right)^2 + \left(\frac{\Delta\mathrm{EF}^{\ell}(\mathbf{x})}{\widetilde{\mathrm{EF}}^{\ell}}\right)^2 + \right.$$
$$\left. + \sum_{i=\ell,r}\left(\frac{\Delta V^i_{\mathrm{v}(aux)}(\mathbf{x})}{V^i_{\mathrm{v}}(t_0)}\right)^2\right) = \frac{1}{2}||\mathbf{w}(\mathbf{x})||_2^2 \rightarrow \min, \tag{4.45}$$

is postulated, with

$$\mathbf{w}(\mathbf{x}) = \left[\frac{\Delta\mathbf{p}(\mathbf{x})}{||\tilde{\mathbf{p}}||_2} \quad \frac{\Delta\mathrm{PVP}^{\ell}(\mathbf{x})}{\widetilde{\mathrm{PVP}}^{\ell}} \quad \frac{\Delta\mathrm{EDP}^{\ell}(\mathbf{x})}{\widetilde{\mathrm{EDP}}^{\ell}} \quad \frac{\Delta\mathrm{EF}^{\ell}(\mathbf{x})}{\widetilde{\mathrm{EF}}^{\ell}} \quad \frac{\Delta V^{\ell}_{\mathrm{v}(aux)}(\mathbf{x})}{V^{\ell}_{\mathrm{v}}(t_0)} \quad \frac{\Delta V^{r}_{\mathrm{v}(aux)}(\mathbf{x})}{V^{r}_{\mathrm{v}}(t_0)}\right]^{\mathrm{T}} \tag{4.46}$$

as the vector of non-dimensionalized least-squares residuals, cf. (4.8). The weighted residuals (pressure weightings $b_p^{i_p}$, $i_p = 1, ..., m_p$, ejection fraction weighting b_{EF}, peak and end-diastolic ventricular pressure weightings b_{PVP} and b_{EDP}, auxiliary volume weightings b_V^i $(i = \ell, r)$) are

$$\left.\begin{aligned}
\Delta\mathbf{p}(\mathbf{x}) &= \begin{bmatrix} b_p^1 \cdot (p_{\mathrm{v}}^{\ell,1}(\mathbf{x}, t_0) - \tilde{p}_{\mathrm{v}}^{\ell,1}) \\ \vdots \\ b_p^{m_p} \cdot (p_{\mathrm{v}}^{\ell,m_p}(\mathbf{x}, t_0 + T_{\mathrm{cycl}}) - \tilde{p}_{\mathrm{v}}^{\ell,m_p}) \end{bmatrix}, \\
\Delta\mathrm{PVP}^{\ell}(\mathbf{x}) &= b_{\mathrm{PVP}} \cdot (\mathrm{PVP}^{\ell}(\mathbf{x}) - \widetilde{\mathrm{PVP}}^{\ell}), \\
\Delta\mathrm{EDP}^{\ell}(\mathbf{x}) &= b_{\mathrm{EDP}} \cdot (\mathrm{EDP}^{\ell}(\mathbf{x}) - \widetilde{\mathrm{EDP}}^{\ell}), \\
\Delta\mathrm{EF}^{\ell}(\mathbf{x}) &= b_{\mathrm{EF}} \cdot (\mathrm{EF}^{\ell}(\mathbf{x}) - \widetilde{\mathrm{EF}}^{\ell}), \\
\Delta V^i_{\mathrm{v}(aux)}(\mathbf{x}) &= b_V^i \cdot (V^i_{\mathrm{v}}(\mathbf{x}, t_0 + T_{\mathrm{cycl}}) - V^i_{\mathrm{v}}(t_0)),\ i = \ell, r.
\end{aligned}\right\} \tag{4.47}$$

In order to solve the optimization problem (4.45), a Levenberg-Marquardt-type algorithm with the iteration rule (4.13) and a regularization parameter update rule according to (4.14) is considered the method of choice.

However, two major hurdles are to overcome:

- The result of the evaluation of (4.45) is governed by a transient solution of a coupled initial boundary value problem, hence multiple solutions of the discrete nonlinear problem (3.32) in a discretized time span $[t_0, t_{N^\star}]$ for which the homeostatic state cycle $N^\star$ has to be found, cf. (2.222). Therefore, an implicit dependence of the objective function on the problem's initial conditions requires some considerations.
- *One* evaluation of the objective function (4.45), meaning the computation of a single cardiac cycle solving (3.32) in a discretized time span $[t_N, t_N + T_{\mathrm{cycl}}]$, is of non-negligible computational cost itself.

Considering these aspects and the fact that $n_\mathrm{p} + 1$ (for the present case, the number of parameters is $n_\mathrm{p} = 5$) forward evaluations per optimization step are necessary if the Jacobian (4.10) is calculated using forward finite differences, cf. sec. 4.1.1, the computational expense and feasibility of the overall parameter estimation process is expected to be not profitable from a computational timing and resources point of view.

In order to address the above-mentioned challenges, a novel *multilevel optimization approach* for the simultaneous estimation of model parameters and homeostatic state initial conditions is presented. The core idea about this method is to construct some "coarse" *reduced-dimensional* surrogate model (RDM) that captures information of the original "fine" *high-dimensional* model (HDM), and to "outsource" a significant amount of optimization work to the computationally cheap RDM.
The generic algorithmic pattern may be depicted as a *V-cycle* that denotes the switches between the two models (levels) and the respective level operations, cf. fig. 4.7. Here, the term *evaluation* means the computation of *one* cardiac cycle in order to determine the result of the objective function, i.e. (4.45). The term *solve* refers to the solution of an optimization problem, here the application of the Levenberg-Marquardt algorithm (4.13) or the Gauss-Newton method (4.12).
The interchange between the models is characterized by transfer operators $\mathbb{T}$. The process is called *restriction* if information is transferred from the HDM to the RDM, and *prolongation* if information is passed from the RDM back to the HDM again. The restriction operator from "fine" to "coarse" is denoted as $\mathbb{T}^{\mathrm{f}}_{\cdot\mathrm{c}}$, and the "coarse" to "fine" prolongation operator is $\mathbb{T}^{\cdot\mathrm{f}}_{\mathrm{c}}$. These operators can be seen as generalizations of the concept of restriction and prolongation as known from multigrid algorithms [28, 29]. Their specific representations will be given in the subsequent sections. Furthermore, "fine" to "fine" prolongations $\mathbb{T}^{\mathrm{ff}}$ and ${}_s\mathbb{T}^{\mathrm{ff}}$ may be defined, which characterize a transfer of information from the HDM of the previous V-cycle or previous solve iteration to the HDM of the current one, e.g. a set of updated initial conditions $\mathcal{I}$ (2.223).
Three different types of RDMs are considered, namely

- a heavily coarsely discretized version of the underlying HDM, denoted as model *C*;
- a 2-dimensional plane strain representation of a bi-ventricular heart, denoted as model *S* (shown in fig. 4.6);
- a reduced-order model of the heart by use of proper orthogonal decomposition, cf. sec. 4.2, denoted as *R*.

It should be noted that all types of RDMs are coupled to the same 0D circulatory system as the respective HDM, thus dimensional reduction addresses the spatially resolved only-ventricular or atrioventricular heart model exclusively.

For other types of problems and with differing formulations of objective functions, nonlinear *multigrid* algorithms for optimization have been proposed, for instance, by Nash [146], Bouman et al. [27], Ye et al. [221] or Borcea [26], while a nice overview is given by Oh et al. [153]. In contrast to some techniques addressed therein or classical multigrid methods for the solution of discretized partial differential equations, where a coarsened grid smoothens the long-wave error component in the solution vector and hence becomes beneficial for the fine grid solver, here

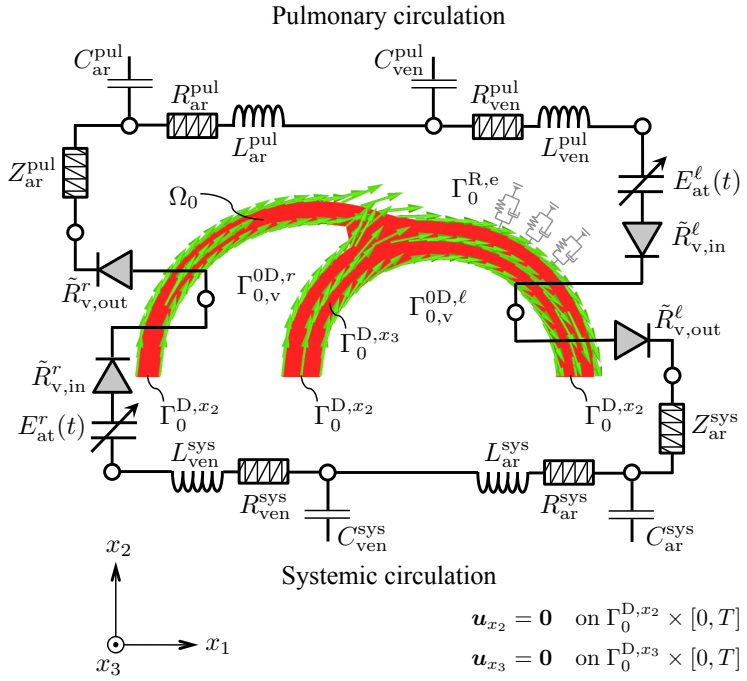

Figure 4.6: 2D surrogate heart model S with systemic and pulmonary circulation (*2Dventr | 0Dsyspul*); muscle fiber direction is in-plane and shown in green.

the same number of degrees of freedom (the parameters) as well as residual entries (number of measurements) is present on both levels. Therefore, the present approach is rather denoted as *multilevel* method.

In the following, two types of novel multilevel algorithms as specializations of the generic V-cycle in fig. 4.7 are presented. They essentially differ with respect to the definitions of inter- and intra-level transfer operators and the coarse level objective function.
The termination criterion of the V-cycle always is

$$E_{\text{cycl}} \leq \epsilon_{\text{cycl}} \quad \text{AND} \quad v \geq 1, \tag{4.48}$$

hence if the periodic (homeostatic) state is reached in terms of E_{cycl} (2.222) and if at least one V-cycle iteration, meaning one visit of the "coarse" level solve has happened. Note that this criterion does not include any information on the magnitude of the objective function (4.45) on the HDM nor information on its gradient norm $||\boldsymbol{\nabla} f||_\infty$, which never was computed during V-cycling.
After finishing the V-cycle, the solution is expected to be sufficiently close to the true minimizer of (4.45) on the HDM, hence the "fine" solve section is entered with the hope of very little further optimization work to solve the HDM optimization problem.
For the two subsequently presented algorithms, the intra-level transfer operator for the last solve step is defined as follows:

$${}_s\mathbb{T}^{\text{ff}} : \begin{cases} \mathcal{I}^{(i)}(t_0) \leftarrow \mathcal{I}^{(v)}(t_0 + T_{\text{cycl}}), & \text{if } E_{\text{cycl}} \leq \epsilon_{\text{cycl}} \text{ OR } ||\boldsymbol{\nabla} f||_\infty > \epsilon_{\text{grad}}, \\ \mathcal{I}^{(i)}(t_0) \leftarrow \mathcal{I}^{(i-1)}(t_0 + T_{\text{cycl}}), & \text{else.} \end{cases} \tag{4.49}$$

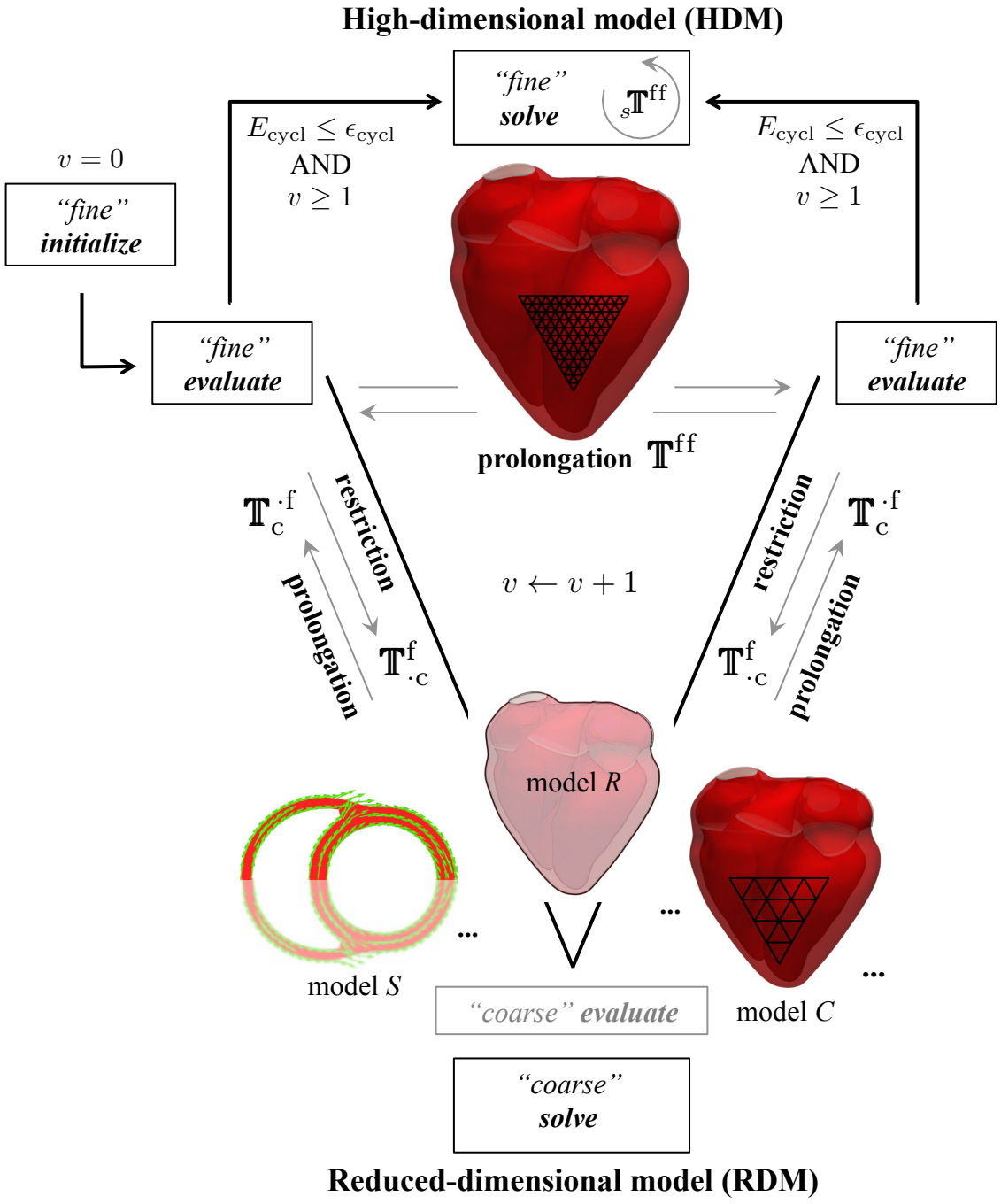

Figure 4.7: Generalized 2-level V-cycle: A high-dimensional model (HDM) optimization problem is accelerated by help of some reduced-dimensional model (RDM); model *S*: "surrogate" 2D plane strain bi-ventricular heart, model *R*: reduced-order heart model using proper orthogonal decomposition on the HDM, model *C*: coarsely discretized version of the HDM; like the HDM, all reduced-dimensional models are coupled to the 0D circulation (drawing neglected in figure for the sake of a better overview).

The first solve, $i = 0$, is entered by updating the initial conditions from the last V-cycle v. An optimization algorithm, here the Gauss-Newton method (4.12), is applied until the gradient norm tolerance is met and *regardless* of a potential violation of the cycle error tolerance. Only *after* convergence in the gradient norm, a further initial condition update is executed for the case that the cycle norm tolerance had been violated during optimization iterations.[3]
Ultimately, the "fine" level solve and thus the whole optimization procedure is considered converged and stops if both conditions, for the cycle error and the HDM gradient norm,

$$E_{\mathrm{cycl}} \leq \epsilon_{\mathrm{cycl}} \quad \text{AND} \quad ||\boldsymbol{\nabla} f||_{\infty} \leq \epsilon_{\mathrm{grad}}, \tag{4.50}$$

are fulfilled.

4.3.1 Full approximation scheme least-squares algorithm *FAS-lsq*

Based upon the above generic V-cycle, a so-called *full approximation scheme least-squares algorithm*, subsequently denoted as *FAS-lsq*, is developed. Despite slight technical modifications, it corresponds to the 2-level optimization algorithm as it has been published in Hirschvogel et al. [86].

Its name and some aspects are adopted from nonlinear multigrid techniques such as the full approximation scheme (FAS) [28, 29, 66]. The basic concept of that approach consists of solving the computationally expensive (fine) HDM nonlinear residual $\mathbf{f}(\mathbf{x}) = \mathbf{0}$ with help of a computationally cheap (coarse) RDM $\mathbf{f}_{\mathrm{c}}(\mathbf{x}_{\mathrm{c}})$. At some initial fine model guess $\mathbf{x} \leftarrow \mathbf{x}^{(0)}$, the fine model evaluation as well as the fine model guess are restricted to the coarse model,

$$\bar{\mathbf{f}}_{\mathrm{c}} := \mathbf{R}\,\mathbf{f}(\mathbf{x}) \quad \text{and} \quad \bar{\mathbf{x}}_{\mathrm{c}} := \mathbf{R}\,\mathbf{x}, \tag{4.51}$$

with a so-called restriction operator $\mathbf{R}$. For the cheap RDM, a modified problem

$$\mathbf{f}_{\mathrm{c}}(\mathbf{x}_{\mathrm{c}}) + \bar{\mathbf{f}}_{\mathrm{c}} - \hat{\mathbf{f}}_{\mathrm{c}} \rightarrow \mathbf{0} \tag{4.52}$$

is solved, with $\hat{\mathbf{f}}_{\mathrm{c}} := \mathbf{f}_{\mathrm{c}}(\bar{\mathbf{x}}_{\mathrm{c}})$, while $\bar{\mathbf{f}}_{\mathrm{c}}$ and $\hat{\mathbf{f}}_{\mathrm{c}}$ are fixed quantities throughout the coarse model iterations. Thereafter, the coarse model estimate $\mathbf{x}_{\mathrm{c}}$ is prolongated to the fine level via

$$\mathbf{x} \leftarrow \mathbf{x} + \mathbf{P}\,(\mathbf{x}_{\mathrm{c}} - \bar{\mathbf{x}}_{\mathrm{c}}) \tag{4.53}$$

with the prolongation operator $\mathbf{P}$.
Technically spoken, if $\mathbf{R} = \mathbf{1}$ and $\mathbf{P} = \mathbf{1}$, the modified problem (4.52) corresponds to shifting the coarse model by its residual difference to the fine model at the current guess, obtaining a coarse model solution which proves beneficial for the fine model solve. Depending on the problem at hand, a hierarchy of different models might be used through recursive application of the above procedure.

[3] A simultaneous initial condition and nonlinear gradient-based optimization iteration update is *not* recommended. It has proven to significantly perturb the gradient calculation since a change in initial conditions essentially changes the topology of the objective function and thus deteriorates convergence behavior of the algorithm.

A similar idea of applying such a method to (unconstrained) optimization problems has been proposed by Nash [146]. Therein, a general optimization problem of the type (4.1) is stated and a (line-search regularized) Newton method (4.4) is applied to solve it. The FAS residual modification is applied to the right-hand side of $(4.4)_1$, which essentially yields a correspondingly modified coarse grid objective function to be minimized. For the case that the optimization problem is non-convex, Nash proposes an additional modification of the objective function in order to guarantee descent.
However, in order to construct the coarse grid optimization problem, a fine grid evaluation of the Newton right-hand side in $(4.4)_1$, hence of the gradient, is necessary, since $(4.51)_1$ has to be computed. For the problem at hand, an HDM *evaluation*, cf. fig. 4.7, would come along with a computationally expensive finite differencing (4.6) for gradient calculation, i.e. $n_\mathrm{p}+1$ evaluations of the objective function.

The central and novel aspect constituting the *FAS-lsq* scheme is not to apply a (Newton right-hand side) residual modification in terms of (4.52), but to apply the modification to the least-squares residuals (4.7), or for the specific problem (4.46), yielding a modified objective function to be minimized for the coarse level iterate $\mathbf{x}_\mathrm{c}$ which is initialized as restriction from the fine level $\mathbf{x}_\mathrm{c} \leftarrow \overline{\mathbf{x}}_\mathrm{c} := \mathbf{R}\,\mathbf{x}$:

$$f_\mathrm{c}(\mathbf{x}_\mathrm{c}) := \frac{1}{2}||\mathbf{w}_\mathrm{c}(\mathbf{x}_\mathrm{c}) + (\overline{\mathbf{w}}_\mathrm{c} - \widehat{\mathbf{w}}_\mathrm{c})\,||_2^2 \rightarrow \min\,. \tag{4.54}$$

Therein, $\widehat{\mathbf{w}}_\mathrm{c} := \mathbf{w}_\mathrm{c}(\overline{\mathbf{x}}_\mathrm{c})$ and $\overline{\mathbf{w}}_\mathrm{c} := \mathbf{R}_\mathrm{w}\mathbf{w}$ are the fixed quantities that remain unaltered during coarse level optimization iterations.
The modified problem is solved until some gradient norm tolerance is met, here in terms of the infinity norm:

$$||\boldsymbol{\nabla} f_\mathrm{c}||_\infty \leq \epsilon_\mathrm{grad}, \tag{4.55}$$

and the new fine level iterate is updated according to (4.53).

The benefit of this approach is that the construction of (4.54) only needs *one evaluation* of the HDM, meaning the computation of one heart cycle. Thus, the whole V-cycle does not require the computation of an HDM gradient, which is only then needed in order to perform the "fine" solve after having met (4.48).

The specific inter-level transfer operators for this algorithm are summarized as

$$\mathbb{T}^\mathrm{f}_{\cdot\mathrm{c}} : \begin{cases} \overline{\mathbf{w}}_\mathrm{c} := \mathbf{R}_\mathrm{w}\mathbf{w}, \\ \mathbf{x}_\mathrm{c} \leftarrow \overline{\mathbf{x}}_\mathrm{c} := \mathbf{R}\,\mathbf{x}, \\ \mathcal{I}_\mathrm{c}^{(v)}(t_0) \leftarrow \mathcal{I}^{(0)}(t_0) \end{cases} \quad \text{and} \quad \mathbb{T}^{\cdot\mathrm{f}}_\mathrm{c} : \mathbf{x} \leftarrow \mathbf{x} + \mathbf{P}(\mathbf{x}_\mathrm{c} - \overline{\mathbf{x}}_\mathrm{c}). \tag{4.56}$$

Without loss of generality, the residual and parameter restriction operators and the parameter prolongation operator are set to identity: $\mathbf{R}_\mathrm{w} = \mathbf{1}$, $\mathbf{R} = \mathbf{1}$, and $\mathbf{P} = \mathbf{1}$.
On the RDM, the initial conditions $\mathcal{I}_\mathrm{c}^{(v)}(t_0)$ remain the same set of (semi-educatedly guessed) initial values $\mathcal{I}^{(0)}(t_0)$ which have been set for initialization of the HDM ($v = 0$). Hence, the RDM will not reach its homeostatic state throughout inter-level iterations.

The intra-level transfer operator that acts between HDMs of two successive V-cycles is

$$\mathbb{T}^{\mathrm{ff}} : \begin{cases} \mathcal{I}^{(v)}(t_0) \leftarrow \mathcal{I}^{(0)}(t_0), & \text{if } v \leq 1, \\ \mathcal{I}^{(v)}(t_0) \leftarrow \mathcal{I}^{(v-1)}(t_0 + T_{\mathrm{cycl}}), & \text{else}, \end{cases} \tag{4.57}$$

meaning that an initial condition update of the HDM happens only if $v > 1$. [4]

4.3.2 Reduced-order model multilevel algorithm *ROM-ml*

The *FAS-lsq* algorithm as it is outlined in sec. 4.3.1 may be generalized to a so-called *reduced-order model multilevel algorithm*, here denoted as *ROM-ml*, if the RDM is constructed directly from the underlying HDM as reduced-order model (ROM) using proper orthogonal decomposition (model *R*, cf. fig. 4.7).
Even though a ROM may be constructed once during V-cycle $v = 0$ after the first "fine" evaluate and then subsequently be utilized as RDM in the *FAS-lsq* scheme, a cost-neutral generalization of that scheme can be achieved if the RDM is simply updated after each V-cycle "fine" evaluate. If done so, the "coarse" evaluate and the least-squares residual restriction in order to form $\widehat{\mathbf{w}}_{\mathrm{c}}$ and $\overline{\mathbf{w}}_{\mathrm{c}}$ in (4.54) may simply be omitted, yielding a RDM objective function of the type

$$f_{\mathrm{c}}(\mathbf{x}_{\mathrm{c}}) := \frac{1}{2}||\mathbf{w}_{\mathrm{c}}(\mathbf{x}_{\mathrm{c}})||_2^2 \rightarrow \min . \tag{4.58}$$

Hence, the delta in least-squares residual errors that has been introduced in (4.54) in order to account for the delta in fine-to-coarse model behavior now is directly incorporated into the RDM itself.
Additionally, one may think of an applicability of this more general approach to different types of objective functions than to least-squares problems only, which is however not considered in this context so far.

The inter-level transfer operators for this algorithm then yield

$$\mathbb{T}^{\mathrm{f}}_{\cdot\mathrm{c}} : \begin{cases} \mathbf{x}_{\mathrm{c}} \leftarrow \mathbf{x}, \\ \mathcal{M}^{(v)}_{\mathrm{RDM}} \leftarrow \mathbb{L}(\mathcal{M}^{(v)}_{\mathrm{HDM}}), \\ \mathcal{I}^{(v)}_{\mathrm{c}}(t_0) \leftarrow \mathcal{I}^{(v)}(t_0) \end{cases} \quad \text{and} \quad \mathbb{T}^{\cdot\mathrm{f}}_{\mathrm{c}} : \mathbf{x} \leftarrow \mathbf{x}_{\mathrm{c}}. \tag{4.59}$$

Therein, $\mathcal{M}_{\mathrm{RDM}}$ and $\mathcal{M}_{\mathrm{HDM}}$ denote the mathematical descriptors for the RDM and HDM, respectively, and the operator $\mathbb{L}$ describes the process of model order reduction, cf. sec. 4.2.

The intra-level transfer operator $\mathbb{T}^{\mathrm{ff}}$ remains identical to (4.57).

4.3.3 Results

The two algorithms are exemplified for the two *LA-HF* and *HA-HF* cases on a porcine ventricular heart model (*p1*). The heart *3Dventr* HDM is discretized using linear displacement-based tetrahedral finite elements with an average edge length of $h \approx 1$ mm (discretization *tet4_1*), hence the

[4] The reason for this simply lies in the presumption that $\mathcal{I}^{(0)}(t_0 + T_{\mathrm{cycl}})$ will be a poor guess if the initial parameter estimate $\mathbf{x}^{(0)}$ is poor, which most often is to be expected.

model is denoted as *3Dventr*$_{tet4\_1}$. For all computations, $n_{\mathrm{step}} = 500$ time steps of equal size are carried out for one cardiac cycle.

For the *FAS-lsq* scheme, two different types of RDMs are considered: the coarsely discretized heart model *C*, which has an average element edge length $h \approx 8$ mm (discretization *tet4_8*), alternatively denoted as *3Dventr*$_{tet4\_8}$, and the 2-dimensional plane strain heart model *S* (cf. fig. 4.6), which is discretized using trilinear displacement-based hexahedral finite elements[5] with an average in-plane element edge length of $h \approx 5$ mm (*2Dventr*$_{hex8\_5}$). For model *C*, $n_{\mathrm{step}} = 200$, and for model *S*, $n_{\mathrm{step}} = 100$ time steps of equal size are used for one cardiac cycle.

In case of the *ROM-ml* algorithm, the reduced-order basis (ROB) is computed by taking snapshots of the HDM every 10th time-step, here resulting in $n_{\mathrm{snap}} = 50$. All reduced-basis vectors are used. On the ROM, $n_{\mathrm{step}} = 200$ time steps of equal size over one cardiac cycle are used.

The models are all coupled to the same vascular model *0Dsyspul*.

For details on the different spatial finite element discretizations of the patient-specific hearts (snapshots, degrees of freedom, comparison), refer to appendix A.1.1. Sketches of the discretizations can be viewed in fig. A.1.

The gradient norm tolerance is chosen to $\epsilon_{\mathrm{grad}} = 0.003 \left\{\frac{1}{\mathrm{kPa}},\ \mathrm{s},\ \frac{\mathrm{mm}^3}{\mathrm{mPa{\cdot}s}},\ \frac{\mathrm{mm}^3}{\mathrm{mPa}}\right\}$ ($\inf$ norm tolerance of gradient, unit depending on largest absolute value). The tolerance for the homeostatic state is chosen to $\epsilon_{\mathrm{cycl}} = 5\ \%$. The perturbation parameters for the gradient calculation are chosen to $\delta x_1 = 10^{-6}$ kPa, $\delta x_2 = 10^{-6}\ \frac{1}{\mathrm{s}}$, $\delta x_3 = 10^{-6}\ \frac{1}{\mathrm{s}}$, $\delta x_4 = 10^{-6}\ \frac{\mathrm{mPa{\cdot}s}}{\mathrm{mm}^3}$ and $\delta x_5 = 10^{-6}\ \frac{\mathrm{mPa}}{\mathrm{mm}^3}$.
The weightings in (4.47) are to $b_p^{i_p} = 10$ ($i_p = 1, ..., m_p$), $b_{\mathrm{PVP}} = 10$, $b_{\mathrm{EDP}} = 10$, $b_{\mathrm{EF}} = 10$, $b_V^{\ell} = 5$ and $b_V^{r} = 0.5$. The Levenberg-Marquardt algorithm for the first "coarse" solve (relating to $v = 0$) is initialized with $\lambda^{0(0)} = 15$, while for the successive V-cycles, its initial value is updated according to $\lambda^{0(v)} \leftarrow \lambda^{0(0)}/(v+1)$. Within the "coarse" solve, λ is updated according to (4.14).

For all optimizations, the same initial parameter guess

$$\begin{aligned}\mathbf{x}^{(0)} &= \begin{bmatrix}\sigma_0^{(0)} & \alpha_{\max}^{(0)} & \alpha_{\min}^{(0)} & R_{\mathrm{ar}}^{\mathrm{sys}\,(0)} & E_{\mathrm{at,A}}^{\ell\,(0)}\end{bmatrix}^{\mathrm{T}} = \\ &= \begin{bmatrix}100\ \mathrm{kPa} & 30\ \frac{1}{\mathrm{s}} & -20\ \frac{1}{\mathrm{s}} & 140\ \frac{\mathrm{mPa}\cdot\mathrm{s}}{\mathrm{mm}^3} & 20\ \frac{\mathrm{mPa}}{\mathrm{mm}^3}\end{bmatrix}^{\mathrm{T}}\end{aligned} \tag{4.60}$$

and some set of semi-educatedly guessed initial conditions $\mathcal{I}^{(0)}$ are chosen.

Table 4.5a and tab. 4.5b show the *LA-HF* results for the algorithm *FAS-lsq* obtained after each V-cycle iteration v as well as for the Gauss-Newton iterations i on the HDM with usage of the surrogate model *S* (*2Dventr*$_{hex8\_5}$) and the coarse model *C* (*3Dventr*$_{tet4\_8}$), respectively. The analogous results for the *HA-HF* case are shown in tab. 4.6.

[5] Of course, a 2-dimensional model would be discretized with 2-dimensional finite elements, e.g. quadrilaterals (*quad4*). However, here a 3-dimensional model (mesh) with Dirichlet fixation of the out-of-plane direction is chosen, which exactly corresponds to the 2-dimensional plane strain case.

Table 4.5: *FAS-lsq* algorithm for model *3Dventr$_{tet4_1}$ | 0Dsyspul*, *LA-HF*: Iteration count v (HDM evaluations); "pseudo" heart cycle $\tilde{N}$; Gauss-Newton iteration count i (HDM solves); parameters σ_0, $\alpha_{\max}$, $\alpha_{\min}$, $R_{\mathrm{ar}}^{\mathrm{sys}}$ and $E_{\mathrm{at,A}}^{\ell}$; objective function f and its gradient norm $||\boldsymbol{\nabla} f||_\infty$; cycle error E_{cycl} on HDM; number of RDM solves n_{c} (1 solve = 6 forward calls); average and total net wall times $\varnothing t_{\mathrm{wall}}$ and t_{wall}, respectively, and net CPU time t_{CPU} (without prestressing, gradient runs and pre-/post-processing)

(a) HDM results obtained accelerated by surrogate model *S* (*2Dventr$_{hex8_5}$*)

v	$\tilde{N}$	σ_0 [kPa]	$\alpha_{\max}$ $\left[\frac{1}{\mathrm{s}}\right]$	$\alpha_{\min}$ $\left[\frac{1}{\mathrm{s}}\right]$	$R_{\mathrm{ar}}^{\mathrm{sys}}$ $\left[\frac{\mathrm{mPa\cdot s}}{\mathrm{mm}^3}\right]$	$E_{\mathrm{at,A}}^{\ell}$ $\left[\frac{\mathrm{mPa}}{\mathrm{mm}^3}\right]$	f	$\|\|\boldsymbol{\nabla} f\|\|_\infty$	E_{cycl} $[-]$	n_{c}
0	1	100.00	30.00	−20.00	140.00	20.00	91.5475	–	0.3591	31
1	1	29.50	13.42	−20.65	88.35	25.40	2.0279	–	0.1856	12
2	2	32.96	20.73	−19.52	109.36	25.42	0.6770	–	0.0624	9
3	3	34.25	21.32	−19.20	116.51	27.49	0.4611	–	0.0514	9
4	4	35.03	18.78	−20.90	110.37	27.08	0.4383	–	0.0599	7
5	5	34.85	17.88	−22.14	106.14	26.11	0.4190	–	0.0465	$\sum:$ 68
i	Gauss-Newton solve on HDM:									
0	6	34.85	17.88	−22.14	106.14	26.11	0.4665	0.0421	0.0235	
1	6	34.57	23.14	−16.11	105.15	27.88	0.4053	0.0189	0.0324	
2	6	34.22	30.40	−11.86	103.80	27.80	0.3573	0.0174	0.0535	
3	6	34.02	36.36	−11.84	103.65	27.75	0.3262	0.0076	0.0501	
4	6	33.95	39.80	−11.28	103.36	27.67	0.3205	0.0032	0.0594	
5	6	33.91	41.03	−11.31	103.37	27.67	0.3198	0.0006	0.0582	
6	7	33.92	41.14	−11.28	103.35	27.66	0.3384	0.1064	0.0287	
7	7	34.61	42.38	−10.63	102.23	26.87	0.2974	0.0065	0.0496	
8	7	34.53	43.45	−10.75	102.73	26.99	0.2962	0.0020	0.0449	

$\varnothing t_{\mathrm{wall}}^{\mathrm{HDM}} = 6.823 \cdot 10^3$ s $\varnothing t_{\mathrm{wall}}^{\mathrm{RDM}} = 0.138 \cdot 10^3$ s

$\sum t_{\mathrm{wall}}^{\mathrm{HDM}} = 15 \cdot \varnothing t_{\mathrm{wall}}^{\mathrm{HDM}} = 102.342 \cdot 10^3$ s $\sum t_{\mathrm{wall}}^{\mathrm{RDM}} = 68 \cdot \varnothing t_{\mathrm{wall}}^{\mathrm{RDM}} = 9.352 \cdot 10^3$ s

$t_{\mathrm{wall}} = \sum t_{\mathrm{wall}}^{\mathrm{HDM}} + \sum t_{\mathrm{wall}}^{\mathrm{RDM}} = 111.694 \cdot 10^3$ s $t_{\mathrm{CPU}} = 112 \cdot \sum t_{\mathrm{wall}}^{\mathrm{HDM}} + 2 \cdot \sum t_{\mathrm{wall}}^{\mathrm{RDM}} = 11.481 \cdot 10^6$ s

(b) HDM results obtained accelerated by coarse model *C* (*3Dventr$_{tet4_8}$*)

v	$\tilde{N}$	σ_0 [kPa]	$\alpha_{\max}$ $\left[\frac{1}{\mathrm{s}}\right]$	$\alpha_{\min}$ $\left[\frac{1}{\mathrm{s}}\right]$	$R_{\mathrm{ar}}^{\mathrm{sys}}$ $\left[\frac{\mathrm{mPa\cdot s}}{\mathrm{mm}^3}\right]$	$E_{\mathrm{at,A}}^{\ell}$ $\left[\frac{\mathrm{mPa}}{\mathrm{mm}^3}\right]$	f	$\|\|\boldsymbol{\nabla} f\|\|_\infty$	E_{cycl} $[-]$	n_{c}
0	1	100.00	30.00	−20.00	140.00	20.00	91.5475	–	0.3591	64*
1	1	35.09	5.42	−14.98	57.85	19.76	5.5362	–	0.2545	12
2	2	32.90	19.50	−24.37	134.69	25.44	1.6246	–	0.2558	10
3	3	38.56	16.07	−22.97	118.03	26.21	1.0005	–	0.0789	8
4	4	34.93	17.39	−24.09	100.85	25.52	0.4395	–	0.0583	6
5	5	35.06	17.62	−23.81	100.45	24.54	0.5305	–	0.0260	$\sum:$ 100
i	Gauss-Newton solve on HDM:									
0	6	35.06	17.62	−23.81	100.45	24.54	0.5447	0.0306	0.0085	
1	6	34.83	22.66	−16.95	107.46	25.38	0.4364	0.0276	0.0255	
2	6	34.59	29.75	−11.78	106.16	25.26	0.3804	0.0167	0.0491	
3	6	34.30	36.56	−11.59	105.94	25.19	0.3408	0.0112	0.0480	
4	6	34.25	40.12	−11.12	105.72	25.13	0.3331	0.0028	0.0564	
5	7	34.21	41.53	−11.11	105.77	25.13	0.3513	0.1028	0.0223	
6	7	34.75	43.73	−10.29	101.49	24.10	0.2994	0.0111	0.0481	
7	7	34.70	43.96	−10.55	102.35	24.26	0.2976	0.0023	0.0394	

$\varnothing t_{\mathrm{wall}}^{\mathrm{HDM}} = 6.845 \cdot 10^3$ s $\varnothing t_{\mathrm{wall}}^{\mathrm{RDM}} = 0.070 \cdot 10^3$ s

$\sum t_{\mathrm{wall}}^{\mathrm{HDM}} = 14 \cdot \varnothing t_{\mathrm{wall}}^{\mathrm{HDM}} = 95.824 \cdot 10^3$ s $\sum t_{\mathrm{wall}}^{\mathrm{RDM}} = 100 \cdot \varnothing t_{\mathrm{wall}}^{\mathrm{RDM}} = 7.042 \cdot 10^3$ s

$t_{\mathrm{wall}} = \sum t_{\mathrm{wall}}^{\mathrm{HDM}} + \sum t_{\mathrm{wall}}^{\mathrm{RDM}} = 102.866 \cdot 10^3$ s $t_{\mathrm{CPU}} = 112 \cdot \sum t_{\mathrm{wall}}^{\mathrm{HDM}} + 28 \cdot \sum t_{\mathrm{wall}}^{\mathrm{RDM}} = 10.929 \cdot 10^6$ s

Table 4.6: *FAS-lsq* algorithm for model *3Dventr$_{tet4_1}$ | 0Dsyspul*, *HA-HF*: Iteration count v (HDM evaluations); "pseudo" heart cycle $\tilde{N}$; Gauss-Newton iteration count i (HDM solves); parameters σ_0, $\alpha_{\max}$, $\alpha_{\min}$, $R_{\mathrm{ar}}^{\mathrm{sys}}$ and $E_{\mathrm{at,A}}^{\ell}$; objective function f and its gradient norm $||\boldsymbol{\nabla} f||_{\infty}$; cycle error E_{cycl} on HDM; number of RDM solves n_{c} (1 solve = 6 evaluations); average and total net wall times $\varnothing t_{\mathrm{wall}}$ and t_{wall}, respectively, and net CPU time t_{CPU} (without prestressing, gradient runs and pre-/post-processing)

(a) HDM results obtained accelerated by surrogate model *S* (*2Dventr$_{hex8_5}$*)

v	$\tilde{N}$	σ_0 [kPa]	$\alpha_{\max}$ $\left[\frac{1}{\mathrm{s}}\right]$	$\alpha_{\min}$ $\left[\frac{1}{\mathrm{s}}\right]$	$R_{\mathrm{ar}}^{\mathrm{sys}}$ $\left[\frac{\mathrm{mPa\cdot s}}{\mathrm{mm}^3}\right]$	$E_{\mathrm{at,A}}^{\ell}$ $\left[\frac{\mathrm{mPa}}{\mathrm{mm}^3}\right]$	f	$\|\|\boldsymbol{\nabla} f\|\|_{\infty}$	E_{cycl} [−]	n_{c}
0	1	100.00	30.00	−20.00	140.00	20.00	30.5241	–	0.4404	21
1	1	59.38	9.74	−14.97	223.16	10.90	2.0635	–	0.4279	15
2	2	65.22	10.15	−15.79	230.28	9.11	0.6856	–	0.1923	10
3	3	65.00	10.65	−15.64	233.92	7.93	0.5339	–	0.1616	8
4	4	65.50	10.13	−15.96	226.00	7.78	0.4890	–	0.1707	6
5	5	65.46	10.04	−16.20	224.27	7.68	0.4883	–	0.1566	4
6	6	65.45	10.14	−15.95	223.78	7.68	0.4887	–	0.1430	3
7	7	65.47	10.16	−16.01	223.45	7.69	0.4912	–	0.1279	4
8	8	65.51	10.21	−15.94	222.60	7.66	0.4908	–	0.1166	2
9	9	65.53	10.21	−16.05	222.32	7.65	0.4936	–	0.1040	4
10	10	65.59	10.24	−15.93	221.48	7.63	0.4929	–	0.0951	2
11	11	65.61	10.24	−16.05	221.26	7.64	0.4956	–	0.0843	4
12	12	65.67	10.26	−15.93	220.61	7.62	0.4953	–	0.0770	1
13	13	65.67	10.26	−15.93	220.61	7.62	0.4985	–	0.0673	5
14	14	65.77	10.20	−16.14	219.99	7.59	0.4989	–	0.0613	2
15	15	65.80	10.18	−16.34	219.78	7.59	0.5008	–	0.0549	2
16	16	65.81	10.23	−16.18	219.59	7.59	0.5011	–	0.0496	$\sum:$ 93
i	Gauss-Newton solve on HDM:									
0	17	65.81	10.23	−16.18	219.59	7.59	0.5112	0.0471	0.0392	
1	17	65.22	11.48	−14.78	217.26	7.78	0.4939	0.0079	0.0491	
2	17	65.30	11.54	−15.02	217.35	7.78	0.4930	0.0002	0.0508	
3	18	65.28	11.58	−14.98	217.35	7.78	0.4978	0.0322	0.0372	
4	18	65.44	11.66	−14.89	216.70	7.92	0.4935	0.0005	0.0434	

$\varnothing t_{\mathrm{wall}}^{\mathrm{HDM}} = 6.754 \cdot 10^3$ s $\quad \varnothing t_{\mathrm{wall}}^{\mathrm{RDM}} = 0.107 \cdot 10^3$ s

$\sum t_{\mathrm{wall}}^{\mathrm{HDM}} = 22 \cdot \varnothing t_{\mathrm{wall}}^{\mathrm{HDM}} = 148.588 \cdot 10^3$ s $\quad \sum t_{\mathrm{wall}}^{\mathrm{RDM}} = 93 \cdot \varnothing t_{\mathrm{wall}}^{\mathrm{RDM}} = 9.930 \cdot 10^3$ s

$t_{\mathrm{wall}} = \sum t_{\mathrm{wall}}^{\mathrm{HDM}} + \sum t_{\mathrm{wall}}^{\mathrm{RDM}} = 158.518 \cdot 10^3$ s $\quad t_{\mathrm{CPU}} = 112 \cdot \sum t_{\mathrm{wall}}^{\mathrm{HDM}} + 2 \cdot \sum t_{\mathrm{wall}}^{\mathrm{RDM}} = 16.662 \cdot 10^6$ s

(b) HDM results obtained accelerated by coarse model *C* (*3Dventr$_{tet4_8}$*)

v	$\tilde{N}$	σ_0 [kPa]	$\alpha_{\max}$ $\left[\frac{1}{\mathrm{s}}\right]$	$\alpha_{\min}$ $\left[\frac{1}{\mathrm{s}}\right]$	$R_{\mathrm{ar}}^{\mathrm{sys}}$ $\left[\frac{\mathrm{mPa\cdot s}}{\mathrm{mm}^3}\right]$	$E_{\mathrm{at,A}}^{\ell}$ $\left[\frac{\mathrm{mPa}}{\mathrm{mm}^3}\right]$	f	$\|\|\boldsymbol{\nabla} f\|\|_{\infty}$	E_{cycl} [−]	n_{c}
0	1	100.00	30.00	−20.00	140.00	20.00	30.5241	–	0.4404	21
1	1	64.48	8.32	−13.64	227.18	9.11	0.9061	–	0.4438	8
2	2	66.17	10.28	−16.59	228.12	8.98	0.8701	–	0.1908	10
3	3	65.48	10.50	−16.01	228.03	7.21	0.5357	–	0.1647	8
4	4	65.02	10.55	−15.98	223.49	7.87	0.4862	–	0.1677	6
5	5	65.17	10.56	−16.03	223.82	7.73	0.4839	–	0.1527	3
6	6	65.18	10.56	−16.02	223.75	7.72	0.4866	–	0.1375	2
7	7	65.23	10.58	−16.02	223.34	7.71	0.4884	–	0.1246	3
8	8	65.32	10.60	−16.04	222.32	7.69	0.4877	–	0.1144	3
9	9	65.36	10.59	−16.08	221.66	7.68	0.4892	–	0.1031	1
10	10	65.36	10.59	−16.08	221.66	7.68	0.4923	–	0.0913	2
11	11	65.42	10.62	−16.10	221.06	7.67	0.4926	–	0.0833	2
12	12	65.47	10.62	−16.10	220.61	7.67	0.4939	–	0.0751	2
13	13	65.51	10.61	−16.11	220.19	7.66	0.4950	–	0.0677	3
14	14	65.59	10.59	−16.12	219.61	7.63	0.4955	–	0.0615	2
15	15	65.60	10.58	−16.15	219.46	7.62	0.4973	–	0.0544	2
16	16	65.64	10.58	−16.16	219.22	7.61	0.4983	–	0.0487	$\sum:$ 78
i	Gauss-Newton solve on HDM:									
0	17	65.64	10.58	−16.16	219.22	7.61	0.5053	0.0385	0.0390	
1	17	65.16	11.66	−14.62	217.15	7.77	0.4943	0.0058	0.0473	
2	17	65.29	11.57	−15.01	217.31	7.77	0.4935	0.0002	0.0484	

$\varnothing t_{\mathrm{wall}}^{\mathrm{HDM}} = 6.746 \cdot 10^3$ s $\quad \varnothing t_{\mathrm{wall}}^{\mathrm{RDM}} = 0.070 \cdot 10^3$ s

$\sum t_{\mathrm{wall}}^{\mathrm{HDM}} = 20 \cdot \varnothing t_{\mathrm{wall}}^{\mathrm{HDM}} = 134.921 \cdot 10^3$ s $\quad \sum t_{\mathrm{wall}}^{\mathrm{RDM}} = 78 \cdot \varnothing t_{\mathrm{wall}}^{\mathrm{RDM}} = 5.479 \cdot 10^3$ s

$t_{\mathrm{wall}} = \sum t_{\mathrm{wall}}^{\mathrm{HDM}} + \sum t_{\mathrm{wall}}^{\mathrm{RDM}} = 140.400 \cdot 10^3$ s $\quad t_{\mathrm{CPU}} = 112 \cdot \sum t_{\mathrm{wall}}^{\mathrm{HDM}} + 28 \cdot \sum t_{\mathrm{wall}}^{\mathrm{RDM}} = 15.265 \cdot 10^6$ s

Table 4.7a shows the *LA-HF* results for the algorithm *ROM-ml* obtained after each V-cycle iteration v as well as for the Gauss-Newton iterations i on the HDM, and tab. 4.7b shows the analogous results for the *HA-HF* case.

Table 4.7: *ROM-ml* algorithm for model *3Dventr$_{tet4_1}$ | 0Dsyspul*: Iteration count v (HDM evaluations); "pseudo" heart cycle $\tilde{N}$; Gauss-Newton iteration count i (HDM solves); parameters σ_0, $\alpha_{\max}$, $\alpha_{\min}$, $R_{\text{ar}}^{\text{sys}}$ and $E_{\text{at,A}}^{\ell}$; objective function f and its gradient norm $||\boldsymbol{\nabla} f||_\infty$; cycle error E_{cycl} on HDM; number of RDM solves n_{c} (1 solve = 6 forward calls); average and total net wall times $\varnothing t_{\text{wall}}$ and t_{wall}, respectively, and net CPU time t_{CPU} (without prestressing, gradient runs and pre-/post-processing)

(a) *LA-HF*

v	$\tilde{N}$	σ_0 [kPa]	$\alpha_{\max}$ $\left[\frac{1}{\text{s}}\right]$	$\alpha_{\min}$ $\left[\frac{1}{\text{s}}\right]$	$R_{\text{ar}}^{\text{sys}}$ $\left[\frac{\text{mPa·s}}{\text{mm}^3}\right]$	$E_{\text{at,A}}^{\ell}$ $\left[\frac{\text{mPa}}{\text{mm}^3}\right]$	f	$\|\|\boldsymbol{\nabla} f\|\|_\infty$	E_{cycl} [−]	n_{c}
0	1	100.00	30.00	−20.00	140.00	20.00	91.5475	–	0.3591	25
1	1	32.39	42.04	−13.74	107.90	25.78	0.3338	–	0.1909	7
2	2	32.43	40.10	−12.42	105.83	25.77	0.3485	–	0.1049	8
3	3	32.98	43.80	−12.04	105.71	24.99	0.4343	–	0.0762	8
4	4	33.38	48.06	−11.43	106.35	21.93	0.3200	–	0.0398	$\sum$: 48
i	Gauss-Newton solve on HDM:									
0	5	33.38	48.06	−11.43	106.35	21.93	0.3780	0.1253	0.0231	
1	5	34.14	44.11	−10.25	103.81	23.03	0.2964	0.0263	0.0624	
2	5	34.10	44.37	−10.78	104.63	23.17	0.2899	0.0026	0.0458	

$\varnothing t_{\text{wall}}^{\text{HDM}} = 6.753 \cdot 10^3$ s $\varnothing t_{\text{wall}}^{\text{RDM}} = 0.742 \cdot 10^3$ s

$\sum t_{\text{wall}}^{\text{HDM}} = 8 \cdot \varnothing t_{\text{wall}}^{\text{HDM}} = 54.024 \cdot 10^3$ s $\sum t_{\text{wall}}^{\text{RDM}} = 48 \cdot \varnothing t_{\text{wall}}^{\text{RDM}} = 35.616 \cdot 10^3$ s

$t_{\text{wall}} = \sum t_{\text{wall}}^{\text{HDM}} + \sum t_{\text{wall}}^{\text{RDM}} = 89.640 \cdot 10^3$ s $t_{\text{CPU}} = 112 \cdot \sum t_{\text{wall}}^{\text{HDM}} + 112 \cdot \sum t_{\text{wall}}^{\text{RDM}} = 10.040 \cdot 10^6$ s

(b) *HA-HF*

v	$\tilde{N}$	σ_0 [kPa]	$\alpha_{\max}$ $\left[\frac{1}{\text{s}}\right]$	$\alpha_{\min}$ $\left[\frac{1}{\text{s}}\right]$	$R_{\text{ar}}^{\text{sys}}$ $\left[\frac{\text{mPa·s}}{\text{mm}^3}\right]$	$E_{\text{at,A}}^{\ell}$ $\left[\frac{\text{mPa}}{\text{mm}^3}\right]$	f	$\|\|\boldsymbol{\nabla} f\|\|_\infty$	E_{cycl} [−]	n_{c}
0	1	100.00	30.00	−20.00	140.00	20.00	30.5241	–	0.4404	22
1	1	63.51	12.86	−16.88	228.65	9.02	0.5471	–	0.4351	14
2	2	64.24	12.19	−15.93	227.77	9.00	0.5937	–	0.1970	9
3	3	64.35	12.04	−15.89	227.46	8.18	0.5079	–	0.1825	7
4	4	64.43	11.99	−15.78	225.15	7.89	0.4898	–	0.1728	6
5	5	64.46	11.99	−15.74	223.95	7.81	0.4883	–	0.1584	5
6	6	64.51	12.02	−15.69	223.18	7.76	0.4883	–	0.1437	3
7	7	64.55	12.06	−15.68	222.68	7.74	0.4897	–	0.1297	3
8	8	64.59	12.10	−15.64	222.05	7.72	0.4908	–	0.1172	3
9	9	64.64	12.14	−15.59	221.39	7.70	0.4917	–	0.1059	2
10	10	64.66	12.17	−15.57	221.05	7.70	0.4933	–	0.0947	3
11	11	64.72	12.20	−15.52	220.31	7.68	0.4940	–	0.0860	2
12	12	64.75	12.19	−15.62	220.03	7.67	0.4966	–	0.0767	3
13	13	64.80	12.23	−15.60	219.53	7.65	0.4975	–	0.0697	2
14	14	64.82	12.25	−15.60	219.31	7.65	0.4991	–	0.0621	2
15	15	64.85	12.27	−15.59	219.03	7.64	0.5003	–	0.0556	2
16	16	64.89	12.24	−15.65	218.74	7.63	0.5018	–	0.0497	$\sum$: 88
i	Gauss-Newton solve on HDM:									
0	17	64.89	12.24	−15.65	218.74	7.63	0.5038	0.0260	0.0399	
1	17	65.05	12.10	−14.49	217.32	7.74	0.4947	0.0018	0.0454	

$\varnothing t_{\text{wall}}^{\text{HDM}} = 6.750 \cdot 10^3$ s $\varnothing t_{\text{wall}}^{\text{RDM}} = 0.748 \cdot 10^3$ s

$\sum t_{\text{wall}}^{\text{HDM}} = 19 \cdot \varnothing t_{\text{wall}}^{\text{HDM}} = 128.257 \cdot 10^3$ s $\sum t_{\text{wall}}^{\text{RDM}} = 88 \cdot \varnothing t_{\text{wall}}^{\text{RDM}} = 65.835 \cdot 10^3$ s

$t_{\text{wall}} = \sum t_{\text{wall}}^{\text{HDM}} + \sum t_{\text{wall}}^{\text{RDM}} = 194.092 \cdot 10^3$ s $t_{\text{CPU}} = 112 \cdot \sum t_{\text{wall}}^{\text{HDM}} + 112 \cdot \sum t_{\text{wall}}^{\text{RDM}} = 21.738 \cdot 10^6$ s

Figure 4.8 shows the final left heart and systemic pressures as well as the left and right ventricular pressure-volume relationships obtained by the algorithm *ROM-ml* (converged *FAS-lsq* results – regardless of the coarse model – are virtually the same). The measured time-resolved left ventricular pressure is denoted by $\tilde{p}_{\mathrm{v}}^{\ell}$ (brown-dotted curves). Measured left ventricular ejection fractions $\widetilde{\mathrm{EF}}^{\ell}$ are shown in top left corner of the pressure-volume loops, along with the computed values EF^{ℓ}.
The *HA-HF* case produces pressure amplitudes that are about a factor 2 greater that for the *LA-HF* situation, however ejection fractions remain virtually the same.

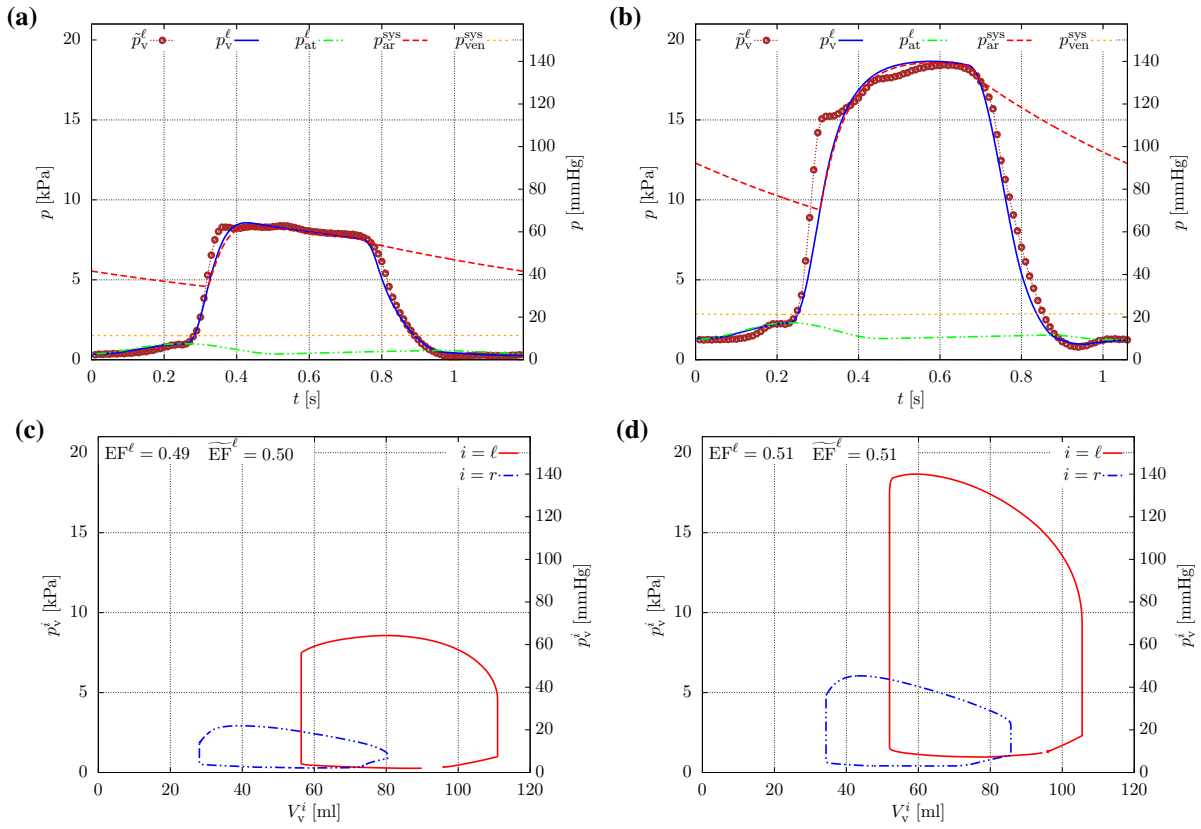

Figure 4.8: Model *3Dventr*$_{tet4\_1}$ | *0Dsyspul*: Outcome of the parameter estimation process, final converged results using *ROM-ml*. **(a)** *LA-HF*: Left heart and systemic pressures over time t, measured pressure is $\tilde{p}_{\mathrm{v}}^{\ell}$ (brown-dotted curve). **(b)** *HA-HF*: Left heart and systemic pressures over time t, measured pressure is $\tilde{p}_{\mathrm{v}}^{\ell}$ (brown-dotted curve). **(c)** *LA-HF*: Left ($i = \ell$) and right ($i = r$) ventricular pressure-volume relationship, measured left ventricular ejection fraction ($\widetilde{\mathrm{EF}}^{\ell}$) and simulated one ($\mathrm{EF}^{\ell}$) in top left corner. **(d)** *HA-HF*: Left ($i = \ell$) and right ($i = r$) ventricular pressure-volume relationship, measured left ventricular ejection fraction ($\widetilde{\mathrm{EF}}^{\ell}$) and simulated one ($\mathrm{EF}^{\ell}$) in top left corner.

4.3.4 Discussion

Novel multilevel (2-level) methods for the simultaneous estimation of stable homeostatic state conditions and key parameters that govern heart work are developed and successfully applied to a patient-specific 3D-0D heart and vascular model under two different types of artificial heart failure conditions. The central idea of the multilevel approach is to reduce the computational burden that would be associated with an optimization problem on a high-fidelity, high-dimensional model (HDM) by help of a computationally inexpensive low-fidelity, reduced-dimensional model (RDM). Here, the HDM has sufficiently fine spatial resolution such that spurious effects like locking phenomena are minimal, cf. the comparisons of the discretizations in appendix sec. A.1.1. A gradient-based nonlinear optimization problem is incorporated into a 2-level V-cycle-type algorithm inspired from nonlinear multigrid techniques, with the essential idea to outsource the gradient-based optimization work to a computationally cheap surrogate RDM. The RDM solve of the optimization problem ultimately produces a set of parameters that is sufficiently close to the true minimum on the HDM such that little computational effort is left to find the optimum. Therefore, the HDM optimization problem is enhanced or accelerated by the 2-level algorithm with the sake of saving computational effort.

The choice of global parameters that are not spatially resolved is reasoned by the type of measurements that were available from the in-vivo experiments. Since at least a pair of measured (end-systolic) pressure and volume (ejection fraction) was available, the calibration of contraction strength (contractility) and afterload (resistance) is a natural choice. These parameters are quickly responsive to medical treatment such as β_1-blockade or phenylephrine. Thus, they exhibit short time scale variability and therefore are prone to be estimated given the data and the experimental setup (cf. Jagschies et al. [98] and the thesis by Jagschies [97] for further details on the in-vivo studies). Passive elastic properties of the myocardium are assumed to remain unaltered during an acute experiment and are not considered for estimation.
Furthermore, the left ventricular pressure measurements were time-resolved, which allowed to additionally calibrate the ventricular upstroke and the relaxation rates, hence the speed of force generation and relief. Finally, end-diastolic pressure was used to calibrate preload, here in terms of left atrial contractility (elastance amplitude).
The calibration procedure is not restricted to these type of measurements or parameters, and would be easily extendable or modifiable if complete synchronized time-resolved pressure-volume data was available.
The problem of low identifiability of parameters [219] which is likely to arise if the parameter space is too large or inappropriate with respect to the (portions of) measured data – meaning the existence of an infinite amount of minima to the optimization problem – is extensively discussed in Hirschvogel et al. [86], and the existence of a well-identifiable minimum is demonstrated therein.

The *FAS-lsq* algorithm was a special variant of multigrid algorithms for optimization as they have been presented, for instance, by Nash [146], and in its specific form requires a least-squares-type of problem to be solved. As elucidated in sec. 4.3.1, choosing a modified coarse objective function (4.54) instead of applying the FAS residual modification to the right-hand side of $(4.4)_1$ is reasoned by avoiding the computation of a gradient by finite differences on the HDM during the V-cycle

iterations. Furthermore, the presented approach is applicable to non-convex problems without the need to account for additional modifications of the coarse grid problem as done in Nash [146]. However, the FAS modification on the least-squares residuals at some point is heuristic and does not necessarily guarantee to provide a close-minimum parameter set for the HDM.
Within this algorithm, two different types of RDMs are considered, namely the same patient-specific heart geometry but heavily coarsely discretized in space (and time) (model *C*), as well as a surrogate 2D plane strain generic heart model with very little degrees of freedom for the efficient computation on a local machine (model *S*).
Both surrogate models yield similar results at the end of the V-cycle iteration for both the low-afterload heart failure (*LA-HF*) and high-afterload heart failure (*HA-HF*) case, cf. tab 4.5 ($v = 5$) and tab. 4.6 ($v = 16$). While contractility, resistance and elastance are generally close to the final values, both models *C* and *S* yield rate parameters $\alpha_{\max}$ and $\alpha_{\min}$ that are only half or twice the final converged values for the *LA-HF* case, but in general are close for the *HA-HF* case. This may be reasoned that the least-squares residuals modification (4.54) is able to account for the delta in model behavior with respect to the scaling of the deformation (i.e., model *C* would require a far higher contractility value to achieve the same deformation as the HDM due to severe locking phenomena exhibited by the former), but probably will struggle if the coarse model's kinematic nature differs too drastically, hence reduced or altered kinematic modes of model *C* or *S* cannot capture the HDM modes sufficiently (i.e., the rate of upstroke or relaxation trigger different distinct modes in the HDM than in the RDM). The better performance of the two models in the *HA-HF* with respect to the rate parameters is not investigated but might be due to the significantly higher base (prestressed) pressure level that somehow moves the models' response upwards in the stress-strain relationship.
However, despite the gaps between some end V-cycle and converged HDM parameters, the objective function f is already close to the minimum (compared to the initial value), hence the classical "valley" problem where large changes in some parameters have only tiny effects on the cost function is observed.
Both, model *C* and *S*, produce comparable additional optimization work that has to be performed on the HDM. Differences of 1–2 iterations are not directly associated to the type of RDM but rather depend on the initial condition update (e.g., last Gauss-Newton iteration ($i = 2$) of tab. 4.6b is lucky to remain below the cycle tolerance, while the same iteration in tab. 4.6a slightly violates it such that extra work has to be performed).
Wall and CPU timing-wise, model *C* exhibits slightly better performance, however model *C* is computed on an HPC cluster and model *S* on a local machine. One iteration is accompanied with the calculation of the gradient, hence six simultaneous simulations are performed with each being assigned two cores which compromises objective time measurements on a local machine.

Projection-based model order reduction techniques have been used in order to generalize the *FAS-lsq* scheme to non-least-squares problems and possibly to more complex (heart) models (*3Datrioventr*) that do not allow for the simple construction of coarse discretizations (with standard meshing schemes, $h \approx 2\ \mathrm{mm}$ is the coarsest possible mesh size for model *3Datrioventr*, cf. appendix sec. A.1.1) or for dimensionality reductions in a straightforward manner.
The novel *ROM-ml* scheme (cf. sec. 4.3.2) does not need a FAS modification of the objective function since the delta in model behavior is directly incorporated into the RDM, here being a reduced-order model (ROM) generated by proper orthogonal decomposition (POD).

End V-cycle parameters, cf. tab. 4.7a (*LA-HF*) and tab. 4.7b (*HA-HF*), are very close to the true HDM optimum, and the additional Gauss-Newton HDM iterations are minimal and are needed to correct for the final initial condition update that is performed when entering the Gauss-Newton scheme.
Wall and CPU timing-wise, *ROM-ml* even performs better than *FAS-lsq* for the *LA-HF* case, even though the ROM is computed on the same 112 cores as the HDM. However, for increasing V-cycle iterations that are required for the *HA-HF* case, wall and CPU times for *ROM-ml* are about a factor of 1.3 larger than for *FAS-lsq*, since the savings in HDM Gauss-Newton iterations is less pronounced than for the *LA-HF* case, and single wall time for a ROM is larger than for models *C* or *S*.

In general, the amount of V-cycle iterations strongly depends on the choice of initial conditions, hence further modifications of the algorithms might be thought of. For example, the homeostatic state may be directly computed exclusively on the ROM without the need to visit the HDM during V-cycling.
Depending on the magnitude of certain parameters, the homeostatic state may be reached fairly rapidly ($v \leq 5$ iterations for the *LA-HF* case) or rather tediously ($v = 16$ iterations for the *HA-HF* case). In general, high vascular resistances and low compliances (as for the latter case) seem to slow down the blood distribution kinetics in the vascular system, hence more cycles are required to reach homeostasis.

5 Applications to ventricular assist device engineering

Congestive heart failure (CHF) [99] as one of the most prevailing disease entities in modern societies drives the development of novel technologies for heart assistance, since the availability of donor organs for transplantation, being the gold standard for heart failure therapies, is continuously reduced [160].
The computational models and parameter estimation methods that were developed in chap. 2–4 here are applied to assess the efficiency of a novel extravascular ventricular assist device (VAD) as it currently is developed in close collaboration with industrial partners, cf. chap. 1 for introductory remarks on vascular assist devices and the following sections for further in-depth explanations.

The main purpose of using computational (in-silico) models is to substantially enhance future processes of individualized implant design and hence to contribute to further mechanistic understanding of heart failure treatment strategies. By using experimental in-vivo data for model calibration and personalization, computational modeling as a tool to describe and predict patient-specific hemodynamic conditions under scenarios of extravascular ventricular support has predictive potential with regard to optimal design and operating conditions of heart assistance implants.
At least three ultimate aims of such computational approaches may be formulated: In-silico models may

- enable to consider a far higher amount of design variants and optimization loops than in-vivo models alone would ever permit;
- allow to gain insights how a treatment influences physiological quantities like cardiac wall stress and strain which are hardly or not at all assessable via experiments; and
- substitute or at least reduce the amount of animal (in-vivo) experiments needed for the reliable and secure design of novel medical devices.

The former aspect is of great interest with regard to disease progression of CHF, as permanently increased diastolic myofiber strain and systolic wall stress are considered the major driving mechanisms of growth and remodeling, namely maladaptive changes in myocardial physiology and morphology [96], cf. the computational models thereof presented in chap. 2, sec. 2.3.
Whereas current left ventricular assist device (LVAD) therapy leads to ventricular unloading and reduction of myocardial stress, the impact on remodeling is subject to current research and still not well understood [22, 25, 32, 55, 100, 118, 215].

This chapter is organized as follows. Section 5.1 presents the general concept of the novel implant and heart assist technology, and sec. 5.2 briefly comments on the experimental in-vivo results that

were obtained from animal studies with the prototype of the implant. Section 5.3 then introduces the computational approach for the interaction modeling of heart and implant, and sec. 5.4 outlines an automated optimization workflow to address specific design questions, e.g. here the optimal positioning of the pneumatic units to achieve a maximum in ventricular stroke work.

5.1 Concept and development of the AdjuCor® biventricular assist device (BiVAD)

The biventricular assist device (BiVAD) is developed in close collaboration with the company AdjuCor® GmbH. The implant is customized to the patient's ventricular shape and size. It consists of a wickerwork-like nitinol shell, a polyurethan sleeve covering the nitinol and three thin-walled polyurethan inflatable pad-like pneumatic units facing the epicardial surface, cf. fig. 5.2. These pads are bellows-like such that high lift with small material straining is achieved when being inflated. Within the manufacturing process, they may be sized and positioned at the anterior and posterior left as well as at the right ventricular epicardial locations according to customized needs of the patient (i.e. at infarct locations). They directly interact with the heart by exerting contact forces onto the epicardial surface. The inflation of the three pads is ECG-controlled and timed according to the QRS-signal (cf. fig. 1.2c for a schematic ECG curve). Support pressure may be varied during systole length.
The individualized design of the shell originates from a CT imaging performed four weeks prior to the in-vivo experiment (fig. 5.1a). Segmentation of the epicardial ventricular contour is carried out at $80\ \%$ diastole ($0.2 \cdot T_{\mathrm{cycl}}$ prior to end-diastolic time t_{ed}) using MIMICS® software (Materialise.com, fig. 5.1b). The obtained stereolithographic (STL) geometry is smoothed and cut at the atrioventricular plane (fig. 5.1c), which is defined by help of the axis from the apex through the aortic valve's center with intercept at the posterior mitral valve leaflet. The positive mould for the implant manufacturing process (fig. 5.1d) is obtained by taking a predefined enlargement (offset) of the segmented ventricular portion of $4\ \mathrm{mm}$ such that the pneumatic units comfortably fit between shell and epicardium without mechanical constraint. Figures 5.1e–g depict the design of the final implant and fig. 5.1h–k the application to the patient via minimally invasive surgery.

5.2 In-vivo experiments on a porcine failing heart model

Here, three pigs from the in-vivo study described in Jagschies et al. [98] are considered, subsequently denoted as *p1*, *p2* and *p3*. After application of anesthesia and placement of the respective catheters for monitoring of pressures, flows and oxygen saturation, the implant was placed via a lower partial sternotomy and partial pericardiotomy. Correct positioning of the individualized implant was checked prior to closing the chest for further assessment of experimental data.
Baseline cardiac function parameters of the healthy heart as well as for two drug-induced heart failure scenarios were recorded without VAD support. The first functional failing heart condition was induced by β_1-receptor blockade that reduced heart rate and contraction strength of the ventricles. It was characterized by low cardiac output and low peripheral vascular resistance leading to very low blood pressure values. In this state, referred to as low-afterload heart failure (*LA-HF*), the hemodynamic effects of gradual increases of left ventricular augmentation pressure

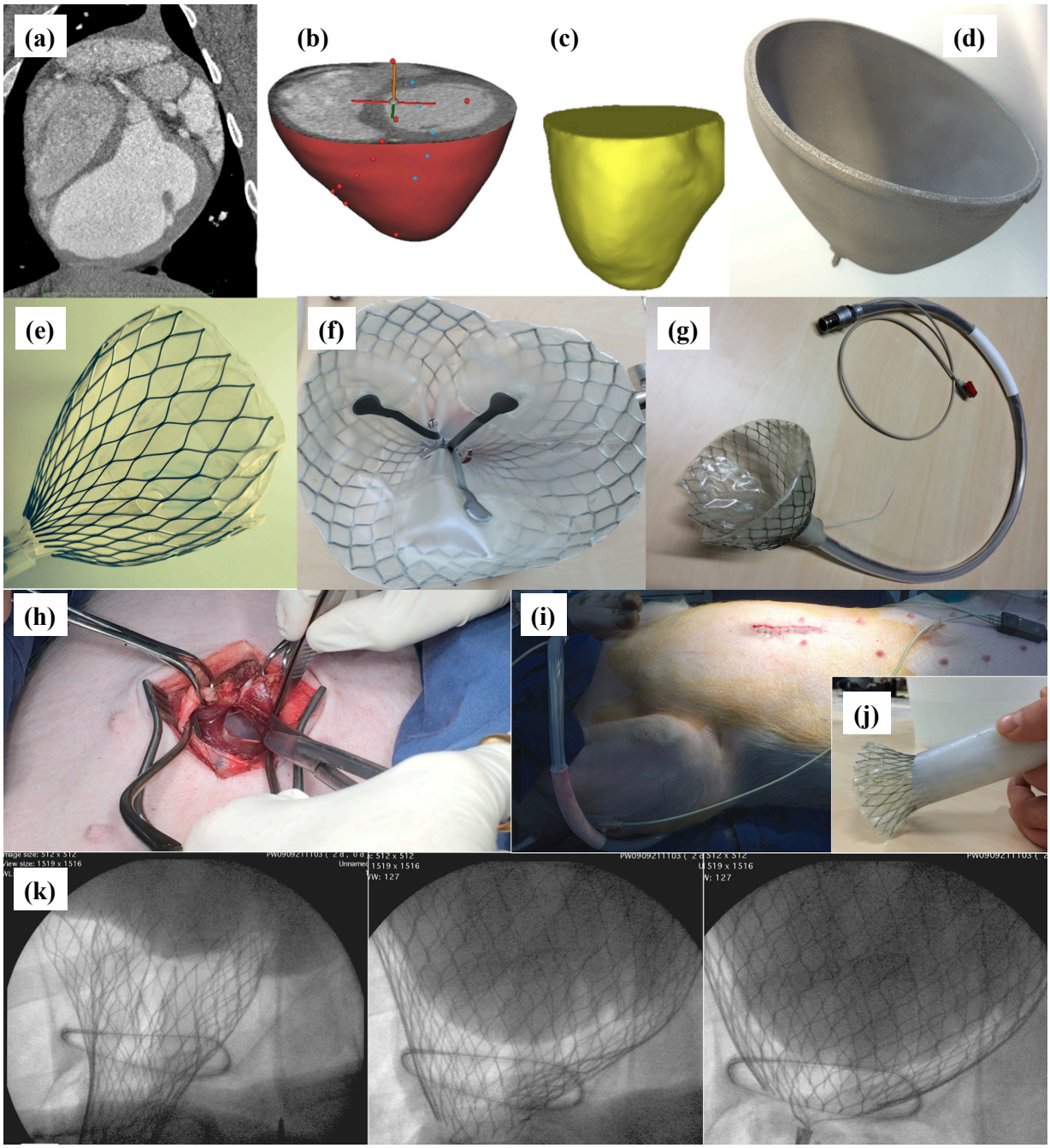

Figure 5.1: Processing chain of implant development and minimally invasive implantation procedure. **(a)** CT image of the patient as basis for segmentation. **(b)** Segmentation of the ventricular portion of the heart by help of MIMICS® software (Materialise.com). **(c)** Final smoothed segmented geometry, ventricular portion of the heart truncated at the atrioventricular plane. **(d)** Enlarged positive mould for the manufacturing process. **(e)–(g)** Final implant including the flexible wickerwork-like nitinol shell, the polyurethan sleeve and the three pad-like pneumatic units as well as the connector cable to the penumatic supply unit. **(h)**,**(i)** Minimally invasive surgery and implantation of the device into a pig. **(j)** Crimping of the device to 30 mm diameter. **(k)** Expansion of the implant beneath the pericardium of the porcine heart.

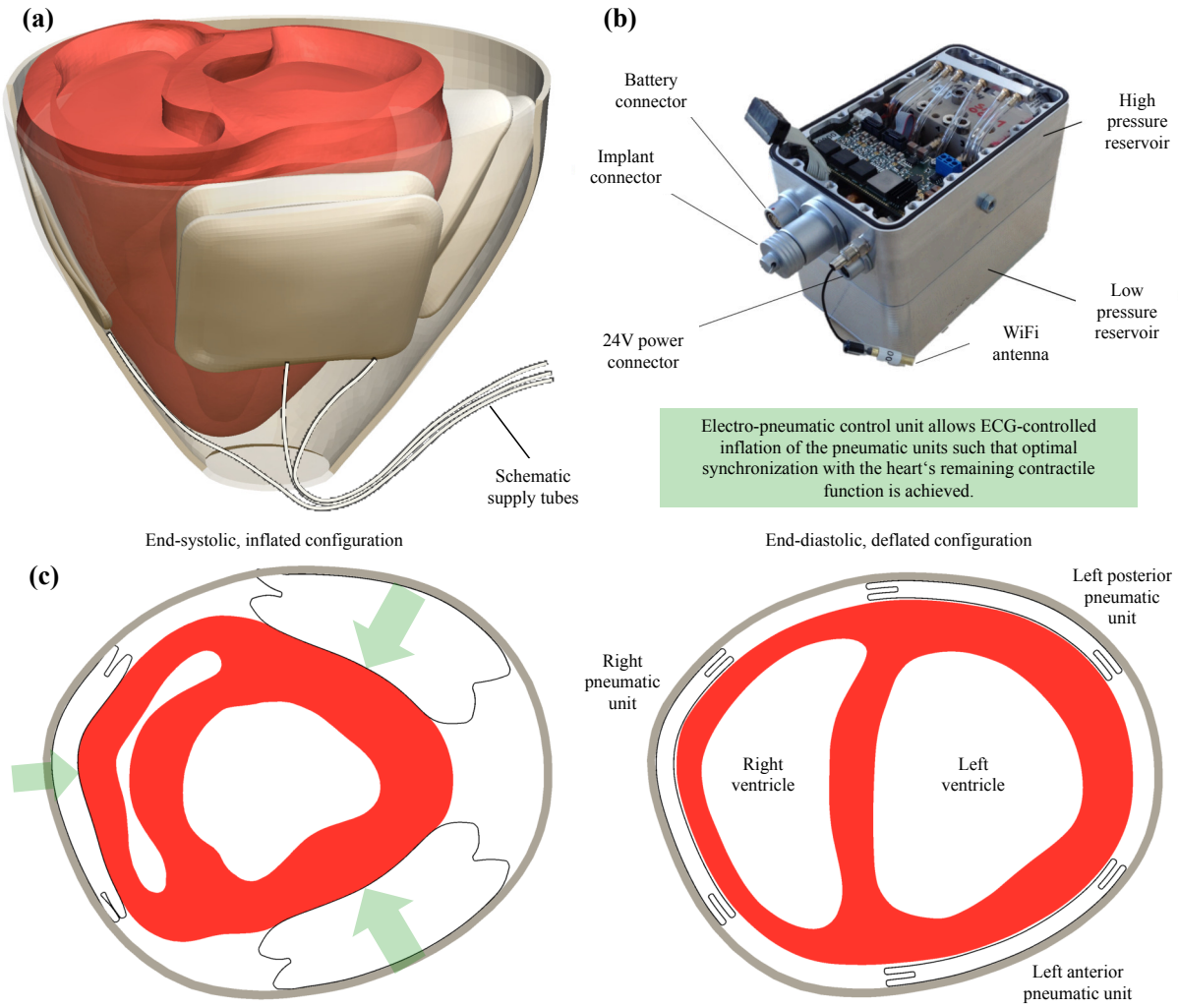

Figure 5.2: Conceptual function of the implant. **(a)** Implant with inflated pads acting on the ventricles in end-systole (simulation, anterior view), schematic supply tubes (not modeled). **(b)** Electro-pneumatic control unit with low- and high-pressure reservoirs, battery, 24V power and implant connectors as well as a WiFi antenna. Pad inflation is controlled via ECG electrodes (not shown) in order to achieve optimal support synchronization with the heart's contraction. **(c)** End-systolic (inflated pads) vs. end-diastolic (deflated pads) configuration, axial slice (simulation).

were assessed.
A similar protocol was conducted for a high-afterload heart failure (*HA-HF*) scenario, which was induced by additional infusion of phenylephrine leading to a constriction of the peripheral arterioles and therefore increased vascular resistance.
Refer also to chap. 4 for estimation of parameters that govern these two distinct states of pharmacologically-induced heart failure.

5.3 Patient-specific modeling of the implant and its ventricular interaction

5.3.1 Parameterized patient-specific implant modeling

The in-silico implant is generated by processing from the positive mould CAD model of the patient-specific epicardial contour. A local φ, z coordinate system for parameterization of the pad locations is introduced, with its origin being the intercept of the atrioventricular plane (AVP) with the axis through the aortic valve and the apex, cf. fig. 5.3a,b. The three pads are denoted with respect to their epicardial position, i.e. left anterior (ℓ_a), left posterior (ℓ_p) and right (r).
Additionally, the patient-specific in-silico implant is parameterized with respect to the pads' wall thickness $d_\mathrm{P}^\mathrm{wall}$, their (radial) depth d_P, the bellows inset h_P^s, the seam inner and outer radii $r_\mathrm{P}^\mathrm{s,i}$ and $r_\mathrm{P}^\mathrm{s,o}$, the corner radius $r_\mathrm{P}^\mathrm{cor}$, and the shell's thickness d_S, cf. fig. 5.3a,b and tab. 5.1 for the specific values of these parameters.
A framework for modeling of the VAD is developed using Trelis® software (csimsoft.com) and Pyhton programming language-based scripting. The processing chain is depicted in fig. 5.4. It is designed such that arbitrary ventricular shapes and individualized positions of the pads may be specified, hence a maximum of flexibility with respect to the patient-specific ventricular geometry and the locations of the pads is given.
The smoothed segmented ventricular contour is imported as STL (fig. 5.4a), enlarged by a uniform offset of $4\ \mathrm{mm}$ (fig. 5.4b), and cut $10\ \mathrm{mm}$ above the AVP prior to extracting the outer surface from the STL (fig. 5.4c). The surface then is duplicated, and sheets that describe the native squared (non-blended) pad geometries are cut out of the duplicate (fig. 5.4d). These sheet positions thereby are governed by their corner points described in the aforementioned φ, z coordinate system. Then, the sheets are thickened, the bellows are created by insetting of a circumferential rim, and outer corners as well as interior and exterior seam edges are blended with defined radii (fig. 5.4e). Surface finite element meshing is performed using quadrilaterals, and mesh offsets of the pads to the inside and of the shell to the outside yield a 3-dimensional hexahedral discretization (fig. 5.4f). Prior to the mesh offsets, the surface pad mesh is exported (fig. 5.4g) such that it may be used as input to optimization algorithms, cf. sec. 5.4.
For the three animal studies presented here, the in-silico CAD model resembles its physical counterpart (the prototype) in terms of functional geometry and positioning of the pads on the epicardial ventricular surface. The in-silico model for this prototype that was established in the year 2013 is denoted as *VAD2013p*.

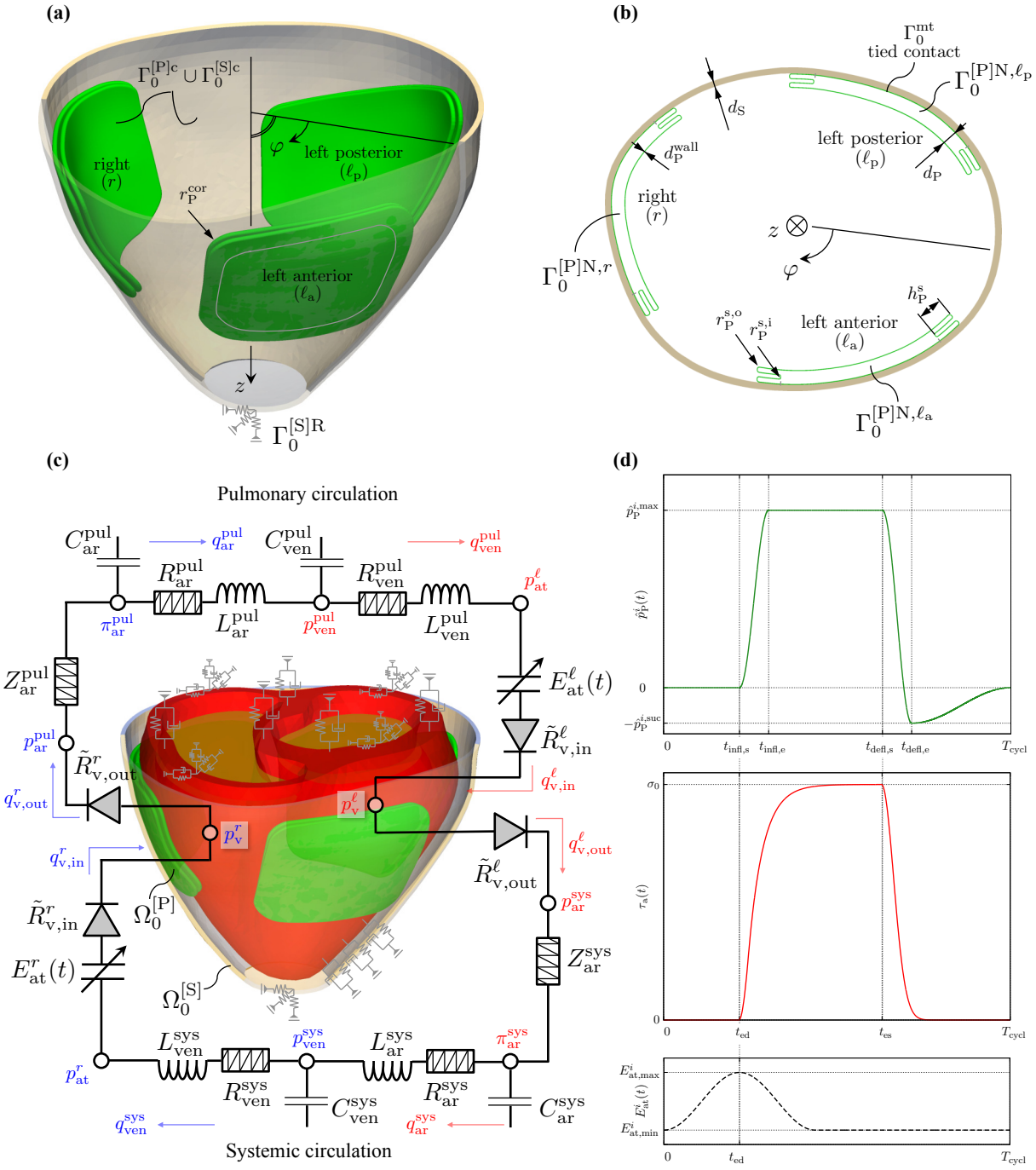

Figure 5.3: Model *3Dventr | 0Dsyspul | VAD2013p*: Computational model of the 3D heart, the 3D VAD and the reduced-order 0D vascular system. **(a)** Anterior view onto the VAD model with left anterior (ℓ_a), left posterior (ℓ_p) and right (r) pneumatic unit. **(b)** Axial slice through the VAD model. **(c)** Anterior view onto the full computational model. **(d)** Driving forces for the simulation plotted over one cardiac cycle $t \in [0, T_{cycl}]$: Prescribed pressure curve $\hat{p}_P^i(t)$ in pads (top), solution $\tau_a(t)$ of the active stress evolution equation for modeling ventricular contraction (prescribed parameterized input function) (middle), prescribed time-varying elastance function $E_{at}^i(t)$ for the 0D atrial models (bottom).

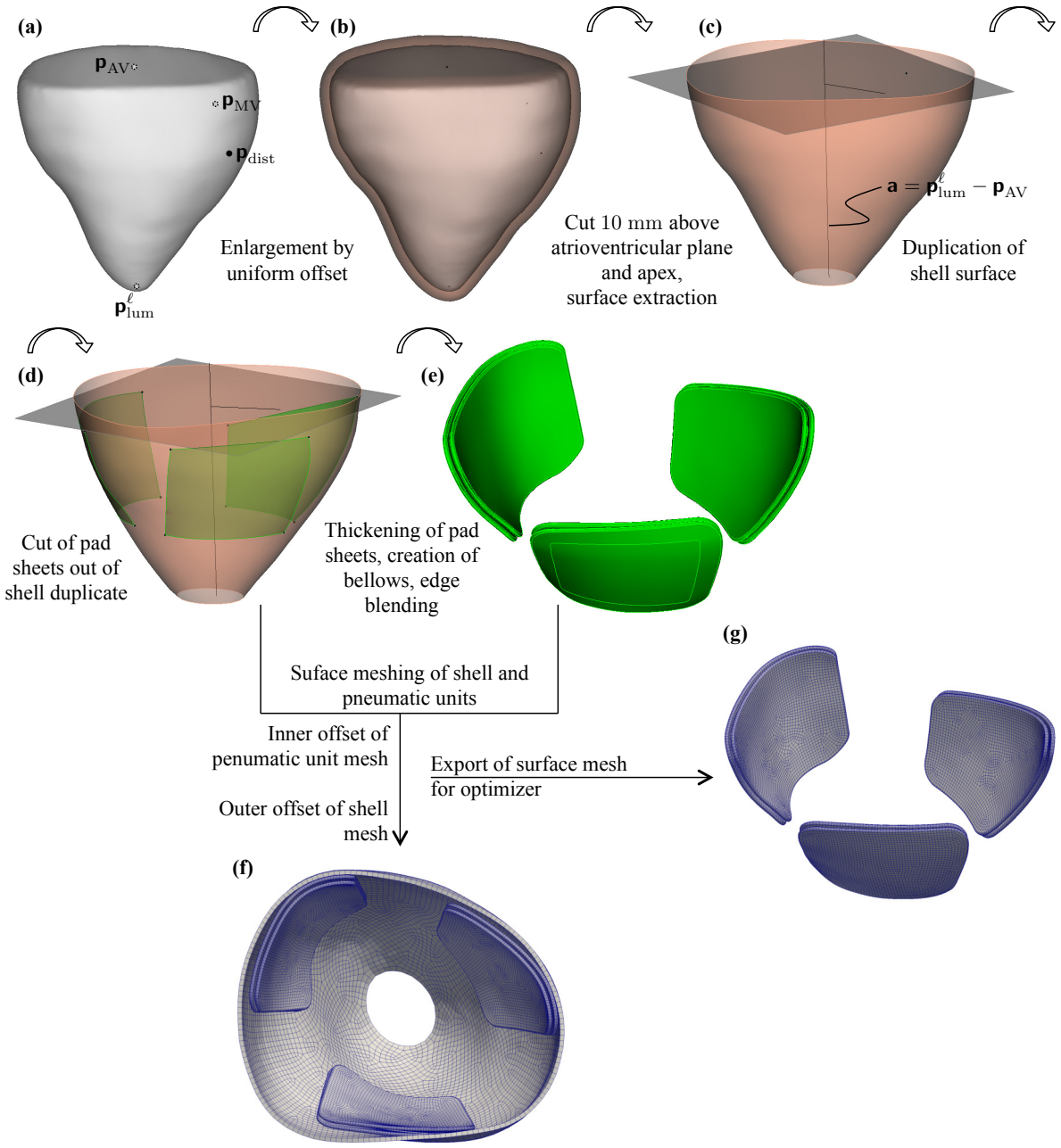

Figure 5.4: Modeling pipeline for the VAD, geometric and discretized model are created in one process. **(a)** Original segmented and smoothed geometry. **(b)** Enlargement by a uniform offset of 4 mm. **(c)** Sheet geometry (surface) obtained after cut 10 mm above atrioventricular plane (AVP) and at the apex, and extraction of the outer surface. **(d)** Duplication of sheet surface, projection of pad corner points onto that surface and cut of pad sheets out of the duplicated surface. **(e)** Thickening of sheet surfaces in radial inner direction, bellow creation by insetting of rim of defined dimension, blending of corner edges as well as interior and exterior circumferential edges at seams. **(f)** Surface meshing of the pad geometries and the shell sheet; creation of 3-dimensional mesh by insetting of pad surface mesh and offsetting of shell surface mesh obainting hexahedral (3D) elements out of quadrilateral (2D) elements. **(g)** Export of surface pad mesh for access of optimizer to mesh node locations.

Table 5.1: Model *VAD2013p*: Common geometrical parameters for the patient-specific biventricular augmentation device (BiVAD)

d_P [mm]	$d_\mathrm{P}^\mathrm{wall}$ [mm]	d_S [mm]	h_P^s [mm]	$r_\mathrm{P}^\mathrm{cor}$ [mm]	$r_\mathrm{P}^\mathrm{s,i}$ [mm]	$r_\mathrm{P}^\mathrm{s,o}$ [mm]
3.5	0.19	1.5	6.5	8.0	0.25	0.6

5.3.2 Model setup and discretization aspects

The computational model for the interaction of the VAD with the heart and the vascular system is presented. Governing equations, discretization methods and solution techniques for the 3D-0D coupled heart-vascular problem are treated in chap. 2 and chap. 3, hence all heart and vascular model-related aspects are not repeated but only sketched in terms of figures and diagrams.
The VAD model *VAD2013p* is decomposed into two mechanically distinct parts, namely the pads (superscript $[\mathrm{P}]$ or subscript P) and the shell (superscript $[\mathrm{S}]$ or subscript S).
During prestressing happening in the time span $[0, t_0]$, cf. sec. 2.2.1.3, the implant remains at rest, and no contact to the epicardium can happen. Thereafter, the transient 3D-0D coupled heart-vascular-VAD problem is solved. Balance equations for the pads and the shell read

$$\boldsymbol{\nabla}_0 \cdot (\boldsymbol{F}^{[\mathrm{P}]} \boldsymbol{S}^{[\mathrm{P}]}) - \rho_{0,\mathrm{P}} \ddot{\boldsymbol{u}}^{[\mathrm{P}]} = \boldsymbol{0} \quad \text{in } \Omega_0^{[\mathrm{P}]} \times [t_0, T] \tag{5.1}$$

and

$$\boldsymbol{\nabla}_0 \cdot (\boldsymbol{F}^{[\mathrm{S}]} \boldsymbol{S}^{[\mathrm{S}]}) - \rho_{0,\mathrm{S}} \ddot{\boldsymbol{u}}^{[\mathrm{S}]} = \boldsymbol{0} \quad \text{in } \Omega_0^{[\mathrm{S}]} \times [t_0, T], \tag{5.2}$$

respectively. The implant is modeled with a hyperelastic material, hence the constitutive equations for the second Piola-Kirchhoff stress are

$$\boldsymbol{S}^{[\mathrm{P}]} = 2\frac{\partial \Psi^{[\mathrm{P}]}}{\partial \boldsymbol{C}^{[\mathrm{P}]}} \qquad \text{and} \qquad \boldsymbol{S}^{[\mathrm{S}]} = 2\frac{\partial \Psi^{[\mathrm{S}]}}{\partial \boldsymbol{C}^{[\mathrm{S}]}}. \tag{5.3}$$

The pads are made out of thin-walled polyurethan (wall thickness $d_\mathrm{P}^\mathrm{wall} = 0.19$ mm) and are modeled by a nearly incompressible Neo-Hookean material law with an Ogden-type volumetric part:

$$\Psi^{[\mathrm{P}]} = \frac{\mu_\mathrm{P}}{2}(\bar{I}_C^{[\mathrm{P}]} - 3) + \frac{\kappa_\mathrm{P}}{4}({J^{[\mathrm{P}]}}^2 - 2\ln J^{[\mathrm{P}]} - 1), \tag{5.4}$$

with the shear modulus μ_P and the bulk modulus κ_P. The shell is modeled by a simple St. Venant-Kirchhoff-type strain energy function,

$$\Psi^{[\mathrm{S}]} = \frac{\nu_\mathrm{S}\mathbb{C}_\mathrm{S}}{2(1+\nu_\mathrm{S})(1-2\nu_\mathrm{S})}(\mathrm{tr}\boldsymbol{E}^{[\mathrm{S}]})^2 + \frac{\mathbb{C}_\mathrm{S}}{2(1+\nu_\mathrm{S})}\mathrm{tr}({\boldsymbol{E}^{[\mathrm{S}]}}^2), \tag{5.5}$$

wherein $\mathbb{C}_\mathrm{S}$ the elastic (Young's) modulus and ν_S Poisson's ratio.

Uniaxial tensile experiments on thin-walled polyurethan samples were carried out in a small-strain regime (uniaxial stretch $\lambda \leq 1.04$). The results thereof are depicted in appendix A.2. A small-strain analytical fit for the shear modulus μ_P was performed assuming perfect incompressibility. However, in the numerical simulation, that constraint was relaxed by choosing an appropriately

large bulk modulus κ_{P} such that a Poisson's ratio of 0.49 is obtained.

The delicate wickerwork-like nitinol architecture of the shell is not explicitly considered but simplistically modeled by a bulk structure of homogeneous thickness. Attempts of simulating the optimal expansion process of this wickerwork structure have been made in the term paper by [53]. The material parameters for the implant are summarized in tab. 5.2.

Table 5.2: Material parameters shear modulus μ_{P}, bulk modulus κ_{P}, reference density $\rho_{0,\mathrm{P}}$ of polyurethan pads; Young's modulus $\mathbb{C}_{\mathrm{S}}$, Poisson's ratio ν_{S}, reference density $\rho_{0,\mathrm{S}}$ of shell

μ_{P} [kPa]	κ_{P} [kPa]	$\rho_{0,\mathrm{P}}$ $[\frac{\mathrm{kg}}{\mathrm{mm}^3}]$	$\mathbb{C}_{\mathrm{S}}$ [kPa]	ν_{S} $[-]$	$\rho_{0,\mathrm{S}}$ $[\frac{\mathrm{kg}}{\mathrm{mm}^3}]$
9346	$467.3 \cdot 10^3$	$1.2 \cdot 10^{-6}$	$5 \cdot 10^5$	0.4	$2 \cdot 10^{-6}$

The inflation of the pads is achieved by a pressure Neumann boundary condition (follower load) acting on their inner lumen (boundaries $\Gamma_0^{[\mathrm{P}]\mathrm{N},i}$):

$$\boldsymbol{t}_0^{[\mathrm{P}]} = -\hat{p}_{\mathrm{P}}^i(t) J^{[\mathrm{P}]} \boldsymbol{F}^{[\mathrm{P}]^{-\mathrm{T}}} \boldsymbol{n}_0^{[\mathrm{P}]} \quad \text{on } \Gamma_0^{[\mathrm{P}]\mathrm{N},i} \times [t_0, T], \quad i = \ell_{\mathrm{a}}, \ell_{\mathrm{p}}, r. \tag{5.6}$$

The pressure inside the pads is controlled by a smooth prescribed time curve, cf. fig. 5.3d (1st plot):

$$\hat{p}_{\mathrm{P}}^i(t) = \begin{cases} 0, & t \le t_{\mathrm{infl,s}}, \\ \frac{1}{2}\hat{p}_{\mathrm{P}}^{i,\max}\left(1 - \cos\frac{\pi(t-t_{\mathrm{infl,s}})}{t_{\mathrm{infl,e}}-t_{\mathrm{infl,s}}}\right), & t_{\mathrm{infl,s}} \le t \le t_{\mathrm{infl,e}}, \\ \hat{p}_{\mathrm{P}}^{i,\max}, & t_{\mathrm{infl,e}} \le t \le t_{\mathrm{defl,s}}, \\ \frac{1}{2}\left(\hat{p}_{\mathrm{P}}^{i,\max} + \hat{p}_{\mathrm{P}}^{i,\mathrm{suc}}\right)\left(1 - \cos\frac{\pi(t-t_{\mathrm{defl,e}})}{t_{\mathrm{defl,e}}-t_{\mathrm{defl,s}}}\right) - \hat{p}_{\mathrm{P}}^{i,\mathrm{suc}}, & t_{\mathrm{defl,s}} \le t \le t_{\mathrm{defl,e}}, \\ \frac{1}{2}\left(-\hat{p}_{\mathrm{P}}^{i,\mathrm{suc}}\right)\left(1 - \cos\frac{\pi(t-T_{\mathrm{cycl}})}{T_{\mathrm{cycl}}-t_{\mathrm{defl,e}}}\right), & t \ge t_{\mathrm{defl,e}}, \end{cases} \quad i = \ell_{\mathrm{a}}, \ell_{\mathrm{p}}, r. \tag{5.7}$$

It is parameterized with respect to the time when inflation starts and ends, $t_{\mathrm{infl,s}}$ and $t_{\mathrm{infl,e}}$, when deflation starts and ends, $t_{\mathrm{defl,s}}$ and $t_{\mathrm{defl,e}}$, as well as with respect to the pad's peak pressures $\hat{p}_{\mathrm{P}}^{i,\max}$ and the suction pressure for deflation, $\hat{p}_{\mathrm{P}}^{i,\mathrm{suc}}$. Here, $t_{\mathrm{infl,s}} = t_{\mathrm{ed}}$ (begin of ventricular contraction) and $t_{\mathrm{defl,s}} = t_{\mathrm{es}}$ (begin of ventricular relaxation). Inflation durations are always assumed to be 0.1 s, thus $t_{\mathrm{infl,e}} = t_{\mathrm{ed}} + 0.1$ s and $t_{\mathrm{defl,e}} = t_{\mathrm{es}} + 0.1$ s. The suction pressure for deflation is set to $\hat{p}_{\mathrm{P}}^{i,\mathrm{suc}} = 0.2\, \hat{p}_{\mathrm{P}}^{i,\max}$.

At the bottom of the shell, denoted by the boundary $\Gamma_0^{[\mathrm{S}]\mathrm{R}}$, a Robin condition is specified:

$$\boldsymbol{t}_0^{[\mathrm{S}]} = -k_{\mathrm{S}} \boldsymbol{u}^{[\mathrm{S}]} \quad \text{on } \Gamma_0^{[\mathrm{S}]\mathrm{R}} \times [0, T]. \tag{5.8}$$

The spring stiffness is chosen to $k_{\mathrm{S}} = 10^3\ \frac{\mathrm{kPa}}{\mathrm{mm}}$.

Between a subset of the pads' backfaces and the shell (common boundary Γ_0^{mt}), matching is enforced:

$$\boldsymbol{u}^{[\mathrm{P}]} = \boldsymbol{u}^{[\mathrm{S}]} \quad \text{on } \Gamma_0^{\mathrm{mt}} \times [t_0, T]. \tag{5.9}$$

Finally, the implant and the heart may exchange contact forces, hence a contact condition is enforced on all implant surfaces that are oriented towards the epicardium, being the boundary $\Gamma^{[\mathrm{P}]\mathrm{c}} \cup \Gamma^{[\mathrm{S}]\mathrm{c}}$:

$$g_{\mathrm{n}} \geq 0, \;\; p_{\mathrm{n}} \leq 0, \;\; p_{\mathrm{n}} g_{\mathrm{n}} = 0 \text{ on } \Gamma^{[\mathrm{P}]\mathrm{c}} \cup \Gamma^{[\mathrm{S}]\mathrm{c}} \times [t_0, T]. \tag{5.10}$$

Therein, g_{n} is the (normal) gap function (2.56) between the two bodies, and p_{n} the (normal) contact traction that is exchanged. Since no frictional nor adhesive forces are considered, $p_{\mathrm{n}} \leq 0$. Refer to sec. 2.1.1.5 for a short introduction to contact and tied contact mechanics.

The absolute model time is $T = t_0 + N^\star T_{\mathrm{cycl}}$, while $N^\star$ is that cycle number fulfilling (2.222) according to sec. 2.2.4.2, where $\epsilon_{\mathrm{cycl}} = 3\ \%$.

The finite element and finite difference discretizations for the heart, the vascular system, and the implant are carried out as detailed in chap. 3. The (frictionless) contact problem between device and heart, eq. (5.10), as well as the meshtying problem between pads and shell, eq. (5.9), are treated with a mortar approach [162]. Contact constraint enforcement is achieved by a penalty law, avoiding the introduction of Lagrange multiplier-type degrees of freedom for the structural problem. The meshtying constraint enforcement is carried out using a Dual Lagrangian multiplier method [163], allowing for a computationally cheap condensation of the meshtying Lagrange multiplier degrees of freedom (interface tractions required to guarantee connectivity) without increasing the size of the resulting linearized system to be solved.

For the ventricular porcine geometry, discretization *tet4_1* is used, cf. fig. A.1 in appendix A.1.1.1. For the implant, discretization *hex8_1* with F-bar element technology [49] is used, evaluating the volumetric part of the deformation gradient at the element's center in oder to bypass spurious volumetric locking phenomena which may be introduced by the near-incompressible polyurethan material model for the pads. The discretization is sketched in fig. A.7 in appendix A.1.1.2.
The discretized patient-specific augmentation device has $237\,030$ (*p1*), $228\,888$ (*p2*) and $222\,684$ (*p3*) degrees of freedom, respectively. The total problem size (including the heart) yields $1\,157\,151$ (*p1*), $1\,043\,235$ (*p2*) and $968\,589$ (*p3*) solid mechanics and 16 0D model unknowns, respectively. The work load for the computations is distributed over $n_{\mathrm{core}} = 112$ Xeon Haswell cores. One heart cycle is computed with $n_{\mathrm{step}} = 500$ time steps of constant size. The adaptive pseudo-transient continuation (PTC) nonlinear solution technique that was introduced in sec. 3.2.2 is used on the structural block of the system matrix for the case that large deflections of the thin-walled pads, especially during deflation, may cause divergence of Newton's method. Additionally, slight perturbations of the contact penalty parameter are introduced in case of non-convergence of the active contact set search which is executed within one semi-smooth monolithic Newton iteration [162, 163]. Time to solution varies between $2\ \mathrm{h}$ (heart-only) and $18\ \mathrm{h}$ (heart and VAD) on this hardware.

5.3.3 Results

The results for three pigs, subsequently referred to as *p1* (filled red diamond), *p2* (thick green diamond) and *p3* (thin blue diamond), are shown. Section 5.3.3.1 shows the validation with experimental in-vivo data. On the one hand, the calibrated results to baseline heart in-vivo data in absence of a functional VAD are shown, and on the other the comparison of simulations with intact VAD to the experimental measurements that have been performed during the experiment. Section 5.3.3.2 then deals with the effects of ventricular augmentation on stroke work, wall stress, and myofiber strain.
The baseline state subsequently is referred to as $\boxed{\text{BL}}$, and four different augmentation scenarios are analyzed, referred to as $\boxed{\text{A1}}$ ($\hat{p}_{\mathrm{P}}^{\ell_{\mathrm{a}},\max} = \hat{p}_{\mathrm{P}}^{\ell_{\mathrm{p}},\max} = \hat{p}_{\mathrm{P}}^{r,\max} = 20$ mmHg), $\boxed{\text{A2}}$ ($\hat{p}_{\mathrm{P}}^{\ell_{\mathrm{a}},\max} = \hat{p}_{\mathrm{P}}^{\ell_{\mathrm{p}},\max} = 40$ mmHg, $\hat{p}_{\mathrm{P}}^{r,\max} = 20$ mmHg), $\boxed{\text{A3}}$ ($\hat{p}_{\mathrm{P}}^{\ell_{\mathrm{a}},\max} = \hat{p}_{\mathrm{P}}^{\ell_{\mathrm{p}},\max} = 60$ mmHg, $\hat{p}_{\mathrm{P}}^{r,\max} = 20$ mmHg), and $\boxed{\text{A4}}$ ($\hat{p}_{\mathrm{P}}^{\ell_{\mathrm{a}},\max} = \hat{p}_{\mathrm{P}}^{\ell_{\mathrm{p}},\max} = 80$ mmHg, $\hat{p}_{\mathrm{P}}^{r,\max} = 20$ mmHg).

5.3.3.1 Validation with experimental data

Calibration to in-vivo baseline data Ventricular 3D-0D heart models (*3Dventr* | *0Dsyspul*) stemming from the three different pigs, cf. fig. 5.5b,c for the initial ventricular and VAD geometry, are calibrated to baseline measurements with help of the parameter estimation methods (*FAS-lsq* scheme) from chap. 4. Low-afterload (*LA-HF*) and high-afterload (*HA-HF*) heart failure states are considered for each animal. The hearts significantly differ in size and shape, cf. data on myocardial wall volume $V(\Omega_0)$ as well as left and right ventricular cavity volume $V_{\mathrm{v}}^{\ell}(t_0)$ and $V_{\mathrm{v}}^{r}(t_0)$ in fig. 5.5b.

Table 5.3: Cardiac cycle time T_{cycl}, end-diastolic time t_{ed}, end-systolic time t_{es}, systemic arterial windkessel time constant $\tau_{\mathrm{ar}}^{\mathrm{sys}}$, measured end-diastolic and end-systolic aortic pressures $\tilde{p}_{\mathrm{ar}}^{\mathrm{sys}}(t_{\mathrm{ed}})$ and $\tilde{p}_{\mathrm{ar}}^{\mathrm{sys}}(t_{\mathrm{es}})$

		T_{cycl} [s]	t_{ed} [s]	t_{es} [s]	$\tau_{\mathrm{ar}}^{\mathrm{sys}}$ [s]	$\tilde{p}_{\mathrm{ar}}^{\mathrm{sys}}(t_{\mathrm{ed}})$ [kPa]	$\tilde{p}_{\mathrm{ar}}^{\mathrm{sys}}(t_{\mathrm{es}})$ [kPa]
p1	*LA-HF*	1.19	0.26	0.75	1.17	4.53	8.27
	HA-HF	1.06	0.23	0.67	0.83	9.07	19.2
p2	*LA-HF*	1.23	0.26	0.9	1.01	3.87	6.93
	HA-HF	1.22	0.27	0.8	1.59	11.1	17.1
p3	*LA-HF*	0.98	0.2	0.67	0.68	3.6	7.6
	HA-HF	1.02	0.2	0.65	0.71	6.53	14.5

The algorithm yields a set of parameters (ventricular contractility σ_0, ventricular upstroke and relaxation rates $\alpha_{\max}$ and $\alpha_{\min}$, systemic arterial resistance $R_{\mathrm{ar}}^{\mathrm{sys}}$, left atrial elastance amplitude $E_{\mathrm{at,A}}^{\ell}$) and 0D model initial conditions that fulfill the homeostatic state criterion (2.222) and minimize (4.45).
Table 5.3 shows patient-specific timing and arterial end-diastolic and end-systolic measurement data which are part of the input to the optimization algorithm. The calibrated parameters (output)

are shown in tab. 5.4. [1] *HA-HF* states yield contractilities and resistances approximately twice as high as compared to *LA-HF* states.
Simulated calibrated pressures over time end ejection fraction data for all three pigs for *LA-HF* and *HA-HF* states are depicted in fig. 5.5a. Those results are subsequently referred to as baseline, BL.

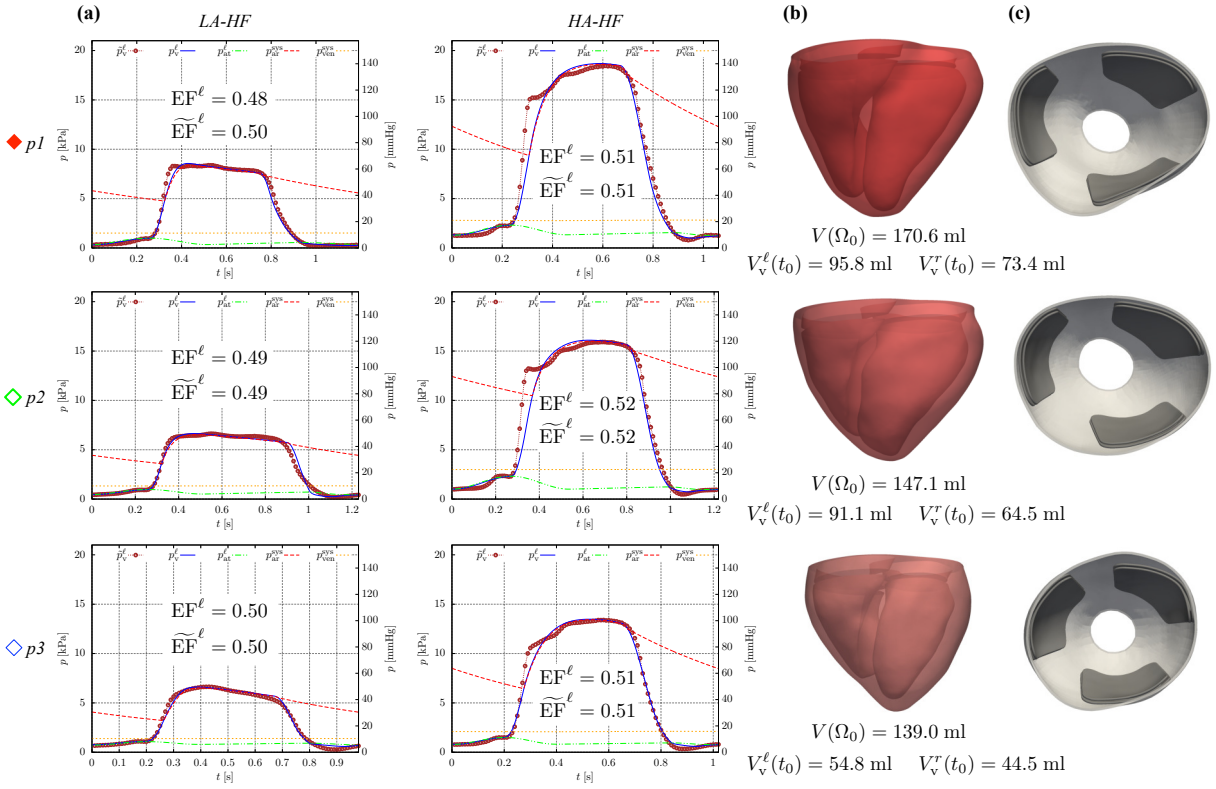

Figure 5.5: Model *3Dventr*$_{tet4\_1}$ | *0Dsyspul*: Baseline (BL) *LA-HF* and *HA-HF* conditions for the three animals as well as initial geometry of myocardium and assist device. **(a)** Simulated left heart and systemic pressures over time, measured left ventricular pressure $\tilde{p}_\text{v}^\ell$ shown as brown dots, simulated and measured left ventricular ejection fraction EF^ℓ and $\widetilde{\text{EF}}^\ell$, calibrated baseline states with *FAS-lsq*, cf. sec. 4.3.1. **(b)** Ventricular geometry (anterior view) with information on the myocardial wall volume $V(\Omega_0)$ as well as left and right ventricular chamber volume $V_\text{v}^\ell(t_0)$ and $V_\text{v}^r(t_0)$, respectively. **(c)** Initial geometry of the ventricular assist device (VAD), top view.

In-silico models show good quantitative and qualitative agreement to experimental data Computational results for the four augmentation scenarios A1–A4 are quantitatively validated against the scatter range of the experimental observations. The comparison to the experiments is shown in fig. 5.6. Furthermore, animal *p1* with A3 augmentation is picked for direct

[1] The very attentive reader might note a slight difference between the *p1* parameters compared to those from the *FAS-lsq* fit presented in tab. 4.5a and tab. 4.6a of chap. 4. This difference stems from minor technical algorithmic modifications that have been introduced prior to generating the ("newer") chap. 4 results compared to the ("older") results presented in this chapter.

Table 5.4: Parameters ventricular contractilty σ_0, ventricular upstroke and relaxation rates $\alpha_{\max}$ and $\alpha_{\min}$, systemic arterial resistance $R_{\mathrm{ar}}^{\mathrm{sys}}$ as well as left atrial elastance amplitude $E_{\mathrm{at,A}}^{\ell}$, calibrated to baseline *LA-HF* and *HA-HF* states with *FAS-lsq*, cf. sec. 4.3.1

		σ_0 [kPa]	$\alpha_{\max}$ $\left[\frac{1}{\mathrm{s}}\right]$	$\alpha_{\min}$ $\left[\frac{1}{\mathrm{s}}\right]$	$R_{\mathrm{ar}}^{\mathrm{sys}}$ $\left[\frac{\mathrm{mPa\cdot s}}{\mathrm{mm}^3}\right]$	$E_{\mathrm{at,A}}^{\ell}$ $\left[\frac{\mathrm{mPa}}{\mathrm{mm}^3}\right]$
p1	*LA-HF*	33.47	41.41	−11.29	103.49	24.78
	HA-HF	64.92	11.73	−14.85	218.56	7.47
p2	*LA-HF*	26.27	20.29	−31.86	94.86	10.44
	HA-HF	58.48	9.83	−18.06	224.82	13.26
p3	*LA-HF*	18.89	25.97	−14.01	118.17	3.74
	HA-HF	37.36	10.05	−17.55	262.08	8.28

comparison of simulated and measured left ventricular pressure increase (fig. 5.6a,a'). Qualitative direct comparison of simulated end-systolic ventricular deformation and CT data which was recorded during the experiment is shown in fig. 5.6c,c'. Figure 5.6b,b' depicts absolute changes in left peak ventricular pressure ($\Delta\mathrm{PVP}^{\ell}$), end-diastolic pressure ($\Delta\mathrm{EDP}^{\ell}$) and stroke volume ($\Delta\mathrm{SV}^{\ell}$) with respect to baseline for all animals *p1*, *p2* and *p3* compared to the scatter range of the experimental data. Animal-averaged simulation results compared to median and interquartile range are shown in tab. 5.5.
Especially peak left ventricular pressure increase $\Delta\mathrm{PVP}^{\ell}$ for the *LA-HF* case and left ventricular stroke volume increase $\Delta\mathrm{SV}^{\ell}$ for the *HA-HF* case are remarkably close to the data's median, while a significant portion of in-silico results lies within or very close to the interquartile range of the data. For the *LA-HF* case, continuous drop in left ventricular end-diastolic pressure can only slightly be observed for *p1*, while *p2* and *p3* exhibit very slight increases above zero. For the *HA-HF* case, *p1* and *p2* $\Delta\mathrm{EDP}^{\ell}$ decreases nearly linearly, while *p3* remains around zero.

Table 5.5: Model *3Dventr*$_{tet4\_1}$ | *0Dsyspul* | *VAD2013p*$_{hex8\_1\,\text{F-bar}}$: Absolute changes in left ventricular stroke volume ($\Delta\mathrm{SV}^{\ell}$), left peak ventricular pressure ($\Delta\mathrm{PVP}^{\ell}$) and left end-diastolic pressure ($\Delta\mathrm{EDP}^{\ell}$) with respect to baseline BL with increasing augmentation scenarios A1–A4 for both *LA-HF* and *HA-HF* cases: measurement data are presented as median (interquartile range), simulation results from the three porcine hearts are presented as average

		$\Delta\mathrm{SV}^{\ell}$ [ml]		$\Delta\mathrm{PVP}^{\ell}$ [mmHg]		$\Delta\mathrm{EDP}^{\ell}$ [mmHg]	
		meas	∅ sim	meas	∅ sim	meas	∅ sim
LA-HF	A1	0.26(−1.38; 4.35)	2.44	2.01(−1.73; 2.68)	3.11	−0.07(−0.14; 0.41)	$-5.52 \cdot 10^{-2}$
	A2	0.16(−1.44; 5.45)	4.07	5.37(−3.47; 8.09)	6.00	0.41(−0.83; 0.74)	−0.13
	A3	1.05(−0.76; 3.48)	4.80	8.49(6.92; 9.15)	8.24	−0.88(−4.30; −0.06)	−0.11
	A4	4.08(0.88; 8.94)	4.31	10.1(5.75; 12.37)	9.66	−1.84(−2.68; −0.95)	0.19
HA-HF	A1	0.87(0.41; 1.57)	1.68	3.79(−4.33; 5.61)	3.61	0.33(−0.52; 1.63)	−0.43
	A2	2.17(−0.14; 2.79)	2.93	4.72(1.97; 11.71)	7.15	0.40(−0.34; 1.44)	−0.84
	A3	3.05(1.95; 3.83)	3.85	7.20(3.14; 9.49)	10.43	−0.80(−1.49; 0.04)	−1.10
	A4	3.13(−2.17; 5.31)	4.41	9.80(3.83; 12.62)	13.16	0.50(−0.40; 1.35)	−1.29

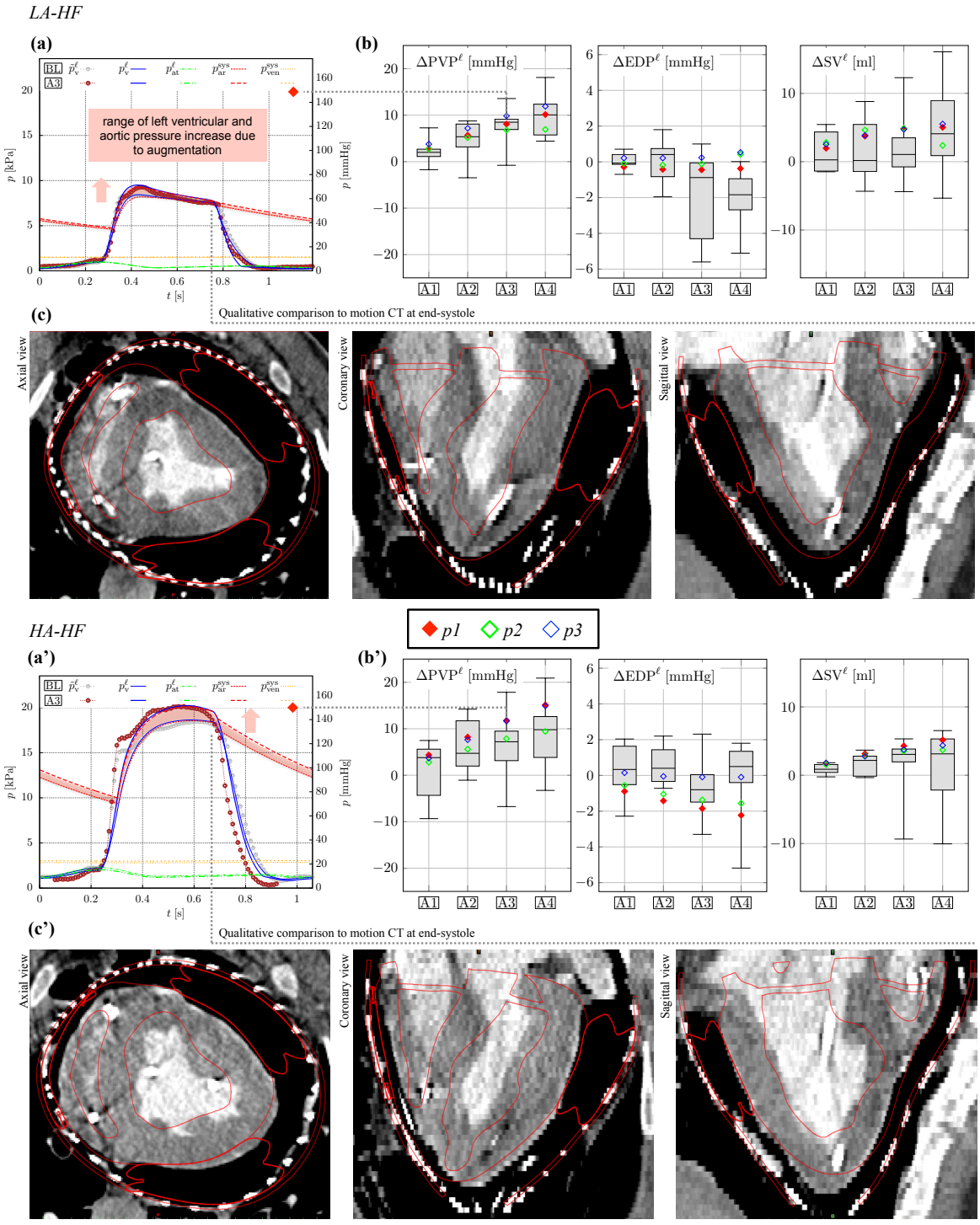

Figure 5.6: Model *3Dventr*$_{tet4\_1}$ | *0Dsyspul* | *VAD2013p*$_{hex8\_1\,\text{F-bar}}$: Validation of simulation results with respect to experimental data, each for *LA-HF* and *HA-HF*. **(a, a')** *p1*: Left heart and systemic pressures over time, baseline BL vs. A3 augmentation, BL measurements are grey dots, A3 measurements are brown dots. **(b, b')** Absolute changes in left peak ventricular pressure (ΔPVP^ℓ), end-diastolic pressure (ΔEDP^ℓ) and stroke volume (ΔSV^ℓ) with respect to baseline with increasing augmentation scenarios A1–A4: Boxplots show measured data from a series of different animal experiments; simulated data is shown as filled red (*p1*), thick green (*p2*) and thin blue (*p3*) diamonds. **(c, c')** *p1* A3: End-systolic qualitative comparison of simulation (red contour) to motion CT data which was recorded during the experiment.

5.3.3.2 Effects on stroke work, wall stress, and myofiber strain

Ventricular augmentation increases left and right ventricular stroke work Figure 5.7a shows left ($i = \ell$) and right ($i = r$) ventricular pressure-volume relationships for animal *p1* for baseline BL and increasing left ventricular augmentations A1–A4, fig. 5.7b depicts the end-systolic deformed configuration for scenario A3 (color is magnitude of displacement $\boldsymbol{u}$), and fig. 5.7c shows relative changes in left (red bars, $i = \ell$) and right (blue bars, $i = r$) ventricular stroke work $\mathrm{SW}^i = \oint_{V_\mathrm{v}^i} p_\mathrm{v}^i \,\mathrm{d}V$ for A1–A4 with respect to baseline BL.
Gradual increase of left ventricular augmentation from $20\ \mathrm{mmHg}$ (A1) to $80\ \mathrm{mmHg}$ (A4) yields left and right ventricular stroke work changes up to $25.7\ \%$ (left) and $34.3\ \%$ (right) (A4 *LA-HF*), as well as $23.1\ \%$ (left) and $16.9\ \%$ (right) (A4 *HA-HF*). Note the change in right stroke work due to only left pad pressure increase, while right pad peak pressure remains at $20\ \mathrm{mmHg}$.

Ventricular augmentation desirably increases afterload but descreases systolic ventricular wall stress The effect of increasing left ventricular augmentation on end-systolic ventricular function, i.e. cavity pressure and wall stress is exemplified for *p1* at *LA-HF* and *HA-HF* states.
Figure 5.8a shows volume-averaged maximum principal wall Cauchy stress, cf. (2.20), $\hat{\sigma}_1 = \frac{1}{V(\Omega)} \int_\Omega \sigma_1 \,\mathrm{d}v$ over the time course of the homeostatic cardiac cycle, and fig. 5.8b depicts the maximum principal wall Cauchy stress σ_1 at end-systole on a deformed coronary cut though the ventricles comparing augmentation A3 with baseline BL. The shading indicates the myofiber orientation that in most regions aligns with the principal direction of σ_1, corresponding to the passive stress the myofibers (and their embedding) sense during cardiac contraction. Figure 5.8c shows the left ventricular cavity pressure over time.
Peak wall stresses and cavity pressures are about twice as high for the high-afterload as compared to the low-afterload heart failure scenario.
The desirable increase in left ventricular systolic pressures (increased afterload) with increasing augmentation comes along with a significant reduction of systolic ventricular wall stress.

Ventricular augmentation decreases preload by reducing end-diastolic volume and myofiber stretch The effect of increasing left ventricular augmentation on end-diastolic ventricular function, i.e. end-diastolic volume EDV and myofiber stretch (2.105) is exemplified for *p1* at *LA-HF* and *HA-HF* states.
Figure 5.9a shows volume-averaged myofiber stretch $\hat{\lambda}_\mathrm{myo} = \frac{1}{V(\Omega)} \int_\Omega \lambda_\mathrm{myo} \,\mathrm{d}v$ over the time course of the homeostatic cardiac cycle, with detail view on the end-diastolic region. Figure 5.9b depicts the myofiber stretch at end-diastole on a coronary cut through the ventricles, comparing augmentation A3 to baseline BL. Finally, fig. 5.9c shows the relative change of left (red bars, $i = \ell$) and right (blue bars, $i = r$) ventricular end-diastolic volume with increasing augmentation with respect to baseline.
With increasing left ventricular augmentation, end-diastolic myofiber stretches are reduced and end-diastolic volumes decrease by $-4\ \%$ (left) and $-3.4\ \%$ (right) (A4 *LA-HF*), as well as $-5.1\ \%$ (left) and $-1.8\ \%$ (right) (A4 *HA-HF*).

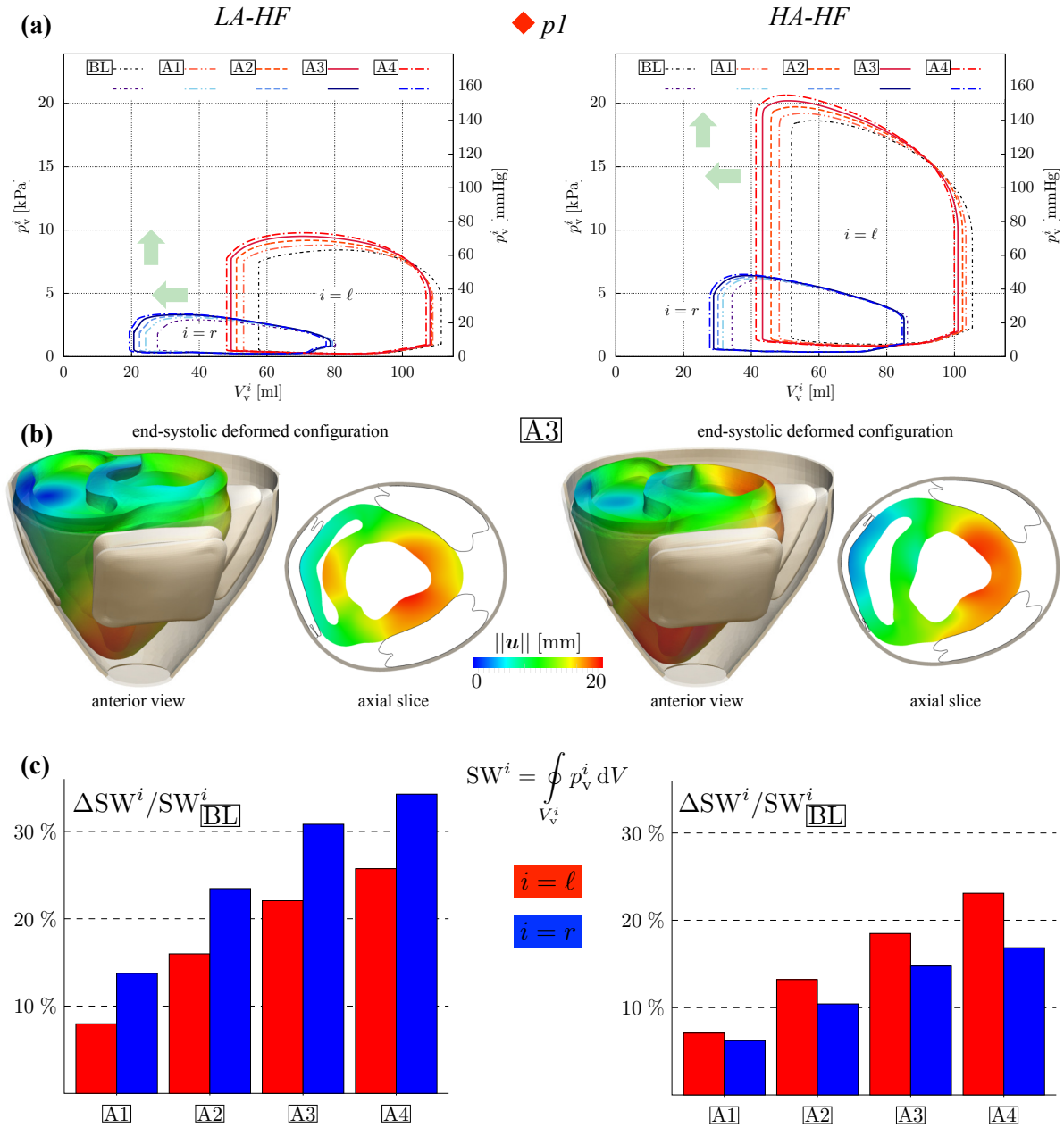

Figure 5.7: Model *3Dventr*$_{tet4\_1}$ | *0Dsyspul* | *VAD2013p*$_{hex8\_1\,\text{F-bar}}$: Ventricular pressure-volume relationships, stroke works for all four augmentation scenarios A1–A4, as well as snapshot of end-systolic deformation for augmentation A3 for *p1*, for both heart failure cases *LA-HF* and *HA-HF*. **(a)** Left and right ventricular pressure-volume relationships. **(b)** Deformation (magnitude of displacement vector $\boldsymbol{u}$) at end-systole, anterior view and axial slice, A3. **(c)** Relative changes in left (red bars) and right (blue bars) ventricular stroke work SW with respect to baseline BL.

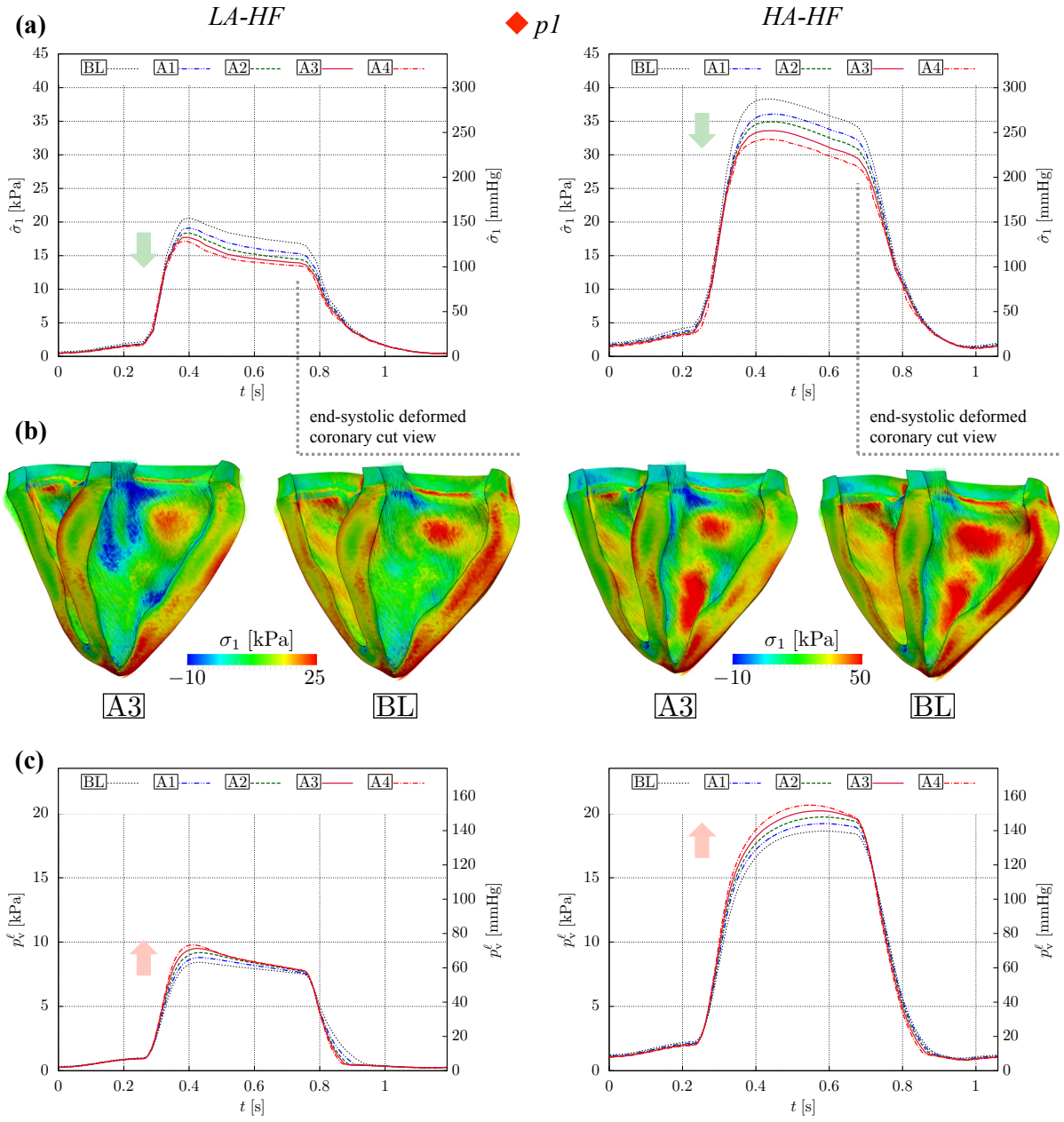

Figure 5.8: Model *3Dventr*$_{tet4\_1}$ | *0Dsyspul* | *VAD2013p*$_{hex8\_1}$ F-bar: Maximum principal wall Cauchy stress for *p1* for baseline BL and the four augmentation scenarios A1–A4, as well as left ventricular pressure, for both heart failure cases *LA-HF* and *HA-HF*. **(a)** Volume-averaged maximum principal wall stress $\hat{\sigma}_1 = \frac{1}{V(\Omega)} \int_\Omega \sigma_1 \, \mathrm{d}v$ over cardiac cycle time, significant decrease with increasing left ventricular augmentation. **(b)** Maximum principal wall stress σ_1 at end-systole, A3 vs. BL, coronary cut, shading shows orientation of myofiber, which approximately aligns with the principal direction of σ_1. **(c)** Left ventricular pressure over time, significant increase with increasing left ventricular augmentation.

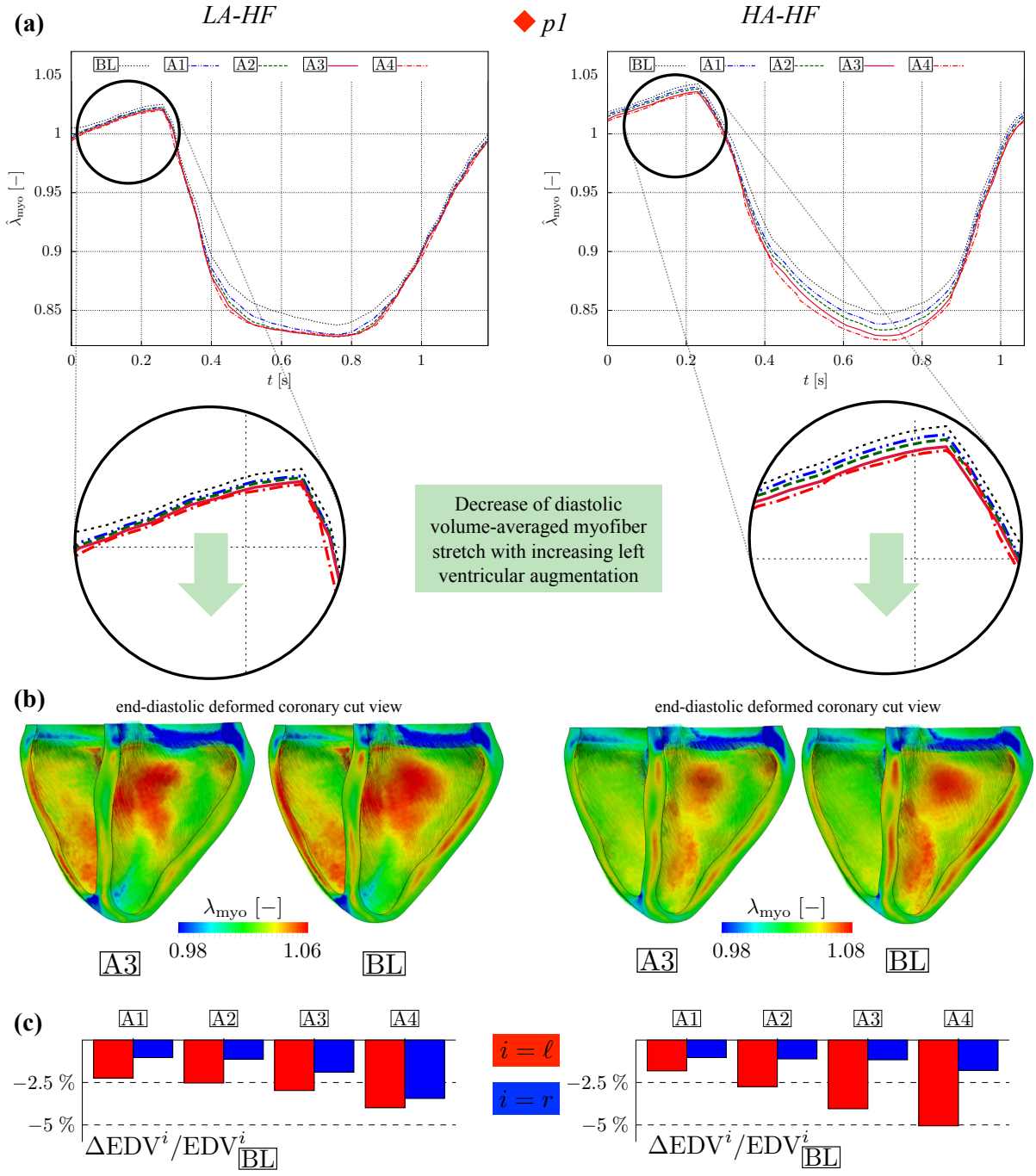

Figure 5.9: Model *3Dventr*$_{tet4\_1}$ | *0Dsyspul* | *VAD2013p*$_{hex8\_1\ \text{F-bar}}$: Myofiber stretch (2.105) for *p1* for baseline BL and the four augmentation scenarios A1–A4, for both heart failure cases *LA-HF* and *HA-HF*. **(a)** Volume-averaged myofiber stretch $\hat{\lambda}_{\text{myo}} = \frac{1}{V(\Omega)} \int_\Omega \lambda_{\text{myo}}\, \mathrm{d}v$ over cardiac cycle time, diastolic decrease with increasing left ventricular augmentation. **(b)** Myofiber stretch λ_{myo} at end-diastole, A3 vs. BL, coronary cut, shading shows orientation of myofiber. **(c)** Relative changes in left (red bars) and right (blue bars) ventricular end-diastolic volume EDV with respect to baseline BL.

5.3.4 Discussion

The driving force for computational modeling of the VAD-heart interaction is to demonstrate that in-silico models not only confirm the experimental results gained from in-vivo models and the therapeutic insights extracted thereof, but also enhance the latter by means of quantities which are not assessable by the experimental setup alone.
In addition, for the first time, it was shown in the in-vivo studies described in Jagschies et al. [98] that a novel therapy of ventricular augmentation by an extravascular biventricular heart assist device exerts direct effects on cardiovascular and ventricular function which may be assessed by help of computational modeling.

The direct comparison of simulated and measured left ventricular pressure, as well as the qualitative comparison to the motion CT image at end-systole was conducted for *p1* with A3 [2]. The magnitude of left ventricular pressure increase due to augmentation is in very good agreement to the catheter measurement for both *LA-HF* and *HA-HF* states. The heart's dislocation at end-systole qualitatively complies with the CT image, even though no further calibration of myocardial constitutive laws or boundary parameters has been conducted. This underpins the well-educated choice of the ventricular material law [89] and the reasonability of boundary parameters (tab. 2.2). However, those values are generic and may be individualized if a higher degree of model fidelity, i.e. with respect to ventricular motion and deformation, is required. Nonetheless, robust data and algorithms for calibration then become crucial with increasing demand for model personalization, naturally again requiring a trade-off between feasibility and model accuracy.

Pressure-volume relationships and stroke work (area enclosed by the pressure-volume curve) of increasing left ventricular augmentation are exemplified for *p1*. Pressure-volume loops exhibit a left- and upward-shift with increasing augmentation, meaning a desirable increase in systolic perfusion pressures and stroke work as well as a reduction in end-diastolic ventricular volume load for both left and right ventricle, even though right ventricular augmentation pressure remains at $\hat{p}_{\mathrm{P}}^{r,\max} = 20\ \mathrm{mmHg}$. The effect of increasing right ventricular function with only-increase of left ventricular augmentation may be explained by the specific locations of the left ventricular pads and the relatively large rightward dislocation of the ventricles, inducing a right ventricular compression even if that pneumatic unit was dysfunctional, cf. fig. 5.7b. and 5.6c,c'.

The three porcine in-silico heart models considered in this contribution were personalized to measurements of time-resolved left ventricular pressure and integral left ventricular ejection fraction data for two contrary states of drug-induced heart failure models: a low-afterload (*LA-HF*) and a high-afterload (*HA-HF*) variant. Furthermore, the three hearts significantly differ in size and shape, cf. data in fig. 5.5b. Thus, the computational model's flexibility with respect to intra- and inter-patient variability is demonstrated.
The calibration procedure, while only limited to integral data, has proven effective and reasonable, since the parameters chosen for calibration are immediately responsive to pharmacological treatment on a short time scale. Thus, specific integral hemodynamics can be reproduced according to

[2] As reported in [98], not all animals were subject to all variants of the experimental protocol. Specifically, *p1* A3 was chosen since this was the highest augmentation scenario which complete pressure and motion CT data had been recorded for.

the measurements at hand, while remaining uncertain parameters of the cardiovascular system had to be chosen relative to the ones estimated according to data from the literature. For further discussion on the parameter estimation procedure and the outcome for those specific low- and high-afterload heart failure cases, refer to [86] and chap. 4.

While computational systolic volume and pressure results remarkably well fit into the scatter range of experimental data, course of end-diastolic pressure with increasing left ventricular augmentation remains inconclusive for both data and model. For the *LA-HF* case, *p1* EDP^{ℓ} drops slightly with *p2* and *p3* virtually remaining unaltered, while the *HA-HF* case produces more pronounced drops in *p1* and *p2* EDP^{ℓ} with hardly any change for *p3*.
Even though the whole mechanisms of blood redistribution in the cardiovascular system due to ventricular augmentation are yet to be fully highlighted by both the computational and the in-vivo models, in-silico parameters governing the venous return in diastolic filling (pulmonary compliances, resistances) remain to be determined more accurately by help of a larger portion of measurements than only left ventricular pressure and ejection fraction. However, an increase in the parameter space will render the parameter estimation process more challenging, and a trade-off between parameter identifiability and model fidelity naturally has to be conducted [219].

Despite a significant and desirable increase of systolic ventricular pressures, the wall stress inside the myocardium at end-systole was monitored and it was shown that a remarkable reduction in maximum principal stress with increasing augmentation is achieved. Thus, even if the (external) afterload is increased, there is a reduction in the *effective* ventricular afterload since the VAD carries are portion of the load the ventricle would have to bear on its own without support. Similar in-silico results have been reported of for a different type of assist device [118].
Furthermore, the drop in end-diastolic volume with increasing augmentation follows a decrease in end-diastolic myofiber stretch, complying with results of cardiac support-induced end-diastolic unloading reported in [143, 179].
Conclusively, in-silico models give insight into mechanical quantities (stresses and strains) which are non-assessable in any experimental setup and therefore are tailored to individualized implant engineering for patients suffering from hypertrophic or dilated cardiomyopathy.
Finally, if combined with computational growth and remodeling methods, in-silico models ultimately may predict how reverse remodeling as consequence of ventricular support may be initiated, i.e. how a VAD has to be engineered to achieve reversal or at least a significant reduction of cardiac disease progression [32, 100, 215].

The implant model itself was dimensioned closely related to the prototype device that has been applied in the respective in-vivo experiments in the year 2013. However, the model focuses on the function of the implant and its effect onto the ventricular myocardium, but currently does not allow for detailed stress analyses inside the pads and the splices between pads and shell due to idealizations that have been undertaken in the modeling process (idealized radii, bellows design, connection to the shell). Furthermore, frictional contact has been neglected for the sake of computational efficiency and feasibility, hence tangential traction forces onto the epicardium and their potential harmful effects are not modeled, but also have to be understood and investigated in an experimental long-term setup prior to designing an elaborated model.
Additionally, the pad pressure is a prescribed function in time, thus no control or feedback control

is modeled for the pad inflation process. For future assessment of the energy consumption that is required to drive the implant at some operating point, the model should be extended towards the pneumatic components and their control systems. First preliminary works thereof may be found in the diploma thesis by [214].

5.4 Optimization methods for implant design and function

Computational in-silico modeling aims at predicting circumstances that are non-assessable within an experimental setup, or those for which an experimental frame has become obsolete due to the proven validated predictability of the model itself. Hence, for a given reliability of the in-silico approach, design variants and alternative operating concepts may be computed and used as input for the engineering process of the "real-world" application.
With regard to the novel heart assist device which has been introduced within the scope of this thesis, a multitude of open questions arise, e.g. the optimal operating pressures of pneumatic units, the pads' ideal shape, material, or location at the ventricular epicardium in order to achieve a maximum in augmentation efficiency – ideally accompanied by a minimum in energy consumption and without compromising the patient's quality of life at any time.

Given the huge amount of operating and design parameters, and the plenty possibly contradictory objectives to be pursued – from an engineering, medical and legal perspective – any formulation of an optimization problem to assess improvements in implant design and function naturally has to be performed in a careful manner and in close interrelation with industrial and medical partners.

Here, a methodological in-silico optimization workflow is presented using the example of optimal circumferential placement of both left ventricular augmentation units (design parameters) in order to achieve a maximum left ventricular stroke work (objective function) at given, fixed augmentation pressures.
A more generalized VAD model for this purpose is presented in sec. 5.4.1, where the peculiarities regarding the 2013 prototype implant have been omitted. The objective function and the workflow are detailed in sec. 5.4.2.
One central part of the optimization procedure is the re-design of the in-silico model on the basis of the finite element mesh, hence on its discretization. For this purpose, a mesh-preserving design adaptation algorithm has been developed that allows for large deflection movement of pads in tangential increments along the epicardial surface. This method as well as its superiority to classical re-design and re-meshing approaches for certain applications are presented in sec. 5.4.3. The results of the optimization problem are depicted in sec. 5.4.4, and a discussion of the outcome, the methods and their implications is performed in sec. 5.4.5.

5.4.1 Generalized VAD model and interaction with the heart

The specific modeling approach for the VAD that was introduced in sec. 5.3.1 relied on the 2013 prototype implant described in sec. 5.1 (*VAD2013p*). Here, the peculiarities of this implant are

omitted for the benefit of a more generalized and also simplified geometric representation: The bellows-like structure of the augmentation units is replaced by a convex rim, and the shell is replaced by a simple back-stabilizing spring (Robin boundary condition). This generalized implant model is subsequently denoted as *VADgen*. It is created using the modeling pipeline depicted in fig. 5.4, however with appropriate modifications (no bellows, no shell). For subsequent computations, the heart model *3Datrioventr* of *p1* together with the circulatory model *0Dsyspulcap* is used. Pad peak pressures are chosen to $\hat{p}_{\mathrm{P}}^{\ell_{\mathrm{a}},\max} = \hat{p}_{\mathrm{P}}^{\ell_{\mathrm{p}},\max} = 60\ \mathrm{mmHg}$ and $\hat{p}_{\mathrm{P}}^{r,\max} = 20\ \mathrm{mmHg}$. Discretization *tet4_2* is chosen for the sake of computational efficiency (cf. appendix A.1.1.1, fig. A.4), and $n_{\mathrm{step}} = 300$ time steps are performed over one cardiac cycle. For the *VADgen* model, discretization *hex8_1* with F-bar element technology is used (cf. appendix A.1.1.2, fig. A.7 for *VAD2013p* for a comparable fineness). The whole model is depicted in fig. 5.10.

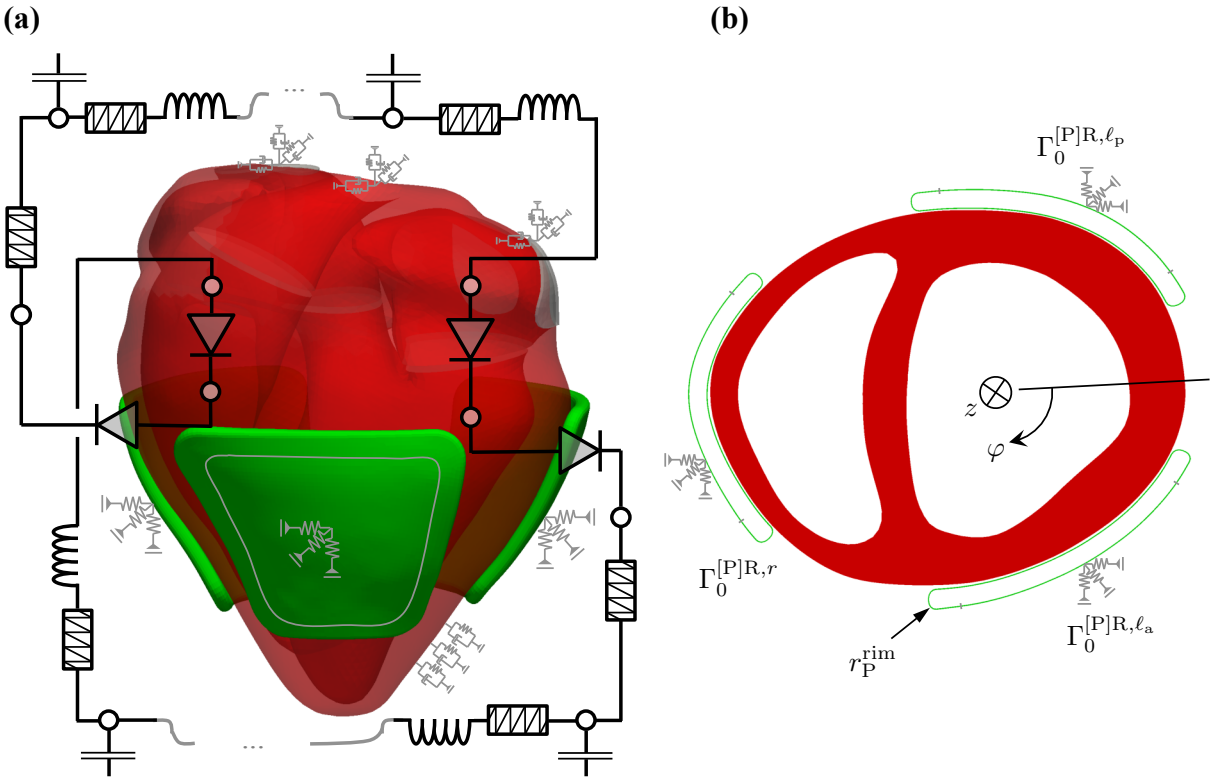

Figure 5.10: Model *3Datrioventr* | *0Dsyspulcap* | *VADgen*: Generalized VAD model interacting with the patient-specific heart. **(a)** Anterior view. **(b)** Axial slice view.

Prior to computing the heart-VAD problem, a reduced set of parameters is calibrated to data from the aforementioned low-afterload heart failure case (*LA-HF*) with the methods presented in chap. 4. Specifically, the rate parameters $\alpha_{\max}$ and $\alpha_{\min}$ in (4.41) are held constant, and only ventricular and atrial contractility σ_0 and $\sigma_{0(at)}$ as well as total systemic arterial resistance $R_{\mathrm{ar}(total)}^{\mathrm{sys}}$ are calibrated by requiring the minimization of (4.45). However, the pressure and auxiliary volume weightings in (4.47) now are $b_p^{i_p} = 0\ (\forall\ i_p)$ and $b_V^i = 0\ (\forall\ i)$, hence the model is only calibrated to peak and end-diastolic left ventricular pressure as well as left ventricular ejection fraction. The parameter estimation is performed using *ROM-ml*, cf. sec. 4.3.2.

Base parameters are listed in tab. 2.3 and tab. 2.6, partly being overridden by the optimized ones and by the specific timing parameters for the *LA-HF* of *p1* that are listed in tab. 5.3.
ROM-ml converged to parameters $\sigma_0 = 68.84$ kPa, $R^{\mathrm{sys}}_{\mathrm{ar}(total)} = 76.61\ \frac{\mathrm{mPa{\cdot}s}}{\mathrm{mm}^3}$ and $\sigma_{0(at)} = 4.09$ kPa within 4 V-cycle and 3 fine level Gauss-Newton iterations with a cycle error of $E_{\mathrm{cycl}} = 0.023$ and an objective function value of $f = 0$ ("perfect fit"). Left heart and systemic pressures as well as left and right ventricular pressure-volume relationships are shown in fig. 5.11.

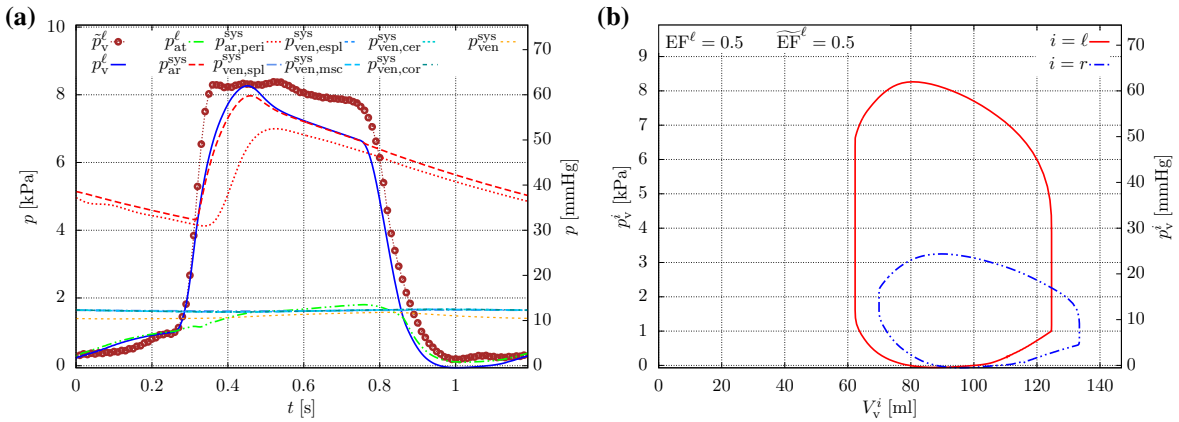

Figure 5.11: Model *3Datrioventr*$_{tet4\_2}$ | *0Dsyspulcap*: Fitted base results using *ROM-ml* to *LA-HF* state of *p1*, without implant. **(a)** Left heart and systemic pressures over time, measured left ventricular pressure $\tilde{p}^{\ell}_{\mathrm{v}}$ in brown dots. Note that calibration was performed only to meet end-diastolic and peak ventricular pressure. **(b)** Left ($i = \ell$) and right ($i = r$) ventricular pressure-volume relationship, perfect match of computed and measured left ventricular ejection fraction EF^{ℓ} and $\widetilde{\mathrm{EF}}^{\ell}$, respectively.

5.4.2 Objective function and design parameters

The optimal (circumferential) placement of both left anterior and left posterior augmentation units in order to achieve a maximum in left ventricular stroke work is (exemplarily) investigated as one possible option for design optimization of the implant.
The design variables are lengths D^{i}_{φ} (and D^{i}_{z}) that a certain augmentation unit ($i = \ell_{\mathrm{a}}$, $i = \ell_{\mathrm{p}}$, $i = r$) moves along the circumferential (and the axial) direction of the epicardial surface – relative to a base implant characterized by $D^{i}_{\varphi} = D^{i}_{z} = 0$.

The optimization task according to (4.1) is

$$\min_{\mathbf{x}\in\mathbb{R}^{n_{\mathrm{p}}}} -\mathrm{SW}^{\ell}(\mathbf{x}). \tag{5.11}$$

Without loss of generality, only the circumferential placement of the left augmentation units is considered, hence the number of parameters is $n_{\mathrm{p}} = 2$ and the parameter vector reads

$$\mathbf{x} = \begin{bmatrix} D^{\ell_{\mathrm{a}}}_{\varphi} & D^{\ell_{\mathrm{p}}}_{\varphi} \end{bmatrix}^{\mathrm{T}}. \tag{5.12}$$

The stroke work is the enclosed area under the pressure-volume relationship and is computed as

$$\mathrm{SW}^{\ell} = \oint_{V_{\mathrm{v}}^{\ell}} p_{\mathrm{v}}^{\ell} \, \mathrm{d}V. \tag{5.13}$$

The gradient-free Nelder-Mead simplex algorithm that was introduced in sec. 4.1.1.2 is used in order to solve (5.11).

A different implementation of this algorithm has been applied to a similar problem in the term paper by [15] (supervised by the author of this work). Therein, a pure structural generic heart model without circulation interacting with a prototype implant model has been used, and the optimal pad placement for minimization of ventricular cavity volume under quasi-static pad inflation has been investigated. The re-design of the implant there has been performed not on the surface mesh but by re-setting the corner sheet points and re-running through the whole model generation pipeline (fig. 5.4) in each iteration.

5.4.3 Mesh-preserving adaptation methods for the discretized implant model

The re-design of the implant is performed on the surface mesh that is present prior to generating the 3-dimensional discretization, cf. fig. 5.4g. This approach essentially has two main advantages compared to re-setting the corner sheet points and re-executing the modeling script:

- the relocated pad has a nearly identical shape than the original one, since the dimensioning via angular and axial coordinates (and hence a dependence from the center axis) is replaced by a defined distance movement along the epicardial surface; and
- the re-designed implant has the same amount of nodes and hence the same degree of freedom map than the original one, which opens the door for the application of projection-based model order reduction techniques in order to increase the efficiency of the computation of design variants.

The mesh-moving algorithm is depicted in the following. Its input are the lengths D_{φ}^{p} and D_{z}^{p} that a certain pad denoted with $p \in [\ell_{\mathrm{a}}, \ell_{\mathrm{p}}, r]$ should move along the epicardial surface in the circumferential and the longitudinal directions, respectively. The algorithm operates by moving small increments Δ_{φ} and Δ_{z} along a tangent plane to the epicardial surface. These increments are recommended to be sufficiently small ($\leq 1 \ \mathrm{mm}$) and here are chosen to $\Delta_{\varphi} = \Delta_{z} = 1 \ \mathrm{mm}$.
The circumferential movement of a node happens along the tangential direction $\mathbf{n}_{\varphi}$ and is scaled by the relation of its distance d to the axis $\mathbf{a} = \mathbf{p}_{\mathrm{lum}}^{\ell} - \mathbf{p}_{\mathrm{AV}}$ (cf. fig. 2.8 or fig. 5.4) and the distance d_{mid} of the pad midpoint $\mathbf{x}_{\mathrm{mid}}^{p}$ to that axis.
Longitudinal movement of a node happens along the modified tangential direction $\bar{\mathbf{n}}_{z}$ that is a blend of the longitudinal direction $\mathbf{n}_{z}$ at that node and the one at the pad midpoint $\tilde{\mathbf{n}}_{z}$ (user-specific blend parameter $a_{z} \in [0, 1]$). For $a_{z} = 1$, the direction $\mathbf{n}_{z}$ is chosen, and the pad geometry would collapse in the limit case that it is moved entirely towards the apex. Otherwise, for $a_{z} = 0$, pad edges become increasingly longer as movement towards the apex takes place, since the circumference gets shorter. Depending on the longitudinal distance, $a_{z} = 0.5$ may be a good

choice, however for a more sophisticated movement, a_z may be designed variable depending on the node distance to the heart axis $\mathbf{a}$.

The following algorithm for the mesh movement is called:

input: $D_\varphi^{\ell_\mathrm{a}}, D_z^{\ell_\mathrm{a}}, D_\varphi^{\ell_\mathrm{p}}, D_z^{\ell_\mathrm{p}}, D_\varphi^{r}, D_z^{r}$ *// total distances that the pads should be moved*
$l_\varphi := 0, l_z := 0$ *// monitored distances that the pads have already been moved*
for $p \in [\ell_\mathrm{a}, \ell_\mathrm{p}, r]$ **do** *// loop over pads to be moved*
  $d_\mathrm{mid} = \frac{||\mathbf{x}_\mathrm{mid}^p - \mathbf{p}_\mathrm{AV}|| \times \mathbf{a}}{||\mathbf{a}||}$ *// distance of pad surface midpoint to axis* $\mathbf{a}$
  compute normal $\mathbf{n}_\mathrm{cross}^p$ at $\mathbf{x}_\mathrm{mid}^p$ of cross-plane spanned by $\mathbf{x}_\mathrm{mid}^p$ and axis $\mathbf{a}$
  // determine length of iteration
  if $\lfloor |D_\varphi^p| \rfloor > \lfloor |D_z^p| \rfloor$ **then**
    $l_\mathrm{iter} = \lfloor |D_\varphi^p / \Delta_\varphi| \rfloor + 1$ *// circumferential component*
  else
    $l_\mathrm{iter} = \lfloor |D_z^p / \Delta_z| \rfloor + 1$ *// longitudinal component*
  end if
  // make increments negative for movement in negative direction
  if $D_\varphi^p < 0$ **then** *// circumferential component*
    $\Delta_\varphi \leftarrow -\Delta_\varphi$
  end if
  if $D_z^p < 0$ **then** *// longitudinal component*
    $\Delta_z \leftarrow -\Delta_z$
  end if
  for $j \in [0, l_\mathrm{iter}]$ **do** *// loop over discrete distance increments*
    // modify last iteration increments such that total lengths are hit
    if $j = \lfloor |D_\varphi^p / \Delta_\varphi| \rfloor$ **then** *// circumferential component*
      if $D_\varphi^p > 0$ **then**
        $\Delta_\varphi \leftarrow D_\varphi^p / \Delta_\varphi - \lfloor D_\varphi^p / \Delta_\varphi \rfloor$
      else
        $\Delta_\varphi \leftarrow D_\varphi^p / \Delta_\varphi - \lceil D_\varphi^p / \Delta_\varphi \rceil$
      end if
    end if
    if $j = \lfloor |D_z^p / \Delta_z| \rfloor$ **then** *// longitudinal component*
      if $D_z^p > 0$ **then**
        $\Delta_z \leftarrow D_z^p / \Delta_z - \lfloor D_z^p / \Delta_z \rfloor$
      else
        $\Delta_z \leftarrow D_z^p / \Delta_z - \lceil D_z^p / \Delta_z \rceil$
      end if
    end if
    for $i \in [0, n_\mathrm{nd}^p]$ **do** *// loop over nodes belonging to pad* p
      project node i with coordinates $\boldsymbol{\xi}^i$ onto epicardial surface $\mathcal{S}_\mathrm{epi}$, obtain $\tilde{\boldsymbol{\xi}}^i$
      compute normal $\mathbf{n}_\mathrm{epi}^i$ of $\mathcal{S}_\mathrm{epi}$ at $\tilde{\boldsymbol{\xi}}^i$
      $\mathbf{n}_\varphi^i = \mathbf{n}_\mathrm{AVP} \times \mathbf{n}_\mathrm{epi}^i$ *// circumferential tangent direction*
      $\mathbf{n}_z^i = \mathbf{n}_\varphi^i \times \mathbf{n}_\mathrm{epi}^i$ and $\tilde{\mathbf{n}}_z^i = \mathbf{n}_\mathrm{cross}^p \times \mathbf{n}_\mathrm{epi}^i$ *// current and midpoint long. tangent direction*

$\bar{\mathbf{n}}_z^i = a_z \mathbf{n}_z^i + (1 - a_z)\tilde{\mathbf{n}}_z^i$ and normalize $\bar{\mathbf{n}}_z^i$ *// modified longitudinal tangent direction*
$d = \frac{||\boldsymbol{\xi}^i - \mathbf{p}_{\mathrm{AV}}|| \times \mathbf{a}}{||\mathbf{a}||}$ *// distance from node to axis* $\mathbf{a}$
if $l_\varphi < |D_\varphi^p|$ **then** *// update node location in circumferential direction*
$\boldsymbol{\xi}^i \leftarrow \boldsymbol{\xi}^i + \Delta_\varphi \frac{d}{d_{\mathrm{mid}}} \mathbf{n}_\varphi^i$
$l_\varphi \leftarrow l_\varphi + ||\Delta_\varphi \mathbf{n}_\varphi^i|| / n_{\mathrm{nd}}^p$
end if
if $l_z < |D_z^p|$ **then** *// update node location in longitudinal direction*
$\boldsymbol{\xi}^i \leftarrow \boldsymbol{\xi}^i + \Delta_z \bar{\mathbf{n}}_z^i$
$l_z \leftarrow l_z + ||\Delta_z \bar{\mathbf{n}}_z^i|| / n_{\mathrm{nd}}^p$
end if
end for
end for
end for

After performing the relocation of the pads, the implant discretization is finalized (step in fig. 5.4f), and the input file for the computation is generated.

5.4.4 Results

Table 5.6 shows the iterations i of the Nelder-Mead simplex algorithm, together with the values of the simplexes spanned by three points in the $D_\varphi^{\ell_\mathrm{a}}, D_\varphi^{\ell_\mathrm{p}}$-plane, the action undertaken by the algorithm, the value of the stroke work (5.13), as well as the error norm E_{fnorm} (4.23).
In the last iteration, the pair $D_\varphi^{\ell_\mathrm{a}}[2] = -5.9947$ mm, $D_\varphi^{\ell_\mathrm{p}}[2] = 8.9998$ mm produced the largest stroke work value of $\mathrm{SW}^\ell = 514.89625487$ mJ and hence is considered as the optimum.
The iterations of the algorithm are visualized by plotting the simplexes in the $D_\varphi^{\ell_\mathrm{a}}, D_\varphi^{\ell_\mathrm{p}}$-plane, cf. fig. 5.12. Iterations $i = 12 \ldots 26$ are visually non-distinguishable, thus the simplex tends to shrink towards zero with increasing iterations as expected.
Figure 5.13 shows the left ventricular pressure-volume relations for the control state (no implant), for the initial simplex, as well as at the optimum. All computations with implant are performed on the first cardiac cycle only; a cycle error (2.222) of ~ 6 % is obtained and tolerated here.

The deformed configurations are visualized in fig. 5.14. The color indicates the magnitude of the displacement (2.2) $||\boldsymbol{u}||$. For better visualization, the implant pads are shown in black (grey). The end-systolic axial views for the initial simplex are depicted in fig. 5.14a, and fig. 5.14b shows the end-systolic axial view for the optimum $D_\varphi^{\ell_\mathrm{a}\star}, D_\varphi^{\ell_\mathrm{p}\star}$. End-diastolic and end-systolic distal views thereof are shown in fig. 5.14c.
Note that there is partial overlap of the left and right ventricular pads for the $D_\varphi^{\ell_\mathrm{a}}[1], D_\varphi^{\ell_\mathrm{p}}[1]$ locations since the pads are "invisible" for one another and therefore per definition cannot come into contact. This fact is of minor importance since such a constellation is purely algorithmic and no valid design state.

5.4.5 Discussion

A generic framework for the optimization of functional design parameters of the ventricular assist device implant is developed. The focus here is set on the determination of the optimal placement

Table 5.6: Iterations i of Nelder-Mead simplex algorithm for model *3Datrioventr*$_{tet4\_2}$ | *0Dsyspulcap* | *VADgen*$_{hex8\_1}$ F-bar, simplex spanned by three points in the $D_{\varphi}^{\ell_a}$, $D_{\varphi}^{\ell_p}$-plane, optimum framed, action of Nelder-Mead algorithm ("cont cont": contraction, and contracted point chosen; "cont renew": contraction, simplex renewed; "exp exp": expanded, and expanded point chosen; "exp refl": expanded, but reflected point chosen; "refl": reflected point chosen), stroke work SW^{ℓ} (5.13), error norm E_{fnorm} (4.23), tolerance $\epsilon_{\mathrm{f}} = 0.0005$ mJ

i	$D_{\varphi}^{\ell_a}[0]$ [mm]	$D_{\varphi}^{\ell_p}[0]$ [mm]	$D_{\varphi}^{\ell_a}[1]$ [mm]	$D_{\varphi}^{\ell_p}[1]$ [mm]	$D_{\varphi}^{\ell_a}[2]$ [mm]	$D_{\varphi}^{\ell_p}[2]$ [mm]	action	SW^{ℓ} [mJ]	E_{fnorm} [mJ]
0	22.5000	20.0000	35.0000	−45.0000	−25.0000	−17.5000	cont cont	504.61458719	20.78034125
1	22.5000	20.0000	−19.3750	24.3750	−25.0000	−17.5000	cont cont	509.65300569	5.06590580
2	0.1562	11.7188	−19.3750	24.3750	−25.0000	−17.5000	cont cont	513.96411492	7.28008694
3	0.1562	11.7188	−19.3750	24.3750	−17.3047	0.2734	cont cont	513.96411492	3.60016619
4	0.1562	11.7188	−3.1738	−3.1934	−17.3047	0.2734	cont cont	513.96411492	1.91529785
5	0.1562	11.7188	−3.1738	−3.1934	−9.4067	2.2681	exp refl	514.13872198	0.17516967
6	0.1562	11.7188	−6.0767	17.1802	−9.4067	2.2681	cont cont	514.33986118	0.30136542
7	−3.7927	10.7214	−6.0767	17.1802	−9.4067	2.2681	cont cont	514.72048914	0.49159469
8	−3.7927	10.7214	−6.0767	17.1802	−7.1707	8.1094	cont cont	514.85135164	0.37332793
9	−3.7927	10.7214	−5.1842	5.5331	−7.1707	8.1094	cont cont	514.85135164	0.11311332
10	−4.9851	8.7713	−5.1842	5.5331	−7.1707	8.1094	cont cont	514.86108588	0.07226649
11	−4.9851	8.7713	−6.5247	9.8941	−7.1707	8.1094	cont cont	514.87147465	0.01601346
12	−4.9851	8.7713	−6.5247	9.8941	−6.4628	8.7211	cont cont	514.87707858	0.01198271
13	−5.7394	9.0395	−6.5247	9.8941	−6.4628	8.7211	refl	514.88363524	0.00976908
14	−5.7394	9.0395	−5.6775	7.8665	−6.4628	8.7211	cont cont	514.88363524	0.00489475
15	−5.7394	9.0395	−5.6775	7.8665	−6.0856	8.5870	cont cont	514.88581433	0.00347119
16	−5.7394	9.0395	−6.0301	9.2866	−6.0856	8.5870	cont cont	514.89213904	0.00749389
17	−5.8986	8.9881	−6.0301	9.2866	−6.0856	8.5870	cont cont	514.89262331	0.00482266
18	−5.8986	8.9881	−6.0301	9.2866	−6.0250	8.8622	cont cont	514.89262331	0.00177862
19	−5.8986	8.9881	−6.0301	9.2866	−5.9947	8.9998	cont cont	514.89625487	0.00388166
20	−5.8986	8.9881	−5.9884	9.1403	−5.9947	8.9998	cont cont	514.89625487	0.00329892
21	−5.9451	9.0291	−5.9884	9.1403	−5.9947	8.9998	cont cont	514.89625487	0.00271498
22	−5.9451	9.0291	−5.9791	9.0773	−5.9947	8.9998	refl	514.89625487	0.00244069
23	−6.0287	9.0480	−5.9791	9.0773	−5.9947	8.9998	refl	514.89625487	0.00183452
24	−6.0287	9.0480	−6.0443	8.9705	−5.9947	8.9998	cont cont	514.89625487	0.00092968
25	−6.0241	9.0166	−6.0443	8.9705	−5.9947	8.9998	cont cont	514.89625487	0.00063488
26	−6.0241	9.0166	−6.0268	8.9893	−5.9947	8.9998	cont cont	514.89625487	0.00019236

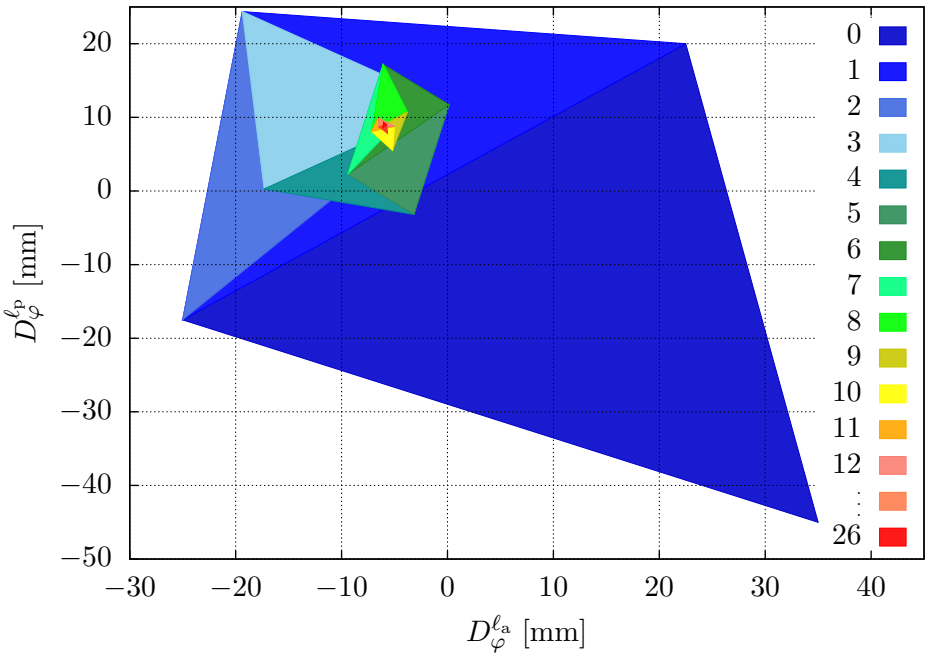

Figure 5.12: Plot of simplexes in the $D_\varphi^{\ell_\mathrm{a}}, D_\varphi^{\ell_\mathrm{p}}$-plane produced by Nelder-Mead algorithm, color bar shows iteration count i. Close-minimum simplex already reached after 12 iterations. Convergence criterion (4.23) with tolerance $\epsilon_\mathrm{f} = 0.0005$ mJ met after 26 iterations.

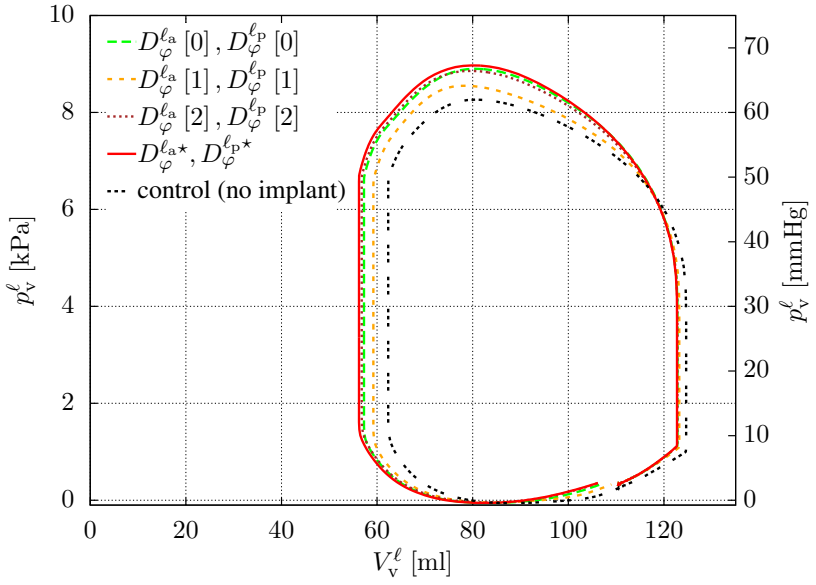

Figure 5.13: Model *3Datrioventr*$_{tet4\_2}$ | *0Dsyspulcap* | *VADgen*$_{hex8\_1\,\mathrm{F\text{-}bar}}$: Left ventricular pressure-volume relationships for the control case (no implant), the initial simplex at $D_\varphi^{\ell_\mathrm{a}}[0], D_\varphi^{\ell_\mathrm{p}}[0]$ (first), $D_\varphi^{\ell_\mathrm{a}}[1], D_\varphi^{\ell_\mathrm{p}}[1]$ (second), $D_\varphi^{\ell_\mathrm{a}}[2], D_\varphi^{\ell_\mathrm{p}}[2]$ (third), as well as at the optimum $D_\varphi^{\ell_\mathrm{a}\star}, D_\varphi^{\ell_\mathrm{p}\star}$.

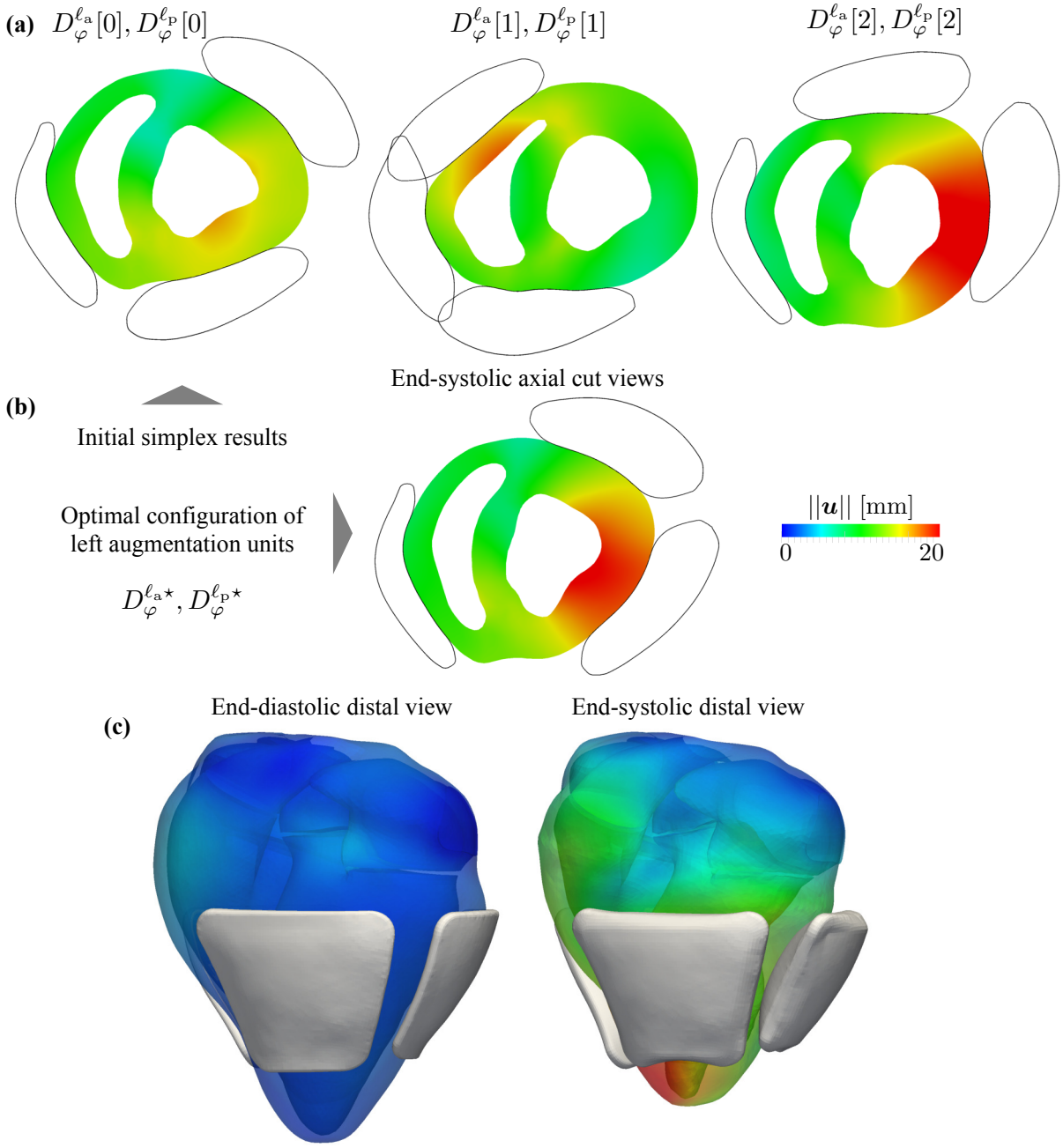

Figure 5.14: Model *3Datrioventr*$_{tet4\_2}$ | *0Dsyspulcap* | *VADgen*$_{hex8\_1\,\text{F-bar}}$: Deformed configurations, color indicates displacement magnitude $||\boldsymbol{u}||$ [mm]. **(a)** End-systolic axial cut views for initial simplex $D_\varphi^{\ell_a}[0], D_\varphi^{\ell_p}[0]$ (first), $D_\varphi^{\ell_a}[1], D_\varphi^{\ell_p}[1]$ (second), $D_\varphi^{\ell_a}[2], D_\varphi^{\ell_p}[2]$ (third). **(b)** End-systolic axial cut view on optimal locations $D_\varphi^{\ell_a\star}, D_\varphi^{\ell_p\star}$. **(c)** End-diastolic (left) and end-systolic (right) distal view for optimum $D_\varphi^{\ell_a\star}, D_\varphi^{\ell_p\star}$.

of the augmentation pads in order to achieve a maximum in ventricular stroke work. Without loss of generality and for demonstrative purposes, the analysis here is restricted to the left ventricular pads and to the location around the ventricular circumference only. However, the framework, in principle, is flexible with respect to the design variables and the objective function and may be extended or modified depending on the requirements for the engineering process.

A gradient-free optimization algorithm is chosen since the underlying forward problem captures non-smooth phenomena such as discretized contact formulations. It was experienced in preliminary studies that the gradient to an objective function that depends on the pad location (be it stroke volume, end-systolic volume, stroke work), hence on a discrete set of nodes that may or may not come into contact, is difficult to compute using a finite difference approach. This may be imagined in the sense that the discretization-dependent situation of contact not necessarily is capable of resolving the difference between the original and a finitely perturbed pad location with sufficient accuracy if that finite perturbation is significantly smaller than the surface mesh size. However, further studies are needed in order to assess if stable smooth gradients may be computed when choosing the finite difference perturbation in the same order of magnitude of the mesh size, or whether a finer mesh may diminish these spurious effects.
The Nelder-Mead simplex algorithm performs as expected and reduces the simplex with increasing iterations, ultimately shrinking it down close to the optimum. For demonstrative purposes, the tolerance was chosen fairly tight and a high number of $i = 26$ iterations is required in order to fulfill it. However, in engineering practice, and especially here due to the relatively small sensitivity of stroke work with respect to circumferential left ventricular pad location, the algorithm already could have been terminated after $i = 7$ iterations as stroke work difference then only affected the first decimal place for increasing iterations.

Currently, the present optimization approach is computationally demanding since it requires to solve the full transient forward problem in most of the cases twice per Nelder-Mead iteration (computation of reflection and potential subsequent action). However, a combination of the present optimization task and method with the 2-level algorithms presented in chap. 4 is straightforward and could increase the computational efficiency. Since the re-design of the implant is entirely performed on the discretization with help of the mesh-moving algorithm presented in sec. 5.4.3, each configuration possesses the same amount of degrees of freedom than the initial one. Therefore, the implant with relocated pads may be computed from a reduced-order model (ROM) that is generated from the initial implant configuration as high-dimensional model (HDM) with help of proper orthogonal decomposition, cf. sec. 4.1.2, and the *ROM-ml* algorithm (sec. 4.3.2) may be chosen to solve the optimization problem. However, preliminary experiences with this approach unveiled difficulties in approximating the adequate behavior using a ROM with significantly differing pad locations generated from the initial implant solution. This is readily reasoned considering the fact that the reduced-order basis (ROB) includes modes which are not at all triggered when computing a configuration with relocated pads, and vice versa the new configuration requires deformation modes which the ROB is devoid of. Hence, globalized ROMs that are generated from multiple HDMs yielding a global ROB may lead to improved ROM behavior, since a larger spectrum of modes are included that enhance the interpolatory abilities of the ROM. However, preliminary studies in this direction still unveiled difficulties to compute

stable interpolations, and the required size of the ROB or different methods of interpolations between HDM solutions in order to obtain a certain accuracy remain to be investigated.

6 Summary and Outlook

Within this thesis, novel computationally efficient and robust patient-specific models for the heart and the circulatory system have been developed. They allow for physiologically meaningful simulations of homeostatic cardiovascular conditions. Their ultimate aim is to be applicable to a wide range of questions that arise in surgery planning, medical intervention, treatment strategies, and here are applied to investigate the impact of a novel extravascular ventricular assist device (VAD) on heart failure scenarios developed in close collaboration with an industrial partner.
A 3-dimensionally (3D) resolved patient-specific geometry of the ventricles (and the atria) is coupled to a 0-dimensional (0D) lumped-parameter closed-loop circulation model. A monolithic computational coupling scheme together with a time-integration of all 0D model governing equations was implemented, and a block-preconditioned GMRES solver was used to efficiently solve the linear 3D-0D coupled system of equations in one monolithic Newton algorithm.
A segmentation workflow for the extraction of the 3D heart geometry out of CT/MRI data as well as an automated process for model generation and finite element meshing that is applicable to arbitrary myocardial geometries has been implemented.
Different types of circulation models are presented, and a gas exchange and dissociation model is straightforwardly incorporated that allows to assess oxygen saturations distributed to different organ compartments.
The model is validated against numerous textbook physiological observations and shows good agreements in behavior for changes in preload, afterload, inotropy, and in presence of valve diseases.
However, for a robust application to different types of cardiovascular conditions, control and feedback control systems should be incorporated into the models, and carbon dioxide and oxygen dissociation functions should be extended to more complex relationships in oder to include the Bohr and Haldane effects as well as temperature dependencies.

The presented 3D-0D model allows to link local phenomena happening on cell scale to global, integral quantities like stroke work and cardiac output and hence is tailored towards the evaluation of the effects that lead to heart failure and possible medical treatment strategies thereof. Growth and remodeling (G&R) models were incorporated by implementing variants of contemporary anisotropic volumetric growth models enhanced by a phenomenological remodeling approach that connects the growth stretch to passive elastic or active tissue properties. The outcome of volume or pressure overload-induced maladaptive changes that arise from a sudden disease event (valve leakage, stenosis, myocardial infarction) was computed by help of a novel multiscale-in-time strategy. Within this algorithm, heart beat and growth time scales are separated and mutually revisited until an outer equilibrium is reached. Reasonable physiological conclusions can be drawn from the presented results, and the G&R models' applicability to investigate possible reverse G&R phenomena after VAD application was not yet shown but readily provided.
For the future, these models should be calibrated using long-term data on myocardial disease

progression, and then could be combined in investigating the aforementioned reversal G&R potential of vascular assist devices.

Novel multilevel parameter estimation methods have been implemented using surrogate modeling techniques and model order reduction by proper orthogonal decomposition. Model order reduction techniques for the first time have been applied to 3D-0D heart-circulation problems, and the performance of the reduced-order model (ROM) with respect to different parametric configurations and sizes of the reduced-order basis was investigated. Stable homeostatic states calibrated to integral volume and time-resolved left ventricular pressure data were obtained in total for three different specific porcine heart geometries and sets of measurements.
However, as discussed, the model order reduction methods still are of some computational expense, and so-called hyper reduction techniques as they recently have been proposed should be incorporated into the ROM framework in order to achieve significant speedups compared to the high-dimensional model.

The calibrated stable homeostatic states were used as input to investigating a novel cardiac compression-based extravascular assist device. A model generation and finite element meshing workflow was established that generates a prototype of the implant according to the design principles set by the industrial partner such that different ventricular shapes and design variants may be easily realized.
The experimental protocols of the acute in-vivo studies then have been replicated in-silico, and a very good agreement of the simulation results to the experimental measurements was shown. Furthermore, the simulation provided access to quantities that are non-assessable in an experimental in-vivo setup: It was shown that gradually increasing left ventricular augmentation pressures reduced end-diastolic myofiber strain and end-systolic wall stress. These results readily give rise to questions how a VAD may reduce G&R stimulants or even initiate reverse G&R after long-term application. However, these findings remain to be ascertained and enhanced both by computational and experimental studies, but have the potential of stimulating further research in this direction.
Furthermore, an optimization framework was proposed that allows to assess the optimal placement of the augmentation pads of the implant in order to achieve a maximum in ventricular stroke work. For this purpose, a mesh-moving algorithm has been developed and a gradient-free optimization algorithm (Nelder-Mead simplex method) was used in order to circumvent difficulties in numerical finite difference gradient calculation in presence of non-smooth computational contact forward problems. An optimal circumferential placement of the left ventricular pads for a maximum in left ventricular stroke work was found, however not without some computational expense of the overall optimization problem.
Therefore, model order reduction techniques as they already have been implemented for the 3D-0D heart-vasculature problem could be a method of choice for the heart-vasculature-VAD model, together with the aforementioned multilevel algorithms that have been developed for parameter estimation. However, current problems that have been encountered using a ROM not only for varying parametric but entirely different structural configurations (varying pad locations essentially mean a different kind of implant with different deformation modes) must be overcome, which could be achieved using global ROMs that are calculated using different realizations of the

implant.

The presented models and methods allow for multiple extensions and enhancements both from a methodological and modeling point of view. Depending on the question at hand, the mechanical models may be readily combined with electrophysiological scalar transport models, and an electro-mechanical coupling would allow to extend the possible applications to questions regarding the excitation-contraction behavior, ventricular or atrial arrhythmia, resynchronization therapies, or similar.
Furthermore, model calibration may be improved and performed with help of measurements stemming from CT or MRI data sets, such as motion tracking or fiber orientation data from diffusion tensor imaging. This could help to identify passive elastic or boundary stiffness parameters as well as fiber directions on an individualized basis and may help to more reliably predict 3D atrioventricular function.

A Appendix

A.1 Integral error analyses of discretizations

Here, integral error analyses for the spatial finite element and temporal finite difference discretizations are performed. Since no analytical solution of the nonlinear 3D-0D forward problem exists, no comparison to a "true" solution but only relative comparisons between different discretizations can be undertaken. These comparisons imply that for decreasing finite element edge length ($h \to 0$ mm) and decreasing finite difference time step size ($\Delta t \to 0$ s), a "true" solution is approximated which is devoid of any discretization-related errors. Strictly speaking, however, there may exist so-called singularity points in the 3D discretized domain (e.g. locations with sharp edges) where the primary variable – the displacement field $\boldsymbol{u}$ (2.2) – may converge, however the derived quantities (stresses and strains) may increase proportional to the mesh refinement, along with a decreasing area of the singularity zone. A prominent example would be a one-sided clamped straight cantilever (uniformly) discretized with solid finite elements and subject to bending forces. At the clamped location, bending around an infinitely small radius happens, hence stresses will tend to infinity at that location for $h \to 0$ mm. Thus, for accurate analyses of stresses and strains, the mesh has to be sufficiently smooth and fine at the locations of interest.
Different discretizations and their influence on integral pressure-volume relationships as well as volume-averaged field data like stresses and strains are shown. However, the discretization procedure always has to consider the specific problem at hand and naturally will be a trade-off between computational feasibility and an expected level of accuracy.
The influence of the spatial discretization is studied in sec. A.1.1, both for the heart and for the ventricular assist device (VAD) implant. The temporal resolution is studied in sec. A.1.2 and only for the prescribed-dynamics heart, hence the 0D model, since large time steps are in general not tolerated for the 3D resolved heart.

A.1.1 Spatial finite element discretizations

Different spatial discretizations are considered for the 3D-0D forward problem, both for the heart (sec. A.1.1.1) and for the VAD models (sec. A.1.1.2). Tetrahedral elements are denoted with *tet4* (4-node linear shape functions) and *tet10* (10-node quadratic shape functions). Hexahedral elements are abbreviated with *hex8* (8-node trilinear shape functions). Quadratic shape functions are not considered for hexahedral elements. A discretization is denoted with the type of finite element plus a number indicating the element edge length in [mm], e.g. *tet10_4* stands for a discretization with quadratic 10-node tetrahedral elements with an element edge length of $h \approx 4$ mm.

A.1.1.1 Heart models

The heart is exclusively discretized with displacement-based tetrahedral finite elements of approximately uniform edge length throughout the whole computational domain $\tilde{\Omega}_0$. Due to the complex patient-specific geometry, other types of elements (e.g. hexahedral ones) are in general not applicable using state-of-the-art meshing software. All computations are carried out using the algorithmic base parameters in tab. 3.1.

For the heart model *3Dventr*, four different levels of finite element edge lengths are considered ($h \approx 8$ mm, $h \approx 4$ mm, $h \approx 2$ mm, $h \approx 1$ mm), each with two different polynomial orders of the finite element ansatz functions (linear 4-node tetrahedral elements, quadratic 10-node tetrahedral elements). Whereas linear 4-node tetrahedral elements in general are known to be prone to severe locking phenomena especially in presence of nearly incompressible material behavior, quadratic 10-node tetrahedrals have significantly better approximation abilities but come along with increased computational effort due to a larger number of degrees of freedom and an increased bandwidth of the tangent matrix. The four discretizations with varying edge lengths are sketched in fig. A.1. Homeostatic state initial conditions have been computed for discretization *tet4_2* according to the procedure described in sec. 2.2.4.1 and then were used to compute one cardiac cycle for all the eight discretizations. Hence, no dependence of the solution on the initial conditions is given. The base parameters from tab. 2.3 and tab. 2.6 are chosen.

Integral results for model *3Dventr* coupled to model *0Dsyspul* are shown for the eight different discretizations *tet4_8*, *tet4_4*, *tet4_2*, *tet4_1*, *tet10_8*, *tet10_4*, *tet10_2* and *tet10_1*: The left and right ventricular pressure-volume relations are shown in fig. A.2; the volume-averaged volumetric (mean, cf. $(2.21)_1$) and deviatoric (von Mises, cf. $(2.22)_2$) stresses, $\hat{\overline{\sigma}} = \frac{1}{V(\Omega)} \int_\Omega \overline{\sigma} \, \mathrm{d}v$ and $\hat{\sigma}_{\mathrm{vM}} = \frac{1}{V(\Omega)} \int_\Omega \sigma_{\mathrm{vM}} \, \mathrm{d}v$, are depicted in fig. A.3a and fig. A.3b, respectively; fig. A.3c shows the volume-averaged myofiber stretch $\hat{\lambda}_{\mathrm{myo}} = \frac{1}{V(\Omega)} \int_\Omega \lambda_{\mathrm{myo}} \, \mathrm{d}v$; and the relative wall volume change $V(\Omega)/V(\Omega_0)$ is depicted in fig. A.3d.

Table A.1 shows the left, right, and total ventricular stroke work SW^ℓ, SW^r, and $\sum_{i=\ell,r} \mathrm{SW}^i$, respectively, as well as the cycle error E_{cycl} (2.222), the number of solid mechanics degrees of freedom $n_{\mathrm{dof}}^{\mathrm{3D}}$, and the number of cores n_{core} that were used for the computation – for the eight discretizations of model *3Dventr* | *0Dsyspul*.

Discretizations *tet4_8*, *tet4_4* and *tet10_8* yield integral results that significantly differ and hence may not be considered for a reliable analysis. However, increasing mesh or polynomial order refinement yields pressure-volume relationships (stroke works), volume-averaged stresses and myofiber strains of acceptable accuracy.

For the heart model *3Datrioventr*, two different levels of finite element edge lengths are considered ($h \approx 2$ mm, $h \approx 1.25$ mm), both again with linear 4-node tetrahedral elements and quadratic 10-node tetrahedral elements. Due to the even more complex geometry of the 4-chamber heart model compared to the only-ventricular model, (uniform) coarser meshing than $h \approx 2$ mm was not possible considering the delicate atrial structures. The two discretizations with varying edge

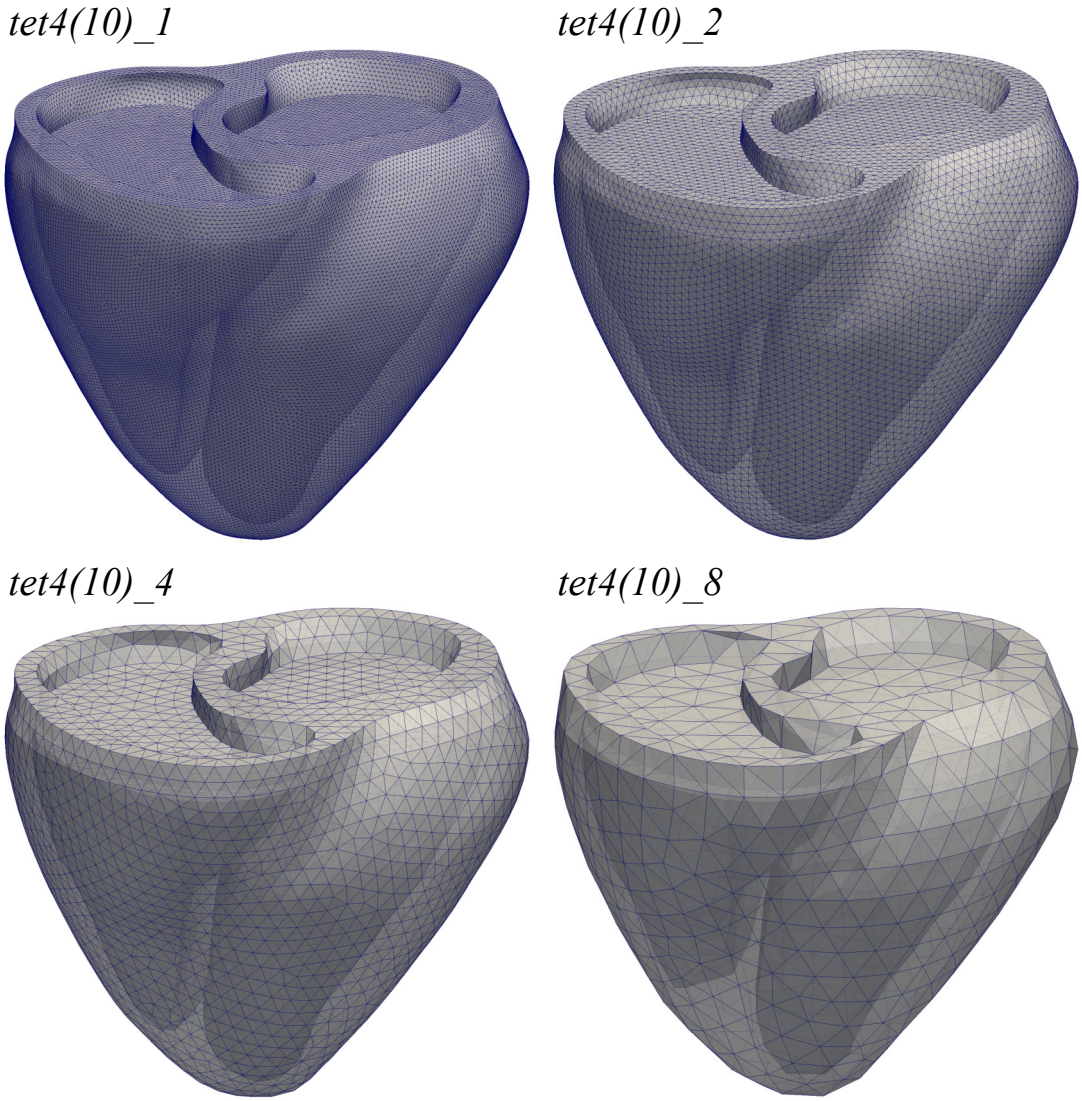

Figure A.1: Model *3Dventr* with the four different spatial discretizations *tet4(10)_1*, *tet4(10)_2*, *tet4(10)_4* and *tet4(10)_8*; either for linear 4-node tetrahedral elements (*tet4*) or quadratic 10-node tetrahedrals (*tet10*).

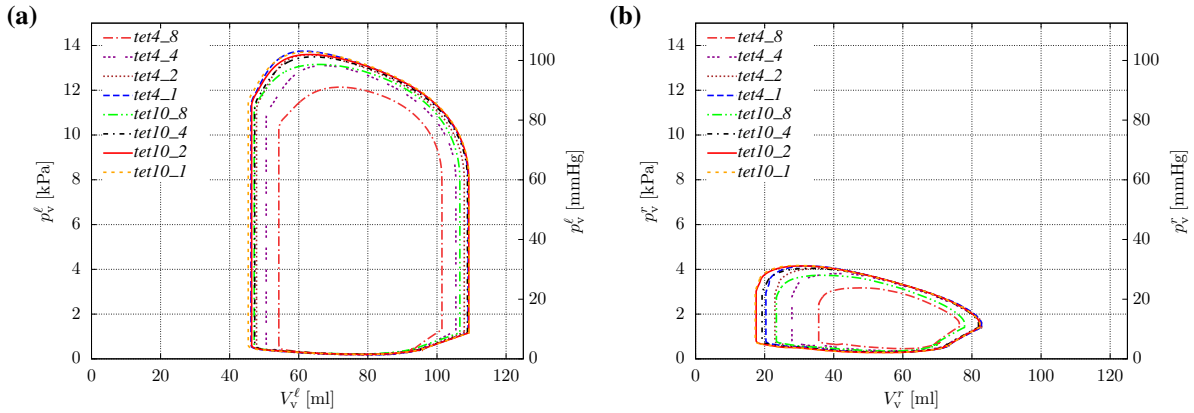

Figure A.2: Model *3Dventr | 0Dsyspul*: Pressure-volume relationships for the eight discretizations *tet4_8*, *tet4_4*, *tet4_2*, *tet4_1*, *tet10_8*, *tet10_4*, *tet10_2* and *tet10_1*. **(a)** Left ventricle. **(b)** Right ventricle.

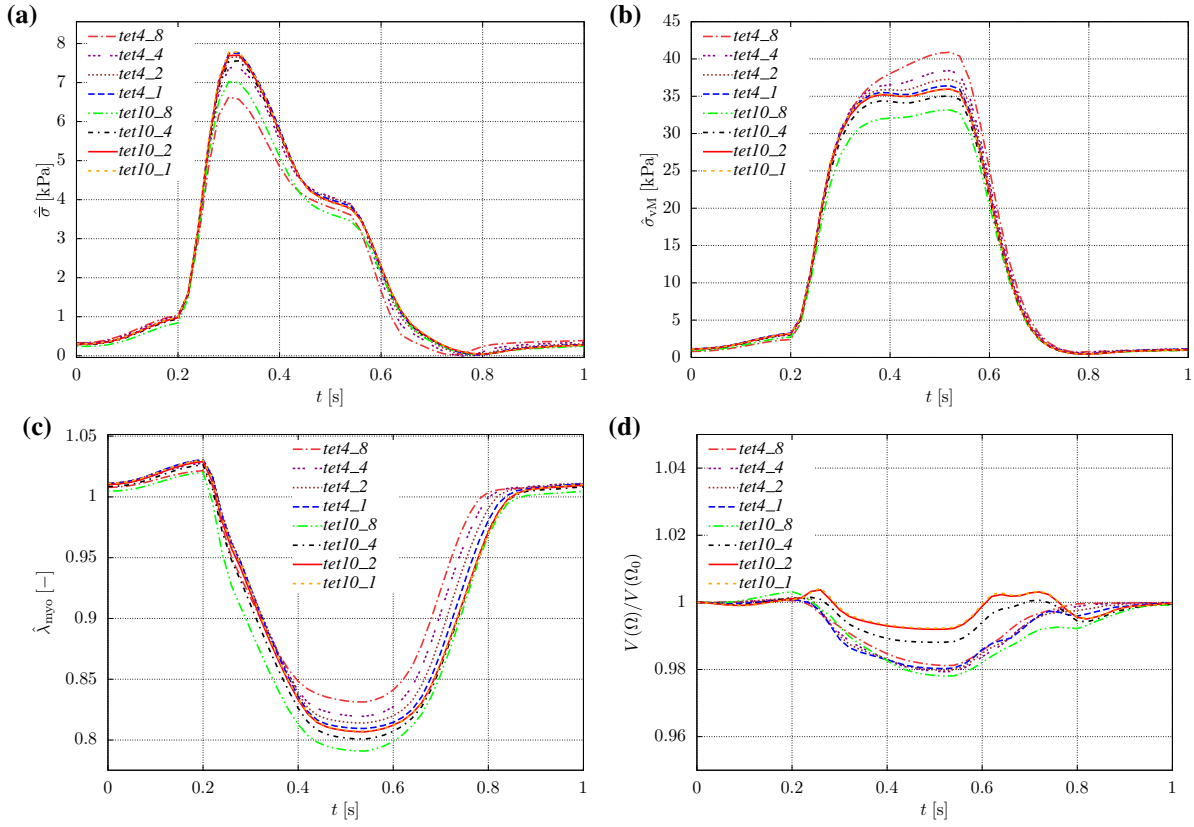

Figure A.3: Model *3Dventr | 0Dsyspul*: Integral volume-averaged data for the eight discretizations *tet4_8*, *tet4_4*, *tet4_2*, *tet4_1*, *tet10_8*, *tet10_4*, *tet10_2* and *tet10_1* over one cardiac cycle $t \in [0, 1\ \mathrm{s}]$. **(a)** Volume-averaged volumetric Cauchy stress (mean stress, cf. $(2.21)_1$), $\hat{\overline{\sigma}} = \frac{1}{V(\Omega)} \int_\Omega \overline{\sigma}\, \mathrm{d}v$. **(b)** Volume-averaged deviatoric Cauchy stress (von Mises stress $(2.22)_2$), $\hat{\sigma}_{\mathrm{vM}} = \frac{1}{V(\Omega)} \int_\Omega \sigma_{\mathrm{vM}}\, \mathrm{d}v$. **(c)** Volume-averaged myofiber stretch, $\hat{\lambda}_{\mathrm{myo}} = \frac{1}{V(\Omega)} \int_\Omega \lambda_{\mathrm{myo}}\, \mathrm{d}v$. **(d)** Relative change of wall volume with respect to undeformed configuration, $V(\Omega)/V(\Omega_0)$.

Table A.1: Model *3Dventr | 0Dsyspul*: Left, right, and total ventricular stroke work SW^ℓ, SW^r, and $\sum_{i=\ell,r} \mathrm{SW}^i$, respectively; cycle error E_{cycl} (2.222), number of 3D solid mechanics degrees of freedom $n_{\mathrm{dof}}^{\mathrm{3D}}$, and number of cores n_{core} used for computation (not less than 28, since 1 node on the cluster possesses 28 cores); all computations carried out with homeostatic state initial conditions from *tet4_2* mesh for comparability; sorted in ascending order with increasing degrees of freedom

	SW^ℓ [mJ]	SW^r [mJ]	$\sum_{i=\ell,r} \mathrm{SW}^i$ [mJ]	E_{cycl} [−]	$n_{\mathrm{dof}}^{\mathrm{3D}}$	n_{core}
tet4_8	521.0	86.3	607.3	0.138	3558	28
tet4_4	642.1	143.0	785.1	0.039	18 582	28
tet10_8	705.0	143.8	848.8	0.085	22 755	28
tet4_2	725.7	169.1	894.8	0.010	126 102	28
tet10_4	739.7	181.7	921.4	0.021	126 501	28
tet10_2	761.4	192.4	953.8	0.035	919 953	168
tet4_1	765.5	182.0	947.5	0.018	920 121	112
tet10_1	779.5	193.8	973.3	0.037	7 017 330	672

lengths are sketched in fig. A.4.
As for model *3Dventr*, homeostatic state initial conditions have been computed for discretization *tet4_2* according to the procedure described in sec. 2.2.4.1 and then were used to compute one cardiac cycle for all the four discretizations in order to exclude dependencies of the solution on the initial conditions. The base parameters from tab. 2.3 and tab. 2.6 are chosen, however without considering the Frank-Starling mechanism, thus choosing ventricular $a_{\mathrm{min}} = 1$ (instead of $a_{\mathrm{min}} = 2/3$) and ventricular $\sigma_0 = 70\ \mathrm{kPa}$ (instead of $\sigma_0 = 100\ \mathrm{kPa}$) such that inotropy is not affected by the preload.

Integral results for model *3Datrioventr* coupled to model *0Dsyspulcap* are shown for the four different discretizations *tet4_2*, *tet4_1.25*, *tet10_2* and *tet10_1.25*: The left and right ventricular as well as left and right atrial pressure-volume relations are shown in fig. A.5; the volume-averaged volumetric (mean, cf. $(2.21)_1$) and deviatoric (von Mises, cf. $(2.22)_2$) stresses, $\hat{\overline{\sigma}} = \frac{1}{V(\Omega)} \int_\Omega \overline{\sigma}\, \mathrm{d}v$ and $\hat{\sigma}_{\mathrm{vM}} = \frac{1}{V(\Omega)} \int_\Omega \sigma_{\mathrm{vM}}\, \mathrm{d}v$, are depicted in fig. A.6a and fig. A.6b, respectively; fig. A.6c shows the volume-averaged myofiber stretch $\hat{\lambda}_{\mathrm{myo}} = \frac{1}{V(\Omega)} \int_\Omega \lambda_{\mathrm{myo}}\, \mathrm{d}v$; and the relative wall volume change $V(\Omega)/V(\Omega_0)$ is depicted in fig. A.6d.

Table A.2 shows the left, right, and total ventricular stroke work SW^ℓ, SW^r, and $\sum_{i=\ell,r} \mathrm{SW}^i$, respectively, as well as the cycle error E_{cycl} (2.222), the number of solid mechanics degrees of freedom $n_{\mathrm{dof}}^{\mathrm{3D}}$, and the number of cores n_{core} that were used for the computation – for the four discretizations of model *3Datrioventr | 0Dsyspulcap*.

The four discretizations all yield integral results that are in a close range to one another. Atrial pressure-volume relationships for the quadratic *tet10* discretizations exhibit a leftward location compared to the linear *tet4* ones. Ventricular pressure-volume relationships (stroke works), volume-averaged stresses and myofiber strains of acceptable accuracy are obtained for the four meshes.

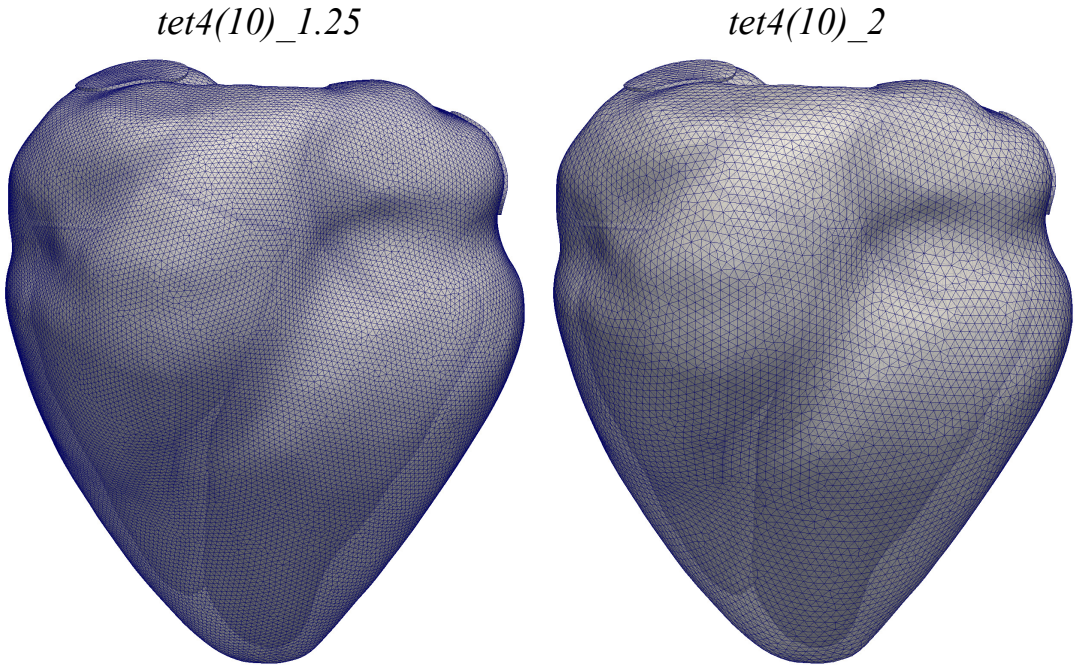

Figure A.4: Model *3Datrioventr* with the two different spatial discretizations *tet4(10)_1.25* and *tet4(10)_2*; either for linear 4-node tetrahedral elements (*tet4*) or quadratic 10-node tetrahedrals (*tet10*).

Table A.2: Model *3Datrioventr* | *0Dsyspulcap*: Left, right, and total ventricular stroke work SW^{ℓ}, SW^{r}, and $\sum_{i=\ell,r} \mathrm{SW}^{i}$, respectively; cycle error E_{cycl} (2.222), number of 3D solid mechanics degrees of freedom $n_{\mathrm{dof}}^{\mathrm{3D}}$, and number of cores n_{core} used for computation (not less than 28, since 1 node on the cluster possesses 28 cores); all computations carried out with homeostatic state initial conditions from *tet4_2* mesh for comparability; sorted in ascending order with increasing degrees of freedom

	SW^{ℓ} [mJ]	SW^{r} [mJ]	$\sum_{i=\ell,r} \mathrm{SW}^{i}$ [mJ]	E_{cycl} [−]	$n_{\mathrm{dof}}^{\mathrm{3D}}$	n_{core}
tet4_2	771.1	259.7	1030.8	0.020	174 876	28
tet4_1.25	816.2	269.1	1085.3	0.019	660 555	112
tet10_2	832.4	266.8	1099.2	0.029	1 262 682	168
tet10_1.25	854.5	276.1	1130.6	0.033	4 937 724	700

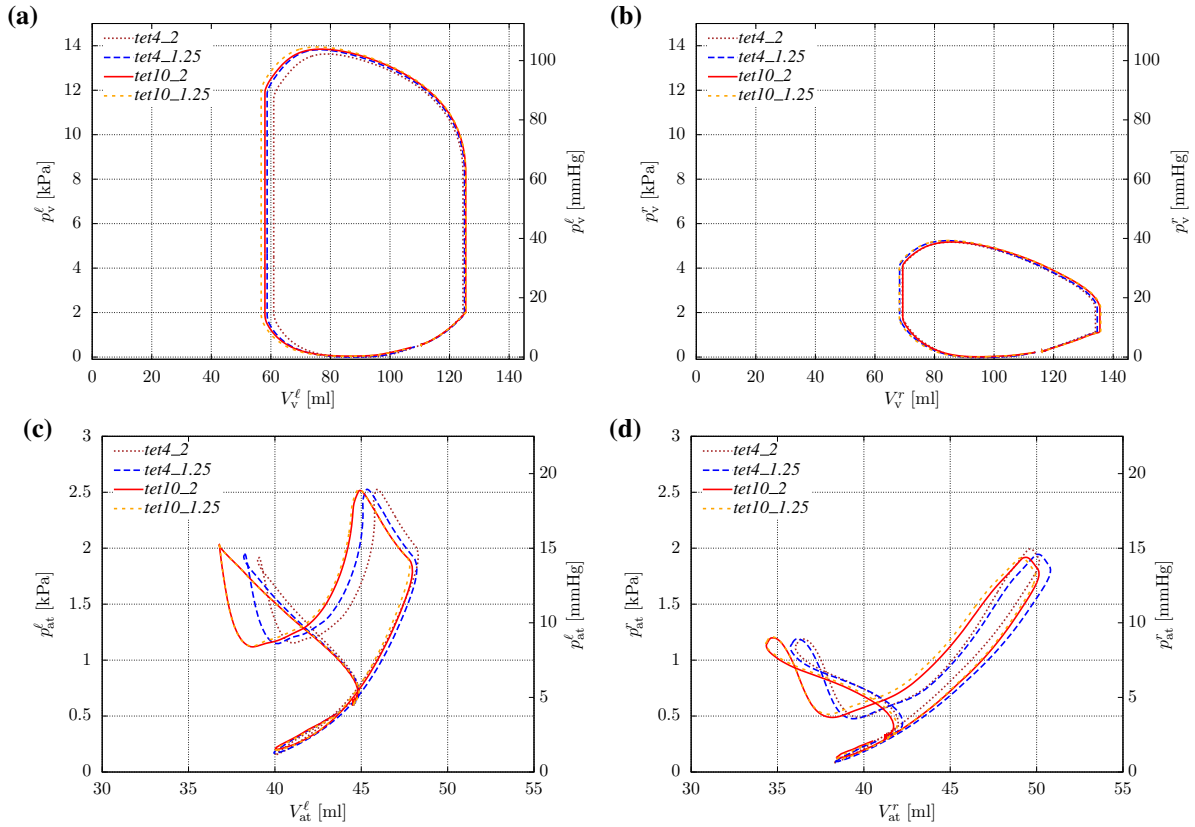

Figure A.5: Model *3Datrioventr | 0Dsyspulcap*: Pressure-volume relationships for the four discretizations *tet4_2*, *tet4_1.25*, *tet10_2* and *tet10_1.25*. **(a)** Left ventricle. **(b)** Right ventricle. **(c)** Left atrium. **(d)** Right atrium.

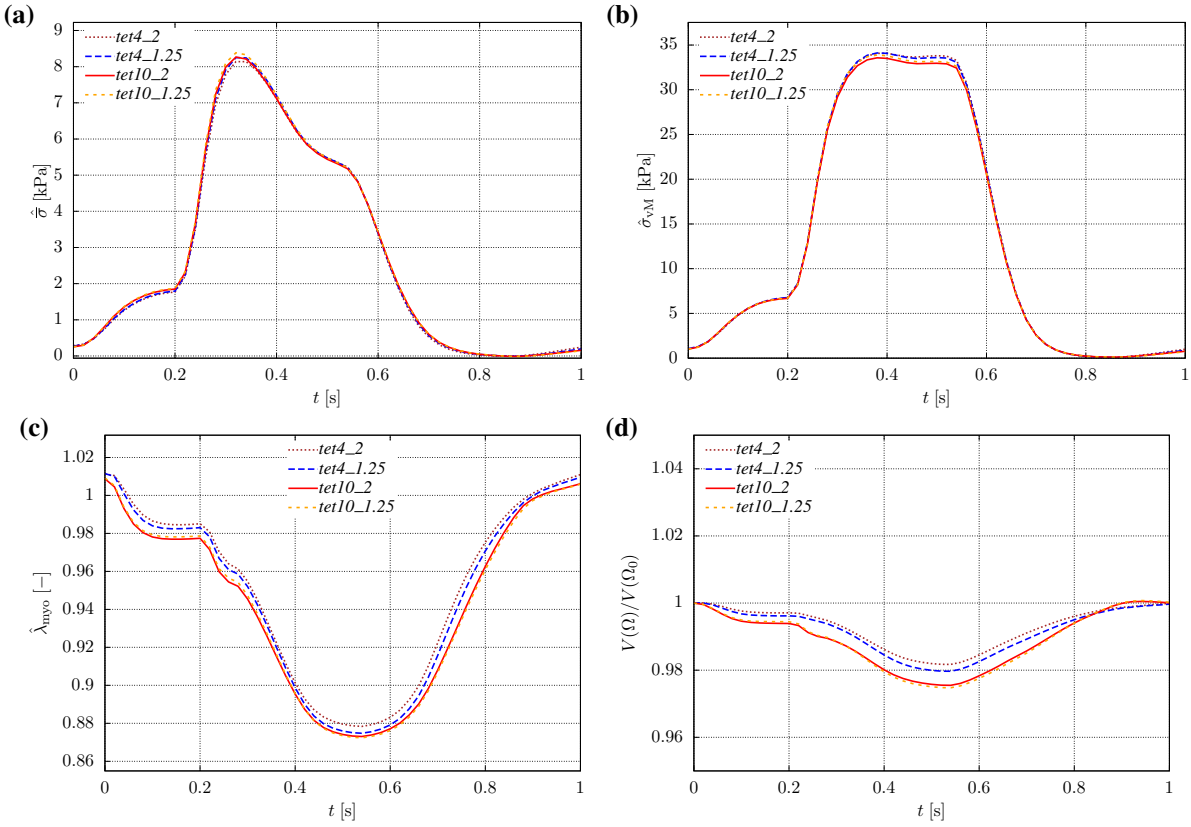

Figure A.6: Model *3Datrioventr | 0Dsyspulcap*: Integral volume-averaged data for the four discretizations *tet4_2*, *tet4_1.25*, *tet10_2* and *tet10_1.25* over one cardiac cycle $t \in [0, 1\ \mathrm{s}]$. **(a)** Volume-averaged volumetric Cauchy stress (mean stress, cf. $(2.21)_1$), $\hat{\overline{\sigma}} = \frac{1}{V(\Omega)} \int_\Omega \overline{\sigma}\, \mathrm{d}v$. **(b)** Volume-averaged deviatoric Cauchy stress (von Mises stress $(2.22)_2$), $\hat{\sigma}_{\mathrm{vM}} = \frac{1}{V(\Omega)} \int_\Omega \sigma_{\mathrm{vM}}\, \mathrm{d}v$. **(c)** Volume-averaged myofiber stretch, $\hat{\lambda}_{\mathrm{myo}} = \frac{1}{V(\Omega)} \int_\Omega \lambda_{\mathrm{myo}}\, \mathrm{d}v$. **(d)** Relative change of wall volume with respect to undeformed configuration, $V(\Omega)/V(\Omega_0)$.

A.1.1.2 VAD models

The VAD model *VAD2013p* is used for the comparison of different discretizations and element technologies. It is entirely discretized using trilinear hexahedral finite elements (*hex8*). Three different mesh sizes that relate to the pad in-plane element edge length are chosen: $h \approx 2$ mm (*hex8_2*), $h \approx 1$ mm (*hex8_1*) and $h \approx 0.5$ mm (*hex8_0.5*). Over the pad thickness $d_{\mathrm{P}}^{\mathrm{wall}}$, 1 element is used. Along the radii $r_{\mathrm{P}}^{\mathrm{s,i}}$ and $r_{\mathrm{P}}^{\mathrm{s,o}}$, element intervals are 2, 4 and 8 for the discretizations *hex8_2*, *hex8_1* and *hex8_0.5*, respectively. Additionally, 1 element is used along the bridges between the two heart-oriented outer radii, the two inner radii and the two shell-oriented outer radii, each having a length of $d_{\mathrm{P}}^{\mathrm{brdg}} = \frac{1}{3}\left(d_{\mathrm{P}} - 4r_{\mathrm{P}}^{\mathrm{s,o}} - 2r_{\mathrm{P}}^{\mathrm{s,i}}\right)$. Over the shell thickness d_{S}, 1 element is used. The in-plane mesh size for the shell is twice as large as for the pads. Refer to tab. 5.1 and fig. 5.3a,b for the dimensions of the implant.

The three different spatial discretizations are depicted in fig. A.7.

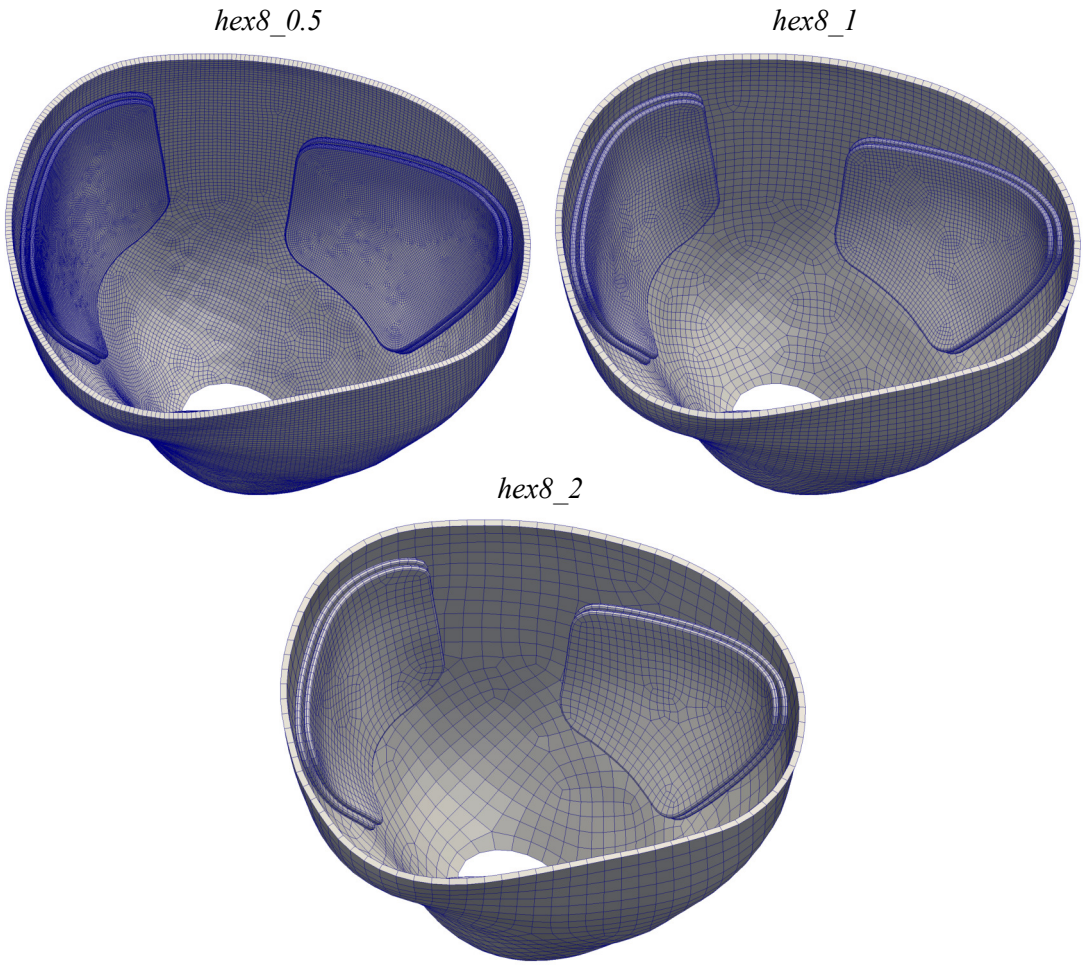

Figure A.7: Model *VAD2013p* with the three different spatial discretizations *hex8_0.5*, *hex8_1*, *hex8_2*.

Furthermore, two different types of finite element technologies are considered. One the one hand, the so-called F-bar technology [49] is used, which evaluates the volumetric part of the deformation gradient at the element's center in order to avoid spurious volumetric locking phenomena. On the other, elements relying on the so-called enhanced assumed strain (EAS) technology are considered, cf. [218] and references therein. The EAS formulation essentially relies on a multi-field variational principe (Hu-Washizu principle) which introduces additional degrees of freedom for the strain field. The specific element formulation allows to perform a condensation of these additional variables at the element level such that the size of the global system of equations remains unaltered. This element technology promises to combat volumetric as well as shear locking phenomena.

One transient cardiac cycle is computed using the heart and vascular model *3Dventr$_{tet4_1}$ | 0Dsyspul* with calibrated homeostatic state conditions and parameters for the low-afterload heart failure scenario (cf. chap. 4). Peak pad pressures in (5.7) are $\hat{p}_{\mathrm{P}}^{\ell_{\mathrm{a}},\max} = \hat{p}_{\mathrm{P}}^{\ell_{\mathrm{p}},\max} = 60\ \mathrm{mmHg}$ and $\hat{p}_{\mathrm{P}}^{r,\max} = 20\ \mathrm{mmHg}$. The pads were deflated without additional suction, hence $\hat{p}_{\mathrm{P}}^{i,\mathrm{suc}} = 0$.

The left and right ventricular pressure-volume relationships as well as the pad volumes $V_{\mathrm{P}}^{i}(t)$ ($i = \ell_{\mathrm{a}}, \ell_{\mathrm{p}}, r$) over time t are shown in fig. A.8 for the three different spatial resolutions using F-bar technology, and for discretization *hex8_1* using standard and EAS elements.
Table A.3 lists total ventricular stroke work $\sum_{i=\ell,r} \mathrm{SW}^{i}$, peak (end-systolic) pad volumes $V_{\mathrm{P}}^{i,\max}$ ($i = \ell_{\mathrm{a}}, \ell_{\mathrm{p}}, r$), the number of VAD degrees of freedom $n_{\mathrm{dof}}^{\mathrm{3D}(\mathit{VAD})}$, as well as the number of cores n_{core} used for the computation.

Table A.3: Model *3Dventr$_{tet4_1}$ | 0Dsyspul | VAD2013p*: Total ventricular stroke work $\sum_{i=\ell,r} \mathrm{SW}^{i}$, peak left anterior, left posterior, and right pad volume $V_{\mathrm{P}}^{\ell_{\mathrm{a}},\max}$, $V_{\mathrm{P}}^{\ell_{\mathrm{p}},\max}$, and $V_{\mathrm{P}}^{r,\max}$, respectively, number of 3D solid mechanics degrees of freedom of the VAD $n_{\mathrm{dof}}^{\mathrm{3D}(\mathit{VAD})}$, and number of cores n_{core} used for computation

	$\sum_{i=\ell,r} \mathrm{SW}^{i}$ [mJ]	$V_{\mathrm{P}}^{\ell_{\mathrm{a}},\max}$ [ml]	$V_{\mathrm{P}}^{\ell_{\mathrm{p}},\max}$ [ml]	$V_{\mathrm{P}}^{r,\max}$ [ml]	$n_{\mathrm{dof}}^{\mathrm{3D}(\mathit{VAD})}$	n_{core}
hex8_2 F-bar	635.2	28.7	28.2	10.1	61 614	112
hex8_1 F-bar	643.6	30.0	29.3	10.5	237 030	112
hex8_0.5 F-bar	645.3	30.4	29.6	11.3	931 152	168
hex8_1 std	612.9	25.0	24.5	11.4	237 030	112
hex8_1 EAS	644.1	29.9	29.2	11.6	237 030	112

End-systolic ventricular volumes are not that sensitive to the VAD discretization, even though peak pad volume is remarkably lower when using hexahedral elements devoid of any technology. The *hex8_1* discretization with F-bar technology yields peak pad volumes comparable to the finer discretization or to that of the same fineness but with EAS technology.
Pad deflation behavior is significantly influenced by the respective discretization (cf. pad volume decays in fig. A.8c–e). Fine resolutions and element technologies allow to resolve more distinct modes in the deformation pattern that however may lead to spurious solutions of the deflated configurations that may compromise ventricular filling. These deflation patterns are most probably not representative for the real-world behavior due to the model idealizations that have been undertaken, cf. chap 5. Hence, if not known better from the experimental data, a deflation process

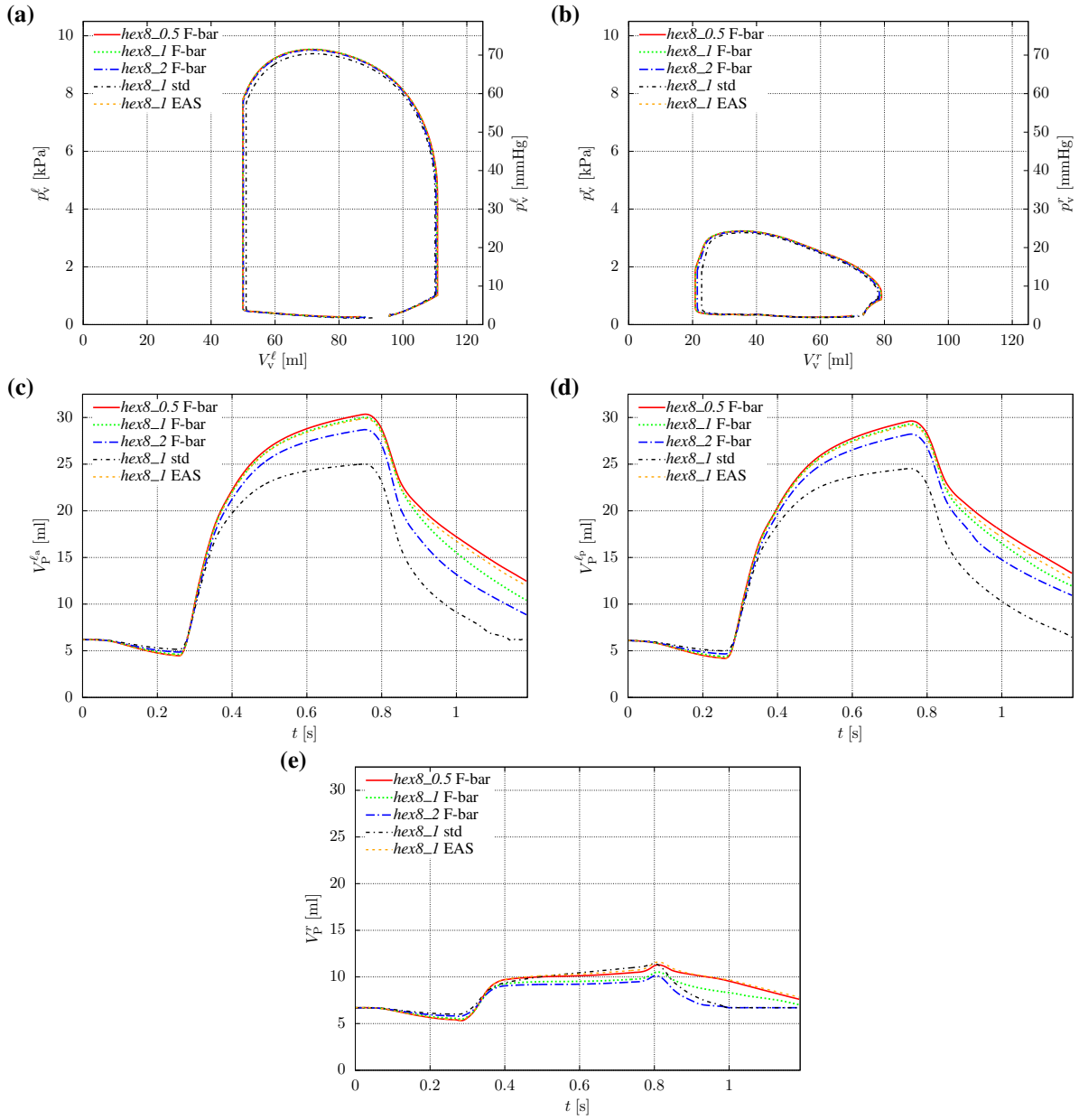

Figure A.8: Model *3Dventr*$_{tet4\_1}$ | *0Dsyspul* | *VAD2013p*: Ventricular pressure-volume relationships as well as pad volumes over time t for the three different VAD discretizations *hex8_2*, *hex8_1* and *hex8_0.5*, as well as comparisons between different element technologies: "std" for standard elements, "F-bar" for the so-called F-bar element technology [49], "EAS" for the enhanced assumed strain technology; all applied to the same heart discretization *tet4_1*. **(a)** Left ventricular pressure-volume loops. **(b)** Right ventricular pressure-volume loops. **(c)** Left anterior pad volume $V_{\mathrm{P}}^{\ell_{\mathrm{a}}}$. **(d)** Left posterior pad volume $V_{\mathrm{P}}^{\ell_{\mathrm{p}}}$. **(e)** Right pad volume V_{P}^{r}.

that minimizes impairment of ventricular filling should be pursued, which is why the suction pressure $\hat{p}_{\mathrm{P}}^{i,\mathrm{suc}}$ in (5.7) was introduced (however note that is was omitted for this convergence study).

A.1.2 Temporal finite difference discretizations

The influence of the time step size Δt (hence the number of performed time steps n_{step} per cardiac cycle) on the solution is studied for the prescribed-dynamics heart (cf. sec. 2.2.3.2). For this purpose, the homeostatic state solution of model *3Datrioventr$_{tet4_2}$* | *0Dsyspulcap* is used as input.

Figure A.9 shows the left and right ventricular pressure-volume relationships, and tab. A.4 shows left, right and total ventricular stroke works SW^{ℓ}, SW^{r} and $\sum_{i=\ell,r}\mathrm{SW}^{i}$, respectively, for the different temporal discretizations with increasing number of time steps $n_{\mathrm{step}} = 8 \ldots 2048$ over one cardiac cycle.

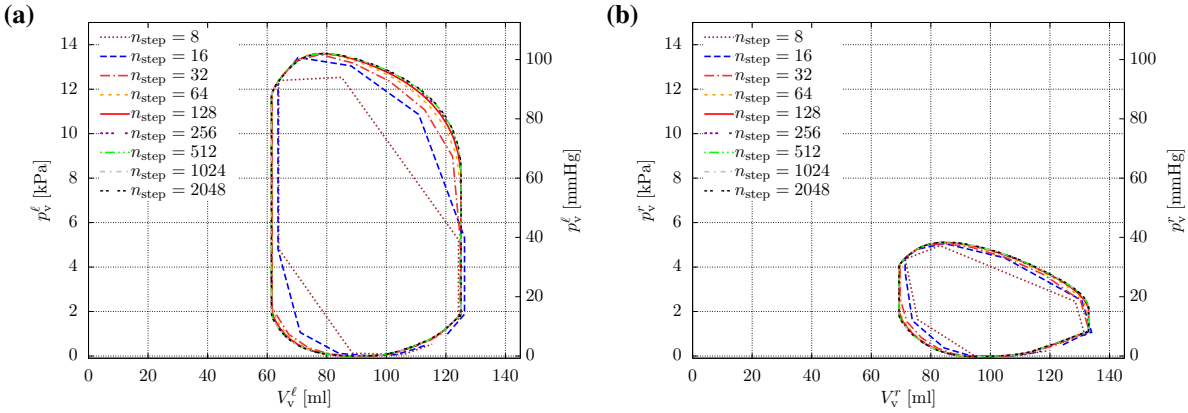

Figure A.9: Model *PrescrHeart$_{3Datrioventr_{tet4_2}}$* | *0Dsyspulcap*: Ventricular pressure-volume relationships for different numbers of time steps n_{step}. **(a)** Left ventricle. **(b)** Right ventricle.

Table A.4: Model *PrescrHeart$_{3Datrioventr_{tet4_2}}$* | *0Dsyspulcap*: Left, right, and total ventricular stroke work SW^{ℓ}, SW^{r}, and $\sum_{i=\ell,r}\mathrm{SW}^{i}$ for different numbers of time steps n_{step}

n_{step}	SW^{ℓ} [mJ]	SW^{i} [mJ]	$\sum_{i=\ell,r}\mathrm{SW}^{i}$ [mJ]
8	546.4	198.7	745.1
16	676.7	227.5	904.3
32	733.5	238.5	971.9
64	755.0	246.7	1001.7
128	764.0	249.9	1013.9
256	767.8	251.2	1019.0
512	769.6	251.9	1021.5
1024	770.5	252.2	1022.7
2048	770.9	252.3	1023.3

Pressure-volume relationships visually are hardly distinguishable for $n_{\mathrm{step}} > 100$, hence changes in stroke work become minor for a further reduction in time step size.

A.2 Small-strain calibration of material parameters for polyurethan

Uniaxial tensile tests have been performed on thin-walled samples of polyurethan in order to determine the mechanical properties of the augmentation pads of the ventricular assist device (VAD) prototype that has been introduced in chap. 5. A nonlinear hyperelastic stress-strain relationship should be derived such that reliable modeling and simulation of the interaction of VAD and heart can be undertaken. Testing was performed similar to a protocol described in the thesis of Maier [132].
The solid red curve in fig. A.10 shows the uniaxial first Piola-Kirchhoff stress P (engineering stress, measured force per measured undeformed cross-sectional area) plotted over the axial stretch λ. Testing results unveiled a strong softening behavior of the material for (engineering) strains $\geq 4\ \%$.

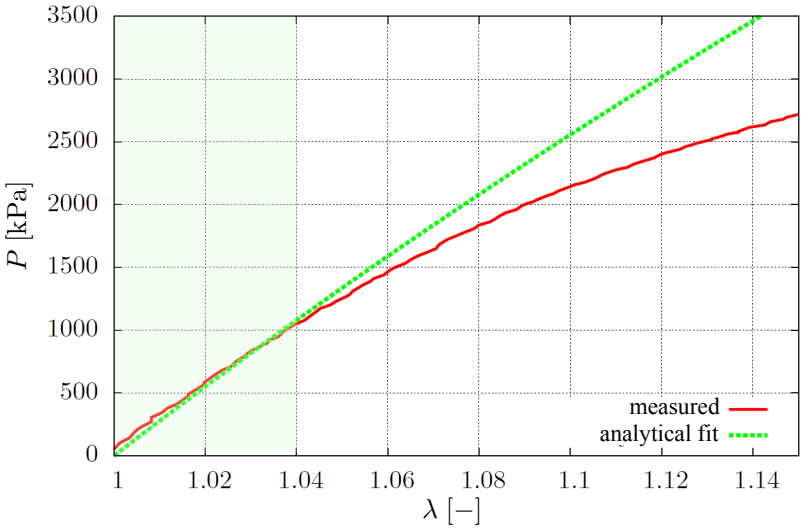

Figure A.10: Uniaxial tensile test on a polyurethan material sample: Uniaxial first Piola-Kirchhoff stress P over uniaxial stretch λ, small-strain analytical fit valid within $\lambda \in [1, 1.04]$.

Since under standard operating conditions the maximum straining of the polyurethan pads was assumed to be "small" (despite undergoing large deflections), softening behavior (which can be associated to effects of visco-plasticity) was neglected. Furthermore, since polyurethan behaves nearly incompressible, a simplifying perfectly incompressible analytical small-strain fit using a Neo-Hookean material has been performed.

Incompressibility requires the third invariant $(2.25)_3$ of the right Cauchy-Green deformation tensor, or equally the determinant J of the deformation gradient to obey

$$J = \lambda_1 \lambda_2 \lambda_3 \stackrel{!}{=} 1, \tag{A.1}$$

where $\lambda_1 \equiv \lambda$ is the stretch in the axial loading direction and $\lambda_2 = \lambda_3 = \frac{1}{\sqrt{\lambda}}$ are the lateral stretches. This means that Poisson's ratio is $\nu = 0.5$, hence the bulk modulus of the material is

$\kappa \to \infty$.

Plugging in the incompressibility constraint into the Neo-Hookean strain energy function yields

$$\Psi = \frac{\mu}{2}\left(\lambda_1^2 + \lambda_2^2 + \lambda_3^2 - 3\right) \overset{J=1}{=} \frac{\mu}{2}\left(\lambda^2 + \frac{2}{\lambda} - 3\right), \tag{A.2}$$

and the first Piola-Kirchhoff stress according to $(2.24)_1$ then reads

$$P = \frac{\partial \Psi}{\partial \lambda} = \mu\left(\lambda - \frac{1}{\lambda^2}\right). \tag{A.3}$$

The material stiffness, hence the uniaxial component of the elasticity tensor (2.34) is

$$\mathbb{C} = \frac{\partial P}{\partial \lambda} = \mu\left(1 + \frac{2}{\lambda^3}\right). \tag{A.4}$$

For the small-strain limit case ($\lambda \to 1$) the elasticity modulus becomes

$$\mathbb{C} = 3\mu, \tag{A.5}$$

which corresponds to the relation between Young's modulus and the shear modulus for incompressible small-strain elasticity [77].

An analytical fit of the shear modulus was performed, cf. the green dashed curve in fig. A.10, yielding a value of

$$\mu = 9346 \text{ kPa}. \tag{A.6}$$

In order to use this data in a displacement-based finite element formulation, the incompressibility constraint has to be relaxed, and a Poisson's ratio of $\nu = 0.49$ is assumed. The bulk modulus then can be calculated via

$$\kappa = \frac{\mu}{1 - 2\nu} = 467.3 \cdot 10^3 \text{ kPa}. \tag{A.7}$$

For the numerical simulation, the split formulation of the strain energy (2.28) with an Ogden-type volumetric part [88] is used together with the parameters (A.6) and (A.7).

Bibliography

[1] G. S. Adair, The hemoglobin system. VI. The oxygen dissociation curve of hemoglobin, *J Biol Chem* **63**, 529–545, 1925.

[2] D. Ambrosi and S. Pezzuto, Active stress vs. active strain in mechanobiology: Constitutive issues, *Journal of Elasticity* **107**, 199–212, 2012.

[3] D. Ambrosi, G. A. Ateshian, E. M. Arruda, S. C. Cowin, J. Dumais, A. Goriely, G. A. Holzapfel, J. D. Humphrey, R. Kemkemer, E. Kuhl, J. E. Olberding, L. A. Taber, and K. Garikipati, Perspectives on biological growth and remodeling, *J Mech Phys Solids* **59**, 863–883, 2011.

[4] D. Amsallem, J. Cortial, and C. Farhat, Towards real-time computational-fluid-dynamics-based aeroelastic computations using a database of reduced-order information, *AIAA Journal* **48**, 2029–2037, 2010.

[5] F. S. Angeli, M. Shapiro, N. Amabile, G. Orcino, C. S. Smith, T. Tacy, A. J. Boyle, K. Chatterjee, S. A. Glantz, W. Grossman, and Y. Yeghiazarians, Left ventricular remodeling after myocardial infarction: characterization of a swine model on β-blocker therapy, *Comp Med* **59**, 272–279, 2009.

[6] A. M. Anwar, M. L. Geleijnse, O. I. I. Soliman, A. Nemes, and F. J. ten Cate, Left atrial Frank-Starling law assessed by real-time, three-dimensional echocardiographic left atrial volume changes, *Heart* **93**, 1393–1397, 2007.

[7] E. E. Apostolakis and N. G. Baikoussis, Methods of estimation of mitral valve regurgitation for the cardiac surgeon, *J Cardiothorac Surg* **4**, 2009.

[8] L. Asner, M. Hadjicharalambous, R. Chabiniok, D. Peresutti, E. Sammut, J. Wong, G. Carr-White, P. Chowienczyk, J. Lee, A. King, N. Smith, R. Razavi, and D. Nordsletten, Estimation of passive and active properties in the human heart using 3D tagged MRI, *Biomechanics and Modeling in Mechanobiology* **15**, 1121–1139, 2016.

[9] M. Astorino, J. Hamers, S. Shadden, and J.-F. Gerbeau, A robust and efficient valve model based on resistive immersed surfaces, *International Journal for Numerical Methods in Biomedical Engineering* **28**, 937–959, 2012.

[10] R. Avazmohammadi, D. S. Li, T. Leahy, E. Shih, J. S. Soares, J. H. Gorman, R. C. Gorman, and M. S. Sacks, An integrated inverse model-experimental approach to determine soft tissue three-dimensional constitutive parameters: application to post-infarcted myocardium, *Biomechanics and Modeling in Mechanobiology* **17**, 31–53, 2018.

[11] P. S. Azevedo, B. F. Polegato, M. F. Minicucci, S. A. R. Paiva, and L. A. M. Zornoff, Cardiac remodeling: Concepts, clinical impact, pathophysiological mechanisms and pharmacologic treatment, *Arq Bras Cardiol* **106**, 62–69, 2016.

[12] J. Baan, E. T. van der Velde, H. G. de Bruin, G. J. Smeenk, J. Koops, A. D. van Dijk, D. Temmerman, J. Senden, and B. Buis, Continuous measurement of left ventricular volume in animals and humans by conductance catheter, *Circulation* **70**, 812–823, 1984.

[13] M. Balajewicz, D. Amsallem, and C. Farhat, Projection-based model reduction for contact problems, *International Journal for Numerical Methods in Engineering* **106**, 644–663, 2016.

[14] G. J. Barclay, D. F. Griffiths, and D. J. Higham, Theta method dynamics, *LMS Journal of Computation and Mathematics* **3**, 27–43, 2000.

[15] M. Bassilious, *Optimierungsverfahren zur Design- und Funktionsverbesserung eines neuartigen extravaskulären Herzunterstützungssystems*, Term paper, Mechanics & High Performance Computing Group, Technische Universität München, 2014.

[16] M. Bassilious, *Ein dimensionsreduziertes Modell des geschlossenen kardiovaskulären Systems gekoppelt an 0D- und 3D-Strukturmechanik-Modelle der Herzventrikel*, Master's thesis, Mechanics & High Performance Computing Group, Technische Universität München, 2015.

[17] J. J. Batzel, F. Kappel, and S. Timischl-Teschl, A cardiovascular-respiratory control system model including state delay with application to congestive heart failure in humans, *J Math Biol* **50**, 293–335, 2005.

[18] A. Ben-Tal, Simplified models for gas exchange in the human lungs, *Journal of Theoretical Biology* **238**, 474–495, 2005.

[19] E. J. Benjamin, M. J. Blaha, S. E. Chiuve, M. Cushman, S. R. Das, R. Deo, S. D. de Ferranti, J. Floyd, M. Fornage, C. Gillespie, C. R. Isasi, M. C. Jiménez, L. C. Jordan, S. E. Judd, D. Lackland, J. H. Lichtman, L. Lisabeth, S. Liu, C. T. Longenecker, R. H. Mackey, K. Matsushita, D. Mozaffarian, M. E. Mussolino, K. Nasir, R. W. Neumar, L. Palaniappan, D. K. Pandey, R. R. Thiagarajan, M. J. Reeves, M. Ritchey, C. J. Rodriguez, G. A. Roth, W. D. Rosamond, C. Sasson, A. Towfighi, C. W. Tsao, M. B. Turner, S. S. Virani, J. H. Voeks, J. Z. Willey, J. T. Wilkins, J. H. Wu, H. M. Alger, S. S. Wong, and P. Muntner, Heart disease and stroke statistics – 2017 update: A report from the American Heart Association, *Circulation* **135**, e146–e603, 2017.

[20] S. A. Berger, Flow in large blood vessels, *Fluid Dynamics in Biology* **141**, 479–518, 1993.

[21] J. Bestel, F. Clément, and M. Sorine, A biomechanical model of muscle contraction, In *Medical Image Computing and Computer-Assisted Intervention (MICCAI'01)*, Volume 2208, pages 1159–1161, Berlin, 2001, Springer-Verlag.

[22] E. J. Birks, S. Drakos, C. Selzman, R. Starling, C. Cunningham, M. Slaughter, D. M. Spevack, A. Salahuddin, P. Alturi, B. Lowes, S. Patel, D. Farrar, F. Kallel, and J. E. Rame, Remission from stage D heart failure (RESTAGE-HF): Early results from a prospective multi-center study of myocardial recovery, *J Heart Lung Transplant* **34**, S40–S41, 2015.

[23] P. J. Blanco and R. A. Feijóo, A 3D-1D-0D computational model for the entire cardiovascular system, *Mecanica Computacional* **XXIX**, 5887–5911, 2010.

[24] G. Blaudszun and D. R. Morel, Relevance of the volume-axis intercept, V0, compared with the slope of end-systolic pressure-volume relationship in response to large variations in inotropy and afterload in rats, *Exp Physiol* **96**, 1179–1195, 2011.

[25] J. P. Boehmer, R. C. Starling, L. T. Cooper, G. Torre-Amione, I. Wittstein, G. W. Dec, D. W. Markham, M. J. Zucker, J. Gorcsan, C. McTiernan, K. Kip, and D. M. McNamara, Left ventricular assist device support and myocardial recovery in recent onset cardiomyopathy, *J Card Fail* **18**, 755–761, 2012.

[26] L. Borcea, A nonlinear multigrid for imaging electrical conductivity and permittivity at low frequency, *Inverse Problems* **17**, 329–359, 2001.

[27] C. A. Bouman and K. D. Sauer, Nonlinear multigrid methods of optimization in Bayesian tomographic image reconstruction, In *Proc. SPIE Conf. Neural and Stochastic Methods in Image and Signal Processing*, Volume 1766, pages 296–306, 1992.

[28] A. Brandt, Multi-level adaptive solutions to boundary-value problems, *Math Comp* **31**, 333–390, 1977.

[29] W. L. Briggs, V. E. Henson, and S. F. McCormick, *A Multigrid Tutorial*, Society for Industrial and Applied Mathematics, 2 Edition, 2000.

[30] M. Broomé, E. Maksuti, A. Bjällmark, B. Frenckner, and B. Janerot-Sjöberg, Closed-loop real-time simulation model of hemodynamics and oxygen transport in the cardiovascular system, *Biomed Eng Online* **12**, 2013.

[31] C. G. Broyden, The convergence of a class of double-rank minimization algorithms. 1. General considerations, *IMA Journal of Applied Mathematics* **6**, 76–90, 1970.

[32] D. Burkhoff, S. Klotz, and D. M. Mancini, LVAD-induced reverse remodeling: basic and clinical implications for myocardial recovery, *J Card Fail* **12**, 227–239, 2006.

[33] M. Caruel, R. Chabiniok, P. Moireau, Y. Lecarpentier, and D. Chapelle, Dimensional reductions of a cardiac model for effective validation and calibration, *Biomechanics and Modeling in Mechanobiology* **13**, 897–914, 2014.

[34] R. Chabiniok, D. Chapelle, P.-F. Lesault, A. Rahmouni, and J.-F. Deux, Validation of a biomechanical heart model using animal data with acute myocardial infarction, In *CI2BM09 – MICCAI Workshop on Cardiovascular Interventional Imaging and Biophysical Modelling, London, UK*, 2009.

[35] R. Chabiniok, P. Moireau, P.-F. Lesault, A. Rahmouni, J.-F. Deux, and D. Chapelle, Estimation of tissue contractility from cardiac cine-MRI using a biomechanics heart model, *Biomech Model Mechanobiol* **11**, 609–630, 2012.

[36] R. Chabiniok, K. K. Bhatia, A. King, D. Rueckert, and N. Smith, Manifold learning for cardiac modeling and estimation framework, In *LNCS: Proc. of 5th international STACOM workshop*, Volume 8896, pages 284–294, Berlin, 2015, Springer-Verlag.

[37] D. Chapelle, P. L. Tallec, P. Moireau, and M. Sorine, An energy-preserving muscle tissue model: formulation and compatible discretizations, *International Journal for Multiscale Computational Engineering* **10**, 189–211, 2012.

[38] K. Chatterjee and J. E. Rame, Systolic heart failure: chronic and acute syndromes, *Crit Care Med* **36**, S44–S51, 2008.

[39] E. W. V. Chaves, *Notes on Continuum Mechanics*, Springer, 2013.

[40] A. Cheng, C. A. Williamitis, and M. S. Slaughter, Comparison of continuous-flow and pulsatile-flow left ventricular assist devices: is there an advantage to pulsatility?, *Ann Cardiothorac Surg* **3**, 573–581, 2014.

[41] T. G. Christiansen and C. Dræby, *Modelling the Respiratory System*, Master's thesis, Roskilde Universitetscenter, 1996.

[42] T. G. Christiansen and C. Dræby, Respiration, In J. T. Ottesen, M. S. Olufsen, and J. K. Larsen (eds.), *Applied Mathematical Models in Human Physiology*, 8, pages 197–247, SIAM: Philadelphia, 2004.

[43] J. Chung and G. M. Hulbert, A time integration algorithm for structural dynamics with improved numerical dissipation: The generalized-α method, *Journal of Applied Mechanics* **60**, 371–375, 1993.

[44] J. N. Cohn, R. Ferrari, and N. Sharpe, Cardiac remodeling – concepts and clinical implications: a consensus paper from an international forum on cardiac remodeling, *Journal of the American College of Cardiology* **35**, 569–582, 2000.

[45] J. A. Collins, A. Rudenski, J. Gibson, L. Howard, and R. O'Driscoll, Relating oxygen partial pressure, saturation and content: the haemoglobin-oxygen dissociation curve, *Breathe (Sheff)* **11**, 194–201, 2015.

[46] A. R. Conn, K. Scheinberg, and P. L. Toint, Recent progress in unconstrained nonlinear optimization without derivatives, *Mathematical Programming* **79**, 397–414, 1997.

[47] R. K. Dash and J. B. Bassingthwaighte, Erratum to: Blood HbO_2 and $HbCO_2$ dissociation curves at varied O_2, CO_2, pH, 2,3-DPG and temperature levels, *Annals of Biomedical Engineering* **38**, 1683–1701, 2010.

[48] T. A. Davis, Algorithm 832: UMFPACK V4.3 – An unsymmetric-pattern multifrontal method, *ACM Trans Math Softw* **30**, 196–199, 2004.

[49] E. A. de Souza Neto, D. Peric, and D. R. J. Owen, Design of simple low order finite elements for large strain analysis of nearly incompressible solids, *International Journal of Solids and Structures* **33**, 3277–3296, 1996.

[50] L. J. Dell'Italia, Q. C. Meng, E. Balcells, I. M. Straeter-Knowlen, G. H. Hankes, R. Dillon, R. E. Cartee, R. Orr, S. P. Bishop, S. Oparil, et al., Increased ACE and chymase-like activity in cardiac tissue of dogs with chronic mitral regurgitation, *Am J Physiol* **269**, H2065–H2073, 1995.

[51] A. Despopoulos, *Color Atlas of Physiology*, Thieme, Stuttgart New York, 5 Edition.

[52] S. Dimmeler, Cardiovascular disease review series, *EMBO Mol Med* **3**, 697, 2011.

[53] A. Ding, *Modellierung eines Formgebungsprozesses einer geflechtartigen Metallstruktur zur optimalen Gestaltung eines Trägers für ein extravaskuläres Herzunterstützungssystem*, Term paper, Mechanics & High Performance Computing Group, Technische Universität München, 2014.

[54] S. Dokos, B. H. Smaill, A. A. Young, and I. J. LeGrice, Shear properties of passive ventricular myocardium, *Am J Physiol Heart Circ Physiol* **283**, 2650–2659, 2002.

[55] S. G. Drakos and M. R. Mehra, Clinical myocardial recovery during long-term mechanical support in advanced heart failure: Insights into moving the field forward, *J Heart Lung Transplant* **35**, 413–420, 2016.

[56] L. M. Ellwein, S. R. Pope, A. Xie, J. J. Batzel, C. T. Kelley, and M. S. Olufsen, Patient-specific modeling of cardiovascular and respiratory dynamics during hypercapnia, *Math Biosci* **241**, 56–74, 2013.

[57] H. Elman, V. E. Howle, J. Shadid, R. Shuttleworth, and R. Tuminaro, A taxonomy and comparison of parallel block multi-level preconditioners for the incompressible Navier-Stokes equations, *Journal of Computational Physics* **227**, 1790–1808, 2008.

[58] J. S. Enciso, E. Adler, and B. H. Greenberg, Current status of the left ventricular assist device as a destination therapy, *US Cardiology Review* **10**, 2016.

[59] C. Farhat, P. Avery, T. Chapman, and J. Cortial, Dimensional reduction of nonlinear finite element dynamic models with finite rotations and energy-based mesh sampling and weighting for computational efficiency, *International Journal for Numerical Methods in Engineering* **98**, 625–662, 2014.

[60] R. Fletcher, A new approach to variable metric algorithms, *The Computer Journal* **13**, 317–322, 1970.

[61] O. Frank, Die Grundform des arteriellen Pulses, *Zeitschrift für Biologie* **37**, 483–526, 1899.

[62] T. Fritz, C. Wieners, G. Seemann, H. Steen, and O. Dössel, Simulation of the contraction of the ventricles in a human heart model including atria and pericardium: Finite element analysis of a frictionless contact problem, *Biomech Model Mechanobiol* **13**, 627–641, 2014.

[63] K. A. Gaar, A. E. Taylor, L. J. Owens, and A. C. Guyton, Pulmonary capillary pressure and filtration coefficient in the isolated perfused lung, *Am. J. Physiol.* **213**, 910–914, 1967.

[64] H. Gao, D. Carrick, C. Berry, B. E. Griffith, and X. Luo, Dynamic finite-strain modelling of the human left ventricle in health and disease using an immersed boundary-finite element method, *IMA Journal of Applied Mathematics* **79**, 978–1010, 2014.

[65] H. Gao, X. Ma, N. Qi, C. Berry, B. E. Griffith, and X. Luo, A finite strain nonlinear human mitral valve model with fluid-structure interaction, *Int J Numer Method Biomed Eng* **30**, 1597–1613, 2014.

[66] M. W. Gee and R. S. Tuminaro, Nonlinear algebraic multigrid for constrained solid mechanics using Trilinos, Technical Report SAND2006-2256, Sandia National Laboratories, 2006.

[67] M. W. Gee, C. T. Kelley, and R. B. Lehoucq, Pseudo-transient continuation for nonlinear transient elasticity, *International Journal for Numerical Methods in Engineering* **78**, 1209–1219, 2009.

[68] M. W. Gee, C. Förster, and W. A. Wall, A computational strategy for prestressing patient-specific biomechanical problems under finite deformation, *International Journal for Numerical Methods in Biomedical Engineering* **1**, 52–72, 2010.

[69] S. Gelman, Venous function and central venous pressure: A physiologic story, *Anesthesiology* **108**, 735–748, 2008.

[70] M. Genet, M. Rausch, L. C. Lee, S. Choy, X. Zhao, G. S. Kassab, S. Kozerke, J. M. Guccione, and E. Kuhl, Heterogeneous growth-induced prestrain in the heart, *J Biomech* **48**, 2080–2089, 2015.

[71] M. Genet, L. C. Lee, B. Baillargeon, J. M. Guccione, and E. Kuhl, Modeling pathologies of diastolic and systolic heart failure, *Ann Biomed Eng* **44**, 112–127, 2016.

[72] M. M. Givertz, Cardiology patient pages: ventricular assist devices: important information for patients and families, *Circulation* **124**, e305–e311, 2011.

[73] S. Göktepe, O. J. Abilez, K. K. Parker, and E. Kuhl, A multiscale model for eccentric and concentric cardiac growth through sarcomerogenesis, *J Theor Biol* **265**, 433–442, 2010.

[74] D. Goldfarb, A family of variable metric updates derived by variational means, *Mathematics of Computation* **24**, 23–26, 1970.

[75] B. A. Goldstein, L. Thomas, J. G. Zaroff, J. Nguyen, R. Menza, and K. K. Khush, Assessment of heart transplant waitlist time and pre- and post-transplant failure: A mixed methods approach, *Epidemiology* **27**, 469–476, 2016.

[76] B. E. Griffith, X. Luo, D. M. McQueen, and C. S. Peskin, Simulating the fluid dynamics of natural and prosthetic heart valves using the immersed boundary method, *International Journal of Applied Mechanics* **1**, 137–177, 2009.

[77] D. Gross, W. Hauger, and P. Wriggers, *Technische Mechanik 4 – Hydromechanik, Elemente der Höheren Mechanik, Numerische Methoden*, Springer, 2012.

[78] K. Gustafson and T. Abe, The third boundary condition – Was it Robin's?, *The Mathematical Intelligencer* **20**, 63–71, 1998.

[79] M. Hadjicharalambous, R. Chabiniok, L. Asner, E. Sammut, J. Wong, G. Carr-White, J. Lee, R. Razavi, N. Smith, and D. Nordsletten, Analysis of passive cardiac constitutive laws for parameter estimation using 3D tagged MRI, *Biomechanics and Modeling in Mechanobiology* **14**, 807–828, 2015.

[80] S. Hales, *Statical Essays: Haemastatics, Volume 2*, Printed for W. Innys and R. Manby, at the west-end of St. Paul's, and T. Woodward, at the Half-Moon between Temple-Gate, Fleetstreet, London, 1733.

[81] F. R. Heinzel, F. Hohendanner, G. Jin, S. Sedej, and F. Edelmann, Myocardial hypertrophy and its role in heart failure with preserved ejection fraction, *J Appl Physiol (1985)* **119**, 1233–1242, 2015.

[82] M. A. Heroux and J. M. Willenbring, Trilinos users guide, Technical Report SAND2003-2952, Sandia National Laboratories, 2003.

[83] U. Hetmaniuk, R. Tezaur, and C. Farhat, Review and assessment of interpolatory model order reduction methods for frequency response structural dynamics and acoustics problems, *International Journal for Numerical Methods in Engineering* **90**, 1636–1662, 2012.

[84] A. V. Hill, The possible effects of the aggregation of the molecules of haemoglobin on its dissociation curves, *J Physiol* **40**, iv–vii, 1910.

[85] G. Himpel, E. Kuhl, A. Menzel, and P. Steinmann, Computational modelling of isotropic multiplicative growth, *Computer Modeling in Engineering and Sciences* **8**, 119–134, 2005.

[86] M. Hirschvogel, M. Bassilious, L. Jagschies, S. M. Wildhirt, and M. W. Gee, A monolithic 3D-0D coupled closed-loop model of the heart and the vascular system: Experiment-based parameter estimation for patient-specific cardiac mechanics, *Int J Numer Method Biomed Eng* **33**, e2842, 2017.

[87] T. S. Hogan, Exercise-induced reduction in systemic vascular resistance: a covert killer and an unrecognised resuscitation challenge?, *Med Hypotheses* **73**, 479–484, 2009.

[88] G. A. Holzapfel, *Nonlinear Solid Mechanics – A Continuum Approach for Engineering*, Wiley Press Chichester, 2000.

[89] G. A. Holzapfel and R. W. Ogden, Constitutive modelling of passive myocardium: A structurally based framework for material characterization, *Phil Trans R Soc A* **367**, 3445–3475, 2009.

[90] L. Hopf, *Strain-based volumetric growth laws for computational modeling of ventricular disease and insufficiency progression*, Bachelor's thesis, Mechanics & High Performance Computing Group, Technische Universität München, 2017.

[91] J. M. Hörmann, *Multiscale electrophysiology simulation of human atria*, Master's thesis, Institute for Computational Mechanics, Technische Universität München, 2013.

[92] J. M. Hörmann, C. Bertoglio, A. Nagler, M. R. Pfaller, F. Bourier, M. Hadamitzky, I. Deisenhofer, and W. A. Wall, Multiphysics modeling of the atrial systole under standard ablation strategies, *Cardiovasc Eng Technol* **8**, 205–218, 2017.

[93] E. W. Hsu, A. L. Muzikant, S. A. Matulevicius, R. C. Penland, and C. S. Henriquez, Magnetic resonance myocardial fiber-orientation mapping with direct histological correlation, *Am J Physiol* **274**, H1627–H1634, 1998.

[94] J. D. Humphrey and K. R. Rajagopal, A constrained mixture model for growth and remodeling of soft tissues, *Math Models Methods Appl Sci* **12**, 407–430, 2002.

[95] T. Ino, L. N. Benson, H. Mikalian, R. M. Freedom, and R. D. Rowe, Determination of left ventricular volumes by Simpson's rule in infants and children with congenital heart disease, *Br Heart J* **61**, 182–185, 1989.

[96] B. M. Jackson, J. H. Gorman, S. L. Moainie, T. S. Guy, N. Narula, J. Narula, M. G. John-Sutton, L. H. Edmunds Jr., and R. C. Gorman, Extension of borderzone myocardium in postinfarction dilated cardiomyopathy, *J Am Coll Cardiol* **40**, 1168–1171, 2002.

[97] L. Jagschies, *Biventricular epicardial augmentation of the failing heart – Investigation of a novel technology in a drug induced porcine failing heart model and using computational modeling*, PhD thesis, Technische Universität München, 2018.

[98] L. Jagschies, M. Hirschvogel, J. Matallo, A. Maier, K. Mild, H. Brunner, R. Hinkel, M. W. Gee, P. Radermacher, S. M. Wildhirt, and S. Hafner, Individualized biventricular epicardial augmentation technology in a drug-induced porcine failing heart model, *ASAIO* **64**, 480–488, 2018.

[99] M. Jessup and S. Brozena, Heart failure, *N Engl J Med* **348**, 2007–2018, 2003.

[100] C. S. Jhun, K. Sun, and J. P. Cysyk, Continuous flow left ventricular pump support and its effect on regional left ventricular wall stress: finite element analysis study, *Med Biol Eng Comput* **52**, 1031–1040, 2014.

[101] D. A. Kass, R. Beyar, E. Lankford, M. Heard, W. L. Maughan, and K. Sagawa, Influence of contractile state on curvilinearity of in situ end-systolic pressure-volume relations, *Circulation* **79**, 167–178, 1989.

[102] J. Keener and J. Sneyd, *Mathematical Physiology II: Systems Physiology*, Volume 8, Springer, New York, 2 Edition.

[103] J. A. Kellum, Determinants of blood pH in health and disease, *Crit Care* **4**, 6–14, 2000.

[104] R. C. P. Kerckhoffs, M. L. Neal, Q. Gu, J. B. Bassingthwaighte, J. H. Omens, and A. D. McCulloch, Coupling of a 3D finite element model of cardiac ventricular mechanics to lumped systems models of the systemic and pulmonic circulation, *Annals of Biomedical Engineering* **35**, 1–18, 2007.

[105] R. C. P. Kerckhoffs, J. H. Omens, and A. D. McCulloch, A single strain-based growth law predicts concentric and eccentric cardiac growth during pressure and volume overload, *Mech Res Commun* **1**, 40–50, 2012.

[106] A. Kilic, S. Emani, C. B. Sai-Sudhakar, R. S. D. Higgins, and B. A. Whitson, Donor selection in heart transplantation, *J Thorac Dis* **6**, 1097–1104, 2014.

[107] O. Kintzel and Y. Başar, Fourth-order tensors – Tensor differentiation with applications to continuum mechanics. Part I: Classical tensor analysis, *ZAMM - Journal of Applied Mathematics and Mechanics / Zeitschrift für Angewandte Mathematik und Mechanik* **86**, 291–311, 2006.

[108] D. Klepach, L. C. Lee, J. F. Wenk, M. B. Ratcliffe, T. I. Zohdi, J. A. Navia, G. S. Kassab, E. Kuhl, and J. M. Guccione, Growth and remodeling of the left ventricle: A case study of myocardial infarction and surgical ventricular restoration, *Mech Res Commun* **1**, 134–141, 2012.

[109] G. Kovacs, A. Olschewski, A. Berghold, and H. Olschewski, Pulmonary vascular resistances during exercise in normal subjects: a systematic review, *Eur Respir J* **39**, 319–328, 2012.

[110] R. D. Krieg, Unconditional stability in numerical time integration methods, *J Appl Mech* **40**, 417–421, 1973.

[111] W. Kroon, T. Delhaas, T. Arts, and P. Bovendeerd, Computational modeling of volumetric soft tissue growth: application to the cardiac left ventricle, *Biomech Model Mechanobiol* **8**, 301–309, 2009.

[112] M. W. Krueger, V. Schmidt, C. Tobón, F. M. Weber, C. Lorenz, D. U. J. Keller, H. Barschdorf, M. Burdumy, P. Neher, G. Plank, K. Rhode, G. Seemann, D. Sanchez-Quintana, J. Saiz, R. Razavi, and O. Dössel, Modeling atrial fiber orientation in patient-specific geometries: A semi-automatic rule-based approach, In *Lecture Notes in Computer Science, Functional Imaging and Modeling of the Heart*, Volume 6666, pages 223–232, Berlin, 2011, Springer-Verlag.

[113] R. Kuperstein, I. Blechman, S. B. Zekry, R. Klempfner, D. Freimark, and M. Arad, Reverse remodeling and the mechanism of mitral regurgitation improvement in patients with dilated cardiomyopathy, *Cardiol J* **22**, 391–396, 2015.

[114] U. Küttler, C. Förster, and W. A. Wall, A solution for the incompressibility dilemma in partitioned fluid-structure interaction with pure Dirichlet fluid domains, *Computational Mechanics* **38**, 417–429, 2006.

[115] A. Laadhari, R. Ruiz-Baier, and A. Quarteroni, Fully Eulerian finite element approximation of a fluid-structure interaction problem in cardiac cells, *International Journal for Numerical Methods in Engineering* **96**, 712–738, 2013.

[116] J. Lang, *Projection-based Parametric Model Order Reduction for 3D-0D Coupled Cardiac Mechanics*, Master's thesis, Institute for Computational Mechanics, Technische Universität München, 2017.

[117] E. H. Lee, Elastic-plastic deformation at finite strains, *J Appl Mech* **36**, 1–6, 1969.

[118] L. C. Lee, L. Ge, Z. Zhang, M. Pease, S. D. Nikolic, R. Mishra, M. B. Ratcliffe, and J. M. Guccione, Patient-specific finite element modeling of the Cardiokinetix Parachute® device: effects on left ventricular wall stress and function, *Med Biol Eng Comput* **52**, 557–566, 2014.

[119] L. C. Lee, M. Genet, G. Acevedo-Bolton, K. Ordovas, J. M. Guccione, and E. Kuhl, A computational model that predicts reverse growth in response to mechanical unloading, *Biomech Model Mechanobiol* **14**, 217–229, 2015.

[120] L. C. Lee, G. S. Kassab, and J. M. Guccione, Mathematical modeling of cardiac growth and remodeling, *Wiley Interdiscip Rev Syst Biol Med* **8**, 211–226, 2016.

[121] L. C. Lee, J. Sundnes, M. Genet, J. F. Wenk, and S. T. Wall, An integrated electromechanical-growth heart model for simulating cardiac therapies, *Biomech Model Mechanobiol* **15**, 791–803, 2016.

[122] R.-M. Lee and N.-C. Tsai, Dynamic model of integrated cardiovascular and respiratory systems, *Mathematical Methods in the Applied Sciences* **36**, 2224–2236, 2013.

[123] I. J. LeGrice, B. H. Smaill, L. Z. Chai, S. G. Edgar, J. B. Gavin, and P. J. Hunter, Laminar structure of the heart: ventricular myocyte arrangement and connective tissue architecture in the dog, *Am J Physiol* **269**, H571–H582, 1995.

[124] K. Levenberg, A method for the solution of certain non-linear problems in least squares, *Quarterly Journal of Applied Mathematics* **II**, 164–168, 1944.

[125] Y. C. Liang, H. P. Lee, S. P. Lim, W. Z. Lin, K. H. Lee, and C. G. Wu, Proper orthogonal decomposition and its applications – Part I: Theory, *Journal of Sound and Vibration* **252**, 527–544, 2002.

[126] Y. C. Liang, W. Z. Lin, H. P. Lee, S. P. Lim, K. H. Lee, and H. Sun, Proper orthogonal decomposition and its applications – Part II: Model reduction for MEMS dynamical analysis, *Journal of Sound and Vibration* **256**, 515–532, 2002.

[127] I.-E. Lin and L. A. Taber, A model for stress-induced growth in the developing heart, *J Biomech Eng* **117**, 343–349, 1995.

[128] Y. Liu, H. Zhang, Y. Zheng, S. Zhang, and B. Chen, A nonlinear finite element model for the stress analysis of soft solids with a growing mass, *International Journal of Solids and Structures* **51**, 2964–2978, 2014.

[129] V. A. Lubarda and A. Hoger, On the mechanics of solids with a growing mass, *International Journal of Solids and Structures* **39**, 4627–4664, 2002.

[130] R. V. Luepker, Cardiovascular disease: Rise, fall, and future prospects, *Annual Review of Public Health* **32**, 1–3, 2011.

[131] J. Lumens, T. Delhaas, B. Kirn, and T. Arts, Three-wall segment (TriSeg) model describing mechanics and hemodynamics of ventricular interaction, *Annals of Biomedical Engineering* **37**, 2234–2255, 2009.

[132] A. Maier, *Computational Modeling of Rupture Risk in Abdominal Aortic Aneurysms*, PhD thesis, Technische Universität München, 2013.

[133] A. Manzoni, A. Quarteroni, and G. Rozza, Model reduction techniques for fast blood flow simulation in parametrized geometries, *International Journal for Numerical Methods in Biomedical Engineering* **28**, 604–625, 2012.

[134] S. Marchesseau, H. Delingette, M. Sermesant, R. C. Lozoya, and C. Tobon-Gomez, Personalization of a cardiac electromechanical model using reduced order Unscented Kalman Filtering from regional volumes, *Medical Image Analysis* **17**, 816–829, 2013.

[135] D. Marquardt, An algorithm for least-squares estimation of nonlinear parameters, *Journal of the Society for Industrial and Applied Mathematics* **11**, 431–441, 1963.

[136] P. I. McConnell, M. P. Anstadt, C. L. D. Rio, T. J. Preston, Y. Ueyama, and B. L. Youngblood, Cardiac function after acute support with direct mechanical ventricular actuation in chronic heart failure, *ASAIO J* **60**, 701–706, 2014.

[137] J. R. McGarvey, T. Shimaoka, S. Takebayashi, C. Aoki, N. Kondo, M. Takebe, G. A. Zsido, A. Jassar, J. H. Gorman, J. J. Pilla, and R. C. Gorman, Minimally invasive delivery of a novel direct epicardial assist device in a porcine heart failure model, *Innovations (Phila)* **9**, 16–21, 2014.

[138] A. Menzel and E. Kuhl, Frontiers in growth and remodeling, *Mech Res Commun* **1**, 1–14, 2012.

[139] L. Michaelis and M. L. Menten, Die Kinetik der Invertinwirkung, *Biochem. Z.*, 333–369, 1913.

[140] C. Mihl, W. R. M. Dassen, and H. Kuipers, Cardiac remodelling: concentric versus eccentric hypertrophy in strength and endurance athletes, *Neth Heart J* **16**, 129–133, 2008.

[141] W. P. Mistiaen, The changes in left ventricular structure-function relationship in aortic valve stenosis, *OA Anatomy* **2**, 1–5, 2014.

[142] M. R. Moreno, S. Biswas, L. D. Harrison, G. Pernelle, M. W. Miller, T. W. Fossum, D. A. Nelson, and J. C. Criscione, Development of a non-blood contacting cardiac assist and support device: An in vivo proof of concept study, *Journal of Medical Devices* **5**, 2011.

[143] D. Morley, K. Litwak, P. Ferber, P. Spence, R. Dowling, B. Meyns, B. Griffith, and D. Burkhoff, Hemodynamic effects of partial ventricular support in chronic heart failure: results of simulation validated with in vivo data, *J Thorac Cardiovasc Surg* **133**, 21–28, 2007.

[144] F. Munzinger, *A lumped-parameter closed-loop circulatory system model coupled to a 3D patient-specific 4-chamber heart model*, Bachelor's thesis, Mechanics & High Performance Computing Group, Technische Universität München, 2016.

[145] A. Nagler, C. Bertoglio, M. W. Gee, and W. A. Wall, Personalization of cardiac fiber orientations from image data using the Unscented Kalman Filter, In *Lecture Notes in Computer Science, Functional Imaging and Modeling of the Heart*, Volume 7945, pages 132–140, Berlin, 2013, Springer-Verlag.

[146] S. G. Nash, A multigrid approach to discretized optimization problems, *Optimization Meth. & Soft.* **14**, 99–116, 2000.

[147] M. L. Neal and J. B. Bassingthwaighte, Subject-specific model estimation of cardiac output and blood volume during hemorrhage, *Cardiovasc Eng* **7**, 97–120, 2007.

[148] J. A. Nelder and R. Mead, A simplex method for function minimization, *The Computer Journal* **7**, 308–313, 1965.

[149] N. M. Newmark, A method of computation for structural dynamics, *ASCE Journal of the Engineering Mechanics Devision* **85**, 67–94, 1959.

[150] Y. Nobuaki, T. Nishi, A. Amano, Y. Abe, and T. Matsuda, Simulation algorithm for the coupling of the left ventricular mechanical model with arbitrary circulation model, In *Conf Proc IEEE Eng Med Biol Soc*, Volume 7, pages 7632–7635, 2005.

[151] D. A. Nordsletten, M. McCormick, P. J. Kilner, P. Hunter, D. Kay, and N. P. Smith, Fluid-solid coupling for the investigation of diastolic and systolic human left ventricular function, *International Journal for Numerical Methods in Biomedical Engineering* **27**, 1017–1039, 2011.

[152] D. A. Nordsletten, S. A. Niederer, M. P. Nash, P. J. Hunter, and N. P. Smith, Coupling multi-physics models to cardiac mechanics, *Prog Biophys Mol Biol* **104**, 77–88, 2011.

[153] S. Oh, A. B. Milstein, C. A. Bouman, and K. J. Webb, Multigrid algorithms for optimization and inverse problems, In *Proc. SPIE Computational Imaging*, Volume 5016, pages 59–70, 2003.

[154] M. S. Olufsen and A. Nadim, On deriving lumped models for blood flow and pressure in the systemic arteries, *Mathematical Biosciences and Engineering* **1**, 61–80, 2004.

[155] J. H. Omens, Stress and strain as regulators of myocardial growth, *Prog Biophys Mol Biol* **69**, 559–572, 1998.

[156] J. H. Omens, E. K. Rodriguez, and A. D. McCulloch, Transmural changes in stress-free myocyte morphology during pressure overload hypertrophy in the rat, *J Mol Cell Cardiol* **28**, 1975–1983, 1996.

[157] M. C. Oz, J. H. Artrip, and D. Burkhoff, Direct cardiac compression devices, *The Journal of Heart and Lung Transplantation* **21**, 1049–1055, 2002.

[158] M. Papageorgiou, M. Leibold, and M. Buss, *Optimierung – Statische, dynamische, stochastische Verfahren für die Anwendung*, Springer Vieweg, 3rd Edition, 2012.

[159] M. E. Pfisterer, A. Battler, and B. L. Zaret, Range of normal values for left and right ventricular ejection fraction at rest and during exercise assessed by radionuclide angiocardiography, *European Heart Journal* **6**, 647–655, 1985.

[160] P. Ponikowski, A. A. Voors, S. D. Anker, H. Bueno, J. G. Cleland, A. J. Coats, V. Falk, J. R. González-Juanatey, V. P. Harjola, E. A. Jankowska, M. Jessup, C. Linde, P. Nihoyannopoulos, J. T. Parissis, B. Pieske, J. P. Riley, G. M. Rosano, L. M. Ruilope, F. Ruschitzka, F. H. Rutten, and P. van der Meer, 2016 ESC guidelines for the diagnosis and treatment of acute and chronic heart failure: The task force for the diagnosis and treatment of acute and chronic heart failure of the european society of cardiology (ESC). Developed with the special contribution of the heart failure association (HFA) of the ESC., *Eur J Heart Fail* **18**, 891–975, 2016.

[161] A. Popp, *Mortar Methods for Computational Contact Mechanics and General Interface Problems*, PhD thesis, Technische Universität München, 2012.

[162] A. Popp, M. W. Gee, and W. A. Wall, A finite deformation mortar contact formulation using a primal-dual active set strategy, *International Journal for Numerical Methods in Engineering* **79**, 1354–1391, 2009.

[163] A. Popp, M. Gitterle, M. W. Gee, and W. A. Wall, A dual mortar approach for 3D finite deformation contact with consistent linearization, *International Journal for Numerical Methods in Engineering* **83**, 1428–1465, 2010.

[164] P. Przybyła, W. Stankiewicz, M. Morzyński, M. Nowak, D. Gaweł, S. Stefaniak, and M. Jemielity, Reduced order model of a human left and right ventricle based on POD method, In A. Wittek, G. Joldes, P. Nielsen, B. Doyle, and K. Miller (eds.), *Computational Biomechanics for Medicine*.

[165] A. Quarteroni (ed.), *Modeling the Heart and the Circulatory System*, Springer Cham Heidelberg New York Dordrecht London, MS&A–Modeling, Simulation & Applications (Vol. 14) Edition, 2015.

[166] A. Quarteroni, G. Rozza, and A. Manzoni, Certified reduced basis approximation for parametrized partial differential equations and applications, *Journal of Mathematics in Industry* **1**, 1–49, 2011.

[167] M. K. Rausch, A. Dam, S. Göktepe, O. J. Abilez, and E. Kuhl, Computational modeling of growth: Systemic and pulmonary hypertension in the heart, *Biomech Model Mechanobiol* **10**, 799–811, 2011.

[168] J. T. Reeves, R. E. Moon, R. F. Grover, and B. M. Groves, Increased wedge pressure facilitates decreased lung vascular resistance during upright exercise, *Chest* **93**, 97S–99S, 1988.

[169] G. Reyes, J. Fernández-Yáñez, H. Rodríguez-Abella, J. Palomo, Á. Pinto, and J. Duarte, Ventricular assist devices as a bridge to transplantation, *Rev Esp Cardiol* **60**, 72–5, 2007.

[170] E. T. Roche, M. A. Horvath, I. Wamala, A. Alazmani, S. E. Song, W. Whyte, Z. Machaidze, C. J. Payne, J. C. Weaver, G. Fishbein, J. Kuebler, N. V. Vasilyev, D. J. Mooney, F. A. Pigula, and C. J. Walsh, Soft robotic sleeve supports heart function, *Sci Transl Med* **9**, 2017.

[171] J. R. Rodarte and K. Rehder, Dynamics of respiration, In *Handbook of Physiology, The Respiratory System, Mechanics of Breathing*, pages 131–144. American Physiological Society, 1986.

[172] E. K. Rodriguez, A. Hoger, and A. D. McCulloch, Stress-dependent finite growth in soft elastic tissues, *J Biomech* **27**, 455–467, 1994.

[173] V. L. Roger, Epidemiology of heart failure, *Circ Res* **113**, 646–659, 2013.

[174] C. Rosendorff, Beta-blocking agents with vasodilator activity, *J Hypertens Suppl* **11**, 37–40, 1993.

[175] M. A. Rossi and S. V. Carillo, Cardiac hypertrophy due to pressure and volume overload: distinctly different biological phenomena?, *Int J Cardiol* **31**, 133–141, 1991.

[176] Y. Saad and M. H. Schultz, GMRES: A generalized minimal residual algorithm for solving nonsymmetric linear systems, *SIAM J Sci and Stat Comput* **7**, 856–869, 1986.

[177] K. Sagawa, L. Maughan, H. Suga, and K. Sunagawa, *Cardiac Contraction and the Pressure-Volume Relationship*, Oxford University Press, New York, 1988.

[178] J. Sainte-Marie, D. Chapelle, R. Cimrman, and M. Sorine, Modeling and estimation of the cardiac electromechanical activity, *Computers & Structures* **84**, 1743–1759, 2006.

[179] A. Saito, M. Shiono, Y. Orime, S. Yagi, K. I. Nakata, K. Eda, T. Hattori, M. Funahashi, Y. Taniguchi, N. Negishi, and Y. Sezai, Effects of left ventricular assist device on cardiac function: experimental study of relationship between pump flow and left ventricular diastolic function, *Artif Organs* **25**, 728–732, 2001.

[180] P. Sajgalik, A. Grupper, B. S. Edwards, S. S. Kushwaha, J. M. Stulak, D. L. Joyce, L. D. Joyce, R. C. Daly, T. Kara, and J. A. Schirger, Current status of left ventricular assist device therapy, *Mayo Clin Proc* **91**, 927–940, 2016.

[181] C. Sansour, On the physical assumptions underlying the volumetric-isochoric split and the case of anisotropy, *European Journal of Mechanics A/Solids* **27**, 28–39, 2008.

[182] N. Saouti, N. Westerhof, P. E. Postmus, and A. Vonk-Noordegraaf, The arterial load in pulmonary hypertension, *Eur Respir Rev* **19**, 197–203, 2010.

[183] E. Schenone, A. Collin, and J.-F. Gerbeau, Numerical simulation of electrocardiograms for full cardiac cycles in healthy and pathological conditions, *Int J Numer Method Biomed Eng* **32**, 2016.

[184] C. H. Selzman and J. Oberlander, The price of progress: destination left ventricular assist device therapy for terminal heart failure, *N C Med J* **67**, 116–117, 2006.

[185] A. Sen, J. S. Larson, K. B. Kashani, S. L. Libricz, B. M. Patel, P. K. Guru, C. M. Alwardt, O. Pajaro, and J. C. Farmer, Mechanical circulatory assist devices: a primer for critical care and emergency physicians, *Crit Care* **20**, 2016.

[186] M. Sermesant, H. Delingette, and N. Ayache, An electromechanical model of the heart for image analysis and simulation, *IEEE Transactions on Medical Imaging* **25**, 612–625, 2006.

[187] D. F. Shanno, Conditioning of quasi-Newton methods for function minimization, *Mathematics of Computation* **24**, 647–656, 1970.

[188] M. Sharan, M. P. Singh, and A. Aminataei, A mathematical model for the computation of the oxygen dissociation curve in human blood, *Biosystems* **22**, 249–260, 1989.

[189] S. M. Shavik, S. T. Wall, J. Sundnes, D. Burkhoff, and L. C. Lee, Organ-level validation of a cross-bridge cycling descriptor in a left ventricular finite element model: effects of ventricular loading on myocardial strains, *Physiol Rep* **5**, e13392, 2017.

[190] O. Siggaard-Andersen and L. Garby, The Bohr effect and the Haldane effect, *Scandinavian Journal of Clinical and Laboratory Investigation* **31**, 1–8, 1973.

[191] O. Siggaard-Andersen, P. D. Wimberley, I. Göthgen, and M. Siggaard-Andersen, A mathematical model of the hemoglobin-oxygen dissociation curve of human blood and of the oxygen partial pressure as a function of temperature, *Clin Chem* **30**, 1646–1651, 1984.

[192] D. G. Silverman, A. B. Jotkowitz, M. Freemer, V. Gutter, T. Z. O'Connor, and I. M. Braverman, Peripheral assessment of phenylephrine-induced vasoconstriction by laser doppler flowmetry and its potential relevance to homeostatic mechanisms, *Circulation* **90**, 23–26, 1994.

[193] R. J. Solaro, Mechanisms of the Frank-Starling law of the heart: The beat goes on, *Biophys J* **93**, 4095–4096, 2007.

[194] B. G. Song, Y. K. On, E. S. Jeon, D. K. Kim, S. C. Lee, S. W. Park, J. K. Oh, K. I. Sung, and P. Park, Atrioventricular reverse remodeling after valve repair for chronic severe mitral regurgitation: 1-year follow-up, *Clin Cardiol* **33**, 630–637, 2010.

[195] N. Stergiopulos, B. E. Westerhof, and N. Westerhof, Total arterial intertance as the fourth element of the windkessel model, *Am. J. Physiol.* **276**, H81–H88, 1999.

[196] D. D. Streeter, H. M. Spotnitz, D. P. Patel, J. Ross, and E. H. Sonnenblick, Fiber orientation in the canine left ventricle during diastole and systole, *Circ Res* **24**, 339–347, 1969.

[197] A. M. Stuart and A. T. Peplow, The dynamics of the theta method, *SIAM Journal on Scientific and Statistical Computing* **12**, 1351–1372, 1991.

[198] S. P. Sutera and R. Skalak, The history of Poiseuille's law, *Annual Review of Fluid Mechanics* **25**, 1–20, 1993.

[199] L. A. Taber and S. Chabert, Theoretical and experimental study of growth and remodeling in the developing heart, *Biomech Model Mechanobiol* **1**, 29–43, 2002.

[200] T. Tanaka, M. Arakawa, T. Suzuki, M. Gotoh, H. Miyamoto, and S. Hirakawa, Compliance of human pulmonary 'venous' system estimated from pulmonary artery wedge pressure tracings–comparison with pulmonary arterial compliance, *Jpn Circ J.* **50**, 127–139, 1986.

[201] M. P. Thon, A. Hemmler, A. Glinzer, M. Mayr, M. Wildgruber, A. Zernecke-Madsen, and M. W. Gee, A multiphysics approach for modeling early atherosclerosis, *Biomech Model Mechanobiol* **17**, 617–644, 2018.

[202] P. R. Trenhago, L. G. Fernandes, L. O. Müller, P. J. Blanco, and R. A. Feijóo, An integrated mathematical model of the cardiovascular and respiratory systems, *Int J Numer Method Biomed Eng* **32**, 2016.

[203] M. Ursino and E. Magosso, Acute cardiovascular response to isocapnic hypoxia. I. A mathematical model, *Am J Physiol Heart Circ Physiol* **279**, 149–165, 2000.

[204] M. Ursino and E. Magosso, Acute cardiovascular response to isocapnic hypoxia. II. Model validation, *Am J Physiol Heart Circ Physiol* **279**, 166–175, 2000.

[205] E. T. van der Velde, D. Burkhoff, P. Steendijk, J. Karsdon, K. Sagawa, and J. Baan, Nonlinearity and load sensitivity of end-systolic pressure-volume relation of canine left ventricle in vivo, *Circulation* **83**, 315–327, 1991.

[206] A. I. Veress, G. M. Raymond, G. T. Gullberg, and J. B. Bassingthwaighte, Left ventricular finite element model bounded by a systemic circulation model, *Journal of Biomechanical Engineering* **135**, 54502, 2013.

[207] W. A. Wall and M. W. Gee, Baci: A parallel multiphysics simulation environment, Technical report, Institute for Computational Mechanics, Technische Universität München, 2008.

[208] W. A. Wall, M. A. Frenzel, and C. Cyron, Isogeometric structural shape optimization, *Computer Methods in Applied Mechanics and Engineering* **197**, 2976–2988, 2008.

[209] H. Watanabe, S. Sugiura, H. Kafuku, and T. Hisada, Multiphysics simulation of left ventricular filling dynamics using fluid-structure interaction finite element method, *Biophys J* **87**, 2074–2085, 2004.

[210] N. Westerhof, J.-W. Lankhaar, and B. E. Westerhof, The arterial windkessel, *Med Biol Eng Comput* **47**, H81–H88, 2009.

[211] M. J. Wilhelm, Long-term outcome following heart transplantation: current perspective, *J Thorac Dis* **7**, 549–551, 2015.

[212] S. R. Wilson, M. M. Givertz, G. C. Stewart, and G. H. Mudge Jr., Ventricular assist devices: the challenges of outpatient management, *J Am Coll Cardiol* **54**, 1647–1659, 2009.

[213] C. M. Witzenburg and J. W. Holmes, A comparison of phenomenologic growth laws for myocardial hypertrophy, *Journal of Elasticity* **129**, 257–281, 2017.

[214] R. Wohlfarth, *Beschreibung und Modellierung der pneumatischen Komponenten des AdjuCor-Herzunterstützungssystems für Herzinsuffizienzpatienten*, Diploma thesis, Mechanics & High Performance Computing Group, Technische Universität München, 2014.

[215] J. Wohlschlaeger, K. J. Schmitz, C. Schmid, K. W. Schmid, P. Keul, A. Takeda, S. Weis, B. Levkau, and H. A. Baba, Reverse remodeling following insertion of left ventricular assist devices (LVAD): a review of the morphological and molecular changes, *Cardiovasc Res* **68**, 376–386, 2005.

[216] J. Wong and E. Kuhl, Generating fibre orientation maps in human heart models using Poisson interpolation, *Computer Methods in Biomechanics and Biomedical Engineering* **17**, 1217–1226, 2014.

[217] P. Wriggers, *Computational Contact Mechanics*, Springer-Verlag Berlin Heidelberg, 2006.

[218] P. Wriggers, *Nonlinear Finite Element Methods*, Springer-Verlag Berlin Heidelberg, 2008.

[219] J. Xi, P. Lamata, S. Niederer, S. Land, W. Shi, X. Zhuang, S. Ourselin, S. G. Duckett, A. K. Shetty, C. A. Rinaldi, D. Rueckert, R. Razavi, and N. P. Smith, The estimation of patient-specific cardiac diastolic functions from clinical measurements, *Medical Image Analysis* **17**, 133–146, 2013.

[220] W. M. Yarbrough, R. Mukherjee, J. S. Ikonomidis, M. R. Zile, and F. G. Spinale, Myocardial remodeling with aortic stenosis and after aortic valve replacement: mechanisms and future prognostic implications, *J Thorac Cardiovasc Surg* **143**, 656–664, 2012.

[221] J. C. Ye, C. A. Bouman, K. J. Webb, and R. P. Millane, Nonlinear multigrid algorithms for Bayesian optical diffusion tomography, In *IEEE Transactions on Image Processing*, Volume 10, pages 909–922, 2001.

[222] A. A. Young, R. Orr, B. H. Smaill, and L. J. Dell'Italia, Three-dimensional changes in left and right ventricular geometry in chronic mitral regurgitation, *Am J Physiol* **271**, H2689–H2700, 1996.

[223] W. Zhang and S. J. Kovács, The diastatic pressure-volume relationship is not the same as the end-diastolic pressure-volume relationship, *Am J Physiol Heart Circ Physiol* **294**, H2750–H2760, 2008.

[224] O. C. Zienkiewicz and Y. M. Xie, A simple error estimator and adaptive time stepping procedure for dynamic analysis, *Earthquake Engineering & Structural Dynamics* **20**, 871–887, 1991.

[225] O. C. Zienkiewicz, R. L. Taylor, and J. Z. Zhu, *The finite element method: Its basis & fundamentals*, Elsevier Butterworth-Heinemann, 2005.

[226] O. C. Zienkiewicz, R. L. Taylor, and J. Z. Zhu, *The finite element method for solid and structural mechanics*, Elsevier Butterworth-Heinemann, 2005.

[227] M. R. Zile, M. Tomita, K. Nakano, I. Mirsky, B. Usher, J. Lindroth, and B. A. Carabello, Effects of left ventricular volume overload produced by mitral regurgitation on diastolic function, *Am J Physiol* **261**, H1471–H1480, 1991.